CWP-516

— Project Review —

Consortium Project on Seismic Inverse Methods for Complex Structures

Estes Park, Colorado, May 10-12, 2005

2004-05 CWP Students and Research Leaders:

Ramzy Al-Zayer
Jyoti Behura
Norm Bleistein
Maarten de Hoop
Pawan Dewangan
Huub Douma
Rodrigo Fuck
Matthew Haney
Ken Larner
Alison Malcolm
Kurang Mehta
Carlos Pacheco
Matt Reynolds
Roel Snieder
John Stockwell
Ilya Tsvankin
Ivan Vasconcelos
Greg Wimpey
Xiaoxia (Ellen) Xu
Yaping Zhu

Visiting Scholars:

Wouter Kimman

CWP Staff:

Michelle Szobody
Program Assistant

Barbara McLenon
Publications Specialist

Center for Wave Phenomena
Colorado School of Mines
Golden, Colorado 80401
(303) 273-3557 fax: (303) 273-3478
email: cwpcsm@dix.mines.edu http://www.cwp.mines.edu

Contents

Data Processing

Seismic Interferometry

Anisotropic Attenuation

Multicomponent Seismology

Migration & Imaging

Faults & Fractures

Acknowledgments

This project review book is prepared for the sponsors of the Consortium Project at the Center for Wave Phenomena. The Consortium Project provides substantial funding for the overall research and educational program at the Center. The Center has also received funds from the following agencies:

- National Science Foundation
- Chemical Sciences, Geosciences and Biosciences Division, Office of Basic Energy Sciences, U.S. Department of Energy
- United States Geological Service (USGS)
- U.S. Civilian Research and Development Foundation (CRDF)

We are extremely grateful for the support of these agencies during the past year and for that of the Consortium sponsors who are listed here.

Amerada Hess Corporation
Anadarko Petroleum Corp.
Aramco
BHP Billiton Petroleum
BP America Inc.
Bureau of Geophysical Prospecting
ChevronTexaco
ConocoPhillips
EnCana
ENI-AGIP E & P Division
ExxonMobil Upstream Research Co.
GMG/AXIS, Inc.
GX Technology
Kerr-McGee Oil & Gas Corporation
Landmark Graphics Corporation
Norsk Hydro A.S.
Petrobras America Inc.
Shell International E & P
Spinnaker Exploration Co.
Statoil Research Centre
Talisman Energy Inc.
Total E & P Services
Union Oil Company of CA
Veritas DGC, Ltd.
WesternGeco L.L.C.

In addition, the Seismic Un*x (SU) project is partially funded by the Society of Exploration Geophysicists.

CWP Policy on Proprietary Printed Material

New printed material that is produced at the Center for Wave Phenomena under Consortium support is presented to Sponsors before it is released to the general public. We delay general publication by 60 days so that Sponsors may benefit directly from their support of the Center for Wave Phenomena.

During this delay, Sponsors may make whatever use of the material inside their organization that they deem proper. However, we expect that all Sponsors will respect the rights of other Sponsors, and of CWP, by not publishing these results externally and independently, in advance of this 60-day delay (even with attribution to CWP). Please refer to your Consortium Membership Agreement under the paragraph entitled "Sponsor Confidentiality Obligation."

Those reports in this book that were produced primarily under consortium support and have not been previously distributed or submitted for publication, will be available for general distribution after July 10, 2005. If you have independently generated results that duplicate or overlap these, and plan to submit them for publication under your own name before this date, please notify us immediately, so that misunderstandings do not arise.

INTRODUCTION

This edition of the report on the Consortium Project at the Center for Wave Phenomena summarizes much of the research conducted within CWP, as it enters its twenty-second year. Note that the papers in this report and those presented orally during the Annual Project Review Meeting, May 10-12, 2005, only partially overlap. Also, in addition to these papers, several last-minute manuscripts will be distributed during the Meeting and mailed to representatives of sponsor companies.

Papers in This Report

The 19 papers in this volume are grouped into the following six categories: data processing, seismic interferometry, anisotropic attenuation, multicomponent seismology, migration and imaging, and faults and fractures. These categories show both similarities to and differences from those of the past few years, indicative of both the continuity and expanding breadth of our research program. Readily, several papers could have been placed in another category, and the categorization could have been different from that selected.

The two papers on *data processing* deal with the practically important issues of nonhyperbolic moveout correction and attenuation of internal multiples. One of the papers presents an efficient and accurate method for nonhyperbolic moveout correction in VTI (transversely isotropic with a vertical symmetry axis) media based on rational interpolation. For large offset-to-depth ratios and models with substantial anellipticity, this method performs better than algorithms based on the widely used nonhyperbolic moveout equation. The high accuracy of the new technique is corroborated using both synthetic and field (land) data. The second paper implements the theory for attenuating imaging artifacts caused by internal multiples that was presented at last year's Project Review Meeting. Synthetic examples illustrate how these artifacts can be estimated as part of the imaging process, resulting in an efficient algorithm.

The field of *seismic interferometry* is rapidly emerging both in industrial and academic research. Five papers on this topic present derivations of the main principles of seismic interferometry and discuss important implementation issues. One of the papers contains an overview of different approaches to interferometry. For simple models of the subsurface, the extraction of the Green's function from sources at the surface can be explained using the principle of stationary phase. The paper shows, however, that when only sources at the surface are used, the reconstructed Green's function contains artifacts caused by spurious multiples that cannot be removed with standard techniques of multiple suppression. The utility of seismic interferometry is not limited to monitoring the subsurface. One of the papers demonstrates how interferometry helps to extract the response of a building from incoherent signals. The building response can be seen either as a sum of normal modes, or as a superposition of propagating waves; this provides complementary information about the response. This application of seismic interferometry can also be helpful in processing of borehole data, and in monitoring mechanical structures such as platforms. Another paper treats the issue of bias in coda-wave interferometry. With the goal of increasing the number of usable independent time windows in interferometry by including windows further into the coda, this paper develops a correction to the cross-correlation coefficient that removes the bias induced by the presence of noise.

Another relatively new topic for CWP is *anisotropic attenuation.* The three papers in this section include both theoretical analysis of attenuation coefficients in anisotropic media and applications to physical-modeling data and to a wide-azimuth field data set. The theoretical contribution extends the Thomsen-style notation for attenuative VTI media to more complicated orthorhombic models. The new notation, based on the same principle as Tsvankin's velocity-anisotropy parameters for orthorhombic media, leads to simple linearized equations for the symmetry-plane attenuation coefficients of all three modes. The attenuation-anisotropy parameters also make it possible to simplify the P-wave attenuation coefficient outside the symmetry planes and develop an analytic framework for inverting P-wave attenuation measurements over fractured reservoirs. Another paper includes physical modeling and analysis of P-wave attenuation anisotropy in a transversely isotropic sample made of phenolic material. Whereas the symmetry axes of the angle-dependent attenuation coefficient and of the velocity function have close orientations, the magnitude of the attenuation anisotropy far exceeds that of the velocity anisotropy. The quality factor Q increases more than tenfold from the symmetry (slow) direction to the isotropy plane (fast direction). The paper devoted to field measurements of attenuation provides estimates of the azimuthally varying P-wave quality factor for the East Decatur field in Texas using the spectral-ratio method and a regularized linear inversion scheme. For the two superbins used in this work, the algorithm yields a substantial magnitude of the azimuthal variation of the effective Q-factor, with the principal directions close to the axes of the corresponding NMO ellipse.

The three papers on *multicomponent seismology* discuss several aspects of the moveout and amplitude analysis of mode-converted PS-waves. One paper demonstrates, with physical-modeling data, that the combination of long-spread reflection traveltimes of PP- and PS-waves can be inverted for the parameters of a horizontal TI layer with a tilted symmetry axis. Application of the modified "PP+PS=SS" method to the PP and PS traveltimes yields the time and offset asymmetry attributes of the PS-waves, which play the critical role in the parameter estimation. The inverted model is validated by reproducing the results of transmission experiments; in particular, the transmitted SV wavefield exhibits a prominent cusp (triplication) accurately predicted by the inversion results. Another paper employs the principle of the PP+PS=SS method to develop an exact technique for constructing the interval traveltime-offset function in a dipping anisotropic (target) layer beneath a horizontally layered overburden. This methodology can be used to estimate the interval parameters of tilted TI formations in such important exploration areas as the Canadian Foothills. Other potential applications are in the dip-moveout inversion for the key time-processing parameter η and in the exact computation of the interval long-spread (nonhyperbolic) moveout. The third paper presents an analytic and numerical study of the small-angle reflection coefficients of the split converted waves PS_1 and PS_2 for a horizontal interface separating two tilted TI halfspaces. While isotropic models predict no P-to-S conversion at normal incidence, the oblique orientation of the symmetry axis results in significant zero-offset PS-wave reflection coefficients reaching 0.1. The developed analytic solutions provide a foundation for AVO-inversion algorithms operating with multicomponent data acquired over tilted TI media.

The section on *migration and imaging* includes three papers. One of them discusses the use of curvelets in common-offset time migration and introduces a procedure based on translating, rotating and dilating curvelets, where the translation and rotation are governed by prestack map time-migration equations. The method is illustrated with synthetic data examples. Another paper is devoted to time-reverse imaging – a technique in which one propagates a pulse through a medium, records the signal and then back-propagates it through the same medium to refocus the energy at the original source location. When the back-propagation velocity is different from that for the forward propagation, the waves refocus at a different location. The shift in the location of the refocused pulse can help to estimate the velocity perturbation. The third paper describes a number of imaging tests with smoothed velocity fields for a simple synthetic 2D model of reflectors beneath salt. Past studies on the smoothing of velocities used for migration have applied smoothing operators to known synthetic velocity. The primary reason for smoothing, however, is that the initial velocities are never known with perfect accuracy. This work shows that, depending on the type of error in the initial velocity model, smoothing of the velocities can improve image, sometimes substantially.

The last section (*faults and fractures*) is devoted to seismic fracture characterization and fault imaging. Conventional fracture-characterization techniques operate with the idealized model of penny-shaped cracks and ignore the roughness (microcorrugation) of fracture surfaces. One of the papers analyzes the NMO ellipses, AVO gradients, and shear-wave polarizations for an effective triclinic medium formed by two microcorrugated, vertical, orthogonal fracture sets in isotropic background rock. Such a model adequately describes the orthogonal fracture networks at Weyburn field in Canada, where the axes of the P-wave NMO ellipse deviate from the fast shear-wave polarization direction. Two other papers are based on Matt Haney's recently defended thesis on imaging fault zones. One of them shows the connection between the fault-zone reflectivity and pore pressure distribution in the South Eugene Island reservoir in the Gulf of Mexico. The other paper describes the evidence of a fluid pulse that propagates along a fault zone with a speed of about 140 meters per year.

OVERVIEW OF DEVELOPMENTS IN CWP

Changes in the Past Year

In August 2004, Ken Larner retired from his position as C.H. Green Professor of Exploration Geophysics and Director of CWP. Ken has been named the University Emeritus Professor at CSM and continues his association with CWP and Geophysics Department as a research professor. We expect that Dave Hale, who has been selected as the new C.H. Green Chair, will work closely with CWP faculty and students.

The leadership of CWP remains strong, with both Ken and Norm Bleistein remaining part of the team, in their "retirement," to support the full-time academic faculty, Martijn de Hoop, Roel Snieder, and Ilya Tsvankin. It has been decided to make CWP Director a rotating position, with Ilya serving the first two- or three-year term. CWP faculty are determined to maintain the balance of applied and long-range projects that has made our consortium one of the premier academic research groups for the past 20 years.

Center Support

This past year the Consortium sponsorship has held steady at 25 companies, despite continuing constraints on corporate budgets for research. We thank the representatives of our sponsor companies for their continued support. A full list of sponsors over the term of the past year appears on the acknowledgment page at the beginning of this volume.

We have received about $500K of government support since last June from the Department of Energy, National Science Foundation, and U.S. Geological Survey. Our industrial and government support for research and education complement one another; each gains from, and strengthens, the other. As a net result, for the present annual fee of $45K, a company participates in a research project whose total funding level is about $1.5M, which gives a leverage factor of over 33.

In addition, the SEG Foundation has continued to provide support for Seismic Unix (SU) software package that is under John Stockwell's leadership.

Joint Projects with Shell International E&P and Total

Roel Snieder and CWP student, Kurang Mehta, are carrying out a collaborative project on seismic interferometry with Rodney Calvert and Jon Sheiman at Shell International E&P. This project aims at optimizing the use of seismic interferometry for imaging and monitoring reservoirs. Though this project is not strictly part of the CWP Consortium, Shell is willing for CWP to share the results with Consortium sponsors, within constraints of Shell's research agreement.

Henri Calandra, of Total in Houston, has been working with and providing support for the research that Alison Malcolm and Martijn de Hoop have been doing in data continuation and attenuation of internal multiples. Total, also, has agreed to make their research results and code available to CWP sponsors.

We encourage similar types of directly sponsored research with other companies that could lead to sharing of results with the Consortium.

Summer Workshop on Subsalt Imaging Problems

Martijn de Hoop and Ken Larner are co-organizers (with Henri Calandra, Chris Corcoran, Joe Higginbotham, Jacques Leveille, and Scott Morton) of the workshop on Subsalt Imaging Problems which will be held July 13-14, 2005, on the CSM campus. The workshop will focus on seismic imaging issues arising from exploration in the Gulf of Mexico. The expected attendance is 60-80 people, evenly divided between industry participants and non-industry researchers.

Interaction with Other Research Projects at CSM and Elsewhere

During this past year, as in previous years, faculty and students of CWP have interacted closely with other industry-funded research projects in the CSM Department of Geophysics. These include the Reservoir Characterization Project (RCP), led by Tom Davis; the Physical Acoustics Laboratory (PAL), led by John Scales and Kasper van Wijk; the Center for Rock Abuse, led by Mike Batzle; and the Gravity/Magnetics Project (GMP), led by Yaoguo Li. Some CWP students receive joint support from these consortia.

In addition, various CWP faculty have engaged in collaborative efforts with researchers elsewhere. Examples include:

- Norm Bleistein
  - Sam Gray, Veritas DGC, Calgary
  - Guanquan Zhang, Academica Sinica, Beijing
  - Yu Zhang and Xu Sheng, Veritas DGC, Houston
- Martijn de Hoop
  - Sergey Goldin, Siberian Branch of the Russian Academy of Sciences
  - Rob van der Hilst and Rod Hager, MIT
  - Chris Stolk, Ecole Polytechnique, Paris
  - Gunther Uhlmann, University of Washington
  - Bjørn Ursin, NTNU, Trondheim, Norway
- Roel Snieder
  - Rick Aster, New Mexico Institute of Technology
  - Rodney Calvert and Jon Sheiman, Shell International E&P
  - Joan Gomberg and Bill Stephenson, US Geological Survey
  - Eldad Haber, Emery University
  - Peter Malin, Duke University
  - Kees Wapenaar, Delft Institute of Technology
- Ilya Tsvankin
  - Andrey Bakulin and Vladimir Grechka, Shell International E&P
  - Pat Berge and Jim Berryman, Lawrence Livermore National Lab
  - Peter Leary, University of Edinburgh
  - Ivan Pšenčík, Czech Academy of Sciences

Travels and Activities of CWP People

Interactions and collaborations that have taken place away from Golden include the following.

- Norm Bleistein
  - Alexander von Humboldt Foundation Senior Fellowship, University of Karlsruhe, Germany (Spring 2005)
  - Visits to IFP and Ecole des Mines in Paris (April 2005)
  - Plans to present two papers at the Workshop on Seismic Waves in Laterally Heterogeneous Media, Czech Rebublic (June 2005)
  - Prepared a full-day short course and two papers for the upcoming BSGF meeting in Salvador de Bahia, Brazil
- Martijn de Hoop (was on sabbatical from CSM this academic year)
  - Several collaborative visits with researchers from Total in Houston and Pau, France, throughout the year
  - Numerous collaborative visits with faculty and students at MIT throughout the year

  - Meeting on Inverse Problems, Helsinki, Finland (May-June 2004)
  - 5th International Conference of AIMS, Pomona, CA (June 2004)
  - Collaborative research with Sergey Goldin on the CRDF grant, Novosibirsk, Russia (July-August 2004)
  - Invited Colloquium at Purdue University, Lafayette (November 2004 and February 2005)
  - IPAM Meeting, Los Angeles (November 2004)
  - Collaborative research with Gunther Uhlmann at the University of Washington (November–December 2004)
  - SRI Workshop near Frankfurt, Germany, as well as collaboration with Bjorn Ursin and others (February–March 2005)

- Ken Larner
  - Keynote Speaker for the annual Canadian SEG Doodletraining Week, Calgary (November 2004). While there, participated as a co-instructor with Brian Russell and Larry Lines for the two-day course "Seismic imaging and inversion"

- Roel Snieder
  - AGU Fall Meeting, San Francisco (December 2004)
  - Annual meeting of the Society of Mining Engineers, Salt Lake City (February 2005)
  - Trips to meetings of the Earth Science Council of the Department of Energy
  - Seismology chair of the organizing committee of the joint Spring Meeting of the American Geophysical Union and SEG

- Ilya Tsvankin
  - Two-day tutorial on seismic anisotropy at BHP Billiton in Houston (June 2004)
  - Technical Program Co-Chairman and member of the Organizing Committee, 11th International Workshop on Seismic Anisotropy, St. John's, Canada (July 2004)
  - Taught the SEG Short Course on Seismic Anisotropy (two days) at the SEG Annual Convention in Denver (October 2004), in Houston (November 2004), at Petrobras in Rio de Janeiro, Brazil (March 2005), and in New Orleans (April 2005)
  - Second edition of the monograph "Seismic signatures and analysis of reflection data in anisotropic media" published by Elsevier (March 2005)

Our students traveled considerably as well. Pawan Dewangan and Yaping Zhu presented papers at the 11th International Workshop on Seismic Anisotropy in St. John's, Canada (July 2004).
Matt Haney, Kurang Mehta, and Greg Wimpey visited Shell Bellaire Research Centre in Houston for extended periods of time to participate in joint research related to Roel Snieder's project with Shell.
Huub Douma and Alison Malcolm traveled to Houston several times doing on-site research with Total.
Huub also spent a month (September 2004) working with Dr. Emmanuel Candes in the Department of Applied and Computational Mathematics at Caltech.
Pawan Dewangan, Tamara Gipprich, Matt Haney, and Alison Malcolm attended the AGU Fall Meeting in San Francisco (December 2004).

Visitors to CWP

CWP has benefited again this year from visits by a number of scientists and friends from other universities and industry. We strongly encourage visits from our sponsor representatives, whether it be for a single day, or for an extended period. Below is a list of those who spent time at CWP.

- Speakers at the Summer School on Mathematical Geophysics and Uncertainty in Earth Models (June 2004): Andrew Curtis (Schulmberger), Chris Farmer (Schlumberger), Eldad Haber (Emery University), Brian Kennett (Australian National University), Alan Levander (Rice University), Stewart Levin (Landmark Graphics), Alberto Malinverno (Schlumberger), Doud Oldenburg (University of British Columbia), George Papanicolaou (Stanford University), Malcolm Sambridge (Australian National University), and Bill Symes (Rice University);

- Anton Duchkov, a graduate student from the Siberian Branch of the Russian Academy of Sciences, collaborating with Martijn (June-July 2004); will return to CWP in October 2005 for a two-year term as a post-doc;
- Maureen Long, a student at MIT, working with Martijn (one week);
- Andrey Bakulin, Shell E&P, collaborating with Ilya and Roel (one week);
- Vladimir Grechka, Shell E&P, collaborating with Ilya;
- Bjørn Ursin, NTNU, Trondheim, Norway, collaborating with Martijn;
- Art Weglein, University of Houston, CWP seminar and SEG Distinguished Lecture;
- Sergey Fomel, University of Texas at Austin, Heiland Lecture;
- Eldad Haber, Emery University, collaborating with Roel;
- Sverre Brandsberg-Dahl, BP, CWP seminar;
- John Etgen, BP, CWP seminar and Heiland Lecture;
- Ray Abma, BP, CWP seminar;
- Bill Dragoset, WesternGeco, CWP seminar and Heiland Lecture;
- Jerry Schuster, University of Utah, Heiland Lecture;
- Christof Stork, WesternGeco, CWP seminar
- Henry Calandra, Total, several visits to work with Martijn de Hoop and Alison Malcolm;
- Jim Gaiser, WesternGeco, Denver, numerous visits as participant in the A(nisotropy)-Team, and speaker.

Students and post-docs

Four CWP students completed their studies this past year: Pawan Dewangan, Alex Grêt, Matthew Haney, and Alison Malcolm.

Anton Duchkov will join CWP as a post-doctoral fellow beginning in October 2005. Anton completed his Ph.D. in December 2004 at the Institute of Geophysics, Novosibirsk, Russia; his advisor was Sergey Goldin.

During the 2004-2005 academic year, CWP provided full or partial funding for 15 students.

Papers at SEG

Once again, CWP students and faculty presented a large number of papers at the SEG Annual Meeting. During the 2004 Annual Meeting in Denver, they gave a total of 13 oral presentations, poster papers, and workshop contributions. A number of these presentations result from the CSM Department of Geophysics requirement that Ph.D. students must complete research papers in two different areas with two separate faculty members (recently, the requirement has been changed to one research paper and a thesis proposal). The two goals of this policy are to broaden students' educational background in geophysics and to encourage them to embark on research early in their Ph.D. studies.

For other meetings where CWP personnel presented papers, see page x, "Travels and Activities of CWP People."

Publications

We recently distributed to our sponsors theses written by CWP graduates: Alex Grêt, Pawan Dewangan and Matthew Haney. The thesis of Alison Malcolm, defended April 1, will be distributed during the upcoming summer. If you did not receive a copy of these publications and would like one, please contact Barbara McLenon at barbara@dix.mines.edu.

Since the 2004 Project Review meeting, 14 papers authored or co-authored by CWP faculty and students have been published and approximately 30 papers are currently under review or in press for publication in a variety of journals. In your meeting folder, you can find a list of recent reports in the CWP list of "Available Papers." The complete list of CWP papers is on our web site at http://www.cwp.mines.edu/bookshelf.html.

On the Web

Samizdat Press, http://samizdat.mines.edu/, the Internet archive that distributes free books and sets of lecture notes, has grown to a listing of 26 titles. The newest additions are "Course of Differential Geometry" and "Multidimensional Geometry," both by Ruslan Sharipov, and "Solving the Sealevel Equation" by Giorgio Spada. Samizdat Press is a creation of John Scales of the CSM Department of Geophysics, and Martin Smith of New England Research.

Computing Environment

The CWP research computing environment includes a 32 processor Linux cluster system. Each of the 16 nodes consists of a dual processor Pentium Xeon 2.4 GHZ PC system with 2 GB of RAM available per processor, and about 160 GB total of hard-disk storage for each node. We have had this unit for nearly two years, and plan to upgrade it with eight more nodes.

Each student and faculty member has a desktop system of 2 Ghz or faster running Linux, with at least 40 GB of storage space per desktop. In addition to these desktop systems, we have purchased a 3.0 Ghz server with .4 Terabytes of disk space. We plan continued expansion of storage and processing capacity.

For data transport, our preferred medium consists of USB hard drives, formatted with the ext3 filesystem. Students make regular use of the following commercial packages: Mathematica, Matlab, NAG95 (Fortran 90/95 compiler), and the Intel compiler (free version).

Software Releases

CWP releases both open-source software as well as software that is proprietary to the Consortium. Most proprietary codes depend heavily on the free software environment, so both of these are relevant to the Consortium. The proprietary period is three years. Some of the codes developed at CWP are part of government-funded research projects, and are required to be released as open source. However, we have descretion as to the classification of other codes. Software developed using in-house resources of sponsor companies generally is not available to us for release.

Tentative plans for future *proprietary* software releases include Alison Malcolm's multiple-suppression research code MULMIG, as well as software related to Huub Douma and Martijn de Hoop's curvelet migration research.

The primary vehicle of *open* software distribution is the CWP/SU:Seismic Un*x (SU) package. This package has been installed at more than 3300 sites in 62 countries (where a country is defined by its independent country code), and has an active worldwide user group.

Release 38 of SU was issued on December 23, 2004, and contained many updates and new software, including the anisotropic migration velocity analysis codes of Debashish Sarkar. Since the beginning of 2005 we have issued 5 beta releases. Future plans include a modification of the SU data format to permit the reading and writing of data in the new SEG Y Rev 1 format.

Annual Project Review Meeting

This year's Annual Project Review Meeting, May 10-12, 2005, will be held for the second time at the Stanley Hotel, Estes Park, Colorado. The historic hotel proved a convenient and hospitable venue for CWP's 20th Anniversary Meeting last year. During the three-day meeting, students and faculty will present more than 20 papers. A tradition of recent years is that, prior to the the Meeting, we hold a tutorial for sponsors on a topic of particular interest within CWP. This year, Roel Snieder will give a two-hour tutorial entitled "Interferometric imaging: Who needs a seismic source?"

WELCOME

With great pleasure, we welcome representatives of our sponsor companies to the 21st Annual Project Review Meeting, and look forward to the opportunity to exchange with you ideas and thoughts about this past year's projects.

Ilya Tsvankin, Director
Center for Wave Phenomena
May 2005

Nonhyperbolic moveout analysis in VTI media using rational interpolation

Huub Douma[1], Alexander Calvert[2] and Edward Jenner[2]
[1] *Center for Wave Phenomena, Colorado School of Mines, Golden, CO 80401-1887, USA*
[2] *GX Technology, 225 East 16th Avenue, Suite 1200, Denver, CO 80203, USA*

ABSTRACT

We present a rational interpolation approach to nonhyperbolic moveout correction in the $t-x$ domain, for qP-waves in homogeneous transversely isotropic media with a vertical symmetry axis. This method has no additional computational overhead compared to using expressions explicit in the relevant parameters, i.e., the anellipticity parameter η and the (zero-dip) normal moveout velocity V_{NMO}. The lack of such additional overhead can be attributed to the observation that, for a fixed value of η and a fixed zero-offset two-way traveltime t_0, the moveout curve for different values of V_{NMO} can be calculated by simple stretching and squeezing of the offset axis, where the amount of stretch or squeeze depends on the change in V_{NMO}. This observation is based on the generally accepted assumptions that the traveltimes of qP-waves in transversely isotropic media, depend mainly on η and V_{NMO}, and that the shear-wave velocity along the symmetry axis has a negligible influence on these traveltimes. The accuracy obtained with this method is as good as that of these approximations. The method can be tuned to be accurate to any offset range of interest, by increasing the order of the interpolation, making it accurate for arbitrary offsets.

We test the method using both synthetic and field data, and compare it with the nonhyperbolic moveout equation of Alkhalifah and Tsvankin (1995). Both data types confirm that for $\eta \gtrsim 0.1$ our method significantly outperforms the nonhyperbolic moveout equation in terms of combined unbiased parameter estimation with accurate moveout correction. A comparison with the shifted hyperbola equation of Fomel (2004) establishes almost identical accuracy of the rational interpolation method and his equation. Under the above-mentioned approximations, we show that the correction factor for the Alkhalifah-Tsvankin equation introduced by Grechka and Tsvankin (1998), is independent of V_{NMO}, and we present a method to estimate its optimal value in practice. This factor can be used to maximize the performance of the Alkhalifah-Tsvankin approximation.

Key words: Moveout analysis, nonhyperbolic, anisotropy, anellipticity, VTI, rational interpolation

Introduction

Over the past two decades, the importance of anisotropy and its influence on seismic data processing have become increasingly appreciated. Since 75% of the clastic infill of sedimentary basins consists of shale formations (Tsvankin, 2001, p.11), and since the transversely isotropic (TI) model adequately describes the intrinsic anisotropy of shales (Sayers, 1994), wave propagation in TI media has attracted much attention. Because the dispersion relations govern the propagation velocities of the different wave modes (and hence the traveltimes used in seismic data processing), and because these relations are nonlinear in the elastic coefficients, many authors have worked on approximations of the dispersion relations in TI media (Dellinger *et al.*, 1993; Tsvankin & Thomsen, 1994; Alkhalifah, 1998; Schoenberg & de Hoop, 2000; Zhang & Uren, 2001; Stovas & Ursin, 2004; Fomel, 2004), with varying levels of accuracy; Fomel's (2004) shifted hyperbola approach seemingly the most accurate of all. Fowler (2003) gives a comparative review of some of these approximations with an emphasis on TI media with a vertical symmetry axis (VTI media).

Here, we propose a rational interpolation scheme for traveltimes of qP-waves in homogeneous VTI media that requires no additional computational overhead compared to methods using approximations explicit in the physical relevant parameters, such as those just mentioned. The choice to use a rational interpolation was motivated by the observation that several of the aforementioned approximations achieve high accuracy through the use of rational approximations [e.g., Schoenberg and de Hoop (2000) and Stovas and Ursin (2004)], and by the form of the nonhyperbolic moveout equation of Tsvankin and Thomsen (1994), which resembles a rational approximation. We refrain from an attempt to derive yet another approximation to traveltimes of qP-waves in such media that is explicit in the relevant parameters. Instead, we simply make use of the facts that the shear-wave velocity along the (vertical) symmetry axis, V_{S0} has negligible influence on the traveltimes of qP-waves in TI media (Tsvankin & Thomsen, 1994; Tsvankin, 1996; Alkhalifah, 1998; Alkhalifah, 2000), and that these traveltimes depend mainly on the anellipticity parameter η and the (zero-dip) normal-moveout velocity V_{NMO} (Alkhalifah & Tsvankin, 1995). That is, the influence of Thomsen parameter δ is only small. We show that these two assumptions cause the influence of V_{NMO} on the nonhyperbolic moveout of qP-waves in a horizontal homogeneous VTI layer, for fixed anellipticity parameter η and two-way zero-offset traveltime t_0, to be a simple horizontal stretch (or squeeze), i.e., along the offset axis, of the moveout curve for some reference value of V_{NMO}, where the amount of stretch (or squeeze) depends on the change in V_{NMO}. This simple observation allows the traveltimes needed for the rational interpolation to be calculated from a small number of precomputed traveltimes stored in a table. Within the limits of the accuracy of the above two approximations, our rational interpolation approach can be tuned to almost arbitrary accuracy at any offset-to-depth ratio (ODR) (or group angle) of interest. A comparison of our approach with the shifted hyperbola approach of Fomel (2004) shows that our method has accuracy almost identical to that of Fomel.

For velocity analysis in VTI media using qP-waves, the nonhyperbolic moveout equation for a single horizontal VTI layer, derived by Tsvankin and Thomsen (1994), is the current standard in seismic data processing. Alkhalifah and Tsvankin (1995) have rewritten this equation in terms of V_{NMO} and η. Even though this approximation is exact at zero offset and infinite offset, Grechka and Tsvankin (1998) mention that at intermediate offsets "this approximation can be somewhat improved by empirically changing the denominator of the nonhyperbolic term." This limited accuracy at intermediate offsets was also noted by other authors [e.g., Zhang and Uren (2001), van der Baan and Kendall (2002), and Stovas and Ursin (2004)]. In an attempt to overcome this limitation in accuracy, Grechka and Tsvankin (1998) introduce a correction factor C in the denominator of the nonhyperbolic term. We show that within the two approximations mentioned above, this correction factor depends only on the ODR and η, and we present a figure that shows C as a function of both ODR and η, for ODR up to four and $0 \leq \eta \leq 1$. We explain how this figure can be used in practice to determine the value of C, that minimizes the bias in the estimated value of η when the nonhyperbolic moveout equation of Alkhalifah and Tsvankin (1995) is used. Through a study of the accuracy of this equation, we establish its limits of applicability.

The motivation for higher accuracy at larger ODR stems from the observation that a larger ODR provides better resolution for the anellipticity parameter η (Alkhalifah, 1997; Grechka & Tsvankin, 1998; Wookey *et al.*, 2002). Hence, improved accuracy at larger ODR can help reduce the uncertainty in inversion for η [within the limits of the trade-off between η and V_{NMO}, as observed by Grechka and Tsvankin (1998)] when large ODR is available in the data. We show that our rational interpolation approach provides significantly more accurate traveltimes than does the currently standard nonhyperbolic moveout equation, especially for larger ODR (larger than two), and for arbitrary levels of anellipticity, with no additional computational overhead. The lack of such overhead stems from the influence of V_{NMO} being limited to a stretch (or squeeze) along the offset axis of the moveout curve for some reference value of V_{NMO}, and for fixed η and t_0.

The outline of this paper is as follows. First, we study the accuracy of the nonhyperbolic moveout equation from Tsvankin and Thomsen (1994) and analyze the influence of the introduction of the correction factor of Grechka and Tsvankin (1998) on this accuracy. Subsequently, we introduce the rational interpolation approach to nonhyperbolic moveout for qP waves in VTI media, and explain the stretch-squeeze influence of V_{NMO} on the moveout curve of qP reflections in a single horizontal homogeneous VTI layer. Subsequently we explain the influence of this observation on the correction factor C in the nonhyperbolic moveout equation. Synthetic tests, for both a single homogeneous horizontal VTI layer and a horizontally layered VTI medium, verify the improved accuracy of the method when compared to the nonhyperbolic moveout equation. Finally these findings are confirmed by an application of the method to field data. Also, a comparison between our

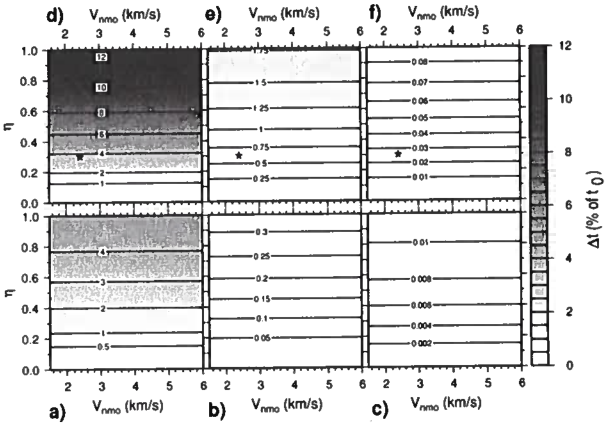

Figure 1. Comparison of the accuracy of the nonhyperbolic moveout equation without the correction factor, i.e., $C = 1$ (a), with the optimal correction factor C (b), and of the [2/2] rational interpolation (c), for a range of models (combinations of η and V_{NMO}) that spans most models of practical interest. Contours are drawn for the maximum absolute percentage error in traveltime (compared to ray-traced traveltimes where ray tracing was done with $V_{S0} = 0$ km/s and $\delta = 0$) for a single horizontal VTI layer, over a range of ODR values up to two. The contoured values are shown in percentage of t_0. Subfigures (d) through (f) show the same contours as in subfigures (a) through (c), except for a range of ODR values up to four. The stars in subfigures (d) through (f) indicate the model parameters used for the residual moveout plots in Figure 4.

method and the shifted hyperbola method of Fomel (2004) establishes the almost identical accuracy of the two methods.

Accuracy of the nonhyperbolic moveout equation

The nonhyperbolic moveout equation of Tsvankin and Thomsen (1994), rewritten in terms of the anellipticity parameter η by Alkhalifah and Tsvankin (1995), is given by

$$t^2(x) = t_0^2 + \frac{x^2}{V_{NMO}^2} - \frac{2\eta x^4}{V_{NMO}^2\left[t_0^2 V_{NMO}^2 + (1+2\eta)\, x^2\right]}, \quad (1)$$

where t_0 is the two-way traveltime at zero offset, x is offset, and V_{NMO} is the (zero-dip) NMO velocity. Note how the moveout reduces to hyperbolic moveout for elliptical anisotropy ($\eta = 0$), as pointed out by Helbig (1983). This equation is exact at both zero offset and infinite offset. In an attempt to increase the accuracy at intermediate offsets, Grechka and Tsvankin (1998) introduce a correction factor. Noting that for a single horizontal VTI layer the absolute error in η is at least twice as large as the relative error in the horizontal velocity $V_{hor} = V_{NMO}\sqrt{1+2\eta}$, they rewrite equation (1) in terms of V_{NMO} and V_{hor},

$$t^2(x) = t_0^2 + \frac{x^2}{V_{NMO}^2} - \frac{\left(V_{hor}^2 - V_{NMO}^2\right) x^4}{V_{NMO}^2\left(t_0^2 V_{NMO}^4 + C V_{hor}^2 x^2\right)}, \quad (2)$$

where C is the above-mentioned correction factor.

Figure 1a show contours of the maximum absolute traveltime difference (in percentage of t_0) between ray-traced traveltimes for a single horizontal VTI layer and the nonhyperbolic moveout equation without the correction factor, for virtually all combinations of η and V_{NMO} of practical interest. The maximum ODR is two, and $t_0 = 1$ s for all models considered. The ray-traced traveltimes were determined with $V_{S0} = 0$ km/s and $\delta = 0$. The differences in the traveltimes are of the order of a percent, which in this case amounts to 10 ms. For a dominant frequency of 50 Hz in surface seismic data, this amounts to a traveltime error of about half a dominant period. Such errors are not negligible, can lead to substantial reduction in stacking power, and thus cause errors in the estimation of η and V_{NMO} in velocity analysis. Note that here we use the true values of η and V_{NMO} for the moveout analysis rather than the best-fit values, since we want to analyze the accuracy of the nonhyperbolic moveout equation for a known model. It is known that the traveltime differences shown in Figure 1a can be reduced by using the best-fit values of η and V_{NMO}, rather than the true ones.

Grechka and Tsvankin (1998) state that, for a single horizontal VTI layer, introducing the coefficient $C = 1.2$ minimizes deviations from the exact traveltimes for the range of offset-to-depth ratio (ODR) $1.5 - 2.5$. They also mention that the correction factor can be used as an optimization parameter by comparison of traveltimes obtained using equation (2) and ray-tracing. Figure 1b is as Figure 1a, except now the optimized correction factor was determined for each combination of η and V_{NMO} shown and then used in equation (2). Note that indeed the introduction of the correction factor reduced the maximum errors in the traveltimes substantially, resulting in errors of the order of a tenth of a percent. A straightforward application of the $C = 1.2$ for all models (not shown here), did reduce the errors somewhat, but the errors were still of the order of a percent. This indicates that a straightforward application of $C = 1.2$ is in general not recommended, except for models where $C = 1.2$ may happen to be the optimal correction factor. It is worth mentioning that in practice the optimal value of C can be determined only approximately because the true values of η and V_{NMO} are unknown. Therefore, Figure 1b represents the best accuracy that can be obtained using the nonhyperbolic moveout equation with the correction factor.

As pointed out by Alkhalifah (1997), a larger maximum ODR (say larger than 1.5) provides increased stability and resolution for the inversion for η using nonhyperbolic moveout. With current acquisition systems, such values of ODR are feasible, especially for shallow targets. Moreover, the need for cost-effective acquisition systems could, with time, increase the maximum ODR in acquisition systems. Also, in near-surface (or shallow) geophysical application, large ODR is common. Figures 1d and 1e are as Figures 1a and 1b, respectively, except that here the maximum ODR is four. The introduction of the optimal correction factor again reduces the errors in traveltime significantly, but the errors are of the order of a percent; that is, they are sizable.

The dependence of nonhyperbolic moveout for a single VTI layer on η and V_{NMO}

From simple geometric considerations, it follows that for a homogeneous horizontal VTI layer, the traveltime is given by

$$t = \frac{V_{P0}\, t_0}{v \cos\psi} , \tag{3}$$

where V_{P0} is the P-wave traveltime along the vertical symmetry axis, ψ is the group angle, and v is the group velocity for propagation in direction ψ. The offset x associated with this traveltime is given by

$$x = V_{P0}\, t_0 \tan\psi . \tag{4}$$

In a TI medium, the phase velocity is given by (Tsvankin, 2001, p.22)

$$\begin{aligned} V(\theta) &= V_{P0}\left\{1 + \epsilon\sin^2\theta - \frac{f}{2}\left(1 - \ldots\right.\right. \\ &\left.\left.\sqrt{\left(1 + \frac{2\epsilon\sin^2\theta}{f}\right)^2 - \frac{2(\epsilon-\delta)\sin^2 2\theta}{f}}\right)\right\}^{1/2} \end{aligned} \tag{5}$$

where θ is the phase angle, ϵ and δ are the Thomsen parameters, and $f \equiv 1 - V_{S0}^2/V_{P0}^2$, with V_{S0} the S-wave phase velocity along the symmetry axis. For such a medium, the group angle is related to the phase angle through (Tsvankin, 2001, p.29)

$$\tan\psi = \frac{\tan\theta + \dfrac{1}{V(\theta)}\dfrac{dV}{d\theta}}{1 - \dfrac{\tan\theta}{V(\theta)}\dfrac{dV}{d\theta}} , \tag{6}$$

while the group velocity v is given by

$$v = V(\theta)\sqrt{1 + \left(\frac{1}{V(\theta)}\frac{dV}{d\theta}\right)^2} . \tag{7}$$

It is known that the qP-wave phase-velocity in TI media depends only weakly on V_{S0} (Tsvankin & Thomsen, 1994; Tsvankin, 1996; Alkhalifah, 1998). For all kinematic problems regarding qP waves, V_{S0} is therefore usually ignored. We likewise set $V_{S0} = 0$ (or $f = 1$) in equation (5). This is the *acoustic approximation* from Alkhalifah (1998; 2000). Note that Alkhalifah and Tsvankin (1995) obtained equation (1) from the nonhyperbolic moveout equation of Tsvankin and Thomsen (1994), by also setting $V_{S0} = 0$. In addition, Alkhalifah and Tsvankin (1995) showed that the time signatures of qP-waves in homogeneous VTI media depend mainly on the (zero-dip) normal-moveout velocity V_{NMO} and the anellipticity parameter η, with an almost negligible influence of V_{P0}. Since we are interested only in traveltime calculations, we can choose $\delta = 0$, and thus $V_{P0} = V_{NMO}$ and $\epsilon = \eta$, in equation (5). That equation then becomes

$$\begin{aligned} V(\theta) &= V_{NMO}\left\{\eta\sin^2\theta + \frac{1}{2}\left(1 + \ldots\right.\right. \\ &\left.\left.\sqrt{\left(1 + 2\eta\sin^2\theta\right)^2 - 2\eta\sin^2 2\theta}\right)\right\}^{1/2} , \end{aligned} \tag{8}$$

while equations (3) and (4) for the traveltime t and the associated offset x, become

$$t = \frac{V_{NMO}\, t_0}{v\cos\psi} , \tag{9}$$

and

$$x = V_{NMO}\, t_0 \tan\psi , \tag{10}$$

respectively. Note that the phase velocity $V(\theta)$ now depends linearly on V_{NMO}. This linearity causes the term $\frac{1}{V(\theta)}\frac{dV}{d\theta}$ in equations (6) and (7) to be independent of V_{NMO}. Since the dependence of the group angle on the anisotropic parameters is governed by the term $\frac{1}{V(\theta)}\frac{dV}{d\theta}$ [cf. equation (6)], the group angle ψ is independent of V_{NMO} and depends only on η. In addition, it follows from equation (7) that the group velocity v depends linearly on V_{NMO} since the phase velocity depends linearly on V_{NMO}. From equations (9) and (10) it then follows that *the traveltime t becomes independent of V_{NMO} and that the associated offset x depends linearly on V_{NMO}*. Also, t_0 is a simple scaling factor for both the traveltime t and the associated offset x. In a single horizontal VTI layer, this means that *for fixed η and t_0, the moveout curve for different values of V_{NMO} can be calculated by simple horizontal stretching and squeezing along the offset axis* (see Figure 2). This important observation is a straightforward consequence of the negligible influence of V_{S0} on qP-wave traveltimes in TI media and the fact that the kinematics of qP-waves in homogeneous VTI media depend mainly on V_{NMO} and η. To make explicit the independence of the traveltimes of V_{NMO}, we rewrite equation (9) as

$$t = \frac{t_0}{v|_{V_{NMO}=1}\cos\psi} , \tag{11}$$

where $v|_{V_{NMO}=1}$ denotes the group velocity calculated for $V_{NMO} = 1$ km/s.

Figure 1a (as well as b-e) shows that the contoured maximum traveltime differences between raytraced traveltimes and traveltimes calculated using the

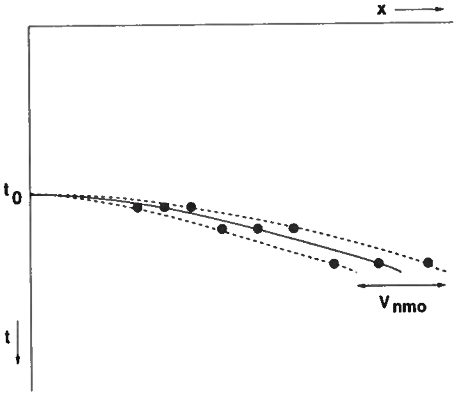

Figure 2. Under the customary assumptions that traveltimes of qP-waves in VTI media depend mainly on η and V_{NMO}, and that the shear-wave velocity along the symmetry axis (V_{S0}) has negligible influence on the traveltimes of qP-waves in such media, the nonhyperbolic moveout curve for fixed η and t_0, but varying V_{NMO}, can be calculated by simple horizontal stretching (or squeezing) along the offset axis. The amount of stretch is determined by the change in V_{NMO}.

nonhyperbolic moveout equation without the correction factor are independent of V_{NMO}. This is now easily understood in light of the previous observation that the nonhyperbolic moveout for fixed η (and t_0) but different values of V_{NMO}, are simply horizontally stretched or squeezed versions of each other. Note that we used $V_{S0} = 0$ and $\delta = 0$ for the ray tracing to determine the traveltime differences shown in Figure 1.

For hard rocks, setting $V_{S0} = 0$ is not as good an approximation as for softer rocks (Tsvankin, personal communication). For such geology (say carbonate reservoirs) it is better to use an 'intelligent estimate' of the V_p/V_s ratio. Note that in this case the traveltimes t are still independent of V_{NMO} because f is simply equal to some appropriately chosen constant value. Therefore, the moveout curves for fixed values of η and t_0 but different values of V_{NMO} are again horizontally stretched or squeezed versions of each other.

Implications for the correction factor C

Rewriting equation (2) in terms of η and V_{NMO} gives

$$t^2(x) = t_0^2 + (x/V_{NMO})^2 - \dots \frac{2\eta\,(x/V_{NMO})^4}{\left[t_0^2 + C\,(1+2\eta)\,(x/V_{NMO})^2\right]} . \qquad (12)$$

Using the observation that the offsets x are linear in V_{NMO}, i.e., using equation (10), it follows that

$$t^2(k) = t_0^2 \left\{ 1 + \frac{k^2}{4} - \frac{\eta k^4}{2\,(4 + C\,[1+2\eta]\,k^2)} \right\} , \qquad (13)$$

where we used $k/2 = \tan\psi$, with k the ODR. This equation shows explicitly that, under the above-mentioned approximations, the traveltimes for a given ODR k (or group angle ψ) are independent of V_{NMO}. Note that using $k/2 = \tan\psi$ in equation (10) gives

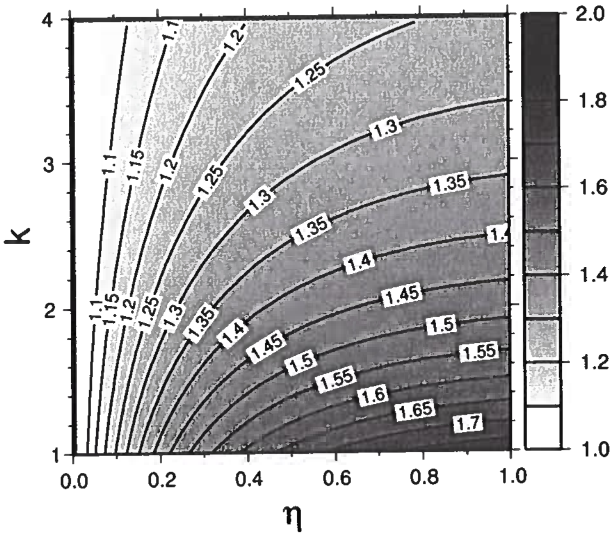

Figure 3. Optimal correction factor C as a function of ODR (k) and η.

$$k = \frac{2x}{t_0 V_{NMO}} . \qquad (14)$$

Strictly, k is a true ODR only if $\delta = 0$. For convenience, we refer to k as the ODR throughout the remainder of this paper.

Under the above-mentioned two approximations, the traveltimes $t(k)$ on the left-hand side of equation (13) are independent of V_{NMO}. It follows that under these approximations the correction factor C is independent of V_{NMO}. Therefore we need only study the dependence of C on η and k. We determine the *optimal* C by minimizing the maximum traveltime difference between ray-traced traveltimes (with $V_{S0} = 0$ km/s and $\delta = 0$) and the traveltimes calculated using equation (13) for different values of η and k. Figure 3 shows a contour plot of C as a function of η and k. Clearly, the optimal C value is not a constant, but rather varies with η and k. Grechka and Tsvankin (1998, p.959) state that, for a single horizontal VTI layer, "introducing the coefficient $C = 1.2$ ... minimizes deviations from the exact traveltimes for the most practical range of offsets $1.5h < x < 2.5h$," where h is the depth of the reflector. Figure 3 shows that for this range of ODR, $C = 1.2$ is optimal only for values of η ranging from 0.08 to 0.18. Therefore, their statement should be understood with the added qualifier that the optimal value of C is close to 1.2 for these particular values of ODR range *in combination* with these particular values of η only.

In practice, neither η or k are known. However, an estimate of V_{NMO} and η can be obtained using equation (12) [or (2)] with $C = 1$. Subsequently, an estimate of

k can be obtained using the estimated value of V_{NMO} in equation (14). Then, the optimal C value can be obtained from Figure 3 using the estimated k and η.

Nonhyperbolic moveout using rational interpolation

Fitting function values at various points (that are not necessarily distinct) using a rational function is usually referred to as *multipoint Padé approximation* (Baker & Graves-Morris, 1981a). Such approximation is also referred to as *N-point Padé approximation*, *Newton Padé approximation*, or *rational interpolation*, depending on the context. Since in this paper, we do not use coincident interpolation points (often referred to as *confluent interpolation points*), we prefer to use the term *rational interpolation*.

A rational approximation to a function $T(x)$ is written as

$$T(x) \approx \frac{N_L(x)}{D_M(x)} , \qquad (15)$$

where $N_L(x)$ is a polynomial of maximum order L, and $D_M(x)$ a polynomial of maximum order M. We denote such an approximation as $[L/M]$ and use the normalization $N_L(0) = T(0)$ and $D_M(0) = 1.0$, after Baker (1975, pp. 5-6). Given $n = L + M$ function values T_i at points x_i, with $i = 1, \ldots, n$, we arrive at a linear system of n equations with n unknowns, the coefficients of the polynomials. Once the coefficients are found, the resulting $[L/M]$ approximant can be used to find the function values $T(x)$ at values of x different from the interpolation points x_i. The solution to this system for the [2/2] rational approximation is given in appendix A.

As with any linear system of equations, the system may be singular. This is a known hazard of rational interpolation. Hence, blind use of rational interpolation can be problematic. There exist reliable algorithms, in the sense that if an interpolant to the function values t_i exists, they find it, whereas if no interpolant exists because the linear system is degenerate, the algorithm exits with an error. An example of such a reliable algorithm is the modified Thacher-Tukey algorithm, e.g., Graves-Morris and Hopkins (1981). Baker and Graves-Morris (1981b, pp. 7-17) give an overview of different algorithms for rational approximations.

Here we use rational interpolation to approximate nonhyperbolic moveout in a horizontal transversely isotropic homogeneous layer with a vertical symmetry axis. Rewriting equation (2) in the form of a rational approximation using the definition of Baker (1975, pp. 5-6), gives

$$t^2(x) = \left\{t_0^2 + \left(A + V_{NMO}^{-2}\right) x^2 + V_{NMO}^{-2} t_0^{-2} \left(A + \ldots \right.\right.$$
$$\left.\left. \left[V_{NMO}^2 - V_{hor}^2\right] / V_{NMO}^4\right) x^4\right\} / \left(1 + A t_0^{-2} x^2\right) , \qquad (16)$$

where $A \equiv C V_{hor}^2 V_{NMO}^{-4}$. This expression reveals that the nonhyperbolic moveout equation can be viewed as a [2/1] rational approximation for t^2 as a function of x^2. Therefore, we could try a [2/1] rational interpolation to approximate nonhyperbolic moveout. In this paper, we choose a [2/2] rational interpolation in an attempt to gain extra accuracy.

To calculate the four unknown coefficients for the [2/2] rational interpolation using equations (A2)-(A5), we need four traveltimes and four associated offsets. Let t_i $(i = 1, \ldots, 4)$ be the traveltime for a fixed ODR k_i (or group angle ψ_i), and let the associated offset be x_i. From the previous section, we know that the traveltimes t_i are independent of V_{NMO} and depend on t_0 through a simple scaling only. This means that the traveltimes t_i needed for the rational interpolation can be calculated from a small subset of traveltimes calculated for a fixed reference value of t_0, denoted as t_0^{ref}, and a range of η values, say from −0.2 to 1.0 in steps of 0.01. This subset can be precomputed and stored in a table. Hence, when the traveltimes t_i for a particular combination of t_0, V_{NMO}, and η are desired, a simple lookup in this table for the particular η combined with scaling with t_0/t_0^{ref} [cf. equation (11)], gives the traveltimes t_i needed for the rational interpolation. That is, the desired traveltime t_i is obtained from

$$t_i = t_i^{table} \left(\frac{t_0}{t_0^{ref}}\right) , \qquad (17)$$

where t_i^{table} is the value of t_i obtained from the table (evaluated for $t_0 = t_0^{ref}$), for ODR k_i and the desired value of η. Evaluating the table for $t_0^{ref} = 1$ s allows the calculation of t_i to be done by scaling of t_i^{table} with t_0 only. Using the given values of V_{NMO} and t_0, the corresponding offsets x_i are then found simply from

$$x_i = \frac{V_{NMO}\, t_0\, k_i}{2} . \qquad (18)$$

The traveltimes and offsets obtained using the method outlined above, allow us to perform velocity-analysis in VTI media using our [2/2] rational interpolation. The efficiency of this approach is comparable to that of current velocity analysis using nonhyperbolic moveout equations (1) or (2), since the small subset of traveltimes for $t_0 = 1$ s and a range of η values, is precomputed and stored in a table. Hence, no computational overhead is required compared to that of current methods. In other words, the nonhyperbolic moveout equation is replaced simply with the rational interpolation formula, and the needed traveltimes are read from the precomputed table.

To precompute the table of traveltimes, a standard anisotropic ray-tracing algorithm can be used. Here, to calculate the traveltimes, we first solve

$$\frac{k_i}{2} = \frac{\tan\theta_i + \left.\dfrac{1}{V_i}\dfrac{dV}{d\theta}\right|_{\theta_i}}{1 - \left.\dfrac{\tan\theta_i}{V_i}\dfrac{dV}{d\theta}\right|_{\theta_i}} , \qquad (19)$$

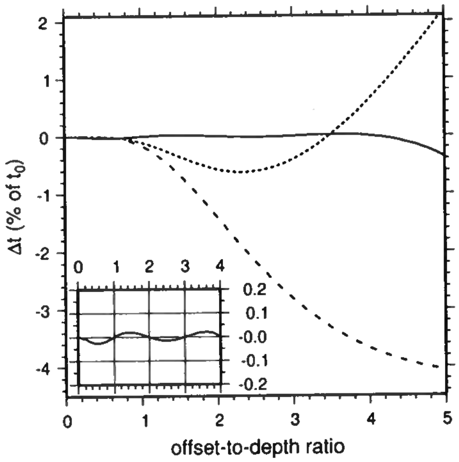

Figure 4. Residual moveout as a function of ODR using the nonhyperbolic moveout equation without the correction factor, i.e., $C = 1$ (dashed), with the optimal correction factor (dotted), and [2/2] rational interpolation (solid). For all three cases the model parameters used are $\eta = 0.3$ and $V_{NMO} = 2.4$ km/s (indicated by the star in Figures 1a-c). The inset shows the residual moveout for the [2/2] rational interpolation on a larger scale. At the interpolated ODR values 1, 2, 3, and 4, the residual moveout is identical zero.

for θ_i numerically, using the Matlab function 'fsolve' which uses an interior-reflective Newton method to solve nonlinear equations (Coleman & Li, 1994; Coleman & Li, 1996). To obtain equation (19) we used $\tan\psi_i = k_i/2$. In equation (19), V_i is the phase velocity associated with ODR k_i. The traveltime is then found through calculation of the group velocity $v_i|_{V_{NMO}=1}$ using equations (8) and (7) with $V_{NMO} = 1$ km/s, and subsequent use of this velocity in

$$t_i^{table} = \frac{t_0^{ref}}{v_i|_{V_{NMO}=1} \cos\left(\tan^{-1}\dfrac{k_i}{2}\right)}, \qquad (20)$$

[cf. equation (11)]. We found that using the group angle as an initial guess for the phase angle generally worked well. We did not investigate different methods to solve for the phase angles θ_i. Using the 'fsolve' function in Matlab, the calculation of a table with four traveltimes for about 100 values of η takes on the order of one minute on a modern PC.

Accuracy comparison between rational interpolation and the nonhyperbolic moveout equation

Figure 1c shows contours of the maximum absolute percentage traveltime difference between ray-traced traveltimes for a single horizontal VTI layer and traveltimes resulting from the [2/2] rational interpolation. Here $t_0 = 1$ s, and the maximum ODR is two. The ODR values used for the rational interpolation are $k_1 = \frac{1}{2}$, $k_2 = 1$, $k_3 = \frac{3}{2}$, and $k_4 = 2$. Here the maximum traveltime errors are of the order $10^{-3}\%$ of t_0 (or 0.01 ms in this case), which is one-to-two orders of magnitude more accurate than that using the nonhyperbolic moveout equation with the optimal correction factor, and two-to-three orders of magnitude more accurate than the accuracy of this equation without the correction factor. With a dominant frequency of 50 Hz, the traveltime errors are about 0.05% of the dominant period, and are hence negligible. Figure 1f shows the same contours, but now for a maximum ODR of four (the ODR values used for the rational interpolation are $k_1 = 1$, $k_2 = 2$, $k_3 = 3$, and $k_4 = 4$). The traveltime errors are now somewhat larger and of the order of $10^{-2}\%$ of t_0 (or 0.1 ms in this case), but still one-to-two orders of magnitude smaller than those for the nonhyperbolic moveout with or without the correction factor. Again, compared to a dominant period of 20 ms, these errors are negligible (0.5% of the dominant period). Hence, rational interpolation achieves a significant improvement in accuracy up to large ODR, and is highly accurate for all models of practical interest, without the use of an optimization parameter such as the correction factor C in the nonhyperbolic moveout equation (2).

We explained earlier that rational interpolation can lead to a degenerate linear system. For our [2/2] rational interpolation, this happens if the moveout is purely hyperbolic. Figure 1, however, shows that for virtually all anisotropic models of practical interest such degeneracy does not occur. Figure 1 was calculated using discrete offsets and discrete values of V_{NMO} and η. If degeneracy would somehow occur for values in the continuous range between the discrete values we used for η and V_{NMO}, adding a small amount of numerical noise (say on the order of 10^{-2} ms) should overcome. Numerical tests showed that adding such a small amount of numerical noise, indeed removed the degeneracy for purely hyperbolic moveout.

Figure 4 shows the residual moveout as a function of ODR for the nonhyperbolic moveout equation without (dashed) and with (dotted) the optimized correction factor, respectively, and for the [2/2] rational interpolation (solid). Here we used $V_{NMO} = 2.4$ km/s*, $\eta = 0.3$ (indicated by the star in Figures 1d-f), and $t_0 = 1$s. Notice that the correction factor introduces a bias in the residual moveout; the undercorrection at intermediate offsets is compensated by an overcorrection at large offsets. The inset shows the residual moveout for the [2/2] rational interpolation at a larger scale. The residual moveout is strictly zero at the specified ODR values of $k_1 = 1$, $k_2 = 2$, $k_3 = 3$, and $k_4 = 4$. We note that

---

*Because of our observation that the traveltime errors do not depend on V_{NMO}, the actual value of V_{NMO} is irrelevant.

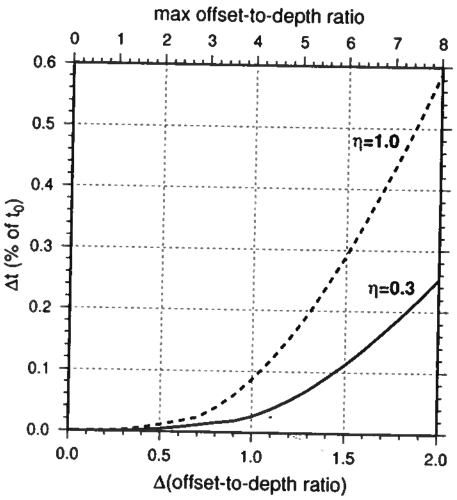

Figure 5. Accuracy of the [2/2] rational interpolation as a function of the separation in ODR of the interpolation traveltimes for $\eta = 0.3$ and $\eta = 1.0$. In both cases $V_{NMO} = 2.4$ km/s. Even if the separation in ODR is two, i.e., the maximum ODR is 8, the percentage errors in traveltime are of the order 10^{-1}.

extrapolation beyond k_4 is dangerous and can result in large errors in traveltimes because the rational approximation starts oscillating with typically increasing amplitudes. The onset of such oscillation can be seen in Figure 4 for ODR values beyond $k_4 = 4$. Rational interpolation should never be used for extrapolation. That is, k_4 should be chosen such that it exceeds the largest offset in the data.

Comparing Figures 1c and 1f, it seems that use of larger intervals of Δk between the k_i causes the maximum traveltime errors to increase. To analyze the influence of Δk, and to see what maximum ODR can be reached with [2/2] rational interpolation with considerable accuracy, Figure 5 shows the maximum absolute percentage traveltime error as a function of Δk. The top horizontal scale of the figure shows the maximum ODR. Here we used $V_{NMO} = 2.4$ km/s and $t_0 = 1$ s, and plot the traveltime errors for two different values of η, i.e., $\eta = 0.3$ (solid) and $\eta = 1.0$ (dashed). Note again that the value of V_{NMO} is irrelevant; errors do not depend on V_{NMO}, as explained previously. The high η value for the dashed curve can be taken as a worst-case scenario with respect to accuracy. For practical values of η, the maximum error in traveltime for ODR values up to 8 (achieved with $k_1 = 2$, $k_2 = 4$, $k_3 = 6$, and $k_4 = 4$), is of the order of a tenth of a percent of t_0. Therefore, for almost all practical cases, our [2/2] rational interpolation provides an accurate nonhyperbolic moveout approximation. If needed, higher-order rational interpolation, combined with $\Delta k = 1$, would obtain extra accuracy.

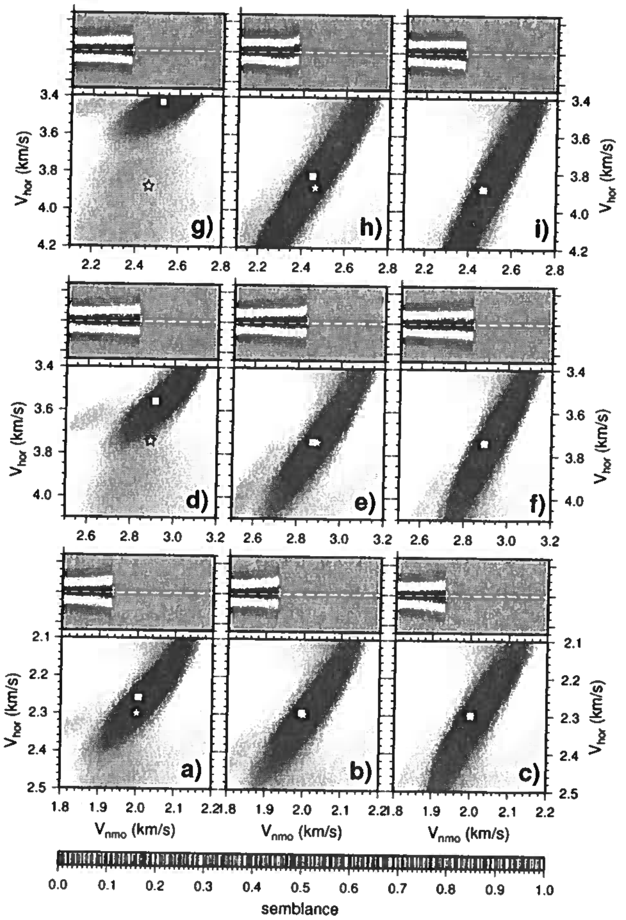

Figure 6. Semblance scans and moveout-corrected gathers, where the moveout correction was done with the parameters related to the maximum semblance values. The model for each subfigure consists of a single horizontal VTI layer, and the maximum ODR is two. For all models, $t_0 = 1$ s. The true model parameters are indicated by the star, and are: $V_{NMO} = 2.0$ km/s and $V_{hor} = 2.3$ km/s (i.e., $\eta = 0.16$) in subfigures a - c; $V_{NMO} = 2.892$ km/s and $V_{hor} = 3.745$ km/s (i.e., $\eta = 0.34$) in d - f (shale under zero confining pressure); and $V_{NMO} = 2.46$ km/s and $V_{hor} = 3.88$ km/s (i.e., $\eta = 0.74$), in g - i (Green River Shale). In the first column, the differences are calculated using equation (2) with $C = 1$, while in the second column the optimal correction factor was used. In the third column the [2/2] rational interpolation was used.

Figure 6 shows semblance scans (at fixed t_0) as a function of V_{NMO} and V_{hor} calculated using the nonhyperbolic moveout equation without the correction factor (a, d, and g), with the optimal correction factor (b, e, and h), and the [2/2] rational interpolation (c, f, and i). In each row of figures the true model parameters (indicated by the star) vary, and are, respectively, $V_{NMO} = 2000$ m/s and $V_{hor} = 2300$ m/s (or $\eta = 0.16$) for a-c, $V_{NMO} = 2892$ m/s and $V_{hor} = 3745$ m/s (or $\eta = 0.34$) for d-f, and $V_{NMO} = 2464$ m/s and $V_{hor} = 3880$ m/s (or $\eta = 0.74$) for g-i; the semblance maxima are indicated by the squares. Note that the synthetic gathers were generated using ray-traced traveltimes, where the ray tracing was done using the true values of δ, i.e., $\delta = 0$ for a-c, $\delta = -0.05$ for d-f, and $\delta = -0.22$ for g-i, while we used $V_{S0} = 0$ km/s for all models.

The model parameters for the lower row of figures correspond to the model parameters used in Figures 1 and 2 of Grechka and Tsvankin (1998). [These parameters were originally chosen because such values of η were observed on field data (Alkhalifah *et al.*, 1996)]. For the middle row, the model parameters correspond to a shale under zero confining pressure, and for the top row, the parameters correspond to Green River shale [see Table 1 in Thomsen (1986) for these two cases]. For all subfigures (i.e., a - i) we used $t_0 = 1$ s and a maximum ODR of two. For the rational interpolation we used $k_1 = \frac{1}{2}$, $k_2 = 1$, $k_3 = \frac{3}{2}$, and $k_4 = 2$. Since for the lower row in Figure 6 the model parameters are identical to those in Figures 1 (and 2) of Grechka and Tsvankin (1998), our Figure 6a is the semblance scan equivalent of Figure 1 in their paper. The C values used in Figures 6b, e, and h were determined in the following way: the estimates of V_{NMO} and V_{hor} determined without the correction factor were used to determine the optimal C-value for this model from Figure 3. This method mimics the way C would be determined in practice.

Figures 6a, d, and g show that the the nonhyperbolic moveout equation (2) without the correction factor obtains high semblance values, but for the wrong values of V_{hor}; V_{NMO} seems largely unbiased. This means that the associated common midpoint (CMP) gathers are well flattened using the wrong value of V_{hor}, hence introducing a bias in the estimated value of V_{hor}, and thus η. The associated moveout corrected gathers for all three models are shown above the semblance scans; the gathers are well flattened with the biased estimate of V_{hor}. Note that for all three models, the semblance maximum (indicated by a square) for the nonhyperbolic moveout equation without the correction factor (Figures 6a, d, and g) indicates a value of η smaller than the true value (a smaller difference between V_{hor} and V_{NMO} than the difference between their true respective values). Hence, this method seems to underestimate η. Without the correction factor, accurate η values are obtained only when the true η values are small (≤ 0.1).

Figures 6b, e, and h indicate that using the correction factor in equation (2) gives maximum semblance values for values of V_{NMO} and V_{hor} that almost coincide with the true values, except for the model with extreme anisotropy (Figure 6h); for this model the method slightly underestimates V_{hor} (and thus η). The associated moveout-corrected CMP gathers are well flattened although careful analysis of the moveout corrected gather for the model with extreme anisotropy indicates a slight residual moveout. Overall, we conclude that even for large levels of anellipticity and ODR up to two, the correction factor in the nonhyperbolic moveout equation (2) allows for accurate estimation of the model parameters V_{NMO} and V_{hor}, even though use of the correction factor leaves some distortion in the moveout correction that becomes more noticeable with increasing anisotropy. Straightforward application of a correction factor $C = 1.2$ (not shown here) provided accurate estimates for the model shown in the bottom row only, for which the optimum C value was close to 1.2. The optimum C values for Figures 6b, e, and h, found from Figure 3, were $C = 1.23$, $C = 1.36$, and $C = 1.46$, respectively. Straightforward application of the [2/2] rational interpolation method provides, for all models, maximum semblances that coincide with the true model parameters, and accurately flattens gathers without any residual moveout (see Figures 6c, f, and i). Of course no optimization is required.

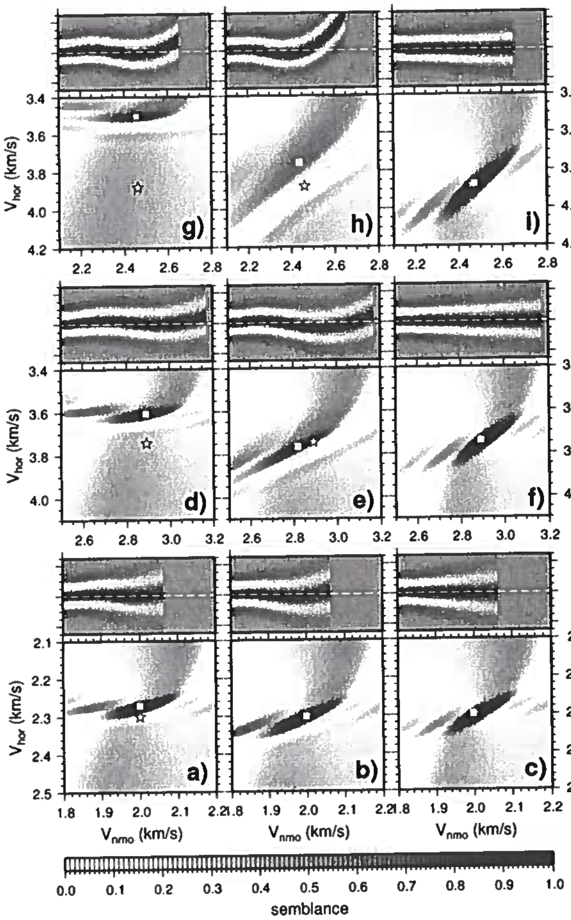

Figure 7. Same as Figure 6, except that the maximum ODR is now four.

Figure 7 shows the same semblance scans and moveout corrected gathers, for the same models and methods as in Figure 6, except that here the maximum ODR is four. For the rational interpolation we used $k_1 = 1$, $k_2 = 2$, $k_3 = 3$, and $k_4 = 4$. Notice that for all models and methods, the peak of the semblance scans is much better defined than in Figure 6; that is, the large semblance values span a much smaller range of V_{hor} (and thus η) values, and a somewhat smaller range of V_{NMO} values. Indeed the higher resolution for η for larger offset ranges was mentioned by Alkhalifah (1997), Grechka and Tsvankin (1998), and Wookey *et al.* (2002). Aside from the improved resolution in η, Figures 7a, d, and g, show again the underestimation of η when the nonhyperbolic moveout equation is used without the correction factor, just as in Figures 6a, d, and g. The maximum semblance, however, now deteriorates with increasing levels of anellipticity, and the associated moveout-corrected CMP gathers clearly indicate a distortion in the moveout, even for the model with $\eta = 0.16$ (see Figure 7a). For the optimum correction factor C (Figures 7b, e, and h), the bias in the estimated values of η is much reduced, but the associated residual moveout is more pronounced than without the use of the correction factor. Again, this is clearly observed even on the model with $\eta = 0.16$ (Figures 7a and b). The rational interpolation method (Figures 7c, f, and i) gives unbiased estimates of η and V_{NMO} *combined with no residual moveout.* This is a direct consequence of the high accuracy of the rational interpolation method shown in Figure 1f for this ODR.

From Figures 6 and 7, for ODR up to two, the nonhyperbolic moveout equation without the correction factor allows for accurate moveout correction for arbitrary levels of anellipticity, but does so with a biased estimate of V_{hor} (and thus η). The bias in η can subsequently be corrected for by determining the optimal value of the correction factor C using Figure 3, and redoing the semblance scans. The value of η determined in this way, is largely unbiased, and results in accurate moveout correction except for the model with extreme anisotropy (see Figures 7g and h), where a slight bias in η and residual moveout correction remains. With increase of ODR up to four, the nonhyperbolic moveout equation no longer gives accurate moveout correction, not even for the model with $\eta = 0.16$. Use of the optimal correction factor C reduces the bias in the estimated value of η, but increases the residual moveout. The rational interpolation method we propose, combines accurate moveout correction with unbiased parameter estimation, for arbitrary levels of anellipticity and ODR up to four. If accuracy is desired for larger offsets, higher-order rational interpolation can be used, or [2/2] rational interpolation can be used with an increased interval between the ODR k_i (say $k_1 = 2$, $k_2 = 4$, $k_3 = 6$, $k_4 = 8$). Figure 5 shows that with the [2/2] rational interpolation we can achieve reasonable accuracy up to ODR of 8.

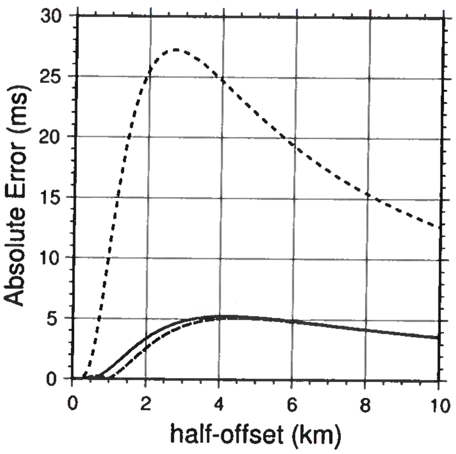

Figure 8. Comparison of accuracy between the nonhyperbolic moveout equation without the correction factor (dotted), the shifted hyperbola method of Fomel (2004) (dashed), and our squeeze-stretch approach (solid), for Greenhorn-shale anisotropy ($\eta = 0.34$ and $V_{NMO} = 2935$ m/s). The absolute traveltime errors are calculated with respect to ray-traced traveltimes. The model parameters are: $V_{P0} = 3094$ m/s, $V_{S0} = 1510$ m/s, $\delta = -0.05$, and $\epsilon = 0.256$ (Greenhorn shale).

Accuracy comparison with the nonhyperbolic moveout approximation of Fomel

Recently, Fomel (2004) proposed a shifted-hyperbola approximation for the group velocity and converted this into the following moveout equation for a single homogeneous horizontal VTI layer,

$$t^2(x) = \frac{3+4\eta}{4\,(1+\eta)} H(x) + \frac{1}{4\,(1+\eta)} \times \ldots \sqrt{H^2(x) + 16\eta\,(1+\eta)\,\frac{t_0^2 x^2}{(1+2\eta)\,V_{NMO}^2}}\,, \quad (21)$$

where $H(x)$ represents the hyperbolic part,

$$H(x) = t_0^2 + \frac{x^2}{(1+2\eta)\,V_{NMO}^2}\,. \quad (22)$$

Fomel (2004) showed that this approximation is significantly more accurate than the nonhyperbolic moveout equation (1) of Alkhalifah and Tsvankin (1995).

Our rational interpolation approach is based on the approximations that (1) the influence of V_{S0} on qP-wave traveltimes in TI media is negligible, and (2) the kinematics of qP-waves in homogeneous VTI media depend mainly on V_{NMO} and η; i.e., we can set $\delta = 0$. Figure 8 shows the traveltime difference between ray-traced traveltimes for a single horizontal VTI layer with Greenhorn-shale anisotropy (Jones & Wang, 1981) and the nonhyperbolic moveout equation (1) form Alkhalifah and Tsvankin (dotted), the shifted hyperbola equation (21) from Fomel (dashed), and traveltimes resulting from ray tracing with $V_{S0} = 0$ km/s and $\delta = 0$

ODR = 2

	C=1.0				**optimal C**				**RI**			
layer	s	V_{NMO}	V_{hor}	η	s	V_{NMO}	V_{hor}	η	s	V_{NMO}	V_{hor}	η
1	1.00	2097	2101	0.00	1.00	2097	2101	0.00	1.00	2099	2101	0.00
2	0.98	2058	2179	0.06	0.98	2056	2188	0.07	0.98	2058	2188	0.07
3	1.00	2271	2839	0.28	0.98	2253	2996	0.38	1.00	2252	3022	0.40
4	0.99	2313	3012	0.35	0.93	2290	3255	0.51	1.00	2282	3285	0.54

ODR = 4

	C=1.0				**optimal C**				**RI**			
layer	s	V_{NMO}	V_{hor}	η	s	V_{NMO}	V_{hor}	η	s	V_{NMO}	V_{hor}	η
1	1.00	2094	2099	0.00	1.00	2094	2099	0.00	1.00	2096	2099	0.00
2	0.95	2029	2207	0.09	0.95	2025	2218	0.10	0.96	2035	2218	0.09
3	0.57	2238	2894	0.34	0.54	2299	2892	0.29	0.84	2189	3158	0.54
4	0.57	2320	3038	0.36	0.57	2300	3152	0.44	0.87	2241	3391	0.64

Table 1. Comparison of obtained semblance values (s), V_{NMO}, V_{hor}, and η,for the three methods, for maximum ODR of two (top) and four (bottom), for a layered medium. The model consists of four horizontal homogeneous VTI layers with the following values of V_{NMO} and η. The parameters for each layer are given in the main text.

but the same values of V_{NMO} and η (solid). The ansitropy parameters are $V_{P0} = 3094$ m/s, $V_{S0} = 1510$ m/s, $\delta = -0.05$, and $\epsilon = 0.256$ (i.e., $V_{NMO} = 2935$ m/s and $\eta = 0.34$), and $t_0 = 646.5$ ms. Except for the solid line, Figure 8 reproduces Figure 7 of Fomel's (2004) paper. Note that the accuracy of the shifted hyperbola approximation is marginally better than the ray-traced traveltimes with $V_{S0} = 0$ km/s and $\delta = 0$ but the same values of V_{NMO} and η. The maximum difference between these two traveltime approximations is about 1 ms (i.e., 0.15% of t_0) for this particular model. From a practical point of view, the two approximations are therefore identical. Even though we have not calculated the solid line with a rational interpolation, we can approximate the solid line to almost arbitrary precision with rational interpolation (i.e., with $[M/N]$ rational interpolation where $M, N > 2$). For ODR up to four, we showed this in Figure 1f using a [2/2] rational interpolation. Since the rational interpolation method that we propose uses traveltimes calculated with $V_{S0} = 0$ km/s and $\delta = 0$, we conclude that the accuracy of our method is basically identical to that of the shifted hyperbola approximation of Fomel (2004). Comparison of semblance scans and moveout corrections calculated using equation (21) and the rational interpolation method (not shown here), for the models and offsets studied in Figures 6 and 7, showed basically no difference between both methods.

Application to horizontally layered VTI media

Up to this point, we have treated only a single horizontal VTI layer. In this section we test the applicability of the rational interpolation method to a horizontally layered VTI medium, and compare its accuracy to that of the nonhyperbolic moveout equation with and without the correction factor. Based on the work of Tsvankin and Thomsen (1994), Grechka and Tsvankin (1998) showed that the nonhyperbolic moveout equation (1) remains valid in horizontally layered media provided the parameters η and V_{NMO} are replaced by 'effective' values that are some average over the vertically heterogeneous overburden. Also, they rewrite the Dix-type inversion procedure, originally introduced by Tsvankin and Thomsen (1994), in terms of η and V_{NMO}. In that method, the effective values of η and V_{NMO}, obtained from applying the single-layer equation (1) to data from a layered medium, are used to estimate the interval values of η and V_{NMO}.

We compare the effective values of η and V_{NMO} obtained using the nonhyperbolic moveout equation, with

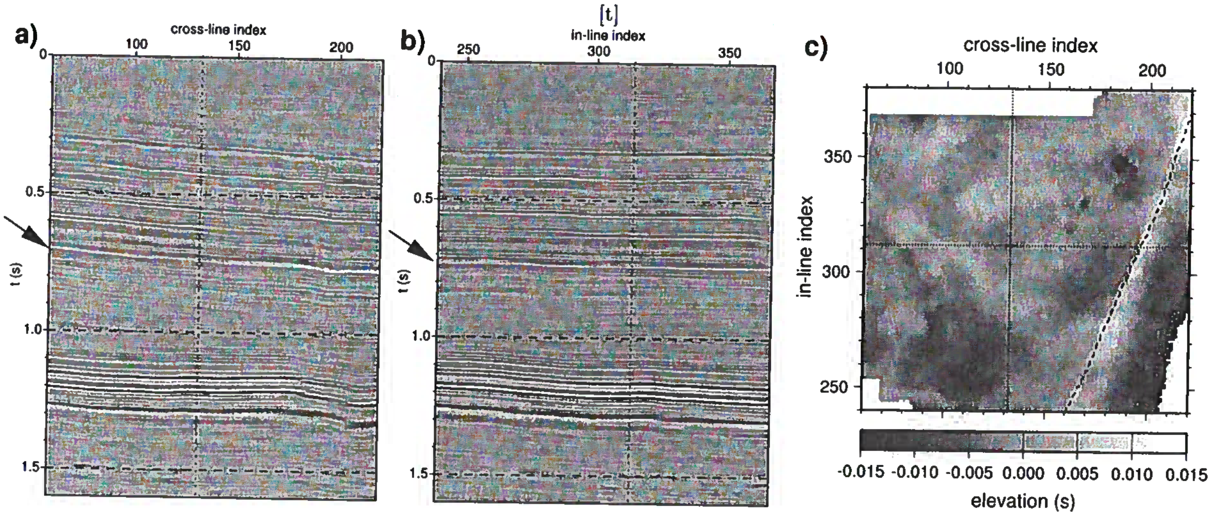

Figure 9. Field data used to test the rational interpolation method. Inline (a), crossline (b), and plan view of the residual topography of the event used for testing (indicated by the arrows in a and b) after removal of the regional dip (c). The dotted lines in c denote the locations of the inline and crossline sections shown in a and b. The dashed line in c denotes the location of a regional fault.

and without the correction factor, and the rational interpolation method, through application of all methods to a horizontally layered medium with the following parameters:

- layer 1 : $h = 1$ km (h is the depth of the bottom of the layer), $V_{NMO} = 2098$ m/s, $V_{hor} = 2098$ m/s, $\eta = 0$, ($V_{P0} = 2000$ m/s, $\epsilon = 0.05$, $\delta = 0.05$),
- layer 2 : $h = 2$ km, $V_{NMO} = 2000$ m/s, $V_{hor} = 2300$ m/s, $\eta = 0.16$, ($V_{P0} = 2000$ m/s, $\epsilon = 0.16$, $\delta = 0$),
- layer 3 : $h = 3$ km, $V_{NMO} = 2892$ m/s, $V_{hor} = 3745$ m/s, $\eta = 0.34$, ($V_{P0} = 3048$ m/s, $\epsilon = 0.255$, $\delta = -0.05$),
- layer 4 : $h = 4$ km, $V_{NMO} = 2460$ m/s, $V_{hor} = 3880$ m/s, $\eta = 0.74$, ($V_{P0} = 3292$ m/s, $\epsilon = 0.195$, $\delta = -0.22$).

For all models we used $V_{S0} = 0$ km/s. Note that here the first layer is elliptically anisotropic, and the second through fourth layers have the same model parameters as those in the models studied in the first through third row of Figures 6 and 7, respectively.

Table 1 shows the results from all three methods for a maximum ODR of two (top) and four (bottom). These results closely resemble the results obtained from the single layer numerical tests shown in Figures 6 and 7. Since all methods are for a single-layer VTI medium only, and because we apply these methods to layered VTI media, the η, V_{NMO}, and V_{hor} values in Table 1 are all 'effective' values. For maximum ODR=2, the nonhyperbolic moveout equation without the correction factor gives consistently lower estimates of η than do the other methods, and the differences increase with depth, i.e., as we increase the level of anellipticity. For that method, the semblance values (indicated with s in Table 1) are high for all layers, indicating high quality moveout correction. Use of the optimal correction factor gives comparable values of η and V_{NMO} to those obtained with the rational interpolation method, for all layers, just as for the single-layer case (see Figure 6). Also, the semblance values from the nonhyperbolic moveout equation with the correction factor slightly decrease with increasing depth (or level of anellipticity), just as for the single-layer case. For maximum ODR=4, the nonhyperbolic moveout equation with and without the correction factor result in decreasing semblance with depth (i.e., increasing level of anellipticity), indicating a lack of ability to accurately moveout-correct the data. Again this is analogous to the results from the single-layer case (Figure 7). That the rational interpolation method has substantially larger semblance values than do the other two methods, for all layers, indicates that this method is able to flatten the gathers best, with the least residual moveout. From a practical point of view, the method that flattens the gathers best, is expected to give the most confidence in the estimated values of η and V_{NMO}. From this point of view, the rational interpolation therefore provides more robust estimates of η and V_{NMO} than do the other two methods, for maximum ODR=4.

It thus seems that the rational interpolation method, which is based on a single horizontal VTI layer, is suitable for application to a horizontally layered medium, at least up to maximum ODR=4 and arbitrary levels of anellipticity. For maximum ODR=2, the nonhyperbolic moveout equation with the correction factor gives comparable estimates of the effective η and V_{NMO} and comparable semblance values to those of the rational interpolation approach. This indicates that for maximum ODR=2, even for extreme levels of anellipticity the effective values of η and V_{NMO} estimated

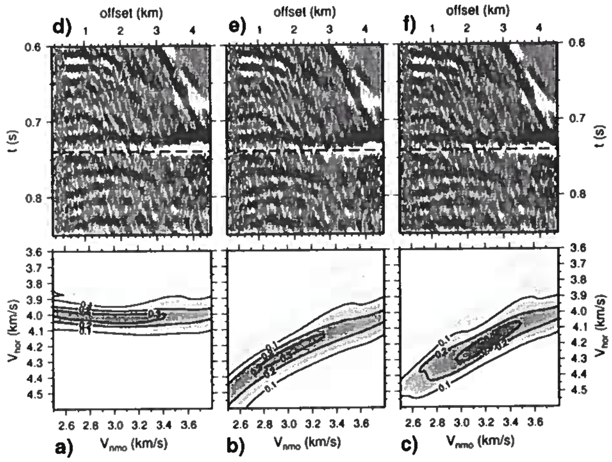

Figure 10. Semblance scans (a-c) for one CMP gather, located at the crossing of the horizontal lines in Figure 9c; its location is also indicated by the dotted lines in Figures 9a and b. The associated moveout corrected gathers are shown in subfigures d-e. The methods used for parameter estimation (i.e., to calculate the semblance scans) and moveout correction are, respectively, nonhyperbolic moveout without (a,d) and with (b,e) the optimal correction factor, and the [2/2] rational interpolation (c,f). A 100-ms window centered around $t_0 = 750$ ms was used in the computation. The contours in a-c indicate the semblance values. Maximum semblance values for the different methods are, respectively, 0.37 (a), 0.32 (b), and 0.40 (c), and the resulting estimates for η and V_{NMO} are, respectively, $\eta = 0.34$ and $V_{NMO} = 3100$ m/s (a), $\eta = 0.45$ and $V_{NMO} = 3100$ m/s (b), and $\eta = 0.33$ and $V_{NMO} = 3250$ m/s (c).

with the rational interpolation method can be used in the Dix-type inversion procedure given by Grechka and Tsvankin (1998). The role of the correction factor in this procedure, however, is currently unclear to us. For maximum ODR=4, the effective values of η and V_{NMO} for substantial anellipticity (say effective η values larger than 0.2) differ substantially between all methods, with the rational interpolation method uniformly giving the best moveout correction (i.e., highest semblance values). This indicates room for extending the rational interpolation method to the vertically heterogeneous case, and thus for developing an inversion procedure based on rational interpolation. It remains to be seen if such an extension is possible.

Field data example

Figures 9a and b show inline and crossline stacked time sections from a land dataset that contains a reflector at about 750-ms two-way traveltime (indicated by the arrows), illuminated with ODR ranging to larger than four. We focus attention on this event throughout the remainder of this section. The geology consists of relatively flat (dip less than two degrees), predominantly shale layers, such that a layered VTI model seems, at first sight, appropriate for these data. Although the structure on the horizon of interest is limited to within ±20 ms of a best-fit planar dip, a subtle NNE-SSW structural trend, associated with deeper faulting (Figure 9c), exists. The dashed line indicates the location of a regional fault. The inline and crossline spacings are both 110 ft.

To test our method, we calculated semblance as a function of V_{NMO} and V_{hor} for the whole dataset over a 100-ms window centered on the event of interest. The offsets used in the analysis were limited to offsets with a maximum ODR of approximately four. Figure 10a-c show the semblance scans for all three methods: (a) the nonhyperbolic equation without and (b) with the optimal correction factor, and (c) the [2/2] rational interpolation, for a randomly selected CMP gather. The location of this gather is indicated by the intersection of the dotted lines in Figure 9c; the location is also indicated by the vertical dotted lines in Figures 9a and b. This gather was generated by collecting traces from a 3-by-3 super bin of adjacent CMPs, and subsequent offset-binning. The change of shape of the semblance contours observed on Figures 10a-c, resembles the change observed from the synthetic data tests; the nonhyperbolic moveout equation without the correction factor exhibits no clear evidence of the inherent tradeoff relation between η and V_{NMO}, whereas the other two methods do display this known trade-off. The semblance peak is most clearly defined for our [2/2] rational interpolation method because of its higher accuracy for such a large ODR range. The derived η, V_{NMO}, and maximum semblance values for the three methods are respectively: 0.34, 3100 m/s, 0.38 (no correction factor); 0.45, 3050 m/s, 0.33 (correction factor); 0.33, 3250 m/s, 0.40 (rational interpolation).

Figure 10d-f shows the moveout-corrected gather for the three methods, whit the semblance-derived values of η and V_{NMO} used for the moveout correction. Note that the residual moveout for the nonhyperbolic moveout equation with and without the correction factor is substantial, whereas the rational interpolation method gives well corrected moveout. The estimated values of η are close to the η value for the modeled results shown in Figure 7d-f. Notice the striking resemblance between the semblance scans and the residual moveouts obtained from both the synthetic and field data (cf. Figure 7d-f). We found that straightforward application of the correction factor $C = 1.2$ resulted in even larger residual moveout than that shown in Figure 10e.

Figure 11a, b, and c show mapviews of the values of η obtained for the event of interest over the entire dataset, using, respectively, the (a) nonhyperbolic moveout equation without and (b) with the optimal correction factor, and (c) the [2/2] rational interpolation method, for maximum ODR of two. The η values ob-

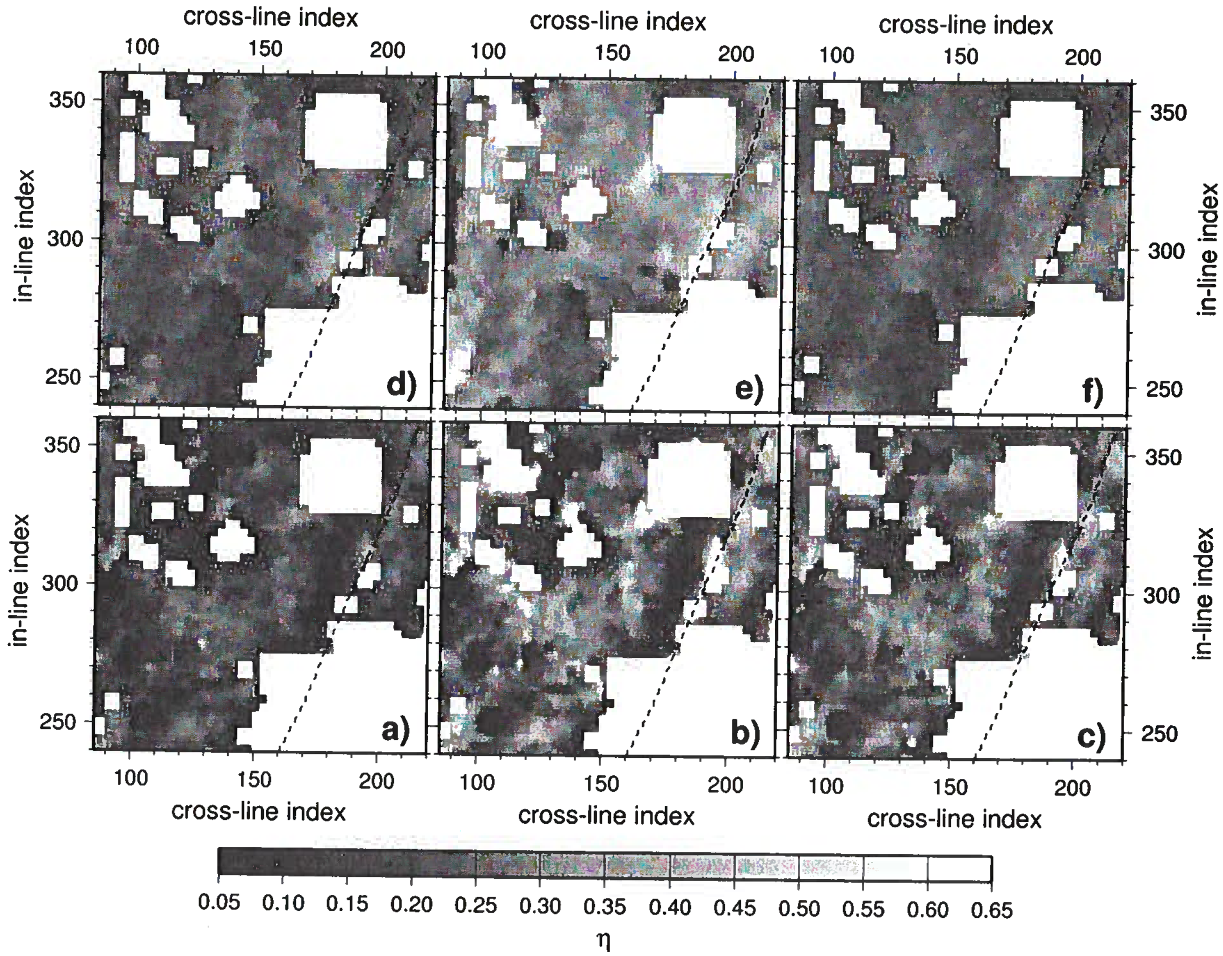

Figure 11. Map view of η derived from the event of interest in the field data with maximum offset of 2250 m, i.e., ODR≈ 2 (a-c), using semblance scans with the nonhyperbolic moveout equation without (a) and with the optimal correction factor (b), and the [2/2] rational interpolation method (c). Subfigures d-f are as a-c, except that the maximum offset is 4500 m, i.e., ODR≈ 4. Estimates of η at locations with poor offset distributions were set to white.

tained using nonhyperbolic moveout equation without the correction factor (a), are generally smaller than the estimated η values from both other methods, just as in our synthetic data examples (cf. Figure 6). The estimates of η obtained using the rational interpolation method (c) and the optimal correction factor approach (b) are quite comparable. This striking similarity is consistent with the results from the synthetic data also. The same comparison for V_{NMO} (not shown) showed that all three methods gave similar estimates of V_{NMO}, just as in the synthetic examples.

Figure 11d, e, and f, are as a, b and c, but here the maximum ODR is four. Notice, that the estimated η values are spatially less variable, for all methods. This can be understood in light of the improved resolution in η for larger ODR, together with the lack of evidence of substantial lateral heterogeneity from the seismic data (cf. Figure 9). Here, the correction-factor approach results in large estimates of η, compared to those of the other methods. From the synthetic tests, we would expect this method to give η values comparable to the estimated η values obtained using rational interpolation. None of our synthetic tests, however, included amplitude-versus-offset (AVO) variations, whereas the field data example clearly does (cf. Figure 10). Some additional synthetic tests (not shown), indicate that the rational interpolation method is less sensitive to such AVO variations than is the nonhyperbolic moveout equation method, with or without the correction factor; this can be explained by the high accuracy of the rational interpolation method†. Therefore, the lack of resemblance between the estimated η values for the correction factor approach and the rational interpolation may be due to

---

† We did not include phase changes with offset in the tests concerning sensitivity to AVO variation.

the AVO variations in the field data. Note that the presence of AVO variations causes semblance based moveout correction to be biased towards the offsets with higher amplitudes. Such bias is especially noticeable when an inaccurate moveout approximation is used to moveout correct the data.

The η values resulting from the rational interpolation method are on average slightly higher than those from the nonhyperbolic moveout equation method without the correction factor; $\eta_{av} = 0.28$ for the rational interpolation method, and $\eta_{av} = 0.25$ for the nonhyperbolic moveout equation method. The lower values of η for the nonhyperbolic moveout equation method without the correction factor are consistent with the results from the synthetic-data tests (cf. Figure 7). For all methods, the η values are high compared to values typically reported from nonhyperbolic moveout analysis [e.g. Toldi *et al.* (1999)]. Of course the relatively high η values are likely a result of the particular lithology of this area. However, most studies reporting estimates of η have been done on marine data, where a substantial waterlayer reduces the effective values of η, hence introducing a bias in what are traditionally considered acceptable values of η.

The [2/2] rational interpolation resulted in more spatially smooth and continuous values of both η (and V_{NMO}) that in some parts correlate somewhat with the geologic trend (cf. Figure 9c). It is important to note that this spatial continuity was not imposed, but followed from a straightforward application of the rational interpolation method presented here. Since the seismic data show no indication of substantial lateral heterogeneity (cf. Figure 9), the relatively smooth spatial variation of η is consistent with the seismic data. This increases our confidence in the η values obtained using the rational interpolation method.

Figure 12a shows the normalized semblance difference between nonhyperbolic moveout equation method with and without the optimal correction factor, for maximum ODR=2. The normalized semblance difference is the difference between the semblances from both methods divided by the semblance for the nonhyperbolic moveout equation method without the correction factor. Figure 12b is as Figure 12a, but it shows the normalized semblance difference between the [2/2] rational interpolation method and the nonhyperbolic moveout equation without the correction factor. For these offsets, all methods result in similar semblances, indicating similar ability to flatten the gathers. This supports our findings from the numerical tests that all methods obtain comparable results in terms of moveout correction, for an ODR range up to two (cf. Figure 6). Figures 12c and d are as 12a and b, except that here the maximum ODR is four. For this range of ODR, the correction-factor approach has on average 7% lower semblance values than does the nonhyperbolic moveout equation without the correction factor, whereas the [2/2] rational interpolation has on average 10% higher semblance values. This supports (for the whole dataset) our findings from the synthetic results that the correction factor approach increases distortion in the moveout correction and that the rational interpolation method results in more accurate moveout correction.

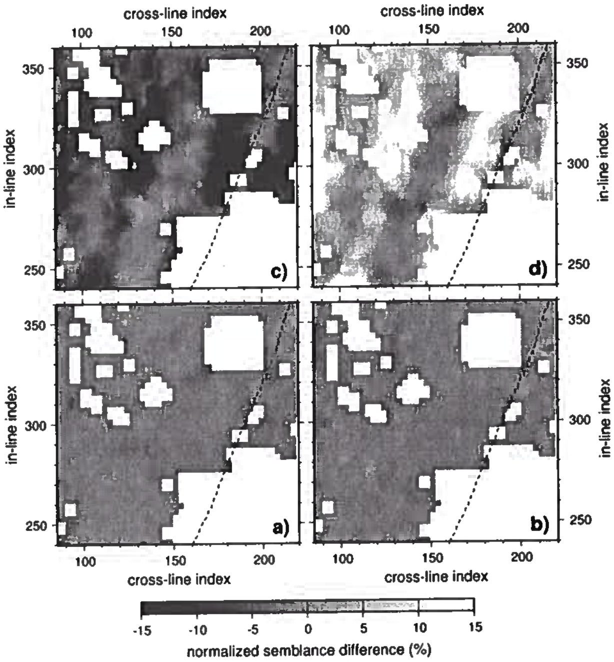

Figure 12. Normalized semblance difference between the nonhyperbolic moveout equation with, and without the correction factor (a), and between the [2/2] rational interpolation method and the nonhyperbolic moveout equation method without the correction factor (b), for a maximum offset of 2250 m, i.e., ODR≈ 2. Subfigures c and d are as a and b, respectively, except for a maximum offset of 4500 m, i.e., ODR≈ 4.

In conclusion, for a maximum ODR larger than two, the [2/2] rational interpolation method provided generally improved moveout correction, improved semblance values, and more spatially continuous estimates of η for this field data example. This supports the applicability of the rational interpolation method to a horizontally layered VTI medium, observed on synthetic data in the previous section. As the numerical tests showed similar results, we expect these findings to generalize to other datasets. For maximum ODR up to two, all methods had similar ability to flatten the gathers, but the nonhyperbolic moveout equation approach gave comparable estimates of η to those of the the rational interpolation method only when the optimal correction factor was used.

Discussion

We have shown that for ODR values up to 8, the [2/2] rational interpolation results in an accuracy of $O(10^{-1})\%$ of t_0 for most models of practical interest. If higher accuracy is desired, or accuracy up to larger ODR is needed (e.g., in near-surface seismic experiments), higher-order polynomials can be used in the rational approximation. The added computation time for inclusion of several extra terms is negligible; hence the efficiency of the proposed method remains essentially the same. We have not done any numerical testing for polynomials of order higher than two.

In the field data example, we treat the overburden of the reflection event of interest as a single horizontal homogeneous VTI layer. As a result, the estimated values of η and V_{NMO} are effective parameters. The geological significance of such effective quantities is difficult to establish, and an approach assuming a layered overburden and resulting interval estimates of η and V_{NMO} would remove this difficulty. Although we do not demonstrate such an approach in this paper, we believe that such an approach is feasible by applying rational interpolation in a layer-stripping fashion. We leave the verification of this idea to a future study. Meanwhile, the single-layer approach outlined here can be used to obtain more accurate estimates of the average (or effective) values of η and V_{NMO} in layered media. Using these values in current Dix-type averaging procedures could lead to better interval estimates of these parameters.

We showed that our rational interpolation approach achieves accuracy almost identical to that of the shifted hyperbola approximation of Fomel (2004). Since we show the applicability of the rational interpolation method to horizontally layered VTI media, the almost identical accuracy of both methods implies the applicability of the shifted hyperbola approximation of Fomel to such media also. For horizontally layered media, a plane-wave decomposition, obtained through a $\tau - p$ transform, is the natural decomposition of the data. This fact was successfully used by Van der Baan and Kendall (2002) and Van der Baan (2004), to obtain interval estimates of η and V_{NMO} from moveout in the $\tau - p$ domain. Even though they successfully estimate interval values of η and V_{NMO}, the acquisition geometry does not always allow a straightforward $\tau - p$ transform. Therefore, there is room to try to extend our $t - x$ based rational interpolation method to render interval estimates of η and V_{NMO}.

The geometry of straight rays involved in velocity analysis for a horizontal homogeneous layer and the geometry of the rays associated with point scattering in a medium with constant velocity are identical. Therefore, the rational interpolation method proposed here is immediately applicable to the problem of post-stack and pre-stack time-migration in VTI media. Larger offsets in the context of moveout velocity analysis are the equivalents of steeper dips in time-migration. Therefore, the increased accuracy for large maximum ODR provided by the rational interpolation for traveltimes of qP-waves in such media suggests improved accuracy when the rational interpolation scheme is used in imaging of steep reflectors in the context of pre and post-stack time-migration in VTI media.

Conclusions

We have presented a rational interpolation approach to nonhyperbolic moveout correction of qP-waves in VTI media. The accuracy of the method was tested using both synthetic and field data and compared with that of the nonhyperbolic moveout equation, which is the current standard in seismic data processing. Both synthetic and field data results confirm that our method significantly outperforms the nonhyperbolic moveout equation in both unbiased parameter estimation and the quality of moveout correction when a maximum ODR larger than two is used. For a single horizontal VTI layer, and for a maximum ODR up to four, the errors from the [2/2] rational interpolation are $O(10^{-2})\%$ of t_0 or less; this is one to two orders of magnitude more accurate than the nonhyperbolic moveout equation of Tsvankin and Thomsen (1994). Even for a maximum ODR up to 8, the traveltime errors resulting from the [2/2] rational interpolation are $O(10^{-1})\%$ of t_0, for virtually all models of practical interest.

Under the customary assumptions that traveltimes of qP-waves in VTI media depend mainly on η and V_{NMO}, and that the influence of V_{S0} on traveltimes of qP-waves in TI media is negligible, we found that the traveltimes in a single horizontal VTI layer, for fixed group-angle, η, and t_0, are independent of V_{NMO}, while the associated offsets are linear in V_{NMO}. As a consequence, therefore, the nonhyperbolic moveout curve for different values of V_{NMO}, but fixed η and t_0, can be calculated by simple horizontal stretching or squeezing, i.e., along the offset axis, where the amount of stretch or squeeze is determined by the change in V_{NMO}. This observation allows us to calculate the traveltimes needed for the interpolation from a small number of traveltimes for a reference value of t_0 (conveniently $t_0^{ref} = 1$ s) and η values ranging from -0.2 to 1.0 in steps of, say, 0.01. This range of η covers most models of practical interest. The few hundred traveltimes for a reference value of t_0 and η values ranging from -0.2 to 1.0, can be precomputed in about a minute on a modern PC and stored in a table. Therefore, the rational interpolation method has no additional computational overhead compared to that of the nonhyperbolic moveout equation method.

We show that the observation of the stretch-squeeze influence of V_{NMO} on the nonhyperbolic moveout causes the correction factor C in the Alkhalifah-Tsvankin nonhyperbolic moveout equation (2) to be independent of V_{NMO}, under the above-mentioned approximations.

This correction factor therefore depends on η and maximum ODR only. We calculated this correction factor for $0 \leq \eta \leq 1$ and maximum ODR between one and four, and presented a contour plot of $C(\eta, ODR)$. If one wants to get the best use out of the Alkhalifah-Tsvankin nonhyperbolic moveout equation (2), this plot can be used in practice to determine the optimal correction factor in the following way; first estimate η and V_{NMO} with the nonhyperbolic moveout equation without the correction factor, then use the estimated V_{NMO} to estimate the maximum ODR using equation (14), and subsequently determine the optimal value of C from Figure 3 using the estimated k and η. For maximum ODR up to four and large levels of anellipticity, tests with synthetic data showed that this correction factor works well to reduce the bias in η that would be obtained if the nonhyperbolic moveout equation without this correction factor was used. The field-data example confirmed this for maximum ODR up to two, but the presence of AVO variation for offsets with maximum ODR between two and four caused this method to fail for ODR up to four. For maximum ODR less than two, this reduction in bias goes together with largely accurate moveout correction, even for strong anellipticity. For ODR up to four, however, the reduction in bias of η goes together with significant distortion in the moveout correction caused by the inaccuracy of the nonhyperbolic moveout equation. In this case the Alkhalifah-Tsvankin nonhyperbolic moveout equation fails to accurately flatten the CMP gathers. The rational interpolation method combines unbiased estimates of η and V_{NMO} with accurate moveout correction in all cases.

From synthetic tests and field data, we found that straightforward application of the correction factor $C = 1.2$, recommended by Grechka and Tsvankin (1998), typically leads to less than satisfactory results. For maximum ODR=4 and $\eta \lesssim 0.1$, the shortcomings in moveout correction and estimated values of η obtained using the nonhyperbolic moveout equation approach without the correction factor are small and probably negligible from a practical point of view. Even though in this particular case satisfactory results can be obtained with the Alkhalifah-Tsvankin nonhyperbolic moveout equation, straightforward application of the rational interpolation method combines unbiased parameter estimation with accurate moveout correction, for arbitrary ODR ranges and arbitrary levels of anellipticity.

Acknowledgment

The authors thank Devon Energy and Mike Ammerman for permission to show these data and Scott Schapper for generating the residual topography map shown in Figure 9c. The careful and critical reviews by Ken Larner and Ilya Tsvankin are much appreciated, as well as the valuable discussions with Ilya Tsvankin, Ken Larner, Vladimir Grechka, Pawan Dewangan, and Ivan Vasconcelos. The first author thanks Matt Haney for pointing out that the nonhyperbolic moveout approximation of Tsvankin and Thomsen (1994) resembles a Padé approximation, thus leading him to study rational approximants.

REFERENCES

Alkhalifah, T. 1997. Velocity analysis using nonhyperbolic moveout in transversely isotropic media. *Geophysics*, **62**, 1839–1854.

Alkhalifah, T. 1998. Acoustic approximations for processing in transversely isotropic media. *Geophysics*, **63**, 623–631.

Alkhalifah, T. 2000. An acoustic wave equation for anisotropic media. *Geophysics*, **65**, 1239–1250.

Alkhalifah, T., & Tsvankin, I. 1995. Velocity analysis for transversely isotropic media. *Geophysics*, **60**, 1550–1566.

Alkhalifah, T., Tsvankin, I., Larner, K., & Toldi, J. 1996. Velocity analysis and imaging in transversely isotropic media: methodology and a case study. *The Leading Edge*, **15**, 371–378.

Baker, G.A. Jr. 1975. *Essentials of Padé Approximations.* Academic Press, Inc., New York.

Baker, G.A. Jr., & Graves-Morris, P. 1981a. *Padé Approximants, part I: Basic Theory.* Addison-Wesley.

Baker, G.A. Jr., & Graves-Morris, P. 1981b. *Padé Approximants, part II: Extensions and Applications.* Addison-Wesley.

Coleman, T.F., & Li, Y. 1994. On the Convergence of Reflective Newton Methods for Large-Scale Nonlinear Minimization Subject to Bounds. *Mathematical Programming*, **67**, 189–224.

Coleman, T.F., & Li, Y. 1996. An Interior, Trust Region Approach for Nonlinear Minimization Subject to Bounds. *SIAM Journal on Optimization*, **6**, 418–445.

Dellinger, J., Muir, F., & Karrenback, M. 1993. Anelliptic approximations for TI media. *J. Seis. Expl.*, **2**, 23–40.

Fomel, S. 2004. On anelliptic approximations for qP velocities in VTI media. *Geophysical Prospecting*, **52**, 247–259.

Fowler, P.J. 2003. Practical VTI approximations: a systematic anatomy. *Journal of Applied Geophysics*, **54**, 347–367.

Graves-Morris, P.R., & Hopkins, T.R. 1981. Reliable rational interpolation. *Num. Math*, **36**, 111–128.

Grechka, V., & Tsvankin, I. 1998. Feasibility of nonhyperbolic moveout inversion in transversely isotropic media. *Geophysics*, **63**, 957–969.

Helbig, K. 1983. Elliptical anisotropy - its significance and meaning. *Geophysics*, **48**, 825–832.

Jones, L.E.A., & Wang, H.F. 1981. Ultrasonic velocities in Cretaceous shales from the Williston Basin. *Geophysics*, **46**, 288–297.

Sayers, C.M. 1994. The elastic anisotropy of shales. *J. Geophys. Res.*, **99 (B1)**, 767–774.

Schoenberg, M. A., & de Hoop, M.V. 2000. Approximate dispersion relations for qP-qSV waves in transversely isotropic media. *Geophysics*, **65**, 919–933.

Stovas, A., & Ursin, B. 2004. New travel-time approximations for a transversely isotropic medium. *J. Geophys. Eng.*, **1**, 128–133.

Thomsen, L. 1986. Weak elastic anisotropy. *Geophysics*, **51**, 1954–1966.

Toldi, J., Alkhalifah, T., Berthet, P., Arnaud, J., Williamson, P., & Conche, B. 1999. Case study of estimation of anisotropy. *The Leading Edge*, **18**, 588–593.

Tsvankin, I. 1996. P-wave signatures and notation for transversely isotropic media: An overview. *Geophysics*, **61**, 467–483.

Tsvankin, I. 2001. *Seismic signatures and analysis of reflection data in anisotropic media.* Elsevier Science Ltd.

Tsvankin, I., & Thomsen, L. 1994. Nonhyperbolic reflection moveout in anisotropic media. *Geophysics*, **59**, 1290–1304.

Van der Baan, M. 2004. Processing of anisotropic data in the $\tau - p$ domain: I-Geometric spreading and moveout corrections. *Geophysics*, **69**, 719–730.

Van der Baan, M., & Kendall, J. M. 2002. Estimating anisotropy parameters and traveltimes in the τ-p domain. *Geophysics*, **67**, 1076–1086.

Wookey, J., Van der Baan, M., Smit, D., & Kendall, J.-M. 2002. Tau-p domain VTI parameter inversions using limited-offset data. *Page F041 of: Extended Abstracts, 64th Meeting, European Association of Geoscientists and Engineers.*

Zhang, F., & Uren, N. 2001. Approximate explicit ray velocity functions and travel times for P-waves in TI media. *Pages 106–109 of: Expanded abstracts of the 71 Ann. Internat. Mtg. Soc. of Expl. Geophys, San Antonio, Texas, USA.*

APPENDIX A: [2/2] RATIONAL INTERPOLATION FOR NONHYPERBOLIC MOVEOUT IN A SINGLE HORIZONTAL VTI LAYER

Using the definition and normalization of the rational approximation outlined in the main text, we can write the [2/2] rational approximation for squared traveltimes T as a function of squared offset X as

$$T(X) \approx \frac{T_0 + n_1 X + n_2 X^2}{1 + d_1 X + d_2 X^2} \quad , \tag{A1}$$

where $T_0 = t_0^2$ is the squared zero-offset two-way traveltime, and $n_{1,2}$ and $d_{1,2}$ are the coefficients of the numerator and denominator of the rational approximant, respectively. Using four squared traveltimes $T_i = t_i^2$, with $i = 1, \ldots, 4$, and four accompanying squared offsets $X_i = x_i^2$ as interpolation points, we arrive at a linear system of four equations with four unknowns, the coefficients $n_{1,2}$ and $d_{1,2}$. Since there are only four coefficients, we simply solve (using Mathematica) for the coefficients in terms of T_i, X_i, and T_0. The resulting expressions for the coefficients are given by

$$\begin{aligned}
d_1 \quad = \quad & ((T_0 - T_4)X_1X_2X_3(T_1X_1(X_2 - X_3) + \ldots \\
& T_3X_3(X_1 - X_2) + T_2X_2(X_3 - X_1)) - \ldots \\
& ((T_1 - T_2)(T_0 - T_3)X_1^2X_2^2 + \ldots \\
& ((T_2 - T_0)(T_1 - T_3)X_1^2 + \ldots \\
& (T_0 - T_1)(T_2 - T_3)X_2^2)X_3^2)X_4 + \ldots \\
& ((T_0 - T_3)X_1X_2(T_1X_1 - T_2X_2 + \ldots \\
& T_4(X_2 - X_1)) - ((T_0 - T_2)(T_1 - T_4)X_1^2 - \ldots \\
& (T_0 - T_1)(T_2 - T_4)X_2^2)X_3 + \ldots \\
& (T_3 - T_4)(T_1X_2 - T_2X_1 + \ldots \\
& T_0(X_1 - X_2))X_3^2)X_4^2)/\ldots \\
& (X_1X_2X_3(T_2(T_3(X_2 - X_3)(X_1 - X_4) - \ldots \\
& T_4(X_1 - X_3)(X2 - X4)) + \ldots \\
& T_1(T_4(X_2 - X_3)(X_1 - X_4) - \ldots \\
& T_3(X_1 - X_3)(X_2 - X_4) + \ldots \\
& T_2(X_1 - X_2)(X_3 - X_4)) + \ldots \\
& T_3T_4(X_1 - X_2)(X_3 - X_4))X_4) \ ,
\end{aligned} \tag{A2}$$

$$\begin{aligned}
d_2 \quad = \quad & (-T_0(X_1 - X_2)(X_1 - X_3)(X_2 - X_3) + \ldots \\
& T_3X_1X_2(X_1 - X_2)(1 + d_1X_3) + \ldots \\
& X_3(T_1X_2(1 + d_1X_1)(X_2 - X_3) + \ldots \\
& T_2X_1(1 + d_1X_2)(X_3 - X_1)))/\ldots \\
& (X_1X_2X_3(T_2X_2(X_1 - X_3) + \ldots \\
& T_3X_3(X_2 - X_1) + T_1X_1(X_3 - X_2))) \ ,
\end{aligned} \tag{A3}$$

$$\begin{aligned}
n_2 \quad = \quad & T_0(X_1 - X_2) + \ldots \\
& T_1(1 + X_1(d_1 + d_2X_1))X_2 - \ldots \\
& T_2X_1(1 + X_2(d_1 + d_2X_2))/\ldots \\
& X_1X_2(X_1 - X_2) \ ,
\end{aligned} \tag{A4}$$

$$n_1 \quad = \quad T_1d_1 - \frac{T_0 - T_1}{X_1} - (n_2 - d_2T_1)X_1 \ . \tag{A5}$$

Note that only the expression for d_1 is explicit in just T_i, X_i, and T_0, whereas d_2 also depends on d_1, n_2 on $d_{1,2}$, and n_1 on n_2 and $d_{1,2}$. Calculating the coefficients $n_{1,2}$ and $d_{1,2}$ using the above expressions and the interpolation traveltimes t_i and offsets x_i, we can use the resulting values of $n_{1,2}$ and $d_{1,2}$ in equation (A1) to evaluate interpolated traveltimes t for offsets x between offsets x_i.

A method for inverse scattering based on the generalized Bremmer coupling series: Practical issues and examples

Alison E Malcolm*, Maarten V. de Hoop* and Henri Calandra†
*Center for Wave Phenomena Colorado School of Mines, Golden, CO 80401, USA
† Total Exploration and Production, Geophysical Research Group 800 Gessner Suite 700
Houston, TX

ABSTRACT

First order internal multiples are a source of coherent noise in seismic images. There are a number of techniques to estimate internal multiples in the data, but few methods exist that estimate imaging artifacts caused by internal multiples. We propose a method to do this in which the artifacts are estimated as part of the imaging process. Our technique is based on a hybrid of the Lippmann-Schwinger scattering series and the generalized Bremmer coupling series. Although we require knowledge of the velocity model this allows us to estimate internal multiples without assumptions inherent to other methods.

Key words: internal multiple attenuation, Bremmer series, downward continuation, imaging artifacts

1 INTRODUCTION

Internal multiples have been recognized as a problem in seismic experiments for a long time (Sloat, 1948). Although there are many techniques to attenuate these multiples in seismic data (Buttkus, 1979; Fokkema *et al.*, 1994; Berkhout & Verschuur, 1997; Verschuur & Berkhout, 1997; Weglein *et al.*, 1997; Jakubowicz, 1998; Kelamis *et al.*, 2002; ten Kroode, 2002; van Borselen, 2002) it is still not possible to estimate multiples in data with sufficient accuracy to remove all the errors they introduce in seismic images. Techniques like the angle-domain filtering proposed by (Sava & Guitton, 2005) are promising because they attenuate multiples directly in the image as opposed to in the data. In this way, even though the multiples are still not completely removed their location in the image is known. Thus, they are less likely to be misinterpreted as primary reflection energy. In this paper, we propose a technique for estimating imaging artifacts caused by internal multiples as part of the imaging process.

Fokkema & van den Berg (1993) use reciprocity to show the possibility of modeling surface-related multiples through a Neumann series expansion. Here, we use a related technique based on a hybrid of the Lippmann-Schwinger and Bremmer series to estimate internal multiples as part of the imaging process. Using a hybrid of the two series allows us to construct an inverse series following the ideas of the Lippmann-Schwinger series, while maintaining a structure consistent with the, convergent, Bremmer series. Because we estimate artifacts in the image rather than the data, we require knowledge of the velocity model. Technically this knowledge is necessary only to the depth of the shallowest reflector involved in the internal multiple (the depth of the up-to-down reflection). Our technique is similar to that of Jakubowicz (1998) in that it uses the techniques of so-called wave-equation migration to model internal multiples. Our method differs from Jakubowicz (1998) in that we propose to estimate the artifacts caused by first order internal multiples in the image rather than estimating the multiples in the data. In addition, Jakubowicz uses implicitly a version of the generalized Bremmer series (de Hoop, 1996) whereas we use a hybrid of the Lippmann-Schwinger and Bremmer series.

The Lippmann-Schwinger series is introduced by Lippmann (1956) to model particle scattering. In the

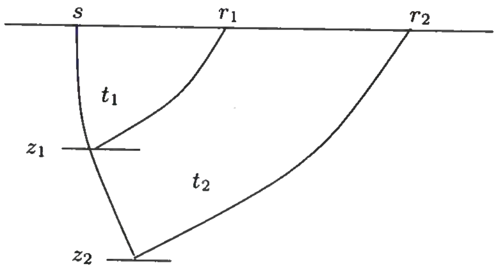

Figure 1. Illustration of the traveltime monotonicity assumption. The assumption states that if $z_1 < z_2$ then $t_1 < t_2$.

development of this series the wave-equation is solved in a known background model, with successive terms in the series being of successively higher order in the contrast operator. The contrast operator is the difference between the operator in the known background model and the true model. This idea is developed further by Moses (1956), and Prosser (1969); and Razavy (1975) where the series is developed for the quantum scattering problem. Weglein *et al.* (1997) uses this series to develop techniques for both surface and internal multiple attenuation; they choose water velocity as the known reference model. ten Kroode (2002) describes the mathematics behind this approach. In particular he notes that the suggested method requires two assumptions. The first assumption is that there are no caustics in the wavefield and the second is the so-called traveltime monotonicity condition. This condition is illustrated in Figure 1 and states that a wave excited at s and scattered at depth z_1 will arrive at the surface in less time than a wave following the same path from s to z_1, but scattering at z_2 instead, whenever z_1 is shallower than z_2.

The Bremmer series was introduced for planarly layered models by Bremmer (1951) and generalized to laterally heterogeneous models by de Hoop (1996). In the Bremmer series, the wavefield is split into up- and down-going constituents; these constituents are then coupled through reflection and transmission operators. Each term involves one more reflection/transmission and propagation step than the previous term. The first term of the series models direct waves, the second models singly scattered (where scattering may be reflection or transmission) waves and so on. The Bremmer series has been applied in many problems (see van Stralen (1997) for an overview) and the convergence of various generalizations of the original series has also been a subject of interest (Atkinson, 1960; Corones, 1975; Gray, 1983; McMaken, 1986). Aminzadeh & Mendel (1980; 1981) propose a method, using the Bremmer series, to attenuate surface-related multiples in a horizontally layered medium.

To estimate artifacts in the image caused by first-order internal multiples (FOIM), we proceed in two steps. We first develop a method to model FOIM, using the hybrid series; this is described in Section 2. Next, we use the modeled FOIM to estimate the artifacts they cause in the image, using ideas from the inverse series in Section 3. In Section 4 we describe an algorithm to perform these two steps at the same time. We illustrate the application of this algorithm to synthetic data in Section 5.

2 THE SCATTERING SERIES

We begin by decomposing the wavefield into its up- and down-going constituents. Following Stolk & de Hoop (2004a), we define

$$\mathsf{Q} = \frac{1}{2}\begin{pmatrix} (Q_+^*)^{-1} & -\mathcal{H}Q_+ \\ (Q_-^*)^{-1} & \mathcal{H}Q_- \end{pmatrix}, \qquad (1)$$

where $\mathcal{H}$ denotes the Hilbert transform in time and * denotes adjoint. This operator relates the propagator for the full wave equation, G, to the propagator for the up-going one way equation, G_-, ($-$ denotes an up-going constituent and $+$ a down-going constituent) via

$$G = Q_-^* G_- \mathcal{H} Q_- \,. \qquad (2)$$

The Q matrix, along with its inverse, diagonalizes the wave operator written as a first order system and thus splits the wavefield into its up- and down-going constituents. The wavefield in the diagonal system, $u_\pm$ is related to the full wavefield, u, via

$$u = Q_+^* u_+ + Q_-^* u_- \,, \qquad (3)$$

applying the Q^{-1} matrix to the the vector $(u_+, u_-)^T$.

Denoting by U_j the vector $(u_{+,j}, u_{-,j})^T$ of up- and down-going wave constituents scattered j times, the terms in the hybrid forward scattering series are related by

$$\delta U_1(\widehat{V}) = D_t^2 \mathsf{L}_0(\widehat{V} U_0), \qquad (4)$$

and

$$\delta U_m(\widehat{V}) = D_t^2 \mathsf{L}_0(\widehat{V} \delta U_{m-1}(\widehat{V})).$$

Here $\widehat{V}$ represents a matrix of reflectivities, and

$$\mathsf{L}_0 = \begin{pmatrix} G_+ & 0 \\ 0 & G_- \end{pmatrix} \qquad (5)$$

denotes the matrix of one-way propagators evaluated in the background velocity model. We use a subscript 0 to indicate the field in the background model and δ to represent a contrast, thus the field U in the true medium is related to that in the background medium by $U = U_0 + \delta U$. Denoting by R the restriction of the wavefield to the acquisition surface (depth $z = 0$), we define $\mathsf{M}_0 = R\mathsf{Q}^{-1}\mathsf{L}_0$. The data are then modeled as

$$\delta D = \begin{pmatrix} d \\ \partial_z d \end{pmatrix} = -D_t^2 \mathsf{M}_0(\widehat{V}(U_0 + \sum_{m \in \mathbb{N}} (-1)^{m+1} \delta U_m(\widehat{V}))). \qquad (6)$$

The leading order term on the right-hand side represents the singly scattered or Born contribution. This contribution is written explicitly in terms of the propagator H of the double-square-root (DSR) (Claerbout, 1985) equation as

$$\begin{aligned} d_1(s_0, r_0, t) \quad = \quad & \tfrac{1}{4} D_t^2 Q^*_{-,r_0}(0) Q^*_{-,s_0}(0) \\ & \int_0^\infty \mathrm{d}z_1 H(0,z) Q_{-,r_1}(z_1) Q_{-,s_1}(z_1) \\ & (E_1 E_2 a)(z_1, s_1, r_1, t_0)\,, \end{aligned} \tag{7}$$

where

$E_1 \quad : k(z,x) \mapsto \delta(r-s) k(z, \frac{r+s}{2}),$

$E_2 \qquad : l(z,r,s) \mapsto \delta(t) l(z,r,s).$

We denote by $a = 2c_0^{-3}\delta c$ the velocity contrast, in which c_0 denotes the smooth background velocity and δc denotes the velocity contrast. Together the E_1 and E_2 operators map the velocity contrast at depth to data at depth.

3 INVERSE SCATTERING

In inverse scattering the goal is to solve for $\widehat{V}$ in terms of the data d (cf. (6)). To this end, we assume that the contrast operator $\widehat{V}$ can be written as a series

$$\widehat{V} = \sum_{m \in \mathbb{N}} \widehat{V}_m(d)\,, \tag{8}$$

where $\widehat{V}_m$ is of order m in the data. Substituting this equation into (6) leads to the following relation between the $\widehat{V}_m(d)$,

$$D_t^2 \mathsf{M}_0(\widehat{V}_m U_0) = D_t^4 \mathsf{M}_0(\widehat{V}_{m-1} \mathsf{L}_0(\widehat{V}_1 U_0))\,. \tag{9}$$

From this it follows that

$$-D_t^2 \mathsf{M}_0(\widehat{V} U_0) = \delta D - \left(\sum_{m \in \mathbb{N}} D_t^2 \mathsf{M}_0(\widehat{V}_m \delta U) \right)\,. \tag{10}$$

If we ignore the second term on the right-hand side, the problem of expressing $\widehat{V}$ in terms of the data reduces to inverse scattering in the Born approximation (Stolk & de Hoop, 2004b). In the context of wave-equation migration, the inverse scattering procedure is split into two parts: downward continuation and imaging.

We apply the adjoint propagator $H(0,z)^*$ to the modeled data in (7) yielding the downward continued data at depth z, for $t > 0$

$$\tilde{d}_1(z) = H(0,z)^* Q^*_{-,s}(0)^{-1} Q^*_{-,r}(0)^{-1} d\,. \tag{11}$$

This downward continuation uses the usual migration velocity model to estimate the data that would have been recorded at the depth z. Next, we apply the imaging condition to the downward continued data

$$a_1(z,.) = M\tilde{d}_1(z) \tag{12}$$

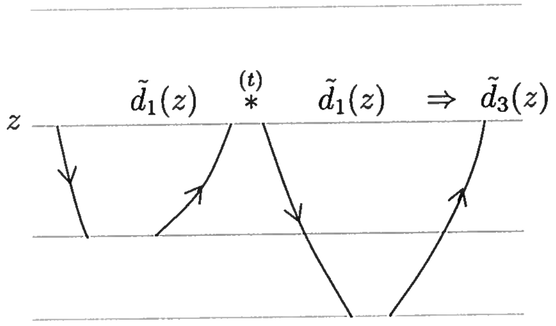

Figure 2. Illustration of equation 13, the estimation of the multiple at the depth z. The lines represent wavepaths rather than rays and do not connect as the imaging condition has not been applied.

where M is the imaging operator discussed by Stolk & de Hoop (Stolk & de Hoop, 2004a). We apply (11)-(12) to (10), from which we obtain an image (first term on the right-hand side) minus artifacts (second term). We compare our method with that of Weglein *et al.* (1997) and ten Kroode (2002) in Appendix B of Malcolm & de Hoop (2005).

The removal of negative times in the construction in (11) is an important step in our algorithm. It can also be computationally expensive to do this because windowing in time requires returning to the time domain. It is also this step that, in practice, imposes a limitation on the thickness of the multiple generating layer from which we can estimate multiples. To be able to attenuate internal multiples in a certain layer it is necessary to be able to remove the primary from the top of the layer without attenuating the reflection from the bottom of the layer.

4 ARTIFACTS DUE TO INTERNAL MULTIPLES IN IMAGING

First modeling internal multiples in the data and then constructing an estimate of the artifacts in the image is computationally expensive. The modeling step requires several propagation steps through the velocity model in addition to the cost of a depth migration needed to estimate artifacts in the image. To avoid these computational costs, we propose an algorithm summarized by the following flow chart

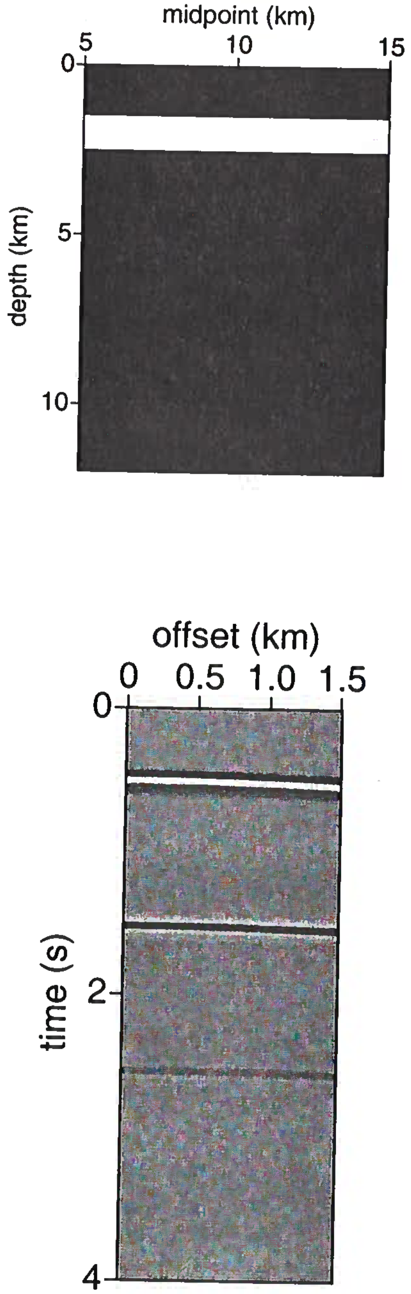

Figure 3. Top: Velocity model for flat example. Bottom: Surface data (CMP) for flat example.

$$\begin{tikzcd}
 & d \arrow[d, "(a)"'] & & \\
a_1(z.,) \arrow[rr, bend left=60, "(e)"] & \tilde{d}_1(z) \arrow[l, "(d)"'] \arrow[r, "(b)"] \arrow[d, "(c)"'] & \tilde{d}_3(z) \arrow[r, "(f)"] \arrow[d, "(c)"] & a_3(z,.) \\
 & \tilde{d}_1(z+\Delta z) \arrow[r, "(+)"] & \tilde{d}_3(z+\Delta z)\,. &
\end{tikzcd}$$

The algorithm can be divided into several steps. First, in (a), we downward continue the data to the depth z. Next we form an estimate, $a(z,x)$, of image from the data in (d). This estimate is used, in (b), to model the internal multiple downward continued to depth z via,

$$\tilde{d}_3(z,s,r,t) = D_t^2 \int Q^*_{-,s'}(z)(E_1 a)(z,s',r')Q^*_{-,r'}(z)$$
$$\tilde{d}_1(z,s',r,\cdot) \overset{(t)}{*} \tilde{d}_1(z,s,r',\cdot)\mathrm{d}s'\mathrm{d}r'\,. \tag{13}$$

Expression (13) is valid upon restricting $\tilde{d}_1$ to $t > 0$ and assumes a point source. If the point source assumption is not satisfied, an estimate of the wavelet should be deconvolved from the estimated multiple. Equation (13) is illustrated in Figure 2. Note the similarity between this expression and that used in the surface-related multiple elimination (SRME) procedure of Fokkema & van den Berg (1993) and Berkhout & Verschuur (1997). An estimate of the artifacts in the image is also made at the current depth in (f).

We then downward continue both the data and the estimated multiples to the next depth. To downward continue the multiples, d_3, we make use of the relation

$$d_3(s_0,r_0,t) = Q^*_{-,r_0}(0)Q^*_{-,s_0}(0)\int_0^\infty \mathrm{d}z H(0,z)\tilde{d}_3(z,.)\,, \tag{14}$$

which states that the multiple, d_3 can be estimated at the surface, $z = 0$ from the multiple, $\tilde{d}_3$ estimated at the depth z. Using relation (14) along with (11) we find that artifact in the image caused by FOIM at the depth z can be estimated by

$$a_3(z,.) = M\tilde{d}_3(z)\,, \tag{15}$$

the analog of (12). This step is (f) of the flowchart. The entire procedure is repeated for subsequent depths, with the estimated multiples at the depth $z+\Delta z$ being added to the multiples downward continued from depth z.

5 EXAMPLES

We begin with a simple, layered, example to illustrate the theory and then proceed to more complicated examples. The first example is a single layer, 1 km thick extending from 1.5 to 2.5 km, with a velocity of 2 km/s embedded in a homogeneous model with velocity 6 km/s.

Synthetic data were computed in this model with finite difference modeling, 101 midpoints were generated with 101 offsets at each midpoint and a spacing of 15 m in both midpoint and offset (we define offset as $(s-r)/2$); 4 seconds of data were recorded at 4 ms sampling. Figure 3 shows the velocity model and the modeled data.

In our method, the data are first downward continued as part of a standard wave-equation migration technique ((a) in the flowchart). The algorithm used to generate the examples shown here uses a pseudo-screen propagator with an implicit finite difference wide-angle correction (Jin *et al.*, 1998). In Figure 4 we show $\tilde{d}_1(z = 1.5)$, a single common-midpoint gather (cmp) downward continued to the depth $z = 1.5$ km of the top of the layer. The primary reflected from the top of the layer is located around $t = 0$, the reflection from the bottom of the layer at about $t = 1$ s and the first order internal multiple at about $t = 2$ s.

We now estimate the multiples at depth using (13). This requires restricting $\tilde{d}_1$ to time $t > 0$. The procedure removes the primary reflection from the current depth (which theoretically arrives at $t = 0$), in this case 1.5 km, before doing the convolution. If this process is not done correctly and energy remains at $t \leq 0$, all subsequent primaries will be duplicated in the estimated multiples section. In this model a simple time-windowing procedure is sufficient, because the reflections are far apart in time. In some situations, we find a τ-p filter to be more effective. This is because we typically see diffraction tails at small positive and negative times caused by the band-limited signal and imperfections in the imaging procedure. A τ-p filter is more effective at removing these tails when they are mixed with later reflections. Figure 4 show the results of applying the τ-p filter to the data.

Once the negative time contributions to the data have been removed, the multiple is estimated with (13), through a convolution with the data in a procedure similar to Surface Related Multiple Elimination (SRME) (Fokkema & van den Berg, 1993; Berkhout & Verschuur, 1997; Verschuur & Berkhout, 1997). The convolved wavefield is multiplied by an estimate of the image at the current depth, in this case $z = 1.5$ km (this is the $(E_1 a)(z, s', r')$ appearing in (13)). This completes (b) of the flowchart. The estimated multiple is shown in Figure 5. The event at about $t = 3$ s in the estimated multiple is a second-order internal multiple. This event is formed from the convolution of a primary with a first-order internal multiple. It is not present in the data panel because it arrives later than the final recorded time.

We now proceed to (c) of the flowchart and propagate both the data and the estimated multiples to the next depth. From the data, an image at the current depth is formed containing both primaries and multiples using (12) ((d) of the flowchart). Another image is also computed at the current depth, containing an estimate of the artifacts caused by FOIM, using (15) ((f) of the flowchart). The image containing both primaries and multiples gives the estimate of $a(z, x)$, which feeds back into the estimation of the multiples through (e) of the flowchart.

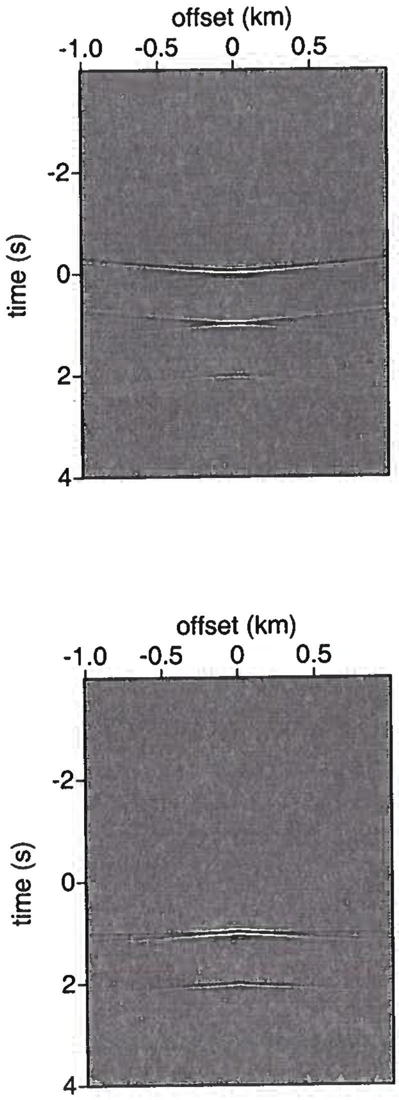

Figure 4. Data downward continued to the 1.5 km, the depth of the first reflector. Top: before the removal of the part of the data at $t \leq 0$. Bottom: after the removal of the part of the data at $t \leq 0$.

Figure 6 compares the estimated multiple to the true multiple. The estimated artifact aligns well with the artifact in the data, despite the fact that we have not accounted for the shape of the source wavelet. (Al-

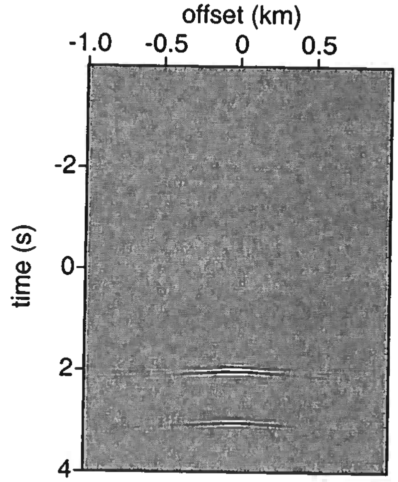

Figure 5. The estimated multiple, in the data, at a depth of 1.5 km; note the agreement with the true multiple in Figure 4.

though the wavelet has not been deconvolved, the data have been shifted so that the peak of the source wavelet is at zero time.)

To illustrate the ability of the method to estimate multiples in more complicated velocity models, we add a low-velocity lens to the model. The resulting velocity model is shown in Figure 7. The layer in this model is the same as the layer in the previous model except that it is 0.5 km deeper to allow more space for the low-velocity lens. The lens is located in the center of the model; it is circular with Gaussian velocity variations, a diameter of 600 m and a maximum contrast of −2 km/s. The addition of the lens has a large influence on the recorded data. A shot record directly above the lens is shown in Figure 8. Note the ringing, perhaps caused by numerical dispersion in the data modeling, that is particularly strong on the multiple. We use a double-square-root propagator that works in midpoint-offset coordinates rather than shot and receiver. To accommodate this choice, we use a subset of the available offsets so that each midpoint has the same number of offsets. The data from a midpoint of 9.8 km are shown in Figure 9. The first arrival is highlighted in this figure to show the triplications caused by the lens more clearly.

To estimate the multiple, we propagate the data to 2 km, the top of the layer, and again show the cmp at midpoint 9.8 km Figure 10 along with the estimated multiples at this depth. Note that the caustic has been removed by the propagation through the lens and that the multiple is accurately estimated. At this point, since we have removed the effects of the lens, the example is essentially the same as the flat case and the multiples are estimated accurately as is shown in Figure 11. Once again, the multiple is relatively weak in the estimated image. This is because of the residual moveout on the common image gather, which is shown in Figure 12.

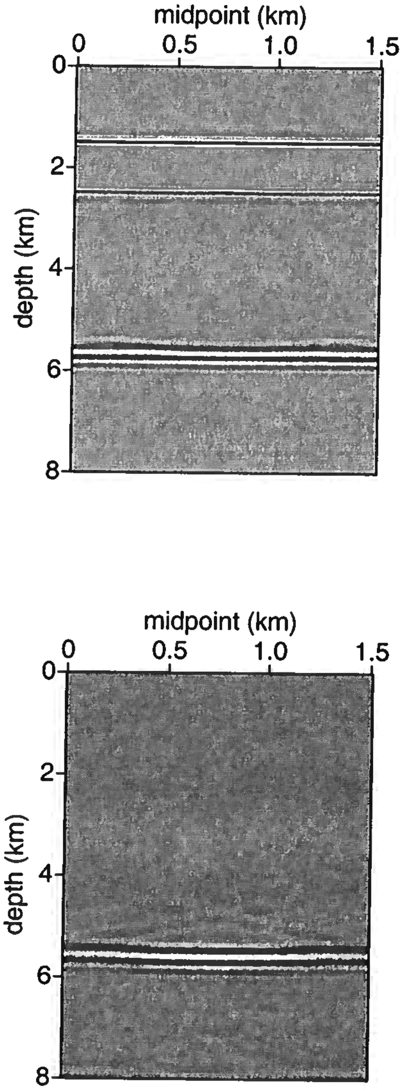

Figure 6. On the top is the image with an artifact from a first-order internal multiple at about 5.7 km depth. On the bottom is the estimated artifact.

To illustrate the dependence of this method on the background velocity model, we perturb the velocity in this section to ascertain the influence of the velocity on the final result. In theory, from equations (14) and (15),

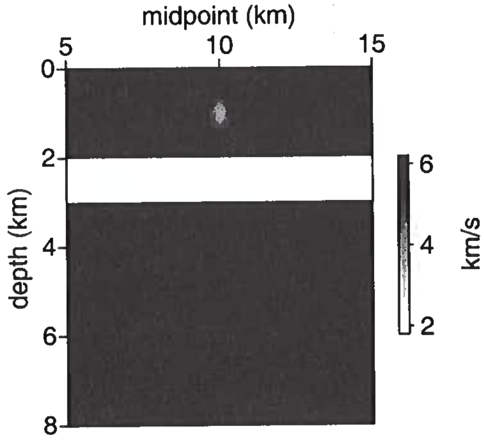

Figure 7. Velocity model, similar to the flat layered example discussed previously, with the addition of a low-velocity lens to demonstrate that the method works in laterally heterogeneous velocity models.

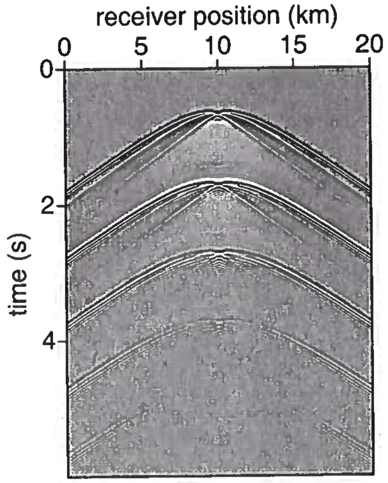

Figure 8. Shot record from $s = 10$ km, directly above the lens. Note the caustic introduced by the lens around zero-offset. The ringing on the second primary (at about 2 s) and the multiple (at about 3 s) is most likely numerical dispersion from the modeling of the data.

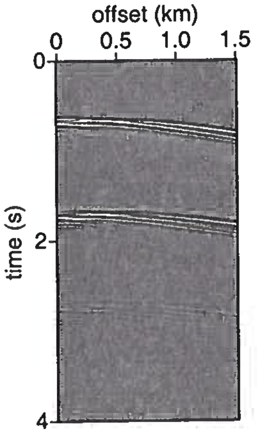

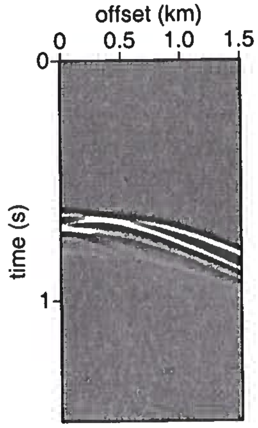

Figure 9. Common midpoint gather at 9.8 km, with only the offsets used to compute the images shown later. Note the triplications caused by the lens. Top: full gather. Bottom: zoom of the primary reflection from the top layer.

knowledge of the velocity is necessary only to the depth of the shallowest reflection, in this case the top of the layer at 2 km depth. To test this we perturb the model in two ways: first we make the layer thicker, and then we add a second lens, with properties identical to the first lens, below the layer. In the first case, we expect the multiple to be imaged at a shallower depth but otherwise to remain unchanged as the perturbation in the velocity is independent of midpoint. Figure 13 shows that we are still able to estimate the artifact accurately despite this error in the velocity model. There is more noise present in the image (left of Figure 13) here than in the correct velocity case (Figure 11). Part of the reason for this is that we have used a smaller agc window

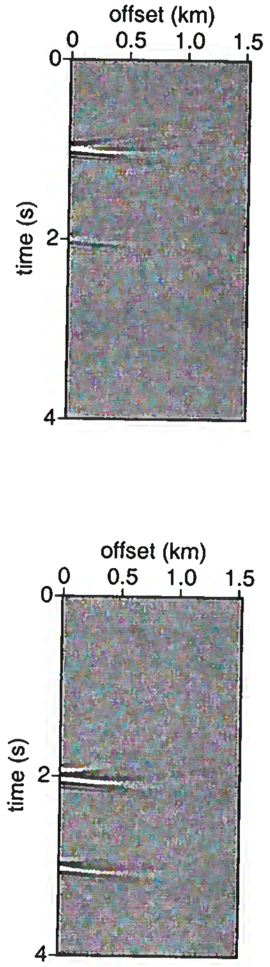

Figure 10. Top: Common midpoint gather at 9.8 km and 2 km depth. Note the disappearance of the multi-pathing as the data are now below the lens. Bottom: estimated multiples at this depth.

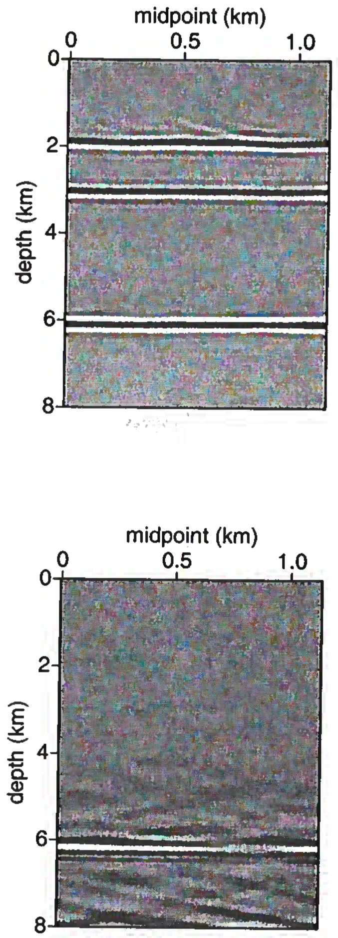

Figure 11. Top: Image with an artifact from the first-order internal multiple at approximately 6 km depth. Bottom: Estimated artifacts from first-order internal multiples.

to enhance the image of the bottom of the layer. In the second case, since the perturbation now depends on midpoint the estimated multiple also depends on midpoint. Although the estimated artifact does not match the image artifact as well in this case as when the correct velocity is used, the estimate remains quite good, as shown in Figure 14.

The theory presented here does require knowledge of the velocity model to the depth of the up to down reflection (top of layer at 2 km depth). To test the sensitivity of the method to errors in this velocity, we remove the lens and estimate the image and the multiple in this incorrect velocity model. The results are shown in Figure 15. Although the estimated artifact remains at roughly the correct depth, there is a phase difference between it and the actual artifact and the variation in the image with midpoint is not accurately estimated. Removing the lens entirely is a large change in the model and thus we expect a large change in the image. In Figure 16, we demonstrate that we can still estimate the multiple with reasonable accuracy when the velocity perturbation is less dramatic. In this case the lens has been moved 0.2 km shallower than in the true velocity model, and with the exception of the phase change between the artifact and our estimate, the result is still good.

The next synthetic model is based on a Shell field in the North Sea. The velocity model is a 2D slice of a 3D velocity model with the steeply dipping reservoir interval added manually. The velocity model is shown in Fig-

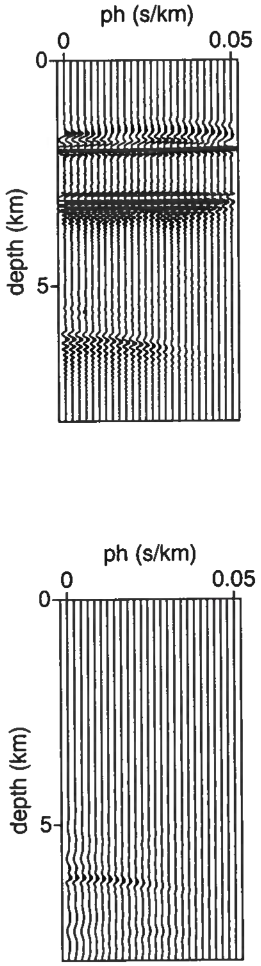

Figure 12. Common image gathers for midpoint 9.8 km. Top: image with artifact. Bottom: estimated artifact.

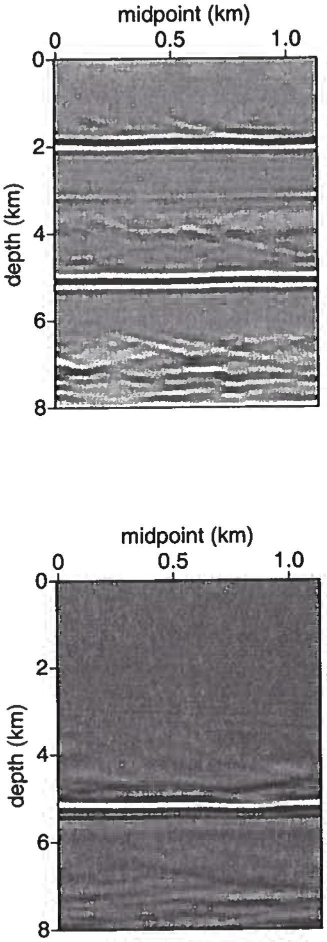

Figure 13. In these images, the reflector has been extended to 3.5 km from 3 km to test the sensitivity of the method to the velocity model. Top: Image with artifacts from internal multiples. Bottom: Estimated artifacts from first-order internal multiples.

ure 17; the chalk layer beginning at about 3 km depth is expected to be the largest generator of internal multiples because of the strong velocity contrast between the chalk and surrounding layers. Some of the layers discussed later are labeled on this figure. The acquisition was designed to simulate a marine experiment. A total of 601 shots were computed with finite differences at a 25 m increment beginning at 15 km and continuing to 30 km. The streamer consists of 241 receivers (hydrophones) spaced at 25 m increments beginning with zero-offset. For the tests shown here we use a subset of 241 midpoints, beginning at 15 km with a spacing of 50 m, with 31 offsets at 50 m spacing beginning at zero-offset. A total of 6 s of data were computed with a 4 ms time sampling interval. A small subset of the available offsets were used to avoid imaging refracted waves visible at long offsets, and to avoid to the extent possible numerical dispersion, which is stronger at larger offsets.

In Figure 18, the data are shown downward continued to a depth of 2.5 km, just above the top of the chalk (the chalk layer is labeled in Figure 17). This figure illustrates that in this instance a simple time windowing is not sufficient. Instead we use a τ-p filter to attenuate the reflection from the top of chalk. By using a τ-p filter rather than a simple time windowing we are also able to apply the filter less frequently as it allows us to remove the entire top of chalk reflection at once, from above the chalk layer.

Figures 19 and 20 compare the estimated artifacts to the true artifacts in the image. The multiples were es-

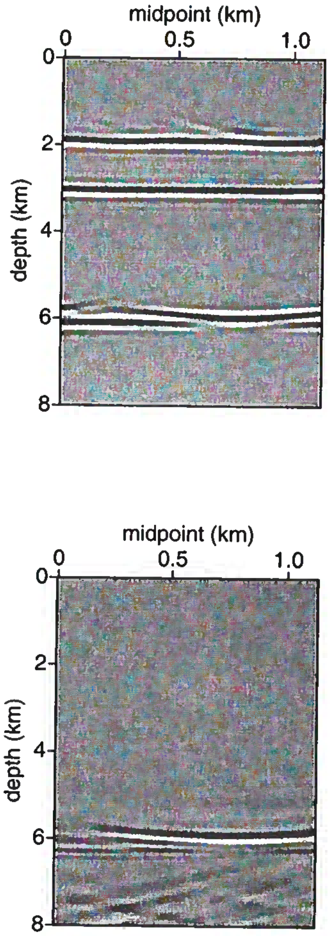

Figure 14. In these images, a second lens has been added beneath the layer to introduce a laterally varying velocity perturbation. Top: Image with artifacts from internal multiples. Bottom: Estimated artifacts from first-order internal multiples.

timated in a depth window from 2.5 to 4.2 km depth and the τ-p filter was applied at 2.5 and 3.25 km. Thus we expect to see the multiples from the top and bottom of the chalk layer. The estimated multiples are imaged at approximately the depth expected based on the velocity model. The multiple at about 4.5 km depth is imaged at the depth expected for an internal multiple entirely within the chalk layer extending from approximately 3 to 4 km depth. The multiples at about 5.5 km are either peg-legs from the bottom of the chalk and the bottom of layer 2 or internal multiples with both deeper scattering points at the bottom of the layer 2. The artifacts caused by these multiples in the image are not easy to see, however, as they are obscured by other ringing in the data.

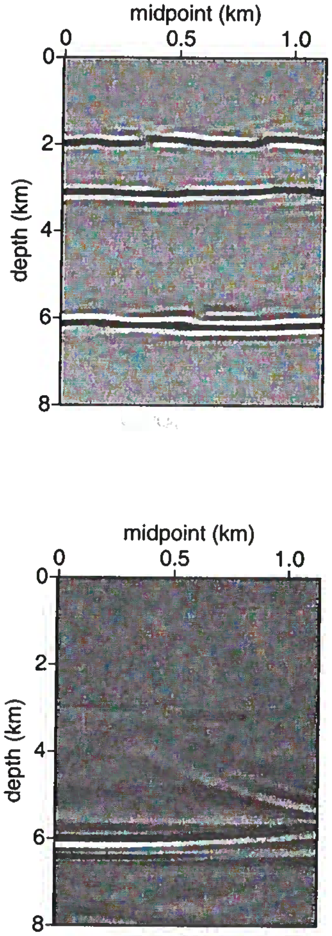

Figure 15. The lens was removed from the velocity model before generating these images. Because this perturbation is above the top of the layer, we expect this to have an impact on the estimated multiple. Note the change in the accuracy of the estimate beneath the lens. Top: Image with artifacts from first-order internal multiples. Bottom: Estimated artifacts from first-order internal multiples.

This ringing does not appear in the estimated artifacts because these estimates are made using the primaries, which arrive at earlier times and are thus less strongly influenced by the ringing. To highlight the multiples as much as possible, we have stacked only the smallest p-values (i.e. the first few traces of the common image gather) to make the image and we have low-passed filtered the image to remove as much of the high-frequency noise visible after the chalk layer as possible, without damaging the imaged structure. In Figure 20 we compare our estimate to one made by ten Kroode (2005), in which he estimates the multiples from the top of the

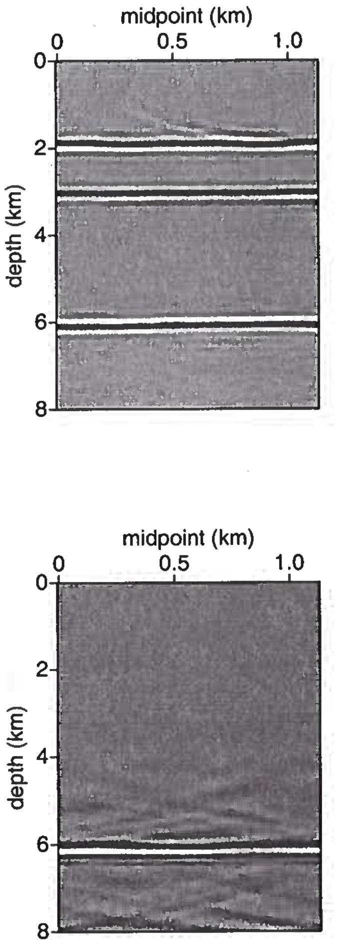

Figure 16. In this model the lens was moved 0.2 km deeper than in the correct velocity model. Because this perturbation is above the top of the layer, we expect this to have an impact on the estimated multiple. Note the phase difference between the estimated artifact and the image. Top: Image with artifacts from first-order internal multiples. Bottom: Estimated artifacts from first-order internal multiples.

chalk layer and compares them to the multiples in the data. This is an extremely coarse comparison as it is not possible to show his image, but the arrows indicate several locations at which artifacts from multiples are present in his image.

6 DISCUSSION

We have described a method to estimate imaging artifacts caused by first-order internal multiples. This method requires knowledge of the velocity model down to the top of the layer that generates the multiple (the depth of the up-to-down reflection). The main computational cost of the algorithm comes from the propagation of the data and the internal multiples. Because two data sets are propagated (the data themselves and the estimated multiples), the cost of the algorithm described here is about twice that of a usual pre-stack depth migration, plus the cost of the removal of negative times. The removal of negatives times can be expensive because it is necessary to return all of the data to the time domain to window the data. Using the τ-p filter reduces this cost because the negative times can be removed less frequently, although the cost of the τ-p transform is much higher than that of a simple time windowing. By estimating the multiple in depth rather than in the data, we avoid difficulties caused by caustics in the wavefield or the failure of the traveltime monotonicity assumption. In addition, estimating artifacts in the image rather than estimating multiples in the data shows clearly which part of the image has been contaminated by internal multiples, even if those multiples are poorly estimated or incompletely subtracted.

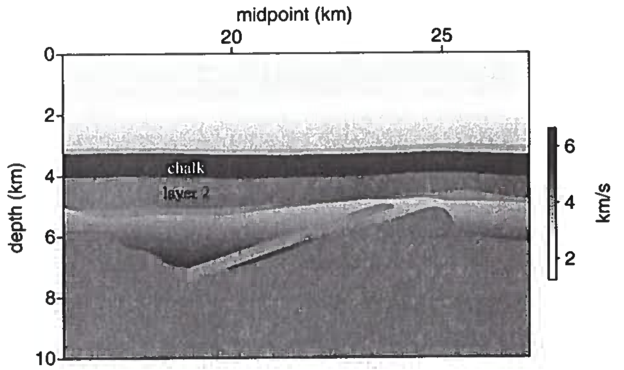

Figure 17. Velocity model for the North Sea example.

7 ACKNOWLEDGMENTS

We thank Total for permission to publish the real data example. We are grateful to Fons ten Kroode and Shell for the North Sea synthetic example. We also appreciate the many helpful discussion with Kris Innanen and Ken Larner as well as the coding assistance from Peng Sheng, Feng Deng, Linbin Zhang and Dave Hale. This work was supported by Total and the sponsors of the Consortium Project on Seismic Inverse Methods for Complex Structures at the Center for Wave Phenomena.

Spurious multiples in seismic interferometry of primaries

Roel Snieder[1], Kees Wapenaar[2], and Ken Larner[1]
[1] *Center for Wave Phenomena, Colorado School of Mines, Golden CO 80401, email rsnieder@mines.edu,*
[2] *Dept. of Geotechnology, Delft University of Technology, Delft, The Netherlands*

ABSTRACT
Seismic interferometry yields the Green's function that accounts for wave propagation between receivers by correlating the waves recorded at these receivers. We present a derivation of this principle based on the method of stationary phase. Although this derivation is applicable to simple media only, it provides insight into the physical principle of seismic interferometry. In a homogeneous medium with one horizontal reflector and without a free surface, the correlation of the waves recorded at two receivers correctly gives both the direct wave and the single-reflected waves. When more reflectors are present a product of the single-reflected waves occurs in the cross correlation that leads to spurious multiples when the waves are excited at the surface only. We give a heuristic argument that these spurious multiples disappear when sources below the reflectors are included. We also extend the derivation to a smoothly varying inhomogeneous background medium.

Key words: siesmic interferometry, stationary phase, multiples

1 INTRODUCTION

Traditionally, imaging techniques are based on the illumination of an object by a coherent source. In many applications coherent sources are not available. Seismic interferometry is a technique in which the Green's function that describes the waves that propagate between two receivers is extracted by computing the correlation of signals recorded at these two receivers. These signals may have been excited by either coherent or incoherent sources. The advantages of this technique are that incoherent noise can be the source of the waves used for imaging and that one can effectively use a wavefield that is excited at one of the receivers, even though no physical source exists at that location.

The first formulation of this technique is due to Claerbout [1968] , who used the phrase "daylight imaging" because the daylight that we use in our vision also provides an incoherent illumination of the objects that we view. His derivation was applicable to layered media. The emergence of the Green's function was subsequently derived for general media using normal-mode theory [Lobkis and Weaver, 2001]. That derivation is applicable only for finite media that have a discrete frequency spectrum. This requirement was relaxed in an alternative derivation based on the representation theorem for one-way wave propagation [Wapenaar et al., 2004], and by using the general representation theorem [Weaver and Lobkis, 2004; Wapenaar, 2004]. Alternative, but equivalent proofs of the emergence of the Green's function have been formulated using the principle of time-reversed imaging [Derode et al., 2003ab; Bakulin and Calvert, 2004; Roux and Fink, 2003]. The relationship between these approaches is shown by Wapenaar et al. [2004] .

The reconstruction of the Green's function from recordings of incoherent signals has been shown observationally using ultrasound [Weaver and Lbkis, 2001; Larose et al., 2004; Malcolm et al., 2004]. Seismic interferometry has been used in helioseismology [Rickett and Claerbout, 1999; Rickett and Claerbout, 2000], in exploration seismology [Bakulin and Calvert, 2004; Schuster et al., 2004], in crustal seismology for the retrieval of the surface wave Green's function [Campillo and Paul, 2003; Shapiro and Campillo, 2004; Shapiro et al., 2005], and for extracting the response of buildings from an incoherent excitation [Snieder, 2005].

The mechanism of seismic interferometry can be explained using the method of stationary phase [Snieder, 2004a]. This is not surprising because the stationary phase approximation is the natural tool to account for the destructive and constructive interference that forms the physical basis of seismic interferometry. The derivation of seismic interferometry with the principle of stationary phase is approximate, but, as shown by Roux et al. [2005] , the stationary phase integral can also be evaluated exactly using elliptical coordinates. This gives exactly the same final result as the stationary phase approximation. The derivation of seismic interferometry based on stationary phase has also been used for waves in a waveguide [Sabra et al., 2005].

The derivation of stationary phase is applicable for simple media only where one can easily account for the different rays that propagate through the media. In this sense the derivation based on stationary phase is less general than derivations based on normal modes, representation theorems, or time-reversed imaging. Despite this limitation, the derivation based on stationary phase is useful because it sheds light on the physics that underlies seismic interferometry. The value of this derivation is mostly didactic, but it also highlights sampling issues and the generation of spurious multiples.

Here we show that singly reflected waves that propagate between two receivers in the subsurface can correctly be reproduced by correlating the waves that have been excited by uncorrelated sources at the surface and are recorded at the two receivers. We derive this for the simplest case for a homogeneous medium without a free surface and flat horizontal reflectors in the subsurface.

In section 2, we derive the general framework for illumination of the subsurface by incoherent sources, and introduce the employed single-scattering model in section 3. In section 4 we show how this leads to the retrieval of the direct wave that propagates between the receivers, and, in section 5, we show that this procedure also correctly leads to the single-reflected wave that propagates between the receivers. The correlation of the single-reflected waves leads to a contribution that is proportional to the square of the reflection coefficient. We show in section 6 that this term is kinematically equivalent to the direct wave that propagates between the receivers. In section 7 we show a numerical example that illustrates the role of stationary phase in seismic interferometry. In section 8, we generalize the derivation to the case of a layered medium with more than one reflector, and we show that the product of singly-reflected waves from different reflectors gives a nonzero contribution to the cross-correlation. We refer to these terms as *spurious multiples* because these terms depend on the product of reflection coefficients, just like real multiples do. The spurious multiples, however, have arrival times that differ from those of real multiples.

2 ILLUMINATING THE SUBSURFACE FROM SOURCES AT THE SURFACE

Consider the problem wherein many sources at the surface $z = 0$ illuminate the subsurface. These sources can be either coherent or incoherent, and the may act either simultaneously or sequentially. The sources are placed at locations $\mathbf{r}_S = (x, y, 0)$ and have a source-time signal $S_S(t)$ that corresponds in the frequency domain to the complex spectrum $S_S(\omega)$. The Earth response that is excited by these sources is recorded at two receivers at locations $\mathbf{r}_A = (x_A, 0, z_A)$ and $\mathbf{r}_B = (x_B, 0, z_B)$, respectively. Without loss of generality, we align the x-axis of the employed coordinate system with the horizontal separation of the sources; hence in this coordinate system the y-coordinate of both sources vanishes.

The source-time functions $S_S(t)$ may be impulsive, but they might also correspond to functions with a more random character, as would be excited by, for example, traffic noise in a land survey or wave noise at the sea-surface during a marine survey. In the sequel we assume that the source time functions for sources at $\mathbf{r}_S$ and $\mathbf{r}_{S'}$ are uncorrelated when averaged over time and that the power spectrum of the source time functions is identical:

$$\int_0^{T_{aver}} S_S(t) S_{S'}(t+\tau) dt = \delta_{SS'} C(\tau) \ , \qquad (1)$$

where T_{aver} denotes the length of the time-averaging and $C(\tau)$ the autocorrelation of the source time functions. The autocorrelation is the Fourier transform of the power spectrum. Since all sources are assumed to have the same power spectrum, they have the same autocorrelation as well.

The source-time functions may have a different character in different imaging experiments. In the virtual-source experiments of Bakulin and Calvert [2004] the shots do not overlap in time. The shots are recorded and processed one after the other, and the cross terms between the shots in expression (1) by definition vanish. The situation is more complicated when truly incoherent sources illuminate the surface. Consider for example the seismic noise generated by waves at the sea-surface. The seismic waves excited at different locations on average are uncorrelated. Snieder [Snieder, 2004a] has shown that for random sources the ensemble average of expression (1) vanishes and that, in a single realization, the ratio of the cross term $S \neq S'$ to the diagonal term $S = S'$ is given by

$$\frac{|\text{cross terms}|}{|\text{diagonal terms}|} \sim \sqrt{\frac{t_{corr}}{N_{sources} T_{aver}}} \ , \qquad (2)$$

where $N_{sources}$ denotes the number of sources and t_{corr} is the temporal width of the cross-correlation $C(\tau)$. This width is inversely proportional to the bandwidth Δf of the sources. The product of the bandwidth and the averaging length T_{aver} is equal to $N_{freedom}$, the number of degrees of freedom in the data [Landau, 1967; Bucci and Franceschetti, 1989]. Therefore the ratio of the cross

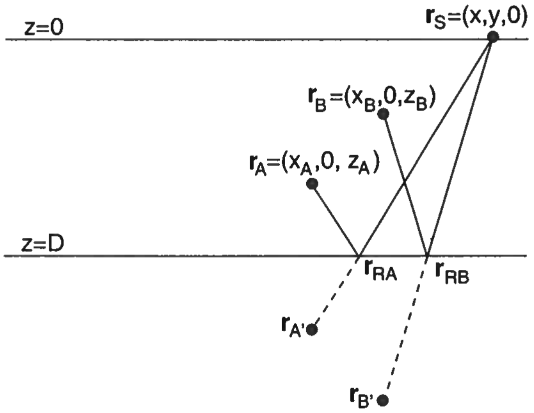

Figure 1. The geometry of an imaging experiment with a source at the surface and two receivers at $\mathbf{r}_A$ and $\mathbf{r}_B$. The mirror image of these receivers in the reflector is indicated at the locations $\mathbf{r}_{A'}$ and $\mathbf{r}_{B'}$, respectively.

terms to the diagonal terms in a single realization is equal to

$$\frac{|\text{cross terms}|}{|\text{diagonal terms}|} \sim \frac{1}{\sqrt{N_{sources} N_{freedom}}} . \qquad (3)$$

It follows from expression (2) that for random, incoherent, source-time functions the cross terms can be made arbitrarily small by increasing the length of the time window over which the averaging is carried out. In the following we assume that the cross-terms $S \neq S'$ can be ignored altogether. In that case, expression (1) corresponds in the frequency domain to

$$S_S(\omega) S_{S'}(\omega) = \delta_{SS'} \left| S(\omega) \right|^2 . \qquad (4)$$

This condition of uncorrelated sources was also used by Wapenaar [2004] , who assumed that the sources are located in the deep subsurface.

We now consider correlation of the waves recorded at two receivers for the special case of an acoustic medium. The waves recorded at the receivers A and B are given by

$$\begin{aligned} u_A(\omega) &= \textstyle\sum_S G^{full}(\mathbf{r}_A, \mathbf{r}_S, \omega) S_S(\omega) , \\ u_B(\omega) &= \textstyle\sum_S G^{full}(\mathbf{r}_B, \mathbf{r}_S, \omega) S_S(\omega) , \end{aligned} \qquad (5)$$

with G^{full} the full Green's function which consists of the direct wave, primaries, and multiples. In the frequency domain the temporal correlation of the waves recorded is given by

$$C_{AB}(\omega) = u_A(\omega) u_B^*(\omega) , \qquad (6)$$

where the asterisk denotes the complex conjugate. Inserting equation (5) in the previous expression gives

$$C_{AB}(\omega) = \sum_{S,S'} G^{full}(\mathbf{r}_A, \mathbf{r}_S) G^{full*}(\mathbf{r}_B, \mathbf{r}_{S'}) S_S(\omega) S_{S'}^*(\omega) . \qquad (7)$$

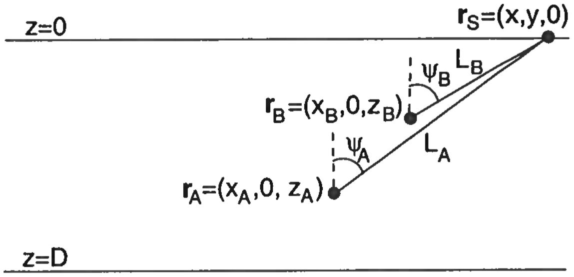

Figure 2. Definition of the geometric variables in the analysis of term 1.

Since the sources are uncorrelated, as stated in expression (4), the cross-terms $S \neq S'$ in this double sum vanish; hence

$$C_{AB}(\omega) = \sum_S G^{full}(\mathbf{r}_A, \mathbf{r}_S) G^{full*}(\mathbf{r}_B, \mathbf{r}_S) \left| S(\omega) \right|^2 . \qquad (8)$$

When the sources are densely distributed along the surface, with n sources per unit surface area, the sum over sources can be replaced by an integration: $\sum_S(\cdots) \rightarrow n \int(\cdots) dx$ over the surface; this gives

$$C_{AB}(\omega) = \left| S(\omega) \right|^2 n \int G^{full}(\mathbf{r}_A, \mathbf{r}_S) G^{full*}(\mathbf{r}_B, \mathbf{r}_S) dx dy , \qquad (9)$$

with x and y the coordinates of the source at the surface as shown in figure 1.

3 A SINGLE-SCATTERING MODEL

In order to better understand the physics of seismic interferometry, we illustrate this technique with a model that consists of a single reflector with plane-wave reflection coefficient r that is embedded in a homogeneous medium. The Green's function in the homogeneous medium is given by

$$G(R) = -\frac{e^{ikR}}{4\pi R} , \qquad (10)$$

with the wavenumber given by $k = \omega / c$, c the wave velocity, and R the distance of propagation. We presume that there is no free surface, so this model does not include any multiply reflected waves. As shown in figure 1, $\mathbf{r}_{RA}$ denotes the reflection point of the wave that propagates to $\mathbf{r}_A$. The full Green's function is the superposition of the direct wave and the single-reflected wave:

$$\begin{aligned} G^{full}(\mathbf{r}_A, \mathbf{r}_S) \; &= G(|\mathbf{r}_A - \mathbf{r}_S|) \\ &\quad + r \; G(|\mathbf{r}_A - \mathbf{r}_{RA}| + |\mathbf{r}_{RA} - \mathbf{r}_S|) , \\ G^{full}(\mathbf{r}_B, \mathbf{r}_S) \; &= G(|\mathbf{r}_B - \mathbf{r}_S|) \\ &\quad + r \; G(|\mathbf{r}_B - \mathbf{r}_{RB}| + |\mathbf{r}_{RB} - \mathbf{r}_S|) . \end{aligned} \qquad (11)$$

In this expression, we used that the reflected wave is given by the Green's function that accounts for the propagation from the source to an image point of the receiver below the reflector. The image points of the receivers A and B are indicated in figure 1 by $\mathbf{r}'_A$ and $\mathbf{r}'_B$, respectively. As shown in that figure, for receiver A the total distance covered by the reflected wave is $|\mathbf{r}_A - \mathbf{r}_{RA}| + |\mathbf{r}_{RA} - \mathbf{r}_S|$.

Inserting equation (11) into expression (9) gives an expression for the correlation, which consists of a sum of four terms:

$$\begin{aligned}
C_{AB}(\omega) &= n\,|S(\omega)|^2 \underbrace{\int G(|\mathbf{r}_A - \mathbf{r}|)G^*(|\mathbf{r}_B - \mathbf{r}|)dxdy}_{T1} \\
&+ n\,|S(\omega)|^2\, r \underbrace{\int G(|\mathbf{r}_A - \mathbf{r}|)G^*(|\mathbf{r}_B - \mathbf{r}_{RB}| + |\mathbf{r}_{RB} - \mathbf{r}|)dxdy}_{T2} \\
&+ n\,|S(\omega)|^2\, r \underbrace{\int G(|\mathbf{r}_A - \mathbf{r}_{RA}| + |\mathbf{r}_{RA} - \mathbf{r}|)G^*(|\mathbf{r}_B - \mathbf{r}|)dxdy}_{T3} \\
&+ n\,|S(\omega)|^2\, r^2 \underbrace{\int G(|\mathbf{r}_A - \mathbf{r}_{RA}| + |\mathbf{r}_{RA} - \mathbf{r}|)G^*(|\mathbf{r}_B - \mathbf{r}_{RB}| + |\mathbf{r}_{RB} - \mathbf{r}|)dxdy}_{T4}\,.
\end{aligned} \tag{12}$$

Term 1 (T1) is the correlation of the direct waves that propagate to the two receivers; this term does not depend on the reflection coefficient. Terms 2 and 3 are proportional to the reflection coefficient r, for this reason they can be expected to account for the single-reflected waves in the Green's function that are extracted from the correlation. Term 4 depends on r^2. In the following, we analyze terms 1-4 in order to establish the connection between the correlation and the Green's function for this simple wave propagation problem.

4 ANALYSIS OF TERM 1

The derivation shown in this section is similar to that in an earlier analysis [Snieder, 2004a]. Using the lengths L_A and L_B, as defined in figure 2, and the Green's function (10), term 1 can be written as

$$T1 = \frac{1}{(4\pi)^2} \int \frac{\exp\left(ik\left(L_A - L_B\right)\right)}{L_A L_B} dxdy\,. \tag{13}$$

The integrand has an oscillatory character, but as we will see, the integrand has a stationary point. For this reason we analyze this integral in the stationary phase approximation [Bleistein, 1984; Snieder, 2004b]. Referring to figure 2, the lengths $L_{A,B}$ are given by

$$L_{A,B} = \sqrt{\left(x - x_{A,B}\right)^2 + y^2 + z^2_{A,B}}\,. \tag{14}$$

The stationary point of the integrand follows by setting the partial x- and y-derivatives of $L = L_A - L_B$ equal to zero. For the y-derivative this gives

$$0 = \frac{\partial L}{\partial y} = \frac{y}{L_A} - \frac{y}{L_B}\,. \tag{15}$$

This derivative vanishes for $y = 0$; hence the condition of stationarity with respect to y implies that the stationary source point lies in the vertical plane of the receivers. The stationarity condition with respect to the x-coordinate gives

$$0 = \frac{\partial L}{\partial x} = \frac{x - x_A}{L_A} - \frac{x - x_B}{L_B} = \sin\psi_A - \sin\psi_B\,, \tag{16}$$

where the angles ψ_A and ψ_B are defined in figure 2. The phase thus is stationary when

$$\psi_A = \psi_B \qquad \text{and} \qquad y = 0\,. \tag{17}$$

The stationarity condition $\psi_A = \psi_B$ is illustrated in figure 3; it implies that the stationary source point at the surface is aligned with the line joining the two receivers. In these figures the receivers are at different depths.

Note that when the receivers are at the same depth ($z_A = z_B$) there is no stationary source position, except for sources infinitely far away. Any attenuation will suppress the contribution of those sources.

Kinematically, expression (13) gives a contribution at a lag-time that is equal to the time it takes for the wave to propagate from receiver B to receiver A because the wave that propagates along the path shown in figure 3 arrives at receiver A with a time delay $|\mathbf{r}_A - \mathbf{r}_B|/c$ compared to the wave that arrives at receiver B. It is nontrivial that the evaluation of the integral in (13) gives a contribution that is also dynamically equal to the Green's function of the waves that propagate between the receivers A and B. In the following we evaluate the integral in the stationary phase approximation.

Evaluating the second derivatives of $L = L_A - L_B$ while using (17) for the stationary point gives

$$\begin{aligned}\frac{\partial^2 L}{\partial x^2} &= \frac{z_A^2}{L_A^3} - \frac{z_B^2}{L_B^3} = \frac{z_A^2}{L_A^2}\frac{1}{L_A} - \frac{z_B^2}{L_B^2}\frac{1}{L_B} \\ &= \cos^2\psi\left(\frac{1}{L_A} - \frac{1}{L_B}\right) ,\end{aligned} \tag{18}$$

and

$$\frac{\partial^2 L}{\partial y^2} = \frac{L_A^2}{L_A^3} - \frac{L_B^2}{L_B^3} = \frac{1}{L_A} - \frac{1}{L_B} . \tag{19}$$

In this example, and the following examples, $\partial^2 L/\partial x \partial y = 0$ at the stationary point, and the two-dimensional stationary phase integral reduces to the product of two one-dimensional stationary phase integrals over the x- and y-coordinates, respectively.

In the following, L_A and L_B are the path lengths for the stationary source position as shown in figure 3. Note that in the geometry of figure 3, $L_A > L_B$ so that $L_A^{-1} - L_B^{-1} < 0$. Evaluating the integral (13) in the stationary phase approximation thus gives

$$\begin{aligned}T1 &= \frac{1}{(4\pi)^2}\frac{\exp\left(ik\left(L_A - L_B\right)\right)}{L_A L_B} \\ &\times e^{-i\pi/4}\sqrt{\frac{2\pi}{k}}\frac{1}{\sqrt{\cos^2\psi\left(\frac{1}{L_B} - \frac{1}{L_A}\right)}} \\ &\times e^{-i\pi/4}\sqrt{\frac{2\pi}{k}}\frac{1}{\sqrt{\frac{1}{L_B} - \frac{1}{L_A}}} ,\end{aligned} \tag{20}$$

Using the relation $k = \omega/c$, we can write this expression as

$$T1 = \frac{c}{8\pi(-i\omega)\cos\psi}\frac{\exp\left(ik\left(L_A - L_B\right)\right)}{L_A - L_B} , \tag{21}$$

The distance $L_A - L_B$ is equal to the receiver separation R shown in figure 3. With expression (10) and including the factor $n\,|S(\omega)|^2$ of expression (12), this gives a total contribution that is equal to

$$T1 = \frac{n\,|S(\omega)|^2\,c}{2\cos\psi} \times \frac{G(R)}{-i\omega} . \tag{22}$$

This means that the contribution of term 1 to the correlation is, in the frequency domain, proportional to the Green's function of the direct wave that propagates between the receivers. Note that this Green's function is multiplied by the source density n at the surface; a denser source distribution gives a stronger correlation than does a less dense one. The Green's function is also multiplied by the power spectrum $|S(\omega)|^2$ of the sources. This power spectrum can be measured, and one can correct for this term. In order to retrieve the Green's function from term 1, one needs to multiply with $-i\omega$. Because of the employed Fourier transform, $f(t) = \int F(\omega)\exp(-i\omega t)d\omega$, this multiplication corresponds to a differentiation in the time domain. This differentiation corrects for the integration that is carried out in the cross-correlation. This need to carry out the differentiation was also noted in other formulations of seismic interferometry, e.g., [Lobkis and Weaver, 2001; Snieder, 2004a; Weaver and Lobkis, 2004].

The term $\cos\psi$ in the denominator is an obliquity factor that corrects for the fact that the length element QQ' of figure 4 perpendicular to the ray corresponds to a line element PP' along the surface whose lengths that are related by $QQ' = PP'/\cos\psi$.

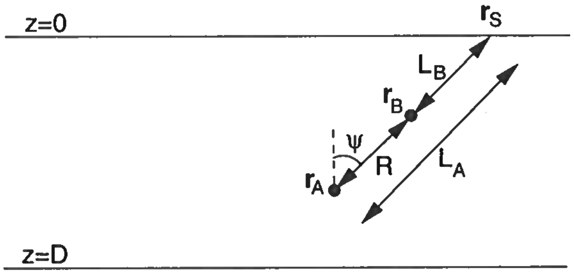

Figure 3. Definition of the geometric variables for the stationary source position in term 1.

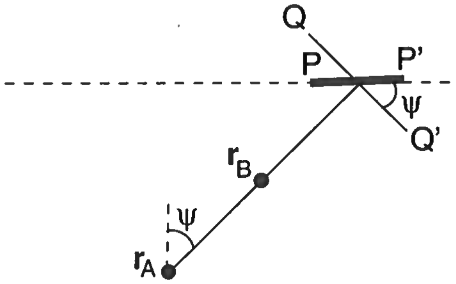

Figure 4. The relation between an element PP' along the surface and the corresponding element QQ' perpendicular to the receiver line.

In the virtual-source experiment of Bakulin and

Calvert [2004], the sources at the surface were placed in a line. In that case there is no integration over the y-coordinate, and the latter terms in expression (20) that come from the y-integration are absent; in that case

$$T1_{line} = \frac{in\,|S(\omega)|^2\,\sqrt{c}}{\sqrt{8\pi}\sqrt{-i\omega}\cos\psi}\sqrt{\frac{1}{L_B} - \frac{1}{L_A}}\,G(R)\,. \quad (23)$$

Note the presence of the factor i and the term $1/\sqrt{-i\omega}$. Correcting for these terms involves a Hilbert transform and a fractional derivative. These correction factors are common in two-dimensional imaging experiments [Yilmaz, 1987; Bleistein et al., 2001; Haney and Snieder, 2005]. Without these corrections the reconstructed Green's function does not have the proper phase and frequency dependence. More seriously, in contrast to equation (22), expression (23) depends explicitly on the distances L_A and L_B. It turns out that when the derivation leading to expression (23) is repeated using the Green's function in two dimensions, an expression analogous to equation (22) is obtained. The presence of the fractional derivatives and the lengths L_A and L_B is thus due to a mismatch between the dimensionality of the physical space through which the waves propagate (3D versus 2D) and the dimensionality of the source distribution (2D versus 1D). The derivation of seismic interferometry by Roux and Fink [2003] is based on wave propagation in three dimensions, while the employed sources are placed along a line. As shown by the example of expression (23), this leads to a Green's function that is kinematically correct, but whose amplitude and phase is not.

A complex overburden located between the surface sources and the receivers in the subsurface acts as a diffusor of seismic waves because the waves radiated from a single source arrive at a receiver from various directions resulting from the scattering and multipathing that has occurred in the overburden. In the experiment of Bukulin and Calvert [2004] the shots were placed on a line at the surface, but the complex overburden in their experiment created multipathing that provided a more diffuse illumination of their receivers in the subsurface that helps to focus the waves onto the virtual sources.

The analysis of this section can be generalized for a heterogeneous medium in which the velocity is sufficiently smooth to warrant the use of ray theory. We show in appendix A that term 1 is then given by

$$T1 = \sum_{stat.\ points} \frac{n|S(\omega)|^2 v_S}{2\cos\psi} \times \frac{G^{ray}(\mathbf{r}_A, \mathbf{r}_B)}{-i\omega}\,, \quad (24)$$

where $G^{ray}(\mathbf{r}_A, \mathbf{r}_B)$ is the ray-geometric Green's function for the waves recorded at $\mathbf{r}_A$ that are generated by a point source at $\mathbf{r}_B$. The summation in this expression is over all the stationary source points on the surface $z = 0$. These points can be found by tracing rays from $\mathbf{r}_A$ to $\mathbf{r}_B$ and by extending these rays to the surface $z = 0$. The angle ψ is the angle between these rays at the surface and the vertical, while v_S is the velocity at the intersection of these rays with the surface.

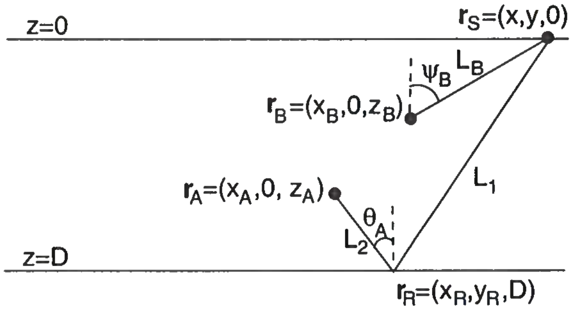

Figure 5. Definition of the geometric variables in the analysis of term 3.

5 ANALYSIS OF TERM 3

The analysis of this term could be achieved by applying the theory of the previous sections to receivers at the image points $\mathbf{r}_{A'}$ and $\mathbf{r}_{B'}$ of figure 1. Here we show explicitly that the cross-correlation correctly produces the single-reflected waves. Using the lengths defined in figure 5 this term is given by

$$T3 = \frac{1}{(4\pi)^2}\int \frac{\exp\left(ik\left(L_1 + L_2 - L_B\right)\right)}{\left(L_1 + L_2\right) L_B}\,dxdy\,. \quad (25)$$

Before we can analyze this expression we need the coordinates of the reflection point $\mathbf{r}_R$ because this determines the lengths L_1 and L_2. The condition that the reflection angle is equal to angle of incidence gives

$$\begin{aligned} x_R &= \frac{(D - z_A)\,x + Dx_A}{2D - z_A}\,, \\ y_R &= \frac{(D - z_A)\,y}{2D - z_A}\,. \end{aligned} \quad (26)$$

Using this, the lengths $L_1$and L_2 are given by

$$\begin{aligned} L_1^2 = &\left(\frac{D}{2D - z_A}\right)^2 (x - x_A)^2 \\ &+ \left(\frac{D}{2D - z_A}\right)^2 y^2 + D^2\,, \end{aligned} \quad (27)$$

and

$$\begin{aligned} L_2^2 = &\left(\frac{D - z_A}{2D - z_A}\right)^2 (x - x_A)^2 \\ &+ \left(\frac{D - z_A}{2D - z_A}\right)^2 y^2 + (D - z_A)^2\,, \end{aligned} \quad (28)$$

while L_B is given by expression (14).

The stationary points of the integral (25) follow

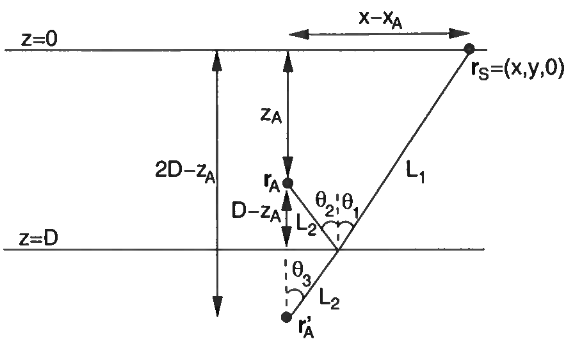

Figure 6. The angles θ_1, θ_2, and θ_3 and their relation to the geometric variables for the reflected wave.

from the first partial derivatives of $L = L_1 + L_2 - L_B$:

$$0 = \frac{\partial L}{\partial y} = \left(\frac{D}{2D - z_A}\right)^2 \left(\frac{y}{L_1}\right) + \left(\frac{D - z_A}{2D - z_A}\right)^2 \left(\frac{y}{L_2}\right) - \frac{y}{L_B} . \tag{29}$$

Again, the stationary source position occurs for $y = 0$; it is located in the vertical plane of the receivers. The condition for stationarity in the x-direction is

$$0 = \frac{\partial L}{\partial x} = \left(\frac{D}{2D - z_A}\right)^2 \left(\frac{x - x_A}{L_1}\right) + \left(\frac{D - z_A}{2D - z_A}\right)^2 \left(\frac{x - x_A}{L_2}\right) - \frac{x - x_B}{L_B} . \tag{30}$$

In order to interpret this last condition geometrically it is useful to relate the ratios in this expression to the angle of incidence at the reflector. Referring to figure 6, the following identities hold: $\cos\theta_1 = D/L_1$, $\cos\theta_2 = (D - z_A)/L_2$, and $\cos\theta_3 = (2D - z_A)/(L_1 + L_2)$. Since these angles are all equal to the angle of incidence θ_A of the reflected wave, we obtain:

$$\cos\theta_A = \frac{D}{L_1} = \frac{D - z_A}{L_2} = \frac{2D - z_A}{L_1 + L_2} . \tag{31}$$

Also, since $x - x_A = L_1 \sin\theta_1 + L_2 \sin\theta_2$, and since both angles are equal to θ_A,

$$\sin\theta_A = \frac{x - x_A}{L_1 + L_2} . \tag{32}$$

Dividing this expression by the last identity of (31) gives

$$\tan\theta_A = \frac{x - x_A}{2D - z_A} . \tag{33}$$

Finally, from (31),

$$\frac{D}{2D - z_A} = \frac{L_1}{L_1 + L_2} , \quad \frac{D - z_A}{2D - z_A} = \frac{L_2}{L_1 + L_2} . \tag{34}$$

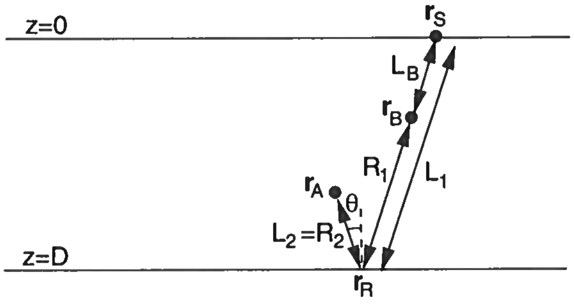

Figure 7. Definition of the geometric variables for the stationary source position for the analysis of term 3.

Using expression (34) in (30), and using (32) to eliminate $x - x_A$, gives, with the relation $(x - x_B)/L_B = \sin\psi_B$,

$$0 = \frac{\partial L}{\partial x} = \sin\theta_A - \sin\psi_B . \tag{35}$$

The integrand thus is stationary when the source position satisfies

$$\theta_A = \psi_B \quad \text{and} \quad y = 0 . \tag{36}$$

This condition is depicted in figure 7: waves radiated from the stationary source position at the surface travel in a straight line from the source through receiver B via a specular reflection to receiver A. Just as in the analysis of term 1, the time delay of this wave recorded at the two receivers is equal to the time it takes the wave to travel from receiver B via the reflector to receiver A. Thus the correlation is kinematically equal to the Green's function for the reflected waves. With the following stationary phase evaluation of the integral (25), we verify that the retrieved Green's function is also dynamically correct.

From expression (27) we get at the stationary point

$$\frac{\partial^2 L_1}{\partial x^2} = \left(\frac{D}{2D - z_A}\right)^2 \frac{D^2}{L_1^3} = \left(\frac{L_1}{L_1 + L_2}\right)^2 \frac{D^2}{L_1^2} \frac{1}{L_1} = \frac{L_1}{(L_1 + L_2)^2} \cos^2\theta . \tag{37}$$

In the second identity we have used expression (34), while the last identity follows from equation (31). In a similar way it follows that

$$\frac{\partial^2 L_2}{\partial x^2} = \frac{L_2}{(L_1 + L_2)^2} \cos^2\theta , \tag{38}$$

and, using (18), we obtain for the curvature of L_B,

$$\frac{\partial^2 L_B}{\partial x^2} = \frac{1}{L_B} \cos^2\theta . \tag{39}$$

In the last expression, we used the stationary phase condition $\psi = \theta$. Combining these results in the path difference $L = L_1 + L_2 - L_B$ gives

$$\frac{\partial^2 L}{\partial x^2} = \cos^2\theta \left(\frac{1}{L_1 + L_2} - \frac{1}{L_B}\right) . \tag{40}$$

Differentiation of (27) gives

$$\frac{\partial^2 L_1}{\partial y^2} \quad \left\{ \left(\frac{D}{2D - z_A} \right)^4 (x - x_A)^2 + \left(\frac{D}{2D - z_A} \right)^2 D^2 \right\} / L_1^3 \, . \tag{41}$$

With expressions (33) and (34) this is equal to

$$\frac{\partial^2 L_1}{\partial y^2} = \left(\frac{D}{L_1} \right)^2 \frac{1}{L_1} \left(\frac{L_1}{L_1 + L_2} \right)^2 \left(\tan^2 \theta + 1 \right) \, . \tag{42}$$

Using the identity $D/L_1 = \cos\theta$ this gives

$$\frac{\partial^2 L_1}{\partial y^2} = \frac{L_1}{(L_1 + L_2)^2} \, . \tag{43}$$

A similar analysis for L_2 gives

$$\frac{\partial^2 L_2}{\partial y^2} = \frac{L_2}{(L_1 + L_2)^2} \, . \tag{44}$$

This gives, for the curvature of L with respect to y,

$$\frac{\partial^2 L}{\partial y^2} = \frac{1}{L_1 + L_2} - \frac{1}{L_B} \, . \tag{45}$$

In these expressions it is understood that all lengths are evaluated at the stationary point.

The stationary phase evaluation of the integral (25) can now be carried out. Keeping in mind that $(L_1 + L_2)^{-1} - L_B^{-1} < 0$, and using the same steps as in section 4, gives

$$T3 = \frac{1}{(4\pi)^2} \frac{\exp(ik(L_1 + L_2 - L_B))}{(L_1 + L_2) L_B} \left(e^{-i\pi/4} \right)^2 \times \frac{2\pi}{k \cos\theta} \left(\frac{1}{L_B} - \frac{1}{L_1 + L_2} \right)^{-1} \, . \tag{46}$$

As shown in figure 7, $L_1 - L_B = R_1$, and $L_2 = R_2$. With the definition (10) for the Green's function this gives after taking the $rn \left| S(\omega) \right|^2$ terms into account:

$$T3 = \frac{n \left| S(\omega) \right|^2 c}{2 \cos\psi} \times r \frac{G(R_1 + R_2)}{-i\omega} \, . \tag{47}$$

Note the resemblance with expression (22) for the contribution of term 1 that gives the direct wave that propagates between the receiver. Expression (47) shows that the contribution of term 3 leads to the singly-reflected wave that propagates from receiver B via the reflector to receiver A. The same corrections must be applied to this term as to term 1 as discussed in section 4.

The same analysis can be applied to term 2 of expression (12), the final result is the complex conjugate of expression (47) so that

$$T2 = \frac{n \left| S(\omega) \right|^2 c}{2 \cos\psi} \times r \left(\frac{G(R_1 + R_2)}{-i\omega} \right)^* \, . \tag{48}$$

The stationary point now lies at the location on the surface such that the direct wave from the source to receiver A propagates along the same path as the wave that travels from the source to the reflector, and ultimately to receiver B.

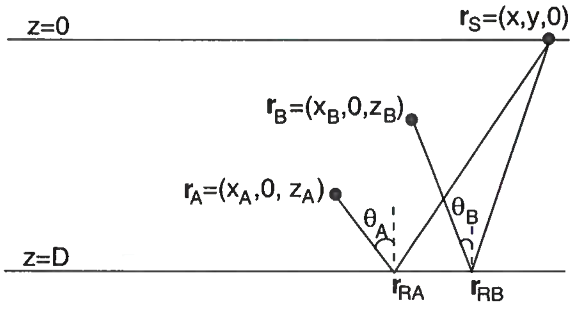

Figure 8. Definition of the geometric variables in the analysis of term 4.

The Green's function in expression (47) is the causal Green's function, while its complex conjugate in equation (48) is the acausal Green's function. It is known that seismic interferometry gives the superposition of the causal and the acausal Green's function [Lobkis and Weaver, 2001; Derode et al., 2003a; Malcolm et al., 2004; Derode et al., 2003b]. The causal Green's function can easily be retrieved from the cross-correlation either by truncating the cross-correlation for $t < 0$, or by averaging the cross-correlation for negative times and positive times.

6 ANALYSIS OF TERM 4

For the analysis of term 4, we carry out the stationary phase analysis of the following integral:

$$T4 = \frac{1}{(4\pi)^2} \int \frac{\exp(ikL)}{X} dx dy \, , \tag{49}$$

with

$$\begin{aligned} L &= \left| \mathbf{r}_A - \mathbf{r}_{RA} \right| + \left| \mathbf{r}_{RA} - \mathbf{r}_S \right| \\ &\quad - \left| \mathbf{r}_B - \mathbf{r}_{RB} \right| - \left| \mathbf{r}_{RB} - \mathbf{r}_S \right| \end{aligned} \tag{50}$$

and

$$\begin{aligned} X &= \left(\left| \mathbf{r}_A - \mathbf{r}_{RA} \right| + \left| \mathbf{r}_{RA} - \mathbf{r}_S \right| \right) \\ &\quad \times \left(\left| \mathbf{r}_B - \mathbf{r}_{RB} \right| + \left| \mathbf{r}_{RB} - \mathbf{r}_S \right| \right) \end{aligned} \tag{51}$$

where all variables are defined in figure 8. The stationary point follows from setting the x- and y-derivatives of the phase equal to zero. As in the previous sections, the stationarity condition with respect to y leads to the condition $y = 0$; this means again that the stationary point lies in the vertical plane of the receivers. Using the same steps that led to expression (35), one finds that the stationarity condition with respect to x is given by

$$0 = \frac{\partial L}{\partial x} = \sin\theta_A - \sin\theta_B \, , \tag{52}$$

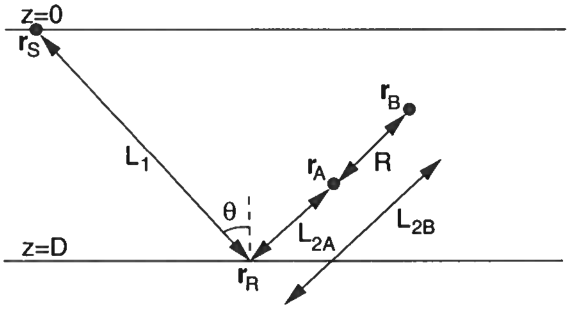

Figure 9. Definition of the geometric variables in the analysis of term 4 for the stationary source position.

where the angles θ_A and θ_B are defined in figure 8. The point of stationary phase thus is defined by the conditions

$$\theta_A = \theta_B \qquad \text{and} \qquad y = 0 \, . \tag{53}$$

This condition of stationary phase corresponds to the source position shown in figure 9. The stationary source position launches two waves that, after reflection at the interface, both propagate along the line that joins the receivers. Since both reflected waves are proportional to r, this contribution to the correlation is proportional to r^2. The correlation of the waves shown in figure 9 is nonzero for a lag-time that is equal to the time it takes for the waves to propagate between the receivers. Kinematically, this term can thus be expected to correspond to the Green's function of the direct wave that propagates between the receivers.

In order to carry out the stationary phase analysis, the second derivatives of the phase is needed. These derivatives follow from the expressions (37), (38), (43) and (44). Using the lengths defined in figure 9, term 4 is given in the stationary phase approximation by

$$\begin{aligned} T4 &= \frac{1}{(4\pi)^2} \frac{\exp(ik(L_1 + L_{2A} - L_1 - L_{2B}))}{(L_1 + L_{2A})(L_1 + L_{2B})} \left(e^{-i\pi/4}\right)^2 \\ & \frac{2\pi}{k\cos\theta} \left(\frac{1}{L_1 + L_{2A}} - \frac{1}{L_1 + L_{2B}} \right)^{-1} . \end{aligned} \tag{54}$$

According to the geometry of figure 9, $R = L_{2B} - L_{2A}$. With the definition (10) for the Green's function this gives, after taking the $r^2 n \left|S(\omega)\right|^2$ terms into account,

$$T4 = \frac{n \left|S(\omega)\right|^2 c}{2\cos\psi} \times r^2 \left(\frac{G(R)}{-i\omega} \right)^* . \tag{55}$$

Apart from the r^2-term and a complex conjugation of the Green's function, this term is similar to term 1 as given in expression (22). The r^2-term arises because both of the waves that are reflected upward from the reflector are proportional to the reflection coefficient. The fact that this contribution is multiplied with r^2 is simply due to the fact that both interfering waves that contribute to this term are proportional to r. The complex conjugate appears because the wave arrives at receiver A before it hits receiver B.

7 A NUMERICAL EXAMPLE

We present a numerical example of the theory. For simplicity we consider the theory in two dimensions. A reflector with reflection coefficient $r = 0.8$ is located at a depth 1500 m below the surface. This is not a small reflection coefficient, but since there is only one reflector and no free surface, this model does not generate any multiple reflections, regardless of how large the reflection coefficient is. The wave velocity is $c = 2000$ m/s, and the receivers are located at $\mathbf{r}_A = (0, 1000)$ m and $\mathbf{r}_B = (300, 500)$ m, respectively. We used noise sources at the surface with a spacing $\Delta x = 20$ m., and a Ricker wavelet with a dominant frequency of 50 Hz for the power spectrum $\left|S(\omega)\right|^2$ of the noise.

The contributions of the sources at the surface to the terms T1-T4 is shown in the left panel of figure 10, while the sum over all source positions is shown in the right panel. The right panel panels shows four distinct arrivals. The arrivals T1 and T3 are causal, while the arrivals T2 and T4 are acausal. T1 is the strongest arrival, because it does not depend on the reflection coefficient. The arrivals T2 and T3 are weaker, because they are the singly reflected waves, while the arrival T4 is the weakest because it varies as r^2.

Note that each of the arrivals in the right panel of figure 10 corresponds to a stationary source point in the left panel of that figure. The nonzero contribution of these arrivals is solely due to the stationary source points, the sources placed at other locations give contributions that interfere desctructively.

Figure 11 shows for term T3 a comparison between the exact waveform, computed with the 2D Green's function, that is shown with the solid line, and the term 3 obtained by summing the correlation over the sources at the surface (shown with crosses). The waveform obtained from seismic interferometry matches the exact waveform well. Note that the shown waveforms do not look like a Ricker wavelet; as theory predicts they are shifted over a phase angle equal to $\pi/4$.

The left panel of figure 10 shows weak arrivals between T1 and T4. These weak arrivals are due to endpoint contributions from the sum over the traces on the left panel of that figure, especially for the endpoints where the arrival time tends to a constant. In the numerical example we tapered the contribution of traces near the endpoints of the source region. Without this tapering these endpoint contributions are much stronger. This is of importance for virtual source imaging [Bakulin and Calvert, 2004] because a careless summation over all source positions may lead to endpoint contributions that could be confused with waves reflected off reflectors in the subsurface.

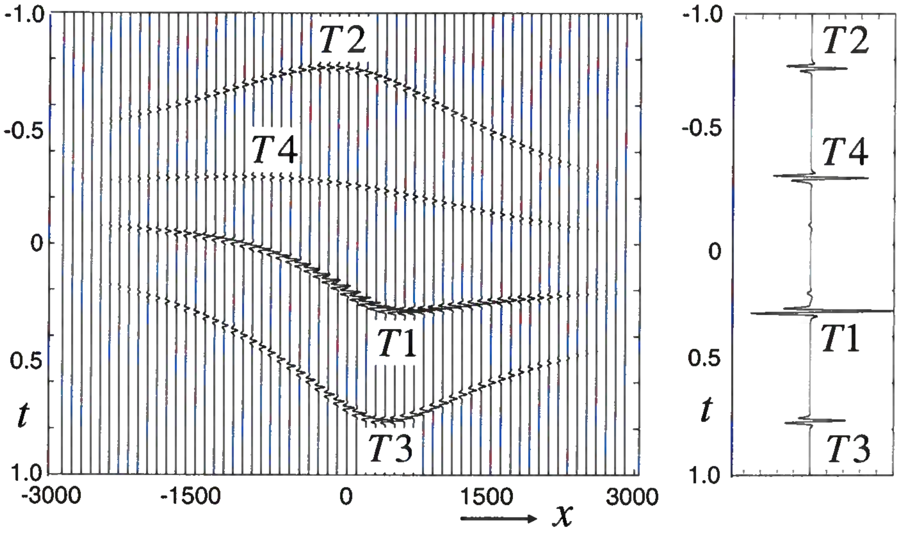

Figure 10. Left panel, the contribution of sources at the surface to the terms T1-T4 as a function of the source position x. For clarity only every fifth source position is shown. Right panel, the sum over all source positions at the surface.

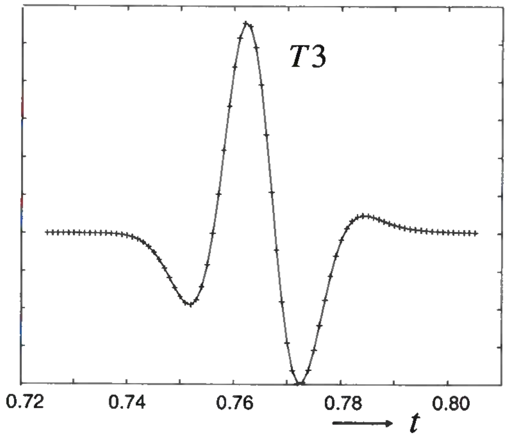

Figure 11. Solid line, the exact arrival for term T3 computed with the 2D Green's function. The crosses indicate the sum of the correlation for term T3 over all sources at the surface. This sum is tapered near the end of the source region.

8 THE CASE OF MORE THAN ONE REFLECTOR

Up to this point the analysis has been based on the assumption of a single reflector in the subsurface. Suppose there are more reflectors at depths D_j with reflection coefficients r_j. Assuming that the wave velocity remains constant, the second term in each of equations (11) needs to be replaced by a sum over all reflectors. In expression (12), the term T1 contains the direct waves only; this term is not influenced by the presence of more than one reflector. The terms T2 and T3 in expression (12) involve the cross term between the direct wave and the single-reflected waves. Since these terms are linear in the reflection coefficients, one can retrieve the sum of all the single reflected waves by summing the terms T2 and T3 over the different reflectors. This means that in the presence of more than one reflector, the cross terms T2 and T3 between the direct wave and the single-reflected waves produce the full set of single reflections.

The term T4 in expression (12) contains the product of the single reflected waves. This means that for more than one reflector this term contains double sum $\sum_{j,j'} r_j r_{j'}(\cdots)$. This double sum can be split into the terms $j' = j$ and the terms $j \neq j'$:

$$\sum_{j,j'} r_j r_{j'}(\cdots) = \sum_j r_j^2(\cdots) + \sum_{j\neq,j'} r_j r_{j'}(\cdots) \qquad (56)$$

Analysis of the first term is identical to that of the term T4 in section ??. This means that one can simply sum expression (55) over all reflectors in the subsurface.

The last contribution that needs to be accounted for is the contribution of the second sum in the right hand side of equation (56) to the term T4. We consider two reflectors at depths D_1 and D_2 with reflection coefficients r_1 and r_2, respectively. The derivation holds for any pair of reflectors. The wave paths associated with two different reflectors to term T4 is shown in figure 12. The integrand in the term T4 of expression (12) now contains a phase term $\exp ikL$ with

$$L = L_1^{(A)} + L_2^{(A)} - L_1^{(B)} - L_2^{(B)} , \qquad (57)$$

where these lengths are defined in figure 12. As before, the phase is stationary with respect to the y-coordinate

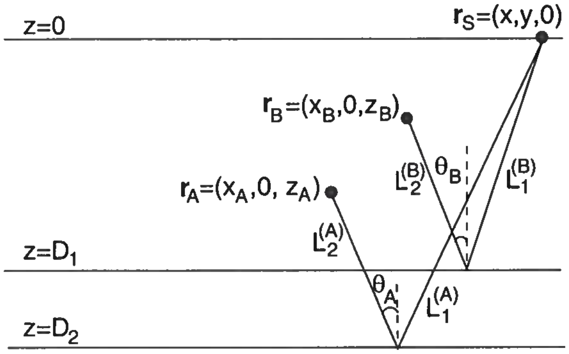

Figure 12. Definition of the geometric variables for the contribution of term 4 from waves reflected off two different reflectors.

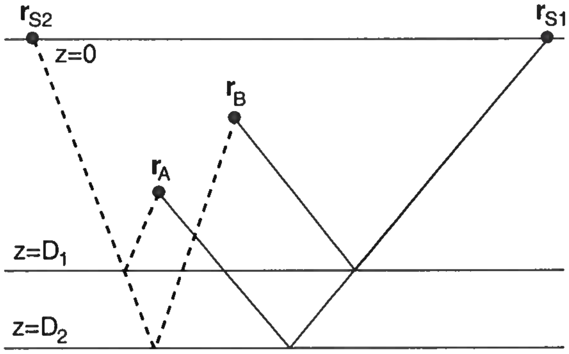

Figure 13. The stationary source points $\mathbf{r}_{S1}$ and $\mathbf{r}_{S2}$ for the correlation of waves reflected from two different reflectors. The corresponding wave paths to the receivers are shown with solid and dashed lines, respectively.

when $y = 0$. The condition that the phase is stationary with respect to x gives the condition

$$0 = \frac{\partial L}{\partial x} = \sin\theta_A - \sin\theta_B \ , \tag{58}$$

where the angles θ_A and θ_B are defined in figure 12. This follows from the derivation that led to the first term in the right hand side of expression (35). The stationary phase condition for this term therefore gives

$$\theta_A = \theta_B \quad , \quad y = 0 \ . \tag{59}$$

The stationary phase condition (59) gives two stationary source points $\mathbf{r}_{S1}$ and $\mathbf{r}_{S2}$ at the surface that are shown in figure 13. The wave paths shown in solid lines indicates the cross correlation of the waves that propagate along the following trajectories: $\mathbf{r}_{S1} \rightarrow$ reflector 1 $\rightarrow \mathbf{r}_B$ and $\mathbf{r}_{S1} \rightarrow$ reflector 2$\rightarrow \mathbf{r}_A$, while the wave paths shown in dashed lines indicate the correlation of the waves that propagate along the following trajectories: $\mathbf{r}_{S2} \rightarrow$ reflector 1 $\rightarrow \mathbf{r}_A$ and $\mathbf{r}_{S2} \rightarrow$ reflector 2 $\rightarrow \mathbf{r}_B$. These wave paths act as the direct and exchange scattering events in quantum mechanics [Lévy-Leblond and Balibur, 1990].

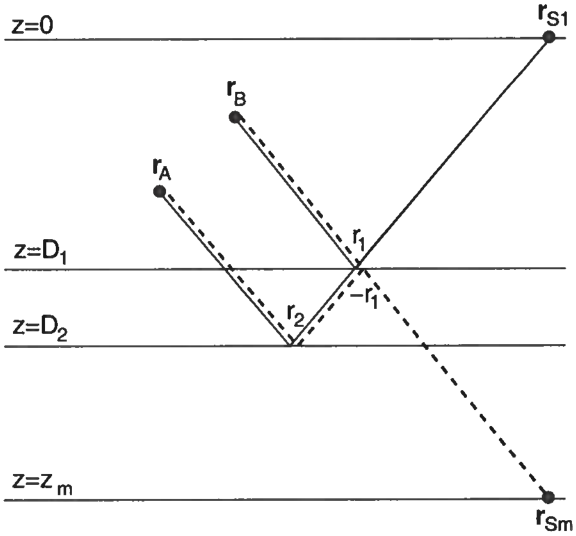

Figure 14. The stationary source points $\mathbf{r}_{S1}$ at the surface $z = 0$ and $\mathbf{r}_{Sm}$ at the surface $z = z_m$ for the correlation of waves reflected from two different reflectors. The corresponding wave paths to the receivers are shown with solid and dashed lines, respectively. The reflection coefficients for the different reflected waves are indicated.

The difference in the travel time of the waves that propagate along the two trajectories shown in the solid lines is not equal to the time it takes to propagate between the receivers. The stationary phase contributions that correspond to these cross terms are nonzero. This implies that the correlation of the waves reflected off different reflectors give stationary phase contributions that are proportional to $r_1 r_2$. These contributions depend on the product of reflection coefficients, hence the correlation of the single-reflected waves from different reflectors gives spurious arrivals that dynamically are equivalent to peg-leg multiples that are reflected once from the free surface and twice from reflectors in the subsurface, because the peg-leg surface multiples are also proportional to $r_1 r_2$.

This is a puzzling conclusion, since theory predicts that the full Green's function can be retrieved when the sources are placed on a closed surface that surrounds the region of interest [Wapenaar et al., 2004; Wapenaar et al., 2005]. The key point is that in the derivation of this paper the sources are placed at the upper surface only. Let us consider what would happen if we also had sources at a surface $z = z_m$ that is located below the reflectors as shown in figure 14.

The reflection response and transmission response of the subsurface are not independent [Claerbout, 1968; Wapenaar et al., 2004]. This suggests that sources below the reflectors are essential for the cancellation of the cross-terms on singly-reflected waves, and we provide a heuristic argument that this is indeed the case.

Consider the situation in figure 14 where sources are present at the surface $z = 0$ above the reflectors, and at the surface $z = z_m$ below the reflectors. The points $\mathbf{r}_{S1}$ and $\mathbf{r}_{Sm}$ on these surfaces are the stationary source points for the cross-terms that correspond to the path indicated with solid lines and dashed lines, respectively. The waves excited at the surface $z = 0$ propagate along the paths shown with solid lines, while the waves excited below the reflectors propagate along the paths shown in dashed lines. These wave paths coincide after their first encounter with reflector 1, hence the contribution of waves radiated from the stationary point; $\mathbf{r}_{S1}$ and $\mathbf{r}_{Sm}$ to the cross-correlation is nonzero for the same delay time. The contribution of the waves excited at $\mathbf{r}_{S1}$ is proportional to $r_1 r_2$, while the contribution of the waves excited at $\mathbf{r}_{Sm}$ is equal to $-r_1 r_2$, because the reflection coefficient of reflector 1 for a downward reflected waves is $-r_1$ rather than r_1. As shown in the examples in the previous sections, it does not matter how far the stationary point is removed from the surface. Therefore, the stationary points $\mathbf{r}_{S1}$ and $\mathbf{r}_{Sm}$ give contributions to the cross-correlation that are equal, but have opposite sign. This means that the sum of the cross terms of the cross-correlation of these two stationary points gives a vanishing contribution.

In practical situations the sources are typically located at the surface $z = 0$ only; this is for example the case in the virtual-source experiment of Bakulin and Calvert [2004]. In that case the cross terms of waves reflected from different reflectors give a non-zero contribution that is proportional to the product of reflection coefficients. These non-zero contributions are proportional to the product of reflection coefficients. Therefore, virtual source imaging introduces spurious multiples when the sources cannot be placed on a closed surface.

9 DISCUSSION

Inserting expression (22), (47), (48) and (55) into equation (12) gives for one reflector the following total contribution to the correlation:

$$C_{AB}(\omega) = \frac{n\,|S(\omega)|^2\,c}{2\cos\psi}\left\{\frac{G(R)}{-i\omega} + r^2\left(\frac{G(R)}{-i\omega}\right)^* \right. \tag{60}$$
$$\left. + r\,\frac{G(R_1+R_2)}{-i\omega} + r\left(\frac{G(R_1+R_2)}{-i\omega}\right)^*\right\} .$$

In the presence of more reflectors, one can sum the last three terms over the different reflectors. The correlation is a weighted average of the causal and acausal Green's function for the direct wave and the singly-reflected waves. Note that for the direct wave, the acausal Green's function is weighted by r^2. This is because the contribution of upgoing waves is r^2 times the contribution to the Green's function from the downgoing waves. In practical applications of seismic interferometry in reflection seismology, this contribution to the direct waves is not relevant because the primary reflections rather than the direct waves are used to image the subsurface.

Note that it is arbitrary how the cross-correlation is defined. When the cross-correlation is defined by $C_{AB}(\omega) = u_A^*(\omega)u_B(\omega)$ instead of expression (6) the roles of the causal and acausal Green's functions are interchanged. Since in practice one extracts the causal Green's function from the correlation, this arbitrariness in the definition of the correlation does not matter.

The four terms in expression (60) correspond to the waves that propagate along the four trajectories shown in figure 15. The waves in the upper diagrams are the direct waves that propagate in opposite directions between the two receivers. The waves in the bottom diagrams are the single-reflected waves that propagate in opposite directions between the receivers. These diagrams provide an illustration of why the correlation leads to the superposition of the causal and acausal Green's function.

In the derivation of this paper we did not explicitly account for the radiation pattern of the point source. It follows from the figure 15 (and figure A1 for a heterogeneous medium) that the paths that render the phase of the correlation stationary correspond to rays that propagate in the same direction to the two receivers. This means that if the source does not radiate energy isotropically, the two receivers are still illuminated with the same source strength. Similarly, when the reflection coefficient depends on the angle of incidence, the stationary phase approximation selects the reflection angle at the angle of the reflected wave that propagates between the receivers A and B, as shown in figure 15.

When more reflectors are present, the contribution of term 4 is proportional to $r_j r_{j'}$. When only sources at the surface $z = 0$ are used, these cross terms lead to spurious multiples that have the same strength as peg-leg multiples. These spurious multiples are not removed by algorithms for the removal of surface-related multiples [Verschuur et al, 1992; van Borselen et al., 1996; Dragoset and Jeričević, 1998] because kinematically they do not correspond to peg-leg multiples.

The analysis of this paper shows that the Green's function is retrieved from the stationary phase contribution from the integration (summation) over all sources. The sources far from the stationary point give an oscillatory contribution that averages to zero. When random noise is used as a source, these source in general are spread out over the surface. When man-made sources are used, however, one may limit these sources to the stationary phase region.

Acknowledgments: We appreciate the comments of John Stockwell, and Kurang Mehta.

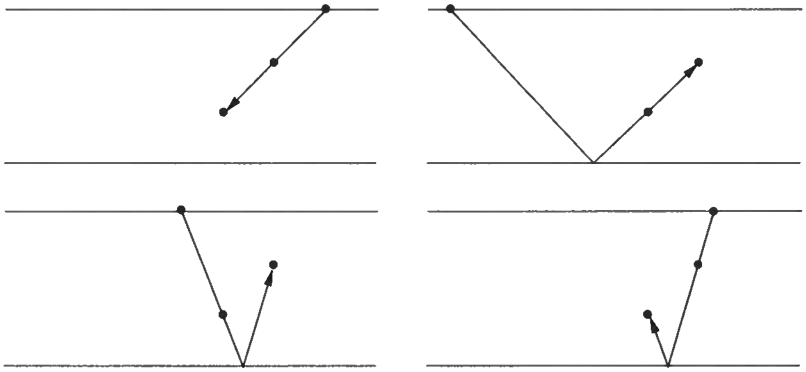

Figure 15. The wave paths that correspond to the stationary contributions to the correlations for the causal direct wave from term 1 (upper left panel), the acausal direct wave from term 4 (upper right panel), the acausal reflected wave from term 2 (lower left panel), the causal reflected wave from term 3 (lower left panel).

REFERENCES

A. Bakulin and R. Calvert. Virtual source: new method for imaging and 4D below complex overburden. *Expanded abstracts of the 2004 SEG-meeting*, pages 2477–2480, 2004.

M. Berrry and C. Upstill. Catastrophe optics: Morphologies of caustics and their diffraction patterns. In E. Wolf, editor, *Prog. in Optics, XVIII*, pages 257–346. 1980.

N. Bleistein. *Mathematical Methods for Wave Phenomena.* Academic Press, Orlando, 1984.

N. Bleistein, J.K. Cohen, and J.W. Stockwell Jr. *Mathematics of Multidimensional Seismic Imaging, Migration, and Inversion.* Springer, New York, 2001.

O.M. Bucci and G Franceschetti. On the degrees of freedom of scattered fields. *IEEE Trans. on Antennas and Propagation*, 37:918–926, 1989.

M. Campillo and A. Paul. Long-range correlations in the diffuse seismic coda. *Science*, 299:547–549, 2003.

V. Cervený and F. Hron. The ray series method and dynamical ray tracing system for three-dimensional inhomogeneous media. *Bull. Seismol. Soc. Am.*, 70:47–77, 1980.

J.F. Claerbout. Synthesis of a layered medium from its acoustic transmission response. *Geophysics*, 33:264–269, 1968.

A. Derode, E. Larose, M. Campillo, and M. Fink. How to estimate the Green's function for a heterogeneous medium between two passive sensors? Application to acoustic waves. *Appl. Phys. Lett.*, 83:3054–3056, 2003a.

A. Derode, E. Larose, M. Tanter, J. de Rosny, A. Tourin, M. Campillo, and M. Fink. Recovering the Green's function from far-field correlations in an open scattering medium. *J. Acoust. Soc. Am.*, 113:2973–2976, 2003b.

W.H. Dragoset and Z. Jeričević. Some remarks on multiple attenuation. *Geophysics*, 63:772–789, 1998.

M. Haney and R. Snieder. Seismic data processing in the stationary phase approximation. *First Break, in press*, 2005.

H.J. Landau. Necessary density conditions for sampling and interpolation of certain entire functions. *Acta Mathematica*, 117:37–52, 1967.

E. Larose, A. Derode, M. Campillo, and M. Fink. Imaging from one-bit correlations of wideband diffuse wave fields. *J. Appl. Phys.*, 95:8393–8399, 2004.

Lévy-Leblond and F. Balibur. *Quantics, Rudiments of Quantum Physics.* North-Holland, Amsterdam, 1990.

O.I. Lobkis and R.L. Weaver. On the emergence of the Green's function in the correlations of a diffuse field. *J. Acoust. Soc. Am.*, 110:3011–3017, 2001.

A. Malcolm, J. Scales, and B.A. van Tiggelen. Extracting the Green's function from diffuse, equipartitioned waves. *Phys. Rev. E*, 70:015601, 2004.

J.E. Rickett and J.F. Claerbout. Acoustic daylight imaging via spectral factorization; helioseismology and reservoir monitoring. *The Leading Edge*, 18:957–960, 1999.

J.E. Rickett and J.F. Claerbout. Calculation of the sun's acoustic impulse response by multidimensional spectral factorization. *Solar Physics*, 192:203–210, 2000.

P. Roux and M. Fink. Green's function estimation using secondary sources in a shallow water environment. *J. Acoust. Soc. Am.*, 113:1406–1416, 2003.

P. Roux, K.G. Sabra, W.A. Kuperman, and A. Roux. Ambioent noise cross correlation in free space: Theoretical approach. *J. Acoust. Soc. Am.*, 117:79–84, 2005.

K.G. Sabra, P. Roux, and W.A. Kuperman. Arrival-time structure of the time-averaged ambient noise cross-correlation in an oceanic waveguide. *J. Acoust. Soc. Am.*, 117:164–174, 2005.

G.T. Schuster, J. Yu, J. Sheng, and J. Rickett. Interferometric/daylight seismic imaging. *Geophys. J. Int.*, 157:838–852, 2004.

N.M. Shapiro and M. Campillo. Emergence of broadband Rayleigh waves from correlations of the ambient seismic noise. *Geophys. Res. Lett.*, 31:L07614, doi10.1029/2004GL019491, 2004.

N.M. Shapiro, M. Campillo, L. Stehly, and M.H. Ritzwoller. High-resolution surface-wave tomography from ambient seismic noise. *Science*, 307:1615–1618, 2005.

R. Snieder. Extracting the Green's function from the correlation of coda waves: A derivation based on stationary phase. *Phys. Rev. E*, 69:046610, 2004a.

R. Snieder. *A Guided Tour of Mathematical Methods for the Physical Sciences.* Cambridge Univ. Press, Cambridge, UK, 2nd edition, 2004b.

R. Snieder. Extracting the building response from an incoherent excitation; theory and application to the Millikan Library in Pasadena, California. *Project Review of the Consortium Project on Seismic Inverse Methods for*

Complex Structures, 2005.

R. Snieder and C. Chapman. The reciprocity properties of geometrical spreading. *Geophys. J. Int.*, 132:89–95, 1998.

R. Snieder and A. Lomax. Wavefield smoothing and the effect of rough velocity perturbations on arrival times and amplitudes. *Geophys. J. Int.*, 125:796–812, 1996.

R.G. van Borselen, J.T. Fokkema, and P.M. van den Berg. Removal of surface-related wave phenomena - the marine case. *Geophysics*, 61:202–210, 1996.

D.J. Verschuur, A.J. Berkhout, and C.P.A. Wapenaar. Adaptive surface-related multiple elimination. *Geophysics*, 57:1166–1177, 1992.

K. Wapenaar. Retrieving the elastodynamic Green's function of an arbitrary inhomogeneous medium by cross correlation. *Phys. Rev. Lett.*, 93:254301, 2004.

K. Wapenaar, J. Fokkema, and R. Snieder. Retrieving the Green's function by cross-correlation: a comparison of approaches. *Submitted to J. Acoust. Soc. Am.*, 2005.

K. Wapenaar, J. Thorbecke, and D. Dragonov. Relations between reflection and transmission responses of three-dimensional inhomogeneous media. *Geophys. J. Int.*, 156:179–194, 2004.

R.L. Weaver and O.I. Lobkis. Ultrasonics without a source: Thermal fluctuation correlations and MHz frequencies. *Phys. Rev. Lett.*, 87:134301–1/4, 2001.

R.L. Weaver and O.I. Lobkis. Diffuse fields in open systems and the emergence of the green's function. *J. Acoust. Soc. Am.*, 116:2731–2734, 2004.

O. Yilmaz. Seismic data processing. In *Investigations in geophysics*, volume 2. Society of Exploration Geophysicists, Tulsa, 1987.

APPENDIX A: SEISMIC INTERFEROMETRY OF THE DIRECT WAVES IN THE RAY-GEOMETRIC APPROXIMATION

In this appendix, we show that the arguments used in this paper for a homogeneous medium can be generalized to heterogenous media where the velocity variations are sufficiently smooth to justify the use of ray theory for the Green's function. In order to avoid complications due to curved reflectors, we analyze only term T1. For simplicity we assume that the density is constant. The ray-geometric Green's function that gives the response at $\mathbf{r}_1$ due to a point source in $\mathbf{r}_2$ is given by expression (15) of [Snieder and Chapman, 1998]:

$$G^{ray}(\mathbf{r}_1,\mathbf{r}_2) = -\frac{1}{4\pi}\sqrt{\frac{v_1}{v_2}}\frac{\exp(i\omega\tau_{12})}{\sqrt{J_{12}}} \; . \tag{A1}$$

In this expression $v_1 = v(\mathbf{r}_1)$, τ_{12} is the travel time for the propagation from $\mathbf{r}_2$ to $\mathbf{r}_1$, and J_{12} is the associated geometrical-spreading factor. Because of reciprocity [Snieder and Chapman, 1998], this Green's function is also equal to

$$G^{ray}(\mathbf{r}_1,\mathbf{r}_2) = -\frac{1}{4\pi}\sqrt{\frac{v_2}{v_1}}\frac{\exp(i\omega\tau_{21})}{\sqrt{J_{21}}} \; . \tag{A2}$$

Note that the travel time is reciprocal:

$$\tau_{12} = \tau_{21} \; , \tag{A3}$$

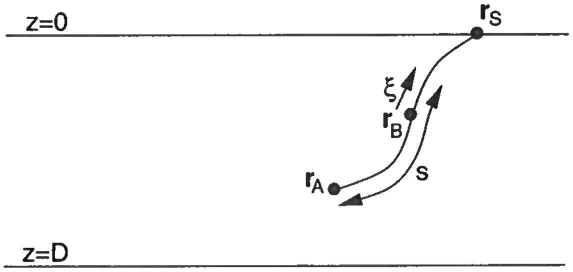

Figure A1. The stationary phase condition for term 1 for a heterogeneous reference medium.

but the geometrical spreading is not [Snieder and Chapman, 1998].

Inserting the Green's function (A2) in term T1 of expression (12) gives

$$T1 = \frac{1}{(4\pi)^2}\int \frac{v_S}{\sqrt{v_A v_B}}\frac{\exp(i\omega(\tau_{SA}-\tau_{SB}))}{\sqrt{J_{SA}J_{SB}}}dxdy \; , \tag{A4}$$

where $v_S = v(\mathbf{r}_S) = v(x,y,0)$, $v_A = v(\mathbf{r}_A)$, and $v_B = v(\mathbf{r}_B)$. By analogy with the situation shown in figure 3 the stationary points in this integral correspond to the rays that propagate from the source S through receiver B to receiver A as shown in figure A1. By virtue of reciprocity, these stationary points can be found by tracing rays from receiver A to receiver B and by continuing these rays to the surface $z = 0$. In general there may be more than one stationary point. In the following we analyze the contribution of one stationary point, but in the end one needs to sum over all stationary points. It may happen, in fact, that the region of stationary phase does not consist of a finite number of points, but of a line or surface area. In that case, point A is a caustic and ray theory breaks down [Berry and Upstill, 1980].

Let the travel time along the ray from A to B to S be given by τ_0. The travel time for an adjacent ray follows from the second-order Taylor expansion in the ray-centered coordinates q_1 and q_2 that measure the perpendicular distance to the ray in two orthogonal directions. According to expression (50) of Cerveny and Hron [1980] the travel time along an adjacent ray is given by

$$\tau = \tau_0 + \frac{1}{2}\mathbf{q}\cdot\mathbf{M}\cdot\mathbf{q} \; , \tag{A5}$$

with $\mathbf{M}$ a matrix of second-order derivatives of the travel time. In the following it is convenient to replace the integration over the surface $z = 0$ in expression (A4) by an integration over the ray-centered coordinates q_1 and q_2. The orientation of these coordinate axes is ambiguous, since any choice of axes perpendicular to the ray is admissible. In the following we choose the q_2-axis to be aligned with the plane $z = 0$, as indicated in figure A2. The other coordinate, q_1, then measures the distance to the ray in the orthogonal direction. As shown in figure A2, the associated q_1-axis makes an angle ψ with the horizontal that is equal to the angle between

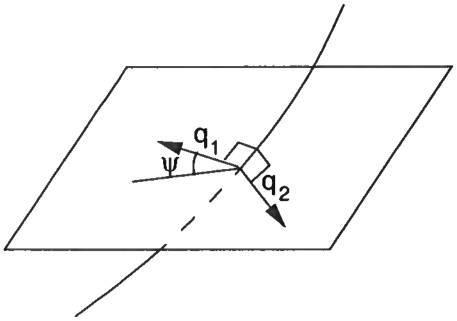

Figure A2. Definition of the ray-centered coordinates q_1 and q_2. The q_2-axis lies in the x, y-plane and is perpendicular to the ray. The angle ψ is the angle between the ray direction and the vertical.

the ray and the vertical. An element dq_2 corresponds to an element dy' in the x, y-plane, while an element dq_1 corresponds to an element $dq_1 = \cos\psi dx'$. We use primed coordinates since the ray direction is not necessarily aligned with the original x-axis. This means that a surface element in the surface integral can be related to a surface element $dq_1 dq_2$ using

$$dxdy = dx'dy' = \frac{1}{\cos\psi} dq_1 dq_2 \,. \tag{A6}$$

This expression can be used to evaluate integral (A4) in the stationary phase approximation. With Taylor expansion (A5) for the rays from A to S and from B to S, this integral in the stationary phase approximation is given by

$$\begin{aligned} T1 &= \frac{1}{(4\pi)^2 \cos\psi} \frac{v_S}{\sqrt{v_A v_B}} \frac{\exp\left(i\omega\left(\tau_{SA} - \tau_{SB}\right)\right)}{\sqrt{J_{SA} J_{SB}}} \\ &\times \int \exp\left(\frac{i\omega}{2} \mathbf{q} \cdot \left(\mathbf{M}_{SA} - \mathbf{M}_{SB}\right) \cdot \mathbf{q}\right) dq_1 dq_2 \,. \end{aligned} \tag{A7}$$

The integration over the q-variables gives [Bleistein, 1984]

$$\begin{aligned} T1 = & \frac{1}{8\pi\omega\cos\psi} \frac{v_S}{\sqrt{v_A v_B}} \frac{\exp\left(i\omega\left(\tau_{SA} - \tau_{SB}\right)\right)}{\sqrt{J_{SA} J_{SB}}} \\ & \frac{\exp\left(i sgn\, \pi/4\right)}{\sqrt{\left|\det\left(\mathbf{M}_{SA} - \mathbf{M}_{SB}\right)\right|}} \,, \end{aligned} \tag{A8}$$

where sgn is the number of positive eigenvalues of $\mathbf{M}_{SA} - \mathbf{M}_{SB}$ minus the number of negative eigenvalues. Using the same reasoning as in the derivation of expression (6.21) of [Snieder and Lomax, 1996], $T1$ is equal to

$$T1 = \frac{i}{8\pi\omega\cos\psi} \frac{v_S}{\sqrt{v_A v_B}} \frac{\exp\left(i\omega\left(\tau_{SA} - \tau_{SB}\right)\right)}{\sqrt{J_{SA} J_{SB} \det\left(\mathbf{M}_{SA} - \mathbf{M}_{SB}\right)}} \,. \tag{A9}$$

Since the points $\mathbf{r}_A$, $\mathbf{r}_B$, and $\mathbf{r}_S$ are located on the same ray,

$$\tau_{SA} - \tau_{SB} = \tau_{AB} \,, \tag{A10}$$

this is the travel time along the ray that joins the receivers A and B. This means that $T1$ is kinematically identical to the Green's function that accounts for the wave propagation between the receivers A and B. In the following we show that expression (A9) also accounts dynamically for this Green's function by using a derivation similar to that presented in [Snieder and Lomax, 1996].

According to expression (68) of Cervený and Hron [1980], the matrix $\mathbf{M}$ is related to the curvature matrix of the wavefronts by the relation

$$\mathbf{M} = \frac{1}{v} \mathbf{K} \,. \tag{A11}$$

Since $\mathbf{M}$ is a 2×2 matrix this, together with expression (A10), implies that

$$T1 = \frac{i}{8\pi\omega\cos\psi} \frac{v_S^2}{\sqrt{v_A v_B}} \frac{\exp\left(i\omega\tau_{AB}\right)}{\sqrt{J_{SA} J_{SB} \det\left(\mathbf{K}_{SA} - \mathbf{K}_{SB}\right)}} \,. \tag{A12}$$

Following equation (76) of Cervený and Hron [1980], the curvature matrix satisfies the following matrix Ricatti equation:

$$\frac{d\mathbf{K}_{SA}}{ds} = \frac{1}{v} \frac{dv}{ds} \mathbf{K}_{SA} - \mathbf{K}_{SA}^2 - \frac{1}{v} \mathbf{V} \,, \tag{A13}$$

where $v = v_S$, and the matrix $\mathbf{V}$ is defined by $V_{ij} = \partial^2 v / \partial q_i \partial q_j$, and where s is the distance along the ray from $\mathbf{r}_A$ through $\mathbf{r}_B$ to the surface, as indicated in figure A1. Using this expression, and the corresponding expression for $\mathbf{K}_{SB}$ it follows that the difference satisfies the following differential equation

$$\frac{d\left(\mathbf{K}_{SA} - \mathbf{K}_{SB}\right)}{ds} = \frac{1}{v} \frac{dv}{ds} \left(\mathbf{K}_{SA} - \mathbf{K}_{SB}\right) - \left(\mathbf{K}_{SA}^2 - \mathbf{K}_{SB}^2\right) \,. \tag{A14}$$

From this it follows after a lengthy calculation that

$$\begin{aligned} \frac{d}{ds} \det\left(\mathbf{K}_{SA} - \mathbf{K}_{SB}\right) &= \frac{2}{v} \frac{dv}{ds} \det\left(\mathbf{K}_{SA} - \mathbf{K}_{SB}\right) \\ &- \left(tr\, \mathbf{K}_{SA} + tr\, \mathbf{K}_{SB}\right) \det\left(\mathbf{K}_{SA} - \mathbf{K}_{SB}\right) \,, \end{aligned} \tag{A15}$$

where tr denotes the trace. According to expression (70) of Snieder and Chapman [1998]

$$tr\, \mathbf{K} = \frac{1}{J} \frac{dJ}{ds} \,. \tag{A16}$$

Using this expression to eliminate the trace of $\mathbf{K}_{SA}$ and $\mathbf{K}_{SB}$ from expression (A15), the result can be integrated to give

$$\frac{d}{ds} \left\{ \frac{J_{SA} J_{SB} \det\left(\mathbf{K}_{SA} - \mathbf{K}_{SB}\right)}{v_S^2} \right\} = 0 \,, \tag{A17}$$

or

$$\frac{J_{SA} J_{SB} \det\left(\mathbf{K}_{SA} - \mathbf{K}_{SB}\right)}{v_S^2} = const. \tag{A18}$$

This expression holds for any point S along the ray in figure A1. The constant can be found by evaluating this expression for a point S along the ray at a small distance ξ beyond the receiver B, as shown in figure A1, and by letting this distance go to zero. At a small distance from receiver B, the medium can be considered to be locally homogeneous, and the curvature matrix attains its value for a homogeneous medium:

$$\mathbf{K}_{SB} = \begin{vmatrix} 1/\xi & 0 \\ 0 & 1/\xi \end{vmatrix} . \tag{A19}$$

In the limit $\xi \rightarrow 0$ these terms dominate the contributions from $\mathbf{K}_{SA}$ in expression (A18) and $\det(\mathbf{K}_{SA} - \mathbf{K}_{SB}) \rightarrow 1/\xi^2$ as $\xi \rightarrow 0$. In that limit the geometrical spreading is given by $J_{SB} = \xi^2$, $J_{SA} \rightarrow J_{BA}$, and $v_S \rightarrow v_B$. Inserting these results in expression (A12) shows that the constant in that expression is given by $const = J_{BA}/v_B^2$. Inserting this in expression (A18) finally gives

$$J_{SA} J_{SB} \det(\mathbf{K}_{SA} - \mathbf{K}_{SB}) = \frac{v_S^2}{v_B^2} J_{BA} , \tag{A20}$$

or

$$\sqrt{J_{SA} J_{SB} \det(\mathbf{K}_{SA} - \mathbf{K}_{SB})} = \pm \frac{v_S}{v_B} \sqrt{J_{BA}} . \tag{A21}$$

At this point, the sign in the right hand side is arbitrary.

This last result can be used to eliminate $\sqrt{\det(\mathbf{K}_{SA} - \mathbf{K}_{SB})}$ from expression (A12), giving

$$T1 = \frac{\pm i v_S}{8\pi\omega \cos\psi} \sqrt{\frac{v_B}{v_A}} \frac{\exp(i\omega\tau_{AB})}{\sqrt{J_{BA}}} . \tag{A22}$$

Following expression (45) of Snieder and Chapman [1998], the reciprocity property of the geometrical spreading is given by $J_{BA} = (v_B/v_A)^2 J_{AB}$; hence

$$T1 = \frac{\pm i v_S}{8\pi\omega \cos\psi} \sqrt{\frac{v_A}{v_B}} \frac{\exp(i\omega\tau_{AB})}{\sqrt{J_{AB}}} . \tag{A23}$$

A comparison with the ray-geometric Green's function (A1) gives

$$T1 = \frac{\mp v_S}{2\cos\psi} \times \frac{G^{ray}(\mathbf{r}_A, \mathbf{r}_B)}{-i\omega} . \tag{A24}$$

After multiplying with the terms $n |S(\omega)|^2$, this result can directly be compared with the corresponding expression (22) for a homogeneous medium. This implies that the lower sign in expression (A21) must be used. After taking the source spectrum and the scatterer density into account, this finally gives equation (24).

CWP-501

Retrieving the Green's function in an open system by cross-correlation: A comparison of approaches

Kees Wapenaar[1], Jacob Fokkema[1], and Roel Snieder[2]
[1] *Department of Geotechnology, Delft University of Technology, Delft, The Netherlands*
[2] *Center for Wave Phenomena, Colorado School of Mines, Golden CO 80401, USA*

ABSTRACT

We compare two approaches for deriving the fact that the Green's function in an arbitrary inhomogeneous open system can be obtained by cross-correlating recordings of the wave field at two positions. One approach is based on physical arguments, exploiting the principle of time reversal invariance of the acoustic wave equation. The other approach is based on Rayleigh's reciprocity theorem. Using a unified notation for both approaches, we discuss their similarities and differences.

Key words: seismic interferometry

1 INTRODUCTION

Since the work of Weaver and Lobkis (2001; 2001), many researchers have shown theoretically and experimentally that the cross-correlation of the recordings of a diffuse wave field at two receiver positions yields the Green's function between these positions. In most cases it is assumed that the diffuse wave field consists of normal modes (with uncorrelated amplitudes) in a closed system. Much less attention has been paid to the theory of Green's function retrieval in arbitrary inhomogeneous open systems. Nevertheless, the first result stems from 1968, albeit for one-dimensional media, when Claerbout (1968) showed that the seismic reflection response of a horizontally layered earth can be synthesized from the autocorrelation of its transmission response. Recently we generalized this to 3-D arbitrary inhomogeneous media (Wapenaar et al., 2002; Wapenaar, 2003; Wapenaar, 2004). Using reciprocity theorems of the correlation type, we showed in those papers that the cross-correlation of transmission responses observed at the earth's free surface, due to uncorrelated noise sources in the subsurface, yields the full reflection response (i.e., the ballistic wave and the coda) of the 3-D inhomogeneous subsurface. Weaver and Lobkis (2004) followed a similar approach for a configuration in which the 3-D inhomogeneous medium is surrounded by uncorrelated sources. Derode et al. (2003a; 2003b) derived expressions for Green's function retrieval in open systems using physical arguments, exploiting the principle of time reversal invariance of the acoustic wave equation. Their approach can be seen as the 'physical counterpart' of our derivations based on reciprocity. In this letter we compare the physical arguments of Derode et al. (2003a; 2003b) with our approach based on Rayleigh's reciprocity theorem (Wapenaar et al., 2002; Wapenaar, 2003; Wapenaar, 2004). Moreover, we indicate the links with 'reverse time migration' and 'frequency domain migration', respectively. We use a unified notation, which facilitates the comparison of both approaches.

2 PHYSICAL ARGUMENTS

In this section we summarize the physical arguments of Derode et al. (2003a; 2003b) for deriving expressions for Green's function retrieval. Consider a lossless arbitrary inhomogeneous acoustic medium in a homogeneous embedding. In this configuration we define two points with coordinate vectors $\mathbf{x}_A$ and $\mathbf{x}_B$. Our aim is to show that the acoustic response at $\mathbf{x}_B$ due to an impulsive source at $\mathbf{x}_A$ [i.e., the Green's function $G(\mathbf{x}_B, \mathbf{x}_A, t)$] can be obtained by cross-correlating passive measurements of the wave fields at $\mathbf{x}_A$ and $\mathbf{x}_B$ due to sources on a surface S in the homogeneous embedding. The derivation starts by considering another physical experiment, namely an impulsive source at $\mathbf{x}_A$ and receivers at $\mathbf{x}$ on S. The response at one particular point $\mathbf{x}$ on S is denoted by $G(\mathbf{x}, \mathbf{x}_A, t)$. Imagine that we record this response for all $\mathbf{x}$ on S, revert the time axis, and feed these time-reverted functions $G(\mathbf{x},\mathbf{x}_A,-t)$ to sources at all $\mathbf{x}$ on S. Huygens' principle states that the wave field at any point $\mathbf{x}'$ in S due to these sources on S is then given by

$$u(\mathbf{x}',t) \propto \oint_S \underbrace{G(\mathbf{x}',\mathbf{x},t)}_{\text{'propagator'}} * \underbrace{G(\mathbf{x},\mathbf{x}_A,-t)}_{\text{'source'}} \mathrm{d}^2\mathbf{x}, \qquad (1)$$

where $*$ denotes convolution and $\propto$ 'proportional to'. According to this equation, $G(\mathbf{x}',\mathbf{x},t)$ propagates the source function $G(\mathbf{x},\mathbf{x}_A,-t)$ from $\mathbf{x}$ to $\mathbf{x}'$ and the result is integrated over all sources on S. Due to the invariance of the acoustic wave equation for time-reversal, the wave field $u(\mathbf{x}',t)$ focusses for $\mathbf{x}' = \mathbf{x}_A$ at $t = 0$. McMechan (1983) exploited this property in a seismic imaging method which has become known as reverse time migration. Derode et al. (2003a; 2003b) give a new interpretation to equation (1). Since $u(\mathbf{x}',t)$ focusses for $\mathbf{x}' = \mathbf{x}_A$ at $t = 0$, the wave field $u(\mathbf{x}',t)$ for arbitrary $\mathbf{x}'$ and t can be seen as the response of a virtual source at $\mathbf{x}_A$ and $t = 0$. This virtual source response, however, consists of a causal and an anti-causal part, according to

$$u(\mathbf{x}',t) = G(\mathbf{x}',\mathbf{x}_A,t) + G(\mathbf{x}',\mathbf{x}_A,-t). \qquad (2)$$

This is explained as follows: the wave field generated by the anti-causal sources on S first propagates to all $\mathbf{x}'$ where it gives an anti-causal contribution, next it focusses in $\mathbf{x}_A$ at $t = 0$ and finally it propagates again to all $\mathbf{x}'$ giving the causal contribution. The propagation paths from $\mathbf{x}'$ to $\mathbf{x}_A$ are the same as those from $\mathbf{x}_A$ to $\mathbf{x}'$, but are travelled in opposite direction. Combining equations (1) and (2), applying source-receiver reciprocity to $G(\mathbf{x},\mathbf{x}_A,-t)$ in equation (1) and setting $\mathbf{x}' = \mathbf{x}_B$ yields

$$G(\mathbf{x}_B,\mathbf{x}_A,t) + G(\mathbf{x}_B,\mathbf{x}_A,-t) \propto \oint_S G(\mathbf{x}_B,\mathbf{x},t) * G(\mathbf{x}_A,\mathbf{x},-t)\mathrm{d}^2\mathbf{x}. \qquad (3)$$

The right-hand side of equation (3) can be interpreted as the integral of cross-correlations of observations of wave fields at $\mathbf{x}_B$ and $\mathbf{x}_A$, respectively, due to impulsive sources at $\mathbf{x}$ on S; the integration takes place along the source coordinate $\mathbf{x}$. The left-hand side is interpreted as the superposition of the response at $\mathbf{x}_B$ due to an impulsive source at $\mathbf{x}_A$ and its time-reversed version. Since the Green's function $G(\mathbf{x}_B,\mathbf{x}_A,t)$ is causal, it can be obtained from the left-hand side of equation (3) by taking the causal part. The reconstructed Green's function contains the ballistic wave as well as the coda due to multiple scattering in the inhomogeneous medium.

3 RAYLEIGH'S RECIPROCITY THEOREM

In this section we summarize our derivation based on Rayleigh's reciprocity theorem (Wapenaar et al., 2002; Wapenaar, 2003; Wapenaar, 2004). This reciprocity theorem relates two independent acoustic states in one and the same domain (De Hoop, 1988; Fokkema and van den Berg, 1993). Consider an acoustic wave field, characterized by the acoustic pressure $p(\mathbf{x},t)$ and the particle velocity $v_i(\mathbf{x},t)$. We define the temporal Fourier transform of a space- and time-dependent quantity $p(\mathbf{x},t)$ as $\hat{p}(\mathbf{x},\omega) = \int \exp(-j\omega t)p(\mathbf{x},t)\mathrm{d}t$, where j is the imaginary unit and ω the angular frequency. In the space-frequency domain the acoustic pressure and particle velocity in a lossless arbitrary inhomogeneous acoustic medium obey the equation of motion $j\omega\rho\hat{v}_i + \partial_i\hat{p} = 0$ and the stress-strain relation $j\omega\kappa\hat{p} + \partial_i\hat{v}_i = \hat{q}$, where ∂_i is the partial derivative in the x_i-direction (Einstein's summation convention applies for repeated lowercase subscripts), $\rho(\mathbf{x})$ the mass density of the medium, $\kappa(\mathbf{x})$ its compressibility and $\hat{q}(\mathbf{x},\omega)$ a source distribution in terms of volume injection rate density. We consider the 'interaction quantity' $\partial_i\{\hat{p}_A\hat{v}_{i,B} - \hat{v}_{i,A}\hat{p}_B\}$, where subscripts A and B are used to distinguish two independent states. Rayleigh's reciprocity theorem is obtained by substituting the equation of motion and the stress-strain relation for states A and B into the interaction quantity, integrating the result over a spatial domain V enclosed by S with outward pointing normal vector $\mathbf{n} = (n_1,n_2,n_3)$ and applying the theorem of Gauss. This gives

$$\int_V \{\hat{p}_A\hat{q}_B - \hat{q}_A\hat{p}_B\}\mathrm{d}^3\mathbf{x} = \oint_S \{\hat{p}_A\hat{v}_{i,B} - \hat{v}_{i,A}\hat{p}_B\}n_i\mathrm{d}^2\mathbf{x}. \qquad (4)$$

Since the medium is lossless, we can apply the principle of time-reversal invariance (Bojarksi, 1983). In the frequency domain time-reversal is replaced by complex conjugation. Hence, when $\hat{p}$ and $\hat{v}_i$ are a solution of the equation of motion and the stress-strain relation with source distribution $\hat{q}$, then $\hat{p}^*$ and $-\hat{v}_i^*$ obey the same equations with source distribution $-\hat{q}^*$ (the asterisk denotes complex conjugation). Making these substitutions for state A we obtain

$$\int_V \{\hat{p}_A^*\hat{q}_B + \hat{q}_A^*\hat{p}_B\}\mathrm{d}^3\mathbf{x} = \oint_S \{\hat{p}_A^*\hat{v}_{i,B} + \hat{v}_{i,A}^*\hat{p}_B\}n_i\mathrm{d}^2\mathbf{x}. \qquad (5)$$

Next we choose impulsive point sources in both states, according to $\hat{q}_A(\mathbf{x},\omega) = \delta(\mathbf{x}-\mathbf{x}_A)$ and $\hat{q}_B(\mathbf{x},\omega) = \delta(\mathbf{x}-\mathbf{x}_B)$, with $\mathbf{x}_A$ and $\mathbf{x}_B$ both in V. The wave field in state A can thus be expressed in terms of a Green's function, according to

$$\hat{p}_A(\mathbf{x},\omega) = \hat{G}(\mathbf{x},\mathbf{x}_A,\omega), \qquad (6)$$

$$\hat{v}_{i,A}(\mathbf{x},\omega) = -(j\omega\rho(\mathbf{x}))^{-1}\partial_i\hat{G}(\mathbf{x},\mathbf{x}_A,\omega), \qquad (7)$$

where $\hat{G}(\mathbf{x},\mathbf{x}_A,\omega)$ obeys the wave equation

$$\rho\partial_i(\rho^{-1}\partial_i\hat{G}) + (\omega^2/c^2)\hat{G} = -j\omega\rho\delta(\mathbf{x}-\mathbf{x}_A), \qquad (8)$$

with propagation velocity $c(\mathbf{x}) = \{\kappa(\mathbf{x})\rho(\mathbf{x})\}^{-\frac{1}{2}}$; similar expressions hold for the wave field in state B. Substituting these expressions into equation (5) and using source-receiver reciprocity of the Green's functions gives

$$2\Re\{\hat{G}(\mathbf{x}_B,\mathbf{x}_A,\omega)\} = \oint_S \frac{-1}{j\omega\rho(\mathbf{x})}\Big(\partial_i\hat{G}(\mathbf{x}_B,\mathbf{x},\omega)\hat{G}^*(\mathbf{x}_A,\mathbf{x},\omega) - \hat{G}(\mathbf{x}_B,\mathbf{x},\omega)\partial_i\hat{G}^*(\mathbf{x}_A,\mathbf{x},\omega)\Big)n_i\mathrm{d}^2\mathbf{x}, \tag{9}$$

where $\Re$ denotes the real part. Note that the left-hand side is the Fourier transform of $G(\mathbf{x}_B,\mathbf{x}_A,t) + G(\mathbf{x}_B,\mathbf{x}_A,-t)$; the products $\partial_i\hat{G}\,\hat{G}^*$ etc. in the right-hand side correspond to cross-correlations in the time domain. Expressions like the right-hand side of this equation have been used by numerous researchers (including the authors) for seismic migration in the frequency domain. Esmersoy and Oristaglio (1988) explained the link with the reverse time migration method, mentioned in the previous section. What is new (compared with migration) is that equation (9) is formulated in such a way that it gives an exact representation of the Green's function $\hat{G}(\mathbf{x}_B,\mathbf{x}_A,\omega)$ in terms of cross-correlations of observed wave fields at $\mathbf{x}_B$ and $\mathbf{x}_A$. Note that, unlike in the previous section, we have not assumed that the medium outside surface S is homogeneous. The terms $\hat{G}$ and $\partial_i\hat{G}$ under the integral represent responses of monopole and dipole sources at $\mathbf{x}$ on S; the combination of the two correlation products under the integral ensures that waves propagating outward from the sources on S do not interact with those propagating inward and vice versa. When a part of S is a free surface on which the acoustic pressure vanishes, then the surface integral in equation (5) and hence in equation (9) need only be evaluated over the remaining part of S. Other modifications of equation (9), including the elastodynamic generalization, are discussed in (Wapenaar et al., 2002; Wapenaar, 2003; Wapenaar, 2004). Van Manen and Robertsson (2005) propose an efficient modelling scheme, based on an expression similar to equation (9).

Next we show with subsequent approximations how equation (9) simplifies to equation (3). First we assume that the medium outside S is homogeneous, with constant propagation velocity c and mass density ρ. In the high frequency regime, the derivatives of the Green's functions can be approximated by multiplying each constituent (direct wave, scattered wave etc.) by $-j\frac{\omega}{c}\cos\alpha$, where α is the angle between the pertinent ray and the normal on S. The main contributions to the integral in equation (9) come from stationary points on S (Snieder, 2004; Schuster et al., 2004; Wapenaar et al., 2004). At those points the ray angles for both Green's functions are identical (see also the example in the next section). This implies that the contributions of the two terms under the integral in equation (9) are approximately equal (but opposite in sign), hence

$$2\Re\{\hat{G}(\mathbf{x}_B,\mathbf{x}_A,\omega)\} \approx \frac{-2}{j\omega\rho}\oint_S \partial_i\hat{G}(\mathbf{x}_B,\mathbf{x},\omega)\hat{G}^*(\mathbf{x}_A,\mathbf{x},\omega)n_i\mathrm{d}^2\mathbf{x}. \tag{10}$$

If we assume that S is a sphere with large enough radius then all rays are normal to S (i.e., $\alpha \approx 0$), hence

$$2\Re\{\hat{G}(\mathbf{x}_B,\mathbf{x}_A,\omega)\} \approx \frac{2}{\rho c}\oint_S \hat{G}(\mathbf{x}_B,\mathbf{x},\omega)\hat{G}^*(\mathbf{x}_A,\mathbf{x},\omega)\mathrm{d}^2\mathbf{x}. \tag{11}$$

Transforming both sides of this equation back to the time domain yields equation (3) (i.e., the result of Derode et al. (2003a; 2003b)), with proportionality factor $2/\rho c$. Finally we consider a variant of our derivation. The Green's function introduced in equation (8) is the response of an impulsive point source of volume injection rate. Let us define a new Green's function $\hat{G}_0$ obeying the same wave equation, but with the source in the right-hand side replaced by $-\rho\delta(\mathbf{x}-\mathbf{x}_A)$, hence $\hat{G}_0 = \frac{1}{j\omega}\hat{G}$. Following the same derivation as above, we obtain instead of equation (11)

$$2j\Im\{\hat{G}_0(\mathbf{x}_B,\mathbf{x}_A,\omega)\} \approx \frac{-2j\omega}{\rho c}\oint_S \hat{G}_0(\mathbf{x}_B,\mathbf{x},\omega)\hat{G}_0^*(\mathbf{x}_A,\mathbf{x},\omega)\mathrm{d}^2\mathbf{x}, \tag{12}$$

where $\Im$ denotes the imaginary part. This expression resembles the results of Weaver and Lobkis (Weaver and Lobkis, 2004) and Snieder (Snieder, 2004), who retrieve the two-sided Green's function from the time-derivative of cross-correlations.

Note that for the derivation of each of the expressions (3) and (9) – (12), we assumed that impulsive point sources were placed on the surface S. This is the approach taken e.g. by Bakulin and Calvert (2004) in their experiment on virtual source imaging. Our derivation also holds for uncorrelated noise sources on S whose source-time function satisfies $s(\mathbf{x},t) * s(\mathbf{x}',-t) = \delta(\mathbf{x}-\mathbf{x}')C(t)$, with $C(t)$ the autocorrelation of the noise. When the noise is distributed over the surface, the cross-correlation of the observations at $\mathbf{x}_A$ and $\mathbf{x}_B$ leads to a double surface integral. The delta function reduces this to the single surface integral in the theory presented here (Wapenaar et al., 2002; Wapenaar, 2003; Derode, et al., 2003b; Wapenaar, 2004; Weaver and Lobkis, 2004; Snieder, 2004). A further discussion is beyond the scope of this letter.

4 NUMERICAL EXAMPLE

We illustrate equation (10) with a simple example. We consider a 2-D configuration with a single diffractor at $(x_1, x_3) = (0, 600)$m in a homogeneous medium with propagation velocity $c = 2000$ m/s, see Figure 1, in which C denotes the diffractor. Further, we define $\mathbf{x}_A = (-500, 100)$m and $\mathbf{x}_B = (500, 100)$m, denoted by A and B in Figure 1. The surface S is a circle with its center at the origin and a radius of 800 m. The solid arrows in Figure 1 denote the Green's function $G(\mathbf{x}_B, \mathbf{x}_A, t)$. We model the Green's functions in equation (10) with the Born approximation, which means

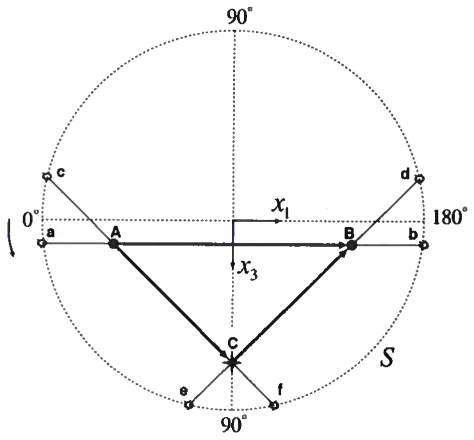

Figure 1. Single diffractor (C) in a homogeneous model. The receivers are at A and B. The integration is carried out along the sources on the surface S. The main contributions come from the stationary points a-d. The contributions from stationary points e and f cancel.

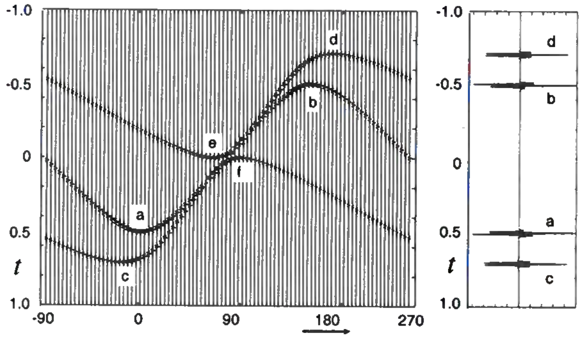

(a) (b)

Figure 2. (a) Time domain representation of the integrand of equation (10). (b) The sum of all traces in (a).

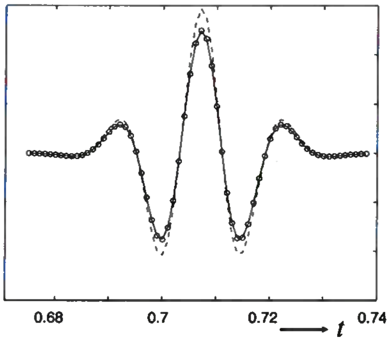

Figure 3. *Zoomed-in version of event c in Figure 2b. The solid line is the directly modelled wave field. The circles represent the integration result of equation (10) (i.e., the sum of the traces in Figure 2a). The dashed line represents the integration result of equation (11).*

that we consider direct waves and first order scattering only. To be consistent with the Born approximation, in the cross-correlations we also consider only the zeroth and first order terms. Figure 2a shows the time-domain representation of the integrand of equation (10) (convolved with a wavelet with a central frequency of 50 Hz). Each trace corresponds to a fixed source position $\mathbf{x}$ on S; the source position in polar coordinates is $(\phi, r = 800)$. The sum of all these traces (multiplied by $rd\phi$) is shown in Figure 2b. This result accurately matches the directly modelled wave field $G(\mathbf{x}_B, \mathbf{x}_A, t) + G(\mathbf{x}_B, \mathbf{x}_A, -t)$ (convolved with a wavelet), see Figure 3. The events labelled 'a' and 'c' in Figure 2 are the direct and scattered arrivals; the events 'b' and 'd' are the corresponding anti-causal arrivals. This figure clearly shows that the main contribution to these events come from Fresnel zones around the stationary points of the integrand (Snieder, 2004; Schuster et al., 2004; Wapenaar et al., 2004). The sources at these stationary points are marked in Figure 1 with the same labels. We discuss event 'c' in more detail. The path 'cCB' in Figure 1 represents the scattered wave in $G(\mathbf{x}_B, \mathbf{x}, t)$, for $\mathbf{x}$ at the stationary point 'c'. The path 'cA' represents the direct wave in $G(\mathbf{x}_A, \mathbf{x}, t)$. By correlating these two waves, the traveltime along the path 'cA' is subtracted from that along the path 'cCB', leaving the traveltime along the path 'ACB', which corresponds to the traveltime of the scattered wave in $G(\mathbf{x}_B, \mathbf{x}_A, t)$. This correlation result is indicated by 'c' in Figure 2a and the integral over the Fresnel zone around this point is event 'c' in Figure 2b. The other events in Figure 2b can be explained in a similar way. Finally, note that there are two more stationary points, indicated by 'e' and 'f' in Figures 1 and 2a, of which the contributions cancel each other.

A similar numerical evaluation of equation (11) yields the result represented by the dashed curve in Figure 3. We observe that the traveltime of the scattered wave is accurately captured by this equation, but the amplitude is slightly overestimated. By increasing the radius of S to 10 000 m we obtained a result with equation (11) that again accurately matches the directly modelled wave field (not shown).

5 CONCLUSIONS

In the literature several derivations have been proposed for Green's function retrieval from cross-correlations. We have shown that the derivation by Derode et al. (Derode, et al., 2003a; Derode, et al., 2003b), which is based on physical arguments, leads essentially to the same result as our derivation based on Rayleigh's reciprocity theorem (Wapenaar et al., 2002; Wapenaar, 2003; Wapenaar, 2004). Moreover, using another definition of the Green's function in Rayleigh's reciprocity theorem, we obtained a representation in terms of the time-derivative of cross-correlations, similar as in Weaver and Lobkis (Weaver and Lobkis, 2004) and Snieder (Snieder, 2004).

REFERENCES

A. Bakulin and R. Calvert. Virtual source: new method for imaging and 4D below complex overburden. In *Soc. Expl. Geophys., Expanded Abstracts*, pages 2477–2480, 2004.

N. N. Bojarski. Generalized reaction principles and reciprocity theorems for the wave equations, and the relationship between the time-advanced and time-retarded fields. *J. Acoust. Soc. Am.*, 74:281–285, 1983.

J. F. Claerbout. Synthesis of a layered medium from its acoustic transmission response. *Geophysics*, 33:264–269, 1968.

A. T. de Hoop. Time-domain reciprocity theorems for acoustic wave fields in fluids with relaxation. *J. Acoust. Soc. Am.*, 84:1877–1882, 1988.

A. Derode, E. Larose, M. Campillo, and M. Fink. How to estimate the Green's function of a heterogeneous medium between two passive sensors? Application to acoustic waves. *Applied Physics Letters*, 83(15):3054–3056, 2003.

A. Derode, E. Larose, M. Tanter, J. de Rosny, A. Tourin, M. Campillo, and M. Fink. Recovering the green's function from field-field correlations in an open scattering medium (L). *J. Acoust. Soc. Am.*, 113(6):2973–2976, 2003.

C. Esmersoy and M. Oristaglio. Reverse-time wave-field extrapolation, imaging, and inversion. *Geophysics*, 53:920–931, 1988.

J. T. Fokkema and P. M. van den Berg. *Seismic applications of acoustic reciprocity.* Elsevier, Amsterdam, 1993.

O. I. Lobkis and R. L. Weaver. On the emergence of the Green's function in the correlations of a diffuse field. *J. Acoust. Soc. Am.*, 110:3011–3017, 2001.

G. A. McMechan. Migration by extrapolation of time-dependent boundary values. *Geoph. Prosp.*, 31:413–420, 1983.

G. T. Schuster, J. Yu, J. Sheng, and J. Rickett. Interferometric/daylight seismic imaging. *Geoph. J. Int.*, 157:838–852, 2004.

R. Snieder. Extracting the Green's function from the correlation of coda waves: A derivation based on stationary phase. *Phys. Rev. E.*, 69:046610–1–046610–8, 2004.

D. J. van Manen, J. O. A. Robertsson, and A. Curtis. Making waves by time reversal. *Phys. Rev. Lett.*, (submitted), 2005.

K. Wapenaar. Synthesis of an inhomogeneous medium from its acoustic transmission response. *Geophysics*, 68:1756–1759, 2003.

K. Wapenaar. Retrieving the elastodynamic Green's function of an arbitrary inhomogeneous medium by cross correlation. *Phys. Rev. Lett.*, 93:254301–1–254301–4, 2004.

K. Wapenaar, D. Draganov, J. Thorbecke, and J. Fokkema. Theory of acoustic daylight imaging revisited. In *Soc. Expl. Geophys., Expanded Abstracts*, pages 2269–2272, 2002.

K. Wapenaar, D. Draganov, J. van der Neut, and J. Thorbecke. Seismic interferometry: a comparison of approaches. In *Soc. Expl. Geophys., Expanded Abstracts*, pages 1981–1984, 2004.

R. L. Weaver and O. I. Lobkis. Ultrasonics without a source: Thermal fluctuation correlations at MHz frequencies. *Phys. Rev. Lett.*, 87:134301–1–134301–4, 2001.

R. L. Weaver and O. I. Lobkis. Diffuse fields in open systems and the emergence of the Green's function (L). *JASA*, 116(5):2731–2734, 2004.

Extracting the building response using seismic interferometry: Theory and application to the Millikan Library in Pasadena, California

Roel Snieder

Center for Wave Phenomena, Colorado School of Mines, Golden CO 80401, email rsnieder@mines.edu

ABSTRACT
The motion of a building depends on the excitation, the coupling of the building to the ground, and the mechanical properties of the building. We separate the building response from the excitation and the ground coupling by deconvolving the motion recorded at different levels in the building, and apply this to recordings of the motion in the Robert A. Millikan Library in Pasadena, California. The waveforms obtained from deconvolution with the motion in the top floor show a superposition of one upgoing and one downgoing wave. The waveforms obtained by deconvolution with the motion in the basement can be formulated either as a sum of upgoing and downgoing waves, or as a sum over normal modes. Since these deconvolved waves for late time have a monochromatic character, they are most easily analyzed with normal-mode theory. For this building we estimate a shear velocity $c = 322\ m/s$ and a quality factor $Q = 20$. These values explain both the propagating waves as well as the normal modes. We show for this application of seismic interferometry that deconvolution of waveforms is superior to correlation.

Key words: seismic interferometry, building response

1 INTRODUCTION

The response of a building to natural or man-made shaking is largely determined by the velocity of shear waves and the attenuation of the building. The shear velocity, together with the geometry of the building, controls the resonant frequencies of the building. The attenuation determines the rate of energy dissipation in the building, which in turn controls the motion of the building for a given excitation.

A complicating factor in the response of a building to shaking is that this response depends both on the properties of the building, as well as on the nature of the coupling to the subsurface (Şafak, 1995). It has been documented that the resonant frequencies of a building can change after heavy precipitation, that changes the coupling between the building and the ground with soil-moisture (Clinton, 2004). In order to fully understand the response of the building, one needs to unravel the properties of the building itself from the coupling of the building to the ground.

The combined response of a building and the ground coupling could be retrieved from an impulsive loading of the building. In general, such an impulsive load cannot be applied for practical reasons, and even if it could, the response of the building to this excitation depends on the properties of the building itself, as well as on the ground coupling. This work is aimed at retrieving the building response from the recording of incoherent shaking of the building, and to unravel the properties of the building itself from the coupling of the building to the subsurface.

We analyze this problem using a technique referred to as seismic interferometry. This technique is based on the correlation of wave recorded at different receivers. When the excitation of the waves is evenly distributed in space, or among the normal modes of the system, this correlation can be shown to lead to the Green's func-

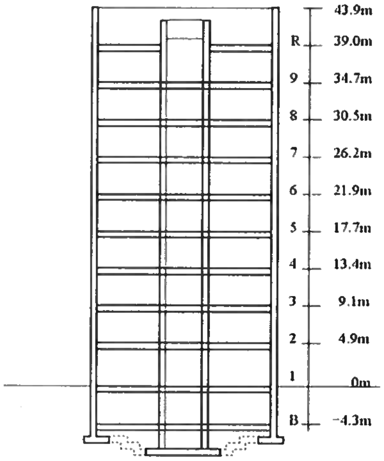

Figure 1. Vertical cross section of the Millikan Library in the north-south direction.

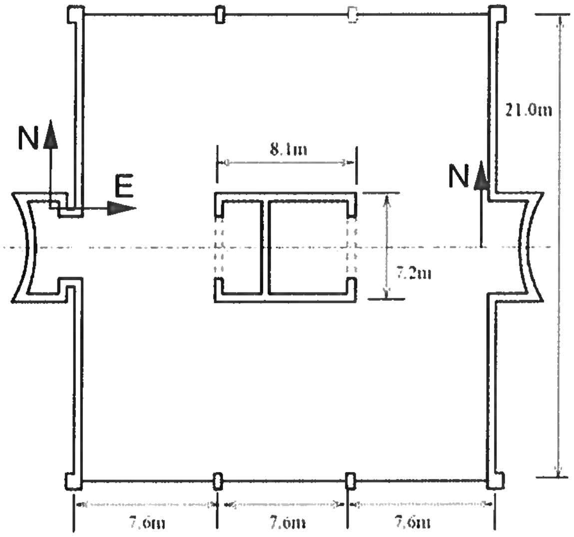

Figure 2. Floor plan of the Millikan Library. On the floors 1-9 seismometers measure the motion in two horizontal directions on the west side of the building, and the north-south motion on the east side, as indicated by the arrows.

tion that accounts for the wave propagation between receivers (Lobkis & Weaver, 2001; Derode *et al.*, 2003; Snieder, 2004a; Wapenaar, 2004; Snieder, 2005; Wapenaar *et al.*, 2005). This technique is valuable as it makes possible the study of the waves that propagate between receivers, without needing a source at one of the receiver locations. It does not matter whether the waves recorded at the receivers are excited by coherent sources or incoherent sources. Here we apply this technique to extract the building response of the Robert A. Millikan Library in Pasadena, California. In contrast to earlier work on seismic interferometry we base our analysis on the deconvolution of the recorded waves at different locations in the building rather than on the correlations.

In section 2 we give details on the Robert A. Millikan Library and the employed recordings of the motion of the building. We describe the deconvolution that we use in section 3. In section 4 we present a simple analytical model of the motion of the building that is based on interfering upgoing and downgoing waves. We show that the deconvolution gives a response that is independent of the excitation and that it does not depend on the coupling of the building with the ground. We show that these deconvolved waves can be interpreted either as propagating waves or as normal modes. We use the deconvolved waves in section 5 to determine the shear velocity and the attenuation of the building. In appendix A we use integration in the complex plane to show how the normal modes of the building can be obtained from the deconvolved waveforms.

2 THE MILLIKAN LIBRARY AND THE RECORDED WAVES

The Robert A. Millikan Library is a 10-story reinforced concrete building located on the campus of the California Institute of Technology in Pasadena, California. Completed in 1967, the building is 21 × 22.9 m in plan, and 43.9 m high from the ground level. The north-south elevation of the building, and the plans for a typical floor and the foundation are given in figures 1 and 2, respectively. There is a 4.3 m deep basement level below the ground. The structural system includes moment-resisting frames and shear walls. The shear walls at the center of the building, form the elevator shaft and carry lateral loads in the north-south direction, whereas the curved shear walls at the north and south ends carry lateral loads in the east-west direction. The foundation system is composed of a central pad 32 feet wide by 4 feet deep that extends between the east and west curved shear walls. In addition, 10 feet wide and 2 feet deep continuous foundation beams run in the east-west direction beneath the columns at the north and south ends of the building. The alluvium under the foundation consists of medium to dense sands mixed with gravels to the bedrock at a distance of about 275 m. The water table is about 11 m deep (Kuroiwa, 1967; Luco *et al.*, 1987). More on the structural system can be found in refs. (Kuroiwa, 1967; Foutch *et al.*, 1975; Foutch, 1976; Luco, 1986; Clinton, 2004).

The building was first instrumented in 1968 with 2 permanent tri-axial accelerometers, located on the roof and the basement. A 10-channel strong motion array was added to the instrumentation in 1979, with channels on the basement, the 6th floor, and the roof. After the 1994 Northridge, California, earthquake, the instrumentation was upgraded to a 36-channel, triggered system with three horizontals at each floor plus three verticals in the basement; the locations and directions of these are shown by the arrows in figure 2. In 2000, the system

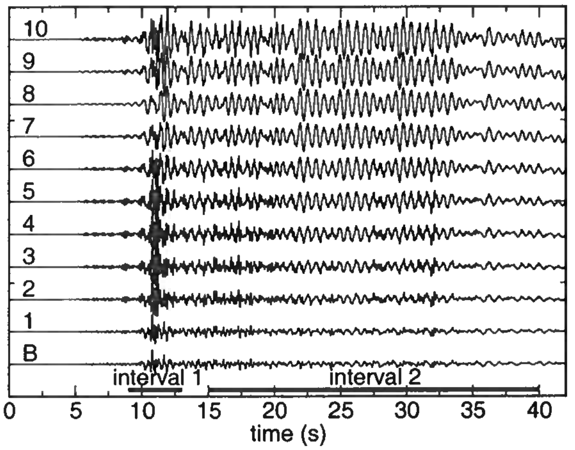

Figure 3. The north-south component of the motion in the west side of the Millikan Library recorded in the basement (B) and the floors indicated by the numbers next to the different traces.

was converted to a 19-bit real-time system recording continuously at 200 Hz. Also, a separate 24-bit tri-axial accelerometer was installed on the 9th floor recording continuously as a CISN (formerly TriNet) station MIK. Figure 2 shows the current sensor layout in the building.

Since its construction, the building has been a field laboratory for researchers in earthquake engineering. A synchronized shaker was permanently installed on the roof of the building in the early 1970's (Hudson, 1962), which is still operational and used for forced vibration testing experiments. A large number of studies on the dynamic behavior of the building have been completed by using vibration data from shaker experiments and real earthquakes (Kuroiwa, 1967; Trifunac, 1972; Udwadia & Trifunac, 1974; Luco, 1986; Luco *et al.*, 1987; Foutch *et al.*, 1975; Foutch, 1976; Foutch & Jennings, 1978; Clinton, 2004).

The recorded motion after an earthquake is shown in figure 3. The P-waves generated by the earthquake arrive before t=9 s, these wave couple weakly to the horizontal motion in the building. The S-wave that arrives around t=11 s is the strongest phase. The surface waves that arrive later excite a resonance in the building with an amplitude that increases with the floor level.

3 THE DECONVOLVED WAVEFORMS

In this study we extract the building response by deconvolving the waves recorded at all floors either with the waveform recorded in the basement, or with the signal recorded at the top floor of the building. The deconvolution of two signals $u_1(\omega)$ and $u_1(\omega)$ is in the frequency domain given by

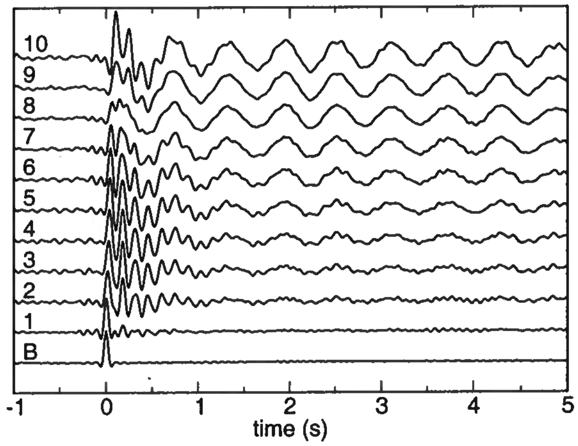

Figure 4. The waveforms of figure 3 at the different floors after deconvolution with the waves recorded in the basement.

$$D(\omega) = u_1(\omega)/u_2(\omega) \; . \qquad (1)$$

This expression is unstable near the notches in the spectrum of u_2 because the denominator goes to zero. In order to stabilize the deconvolution we used the following estimator for the deconvolution instead:

$$D(\omega) = \frac{u_1(\omega)u_2^*(\omega)}{|u_2(\omega)|^2 + \varepsilon} \; , \qquad (2)$$

where the asterisk denotes the complex conjugation. When $\varepsilon = 0$ this expression reduces to expression (1). In this study the parameter ε was set to 10% of the average spectral power.

The waveforms deconvolved with the signal recorded in the basement are shown in figure 4. The deconvolved wave in the basement is a single spike because a signal deconvolved with itself is a delta function. The deconvolved waves at all the floors are causal, i.e. they vanish for $t < 0$. The first onset of the deconvolved waves is a wave that propagates upward in the building. A reflection of this wave by the top of the building is visible as the second peak in the waves that propagates downward in the building. The early part of the deconvolved waves consist of a superposition of upward and downward propagating waves. Since these waves interfere, it is difficult to identify the individual upward and downward propagating waves. The later part of the deconvolved waves consists of the resonance of the building. This resonance grows in amplitude with the floor level, and is fairly monochromatic.

The waveforms deconvolved with the signal recorded in the basement are fairly complex. In contrast, as shown in figure 5, the waveforms deconvolved with the signal recorded at the top floor are much simpler. These deconvolved waves are acausal and consist of the superposition of one upgoing wave and one downgoing

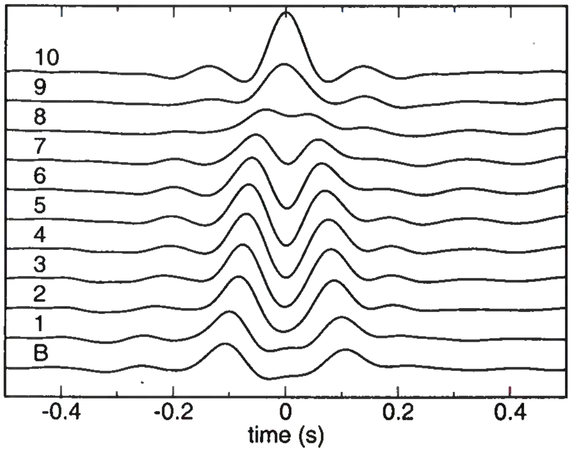

Figure 5. The waveforms of figure 3 at the different floors after deconvolution with the waves recorded at the top floor.

wave. There is little indication that these upgoing and downgoing waves are reflected within the building. The reflection coefficients by the floors within the building (Şafak, 1999) therefore must be small. The reflection coefficient for elastic waves by a floor in the building depends on the product of the frequency and the mass of the floor (Doyle, 1989; Şafak, 1999). This means that the absence of waves reflected off the floors in the building may be due to the relatively low frequencies in the waveforms used in this study. In addition, the dominant wavelength of the employed waves spans several floors, this further suppresses reflections generated by the individual floors because a medium with small-scale variations can be treated as an effective medium that behaves like a homogeneous medium with properties that are determined by the background velocity and the embedded scatterers (Frisch, 1968; Keller & Karal, 1966; Tatarskiĭ & Gertsenshteiň, 1963).

The deconvolved waveforms in the figures 4 and 5 are computed from the full waveforms shown in figure 3. It is, however, not necessary to use the full waveforms. We have also deconvolved the signals using the time intervals 1 and 2 as shown in figure 3. Interval 1 straddles the S-wave arrival and is 4 s long, while interval 2 contains the surface wave arrivals and has a duration of 25 s. Both intervals were padded with zeroes to a duration of 40 s. The signals deconvolved with the waves recorded in the basement for each of the intervals are shown in figure 6. The thick line denotes the deconvolved waveforms from interval 1 while the thin line denotes the deconvolved waves from interval 2.

The similarity of the waves deconvolved over different time intervals is striking. Note how the deconvolved waves from interval 1 display the resonance of the building, despite the fact that these waves are based on the impulsive S-wave arrival only. The broadband nature of the S-wave ensures that sufficient low-frequency information is present to reproduce the resonance. Note also that the deconvolved waves from interval 2 are based on the surface wave signal. Nevertheless, these deconvolved waves display the upward and downward propagating waves early in the deconvolved signal.

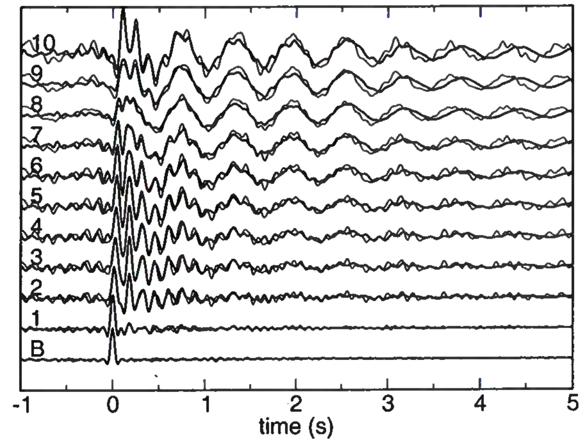

Figure 6. The waveforms of figure 3 at the different floors after deconvolution with the waves recorded in the basement using only part of the data of figure 3. The deconvolved waves shown in thick lines are obtained by using only the data in interval 1 of figure 3, while the deconvolved waves shown in the thin lines are computed from the data in interval 2 of figure 3.

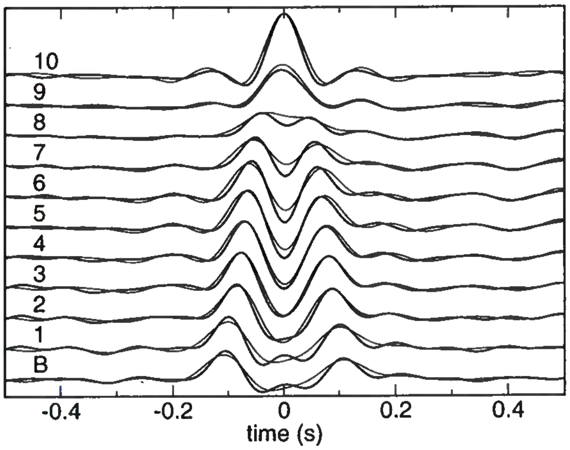

Figure 7. The waveforms of figure 3 at the different floors after deconvolution with the waves recorded in the top floor using only part of the data of figure 3. The deconvolved waves shown in thick lines are obtained by using only the data in interval 1 of figure 3, while the deconvolved waves shown in the thin lines are computed from the data in interval 2 of figure 3.

The recorded waves in interval 2 are dominated by low-frequency surface waves. These waves visually mask the higher frequency components in interval 2. The deconvolution equalizes the frequency content and therefore brings out the high-frequency propagating waves in figure 6. Interval 1 is shorter than interval 2, and one might think that interval 1 therefore contains less information than interval 2. Because of the impulsive character of the S-wave, the waves in interval 1 have a larger bandwidth than the waves in interval 2. This larger bandwidth helps stabilize the deconvolution. The similarity of the deconvolved waves for the intervals 1 and 2 shown in the the figures 6 and 7 implies that for the level of shaking used in this study the building responds linearly.

The waves deconvolved with the signal recorded at the top floor for interval 1 and interval 2 is shown in figure 7 with a thick and thin line, respectively. As in the preceding figure, these deconvolved waves are similar. This implies that the S-wave and the surface wave both contain information about the upward and downward propagating waves in the building. The deconvolution defined in equation (2) and the choice of ε are not optimized. A more careful choice of the deconvolution algorithm could make the deconvolved waves from the intervals 1 and 2 even more similar.

The deconvolved waves behave in the same way as a hologram. A part of a hologram can be used to reconstruct the image, albeit with a degraded resolution compared to the image of the full hologram (Lauterborn *et al.*, 1995). As shown in the figures 6 and 7, the deconvolved waves that are computed from different sub-intervals of the whole signal lead to the same deconvolved waves.

4 A SIMPLE MODEL FOR THE WAVE PROPAGATION IN THE BUILDING

In this section we present a simple model for the wave propagation for the building. The base of the building is exposed to an external motion $s(t)$ with Fourier transform $S(\omega)$. In this model, the wave propagates upward in the building with a velocity c that is the shear velocity of the building. At the top of the building with height H the waves are reflected with reflection coefficient $+1$. During the upward and downward propagation the waves attenuate; for a wave that travels over a distance L this is described by an attenuation operator $A(L,t)$. For a constant Q-model, this attenuation operator is in the frequency domain given by (Aki & Richards, 2002):

$$A(L,\omega) = \exp\left(-\gamma\,|\omega|\,L/c\right) \ , \tag{3}$$

where γ is related to the quality factor by

$$\gamma = 1/2Q \ . \tag{4}$$

The downward propagating waves reflect off the base of the building with a reflection coefficient $R(\omega)$ that corresponds in the time domain to a reflection operator $r(t)$. A wave $S(t)$ that travels upward in the building is given by $S(t-z/c)$. When the wave reflects off the top of the building, with reflection coefficient $+1$, the downgoing wave is given by $S(t-(2H-z)/c$. When this downgoing wave reflects off the base of the building, it is deconvolved with the reflection operator $r(t)$. The wave that then travels upward is given by $r(t) * S(t-(2H+z)/c)$. The delay time $2H/c$ accounts for the time needed to propagate once up and down the building. This process can be continued for all the upward and downward propagating waves and is similar to the treatment of water-layer reverberations of Backus (Backus, 1959). After a convolution with the attenuation operators for each upward and downward going wave, the total response of the building is in the time domain given by

$$\begin{aligned} u(z,t) \quad &= A(z,t) * s\left(t-\frac{z}{c}\right) \\ &+A(2H-z,t) * s\left(t-\frac{2H-z}{c}\right) \\ &+r(t) * A(2H+z,t) * s\left(t-\frac{2H+z}{c}\right) \\ &+r(t) * A(4H-z,t) * s\left(t-\frac{4H-z}{c}\right) \\ &+\cdots \end{aligned} \tag{5}$$

With the wave number defined by

$$k = \omega/c \ , \tag{6}$$

and for the attenuation model (3), this expression is in the frequency domain given by

$$u(z,\omega) = \sum_{n=0}^{\infty} S(\omega)R^n(\omega) \quad \left\{ e^{ik(2nH+z)} e^{-\gamma|k|(2nH+z)} \right. \\ \left. + \, e^{ik(2(n+1)H-z)} e^{-\gamma|k|(2(n+1)H-z)} \right\} . \tag{7}$$

In this expression n counts the number of bounces off the base of the building. The first term denotes the upward propagating waves, while the last term accounts for the downward propagating waves that have bounced n times in the building.

The motion at height z deconvolved with the motion at the top floor is denoted by $T(z,\omega)$, so that in the frequency domain

$$T(z,\omega) \equiv \frac{u(z,\omega)}{u(z=H,\omega)} . \tag{8}$$

Similarly, the motion deconvolved with the motion at the bottom floor is denoted by $B(z,\omega)$, hence

$$B(z,\omega) \equiv \frac{u(z,\omega)}{u(z=0,\omega)} . \tag{9}$$

Let us first analyze $T(\omega)$. Inserting expression (7) in the numerator and denominator of the definition (8) gives

$$T(z,\omega) = \frac{\sum_{n=0}^{\infty} S(\omega)R^n(\omega) \left\{ e^{ik(2nH+z)} e^{-\gamma|k|(2nH+z)} + e^{ik(2(n+1)H-z)} e^{-\gamma|k|(2(n+1)H-z)} \right\}}{2\sum_{n=0}^{\infty} S(\omega)R^n(\omega) e^{ik2(n+1)H} e^{-\gamma|k|2(n+1)H}} . \tag{10}$$

This expression can also be written as

$$T(z,\omega) = \frac{\left\{ e^{ik(z-H)} e^{-\gamma|k|(z-H)} + e^{ik(H-z)} e^{-\gamma|k|(H-z)} \right\} \sum_{n=0}^{\infty} S(\omega)R^n(\omega) e^{ik2(n+1)H} e^{-\gamma|k|2(n+1)H}}{2\sum_{n=0}^{\infty} S(\omega)R^n(\omega) e^{ik2(n+1)H} e^{-\gamma|k|2(n+1)H}} . \tag{11}$$

The excitation $S(\omega)$ and the sum with the reverberations in the numerator and the denominator cancel, so that

$$T(z,\omega) = \frac{1}{2} \left\{ e^{ik(z-H)} e^{-\gamma|k|(z-H)} + e^{ik(H-z)} e^{-\gamma|k|(H-z)} \right\} . \tag{12}$$

This means that $T(z,\omega)$ accounts for the sum of one attenuating upgoing wave and one downgoing wave. Since $z < H$, the upgoing wave is acausal. The cancellation of the sum over reverberations means that $T(z,\omega)$ is independent of the reverberations in the building. The cancellation of the reflection coefficient $R(\omega)$ implies that $T(z,\omega)$ does not depend on the coupling of the building to the subsurface. The cancellation of $S(\omega)$ means that the deconvolved response in independent of the excitation of the building.

A similar analysis can be applied to the building response deconvolved with the motion at the base. Inserting expression (7) in the numerator and denominator of expression (9) gives

$$B(z,\omega) = \frac{\sum_{n=0}^{\infty} S(\omega)R^n(\omega) \left\{ e^{ik(2nH+z)} e^{-\gamma|k|(2nH+z)} + e^{ik(2(n+1)H-z)} e^{-\gamma|k|(2(n+1)H-z)} \right\}}{\sum_{n=0}^{\infty} S(\omega)R^n(\omega) \left\{ e^{ik2nH} e^{-\gamma|k|2nH} + e^{ik2(n+1)H} e^{-\gamma|k|2(n+1)H} \right\}} . \tag{13}$$

Factoring out the summations this can be written as

$$B(z,\omega) = \frac{\left\{ e^{ikz} e^{-\gamma|k|z} + e^{ik(2H-z)} e^{-\gamma|k|(2H-z)} \right\} \sum_{n=0}^{\infty} S(\omega)R^n(\omega) e^{ik2nH} e^{-\gamma|k|2nH}}{\left\{ 1 + e^{2ikH} e^{-2\gamma|k|H} \right\} \sum_{n=0}^{\infty} S(\omega)R^n(\omega) e^{ik2nH} e^{-\gamma|k|2nH}} . \tag{14}$$

The summation over the reverberations, the reflection coefficient $R(\omega)$, and the excitation $S(\omega)$ cancel, so that

$$B(z,\omega) = \frac{e^{ikz} e^{-\gamma|k|z} + e^{ik(2H-z)} e^{-\gamma|k|(2H-z)}}{1 + e^{2ikH} e^{-2\gamma|k|H}} . \tag{15}$$

Just as for the signals deconvolved with the top floor, this deconvolved signal depends neither on the coupling with the ground nor on the excitation.

The deconvolved response $T(z,\omega)$ is the superposition of one acausal upgoing wave and one causal downgoing wave. Such a simple interpretation cannot be applied to $B(z,\omega)$ because the numerator depends on frequency. The deconvolved response can be interpreted in two ways: as a superposition of traveling waves, or as a superposition of modes. The traveling wave interpretation is obtained by using the following geometric series:

$$\frac{1}{1 + e^{2ikH} e^{-2\gamma|k|H}} = \sum_{n=0}^{\infty} (-1)^n \, e^{2iknH} e^{-2\gamma|k|nH} . \tag{16}$$

Because of the attenuation this sum is guaranteed to converge. Inserting this in equation (15) gives $B(z,\omega)$ as an infinite sum of upgoing and downgoing traveling waves:

$$\begin{aligned} B(z,\omega) = \quad & \sum_{n=0}^{\infty} (-1)^n \left\{ e^{ik(z+2nH)} e^{-\gamma|k|(z+2nH)} \right. \\ & \left. + e^{ik(2(n+1)H-z)} e^{-\gamma|k|(2(n+1)H-z)} \right\} . \end{aligned} \tag{17}$$

The difference with expression (15) is that the frequency-dependent denominator has disappeared. Note that since the argument of each of the complex exponentials is positive, $B(z,\omega)$ is a causal function. This deconvolved response is an infinite sum of upgoing and downgoing attenuated waves. This sum differs from the sum of upgoing and downgoing waves in the building, because $B(z,\omega)$ does not depend on the ground coupling, whereas the original sum of upgoing and downgoing waves (7) does depend on the ground coupling through the reflection coefficient $R(\omega)$.

In expression (17) the reflection coefficient at the base of the building is equal to -1, because the wave that has bounced n times off the base of the building is proportional to $(-1)^n$. There is a simple explanation for this (Jon Sheiman, personal communication, 2004). The deconvolution of the motion of the basement with itself gives, by definition, a bandpass-filtered delta function as shown in the bottom trace of figure 4. When the wave that has reflected off the top of the building propagates downward, it must give a vanishing contribution at the base of the building because the deconvolved wave at that level vanishes for $t > 0$. The motion at the base can only vanish when an upward propagating wave is launched upward with the opposite polarity as the downward propagating wave that strikes the basement. This corresponds to a reflection coefficient for the deconvolved waves that is equal to -1 rather than the reflection coefficient $R(\omega)$ of the subsurface. It has been shown earlier that interferometric imaging can be used to determine waveforms for the system with different boundary conditions than the physical boundary conditions (Riley & Claerbout, 1976; Wapenaar *et al.*, 2004). Riley and Claerbout (Riley & Claerbout, 1976) coined the phrase *Noah's deconvolution* for this technique.

An alternative way to interpret $B(z,\omega)$ is based on normal modes. Using the inverse Fourier transform, and expression (6), the deconvolved response is in the time domain given by

$$B(z,t) = \int_{-\infty}^{\infty} \frac{e^{-i\omega(t-z/c)} e^{-\gamma|\omega|z/c} + e^{-i\omega(t-(2H-z)/c)} e^{-\gamma|\omega|(2H-z)/c}}{1 + e^{2i\omega H/c} e^{-2\gamma|\omega|H}} d\omega . \tag{18}$$

As shown in appendix A this integral can be solved by contour integration. The integrand has simple poles when

$$1 + e^{2i\omega H/c} e^{-2\gamma|\omega|H} = 0 , \tag{19}$$

the location of the poles in the lower half-plane is shown in figure 8. For $t > (2H - z)/c$, the contour must be closed in the lower half plane, and as shown in appendix A the integral (18) can be written as a sum of damped normal modes:

$$\begin{aligned} B(z,t) = \quad & \frac{4\pi c}{H} \sum_{m=0}^{\infty} (-1)^{m+1} \exp(-\gamma\omega_m t) \\ & \times \cos\left(\frac{\omega_m (H-z)}{c}\right) \sin(\omega_m t) \ , \end{aligned} \tag{20}$$

with

$$\omega_m = \frac{(m + 1/2)\, \pi c}{H} \qquad m = 0, 1, 2, \cdots \tag{21}$$

It should be noted that these normal modes are not the normal modes of the building, because its normal modes depend in general on the coupling to the ground. The normal modes in the sum (20) are independent of the reflection coefficient $R(\omega)$, hence the normal modes in the deconvolved response depend on the properties of the building only. This is consistent with the traveling wave formulation of expression (17), where the reflection coefficient for the deconvolved wave is equal to -1 rather than the reflection coefficient $R(\omega)$ of the subsurface.

Each term in the sum (20) is exponentially damping. The term with the fundamental mode ($m = 0$) has the smallest damping. This means that for large times ($t \gg 2H/\pi c$) the fundamental mode dominates and hence

$$B(z,t) \approx \frac{4\pi c}{H} \exp(-\gamma\omega_0 t) \cos\left(\frac{\omega_0 (H-z)}{c}\right) \sin(\omega_0 t) \ , \tag{22}$$

with

$$\omega_0 = \frac{\pi c}{2H} . \tag{23}$$

The period that corresponds to this angular frequency is given by

$$T_0 = \frac{4H}{c} \ . \tag{24}$$

Note that this is the time needed to propagate up and down the building twice. This period is determined by the factor $(-1)^m$ in expression (17). Because of this factor the wave changes polarity if it propagates up and down the building once. If the wave travels up and down the building twice and covers a distance $4H$, the polarity changes twice and the reverberating wave reinforces itself to form a resonance.

5 INTERPRETATION OF THE DECONVOLVED WAVEFORMS

The theory of the previous section agrees with the deconvolved waves in the figures 4 and 5. Let us first consider the waves deconvolved with the waves at the top floor as shown in figure 5. These deconvolved waves are given by expression (12) that gives the superposition of an acausal upgoing wave and a causal downgoing wave; both waves are clearly visible in figure 5. Given the floor spacing of 4.27 m (Clinton, 2004) these waves can be used to estimate the shear velocity in the building. It follows from eexpression (12) that if there is no attenuation ($\gamma = 0$), and if the data have infinite bandwidth, that the deconvolution is in the time domain given by a superposition of upward and downward propagating delta functions

$$T(z,t) = \pi \left\{ \delta\left(t - \frac{z-H}{c}\right) + \delta\left(t + \frac{z-H}{c}\right) \right\} \ . \tag{25}$$

(In deriving this result expression (6) is used.) The attenuation and the finite bandwidth of the data cause the broader pulses shown in figure 5.

We measured the arrival time of the upward and downward propagating waves by picking the maximum of these waves. These arrival times are shown in figure 9. The distance is measured relative to the position of the accelerometer at the top floor. For the upward propagating wave this distance is given a negative value. For the floors 4-10 the upward and downward propagating waves overlap. This may bias the travel time measurements. The travel times at these floors are indicated with open squares. The travel time determined from the waves recorded in the basement may be biased by the presence of the solid earth below the basement, these travel times are also indicated with open squares. Despite these reservations, the measurements in figure 9 display a fairly linear dependence of the travel time with distance, this indicates a constant shear velocity in the building.

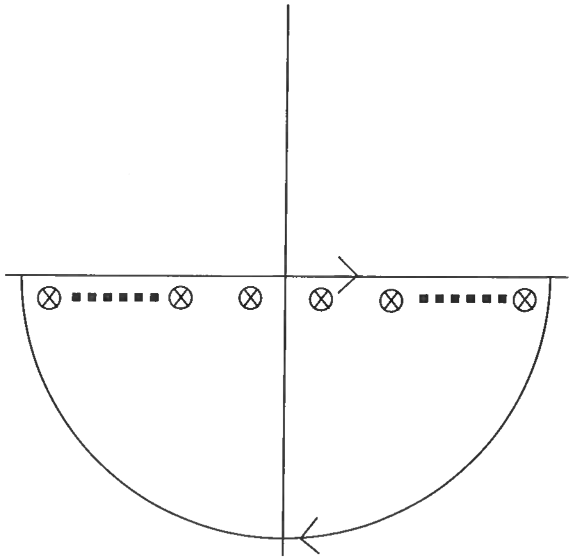

Figure 8. The location of the poles in the complex ω-plane and the contour integration that is used for $t > (2H - z)/c$.

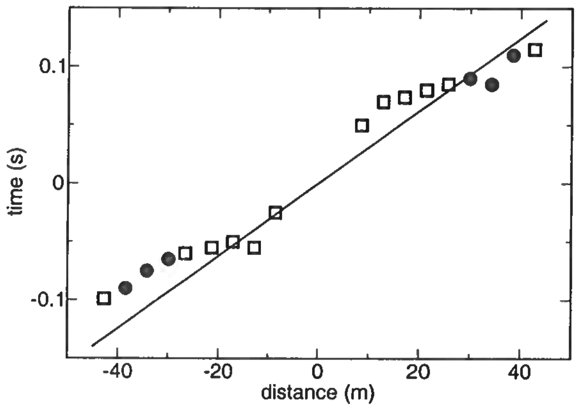

Figure 9. The arrival times of the upgoing and downgoing waves in figure 5. A negative distance/time corresponds to the upgoing wave, a positive distance/time to the downgoing wave. The travels times at the floors 1-3 are marked with solid circles. The solid line indicates the travel time predicted for the shear velocity inferred from the normal mode measurements that give a velocity of 322 m/s.

According to expression (12), the upward and downward propagating waves both decay due to attenuation. This attenuation can be seen in figure 5 because the downward going wave has a consistently smaller amplitude than the upward propagating wave. The absolute value of the amplitude at different floors cannot be compared with great accuracy, because the absolute amplitude is affected by the receiver coupling and other uncertainties. The ratio of the amplitude of the downgoing wave and the upgoing wave, however, does not depend on the receiver coupling. Figure 10 shows the natural logarithm of the ratio of the downgoing wave and the upgoing wave at each floor. The amplitude mea-

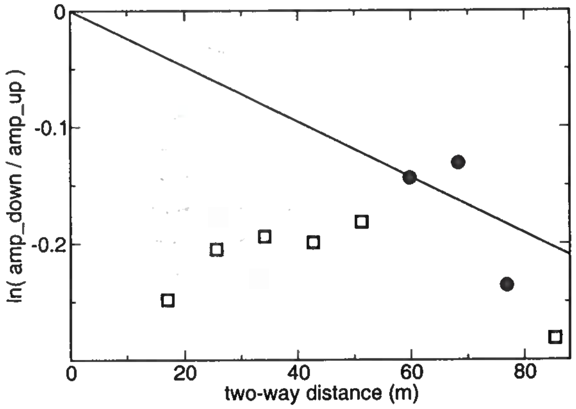

Figure 10. The natural logarithm of the ratio of the amplitudes of the upgoing and downgoing waves of figure 5 as a function of the two-way distance to the top of the building. The amplitude ratio for the floors 1-3 is indicated with solid circles. The log-amplitude ratio predicted by the attenuation of expression (28) is shown with the straight line.

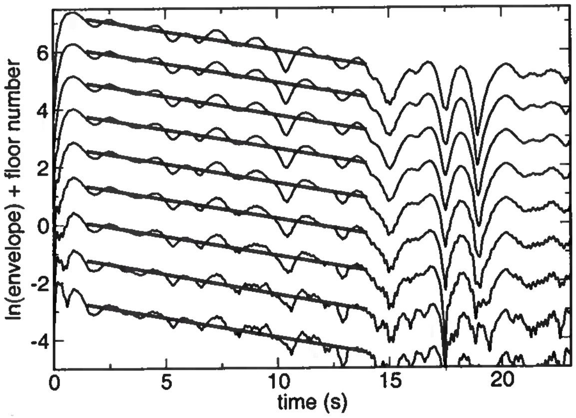

Figure 11. The natural logarithm of the envelope of the deconvolved waves in figure 4 after applying a bandpass filter with corner frequencies of 1 Hz and 3 Hz, respectively. For clarity the floor number is added to each curve. The best-fitting straight line to each curve is indicated with thick solid lines.

surements in the floors 4-10 and in the basement are likely to be unreliable because of the interference of the upgoing and downgoing waves and the presence of the solid earth below the basement, respectively. The amplitude ratios at these levels are indicated with open squares. The amplitude ratio for the floors 1-3 is indicated by solid circles and are most reliable. The two-way distance is measured relative to the receiver at the top floor. The scatter in the amplitude ratio is considerable because the amplitude difference between the upgoing and downgoing waves is fairly small. In a taller building these amplitude differences would be larger, and the attenuation can be determined with greater accuracy.

According to expressions (17) and (20), the signals deconvolved with the bottom floor can be seen either as a superposition of upward and downward propagating waves, or as a sum of normal modes. The interpretation in terms of propagating waves is most useful for the early part of the deconvolved waves in figure 4. In that figure, the upward and downward propagating waves are not as clear as in figure 5 for the waves deconvolved with the signals at the top floor, because in figure 5 only one upgoing wave and one downgoing wave are present, whereas according to expression (17) many upgoing and downgoing waves interfere with each other in figure 4. For this reason we analyze the waves deconvolved with the signal in the basement in figure 4 from the normal mode point of view as formulated in expression (20). Since the fundamental mode is much stronger than the higher modes, we use the expressions (22) through (24) in the following.

The amplitude spectrum of the deconvolved waves of figure 4 averaged over all the floors has a pronounced peak at 1.72 Hz. This reflects the monochromatic nature of the resonance. Given that the height of the building measured to the basement is 47 m, this gives with expression (24) a shear velocity of

$$c = 322\ m/s\ . \tag{26}$$

The travel time as a function of distance for this velocity is indicated by the solid line in figure 9. The proximity of this travel time curve to the arrival times of the upward and downward propagating waves, shows that the traveling waves and the normal modes predict a shear velocity that is similar. This provides a consistency check on the analysis. A systematic difference between the velocity of the propagating waves and the normal modes can be due to dispersion caused by the internal structure in the building, and to amplitude variations between floors that are ignored in expression (4) that forms the basis of the mathematical model of section 4.

According to expression (22) the resonance decays with time due to anelastic attenuation. In order to quantify the attenuation we bandpass filtered the deconvolved waves of figure 4 with a Butterworth filter with cutoff frequencies of 1 and 3 Hz, respectively. This filter extracts the fundamental mode from the waveforms. The natural logarithm of the envelope of the bandpass-filtered waveforms is shown in figure 11. Since the resonance is weak for the lowest floor, we used only the top 9 floors in the normal-mode analysis. We added the floor number to each curve in order to separate them in the figure. Since only the slope depends on the attenuation this offset does not affect the analysis. Note that, apart from some fluctuations, the envelope of the deconvolved waves decays with time. This contrasts the original waveforms in figure 3 that do not decay with time because the motion is continuously excited by the surface waves. The deconvolution extracts the decay of the resonance with time, this makes it possible to measure the anelastic attenuation in the building.

Between 1.5 s and 14 s the logarithm of the envelope decays linearly with time, this is consistent with the exponential decay in expression (22). For later times the resonance is of the same order of magnitude as the ambient noise, and the exponential decay is not valid. In order to determine the attenuation we fitted straight lines to the curves for 1.5 s < t < 14 s. The least-squares fit of the envelopes is shown by the solid lines in figure 11. The slopes are similar and the average slope is given by

$$slope = -0.1321 \pm 0.0017\, s^{-1}\ . \qquad (27)$$

The error is determined by the standard deviation of the slope for the deconvolved waves at different floors. According to the expressions (4) and (22) the slope is equal to $-\omega/2Q$. For the resonant frequency of 1.72 Hz, this gives

$$Q = 20.45\ . \qquad (28)$$

This value of the attenuation can be compared with the attenuation of the propagating waves shown in figure 10. The propagating waves in figure 5 have a dominant frequency of about $f = 5Hz$. The propagating waves decay with distance as $\exp(-\pi f z/Qc)$. For the value of Q given above, and a velocity of 322 m/s, this decay is shown by the solid line in figure 10. The variability in the amplitude measurements in that figure is fairly large. For the lower three floors where the upgoing and downgoing waves don't interfere, the attenuation inferred from the resonance agrees will with amplitude decay determined from the propagating waves as indicated with the solid circles. The comparison of the attenuation from the normal modes and the propagating waves provides a consistency check on the employed model of wave propagation in the building.

6 DISCUSSION

We have shown that the deconvolution of the motion recorded at different floors in the building is an effective tool for extracting the building response. The deconvolution with respect to the signals recorded in the basement and the top floor provide complementary information. The deconvolution with the signal recorded at the top floor gives a one upgoing and one downgoing propagating wave that clearly are separated. The deconvolution with the waveforms recorded in the basement provides information on the fundamental mode of the building.

The deconvolved waves are independent of the excitation and of the ground coupling. This can be seen in expressions (12) and (15) that are independent of the excitation $S(\omega)$ and the reflection coefficient $R(\omega)$ at the base of the building. Suppose that instead of the deconvolution we had used the correlation, as is common in interferometric imaging (Lobkis & Weaver, 2001; Derode *et al.*, 2003; Snieder, 2004a; Wapenaar, 2004; Snieder, 2005). In the frequency domain, the correlation of the waves recorded at height z with those in the basement is given by

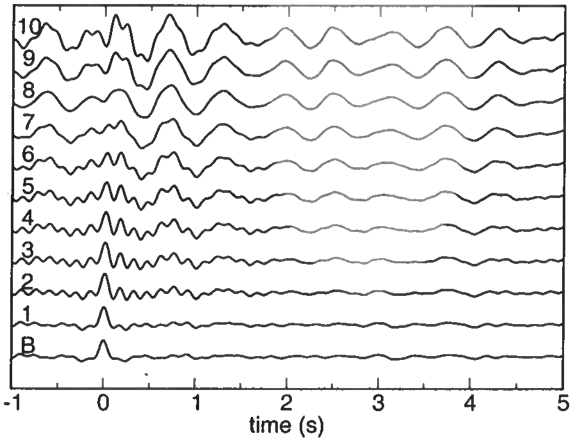

Figure 12. The waveforms of figure 3 at the different floors after correlation with the waves recorded in the basement.

$$C(z,\omega) = u(z,\omega)u^*(z=0,\omega)\ . \qquad (29)$$

When equation (7) is inserted in this expression, the result contains the power spectrum $|S(\omega)|^2$ of the excitation as well as products of the reflection coefficient $R(\omega)$. In contrast to this, the deconvolved waves of expressions (12) and (15) depends on neither of these quantities. It is instructive to consider the waveforms obtained from correlation with the signal in the basement as defined by equation (29), these correlated waveforms are shown in figure 12. This figure should be compared with figure 4 for the deconvolved waves. The deconvolved waves are causal while the waveforms obtained by correlation are not. This is due to the fact that the waveforms computed by correlation depends on the power spectrum $|S(\omega)|^2$ of the excitation. The multiplication with the power spectrum in the frequency domain corresponds in the time domain to a convolution with the autocorrelation of the excitation. For the surface waves that excite the building, this autocorrelation has a fairly long time duration. This leads to a-casual arrivals in the correlated waves of figure 12. Note that the waveforms computed from correlation show neither the upgoing and downgoing waves nor the clear resonance of the deconvolved waves of figure 4. This means that for this application deconvolution is superior to correlation.

Expression (12) can be generalized for SH-waves in an arbitrary layered medium. In this case the deconvolved waves $T(z,\omega)$ are equal to the P_{11}-element of the propagator matrix (Trampert *et al.*, 1993). This contrasts formulations of seismic interferometry based on correlation where the Green's function is obtained (Lobkis & Weaver, 2001; Derode *et al.*, 2003; Snieder, 2004a; Wapenaar, 2004; Snieder, 2005). According to expression (7.43) of Aki and Richards (Aki & Richards, 2002), the P_{11}-element of the propagator matrix for SH-waves in a lossless homogeneous medium is given by

$$P_{11}(z,H) = \cos k(z-H) = \frac{1}{2}\left(e^{ik(z-H)} + e^{ik(H-z)}\right) . \tag{30}$$

Apart from terms that depend on the attenuation this expression is identical to equation (12). We can show that this is also the case for a general layered medium that has internal reflections.

The deconvolved waves can be used to estimate the shear velocity and attenuation in the Millikan Library. The waves deconvolved with the motion in the top floor lead to clear upgoing and downgoing waves. The velocity of propagation can be measured from the arrival time of these waves, while the ratio of the amplitude of the upgoing and downgoing waves constrains the attenuation. The waveforms obtained by deconvolution with the motion in the basement gives the motion of the fundamental mode of the building. The frequency and temporal decay constrain the shear velocity and attenuation as well. As shown in figures 9 and 10, these complementary pieces of information are consistent. This shows that the deconvolution of the motion in the building recorded at different levels can successfully be used to eliminate the imprint of the excitation and the ground coupling, and that the values of the shear velocity and attenuation from propagating waves and from the fundamental mode are consistent.

Acknowledgments: We appreciate the insights that we got from discussions with Jon Sheiman, Rodney Calvert, Huub Douma, Ken Larner and Matt Haney.

REFERENCES

Aki, K., & Richards, P.G. 2002. *Quantitative Seismology.* Second edn. Sausalito: Univ. Science Books.

Backus, M.M. 1959. Water reverberations – their nature and elimination. *Geophysics*, **24**, 233–261.

Clinton, J.F. 2004. *Modern digital seismology - Instrumentation, and small amplitude studies in the engineering world.* Ph.D. thesis, California Institute of Technology.

Derode, A., Larose, E., Campillo, M., & Fink, M. 2003. How to estimate the Green's function for a heterogeneous medium between two passive sensors? Application to acoustic waves. *Appl. Phys. Lett.*, **83**, 3054–3056.

Doyle, J.F. 1989. *Wave propagation in structures: An FFT-based spectral analysis methodology.* New York: Springer.

Foutch, D.A. 1976. *A Study of the Vibrational Characteristics of Two Multistorey Buildings.* Ph.D. thesis, California Institute of Technology.

Foutch, D.A., & Jennings, P.C. 1978. Foundation response of a nine-storey reinforced concrete building. *Bull. Seismol. Soc. Am.*, **68**, 219–229.

Foutch, D.A., Luco, J.E., Trifunac, M.D., & Udwadia, M.E. 1975. Full scale, three dimensional tests of structural deformation during forced excitation of a nine-storey reinforced concrete building. *Pages 206–215 of: Proceedings, U.S. National Conference on Earthquake Engineering.*

Frisch, U. 1968. Wave Propagation in Random Media. *Pages 75–198 of:* Bharucha-Reid, A.T. (ed), *Probabilistic methods in applied mathematics.* Academic Press.

Hudson, D.E. 1962. *Synchronized vibration generators for dynamic tests of full-scale structures.* Technical report, Earthquake Engineering Research Laboratory, California Institute of Technology.

Keller, J.B., & Karal, F.C. 1966. Effective Dielectric Constant, Permeability, and Conductivity of a Random Medium and the Velocity and Attenuation Coefficient of Coherent Waves. *J. Math. Phys.*, **7**, 661–670.

Kuroiwa, J.H. 1967. *Vibration Test of a Multistorey Building.* Ph.D. thesis, California Institute of Technology.

Lauterborn, W., Kurz, T., & Wiesenfeldt, M. 1995. *Coherent Optics, Fundamentals and Applications.* Berlin: Springer-Verlag.

Lobkis, O.I., & Weaver, R.L. 2001. On the emergence of the Green's function in the correlations of a diffuse field. *J. Acoust. Soc. Am.*, **110**, 3011–3017.

Luco, J., Trifunac, M., & Wong, H. 1987. On the apparent change in dynamic behavior of a 9-story reinforced-concrete building. *Bull. Seismol. Soc. Am.*, **77**, 1961–1963.

Luco, J. E. 1986. *Soil-structure interaction effects on forced vibration tests.* Los Angeles, California: Technical Report Report 86-05, University of Southern California, Department of Civil Engineering.

Riley, D.C., & Claerbout, J.F. 1976. 2-D multiple reflections. *Geophysics*, **41**, 592–620.

Şafak, E. 1995. Detection and identification of soil-structure interaction in buildings from vibration recordings. *J. Struct. Eng.*, **121**, 899–906.

Şafak, E. 1999. Wave-propagation formulation of seismic response of multistory buildings. *J. Struct. Eng.*, **125**, 426–437.

Snieder, R. 2004a. Extracting the Green's function from the correlation of coda waves: A derivation based on stationary phase. *Phys. Rev. E*, **69**, 046610.

Snieder, R. 2004b. *A Guided Tour of Mathematical Methods for the Physical Sciences.* 2nd edn. Cambridge, UK: Cambridge Univ. Press.

Snieder, R. 2005. Spurious multiples in interferometric imaging of primaries. *Geophysics, submitted.*

Tatarskiĭ, V.I., & Gertsenshteĭn, M.E. 1963. Propagation of waves in a medium with strong fluctuations in refractive index. *Soviet Phys. JETP*, **17**, 458–463.

Trampert, J., Cara, M., & Frogneux, M. 1993. SH propagator matrix and Q_s estimates from borehole- and surface-recorded earthquake data. *Geophys. J. Int.*, **112**, 290–299.

Trifunac, M.D. 1972. Comparisons between ambient and forced vibration experiments. *Int. J. Earthquake Eng. and Struct. Dyn.*, **1**, 133–150.

Udwadia, F.E., & Trifunac, M.D. 1974. Time and amplitude dependent response of structures. *Int. J. Earthquake Eng. and Struct. Dyn.*, **2**, 359–378.

Wapenaar, K. 2004. Retrieving the elastodynamic Green's function of an arbitrary inhomogeneous medium by cross correlation. *Phys. Rev. Lett.*, **93**, 254301.

Wapenaar, K., Thorbecke, J., & Dragonov, D. 2004. Relations between reflection and transmission responses of three-dimensional inhomogeneous media. *Geophys. J. Int.*, **156**, 179–194.

Wapenaar, K., Fokkema, J., & Snieder, R. 2005. Retrieving the Green's function by cross-correlation: a comparison of approaches. *Submitted to J. Acoust. Soc. Am.*

APPENDIX A: EVALUATION OF THE FOURIER INTEGRAL (18)

In this appendix we evaluate the Fourier integral (18) using complex integration. For $t > (2H - z)/c$ the integration along the real ω-axis must be closed in the lower half plane to obtain a vanishing contribution of the semi-circular integration path that is added in the contour integration (Snieder, 2004b). The value of the contour integral over the path shown in Figure 8 is determined by the poles of the integrand in expression (18) in the lower half-plane. The pole-positions are determined by expression (19). To first order in γ the poles are located at

$$\omega_* = \pm\omega_m - i\gamma\omega_m \qquad (m = 0, 1, 2, \cdots) , \tag{A1}$$

with ω_m given by expression (21). There are infinitely many poles at locations in the lower half-plane as shown in Figure 8.

The terms in the integrand in expression (18) are of the form

$$I = \int_{-\infty}^{\infty} \frac{f(\omega)}{1 + e^{i\omega\tau} e^{-\gamma|\omega|\tau}} d\omega , \tag{A2}$$

where $f(\omega)$ is an analytic function. Setting $\omega = \omega_* + \xi$ and using a first-order Taylor expansion in ξ gives

$$1 + e^{i\omega\tau} e^{-\gamma|\omega|\tau} = -i\xi\tau + O\left(\xi^2\right) . \tag{A3}$$

This implies that the poles are simple and that the residue for the pole at ω_* is given by

$$Res \frac{f(\omega)}{1 + e^{i\omega\tau}} = \frac{f(\omega_*)}{-i\tau} , \tag{A4}$$

Together with the factor $-2\pi i$ from the counter-clockwise contour integration, this gives a contribution $2\pi f(\omega_*)/\tau$ to the the complex integral. Using this in the integral (18) and taking the poles in the 3rd and 4th quadrant into account gives:

$$\begin{aligned} B(t) = \tfrac{2\pi c}{H} \quad & \textstyle\sum_{m=0}^{\infty} e^{-\gamma\omega_m t} \left\{\cos\left(\omega_m(t - z/c)\right)\right. \\ + \quad & \left.\cos\left(\omega_m(t - (2H - z)/c)\right)\right\} . \end{aligned} \tag{A5}$$

Using trigonometric identities the terms in curly brackets equals

$$\begin{aligned} & \cos\left(\omega_m(t - z/c)\right) + \cos\left(\omega_m(t - (2H - z)/c)\right) \\ & = 2\cos\left(\omega_m H/c\right)\cos\left(\omega_m(H - z)/c\right)\cos(\omega_m t) \\ & -2\sin\left(\omega_m H/c\right)\cos\left(\omega_m(H - z)/c\right)\sin(\omega_m t) . \end{aligned} \tag{A6}$$

According to expression (21), $\cos(\omega_m H/c) = 0$ and $\sin(\omega_m H/c) = (-1)^m$, so that

$$\begin{aligned} & \cos\left(\omega_m(t - z/c)\right) + \cos\left(\omega_m(t - (2H - z)/c)\right) = \\ & 2(-1)^{m+1}\cos\left(\omega_m(H - z)/c\right)\sin(\omega_m t) . \end{aligned} \tag{A7}$$

Using this in equation (A5) gives expression (20).

The theory of coda wave interferometry

Roel Snieder

Center for Wave Phenomena, Colorado School of Mines, Golden CO 80401, email rsnieder@mines.edu

ABSTRACT
Coda waves are sensitive to changes in the subsurface because the strong scattering that generates these waves causes coda waves to repeatedly sample a limited region of space. Coda wave interferometry is a technique that exploits this sensitivity to estimate weak changes in the medium from a comparison of the coda waves before and after the perturbation. Here I present the general theory of coda wave interferometry, and show how the time-shifted correlation coefficient can be used to estimate the mean and variance of the travel time perturbation caused by the perturbation of the medium. This mean and average are defined based on the intensity of the coda waves. I show how this general theory can be used to estimate changes in the wave velocity, in the location of scatterer positions, and in the source location.

Key words: coda wave interferometry

Preface

In December 2004, a symposium was held at the Fall Meeting of the American Geophysical Union in honor of Keiiti Aki. He is known not only for writing the seminal textbook "Quantitative Seismology" with Paul Richards, but also for his prolific and groundbreaking research in seismology, and for his caring and creative frame of mind. Aki is one of the pioneers in the analysis of coda waves; he developed and implemented the analysis of the decay rate of these waves as a tool to monitor time-lapse changes in the Earth. He carried out numerous studies to apply this to monitor fault zones and volcanoes with the ultimate goal to develop better tools for hazard assessment.

Aki's use of coda waves has focused on the amplitude of these waves. At the Colorado School of Mines we developed a new technique, coda wave interferometry, that takes the phase information of these waves into account as well. This provides a tool to monitor time-lapse changes in the subsurface based on changes in the waveforms in the coda. We have applied this to measure velocity changes in rocks due to changes in the temperature or stress, to monitor stress changes in a mining environment, to determine the distance between earthquakes, and for volcano monitoring. We look forward to collaborate with our sponsors on the application of coda wave interferometry to reservoir monitoring.

The following paper gives the theory of coda wave interferometry. It will appear in the special issue of Pure and Applied Geophysics titled "Advances in Studies of Heterogeneities in the Earth Lithosphere: The Keiiti Aki Volume II." The treatment of this paper is general and can be used to a variety of different applications. The work on coda wave interferometry has been largely financed completely with financial support from the National Science Foundation.

1 INTRODUCTION

The seismic coda constitutes the tail of strongly scattered waves in a seismogram. Aki was one of pioneers in using the seismic coda [Aki and Chouet, 1975] . He used the temporal decay of the seismic coda as measure of the scattering in the earth, and proposed to use changes of coda Q to monitor changes in the stress in the subsurface [Aki, 1985; Jin and Aki, 1986]. This approach considers the amplitude of the coda waves, but does not use the phase information in the coda.

Here I present the theory of coda wave interferometry, a technique to monitor time-lapse changes based on the phase and amplitude information of coda waves.

In a strongly-scattering medium, the waves repeatedly sample the same region in space. Such a medium therefore works as a natural interferometer. Just as in a man-made interferometer [Lauterborn et al., 1995] the multiply-scattered waves are extremely sensitive to minute changes in the medium. In coda wave interferometry we exploit this sensitivity to measure small changes in the medium.

This idea is not new, the sensitivity of coda waves has been used to estimate velocity changes in fault zones [Poupinet et al., 1984], in volcanoes [Ratdomopurbo and Poupinet, 1995; Matsumoto et al., 2001] , in a mining environment [Grêt et al., 2004] , and in ultrasound experiments [Roberts et al, 1992; Snieder et al., 2002; Grêt et al., 2005] . Temporal changes in the coda waves within a a couple of days have been observed in a volcano . In the physics community a related technique called diffusing wave spectroscopy [Weitz and Pine, 1993; Cowan et al., 2002] has been used to monitor fluidized suspensions [Cowan et al., 2000; Page et al., 2000].

In this work I present the theory of coda wave interferometry. Because of the generality of the derivation, it can be applied to a a number of different applications of coda wave interferometry. The theory is based on the path summation (section 2). This is a formulation of scattering that states that the total wave field is the superposition of the waves that propagate along all possible scattering paths. In section 3 I show how the changes in the coda waves can be characterized with the time-shifted correlation coefficient. This quantity is related to the distribution of the travel time perturbation when averaged over all scattering paths (section 4). In principle, the distribution of the travel time perturbation can be obtained from the time-shifted correlation coefficient, but I show in section 5 how in practical application the mean and variance of the travel time perturbation can be obtained from the time-shifted correlation coefficients. In section 6 I apply the theory to three examples; a change in the velocity, uncorrelated perturbations of the scatterer locations, and a change in the source position.

2 THE PATH SUMMATION AND THE CHANGE IN THE WAVES

The theory of coda wave interferometry is based on the path summation where the wavefield at a given location is written as a sum of the waves that propagate along all possible paths [Snieder, 1999]:

$$u(t) = \sum_P S_P(t) \ . \tag{1}$$

The path summation is valid when the wavefield can be written as a discrete sum over all possible scattering paths, and expression (1) simply states that the total wavefield is the sum of the waves that have propagated along all possible scattering paths. I use a scalar notation, but expression (1) is also valid for elastic waves; in that case equation (1) can be used for each of the components of the wave motion. For elastic waves conversions between P and S-waves occur at the scatterers; in that case the path summation includes a sum P and S waves for each segment of the scattering path, so that $\sum_P$ includes all the possible wave conversions along each path as well.

A perturbation of the medium leads to a perturbation of the waves. I assume that the scattering properties of the scatterers in the medium do not change, but that either the propagation velocity, the position of the scatterers, or the source position is weakly perturbed. These perturbations correspond to a change in the phase of the wave propagation changes, the geometrical spreading, and the scattering angle for every scattering event.

Let us consider a wave that propagates over a distance l between scatterers. The average distance between the scatterers, as seen by the waves, is given by the scattering mean free path [Lagendijk and van Tiggelen, 1996; van Rossem and Nieuwenhuizen, 1999]. In the frequency domain the propagation over this distance corresponds to a phase shift $\exp(ikl)$. Let us first consider a change δl in the path length. This change corresponds to a phase change $\exp(ik\delta l) = 1 + i\delta kl$, so that a change in the path length gives the following change in the wavefield:

$$|\delta u|^{phase} \sim |k\delta l u| \ . \tag{2}$$

In three dimensions the geometrical spreading for each segment of propagation varies as $1/l$, hence the change in the wavefield due to the geometrical spreading associated with a change in path length is given by

$$|\delta u|^{spreading} \sim \left| \frac{\delta l}{l} u \right| \ . \tag{3}$$

A change δl in the scatterer position leads to a change in the scattering angle that is of the order $\delta\theta \sim \delta l/l$. When the scattering amplitude, or source radiation pattern, varies as $\cos m\theta$ or $\sin m\theta$, the change in the wavefield due to this change in scattering angle is of the order

$$|\delta u|^{angle} \sim |m\delta\theta|\, u = \left| \frac{m\delta l}{l} u \right| \ . \tag{4}$$

The change is the phase of the wavefield dominates when the right hand side expression (2) is larger than both (3) and (4). Since in general $|m| > 1$ this conditions imply that the change in the phase is dominant when

$$\frac{l}{\lambda} > \frac{|m|}{2\pi} \ , \tag{5}$$

where the wavelength is given by $\lambda = 2\pi/k$. This means that the change in the phase dominates the change of the wavefield when the scattering mean free path is much larger than a wavelength. If this condition is not satisfied the waves are localized [van Tiggelen, 1999] and the theory of this paper does not hold.

This means that when the distance between the scatterers is changed, the change in the phase is the most important change. It follows from expression (2) that the change in the phase varies linearly with frequency, because $k = \omega/c$. Such a change in the phase corresponds in the time-domain a change in the phase corresponds to a change in the arrival time of the wave. A change in the velocity of propagation also gives a change in the arrival time of the wave. I denote the change in the travel time of the wave that propagates along path P by τ_P. This means that the perturbed wavefield is given by

$$\tilde{u}(t) = \sum_P S_P(t - \tau_P) \ . \tag{6}$$

This expression should be compared with equation (1) for the unperturbed wave.

3 MEASURING THE CHANGE IN THE WAVEFIELD

The unperturbed and perturbed waves can be compared using the time-shifted correlation coefficient defined as

$$R(t_s) = \frac{\int_{t-T}^{t+T} u(t')\tilde{u}(t'+t_s)dt'}{\sqrt{\int_{t-T}^{t+T} u^2(t')dt' \int_{t-T}^{t+T} \tilde{u}^2(t')dt'}} \ . \tag{7}$$

In this expression t_s is the time shift of the unperturbed and perturbed waves in the correlation. The correlation is computed of a finite time-window with center-time t and window length $2T$. Let us first analyze the numerator of this expression that is given by

$$N(t_s) = \int_{t-T}^{t+T} u(t')\tilde{u}(t'+t_s)dt' \ . \tag{8}$$

Inserting the expressions (1) and (6) in this equation gives a double sum $\sum_{PP'}$over paths. Such a double sum can be divided into diagonal terms, for which $P = P'$, and cross-terms $P \neq P'$:

$$\sum_{PP'}(\cdots) = \sum_{P=P'}(\cdots) + \sum_{P\neq P'}(\cdots) \ , \tag{9}$$

with equations (1) and (6) this gives:

$$\begin{aligned} N(t_s) \ &= \textstyle\sum_P \int_{t-T}^{t+T} S_P(t')S_P(t'+t_s-\tau_P)dt' \\ &+ \textstyle\sum_{P\neq P'} \int_{t-T}^{t+T} S_P(t')S_{P'}(t'+t_s-\tau_{P'})dt' \ . \end{aligned} \tag{10}$$

The cross-terms are uncorrelated, this means that on average the cross terms integrate to zero. In a single realization this is not necessarily the case, and the second term in expression (10) may not be zero. Snieder [2004] estimated the magnitude of the cross terms $\sum_{P\neq P'}$ to the diagonal terms $\sum_{P=P'}$, and showed that when the DC-component of the signal vanishes that in a single realization

$$\frac{|\text{cross terms}|}{|\text{diagonal terms}|} \sim \sqrt{\frac{T_{corr}}{2T}} \ , \tag{11}$$

where T_{corr} is the width of the autocorrelation of the signal in the time domain. This width is proportional to $1/\Delta f$, with Δf the bandwidth of the signal. This means that the ratio in expression (11) can also be written as

$$\frac{|\text{cross terms}|}{|\text{diagonal terms}|} \sim \sqrt{\frac{1}{\Delta f \ 2T}} \ . \tag{12}$$

The bandwidth times the window length is the number of degrees of freedom in the signal [Bucci and Franceschetti, 1989; Landau, 1967] , hence the ratio of the cross-terms to the diagonal terms is for a single realization equal to $1/\sqrt{N}$, with N the number of degrees of freedom in the data. The important point of expression (11) is that the cross-terms decrease when the window length is increased. Note that this argument does not hold for monochromatic data, because in that case $\Delta f = 0$ and the right hand side of expression (12) cannot be reduced by increasing the window length. This means that in order to ignore the cross-terms both the window length and the bandwidth must be sufficiently large.

In the following I assume that this indeed the case and that the cross-terms can be ignored, in this approximation

$$N(t_s) = \sum_P \int_{t-T}^{t+T} S_P(t')S_P(t'+t_s-\tau_P)dt' \ . \tag{13}$$

This integral can be written as a sum of the cross-correlations of the waves that have propagated along the individual paths that is defined as

$$C_P(t_0) \equiv \int_{t-T}^{t+T} S_P(t')S_P(t'+t_0)dt' \ . \tag{14}$$

With this definition $I(t_s)$ can be written as

$$N(t_s) = \sum_P C_P(t_s - \tau_P) \ . \tag{15}$$

A similar treatment can be applied to the terms in the denominator of equation (7), this gives

$$\int_{t-T}^{t+T} u^2(t')dt' = \int_{t-T}^{t+T} \tilde{u}^2(t')dt' = \sum_P C_P(0) \ . \tag{16}$$

In deriving this result the same approximations are used as in the derivation of expression (15), specifically the cross-terms $\sum_{P\neq P'}$ are ignored. Inserting the expressions (15) and (16) into the definition (7) of the correlation coefficient gives

$$R(t_s) = \frac{\sum_P C_P(t_s - \tau_P)}{\sum_P C_P(0)} \ . \tag{17}$$

Before we analyze this correlation coefficient I introduce another approximation. In the frequency domain the definition (14) for the correlation of S_P corresponds to

$$C_P(\omega) = S_P^*(\omega)S_P(\omega)\exp(i\omega t_0) = |S_P(\omega)|^2 \exp(i\omega t_0) \ . \tag{18}$$

I assume that the waves that propagate along the different trajectories have a power spectrum with the same shape, but that the amplitude of each of these waves may be different. Note that this does not imply that the waves $S_P(t)$ are the same, because the phase spectrum may be different. In fact, the phase spectrum will be different because these waves have different arrival times. Since the autocorrelation is the Fourier transform of the power spectrum, the assumption that shape of the the power spectrum of the waves is the same implies that up to a constant the autocorrelation also is the same, so that

$$C_P(t_0) = I_P C(t_0) \qquad \text{with} \qquad C(0) = 1 \; . \tag{19}$$

In this expression $C(t_0)$ is the autocorrelation of the $S_P(t)$ normalized at its maximum for $t_0 = 0$, while I_P measures the intensity of the wave that has propagated along path P. Using these results the correlation coefficient is given by

$$R(t_s) = \frac{\sum_P I_P C(t_s - \tau_P)}{\sum_P I_P} \; . \tag{20}$$

4 THE PROBABILITY DENSITY FUNCTION OF THE TRAVEL TIME PERTURBATION

The time-shifted cross correlation coefficient can be determined from the recorded waves using expression (7). The goal is to infer properties of the travel time perturbation from this measurement. One way to achieve this is to define the normalized energy of the arrivals in the employed time window with a travel time shift between τ and $\tau + d\tau$ as $P(\tau)d\tau$. This definition implies that

$$P(\tau)d\tau = \frac{\sum_{P \text{ such that } \tau<\tau_P<\tau+d\tau} I_P}{\sum_{all\ P} I_P} \; . \tag{21}$$

The sum in the numerator is all paths that have a travel time change between τ and $\tau + d\tau$. Since the denominator contains a sum over all paths, and hence all relevant values of τ, the function $P(\tau)$ is normalized:

$$\int_{-\infty}^{\infty} P(\tau)d\tau = 1 \; . \tag{22}$$

The definition (21) consists of a ratio of positive numbers, therefore $P(\tau)$ is positive and normalized. For this reason it has the same properties as a probability density function. Using statistical jargon, we use the following definition of an expectation value:

$$\langle f(\tau)\rangle \equiv \int_{-\infty}^{\infty} P(\tau)f(\tau)d\tau \; . \tag{23}$$

Using expressions (21) this can also be written in the path summation as

$$\langle f(\tau)\rangle \equiv \frac{\sum_P I_P f(\tau_P)}{\sum_P I_P} \; . \tag{24}$$

With the definitions (21) and (24), equation (20) can be written as

$$R(t_s) = \langle C(t_s - \tau)\rangle = \int P(\tau)C(t_s - \tau)d\tau \; . \tag{25}$$

The first identity shows that coda wave interferometry leads to a weighted average of a function of the travel time perturbation. The coda waves travel along all possible paths, and the contribution of the travel time perturbation is averaged over all possible paths with a weight function given by the intensity of the waves for each path.

The second identity of expression (25) states that the time-shifted correlation coefficient is given by the convolution of $P(\tau)$ with $C(\tau)$. The time-shifted correlation coefficient $R(t_s)$ follows from the recorded waves. The function $C(t)$ follows from the power spectrum of the recorded waves, and is known as well. In principle $P(\tau)$ can the be obtained from expression (25) by deconvolution. This provides direct information on the distribution of the travel time perturbations over the paths that have arrivals within the employed time window. Note that in this approach we do not need to assume that the travel time perturbation is small.

In practice this deconvolution approach may not work well for the retrieval of $P(\tau)$. In the frequency domain, the right hand side of expression (25) corresponds to the multiplication of the frequency spectra of P and C. The frequency spectrum of $C(\tau)$ is the power spectrum of the data. In general, there is no guarantee that the frequency spectrum of $P(\tau)$ overlaps with the power spectrum of the data. This would only be the case when the distribution of the travel time perturbation peaks near the dominant period of the waves. Since we cannot be sure that this condition is satisfied in a given experiment we take a different approach and extract the first and second moments of the travel time perturbation from expression (25).

5 EXTRACTING THE MOMENTS OF THE TRAVEL TIME PERTURBATION FROM THE CORRELATION

In this section we assume that the travel time perturbations do not change vary much among all the different paths with arrivals within the employed time window. Specifically, we assume that we can use a second-order Taylor expansion of $C(t)$. The autocorrelation is an even function, with $C(0) = 1$, the second-order Taylor expansion is given by

$$C(t) = 1 - \frac{1}{2}\ddot{C}(t = 0)t^2 \; , \tag{26}$$

where the dots denote the second time derivative. In the following I consider the situation before the perturbation. In that case $\tau_P = 0$, and expression (20) gives

$$C(t) = R(t) \; , \tag{27}$$

where $R(t)$ is the correlation coefficient defined in expression (7) with the unperturbed state equal to the perturbed state: $u = \tilde{u}$. Using this in expression (27) gives

$$C(t) = \frac{\int u(t')u(t'+t)dt'}{\int u^2(t')dt'} , \tag{28}$$

where the integration is over the time-window under consideration. Note that it follows from this expression that $C(0) = 1$, as required in equation (19).

Differentiating expression (28) twice with respect to time gives

$$\ddot{C}(t) = \frac{\int u(t')\frac{d^2u(t'+t)}{dt^2}dt'}{\int u^2(t')dt'} = \frac{\int u(t')\frac{d^2u(t'+t)}{dt'^2}dt'}{\int u^2(t')dt'} , \tag{29}$$

where second derivative in the last term is with respect to t'. Setting $t = 0$, and using an integration by parts gives under the assumption that u vanishes at the end of the integration interval:

$$\ddot{C}(0) = -\frac{\int \dot{u}^2(t')dt'}{\int u^2(t')dt'} . \tag{30}$$

In practice, one tapers the integrand in the correlation coefficient (7) in order to suppress truncation artifacts. This taper ensures that the integrand of expression (7) indeed vanishes at the endpoint of the interval. The right hand side of expression (30) has the physical dimension *frequency*^{2}; for this reason I introduce the following definition of the mean squared angular frequency:

$$\overline{\omega^2} \equiv \frac{\int \dot{u}^2(t')dt'}{\int u^2(t')dt'} . \tag{31}$$

Note that this quantity can directly be computed from the recorded data. Using this result in the expressions (26) and (30) gives the following second-order Taylor expansion:

$$C(t) = 1 - \frac{1}{2}\overline{\omega^2}t^2 . \tag{32}$$

Inserting this result in expression (20) gives

$$R(t_s) = 1 - \frac{1}{2}\overline{\omega^2}\frac{\sum_P I_P(t_s - \tau_P)^2}{\sum_P I_P} . \tag{33}$$

It follows by differentiation that the correlation coefficient attains its maximum when

$$0 = \frac{dR(t_s)}{dt_s} = -\overline{\omega^2}\frac{\sum_P I_P(t_s - \tau_P)}{\sum_P I_P} . \tag{34}$$

This maximum is reached for

$$t_s = t_{\max} = \frac{\sum_P I_P \tau_P}{\sum_P I_P} . \tag{35}$$

This equation states that the correlation coefficient attains its maximum for a time shift that is equal to the intensity-weighted travel time perturbation. According to the notation of expression (24) this result can also be written as

$$t_{\max} = \langle \tau \rangle . \tag{36}$$

The value $R_{\max}$ of the correlation coefficient at its maximum follows by replacing t_s in expression (33) by the average $\langle \tau \rangle$, thus

$$R_{\max} = 1 - \frac{1}{2}\overline{\omega^2}\frac{\sum_P I_P(\tau_P - \langle \tau \rangle)^2}{\sum_P I_P} . \tag{37}$$

Using expression (24) the ratio in the last term satisfies

$$\frac{\sum_P I_P(\tau_P - \langle \tau \rangle)^2}{\sum_P I_P} = \left\langle (\tau - \langle \tau \rangle)^2 \right\rangle = \sigma_\tau^2 , \tag{38}$$

where σ_τ^2 is the variance of the travel time perturbation. Combining this result with expression (37) gives

$$R_{\max} = 1 - \frac{1}{2}\overline{\omega^2}\sigma_\tau^2 . \tag{39}$$

The time-shifted correlation coefficient can for every employed time window be computed from expression (7) given the data before and after the perturbation, and according to expression (36) the time-shifted correlation coefficient attains its maximum for a shift time that is equal to the mean travel time perturbation. According to equation (39) the value of the time-shifted correlation coefficient gives the variance of the travel time perturbation. This means that if the unperturbed and perturbed waveforms are known, the mean and variance of the travel time perturbation can be computed. Computing the two lowest moments of the distribution of the travel time perturbation is a less ambitious goal than determining the distribution $P(\tau)$ of the travel time perturbations from equation (25), but as we will see in the examples of the next section the mean and variance of the travel time perturbation are useful in a number of practical applications.

The data may be contaminated with noise. The noise has two effects on the time-shifted cross correlation coefficient. First, the noise introduces fluctuations in the estimated coefficient. Without knowing the noise there is no way to eliminate these fluctuations other than using non-overlapping time windows of the coda to obtain independent estimates of the cross-correlation. Second, noise leads to a bias because noise lowers the value of the cross-correlation. This bias can be estimated given the energy in the noise ($\langle n^2 \rangle$) and the energy of the noise-contaminated data ($\langle u^2 \rangle$). Douma and Snieder [2005] show that the bias in the correlation coefficient can be accounted for by using the corrected correlation coefficient that is related to the uncorrected coefficient by the following relation

$$R_{corr} = R / \sqrt{1 - \frac{\langle n^2 \rangle}{\langle u^2 \rangle}}\sqrt{1 - \frac{\langle \tilde{n}^2 \rangle}{\langle \tilde{u}^2 \rangle}} . \tag{40}$$

The noise levels $\langle n^2 \rangle$ and $\langle \tilde{n}^2 \rangle$ before and after the perturbation can be estimated from the data recorded before the first-arriving waves.

6 EXAMPLES

In this section I consider three different perturbations that are of relevance for practical applications; a constant velocity perturbation, random displacement of scatterers, and a perturbation in the source position.

6.1 A constant velocity perturbation

Suppose that in a medium the velocity is perturbed with a perturbation δv, and that the relative velocity perturbation $\delta v/v$ is the same at every location in space. The unperturbed travel time is given by

$$t = \int_P \frac{1}{v} ds \,, \tag{41}$$

where the integration is along path P. The perturbed travel time is to first order in the velocity perturbation given by

$$t + \tau_P = \int_P \frac{1}{v + \delta v} ds = \int_P \left(\frac{1}{v} - \frac{\delta v}{v^2} \right) ds \,. \tag{42}$$

With expression (41) this gives

$$\tau_P = -\int_P \frac{1}{v} \frac{\delta v}{v} ds = -\left(\frac{\delta v}{v} \right) \int_P \frac{1}{v} ds \,, \tag{43}$$

where I used in the last identity that the relative velocity perturbation is assumed to be constant. With expression (41) the travel time perturbation can be written as

$$\tau_P = -\left(\frac{\delta v}{v} \right) t \,. \tag{44}$$

Note that the velocity v is not necessarily constant. According to expression (44), the travel time perturbation depends on the arrival time of the wave only, but is independent of the particular path. This means that in a small time window the mean travel time perturbation is also given by

$$t_{max} = \langle \tau \rangle = -\left(\frac{\delta v}{v} \right) t \,. \tag{45}$$

Since the travel time perturbation is the same for all trajectories, the variance of the travel time perturbation vanishes

$$\sigma_\tau^2 = 0 \,. \tag{46}$$

As shown in expression (36), the mean travel time perturbation is equal to the shift time that gives the maximum of the time-shifted correlation coefficient, this quantity can easily be retrieved from the data. According to expression (45) the relative velocity change then follows from

$$\left(\frac{\delta v}{v} \right) = -\frac{t_{max}}{t} \,. \tag{47}$$

This has been applied by Snieder et al. [2002] to measure the velocity change in a granite sample with temperature. In their experiment coda wave interferometry is sufficiently sensitive to detect a velocity change of about 0.1%. This change in the velocity can be inferred from different non-overlapping time windows in the coda. This redundancy serves as a consistency check on the method, and can be used for error estimation. In these measurements the estimated error in the velocity change was about 0.02% [Sniedet et al., 2002] . Grêt et al. [Grêt et al., 2005] applied this technique also to measure the velocity change in rocks due to changes in the stress state in laboratory conditions, and in a mining environment [Grêt et al., 2004].

For elastic waves there are two wave velocitites. It follows from the intensity-averaged travel time perturbation (35) that for elastic waves the inferred velocity change is a weighted average of the change in the P-wave and S-wave velocities [Snieder, 2002]:

$$\frac{\delta v}{v} = \frac{\beta^3}{2\alpha^3 + \beta^3} \frac{\delta \alpha}{\alpha} + \frac{2\alpha^3}{2\alpha^3 + \beta^3} \frac{\delta \beta}{\beta} \,. \tag{48}$$

where α and β are the velocities of P-waves and S-waves, respectively. Since $\beta < \alpha$ the perturbation in the shear velocity dominates the perturbation in the P-wave velocity. For example, for a a Poisson medium ($\alpha = \sqrt{3}\beta$):

$$\frac{\delta v}{v} = 0.09 \frac{\delta \alpha}{\alpha} + 0.91 \frac{\delta \beta}{\beta} \,. \tag{49}$$

The theory of this section is valid when the relative velocity change is independent of location. In realistic situations this is not necessarily the case. The theory can be extended for situations where the relative velocity change depends on position. In that case the mean travel time change is linearly related to the velocity change:

$$\langle \tau \rangle = \int K(\mathbf{r}, t) \delta v(\mathbf{r}) dV \,, \tag{50}$$

where the kernel $K(\mathbf{r}, t)$ depends on the intensity-weighted average over all scattering paths. This expression can be used as the basis of a standard linear inversion for the velocity change $\delta v(\mathbf{r})$ given the mean travel time change observed for different source-receiver pairs and different time windows. The kernel $K(\mathbf{r}, t)$ has been derived both for single-scattered waves [Pacheco and Snieder, 2005a] as well as for strongly scattered waves [Pacheco and Snieder, 2005b].

6.2 Random displacement of scatterers

As a second example we consider a perturbation that consists of uncorrelated movement of the scatterers. This is of relevance for studying the motion of particles in colloidal suspensions [Heckmeier and Maret, 1997] and of bubbles in a turbulent fluid [Cowan et al., 2000; Page et al., 2000]. The theory presented here is equivalent to diffusing wave spectroscopy [Cowan at al., 2002;

Weitz and Pine, 1993], although the derivation is different.

Let us consider scatterers that move independently in three dimensions and that have a root mean square displacement δ between the two measurements of the waves that are used to study the motion of the scatterers. On average the path length for each scattered wave does not change, hence the mean perturbation of the travel time vanishes:

$$\langle \tau \rangle = 0 \,. \tag{51}$$

Some scattering paths are longer, while other scattering paths are shorter, therefore the variance of the travel time perturbation is nonzero.

We compute the variance of the travel time by using that for a wave that has scattered n times, the variance in the path length is given by [Snieder and Scales, 1998]:

$$\sigma_L^2 = 2n\left(1 - \overline{\cos\theta}\right)\delta^2 \,. \tag{52}$$

In this expression $\overline{\cos\theta}$ is the average of the cosine of the scattering angle over all paths in the employed time window. The number of scatterers encountered is related to the travel time by $n = vt/l$, where v is the wave velocity and l the scattering mean free path. Using this in expression (52) gives

$$\sigma_L^2 = \frac{2vt\delta^2}{l_*} \,, \tag{53}$$

where l_* is the transport mean free path. This is the distance of propagation over which the scattered wave has lost all information about its direction of propagation [Lagendijk and van Tiggelen, 1996; van Rossum and Nieuwenhuizen, 1999]. For a constant velocity the variance in the path travel time is related to the variance in the path length by $\sigma_\tau = \sigma_L/v$, so that

$$\sigma_\tau^2 = \frac{2t\delta^2}{vl_*} \,, \tag{54}$$

With expression (39) this means that the measured maximum of the cross-correlation is related to the mean displacement of the scatterers by

$$R_{max} = 1 - \frac{\overline{\omega^2}\delta^2 t}{vl_*} \,. \tag{55}$$

Given a measured value of the maximum of the cross-correlation, one can infer the mean scatterer displacement δ from this expression if the wave velocity and the transport mean free path is known. Snieder et al. [2002] show in a numerical experiment that the mean scatterer displacement can correctly be retrieved from the coda waves. The scatterer displacement can be computed from several non-overlapping time windows of the coda, and they show how this redundancy can be used to compute error bounds on the scatterer displacement inferred from the coda waves.

6.3 A displaced source position

The relative distance between earthquakes can be found from the absolute location of the events, but in this approach errors in the employed velocity model may lead to large errors in the distance between the events [Pavlis, 1992] . An alternative approach is the double-difference method where the relative event location is computed from the differential travel time of the direct arrivals [Shearer, 1997; Astiz and Shearer, 2000; Walhauser and Ellsworth, 2002] . Coda wave interferometry can also be used to determine the relative distance between earthquakes, provided the source mechanisms of the events are identical. This provides additional information on the relative position between events that can be used in addition to the constraints obtained from the double-difference method.

Let us consider two nearby seismic sources with the same source mechanism. When the source position is perturbed over the distance $\mathbf{r}$, the distance from the source to the first scatterer along every scatterer path is perturbed. The distance between the scatterers is unperturbed, so we only need to account for the change in the distance to the first scatterer along every scattering path. For this reason it does not matter if the wave travels from the first scatterer along every path directly to the receiver, or whether the wave visits many other scatterers first. The theory of this section therefore is applicable both for single scattering as well as for multiple scattering.

For a scattering path P with take-off direction $\hat{\mathbf{t}}_P$ at the source, the perturbation in the travel time is given by

$$\tau_P = -\frac{(\hat{\mathbf{t}}_P \cdot \mathbf{r})}{v} \,. \tag{56}$$

For a scattering path where the wave leaves the source as a P-wave, v is the P-wave velocity at the source location, whereas for a path where the wave leaves the source as an S-wave, v denotes the shear velocity. When the scatterers are distributed homogeneously, some paths are longer when the source location is perturbed, while others are shorter. The resulting mean travel time perturbation vanishes [Snieder and Vrijlandt, 2005] . This can be shown by integrating the travel time perturbation (56) over all take-off directions.

The variance of the travel time perturbation, however, is nonzero, because some paths are longer when the source location is perturbed while others are shorter. The variance of the travel time perturbation depends on the type of source (explosion, point force, double couple), as well as on the orientation of the perturbation of the source location relative to the source mechanism [Snieder and Vrijlandt, 2005]. An important application is the location of aftershocks. In that case all events are located in the plane of the fault-plane of the main shock. Snieder and Vrijlandt [2005] show that in this case the variance of the travel time is given by

$$\sigma_\tau^2 = \frac{\left(\frac{6}{\alpha^8} + \frac{7}{\beta^8}\right)}{7\left(\frac{2}{\alpha^6} + \frac{3}{\beta^6}\right)} r^2 . \tag{57}$$

In this expression α is the P-wave velocity, and β denotes the shear-wave velocity. This expression depends on both velocities, because the path summation includes waves that leave the source as a P-wave, as well as waves that leave the source as an S-wave. The P- and S-wave velocities in expression (57) are raised to high powers. Since $\beta < \alpha$, the terms with the shear velocity dominate. Note that expression (57) depends on the distance r between the events, but not on their relative orientation in the fault plane. The reason for this is that the averaging (38) in this application involves an integration over all take-off directions. In this directional averaging information on the direction of the event separation is lost.

Expression (57) can be used to estimate the source separation in the following way. For several time windows in the coda the time-shifted correlation coefficient can be computed from expression (7). Using expression (39), the maximum of this function can be equated to the variance of the travel time perturbation given by equation (57). The resulting expression can then be solved for the event separation r. In the presence of significant noise, the correction factor of equation (40) can be used to eliminate the bias in the cross-correlation due to noise.

Snieder and Vrijlandt [2005] applied this technique to events on the Hayward Fault, California, and showed that the event separation obtained from the coda waves agrees with the event separation of the same events determined by Waldhauser and Ellsworth [2002] with the double-difference method.

Note that the estimation of the event separation can be carried out with a single station. An error estimate of the event separation can be obtained by comparing the event separation inferred from different non-overlapping time windows in the coda.

7 DISCUSSION

The main result of the theory of this paper is that the time-shifted correlation coefficient of expression (7) can be related to the mean and variance of the travel time perturbation. According to expression (36), the mean travel time perturbation follows from the shift time that gives the maximum of the time-shifted correlation coefficient, and equation (39) relates the maximum of the cross-correlation coefficient to the variance of the travel time perturbation. This means that the mean and variance of the travel time perturbation can be obtained from a comparison of the coda waves before and after the perturbation. Additive random noise leads to a bias in the maximum of the correlation coefficient, this bias can be removed using the correction factor of expression (40).

The present theory can be applied to a constant change in the velocity, to uncorrelated perturbations in the locations of the scatterers, and to changes in the source position. For a change in the velocity (section 6.1), the means travel time perturbation is nonzero (equation (45)), but the variance of the travel time perturbation is zero (expression (46)). For random perturbations in the scatterer location the mean travel time perturbation vanishes (expression (51)), but according to equation (52) the variance of the travel time is nonzero and depends linearly on time. This contrasts the case of a perturbation in the source position where the mean travel time perturbation also vanishes and where according to expression (57) the variance is nonzero and independent of time. In general, it may not be obvious how a medium is perturbed. As shown above, the three different perturbation leave a different imprint on the mean and the variance of the travel time perturbation. Since these quantities can be estimated for several independent windows of the coda waves using the time-shifted correlation coefficient, it is possible to discriminate between these different perturbations using the recorded coda waves.

REFERENCES

K. Aki. Theory of earthquake prediction with special reference to monitoring of the quality factor of lithosphere by the coda method. *Earthquake Res. Bull.*, 3:219–230, 1985.

K. Aki and L.B. Chouet. Origin of coda waves: source, attenuation, and scattering effects. *J. Geophys. Res.*, 80:3322–3342, 1975.

L. Astiz and P.M. Shearer. Earthquake locations in the inner Continental Borderland, offshore southern California. *Bull. Seism. Soc. Am.*, 90:425–449, 2000.

O.M. Bucci and G Franceschetti. On the degrees of freedom of scattered fields. *IEEE Trans. on Antennas and Propagation*, 37:918–926, 1989.

M.L. Cowan, I.P. Jones, J.H. Page, and D.A. Weitz. Diffusing acoustic wave spectroscopy. *Phys. Rev. E*, 65:066605–1/11, 2002.

M.L. Cowan, J.H. Page, and D.A. Weitz. Velocity fluctuations in fluidized suspensions probed by ultrasonic correlation spectroscopy. *Phys. Rev. Lett.*, 85:453–456, 2000.

H. Douma and R. Snieder. Correcting for bias due to noise in coda wave interferometry. *Submitted to Geophys. J. Int.*, 2005.

A. Grêt, R. Snieder, R.C. Aster, and P.R. Kyle. Monitoring rapid temporal changes in a volcano with coda wave interferometry. *Geophys. Res. Lett., in press*, 2005.

A. Grêt, R. Snieder, and J. Scales. Time-lapse monitoring of rock properties with coda wave interferometry. *Submitted to J. Geophys. Res.*, 2005.

R. Grêt, A.and Snieder and U. Ozbay. Monitoring stress change in an undergraound mining environment with coda wave interferometry. *Submitted to the J. of Mining Applications*, 2004.

M. Heckmeier and G. Maret. Dark speckle imaging of colloidal suspensions in multiple light scattering media. *Progr. Colloid. Polym. Sci.*, 104:12–16, 1997.

A. Jin and K. Aki. Temporal changes in the coda Q before the Tangshan earthquake of 1976 and the Haicheng earthquake of 1975. *J. Geophys. Res.*, 91:665–673, 1986.

A. Lagendijk and B.A. van Tiggelen. Resonant multiple scattering of light. *Phys. Rep.*, 270:143–215, 1996.

H.J. Landau. Necessary density conditions for sampling and interpolation of certain entire functions. *Acta Mathematica*, 117:37–52, 1967.

W. Lauterborn, T. Kurz, and M. Wiesenfeldt. *Coherent Optics, Fundamentals and Applications.* Springer-Verlag, Berlin, 1995.

S. Matsumoto, K. Obra, K. Yoshimoto, T. Saito, A. Ito, and A. Hasegawa. Temporal changes in P-wave scatterer distribution associated with the M6.1 earthquake near Iwate volcano, northeastern Japan. *Geophys. J. Int.*, 145:48–58, 2001.

C. Pacheco and R. Snieder. Localizing time-lapse changes with multiply scattered waves. *Submitted to J. Acoust. Soc. Am.*, 2005.

C. Pacheco and R. Snieder. Localizing time-lapse changes with single scattered waves. *Submitted to Geophys. J. Int.*, 2005.

J.H. Page, M.L. Cowan, and D.A. Weitz. Diffusing acoustic wave spectroscopy of fluidized suspensions. *Physica B*, 279:130–133, 2000.

G. Pavlis. Appraising relative eartquake location errors. *Bull. Seism. Soc. Am.*, 82:836–859, 1992.

G. Poupinet, W.L. Ellsworth, and J. Fréchet. Monitoring velocity variations in the crust using earthquake doublets: an application to the Calaveras Fault, California. *J. Geophys. Res.*, 89:5719–5731, 1984.

A. Ratdomopurbo and G. Poupinet. Monitoring a temporal change of seismic velocity in a volcano: Application to the 1992 eruption of Mt. Merapi (Indonesia). *Geophys. Res. Lett.*, 22:775–778, 1995.

P.M. Roberts, W. Scott Phillips, and M.C. Fehler. Development of the active doublet method for measuring small velocity and attenuation changes in solids. *J. Acoust. Soc. Am.*, 91:3291–3302, 1992.

P.M. Shearer. Improving local earthquake locations using the L_1-norm and waveform cross-correlation: Application to the Whittier Narrows California aftershock sequence. *J. Geophys. Res.*, 102:8269–8283, 1997.

M. Snieder and M. Vrijlandt. Constraining relative source locations with coda wave interferometry: Theory and application to earthquake doublets in the Hayward Fault, California. *J. Geophys. Res., in press*, 2005.

R. Snieder. Imaging and averaging in complex media. In J.P. Fouque, editor, *Diffuse waves in complex media*, pages 405–454. Kluwer, Dordrecht, 1999.

R. Snieder. Coda wave interferometry and the equilibration of energy in elastic media. *Phys. Rev. E*, 66:046615–1,8, 2002.

R. Snieder. Extracting the Green's function from the correlation of coda waves: A derivation based on stationary phase. *Phys. Rev. E*, 69:046610, 2004.

R. Snieder, A. Grêt, H. Douma, and J. Scales. Coda wave interferometry for estimating nonlinear behavior in seismic velocity. *Science*, 295:2253–2255, 2002.

R. Snieder and J.A. Scales. Time reversed imaging as a diagnostic of wave and particle chaos. *Phys. Rev. E*, 58:5668–5675, 1998.

M.C.W. van Rossum and Th.M. Nieuwenhuizen. Multiple scattering of classical waves: microscopy, mesoscopy and diffusion. *Rev. Mod. Phys.*, 71:313–371, 1999.

B.A. van Tiggelen. Localization of waves. In J.P. Fouque, editor, *Diffuse waves in complex media*, pages 1–60. Kluwer, Dordrecht, 1999.

F. Waldhauser and W.L. Ellsworth. Fault structure and mechanics of the Hayward Fault, California, from double-difference earthquake locations. *J. Geophys. Res.*, 107:10.1029/2000JB000084, 2002.

D.A. Weitz and D.J. Pine. Diffusing wave spectroscopy. In W. Brown, editor, *Dynamic light scattering, The method and some applications*, pages 652–720. Clarendon Press, Oxford, 1993.

CWP-496P

Correcting for bias due to noise in coda wave interferometry

Huub Douma and Roel Snieder
Center for Wave Phenomena, Colorado School of Mines, Golden, CO 80401-1887, USA

ABSTRACT
Coda wave interferometry (CWI) utilizes multiply scattered waves to diagnose small changes in a medium by using the scattering medium as an interferometer. Since the medium is usually stationary over the duration of a seismic experiment, different (non-overlapping) time windows in the coda allow for independent estimates of the medium perturbation. If the seismograms are contaminated with noise, only those time windows can be used for which the amplitude of the coda is above the ambient noise level. This limits the usable number of independent time windows. Here, we show how bias due to noise in CWI can be accounted for, by deriving a correction factor for the cross-correlation coefficient. This correction factor allows more time windows further into the decaying coda to be used, and hence allows for a reduction of the error bars on the medium perturbation estimates. We demonstrate the validity of this correction factor by using data from a numerical experiment and field measurements. These experiments involve the displacement of point scatterers and a change in the source location, respectively. The application of our correction factor is not limited to CWI, but can be used to correct for bias induced by noise in any application that uses cross-correlation between different signals that are contaminated with noise.

Key words: Scattering, seismic coda, monitoring, noise, earthquake location

Introduction

Multiply scattered wavefields have been experimentally shown to be remarkably stable with respect to perturbations of the boundary conditions of experiments with multiply scattered waves (Derode *et al.*, 1995; Derode *et al.*, 1999). Due to this stability, the information carried by multiply scattered waves has been successfully used in an industrial context [e.g. Fink (1997)]. Coda wave interferometry (Snieder *et al.*, 2002; Snieder, 2002; Grêt *et al.*, 2004b; Grêt *et al.*, 2004c; Snieder, 2004a) uses multiply scattered waves to detect small changes by using the scattering medium as an interferometer. Since multiply scattered waves dominate the final portions of a seismogram, they are usually referred to as coda waves just as, in musical notation, the coda denotes the closing part of a musical piece. Hence the name *coda wave interferometry* (CWI). Since CWI uses multiply scattered waves, it is inherently more sensitive to changes in the medium than are techniques based on single scattering, as multiply scattered waves sense changes in the medium multiple times.

In parallel, but independently, diffusing acoustic wave spectroscopy (DAWS) (Page *et al.*, 2000; Cowan *et al.*, 2002) was developed as the classical equivalent of diffusing wave spectroscopy (DWS) (Maret & Wolf, 1987; Pine *et al.*, 1988; Yodh *et al.*, 1990; Weitz & Pine, 1993). In DWS light is used to study different aspects of strongly scattering media, whereas in DAWS classical waves are used to probe such media. DWS has been used in many applications such as, e.g., determining the aging of foams, particle sizing, and determining the motion of particles in fluidized suspensions on ångström length scales (Weitz & Pine, 1993). So far, DAWS has mainly been used to determine the relative mean square displacement of fluidized suspensions of particles (Page *et al.*, 1999; Cowan *et al.*, 2000; Page *et al.*, 2000; Cowan *et al.*, 2002). CWI has been succesfully used to measure the nonlinear dependence of seismic velocity in rocks on temperature (Snieder *et al.*, 2002), to monitor volcanos (Grêt *et al.*, 2004a), and to estimate source displacement (Snieder & Vrijlandt, 2004). The ability to use CWI to determine the relative mean square displacement of point scatterers from noise-free waveforms was established using a numerical experiment by (Snieder *et al.*, 2002). Both CWI and DAWS use the amplitude information as well as the phase information of the multiply scattered wavefields, and are both based on a path summation approach to model the multiply scattered wavefields. Hence, both methods are in principle the same, but have been used for different applications.

CWI is based on a measure of cross-correlation between multiply scattered wavefields recorded before and after a medium has changed. The cross-correlation coefficients calculated for different (non-overlapping) time windows provide independent estimates of the medium perturbations. These independent estimates in turn allow for the calculation of error estimates of the perturbation; the larger the number of independent (unbiased) measurements, the smaller the error estimates.

When the coda is contaminated with noise, the number of independent time windows that can be used is limited to traveltimes where the ambient noise level is small compared to the amplitudes of the multiply scattered waves. To be able to use as many independent time windows as possible, and hence reduce the error bars on the inferred perturbation, it is important to correct the cross-correlation function for the bias caused by noise. In this paper, we show how this bias in CWI can be corrected for, by deriving a correction factor for the cross-correlation coefficient. We demonstrate its validity by using data from a numerical experiment involving the displacement of point scatterers, and field data involving the displacement of the source location.

The organization of this paper is as follows. We first review the principles of CWI and then derive the noise correction factor. Subsequently we show the validity of the correction factor using the numerical and field experiments mentioned above. We conclude with a short discussion of the results. In appendix A we derive a condition for the reliability of the correction factor. This condition can be used to determine the time windows in the coda where the correction factor is reliable.

Coda wave interferometry

Coda wave interferometry is based on a path summation approach, which is a generalization of the Neumann series solution of the Lippmann-Schwinger equation for scattering of classical waves [e.g. Snieder (1999)]. This path summation can be represented as

$$u_u(t) = \sum_T A_T(t) \,, \tag{1}$$

where T denotes the different trajectories the waves have traveled, and the function $A_T(t)$ denotes the contribution of trajectory T to the multiply scattered wavefield. The subscript in $u_u(t)$ denotes that the wavefield is recorded from the unperturbed medium. Here, for simplicity, we treat acoustic waves, but the theory has been generalized to elastic waves (Snieder, 2002).

Now suppose the medium has changed, and that the main contribution of the change to the wavefields is a perturbation of the traveltime of each trajectory T. [This is obviously not universally true for any type of perturbation of the medium, and limits the applicability of our subsequent results to certain types of perturbations. For the perturbations studied in this paper however, i.e., small displacement of the scatterers and change in the source location, this turns out to be an acceptable assumption.] Using this, we can write the multiply scattered wavefield in the perturbed medium, denoted by $u_p(t)$, as

$$u_p(t) = \sum_T A_T(t - \tau_T) \,, \tag{2}$$

with τ_T the change in the traveltime for trajectory T due to the perturbation in the medium.

To measure the change in waveform due to the medium perturbation, we define the correlation coefficient $r(t, t_s, t_w)$ as

$$r(t, t_s, t_w) \equiv \frac{(u_u, u_p)_{(t,t_s,t_w)}}{\sqrt{(u_u, u_u)_{(t,0,t_w)}\,(u_p, u_p)_{(t,0,t_w)}}} \,, \tag{3}$$

with

$$(u_u, u_p)_{(t,t_s,t_w)} \equiv \int_{t-t_w}^{t+t_w} u_u(t')u_p(t' + t_s)dt' \,, \tag{4}$$

where t_s is the time-shift in the cross-correlation, and $2t_w$ is the length of the time window. The maximum of this correlation coefficient occurs at time-shift $t_s = \langle\tau\rangle$, where $\langle\tau\rangle$ is the mean traveltime change given by (Snieder, 2002)

$$\langle\tau\rangle \equiv \frac{\sum_T A_T^2 \tau_T}{\sum_T A_T^2} \,. \tag{5}$$

Using equations (1) and (2) in equation (3), Snieder *et al.* (2002) and Snieder (2002) show that the maximum value of this cross-correlation function, $r_{\max}^{(t,t_w)}$, is given by

$$r_{\max}^{(t,t_w)} = 1 - \frac{1}{2}\overline{\omega^2}\sigma_\tau^2 \,, \tag{6}$$

where the frequency $\overline{\omega^2}$ is given by

$$\overline{\omega^2} \equiv \frac{\int_{t-t_w}^{t+t_w} \dot{u}_u^2(t')dt'}{\int_{t-t_w}^{t+t_w} u_u^2(t')dt'} \,. \tag{7}$$

Here, $\dot{u}$ denotes the time derivative of $u(t)$. The variance of the traveltime perturbation, σ_τ^2, is given by

$$\sigma_\tau^2 \equiv \frac{\sum_T A_T^2 (\tau_T - \langle\tau\rangle)^2}{\sum_T A_T^2} \,. \tag{8}$$

In expression (8) and equation (5), the summations concern only trajectories with arrival times in the window with central window time t and window duration $2t_w$. In deriving equation (6), it is assumed that the double sums over trajectories T and T' with $T \neq T'$ are on average incoherent, and used a second-order Taylor expansion of the cross-correlation function in the quantity $\tau_T - \langle \tau \rangle$ (Snieder, 2002). The latter approximation is valid when the traveltime perturbation due to the medium perturbation is smaller than the dominant period of the multiply scattered wavefields. Snieder (2004b) showed that the double sums over trajectories T and T' with $T \neq T'$, are proportional to $1/\sqrt{t_w \Delta f}$, with Δf the bandwidth of the signal, so that their importance thus reduces for larger time windows and larger bandwidth data.

Correcting for the bias due to noise

So far, we assumed the waveforms $u_u(t)$ and $u_p(t)$ to be free of noise. To study the influence of noise on CWI, we derive a correction factor for the correlation coefficient when the waveforms $u_u(t)$ and $u_p(t)$ are contaminated with noise. We define

$$u'_u(t) = u_u(t) + n_u(t)\,, \quad u'_p(t) = u_p(t) + n_p(t)\,, \tag{9}$$

where $u'_u(t)$ and $u'_p(t)$ are the noise-contaminated signals, $u_u(t)$ and $u_p(t)$ the noise-free waveforms, and $n_u(t)$ and $n_p(t)$ the noise signals for the unperturbed and perturbed wavefields, respectively. Using the noise-contaminated signals, we define the noise-contaminated cross-correlation coefficient as

$$r'(t, t_s, t_w) = \frac{\left(u'_u, u'_p\right)_{(t,t_s,t_w)}}{\sqrt{\left(u'_u, u'_u\right)_{(t,0,t_w)} \left(u'_p, u'_p\right)_{(t,0,t_w)}}}\,. \tag{10}$$

Our aim is to derive a correction factor $c(t, t_s, t_w)$ such that

$$r(t, t_s, t_w) \approx c(t, t_s, t_w) r'(t, t_s, t_w)\,. \tag{11}$$

Throughout the remaining derivation, we assume that these noise signals are identically and independently distributed (i.i.d.), and wide-sense stationary with zero mean [i.e., the mean is zero for all times, and the autocorrelation depends only on the time shift t_s (Papoulis, 1991, p. 298)].

Using equation (9), we find

$$\begin{aligned}
\left(u'_u, u'_p\right)_{(t,t_s,t_w)} &= \left(u_u, u_p\right)_{(t,t_s,t_w)} + \left(u_u, n_p\right)_{(t,t_s,t_w)} \\
&\quad + \left(u_p, n_u\right)_{(t,t_s,t_w)} \\
&\quad + \left(n_u, n_p\right)_{(t,t_s,t_w)}\,, \qquad (12) \\
\left(u'_u, u'_u\right)_{(t,0,t_w)} &= \left(u_u, u_u\right)_{(t,0,t_w)} + 2\left(u_u, n_u\right)_{(t,0,t_w)} \\
&\quad + \left(n_u, n_u\right)_{(t,0,t_w)}\,, \qquad (13) \\
\left(u'_p, u'_p\right)_{(t,0,t_w)} &= \left(u_p, u_p\right)_{(t,0,t_w)} + 2\left(u_p, n_p\right)_{(t,0,t_w)} \\
&\quad + \left(n_p, n_p\right)_{(t,0,t_w)}\,. \qquad (14)
\end{aligned}$$

In equations (12)-(14), terms of the form $(u, n)_{(t,t_s,t_w)}$ appear, where $u = u(t)$ is a deterministic signal and $n = n(t)$ a realization of a stochastic process. Using that the noise signals have zero mean, we then find that

$$(u, n)_{(t,t_s,t_w)} \approx 0\,, \tag{15}$$

provided the window length t_w is at least several dominant periods of the noise-contaminated signal. For the terms $(n_u, n_p)_{(t,t_s,t_w)}$ and $(n_p, n_u)_{(t,t_s,t_w)}$ in equations (12)-(14), we use the independence of the noise realizations to find

$$(n_u, n_p)_{(t,t_s,t_w)} \approx 0\,, \tag{16}$$

with the same assumption for the window length t_w as used in equation (15). Approximations (15) and (16) become more accurate with increasing window lengths.

Using equations (15) and (16) in equations (12)-(14), it follows that

$$\begin{aligned}
\left(u'_u, u'_p\right)_{(t,t_s,t_w)} &\approx \left(u_u, u_p\right)_{(t,t_s,t_w)}\,, \qquad (17) \\
\left(u'_u, u'_u\right)_{(t,0,t_w)} &\approx \left(u_u, u_u\right)_{(t,0,t_w)} \\
&\quad + \left(n_u, n_u\right)_{(t,0,t_w)}\,, \qquad (18) \\
\left(u'_p, u'_p\right)_{(t,0,t_w)} &\approx \left(u_p, u_p\right)_{(t,0,t_w)} \\
&\quad + \left(n_p, n_p\right)_{(t,0,t_w)}\,. \qquad (19)
\end{aligned}$$

Using these approximations in equation (10), and substituting the resulting expression in equation (11), it follows that the correction factor $c(t, t_s, t_w)$ is approximately given by

$$c(t, t_s, t_w) \approx \left(1 - \frac{(n_u, n_u)_{(t,0,t_w)}}{(u'_u, u'_u)_{(t,0,t_w)}}\right)^{-\frac{1}{2}} \left(1 - \frac{(n_p, n_p)_{(t,0,t_w)}}{(u'_p, u'_p)_{(t,0,t_w)}}\right)^{-\frac{1}{2}} \tag{20}$$

This correction factor $c(t, t_s, t_w)$ depends on the unknown noise signals $n_u(t)$ and $n_p(t)$. In practice, assuming the noise is stationary, we can estimate these noise signals using the recorded wavefields $u_u(t)$ and $u_p(t)$ before $t = 0$ of the experiment. This gives us estimated noise signals $\tilde{n}_u(t)$ and $\tilde{n}_p(t)$. Replacing $n_u(t)$ and $n_p(t)$ in equation (20) with their estimated counterparts, is a good approximation only if the terms of the form $(u, n)_{(t,t_s,t_w)}$ and $(n_u, n_p)_{(t,t_s,t_w)}$ in equations (12)-(14) are small compared to the remaining terms. Hence, for this replacement to be valid, we want the following inequalities to hold:

$$\begin{aligned}
&|(u_u, n_p)_{(t,t_s,t_w)} + (u_p, n_u)_{(t,t_s,t_w)} + (n_u, n_p)_{(t,t_s,t_w)}| \\
&\qquad \ll |(u_u, u_p)_{(t,t_s,t_w)}|\,, \qquad (21) \\
&\qquad 2|(u_u, n_u)_{(t,0,t_w)}| \\
&\qquad \ll |(u_u, u_u)_{(t,0,t_w)} + (n_u, n_u)_{(t,0,t_w)}|\,, \qquad (22) \\
&\qquad 2|(u_p, n_p)_{(t,0,t_w)}| \\
&\qquad \ll |(u_p, u_p)_{(t,0,t_w)} + (n_p, n_p)_{(t,0,t_w)}|\,. \qquad (23)
\end{aligned}$$

In appendix A we rewrite these three inequalities into one inequality that can be evaluated using only the noise

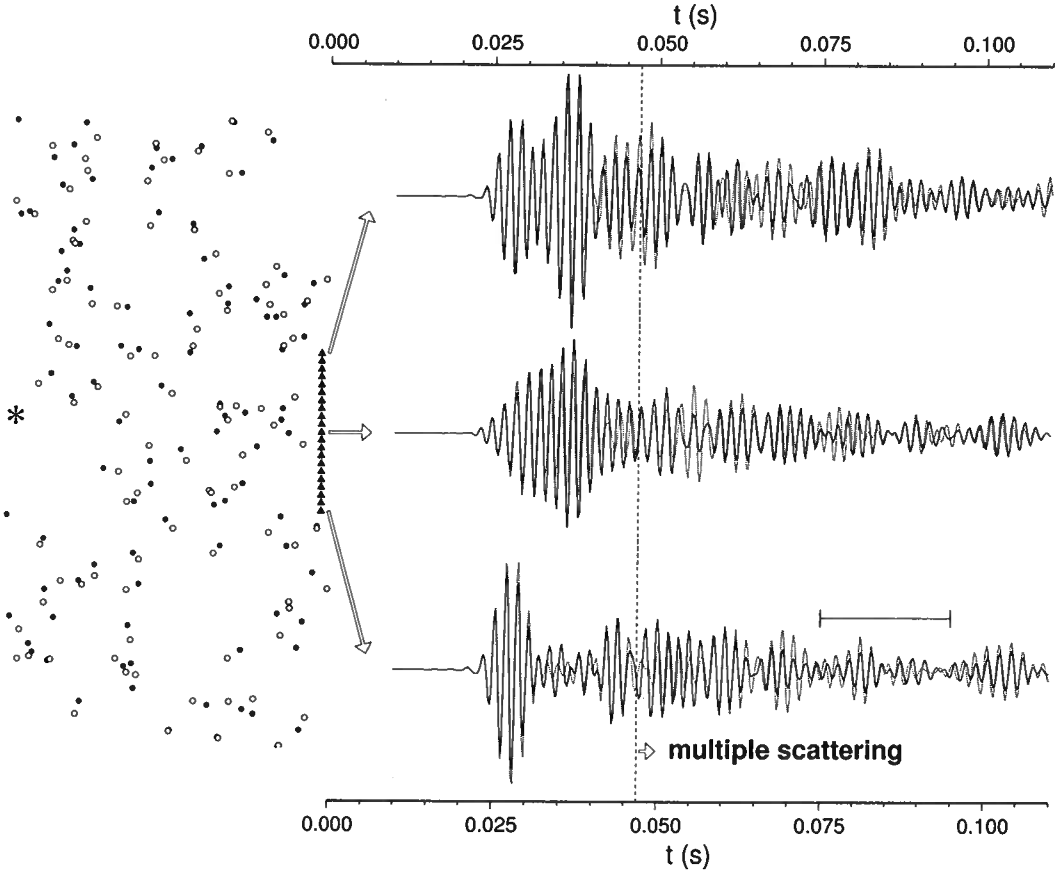

Figure 1. Unperturbed (filled circles) and perturbed (open circles) locations of the point scatterers in the medium. For display purposes the differences between the unperturbed and perturbed locations are magnified by a factor 10. The star denotes the source and the triangles the receivers. The modeled seismograms are shown for three receivers. The drawn seismograms are related to the unperturbed scatterer locations, and the dotted seismograms to the perturbedlocations. For times later than $t = 4.7 \times 10^{-2}$s (marked by the dotted line), the waves have scattered more than four times. The horizontal bar indicates the window length for the time-windowed cross-correlations used to calculate the RMS displacement δ shown in figure 2.

contaminated signals $u'_u(t)$ and $u'_p(t)$, and an estimated noise signal $n_O(t)$. The resulting inequality [equation (A5)] then determines if a certain time window has a reliable correction factor associated with it, when the unknown noise signals $n_u(t)$ and $n_p(t)$ in equation (20) are replaced with $n_O(t)$. Replacing $n_u(t)$ and $n_p(t)$ with $n_O(t)$ in equation (20), the correction factor is given by

$$c(t, t_s, t_w) \approx \left(1 - \frac{(n_O, n_O)_{(t,0,t_w)}}{(u'_u, u'_u)_{(t,0,t_w)}}\right)^{-\frac{1}{2}} \left(1 - \frac{(n_O, n_O)_{(t,0,t_w)}}{(u'_p, u'_p)_{(t,0,t_w)}}\right)^{-\frac{1}{2}} \quad (24)$$

and is considered reliable if inequality (A5) is satisfied with an appropriate value of γ [$O(10^{-1})$].

To derive condition (A5), we assume that the noise is stationary and that $n_u(t)$ and $n_p(t)$ have about the same noise levels, (i.e., the same variance). If the noise levels of $n_u(t)$ and $n_p(t)$ are substantially different, separate noise estimates of $n_u(t)$ and $n_p(t)$ can be used in equation (20) to calculate the correction factor. In this case condition (A5) does not apply, and a new condition could be derived. To avoid belaboring the point, we refrain from such a treatment.

Displacement of the scatterers

The problem of inferring the average displacement of scatterers in a strongly scattering medium from the multiply scattered wavefields, has been used to study fluidized particle suspensions (Weitz & Pine, 1993; Heckmeier & Maret, 1997; Page *et al.*, 1999; Cowan *et al.*, 2000; Page *et al.*, 2000; Cowan *et al.*, 2002). In geophysics, this problem may be relevant when a strongly scattering region in the earth is strained, causing the scattering heterogeneities to move. In such a situation the displacement of the scatterers is not expected to be random, but will be correlated among scatterers.

Here, we present a numerical experiment with point scatterers in a homogeneous background model, where we randomly perturb the scatterer locations and use CWI to infer their root-mean-square (RMS) displacement. Although this experiment is not directly related to a changing strain in the earth, it serves the purpose of testing the workings of our correction factor.

Snieder & Scales (1998) showed that for independent perturbations of the scatterer positions and isotropic scattering, the variance of the path length L is given by

$$\sigma_L^2 = 2n\delta^2 \,, \tag{25}$$

where n is the number of scatterers in the path, and δ is the RMS displacement of the scatterers in the direction of either coordinate axis (horizontal and vertical for two dimensions). Note that Snieder and Scales assume all directions of random displacement to be equally likely. As a result, the RMS displacement is the same in each direction (horizontal and vertical for 2D), i.e., for 2D the true RMS displacement would be $\sqrt{2}\delta$. Using that the number of scatterers is on average given by $n = vt/l^*$, with l^* the transport mean free path (Lagendijk & van Tiggelen, 1996) and v the velocity, and using $L = vt$, it follows that the variance of the traveltime perturbations is given by

$$\sigma_\tau^2 = \frac{2\delta^2 t}{vl^*} \,. \tag{26}$$

Inserting this in equation (6), it follows that the RMS displacment δ can be found from

$$\delta = \sqrt{\left(1 - r_{\max}^{(t,t_w)}\right) \frac{vl^*}{\overline{\omega^2} t}} \,. \tag{27}$$

Since the perturbations of the scatterer locations are assumed to be independent, and since the scattering is assumed to be isotropic, the mean traveltime perturbation $\langle\tau\rangle = 0$. This means that the maximum of the cross-correlation function $r_{\max}^{(t,t_w)}$ occurs at zero lag, i.e., $t_s = 0$.

Figure 1 shows the setup of our numerical experiment to test the inference of the scatterer displacements from the seismic coda using equation (27). This experiment was also outlined by Snieder *et al.* (2002). One hundred point scatterers (solid dots) are contained in an area of 40×80 m^2, and the waveforms are calculated using a numerical implementation (Groenenboom & Snieder, 1995) of Foldy's method (Foldy, 1945). The resulting seismograms are shown by the solid lines for three locations on the edge of the area, and the source location is indicated by the asterisk. In these calculations the scattering amplitude was set to $-4i$, in order to get the maximum possible scattering strength as constrained by the optical theorem [(Groenenboom & Snieder, 1995); in their notation we used $\gamma = 4$]. The background velocity equalled 1500 m/s and the source spectrum $S(\omega) = e^{-\omega^2/\omega_0^2}$, with ω the angular frequency, $\omega_0 = 2\pi f_0$, and $f_0 = 600$ Hz. The frequency band used was 400 – 800 Hz, with a resulting dominant frequency of about 500 Hz due to tapering on either side of the spectrum. Since in our experiment we have isotropic scattering, the transport mean free path equals the mean free path, i.e., $l^* = l$. The mean free path in our experiment was measured to be $l = 17.6$ m, which, using $n = vt/l$, can be used to infer that after $t = 4.7 \times 10^{-2}$ s the waves are on average scattered more than four times. This time is indicated in Figure 1 by the dotted vertical line. The perturbed scatterer locations are indicated by the open circles in Figure 1. For display purposes the displacements are magnified by a factor 10. The actual RMS displacement $\delta_{\text{true}} = 8 \times 10^{-2}$ m in both the horizontal and vertical direction. *This displacement equals just* 1/38 *of the dominant wavelength* (the dominant wavelength $\lambda = 3$ m). The resulting waveforms calculated using the displaced scatterers are shown for three receivers by the dotted lines.

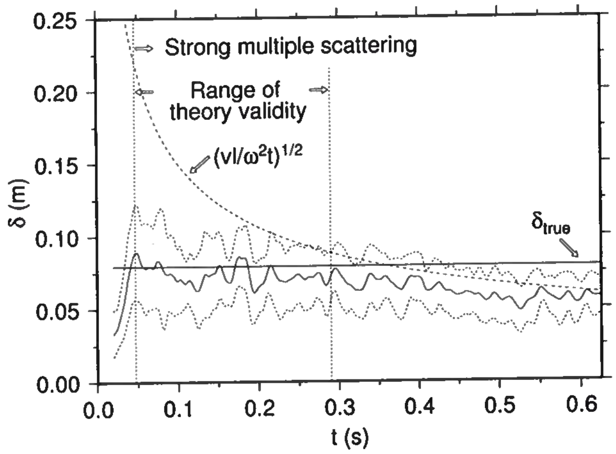

Figure 2. Inferred RMS displacement δ as a function of the center window time t (solid line) plus or minus one standard deviation (dotted lines). The true value of δ is indicated by the horizontal solid line. The range of validity of CWI is indicated by the vertical lines. The half-window time t_w used in calculating the time windowed correlation coefficient equals 0.01s.

Figure 2 shows the inferred value of δ [using equation (27)] as a function of the central window time t, where the estimated values for δ from all 21 receivers were averaged. [The receiver spacing was chosen such that the calculated multiply scattered waveforms were uncorrelated, meaning they can be treated as independent.] The dotted lines show the average inferred value of δ as a function of time plus or minus one standard deviation. The half-window duration t_w was 10^{-2} s, resulting in a window length of 10 dominant periods, and $\sqrt{\overline{\omega^2}} = 3.66 \times 10^3$ rad/s. The vertical dotted lines indicated the range of validity of equation (27). For early times (i.e., $t < 4.7 \times 10^{-2}$ s) the relation $n = vt/l$ for the number of scatterings used in the derivation

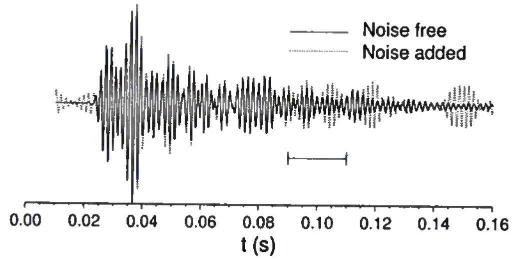

Figure 3. An example signal without noise (drawn) and with noise (dotted). The horizontal bar indicates the window length for the time-windowed cross-correlations used to calculate the RMS displacement δ shown in figure 4.

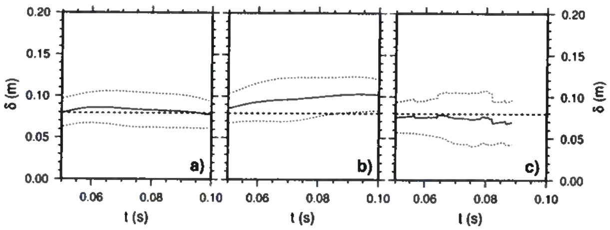

Figure 4. Inferred value of δ as a function of the central window time t, obtained using equation (27) with the noise-free signals (a), with the noise-contaminated signals and no application of the correction factor (b), and with the noise-contaminated signals and application of the correction factor using equation (24) (c).

of equation (27) is not valid, and for late times (i.e., $t > 2.9\times10^{-1}$ s), the second-order Taylor approximation of the auto-correlation of the source signal is inaccurate by more than 15%. This latter time is indicated by the rightmost dotted vertical line in Figure 2. Within the range of validity of equation (27), the true displacement is recovered within the range given by the average RMS displacement plus or minus one standard deviation. For late times, the correlation coefficient is close to zero and, according to equation (27), the inferred value of δ is then given by $\sqrt{vl/\left(\overline{\omega^2}t\right)}$. This function is indicated by the dashed line in Figure 2 and indeed agrees well with the inferred value of δ for late times. For these times the inferred value of δ is of course no longer a good estimate of the true RMS displacement.

As mentioned in the introduction, when the wavefields are contaminated with noise, the number of independent time windows that can be used is limited to traveltimes where the ambient noise level is small compared to the amplitudes of the multiply scattered waves. In order to be able to use as many independent time windows as possible, and hence reduce the error bars on the inferred perturbation, it is important to correct the cross-correlation function for the bias due to the noise. To test the correction factor in equation (24), we added band-limited noise to the waveforms for all 21 receivers from our numerical experiment. The bandwidth of the noise was the same as that of the noise-free signals (i.e., 400 – 800 Hz). Figure 3 shows a waveform with and without the added noise. Using the noise-contaminated waveforms, we again calculated the inferred values of δ both with and without the correction factor; see Figure 4c and 4b respectively. For reference, Figure 4a shows the inferred value of δ when the noise-free signals were used. Figure 4b shows that the noise induces a bias in the estimated value of δ; the presence of noise reduces the correlation between the unperturbed and perturbed waveforms, and causes the inferred values of δ, calculated using equation (27), to be larger. For early times, the true value of δ is embedded within the average value of δ plus or minus one standard deviation, but the estimated average value of δ is too high, especially for later times, where the lower amplitude values of the coda result in lower signal-to-noise ratios. Figure 4c shows that the correction factor from equation (24) accurately accounts for the bias due to the noise. The noise estimates were obtained using the signal before the main first arrival in the seismograms. In the calculation of the results shown in Figure 4c, we used condition (A5) for each receiver, with $\gamma = 0.125$ to select the time windows used for the inversion of δ [note that this is a different γ than that used by Groenenboom & Snieder (1995)]. As a result, the number of receivers that had usable time windows for a given central window time t, varies for different t. This causes the jagged appearance of the average inferred value of δ (and the standard deviation). We used a time window only when at least seven receivers (i.e., 30% of the receivers) satisfied condition (A5) at the central window time t. After $t \approx 9 \times 10^{-2}$ s fewer than seven time windows satisfied condition (A5) with $\gamma = 0.125$, and hence the correction factor was judged unreliable. As a result, the noise-corrected estimates of the RMS displacement are not shown for times larger than $t \approx 9 \times 10^{-2}$ s.

Source separation

Snieder & Vrijlandt (2004) used CWI to estimate the distance between seismic events having the same source mechanism, that are recorded at a single station. They derive the imprint of a change in source location on the variance of the traveltime differences, and then use equation (6) to infer this change from the maximum of the cross-correlation function, i.e., $r_{\max}^{t,t_w}$. For two double-couple sources with a source separation in the fault plane, they show that the relation between the source displacement Δs and the variance of the traveltimes σ_τ^2 is given by

$$\sigma_\tau^2 = \frac{\left(\frac{6}{\alpha^8} + \frac{7}{\beta^8}\right)}{7\left(\frac{2}{\alpha^6} + \frac{3}{\beta^6}\right)} (\Delta s)^2 , \tag{28}$$

where α and β are the P and S wave velocities, respectively. Different non-overlapping time-windows provide independent estimates of the source separation. These independent estimates in turn allow for the calculation of error estimates of the source separation.

Figure 5a shows two seismograms (events 242003 and 242020) from earthquakes on the Hayward fault, California (Waldhauser & Ellsworth, 2000), recorded at station CSP of the Northern California Seismic Network. The recorded signal before the arrival of the P wave shows that the noise level is considerable. Figure 5b shows the maximum of the time-windowed cross-correlation function without the correction factor (thin line) and with the correction factor (thick line) applied, and Figure 5c shows the inferred values of the source separation using equation (28). Here the estimate of the noise, i.e., $n_0(t)$, was obtained from the waveforms before the first arrivals. The half-window duration t_w used is 5 s (the full window length is indicated by the horizontal bar in Figure 5a), and the P and S wave velocities used to calculate the source displacement are α = 5750 m/s and β = 3320 m/s, respectively. Note that we used overlapping time windows, since we plot $r_{\max}^{(t,t_w)}$ simply as a continuous function of the central window time t. Of course, non-overlapping windows could be used to ensure independent estimates of the source separation.

Figure 5b shows that the corrected values of $r_{\max}^{(t,t_w)}$ maintain a fairly constant level for times t late in the coda, whereas the uncorrected values decrease earlier in the coda because the noise decreases the similarity between both waveforms. As a result, the inferred values of the source separation using equation (28) are more or less constant for larger traveltimes when the corrected values of $r_{\max}^{(t,t_w)}$ are used (Figure 5c). This indicates that the correction factor $c(t, t_s, t_w)$ given by equation (24), accurately corrects for the influence of the noise on the cross-correlation function. For very large times (say $t > 40$ s) the corrected values are more variable because the correction factor becomes unreliable. We purposely showed the times where the corrected values become variable, to indicate the level of variation caused by an unreliable correction factor. Of course, the time where the correction factor becomes unreliable could have been estimated using condition (A5) with an appropriate value of γ [$O(10^{-1})$].

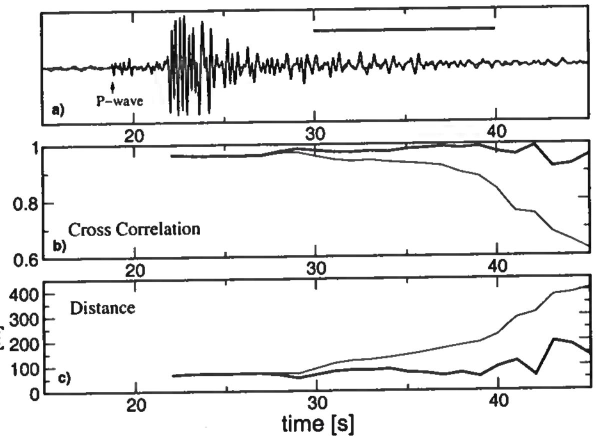

Figure 5. Two seismograms from two earthquakes on the Hayward fault, California, recorded at station CSP of the Northern California Seismic Network (a), their cross-correlation maximum $r_{max}^{(t,t_w)}$ (b), uncorrected (thin line) and corrected (thick line), and the inferred source displacement (c) using both the uncorrected (thin line) and corrected (thick line) values of $r_{max}^{(t,t_w)}$ shown in (b). The horizontal line in (a) indicates the window length used in the cross-correlation.

Conclusion

We have derived a factor that corrects for the influence of noise on the cross-correlation function, and have shown its accuracy using both numerical and field data. The application of this correction factor is shown in the context of CWI, for the inference of the RMS displacement of scatterers and a displacement of the source, from multiply scattered wavefields. For the displacement of the scatterers, we showed that in the presence of noise, a displacement of *only* 1/38 *from the dominant wavelength* can be succesfully retrieved from the cross-correlation between the unperturbed and perturbed signals. This shows the power of CWI when compared to methods that use singly-scattered waves only.

Since for both the scatterer displacement and source separation cases, the perturbation is independent of the traveltimes of the multiply scattered waves, using non-overlapping time windows to estimate the perturbations provides a consistency check of the method, and allows the calculation of error estimates. In this context, our correction factor is relevant, as it increases the number of usable time windows and hence allows for a reduction of the error estimates. In addition the correction factor adjusts for bias in the cross-correlation induced by the noise. Since our factor depends on an estimate of the noise level in the data, we present a condition that allows determination of the reliability of the correction. This condition can be verified using only noise contaminated signals and an estimate of the noise level in the data. Using this condition, the time windows used in the windowed cross-correlation can be judged to be reliable or not.

The use of the proposed correction factor is of course not limited to CWI. Any application that uses cross-correlations between different and noisy signals, and needs to correct for bias induced by noise, can benefit from the correction factor presented here.

ACKNOWLEDGMENTS

We thank Mark Vrijlandt for making Figure 5, and Ken Larner for his critical review. In addition, we thank Western Geophysical (now WesternGeco), in particular Peter Nuttal, for funding a three-month visit of H.D. to the Center for Wave Phenomena at the Colorado School of Mines in the summer of 2000, that formed the basis for this work. This work was supported by the NSF (grant EAR-0106668) and by the sponsors of the Consortium Project on Seismic Inverse Methods for Complex Structures at the Center for Wave Phenomena.

REFERENCES

Cowan, M.L., Page, J.H., & Weitz, D.A. 2000. Velocity fluctuations in fluidized suspensions probed by ultrasonic correlation spectroscopy. *Phys. Rev. Lett.*, **85**, 453–456.

Cowan, M.L., Jones, I.P., Page, J.H., & Weitz, D.A. 2002. Diffusing Acoustic Wave Spectroscopy. *Phys. Rev. E*, **65**, 066605–1/11.

Derode, A., Roux, P., & Fink, M. 1995. Robust acoustic time reversal with high-order multiple scattering. *Phys. Rev. Lett.*, **75**, 4206–4209.

Derode, A., Tourin, A., & Fink, M. 1999. Ultrasonic pulse compression with one-bit time reversal through multiple scattering. *J. Appl. Phys.*, **85**, 6343–6352.

Fink, M. 1997. Time-reversed Acoustics. *Physics Today*, **50**, 34–40.

Foldy, L.O. 1945. The Multiple scattering of waves. *Phys. Rev.*, **67**, 107–119.

Grêt, A., Snieder, R., Aster, R.C., & Kyle, P.R. 2004a. Monitoring rapid temporal changes in a volcano with coda wave interferometry. *Submitted to Geophys. Res. Lett.*

Grêt, A., Snieder, R., & Ozbay, U. 2004b. Monitoring stress change in an underground mining environment with coda wave interferometry. *Submitted to the J. of Mining Applications.*

Grêt, A., Snieder, R., & Scales, J. 2004c. Time-lapse monitoring of rock properties with coda wave interferometry. *Submitted to J. Geophys. Res.*

Groenenboom, J., & Snieder, R.K. 1995. Attenuation, dispersion, and anisotropy by multiple scattering of transmitted waves through distributions of scatterers. *J. Acoust. Soc. Am.*, **98**(6), 1–11.

Heckmeier, M., & Maret, G. 1997. Dark Speckle Imaging of Colloidal Suspensions in Multiple Light Scattering Media. *Progr. Colloid. Polym. Sci.*, **104**, 12–16.

Lagendijk, A., & van Tiggelen, B.A. 1996. Resonant Multiple Scattering of Light. *Phys. Rep.*, **270**, 143–215.

Maret, G., & Wolf, G.E. 1987. Effect of Brownian Motion of Scatterers. *Z. Phys. B*, **65**, 409–413.

Page, J.H., Jones, I.P., Schriemer, H.P., Cowan, M.L., Sheng, P., & Weitz, D.A. 1999. Diffusive transport of acoustic waves in strongly scattering media. *Physica B*, **263-264**, 37.

Page, J.H., Cowan, M.L., & Weitz, D.A. 2000. Diffusing acoustic wave spectroscopy of fluidized suspensions. *Physica B*, **279**, 130–133.

Papoulis, A. 1991. *Probability, Random Variables, and Stochastic Processes.* McGraw-Hill Inc.

Pine, D.J., Weitz, D.A., Chaikin, P.M., & Herbolzheimer, E. 1988. Diffusing Wave Spectroscopy. *Phys. Rev. Lett*, **60**, 1134–1137.

Snieder, R. 2004a. Coda wave interferometry. *Pages 54–56 of: 2004 McGraw-Hill yearbook of science & technology.* New York: McGraw-Hill.

Snieder, R. 2004b. Extracting the Green's function from the correlation of coda waves: A derivation based on stationary phase. *Phys. Rev. E*, **69**, 046610.

Snieder, R., & Vrijlandt, M. 2004. Constraining Relative Source Locations with Coda Wave Interferometry: Theory and Application to Earthquake Doublets in the Hayward Fault, California. *submitted to J. Geophys. Res.*

Snieder, R.K. 1999. Imaging and averaging in complex media. *Pages 405–454 of:* Fouque, J.P. (ed), *Diffuse waves in complex media.* Kluwer, Dordrecht.

Snieder, R.K. 2002. Coda wave interferometry and the equilibration of energy in elastic media. *Phys. Rev. E*, **66**, 046615–1,8.

Snieder, R.K., & Scales, J.A. 1998. Time reversed imaging as a diagnostic of wave and particle chaos. *Phys. Rev. E*, **58**, 5668–5675.

Snieder, R.K., Grêt, A., Douma, H., & Scales, J. 2002. Coda Wave Interferometry for estimating nonlinear behavior in seismic velocity. *Science*, **295**(22 March), 2253–2255.

Waldhauser, F., & Ellsworth, W. 2000. A double-difference earthquake location algorithm: Method and application to the northern Hayward fault, California. *Bull. Seism. Soc. Am.*, **90**, 1353–1368.

Weitz, D.A., & Pine, D.J. 1993. Diffusing Wave Spectroscopy. *Page 652 of:* Brown, W. (ed), *Dynamic Light Scattering.* Clarendon Press, Oxford.

Yodh, A.G., Kaplan, P.D., & Pine, D.J. 1990. Pulsed diffusing-wave spectroscopy: High resolution through nonlinear optical gating. *Phys. Rev. B*, **42**, 4744–4747.

APPENDIX A: A CONDITION TO ESTIMATE THE RELIABILITY OF THE CROSS-CORRELATION CORRECTION FACTOR

Equation (20) for the correction factor of the cross-correlation coefficient, depends on the unknown noise functions $n_u(t)$ and $n_p(t)$. In practice, we don't know these noise functions, and can at best estimate the average noise levels. Since in practice we often only have one estimate of the noise level, as opposed to some ensemble average, we want the correction factor to be reliable when the unknown noise signals in equation (20) are replaced by a single estimate of the noise. If inequalities (21)-(23) are satisfied, the correction factor will only weakly depend on the estimate of the noise signals. Here we rewrite these inequalities into one inequality that can be verified using the noise contaminated signals and an estimate (or single realization) of the noise $n_0(t)$.

To write inequalities (21)-(23) as a single one, we first add the left- and right-hand sides of equations (21)-(23), while multiplying equation (21) by two for convenience in the further derivation. This gives

$$\begin{gathered} 2\left(|(u_u,n_p)_{(t,t_s,t_w)}+(u_p,n_u)_{(t,t_s,t_w)}+(n_u,n_p)_{(t,t_s,t_w)}|+|(u_u,n_u)_{(t,0,t_w)}|+|(u_p,n_p)_{(t,0,t_w)}|\right) \\ \ll \\ 2|(u_u,u_p)_{(t,t_s,t_w)}|+(u_u,u_u)_{(t,0,t_w)}+(n_u,n_u)_{(t,0,t_w)}+(u_p,u_p)_{(t,0,t_w)}+(n_p,n_p)_{(t,0,t_w)}\,, \end{gathered} \tag{A1}$$

where we have used that zero-lag auto-correlations are positive definite. If conditions (21)-(23) hold, equations (17)-(19) from the main text are good approximations. We can use these approximations, together with the linearity of $(\cdot\,,\cdot)_{(t,t_s,t_w)}$ and equation (9), to approximate inequality (A1) as

$$\begin{gathered} 2|(u'_u,n_p)_{(t,t_s,t_w)}+(u'_p,n_u)_{(t,t_s,t_w)}-(n_u,n_p)_{(t,t_s,t_w)}| \\ +2|(u'_u,n_u)_{(t,0,t_w)}-(n_u,n_u)_{(t,0,t_w)}|+2|(u'_p,n_p)_{(t,0,t_w)}-(n_p,n_p)_{(t,0,t_w)}| \\ \ll \\ 2|(u'_u,u'_p)_{(t,t_s,t_w)}|+(u'_u,u'_u)_{(t,0,t_w)}+(u'_p,u'_p)_{(t,0,t_w)}\,. \end{gathered} \tag{A2}$$

Since in CWI we assume that the travel-time perturbations in the time window $[t-t_w,t+t_w]$ are small, we expect a positive cross-correlation between the signals $u'_u(t)$ and $u'_p(t)$ for times where CWI is valid. Using this, we can write condition (A2) as

$$\begin{gathered} |(u'_u+u'_p,n_0)_{(t,t_s,t_w)}|+|(u'_u,n_0)_{(t,0,t_w)}-(n_0,n_0)_{(t,0,t_w)}|+|(u'_p,n_0)_{(t,0,t_w)}-(n_0,n_0)_{(t,0,t_w)}| \\ \ll 2([u'_u+u'_p]/2,[u'_u+u'_p]/2)_{(t,0,t_w)} \end{gathered} \tag{A3}$$

where we substituted for both noise signals $n_u(t)$ and $n_p(t)$ the estimated noise signal $n_0(t)$, and we assumed $\left|(n_u,n_p)_{(t,t_s,t_w)}\right| \ll \left|(u'_u,n_p)_{(t,t_s,t_w)}+(u'_p,n_u)_{(t,t_s,t_w)}\right|$ to eliminate the $(n_u,n_p)_{(t,t_s,t_w)}$ term. The latter approximation is more appropriate for larger signal-to-noise ratios, larger time windows, and uncorrelated noise realizations $n_u(t)$ and $n_p(t)$. Note that substituting a single noise signal for both unknown noise signals $n_u(t)$ and $n_p(t)$ is appropriate only, if both noise signals have similar noise levels. Dividing both sides of condition (A3) by $(n_0,n_0)_{(t,0,t_w)}$ (which is positive definite), and defining the ratio

$$\Gamma(t,t_w) \equiv \frac{([u'_u+u'_p]/2,[u'_u+u'_p]/2)_{(t,0,t_w)}}{(n_0,n_0)_{(t,0,t_w)}}\,, \tag{A4}$$

inequality (A3) leads to

$$\frac{1}{2}\left(\left|\frac{(u'_u+u'_p,n_0)_{(t,t_s,t_w)}}{(n_0,n_0)_{(t,0,t_w)}}\right|+\left|\frac{(u'_u,n_0)_{(t,0,t_w)}}{(n_0,n_0)_{(t,0,t_w)}}-1\right|+\left|\frac{(u'_p,n_0)_{(t,0,t_w)}}{(n_0,n_0)_{(t,0,t_w)}}-1\right|\right)/\Gamma(t,t_w) \le \gamma\,, \tag{A5}$$

where γ is $\mathrm{O}(10^{-1})$. Here $\sqrt{\Gamma(t,t_w)}$ can be interpreted as the average signal-to-noise ratio.

Condition (A5) is satisfied only for time windows that have a large average signal-to-noise ratio. The l.h.s of condition (A5) can be evaluated using the noise contaminated signals $u'_u(t)$ and $u_p(t)$, and an estimated noise signal $n_0(t)$. This condition can thus be used as a selection criterion to determine which time windows have reliable correction factors associated with them, when an estimated noise signal $n_0(t)$ is used (i.e., when equation (24) is used to calculate the correction factor). Note that γ can be interpreted as the inverse of the signal-to-noise ratio.

CWP-504

Estimation of azimuthally varying attenuation from surface seismic data

Ivan Vasconcelos* and Edward Jenner†
* *Center for Wave Phenomena, Department of Geophysics, Colorado School of Mines, Golden, CO 80401, USA*
† *GX Technology - Axis Imaging Division, 225 East 16th Avenue, Suite 1200, Denver, CO 80203, USA*

ABSTRACT

Observing the azimuthally varying seismic attenuation in data that show azimuthal velocity anisotropy could contribute not only to the interpretation of the subsurface symmetry systems, but also to the characterization of its physical parameters. In this paper, we estimate azimuthal variations of the P-wave effective quality factor (Q) from field surface seismic data. We also provide an interpretation of our results taking into account the NMO ellipse parameters measured from the data, and potential bias caused by systematic noise. By assuming that Q is frequency independent, and the medium at each particular azimuth the medium is laterally homogeneous, we use the spectral ratio method and a regularized linear inversion scheme to estimate the quality factor in azimuth-sectored data. The regularization parameters are chosen by a χ^2 criterion that is based on estimates of the variance in the field data. Tests on synthetic data show that this regularized inversion provides robust estimates of Q for signal-to-noise ratios lower than those observed in the data. Application of this methodology to P-wave data from the East Decatur Field in Texas yields non-negligible azimuthal variations in Q. The azimuthal signature of attenuation appears to be consistent with the effective NMO ellipse from the same interface. However, data residuals show non-random structures that suggest a strong systematic component to the noise. We provide a brief analysis of scattering-related absorption and of frequency imprints of source-receiver arrays as possible sources of systematic noise.

Key words: attenuation, azimuthal anisotropy, regularized inverse solution

1 INTRODUCTION

An important dynamic effect for wave propagation in elastic media is attenuation. In media containing aligned cracks on scales smaller than the dominant seismic wavelength there should be azimuthally variable signatures of attenuation. These azimuthal attenuation variations may be valuable tools in identifying and characterizing fractures in the subsurface. Fractured formations are also known for showing azimuthal velocity anisotropy signatures. Jenner (2001) used azimuthally varying normal-moveout (NMO) velocities and AVO signatures from P-waves to identify fracture zones at the Weyburn field in Canada. Adding shear-wave splitting analysis to the information obtained by Jenner (2001), Cardona (2002) was able to interpret the predominant anisotropic symmetry systems at the reservoir level at Weyburn. Cardona (2002) also suggested that shear-wave splitting at vertical incidence could be affected by changes in saturation for certain fracture rheologies.

It is somewhat intuitive to expect that formations that are anisotropic with respect to velocities should have associated signatures of attenuation anisotropy. Indeed, experiments conducted in anisotropic physical models (Hosten et al., 1987; Arts and Rasolofosaon, 1992) showed that not only attenuation has a directional dependence but also the magnitude of its anisotropy can be more significant than that of velocity. Another experiment conducted by Prasad and Nur (2003) relates P-wave attenuation anisotropy to the texture of sedimentary rocks. Clark et al. (2001) estimated azimuthal variations of attenuation from four sail-line profiles extracted from a 3D marine dataset acquired offshore West Africa. Their interpretation of the principal orientation of the azimuthally variable attenuation is consistent with fracture orientations infered from azimuthally variable AVO.

Taking attenuation into account is also important because of its sensitivity to fluid content. Through 1D Biot equations for poroelastic media, Gurevich et al. (1997) provided an analytical description on how interlayer flow caused by wave displacement influences attenuation. From crosswell data collected at the Buena Vista Hills field, Hackert et al. (2001) used attenuation estimates in lithology identification which served as input to a later study by Parra et al. (2002), who used the information of higher attenuation zones to characterize fluid infill in fractured shale formations. Obtaining azimuthally variable estimates of attenuation can help not only in estimating the orientation of fractures, but also in characterizing some of their physical properties (Rathore et al., 1995; Lynn et al., 1999).

A common parameter used in attenuation estimation is the quality factor, or Q, which is inversely proportional to attenuation. There are many methodologies available for estimating Q. Dasgupta and Clark (1998) use the spectral ratio method to invert for Q using stacked power spectra extracted from stretch-compensated NMO-corrected gathers. In a physical modeling experiment Zhu (2005a) applies the spectral ratio method to analyze variations of attenuation with polar angle. Using prestack data, Hicks and Pratt (2001) apply a tomographic approach based on local descent methods to estimate the quality factor. Also in the context of surface seismic data, Zhang and Ulrych (2002) use the peak frequency shift in the power spectra from different time windows to invert for Q. Quan and Harris (1997) also rely on the peak frequency shift method in crosswell tomography to estimate attenuation. According to Mateeva (2003), Q can be estimated reliably from surface seismic as long as the subsurface can be described by a model with stationary reflectivity, bounded by a free surface. The methodology we describe in this paper makes use of the spectral ratio method (Mateeva, 2003; Dasgupta and Clark, 1998; White, 1992) to estimate Q.

Estimating Q related to intrinsic absorption may prove to be an involved procedure as scattering from thin layering also contributes to attenuation. In this paper, we use the term *effective Q* to refer to the total attenuation effect that is due to both intrinsic and scattering absorption. Mateeva (2003) describes a methodology to separate intrinsic absorption from multiple scattering effects in the context of check-shot VSP experiments. Her approach relies on well log reflectivity data to model only the scattering component of attenuation, which is then removed from the effective Q measurements. In Vasco et al. (1996) scattering absorption is predicted analytically by ray perturbation theory. We chose to model the scattering component of absorption in an approach similar to Mateeva (2003). With well log information, we can generate synthetic common-shot gathers using the reflectivity method (Müller, 1985) with only layering-induced absorption.

The main goal of this paper is to devise and implement a methodology that allows for azimuthally varying estimates of the quality factor. This project was inspired by the observation of azimuthal velocity anisotropy signatures in the East Decatur field that are likely caused by fracturing in the reservoir level. This observation suggested that there would be attenuation anisotropy signatures associated with velocity anisotropy. By assuming our model to be horizontally layered, laterally homogeneous and that Q only varies with azimuth we impose that any two trace pairs in a certain azimuth should yield the same estimate of Q. In practice we enforce the roughness penalty by means of Tikhonov regularization (Hansen, 1998). Since the reliability of our estimates is an important issue, error estimation is done by linear error propagation (Hansen, 1998; van Wijk et al., 2002). In order to obtain estimates of the variance in the data that are independent of model parameters, we use a nonparametric fitting approach (van Wijk et al., 2002; Grey and Silverman, 1994). We apply our methodology first to synthetic data and then to data from the East Decatur field. To describe one of the systematic noise components of the estimates from East Decatur we predicted the frequency response of scattering attenuation. Another source of systematic noise in our estimates are frequency distortions caused by stacking records from source and receiver arrays. Such noise is analyzed by computing the transfer functions of source and receiver arrays with the acquisition geometry of the East Decatur data. A simple formalism for computing array transfer functions is covered in Appendix B.

2 ESTIMATING THE QUALITY FACTOR

Since the objective of our study is to determine whether or nor it is possible to measure azimuthal variations of attenuation from the East Decatur field data, we need to design an inversion methodology that yields robust solutions in the presence of noise. Furthermore, it is of great importance for the chosen methodology to provide meaningful error estimates to determine if measured azimuthal variations of Q are representative of physical phenomena.

The vast majority of existing methods for Q inversion assume 2D media. The main reason for this is that until recently there were no models that presented a closed-form description of the azimuthal variation of Q.

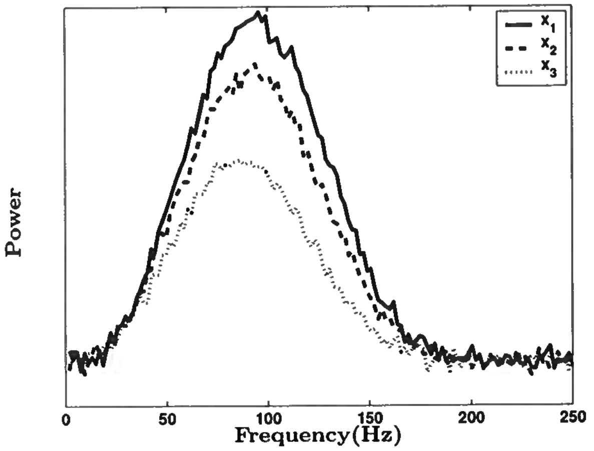

Figure 1. Noise-contaminated power spectra of the reflected signal for three traces with offsets $x_1 > x_2 > x_3$. Model parameters are the P-wave velocity $V = 2.0$ km/s, $Q = 250$ and the reflector depth 1 km. The source pulse was modeled with a Ricker wavelet. The bandwidth used in the inversion tests is $30 - 80Hz$.

In this paper, we assume that any vertical plane represents a section of horizontally layered, laterally homogeneous and isotropic medium. Such assumption allows us to use all data within a given narrow azimuth sector to obtain an estimate of the quality factor at that azimuth. It is therefore necessary to assume that the azimuthal variation of Q within a sector is negligible such that the medium can be considered as laterally homogeneous with respect to attenuation.

In a homogeneous isotropic attenuative medium, the spectrum of the signal at a certain trace j is given by:

$$S_j(f) = A_j\, W(f)\, e^{-\frac{\pi f t_j}{Q}} \tag{1}$$

where f is frequency, t_j is traveltime, Q is the quality factor of the medium and $W(f)$ is the spectrum of the source pulse. Here we will consider amplitude effects due to angle-varying reflectivity and geometrical spreading to be frequency independent, and these effects are accounted for by the term A_j in equation (1). From equation (1) we can see that attenuation in a homogeneous medium at a given frequency is a function of only the traveltimes, and Q . If we consider two signals recorded in the same medium and with the same source pulse, by dividing the spectra $S_1(f)$ and $S_2(f)$ of the waveforms recorded at traveltimes t_1 and t_2, we find:

$$\frac{S_1(f)}{S_2(f)} = \frac{A_1\, e^{-\frac{\pi f t_1}{Q}}}{A_2\, e^{-\frac{\pi f t_2}{Q}}} \tag{2}$$

Taking the logarithm of equation (2) gives;

$$\ln\left[\frac{S_1(f)}{S_2(f)}\right] = \ln\left[\frac{A_1}{A_2}\right] - \frac{\pi f}{Q}(t_1 - t_2) \tag{3}$$

Equation (3) shows that the quality factor Q can be directly estimated from the slope of the ratio of the spectra (in logarithmic scale) for any two traces, if the difference in traveltime between the traces is known. This is the so-called spectral ratio method for inverting for Q (Mateeva, 2003; Dasgupta and Clark, 1998; White, 1992). For later discussion, note that in equation (3) the absorption-related effects are contained in the slope term (frequency dependent), whereas all frequency-independent effects are contained in the intercept term.

According to equation (3), any two traces with a given azimuth can be used to obtain an estimate of Q. In an ideal case, this means that if we had an estimate for the quality factor for each possible trace pair for a gather with a fixed azimuthal orientation, then Q should always be the same. The methodology presented here seeks to take advantage of this "redundancy" by introducing a regularization operator. If there are N possible trace combinations in our azimuth gather, we can take the i^{th} trace pair and write our inverse problem based on equation (3) in the form of the following linear system:

$$\mathbf{A}_i \mathbf{m}_i = \mathbf{d}_i, \tag{4}$$

where,

$$\mathbf{A}_i = \begin{pmatrix} -\pi f_1 \Delta t_i & 1 \\ -\pi f_2 \Delta t_i & 1 \\ \cdot & \cdot \\ \cdot & \cdot \\ -\pi f_n \Delta t_i & 1 \end{pmatrix}, \tag{5}$$

$(f_1, f_2, ..., f_n)$ are the sampled frequency values corresponding to the spectral ratio values in $\mathbf{d}_i$ (left-hand side of equation (3)), and Δt_i is the traveltime difference between the two traces in the i^{th} trace pair. The matrix $\mathbf{m}_i$ contains the intercept and slope (proportional to $1/Q$) model parameters from the two terms in equation (3). Δt_i is computed from the hyperbolic two-way traveltime at each trace, taking into account the elliptical form of the azimuthal variation of normal-moveout velocity (Grechka and Tsvankin, 1998).

Our model objective function to be minimized in the inversion is designed in the following manner:

$$f(\mathbf{m}_i, \mathbf{s}) = \sum_{i=1}^{N} ||\mathbf{A}_i \mathbf{m}_i - \mathbf{d}_i||^2 + \lambda^2 ||\mathbf{R}\mathbf{s}||^2; \tag{6}$$

$\mathbf{s}$ is a $N \times 1$ matrix whose elements are the slope model parameters from all $\mathbf{m}_i$ ($1/Q$, Appendix A), $\mathbf{R}$ is a regularization matrix and λ is its regularization weighting parameter. This particular choice of $\mathbf{s}$ assures that we regularize our inverse problem only with respect to the slope term in equation (3), without imposing

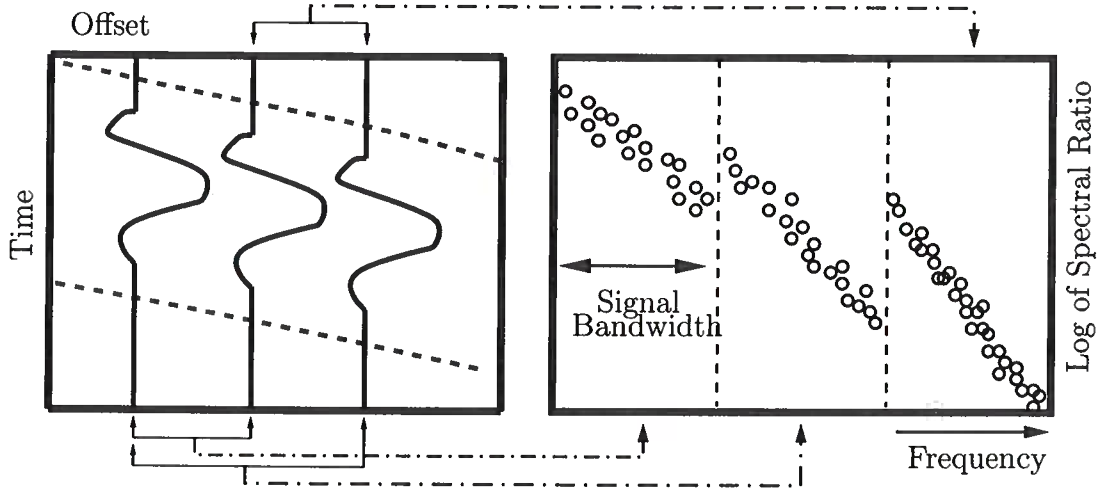

Figure 2. Generation of the data vector **d** (equation 8) from seismic traces using equation (6). Seismic data is sorted according to the CMP number and offset (left hand side). The waveform of the reflection event of interest is windowed on each trace (red dotted lines denote the time window). Then, for any two traces, we compute the ratio of the power spectra of the event (in logarithmic scale) on a sample-by-sample basis, which yields the data points on the right hand side panel in the figure. Each pair of traces provides the data $\mathbf{d}_i$, separated by the dashed lines.

any assumptions on the frequency-independent intercept term. The form of the objective function in equation (6) falls into the category of direct regularization methods known as Tikhonov regularization (Hansen, 1998).

The first term in equation (6) seeks to minimize the total misfit between the data (the spectral ratio) measured for each trace combination and data predicted by its corresponding $\mathbf{m}_i$. This term would be sufficient to carry out the inversion if the model assumptions were correct and the data were noise-free. Acknowledging the existence of non-negligible variance in our data, the second term in equation (6) penalizes the norm of **R** times the model. This allows us to find a solution that does not provide the minimum misfit, but complies to the model constraints enforced by **R**s. In our case, **R** is the sum of the first and second derivative operators. The regularized inverse operator related to the objective function in equation (6) can be found from its normal equations followed by simple linear operations that reduce our inverse problem to a single linear system. These steps are described in Appendix A. Our regularized inverse solution has the same form as the standard Tikhonov regularized inverse:

$$\mathbf{m}^{\dagger} = \mathbf{A}^{\dagger}\mathbf{d}, \tag{7}$$

where $A^{\dagger}$ is the so-called regularized pseudo-inverse operator,

$$\mathbf{A}^{\dagger} = (\mathbf{A}^T\mathbf{A} + \lambda^2\mathbf{R}^T\mathbf{R})^{-1}\mathbf{A}^T. \tag{8}$$

Substituting equation (8) into equation (7) gives

$$\mathbf{m}^{\dagger} = (\mathbf{A}^T\mathbf{A} + \lambda^2\mathbf{R}^T\mathbf{R})^{-1}\mathbf{A}^T\mathbf{d}. \tag{9}$$

The relationship between the matrices in equation (6) and in equation (9) are described in Appendix A. Of course, it would be simpler to just apply the Generalized Least Squares (GLS) solution (Hansen, 1998; Green and Silverman, 1994) and get independent estimates of attenuation for each trace pair. However, as we will see later on, if estimates of Q obtained independently for each pair, the actual inverted values for two noise-contaminated, closely neighboring trace pairs may be different by a factor of three. So, if we chose the best possible fit to the data (the GLS solution) we would violate the homogeneity assumption made in equation (3).

As mentioned earlier, it is important to provide meaningful model variances, such that the final results can be properly interpreted. The variance in the model parameters can be directly estimated from the inverse operator $\mathbf{A}^{\dagger}$ [equation (8)] and the data covariance matrix (Hansen,1998; van Wijk et al., 2002). For our particular case, we assume the data covariance matrix is a diagonal matrix of the data variances $\sigma_{d,i}$. To estimate the variance in the data ($\sigma_{d,i}$) we follow the approach described in van Wijk et al. (2002) and minimize the function

$$g(\mu_i) = ||\mu_i - \mathbf{d}_i||^2 + \lambda_{d,i}^2||\mathbf{R}_d\mu_i||^2 \tag{10}$$

with respect to μ_i, for a chosen operator $\mathbf{R}_d$. This gives us an estimate μ_{i,λ_d} for a given λ_d, a smoothed version of our data vector $\mathbf{d}_i$ according to the structure imposed by the operator $\mathbf{R}_d$. This type of fitting procedure is also know as nonparametric regression (Green and Silverman, 1994). If $\mathbf{R}_d$ is chosen so that it represents a certain structure present in the data, then the variance of $\mu_{i,\lambda_d} - d_i$ yields an estimate of $\sigma_{d,i}$ (van Wijk et al., 2002), the data variance with respect to the

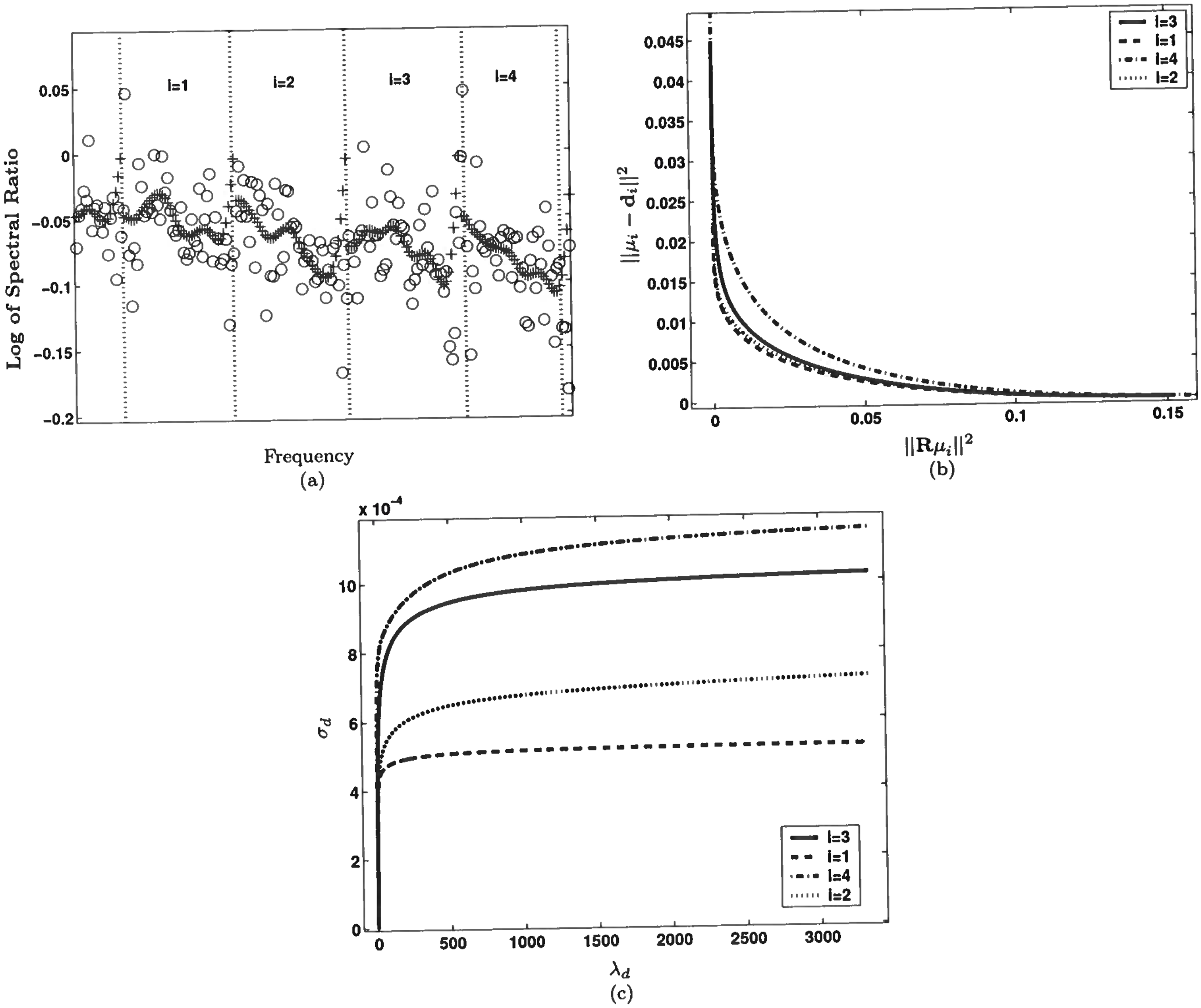

Figure 3. (a) Data from vectors $\mathbf{d}_i$ (equation 6) as in Figure 2(circles) and the smoothed data μ_i (equation 10, crosses). $\mathbf{d}_i$ were computed from noise-contaminated power spectra (Figure 1). The choice of $\lambda_{d,i}$ that gives μ_i can be done by picking $\lambda_{d,i}$ that yields the maximum curvature of L-curves in (b); for this value of $\lambda_{d,i}$ the data variance is approximately constant (c). Each of the four curves in (b,c) pertain to the data vectors $\mathbf{d}_i$ in (a). The data in (a) with $i = 1, 2, 3, 4$ have respectively increasing differences in offset.

structure predicted by $\mathbf{R}_d$. In our particular application we expect the data to have a linear dependence on frequency, hence we choose $\mathbf{R}_d$ to be a second derivative operator. The procedure of choosing the optimum λ_d will be described in the next section.

Another separate issue is determining the solution $\mathbf{m}^\dagger$. Once the regularized inverse operator is established, we can apply it to our data and obtain a regularized model. As in any other regularization problem, the choice of the weighting parameter λ determines $\mathbf{m}^\dagger$. For our particular application we apply a combined L-curve/χ^2 criterion. If the L-curve criterion (Hansen, 1998) alone is used, and the L-Curve varies smoothly, there is a wide range of λ values that satisfy the criterion but would result in vastly different models. If an estimate of the variance in the data is available, setting its corresponding χ^2 to some confidence level allows one to compute a misfit cut-off for the L-curve that gives the best λ (van Wijk et al., 2002).

There are important practical issues related to the inversion methodology discussed above. To use equation 3 in our inversion scheme, we need to make an extra assumption. Since at a particular azimuth our model is supposed to consist of homogeneous layers with horizontal interfaces, while equation (3) is valid for homogeneous half-spaces, the contrasts between layers are assumed to be small and raypaths should be close to vertical. In practice, this assumption is enforced by only taking into account only near-offset traces (i.e., offset-to-depth ratio less than 1).

The forward operator $\mathbf{A}_i$ [equation (3)] and the data vector $\mathbf{d}_i$ pertain to a windowed portion of the corresponding traces containing the reflection event of interest. The center of window is equal to to the traveltime of the event predicted using the estimated moveout parameters for the corresponding CMP gather. Once the window center positions are determined, the windowing is carried out with a Hanning-type taper (Priestley, 1981). Mateeva (2003) discussed some of the implications of windowing in the Q estimation process. Her studies show that the window size imposes a bias on attenuation estimates, and this bias decreases with increasing window size. Our window size was typically on the order of 1.5 times the dominant wavelength of the signal. Mateeva (2003) also shows that windowing data with no tapering can severely distort estimates of Q, but the choice of the tapering function has little influence on the results.

After windowing, we pad the time series with zeros (for as many as ten times the length of the windowed series) to ensure a dense enough sampling of the power spectra. Next, we determine the signal frequency bandwidth by comparing the spectrum of our windowed time series with the spectra from far-offset traces for time windows positioned before the first arrival. The reason for this is that data before the first arrival should be representative of background noise.

3 SYNTHETIC DATA TESTING

Since one of our assumptions about the data is that each vertical plane can be treated as a horizontally layered, laterally homogeneous medium, the main focus of our synthetic data test is to assess the performance of our inversion methodology on CMP-sorted, surface seismic data that would represent an azimuth sector. Given that our main objective is to study the robustness of the regularized inverse operator in the presence of noise, the simplest model for our synthetic example is that of a homogeneous, isotropic, attenuative layer. For such a model, we can predict the the power spectrum of the signal at any trace simply by using equation (1), and having as input our medium parameters and the power spectrum of the source pulse. The synthetic data were then modeled with P-wave velocity $V = 2.0$km/s, $Q = 250$, a reflector depth of 1km and a Ricker source wavelet. The data was then contaminated with Gaussian random noise. Noise variances in the synthetic spectra were chosen to be at least two orders of magnitude larger than that of real data traces for times before the first arrival. Figure 1 shows noise-contaminated power spectra of the reflected signal from four traces. Figure 1 also illustrates that as the traveltime increases (with increasing offset), the frequency peak of the power spectrum shifts towards lower frequencies. This behavior should always be observed in data for media were the constant Q assumption is valid, and the attenuation coefficient is proportional to frequency.

Once the synthetic power spectra were generated, we computed the data vectors $\mathbf{d}_i$ [equation 6)] by taking the natural logarithm of the ratio between the spectra of all possible trace pairs (Figure 2). Before we can find the regularized inverse solution, it is necessary to estimate $\sigma_{d,i}$ (the variance in the data). After many iterations over the value of $\lambda_{d,i}$ we produce the L-curves in Figure 3b. The choice of $\lambda_{d,i}$ can be made by picking some point where the L-curve has the maximum curvature. Another option for the choice of $\lambda_{d,i}$ comes from the curves in Figure 3c that show that as $\lambda_{d,i}$ increases, the data variance increases rapidly at first and then becomes approximately constant. A natural choice for the regularization parameter would be the value $\lambda_{d,i}$ at which the increase data variance is negligible. After establishing the optimum value for the regularization parameter, we can predict the modified data vector μ (Figure 3a) and the total data variance. For the data with the highest offset difference between the two traces ($i = 4$) the corresponding σ_d is smallest (Figure 3). This happens because all power spectra had their samples randomly distorted with the same variance and the ratios that correspond to spectra with a higher attenuation difference will show smaller variance. If the noise in our data is limited to random fluctuations in the power spectra, traces with larger offset differences will give more stable estimates of Q. As to the issue of how reliable the estimates of the data variances ($\sigma_{d,i}$) are, we refer to the work of van Wijk et al. (2002).

With an estimate for the variance in the data, we set a threshold for the maximum tolerable misfit for a certain confidence level, according to the χ^2 test for goodness of fit (van Wijk et al., 2002). This threshold can then be used to decide the amount of regularization we can impose in our data. In practice, we wish to be conservative about the model smoothness in such a way we choose the value of λ (equation 9) that provides a misfit under the confidence level threshold. Figure 4 illustrates the L-curve for $\mathbf{R}$, with the corresponding misfit threshold set by the χ^2 criterion. For the chosen λ we can find the regularized inverse solution (Figure 5a,c). Figure 5a,c shows that the regularized inverse solution is closer to the true model than the standard generalized least squares (GLS) solution. We can also observe that there is some structure in the regularized inverse solutions. This structure is related to the ordering of the data vectors $\mathbf{d}_i$ within d, which in turn is related to how traces are sorted in the input data.

If the data variance estimation procedure provided perfect estimates and we decided to push the regularization to higher confidence levels, the structure of the regularized solution would be somewhat less smooth, depending on where the misfit threshold (determined from χ^2) intersects the L-curve. The regularized inverse solution in Figure 5c is less structured and closer to true model than in Figure 5a because its solution requires less regularization, since the data variance estimate is smaller. Figures 5b,d show the fit of the regularized and GLS solutions, for most trace pairs it is hard to visually distinguish the regularized from the non-regularized fit. This difference is small because the traveltime difference between traces is small, which translates into small differences in attenuation magnitudes. However, the differences between the regularized and non-regularized solutions for the same data are quite noticeable.

There may be cases when a structure in the solution induced by the use of differencing-type regularization operators is unwanted (e.g. if the structure is very steep). Another option for regularizing our problem is to penalize the norm of the residuals between each model parameter and the mean (exemplified in Appendix A). This particular choice of $\mathbf{R}$ will eliminate the structures caused by applying differencing type regularization operators. However, since the cause of structured solutions usually is the presence of extreme values, depending on the difference between the outlier values and the mean of the remaining solutions, the overall mean of the model parameter shifts towards the outliers.

4 EAST DECATUR FIELD DATA

Our field data study was conducted on prestack 3-D wide-azimuth P-wave data acquired over the East Decatur field, located in North Texas. The formation of interest is the Barnett formation, which is composed of thick fractured shale beds. The Barnett shale is one of the largest producing gas reservoirs in the United States, and it has been reported that its best production rates come from wells drilled in areas where natural fractures were present. Hence, the detection of natural fractures a crucial step toward identifying and characterizing areas of better production for reservoirs like the Barnett shale.

Figure 6 shows an Inline section from the the East Decatur field data after 3-D zero-offset migration. The subsurface geology at the East Decatur field is close to horizontally layered (as dips are in the order of 2°), with mild lateral velocity variations. Apart from the structural simplicity, this particular dataset was chosen for pronounced lateral variations of the P-wave azimuthal anisotropy. Figure 7 shows NMO ellipse parameters for the reflection at the bottom of the Barnett formation. For this field, azimuthal anisotropy is mainly attributed to fractures in the Barnett shale beds since the interval NMO ellipse orientations coincide with fracture orientations from well observations and geologic data. The pronounced azimuthal velocity anisotropy signatures related to intrinsic properties (fracturing) of the Barnett formation immediately raised the question of whether there should associated azimuthal variations of attenuation anisotropy. The goal of the project was to obtain azimuthally variable estimates of the total effective attenuation and check if the results are in agreement with fracture orientations and velocity anisotropy signatures.

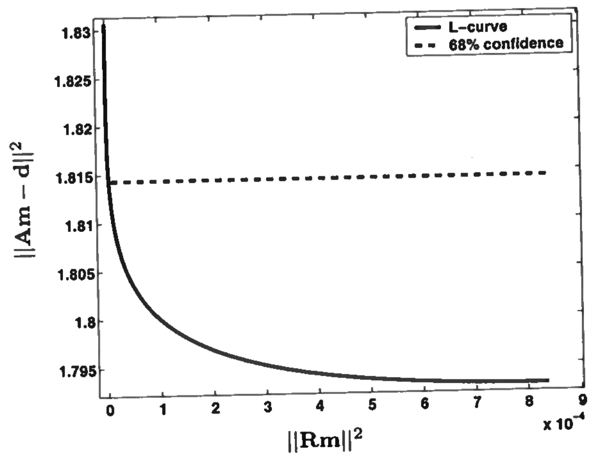

Figure 4. L-Curve for R [equation (8)]. Picking the value of λ corresponds to the misfit at the 68% confidence level results in the smoothest possible model according to the data variance.

We applied the inversion methodology described above to estimate the azimuthally varying Q. The seismic data were sorted into CMP geometry, and the only pre-processing step applied was source-receiver statics. Because the windowing of the desired events is based on predicting reflected traveltimes, static corrections are important to assure proper windowing. Here, we show the azimuthal attenuation analysis for two 9×9 superbins, hereafter referred to as CMP1 (inline coordinate 1380, crossline 5285, Fig. 7) and CMP2 (inline 1398, crossline 5292), respectively. Traces were then sorted into 5° azimuth bins and the inversion for each bin was conducted for the horizon at approximately 1.3 s, interpreted as the reflection from the bottom of the Barnett formation. The window length was set constant to 98 samples, Figure 8a shows waveforms extracted from data traces. Their corresponding power spectra are displayed in Figure 8b. The real data spectra are smoother than the spectra in Figure 1 because random

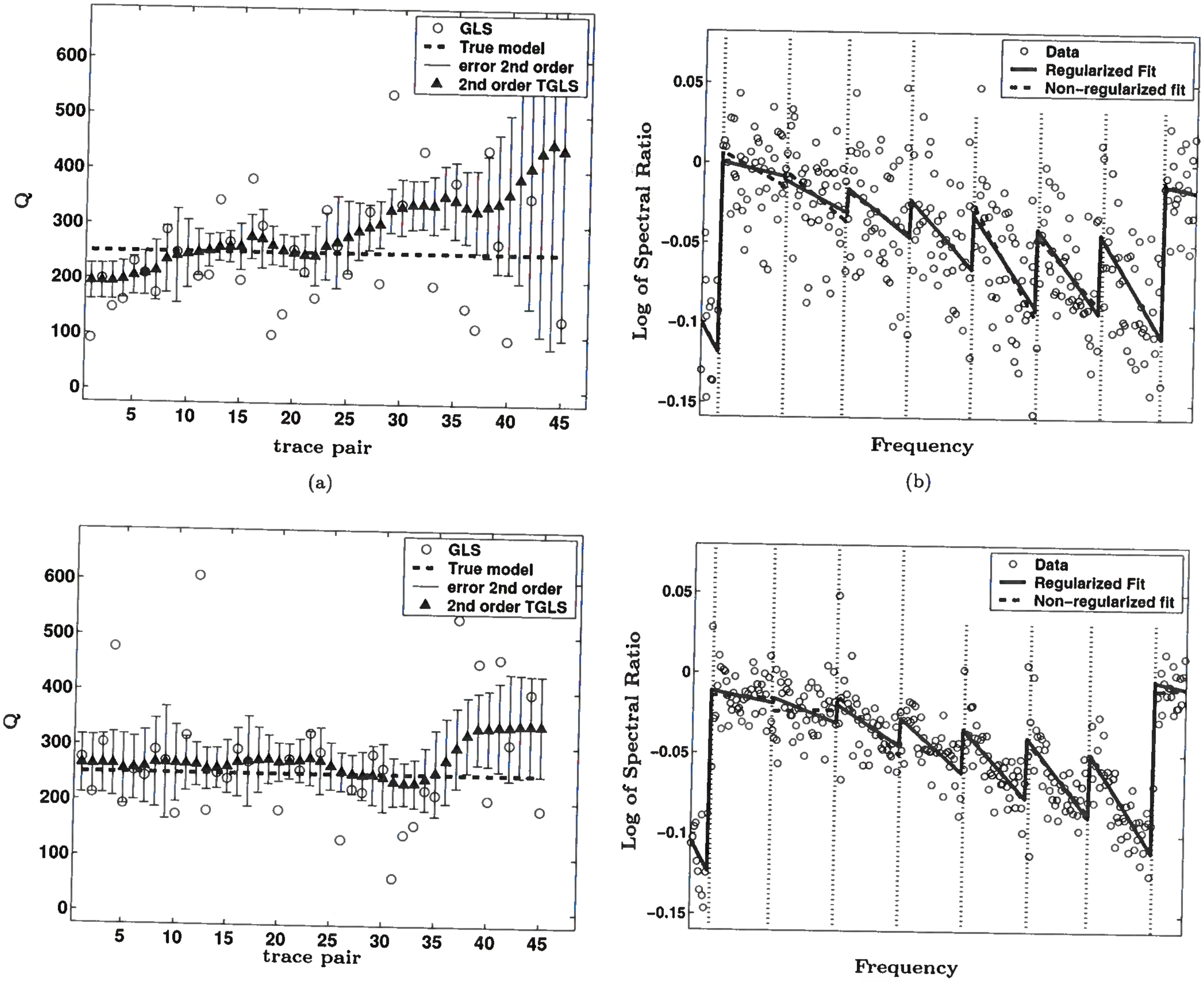

(a) (b) (c) (d)

Figure 5. Inversion results for the synthetic data with different signal-to-noise ratios. The power spectra that generated data for (a,b) are distorted with twice the variance as the spectra for the results in (c,d). (a) and (b) show the Q estimates from the Tikhonov generalized least squares solution (TGLS, 2^{nd} order stands for the use of a first and second derivative operators in R, Appendix A) and the standard generalized least squares. The error bars represent the variance in the model parameters. (c) and (d) are the models fitted to the data, where the regularized fits are related to the TGLS solutions and the non-regularized fits pertain to the GLS solutions.

noise levels are likely smaller than those in synthetic tests.

Once the reflection event at a given azimuth bin has been windowed, we can set up our data space d [equation (8)] from the data vectors $\mathbf{d}_i$ computed for all trace pair combinations from offset-to-depth ratios up to 1.0. Next we estimate the variance in the data, which, from a simple visual examination of the smoothness of the power spectra (Figure 8) is expected to be less than the that in our synthetic examples. However, although there is little random noise in the spectra, we observe pronounced, repeatable, nonlinear structures in the spectral ratios (Figure 9b).

The algorithm described above treats these structures in the fit residuals as random noise. Clearly, the presence of non-random repeatable structures point to

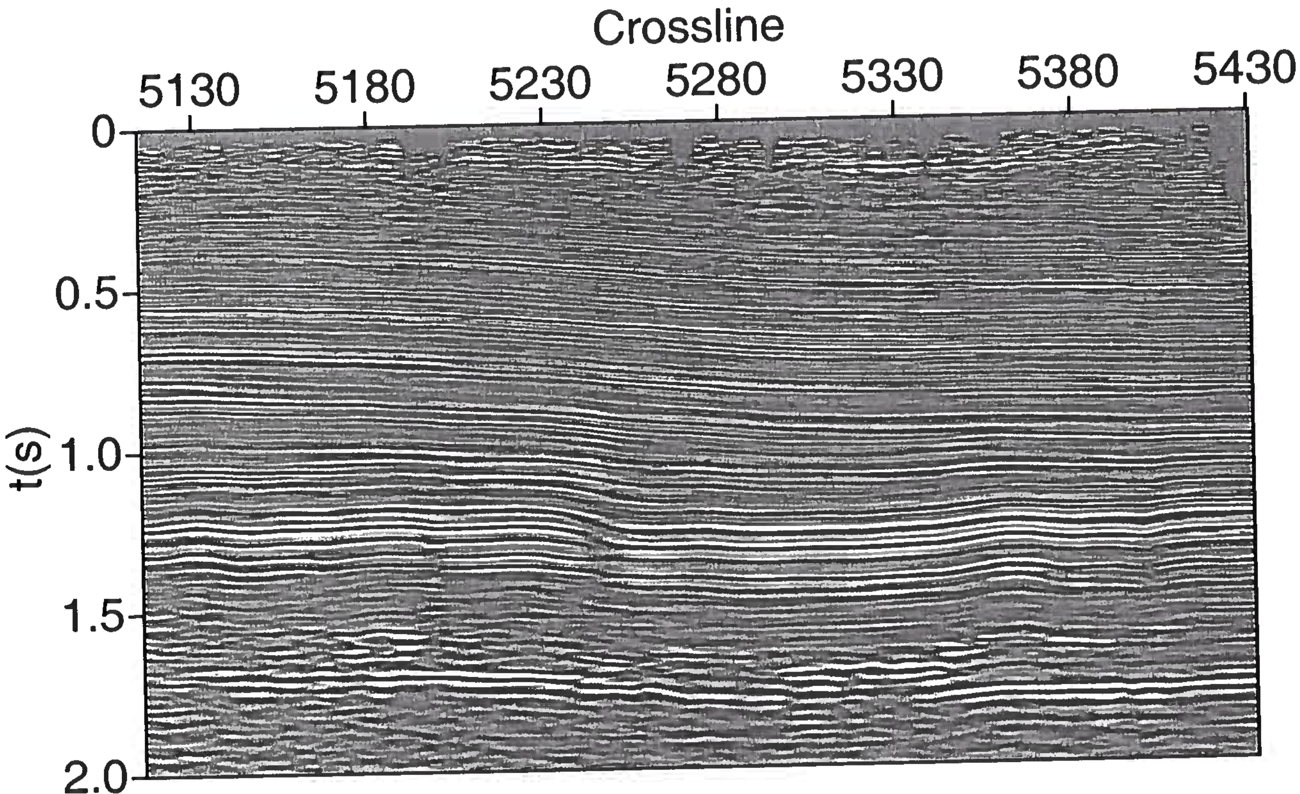

Figure 6. Post-stack migrated image of the East Decatur field data at Inline 1350. The Barnett shale formation is located approximately in the 1.0 s to 1.3 s interval. The overburden is composed of sand/shale sequences.

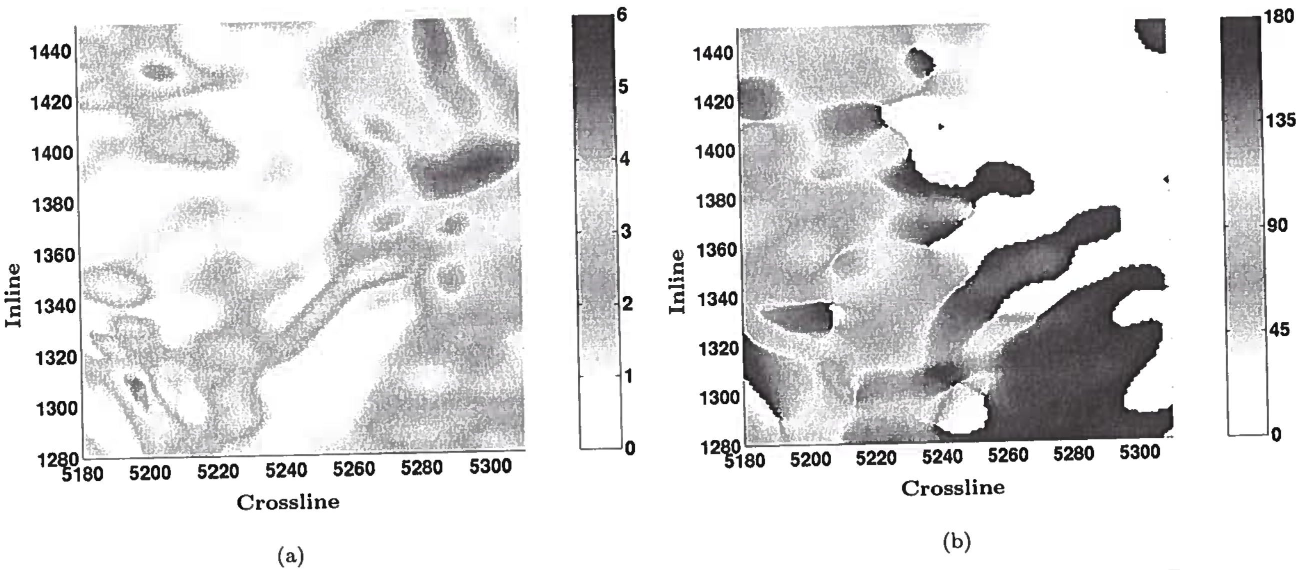

(a)

(b)

Figure 7. Parameters of P-wave NMO ellipses for the reflection from the bottom of the Barnett formation in the East Decatur field. (a) The magnitude of azimuthal anisotropy (NMO ellipse eccentricities) in percent.(b) The orientation of the semi-major axis of the NMO ellipses with respect to North. The two CMPs analyzed (CMP1 and CMP2) lie within the area of stronger azimuthal anisotropy in the upper right-hand corner of the area, respectively with coordinates (*Inline* 1380, *Crossline* 5285) and (*Inline* 1392, *Crossline* 5292). Increasing Crossline coordinates point to the North.

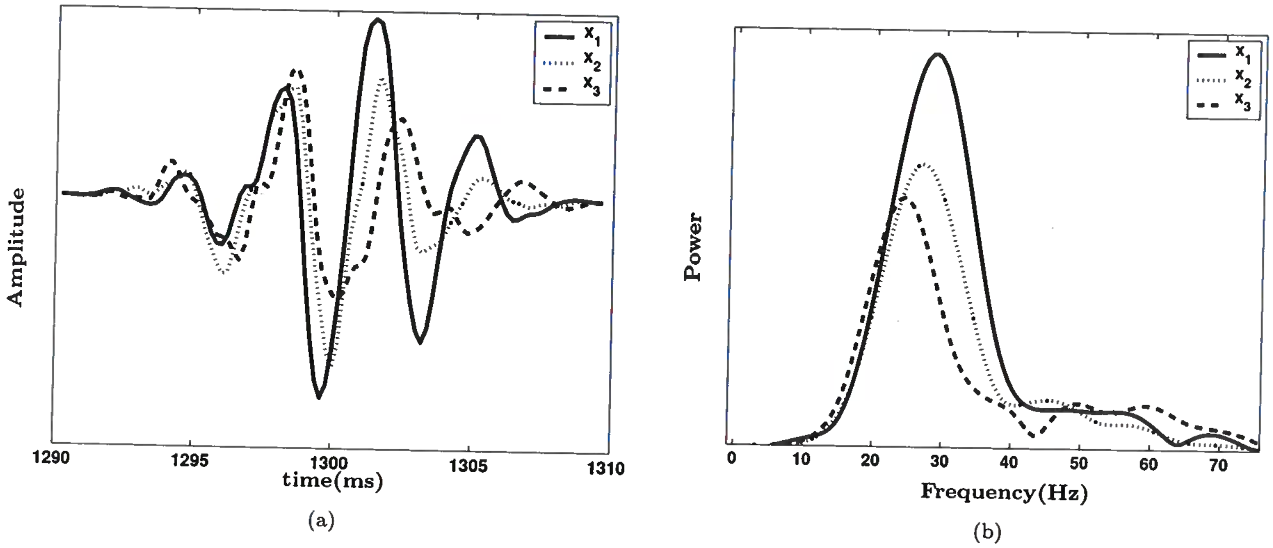

(a)

(b)

Figure 8. Widowed data from CMP1 for a 5° azimuth bin at an azimuth of 40° (a), and their corresponding power spectra (b). Offsets are x_1 = 1614 m, x_2 = 1661 m and x_3 = 1708 m. The inversion was carried out considering frequency samples from 25-50 Hz.

the fact that the assumptions do not account for all the relevant physical phenomena behind the data, although the model can represent a component of the data(Green and Silverman, 1994; Gu, 2002). In other words, we can take advantage of the fact that the regularization parameters can be tuned to set how much we impose a model structure. Then, it is possible to fit a linear component of the spectral ratio by trying to account for the fact that the data variances may be overestimated due to the presence of correlated noise components. We do this in practice by setting our λ to a value that corresponds to a misfit lower than the threshold set by the estimated σ_d. We can then try to pick a value of λ such that we get a model with reduced norm, at the same time being conservative towards the regularization as we try to keep the misfit and the regularization-induced bias as small as possible. Figure 9 shows the estimated model and corresponding data fit obtained following this approach, before and after regularization. To find the value of Q for a given azimuth, we chose to take the median of the regularized Q measurements for each trace pairs to minimize the contribution of outliers.

The effective quality factor for 5° azimuth bins with 20° azimuth increments are displayed for both superbins in Figure 10. It is clear from Figure 10 that if our assumptions and estimates of the variance in the data are accurate, there is a non-negligible azimuthal signature of attenuation. The direction of maximum attenuation (lowest Q) is close to the semi-minor axis of the NMO ellipse, approximately oriented East-West (Figure 7). If the fractures in the shale are fluid-filled, a possible physical interpretation is that waves traveling perpendicular to the most prominent set of fractures should have smaller velocities and experience higher attenuation. It is also interesting to observe that the magnitude of azimuthal attenuation anisotropy is much larger than that of azimuthal NMO velocity anisotropy. The interpretation of these results, however, has to include systematic components, which is discussed next.

If all or some of the nonlinear structure in the data is related to physical phenomena, it is not clear whether or not a linear fit to the data makes any physical sense. Here, we attempt to model nonlinear noise due to different physical phenomena, evaluate its influence on the data, and briefly discuss how it should be dealt with. Correcting for possible sources of noise and employing more involved parameter fitting techniques such as semiparametric fitting and residuals analysis (Grey and Silverman, 1998; Gu, 2002) would be preferable. These procedures, however, are beyond the scope of this paper.

We attribute the nonlinearities in the spectral ratios to two distinct physical phenomena. First, in our measurements we cannot separate the contribution of intrinsic absorption from that of layering-induced absorption. As it is discussed by Mateeva (2003), the attenuation caused by multiple scattering may influence the data in different ways, depending on the media properties. Second, for the East Decatur field, the data were

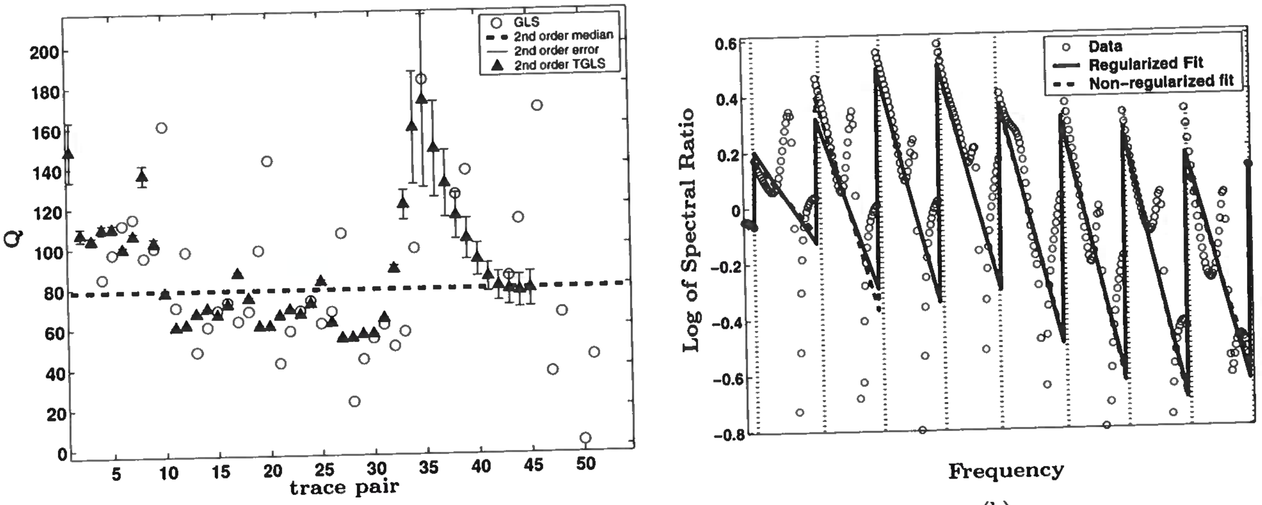

(a)

(b)

Figure 9. Inverted parameter Q for a 5° azimuth bin from CMP1 at 40° azimuth (a), and the corresponding data fit (b). When compared to the synthetic results in Figure 5, Q measurements in (a) are more scattered, and the fit residuals in (b) exhibit non-random, repeatable structures.

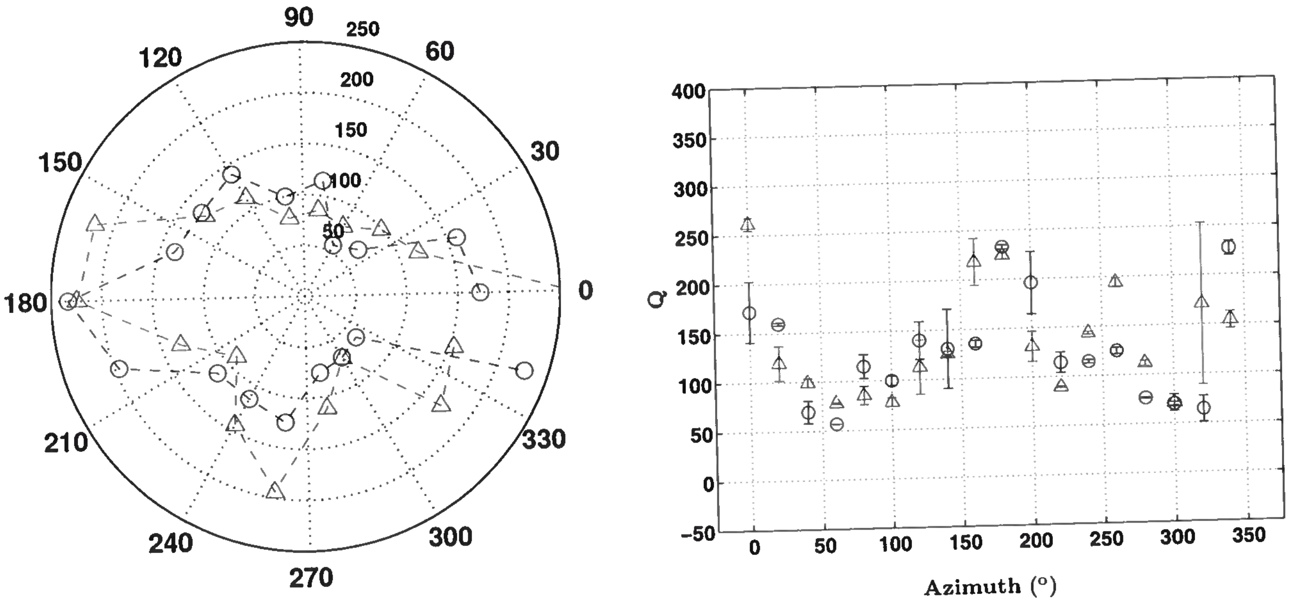

(a)

(b)

Figure 10. Estimates of the effective quality factor at different azimuths shown in a polar plot (a) and with error estimates (b). The results from CMP1 are marked by the blue circles, and from from CMP2 by red triangles. The error bars in (b) are computed as the average standard deviation of the model variances for each trace pair within a sector (Figure 9). The azimuth is with respect to the North. The average orientation of the semi-major axis of the NMO ellipses is North-South.

acquired using source and receiver arrays. Since the response of each array component is simply stacked to form the data, the signature of the source-receiver arrays is frequency dependent (Appendix B).

For our particular dataset, it is also important to find out if multiple scattering due to thin layering could add a nonlinear component to the spectral ratios, and if this component has a structure that correlates to that observed in the data (Figure 9b). Using velocities (compressional and shear-wave) and densities from well logs, we generated a synthetic seismogram (Figure 11) for East Decatur with the reflectivity method (Muller, 1985). This method produces a complete wave-field with all multiples but no intrinsic absorption. Figure 12a shows that there is a clear offset-dependent nonlinear frequency imprint of scattering-induced attenuation in the spectral ratios. The data structure in Figure 12b is somewhat different from that observed in field data (e.g. Figure 9b), as field structures not only vary with offset, but also differ from one azimuth bin to another.

Even though layering-induced absorption causes nonlinear behavior in the spectral ratios, its influence should be azimuthally independent, as long as the medium is laterally homogeneous. This means that the bias in the estimates of Q related to multiple scattering should be the same at all azimuths. Also, in Figure 12 we can observe that the bias in the fitted slopes introduced by thin layering is offset dependent. This implies that if our data is not corrected for scattering absorption, the regularized solution may contain a structure related to the bias in each Q measurement, depending on how regularized the solution is. If too much smoothing (regularization) is applied to uncorrected data, it is difficult to assess how the bias from scattering absorption translates into errors in the estimated model parameters.

As discussed before, use of source and receiver arrays in acquisition creates frequency signatures that may distort the spectral ratios. In Appendix B we show how to obtain the frequency signatures of arrays for a simple homogeneous, isotropic model. For East Decatur field data, receiver arrays are composed of eight sensors, each at a distance of two meters from the center of the array with equal step in azimuth. Source arrays are made of a line of three vibrator trucks, with a 20 m separation between the trucks. The source line is always oriented in the direction 45°N. Because the spacing between the sources is considerably bigger than that between receivers in their respective arrays, the source array should produce a more substantial distortion in the power spectra. Also, there should be some azimuthal dependence of the source-receiver transfer function because the sources are set in a line with a fixed orientation for any source-receiver azimuth. The maximum contribution of the source array should be for the source-receiver azimuth that coincides with the source array orientation, and the minimum should correspond to the orthogonal direction (Appendix B). Using the results of Appendix B, we computed the frequency signatures of the source-receiver arrays for East Decatur data (Figure 13a,c). The biggest deviations of the spectral ratios occur at the 45°N direction, while they become negligible at the 135°N direction (Figure 13b,d). These azimuths coincide with the predicted directions of the maximum and minimum contribution of the source array, which confirms that the influence of the receiver array is relatively minor. Figure 13 also suggests that the bias in the spectral ratios induced by the source and receiver arrays varies with both offset and azimuth. Furthermore, the frequency dependence of this bias within the signal bandwidth can be considered as approximately linear. Hence, there will be an apparent azimuthal variation of attenuation due only to the particular geometry of the source and receiver arrays.

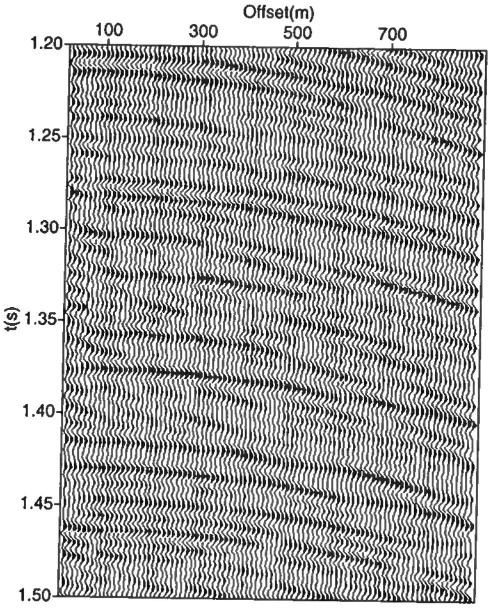

Figure 11. Synthetic seismogram of East Decatur data. The seismogram was computed using the reflectivity method with well log data as input. The event of interest in the seismogram is at approximately 1.28 s.

5 DISCUSSION AND CONCLUSION

With the objective of estimating the azimuthally varying attenuation, we proposed a methodology that assumes that at each azimuth the medium can be considered, as horizontally layered and laterally homogeneous. The methodology includes a search for a pseudo-inverse operator that can both fit the spectral ratio data and honor the model assumptions. In the regularization we

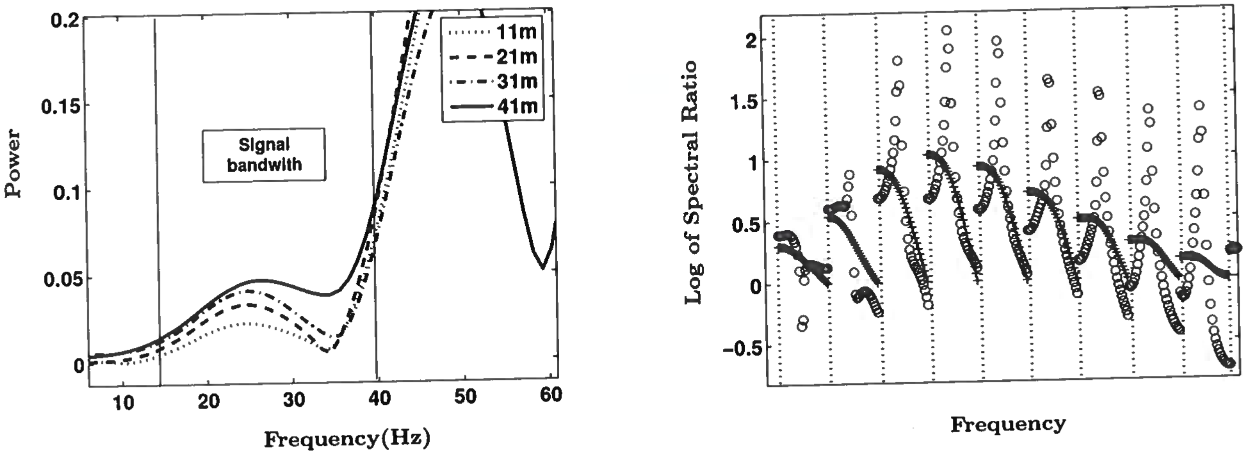

(a)

(b)

Figure 12. (a) Power spectra for the data modeled with the reflectivity method for the event of interest in Figure 11 at offsets 11, 21, 31 and 41 m. (b) Data vectors $\mathbf{d}_i$ (circles) and their smoothed versions μ_i (crosses), used to predict the variance in the data. The data in (b) are computed for the same bandwidth as the spectral ratios for the field data in Figure 9.

use equally weighted first and second derivatives operators to impose smoothness on the estimates of Q within each azimuth bin. This methodology is also designed to provide reliable error estimates. The variances in the model parameters are computed from the regularized pseudo-inverse operator and from the data variances obtained with a nonparametric fitting technique. The estimates for data variance also provide the basis for choosing the regularization weighting parameter.

Noisy synthetic data were generated by distorting power spectra with uncorrelated Gaussian noise. For this type of noise, estimates of Q from traces with larger traveltime differences tend to be more stable because the data variances are smaller. This synthetic test shows that even for signal-to-noise ratios smaller than those typically observed in real data, the regularized inverse solution is considerably closer to the true model than the standard generalized least squares (GLS) solution. While the regularized solution is always smoother than the GLS solution, for data with higher noise levels, it may contain structures that related to the particular order of the input data. In our case, this order is associated to the sorting of the field data traces.

In the East Decatur dataset, we applied our inversion methodology to two 9 x 9 CMP-sorted superbins that lie within one of the areas of strongest azimuthal velocity anisotropy. Since most of the azimuthal anisotropy observed in the East Decatur is is believed to be caused by the fracturing in the Barnett shale formation, our studies focused on the reflection from its bottom. The only pre-processing step applied to the data was source-receiver statics correction, which is necessary because the position of the window around the signal depends on reflected traveltimes computed from moveout parameters.

In contrast to the synthetic data, the spectral ratios from the field gathers contained very little random noise. Instead, we observed a strong nonlinear systematic component to the noise, which produces nonlinear structures in the spectral ratios. Because our methodology cannot separate systematic and random components of the noise, the data variance may be overestimated. In evaluating the linear component of the spectral ratios, we chose to avoid smoothing the data too much, keeping the misfit under the 68% confidence level threshold and the regularization-induced bias as small as possible. In this context, our results for the inversion for Q in 5° azimuth sectors from both superbins show a similar azimuthally variable signature. The direction of the maximum attenuation is approximately East-West, which coincides with the average orientation of the semiminor axis of the P-wave NMO ellipse.Taking fluid-filled fractures with a single predominant orientation as a model for the Barnett shale, maximum attenuation occurs in the direction perpendicular to the fracture strike. An important observation is that the magnitude of the azimuthal variations of attenuation is much larger than that of NMO velocities. In the context of East Decatur field, this suggests that attenuation measurements are much more sensitive to the anisotropy induced by the presence of fluid-filled cracks.

We considered two possible causes for systematic noise in the spectral ratios: absorption effects due to thin layering and frequency distortions caused by stacking the response of source and receiver arrays. We analyzed the first case by computing spectral ratio data for synthetic seismograms generated with the reflectivity

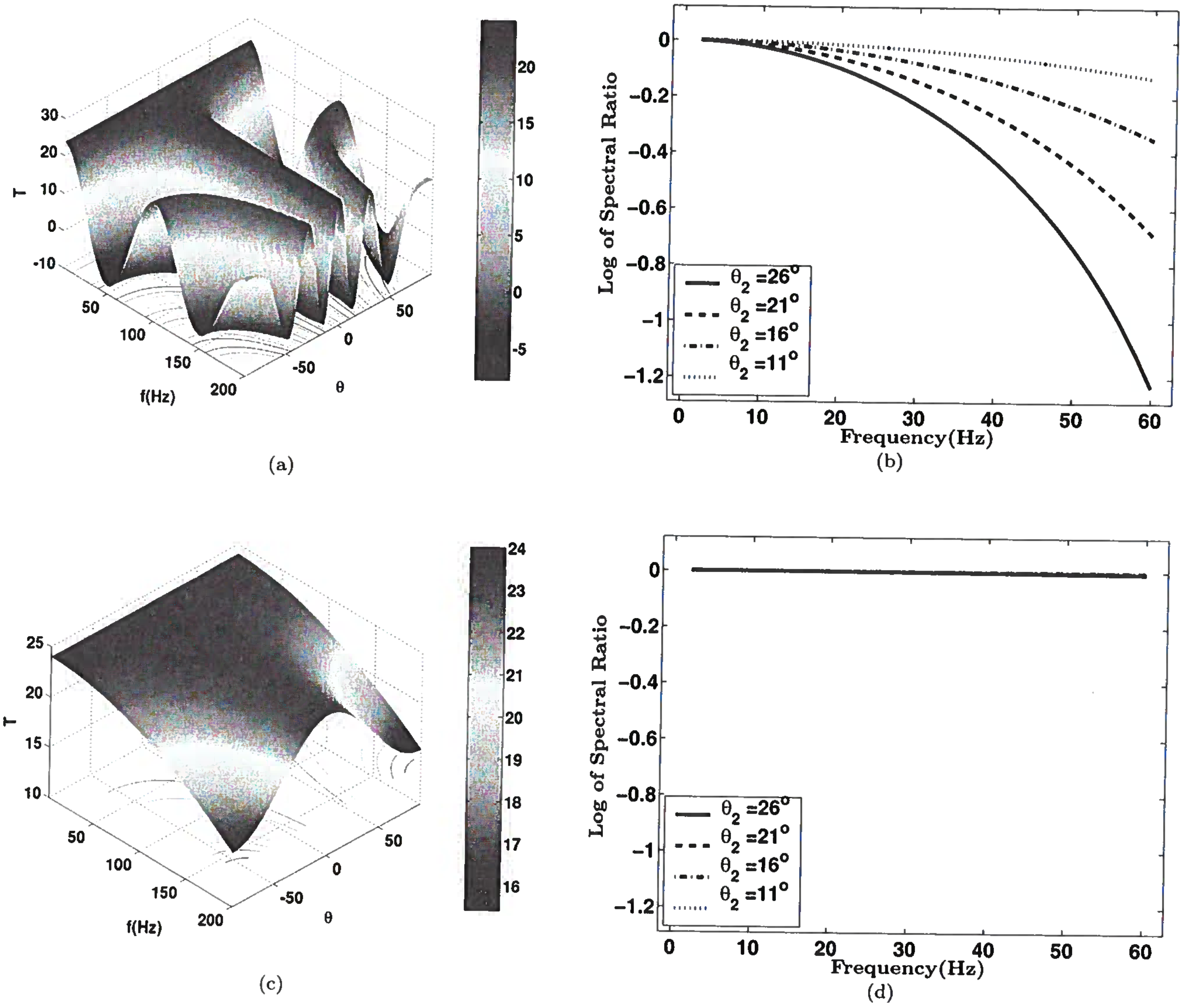

(a) (b)

(c) (d)

Figure 13. Transfer functions T, (a) and (c), of the source and receiver arrays combined as a function of the emergence angle θ and frequency ω. (a) Source-receiver transfer function for the source-receiver azimuth that yields the maximum frequency distortion (azimuth 45°N), and (c), the source-receiver azimuth that gives the smallest frequency distortion. The frequency signatures in (a) and (c) translate into the signatures in the spectral ratios shown, respectively, in (b) and (d). Each curve on the spectral ratio plots is computed between one of the signals with the from the legend and a signal with the 5° emergence angle. The same source and receiver array geometries used here were employed in the East Decatur field data acquisition. The emergence angles θ are directly related to offsets.

method. This way can generate shot gathers accounting only for the attenuation caused by multiple scattering for the reflectivity properties of the East Decatur field. Spectral ratios from the modeled data showed nonlinear features that change from one trace pair to the other, which suggests that the bias in slope estimation introduced by layering-induced absorption is a function of the trace offsets. For a horizontally layered, laterally homogeneous medium, attenuation effects due to multiple scattering are independent of azimuth.

To examine the frequency signatures of the source and receiver arrays, we computed their corresponding transfer functions using the source and receiver array geometries from field data. The frequency distortions introduced by the receiver array are negligible compared to those caused the source array. Also, since the sources are set up in a line with fixed orientation, its frequency signatures are azimuthally dependent. These signatures translate into the spectral ratios with a weak nonlinear dependence on frequency. The source and receiver arrays introduce a negative bias in slope estimates from spectral ratios, which is a function of both offset and azimuth. This generates an apparent azimuthally variable attenuation effect due only to the source and receiver array geometry, where attenuation is strongest at the 45°N direction and weakest at 135°N.

By accounting for layering-induced absorption and for the array transfer functions we could not completely reproduce the structures in the spectral ratios from field data. Strictly, in attenuative media reflectivity and geometrical spreading should be frequency dependent because of velocity dispersion. These effects would be dependent on incidence angle, which in turn would yield structures in the spectral ratios that should vary with offset. Source and receiver radiation patterns in lossy media also become frequency dependent, and their effects in spectral ratios should be corrected for.

In azimuthally anisotropic attenuative medium, intrinsic absorption will have a dependence in polar angle as well as in azimuth (Zhu, 2005b). For the results presented in this paper we ignored the influence of the polar angle. However, the methodology presented here could be applied to trace clusters with different offset ranges to obtain an estimate of the dependence of attenuation with polar angle. With closed form expressions for anisotropic attenuation in terms of anisotropic parameters as in Zhu and Tsvankin (2004, 2005b), the methodology described here could be applied to characterize anisotropic attenuation. Furthermore, our inversion procedure can be applied to other types of datasets with redundant wave-field information (e.g. walkaway vertical seismic profiles, tomographic experiments), and to time lapse studies.

6 ACKNOWLEDGMENTS

We greatly appreciate the input given by Alex Calvert (GX Tech., AXIS) throughout the course of the project. We are thankful to Roel Snieder (CWP) for his help on the issue of array transfer functions. I.V. is grateful to Huub Douma, Ken Larner and CWP colleagues for insightful discussions. Our appreciation also goes to Ilya Tsvankin and Kasper van Wijk for reviewing this paper. We would like to thank GX Technology (AXIS Imag. Div.) and Devon Energy for giving permission to publish these results.

REFERENCES

Arts, R. J., and Rasolofosaon, P. N. J., 1992, Approximation of velocity and attenuation in general anisotropic rocks: 62^{nd} Ann. Intl. Mtg. Soc. Expl. Geophys., Expanded Abstracts, 640-643.

Cardona R., 2002, Fluid Substitution Theories and Multicomponent Seismic Characterization of Fractured Reservoirs: Ph.D. thesis, Colorado School of Mines.

Clark, R. A., Carter, A. J., Nevill, P. C., and Benson, P. M., 2001, Attenuation measurements from surface seismic - azimuthal variation and time lapse case studies: 63^{rd} EAGE Conference and Technical Exhibition, Expanded Abstracts, L-28.

Dasgupta, R., and Clark, R. A., 1998, Estimation of Q from surface seismic reflection data: Geophysics, **63**, 2120-2128.

Grechka, V., and Tsvankin, I., 1998, 3-D description of normal moveout in anisotropic inhomogeneous media. Geophysics **63**, 1079-1092.

Grey, P. J., and Silverman, and B. W., 1994, Nonparametric regression and generalized linear models: Monographs on Statistics and Applied Probability, **58**, Chapman & Hall.

Gu, C., 2002, Smoothing spline ANOVA models: Springer-Verlag New York, Inc.

Gurevich, B., Zyrianov, V. B., and Lopatnikov, S. L., 1997, Seismic attenuation in finely layered porous rocks: Effects of fluid flow and scattering: Geophysics, **62**, 319-324.

Hackert, C. L., Parra, J. O., Brown, R. L., and Collier, H. A., 2001, Characterization of dispersion, attenuation, and anisotropy at the Buena Vista Hills field, California: Geophysics, **66**, 90-96.

Hansen, P. C., 1998, Rank deficient and discrete ill-posed problems: numerical aspects of linear inversion: Society for Industrial and Applied Mathematics.

Hicks, G. J., and Pratt, R. G., 2001, Reflection waveform inversion using local descent methods: Estimating attenuation and velocity over a gas-sand deposit: Geophysics, **66**, 598-612.

Hosten, B., Deschamps, M., and Tittman, B. R., 1987, Inhomogeneous wave generation and propagation in lossy anisotropic rocks: application to the characterization of viscoelastic composite materials: J. Acoust. Soc. Am., **82**, 1763-1770.

Jenner, E., 2001, Azimuthal Anisotropy of 3-D Compressional Wave Seismic Data, Weyburn Field, Saskatchewan, Canada: Ph.D. thesis, Colorado School of Mines.

Lynn, H. B., Campagna, D., Simon K. M., and Beckham, W. E., 1999, Relationship of P-wave seismic attributes, azimuthal anisotropy, and commercial gas pay in 3-D P-wave multiazimuth data, Rulison Field, Piceance Basin, Colorado: Geophysics **64**, 1293-1311.

Mateeva, A., 2003, Thin horizontal layering as a stratigraphic filter in absorption estimation and seismic deconvolution: Ph.D. thesis, Colorado School of Mines.

Müller, 1985, The reflectivity method: a tutorial: Journal of Geophysics **58**, 153-174.

Parra, J. O., Hackert, C. L., and Xu, P., 2002, Characterization of low Q zones at the Buena Vista Reservoir, California: Geophysics, **67**, 1061-1070.

Prasad, M., and Nur, A., 2003, Velocity and attenuation anisotropy in reservoir rocks: 73^{rd} Ann. Intl. Mtg. Soc. Expl. Geophys., Expanded Abstracts, 1652-1655.

Quan, Y., and Harris, J. M., 1997, Seismic attenuation tomography using the frequency shift method: Geophysics, **62**, 895-905.

Rathore, J. S., Fjaer, E., Holt R. M., and Renlie, L., 1995, Acoustic anisotropy of a synthetic sandstone with a controlled crack geometry: Geophys. Prosp., **43**, 805-829.

Vasco, D. W., Peterson Jr., J. E., Majer, and E. L., 1996, A simultaneous inversion of seismic traveltimes and amplitudes for velocity and attenuation: Geophysics, **61**, 1738-1757.

van Wijk, K., Scales, J. A., Navidi, W., and Tenorio, L., 2002, On estimating errors in inverse calculations: Geophysical Journal Intl., **149**, 624-632.

White, R. E., 1992, The accuracy of estimating Q from seismic data: Geophysics, **57**, 1508-1511.

Zhang, C., and Ulrych, T. J., 2002, Estimation of quality factors from CMP records: Geophysics, **67**, 1542-1547.

Zhu, Y., and Tsvankin, I., 2004, Plane-wave propagation and radiation patterns in attenuative TI media: CWP Project Review, CWP-479, 125-142.

Zhu, Y., and Tsvankin, I., 2005a, Physical modeling and analysis of P-wave attenuation anisotropy in transversely isotropic media: CWP Project Review.

Zhu, Y., and Tsvankin, I., 2005b, Plane-wave attenuation anisotropy in orthorhombic media: CWP Project Review.

APPENDIX A: THE TIKHONOV GENERALIZED LEAST SQUARES SOLUTION

Since our objective is to impose smoothness in the measurements of Q from one trace pair to another, it is important to incorporate the linear systems from all trace pairs into a single linear system that sets up the so-called generalized least squares problem.

Our model objective function is:

$$f(\mathbf{m}_i, \mathbf{s}) = \sum_{i=1}^{N} ||\mathbf{A}_i\mathbf{m}_i - \mathbf{d}_i||^2 + \lambda^2||\mathbf{R}\mathbf{s}||^2 ; \qquad \text{(A1)}$$

where the forward operators:

$$\mathbf{A}_i = \begin{pmatrix} -\pi f_1 \Delta t_i & 1 \\ -\pi f_2 \Delta t_i & 1 \\ \cdot & \cdot \\ \cdot & \cdot \\ -\pi f_n \Delta t_i & 1 \end{pmatrix}, \qquad \text{(A2)}$$

for the i^th trace pair. There are n frequency samples in the signal bandwidth and Δt_i is traveltime difference between the two traces. The model parameters matrices $\mathbf{m}_i$:

$$\mathbf{m}_i = \begin{pmatrix} \frac{1}{Q_i} \\ a \end{pmatrix}, \qquad \text{(A3)}$$

where Q_i is the Q measurement and a is the intercept of the line fitted to the spectral ratio. The data $\mathbf{d}_i$ contain the values of the natural logarithm of the spectral ratio that correspond to the frequency samples in $\mathbf{A}_i$. The vector $\mathbf{s}$ in equation (A1) contains all of the elements equal to the $1/Q_i$ elements from all of the $\mathbf{m}_i$ matrices, sich that:

$$\mathbf{s} = \begin{pmatrix} \frac{1}{Q_1} \\ \frac{1}{Q_2} \\ \cdot \\ \cdot \\ \frac{1}{Q_N} \end{pmatrix}. \qquad \text{(A4)}$$

To find the solutions that minimize equation (A1), we must differentiate it with respect to all model vectors $(\mathbf{m}_1, \mathbf{m}_2, ..., \mathbf{m}_N, \mathbf{s})$, and set the result to zero:

$$\sum_{i=1}^{N} \frac{\partial}{\partial \mathbf{m}_i}||\mathbf{A}_i\mathbf{m}_i - \mathbf{d}_i||^2 + \lambda^2 \frac{\partial}{\partial \mathbf{s}}||\mathbf{R}\mathbf{s}||^2 = 0; \qquad \text{(A5)}$$

From which we obtain the following normal equations:

$$\sum_{i=1}^{N} \mathbf{A}_i^T\mathbf{A}_i\mathbf{m}_i + \lambda^2\mathbf{R}^T\mathbf{R}\mathbf{s} = \sum_{i=1}^{N} \mathbf{A}_i^T\mathbf{d}_i ; \qquad \text{(A6)}$$

Let $\mathbf{A}$ be a matrix that contains all of our $\mathbf{A}_i$'s [equation (A2)] such that:

$$\mathbf{A} = \alpha_{k,l}, \qquad \text{(A7)}$$

here $\alpha_{k,l}$ are the elements of $\mathbf{A}$ with row k and column l. From here on we will use k and l to denote respectively row and column indices of any matrix. Its only nonzero elements are

$$\alpha_{x+n(i-1),2i-1} = -\pi f_x \Delta t_i, \ 1 < x < n \qquad \text{(A8)}$$

and

$$\alpha_{x+n(i-1),2i} = 1, \ 1 < x < n \qquad \text{(A9)}$$

where $1 < i < N$ and maps elements from $\mathbf{A}$ to the corresponding i^th trace combination. The index x scans over frequency samples. The matrix $\mathbf{A}$ has N times n (Nn) rows and $2N$ columns, and contains the information from the forward operators of all trace pair combinations. With $\mathbf{A}$ we can set up a linear system:

$$\mathbf{A} = \mathbf{m}\mathbf{d} \qquad \text{(A10)}$$

where $\mathbf{m}$ contains all model matrices $\mathbf{m}_i$ and $\mathbf{d}$ contains all data matrices $\mathbf{d}_i$.

Now, to go from the normal equation in equation (A6) to the final form of the pseudo-inverse solution, let's rewrite the matrices $\mathbf{A}_i$, $\mathbf{m}_i$ and $\mathbf{d}_i$ in the following manner:

$$\mathbf{A}_i = \mathbf{\Gamma}_i\mathbf{A}, \qquad \text{(A11)}$$

$$\mathbf{m}_i = \mathbf{\Omega}_i\mathbf{m}, \qquad \text{(A12)}$$

$$\mathbf{d}_i = \mathbf{\Gamma}_i\mathbf{d}, \qquad \text{(A13)}$$

where

$$\mathbf{\Gamma}_i = \gamma_{k,l}, \qquad \text{(A14)}$$

$$\mathbf{\Omega}_i = \omega_{k,l}, \qquad \text{(A15)}$$

with nonzero elements

$$\gamma_{x+n(i-1),x+n(i-1)} = 1;\ 1 < x < n\,,\ 1 < i < N \quad \text{(A16)}$$

$$\omega_{2i-1,2i} = 1;\ 1 < i < N \quad \text{(A17)}$$

both $\mathbf{\Gamma}_i$ and $\mathbf{\Omega}_i$ are square matrices of dimensions Nn and $2N$, respectively. Thus our new $\mathbf{A}_i$'s dimensions are $Nn \times 2N$, $\mathbf{m}_i$ is now $2N \times 1$ and $\mathbf{d}_i$ is $Nn \times 1$. Also, with the objective of designing the pseudo-inverse operator, we can simply replace $\mathbf{s}$ by $\mathbf{m}$, and make sure $\mathbf{R}$ only operates on the slope terms by setting his elements that correspond to intercept terms to zero. This way, we can use equation (A12) and equation (A13) to rewrite equation (A6):

$$(\sum_{i=1}^{N} \mathbf{A}_i^T \mathbf{A}_i \mathbf{\Omega}_i)\mathbf{m} + \lambda^2 \mathbf{R}^T \mathbf{R}\mathbf{m} = (\sum_{i=1}^{N} \mathbf{A}_i^T \mathbf{\Gamma}_i)\mathbf{d}\,; \quad \text{(A18)}$$

From equation (A11) and equation (A16), the sum of all $\mathbf{A}_i$ over N results in $\mathbf{A}$. Likewise, summing $\mathbf{\Omega}_i$ and $\mathbf{\Gamma}_i$ over N results in identity matrices. When then get:

$$\mathbf{A}^T \mathbf{A}\mathbf{m} + \lambda^2 \mathbf{R}^T \mathbf{R}\mathbf{m} = \mathbf{A}^T \mathbf{d}\,; \quad \text{(A19)}$$

From which we obtain the pseudo-inverse solution:

$$\mathbf{m}^\dagger = (\mathbf{A}^T \mathbf{A} + \lambda^2 \mathbf{R}^T \mathbf{R})^{-1} \mathbf{A}^T \mathbf{d}. \quad \text{(A20)}$$

To provide an example of the regularization operator $\mathbf{R}$, let us consider:

$$\mathbf{R} = \begin{pmatrix} 1-\frac{1}{N} & 0 & -\frac{1}{N} & 0 & \dots & 0 & -\frac{1}{N} \\ -\frac{1}{N} & 0 & 1-\frac{1}{N} & 0 & \dots & 0 & -\frac{1}{N} \\ \cdot & \cdot & \cdot & \cdot & \cdot & \cdot & \cdot \\ \cdot & \cdot & \cdot & \cdot & \cdot & \cdot & \cdot \\ -\frac{1}{N} & 0 & -\frac{1}{N} & 0 & \dots & 0 & 1-\frac{1}{N} \end{pmatrix}. \quad \text{(A21)}$$

This would be the regularization operator to be used if we choose to penalize the norm of the residuals from the mean of the model parameters. All the zeros in equation (A21) correspond to the intercept terms in $\mathbf{m}$.

APPENDIX B: TRANSFER FUNCTIONS OF SOURCE AND RECEIVER ARRAYS

Let us consider an array geometry according to Figure A1. From such geometry, we can define the quantities $R = |\vec{r} - \vec{c}|$ and $d(\vec{p}) = |\vec{p} - \vec{c}|$. If we simply stack the responses of the array components, then the total displacement $\vec{u}$ of the array:

$$\vec{u}(\omega, \vec{r}) = S(\omega) \int_C G(\vec{r}, \vec{p}) d\vec{p} \quad \text{(B1)}$$

where $S(\omega)$ is the source function in the frequency domain, and $G(\vec{r}, \vec{p})$ is the Green's function of the medium between $\vec{r}$ and $\vec{p}$. C is a closed contour (away from the origin) over which array elements are placed.

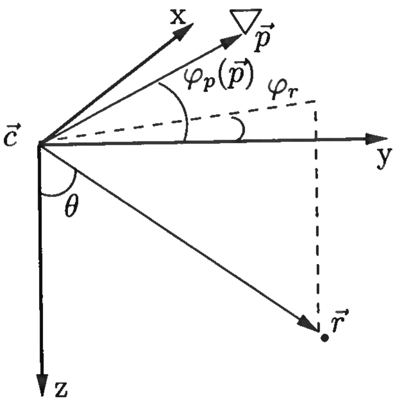

Figure A1. The array geometry used to derive the array's transfer function. An array centered at $\vec{c}$ has n array components with position denoted by $\vec{p}$. The array records an arrival from $\vec{r}$ that makes an emergence angle θ with the vertical. The array element at $\vec{p}$ makes an angle of φ_p with the x-axis, and $\vec{r}$ makes an angle of φ_r.

For a point force source in a homogeneous, isotropic medium:

$$G(\vec{r}, \vec{p}) = \frac{e^{ik|\vec{r} + d(\vec{p})\mathbf{x}_1(\vec{p})|}}{|\vec{r} + d(\vec{p})\mathbf{x}_1(\vec{p})|}, \quad \text{(B2)}$$

k being wavenumber, and $\mathbf{x}_1(\vec{p})$ is a unit vector with the same orientation as $\vec{p} - \vec{c}$. For convenience, in equation (B2) we set the array center $\vec{c}$ to the origin of the coordinate frame. Then putting equation (B2) in equation (B1) we get:

$$\vec{u}(\omega, \vec{r}) = S(\omega) \int_C \frac{e^{ik|\vec{r} + d(\vec{p})\mathbf{x}_1(\vec{p})|}}{|\vec{r} + d(\vec{p})\mathbf{x}_1(\vec{p})|} d\vec{p}; \quad \text{(B3)}$$

and, if we assume $R >> d(\vec{p})$:

$$\vec{u}(\omega, \vec{r}) = \frac{S(\omega)}{R} \int_C e^{ik|\vec{r} + d(\vec{p})\mathbf{x}_1(\vec{p})|} d\vec{p} \quad \text{(B4)}$$

Now, we can write

$$|\vec{r} + d(\vec{p})\mathbf{x}_1(\vec{p})|^2 = R^2 + 2d(\vec{p})[\vec{r}.\mathbf{x}_1] + d^2(\vec{p}), \quad \text{(B5)}$$

with

$$\vec{r}.\mathbf{x}_1 = R\, sin\theta\, cos(\varphi_p(\vec{p}) - \varphi_r). \quad \text{(B6)}$$

Because $R >> d(\vec{p})$ we can drop the term quadratic on $d(\vec{p})$. Next, by taking the square root of equation (B5) and performing a Taylor expansion of the radical on the right-hand side we get:

$$|\vec{r} + d(\vec{p})\mathbf{x}_1(\vec{p})|^2 = R + d(\vec{p})\, sin\theta\, cos(\varphi_p(\vec{p}) - \varphi_r). \quad \text{(B7)}$$

Which, if replaced in equation (B4), gives:

$$\vec{u}(\omega, \vec{r}) = S(\omega) \frac{e^{ikR}}{R} \int_C e^{ikd(\vec{p})\, sin\theta\, cos(\varphi_p(\vec{p}) - \varphi_r)} d\vec{p} \quad \text{(B8)}$$

or

$$\vec{u}(\omega, \vec{r}) = S(\omega)\, G(\vec{r}, \vec{c})\, T(\omega). \quad \text{(B9)}$$

Equation (B8) represents the total displacement $\vec{u}$ in terms of the source function $S(\omega)$, the Green's function at the center of the array $G(\vec{r}, \vec{c})$ and the transfer function of the array:

$$T(\omega) = \int_C e^{ikd(\vec{p})\, sin\theta\, cos(\varphi_p(\vec{p}) - \varphi_r)} d\vec{p}, \qquad \text{(B10)}$$

or simply,

$$T(\omega) = 1 + \int_C e^{ikd(\vec{p})\, sin\theta\, cos(\varphi_p(\vec{p}) - \varphi_r)} d\vec{p}, \qquad \text{(B11)}$$

for an array with a component in its center. From equation (B10) we can see that if $d(\vec{p})$ is constant and the array geometry is such that for an array component with a given azimuth φ_p there is another component with azimuth $\varphi_p + \pi$ (i.e. C is symmetric with respect to the coordinate axes in the surface plane), $T(\omega)$ is a purely real function. The consequence of this is that there are only amplitude distortions related to stacking the response of array components, while arrival phases suffer no distortions. This is the case for the geometries in the East Decatur field data.

To incorporate the effects of both the source transfer function $T_s(\omega)$ and the receiver's $T_r(\omega)$ into the source-receiver array function $T_s r(\omega)$ we simply take the product:

$$T(\omega) = T_s(\omega)\, T_r(\omega), \qquad \text{(B12)}$$

with, for example,

$$T_r(\omega) = \int_{C_r} e^{ikd_r\, sin\theta\, cos(\varphi_{p_r}(\vec{p_r}) - \varphi_r)} d\vec{p_r}, \qquad \text{(B13)}$$

$$T_s(\omega) = 1 + \int_{C_s} e^{ikd_s\, sin\theta\, cos(\varphi_{p_s}(\vec{p_s}) - \varphi_r - \pi)} d\vec{p_s}, \qquad \text{(B14)}$$

these being the transfer functions to be used for East Decatur field geometries. The distance $d(\vec{p})$ is constant for both source d_s and receiver d_r. Since $\vec{r}$ is between the source and receiver, we add $-\pi$ to the argument of the cosine in the exponential of either the source or receiver array transfer function, in this case, to $T_s(\omega)$.

Plane-wave attenuation anisotropy in orthorhombic media

Yaping Zhu and Ilya Tsvankin
Center for Wave Phenomena, Department of Geophysics, Colorado School of Mines, Golden, CO 80401

ABSTRACT

Orthorhombic velocity and attenuation models are needed in the interpretation of the azimuthal variation of seismic signatures recorded over fractured reservoirs. Here, we develop an analytic framework for describing the attenuation coefficients in orthorhombic media with orthorhombic attenuation (i.e., the symmetry of both the real and imaginary parts of the stiffness tensor is orthorhombic).

The analogous form of the Christoffel equation in the symmetry planes of orthorhombic and VTI (transversely isotropic with a vertical symmetry axis) media helps to obtain the symmetry-plane attenuation coefficients by adapting the existing VTI equations. To take full advantage of this equivalence with transverse isotropy, we introduce a set of attenuation-anisotropy parameters similar to the VTI parameters ϵ_Q, δ_Q, and γ_Q. This notation, based on the same principle as Tsvankin's velocity-anisotropy parameters for orthorhombic media, leads to simple linearized equations for the symmetry-plane attenuation coefficients of all three modes (P, S_1, and S_2).

The attenuation-anisotropy parameters also allow us to simplify the P-wave attenuation coefficient $\mathcal{A}_P$ outside the symmetry planes under the assumption of weak attenuation and weak velocity and attenuation anisotropy. The approximate $\mathcal{A}_P$ has the same form as the linearized phase-velocity function, with Tsvankin's velocity parameters $\epsilon^{(1,2)}$ and $\delta^{(1,2,3)}$ replaced by the attenuation parameters $\epsilon_Q^{(1,2)}$ and $\delta_Q^{(1,2,3)}$. The exact attenuation coefficient $\mathcal{A}_P$, however, also depends on the velocity-anisotropy parameters, while the body-wave velocities are almost unperturbed by the presence of attenuation.

The reduction in the number of parameters responsible for the P-wave attenuation and the simple approximation for the coefficient $\mathcal{A}_P$ provide a basis for inverting P-wave attenuation measurements from orthorhombic media. The attenuation processing has to be preceded by anisotropic velocity analysis that can be performed (in the absence of pronounced velocity dispersion) using existing algorithms for nonattenuative media.

Key words: attenuation, orthorhombic symmetry, anisotropy parameters, plane waves, linearized approximation

1 INTRODUCTION

Effective velocity models of fractured reservoirs often have orthorhombic or an even lower symmetry (Schoenberg and Helbig, 1997; Bakulin et al., 2000). It is likely that polar and azimuthal velocity variations in orthorhombic formations are accompanied by directionally dependent attenuation. Indeed, systems of aligned fractures or pores are among the most common physical reasons for anisotropic attenuation (e.g., Mavko and Nur, 1979; Akbar, 1993; Pointer et al., 1996).

Physical modeling shows that the P-wave attenuation coefficient in the direction perpendicular to aligned pores or fractures is higher than that parallel to the pores (Akbar, 1993). Similar results were obtained by Zhu and Tsvankin (2005b) for a synthetic material, in which thin layers of paper bonded with phenolic resin (i.e., aligned heterogeneities) create extremely strong attenuation anisotropy. Pointer et al. (1996) found that significant dissipation of energy is caused by the movement of fluids in interconnected pathways (crack-pore networks). The relationship between the azimuthal variation of attenuation and horizontal permeability measured over a fractured reservoir was discussed by Lynn et al. (1999). On the whole, existing experimental data indicate that both velocity and attenuation in fractured rocks vary with angle, with the type and magnitude of the anisotropy controlled by such factors as the shape, distribution, and orientation of aligned fractures and pores.

When the dominant wavelength is much larger than the characteristic size of heterogeneities, the scattering phenomena can be ignored, and the medium can be treated as effectively homogeneous. This paper is devoted to the attenuation of plane waves propagating in a homogeneous medium that has orthorhombic symmetry for both the velocity function and attenuation coefficient. As in our previous work on transversely isotropic (TI) media (Zhu and Tsvankin, 2004, 2005a,b), we study the *normalized* attenuation coefficient defined as

$$\mathcal{A} \equiv \frac{k^I}{k}\,, \tag{1}$$

where k and k^I are the real and the imaginary parts of the wavenumber, respectively. The coefficient $\mathcal{A}$ determines the rate of the amplitude decay per wavelength. The two main assumptions used here to simplify the analytic description of attenuation are as follows:

1) Wave propagation is "homogeneous," which means that the real and the imaginary parts of the wave vector are parallel to each other ($\mathbf{k}^I \parallel \mathbf{k}$).

2) The symmetry of the imaginary part of the stiffness matrix (or stiffness tensor) coincides with that of the real part. This assumption ensures that the quality-factor matrix $\mathbf{Q}$ (Carcione, 2001; Zhu and Tsvankin, 2004, 2005a) has the same structure as the real part of the stiffness matrix that governs the velocity anisotropy.

The main challenge in describing the attenuation anisotropy in orthorhombic materials is in the large number of parameters that control the attenuation coefficients. Because of the coupling between the velocity and attenuation anisotropy, the coefficient $\mathcal{A}$ depends (for a fixed orientation of the symmetry planes) on the nine real stiffness coefficients and nine elements of the quality matrix. Here, we show that significant simplifications can be achieved by extending the principle of Tsvankin's (1997, 2001) notation for velocity anisotropy to attenuative orthorhombic media.

The equivalence between the complex Christoffel equation in the symmetry planes of orthorhombic and VTI (TI with a vertical symmetry axis) media makes it possible to obtain the symmetry-plane attenuation coefficients from the corresponding VTI equations. As shown by Zhu and Tsvankin (2004, 2005a), attenuation anisotropy in VTI media can be conveniently described by the Thomsen-style parameters ϵ_Q, δ_Q, and γ_Q. Adapting the results of Zhu and Tsvankin (2004, 2005a) for the symmetry planes of orthorhombic media, we introduce a set of seven anisotropy parameters that fully characterizes (in combination with the velocity parameters) directionally-dependent attenuation in orthorhombic materials. Linearizing the P-wave attenuation coefficient in the limit of weak attenuation and weak anisotropy yields a simple expression outside the symmetry planes that has the same form as Tsvankin's (1997, 2001) weak-anisotropy approximation for the velocity function. The accuracy of the approximate attenuation coefficient is verified using numerical tests for models with substantial attenuation and velocity anisotropy.

2 CHRISTOFFEL EQUATION FOR ATTENUATIVE ORTHORHOMBIC MEDIA

A harmonic plane wave propagating in an attenuative medium has the form

$$\tilde{\mathbf{u}} = \tilde{\mathbf{U}} \exp\left[i(\omega t - \tilde{\mathbf{k}}\mathbf{x})\right], \tag{2}$$

where $\tilde{\mathbf{U}}$ is the polarization vector, and $\tilde{\mathbf{k}} = \mathbf{k} - i\mathbf{k}^I$ is the wave vector (both vectors are complex). We consider plane-wave propagation in orthorhombic media with orthorhombic attenuation, which means that the symmetry of the imaginary part of the stiffness matrix is identical to that of the real part. Then it is convenient to choose a Cartesian coordinate system aligned with the "natural" coordinate frame of the model, so that each coordinate plane coincides with one of the symmetry planes.

Substituting the plane wave (2) into the wave equation yields the following Christoffel equation:

$$\begin{bmatrix} \tilde{c}_{11}\tilde{k}_1^2 + \tilde{c}_{66}\tilde{k}_2^2 + \tilde{c}_{55}\tilde{k}_3^2 - \rho\omega^2 & (\tilde{c}_{12} + \tilde{c}_{66})\tilde{k}_1\tilde{k}_2 & (\tilde{c}_{13} + \tilde{c}_{55})\tilde{k}_1\tilde{k}_3 \\ (\tilde{c}_{12} + \tilde{c}_{66})\tilde{k}_1\tilde{k}_2 & \tilde{c}_{66}\tilde{k}_1^2 + \tilde{c}_{22}\tilde{k}_2^2 + \tilde{c}_{44}\tilde{k}_3^2 - \rho\omega^2 & (\tilde{c}_{23} + \tilde{c}_{44})\tilde{k}_2\tilde{k}_3 \\ (\tilde{c}_{13} + \tilde{c}_{55})\tilde{k}_1\tilde{k}_3 & (\tilde{c}_{23} + \tilde{c}_{44})\tilde{k}_2\tilde{k}_3 & \tilde{c}_{55}\tilde{k}_1^2 + \tilde{c}_{44}\tilde{k}_2^2 + \tilde{c}_{33}\tilde{k}_3^2 - \rho\omega^2 \end{bmatrix} \cdot \begin{Bmatrix} \tilde{U}_1 \\ \tilde{U}_2 \\ \tilde{U}_3 \end{Bmatrix} = 0\,, \tag{3}$$

where $\tilde{c}_{ij} = c_{ij} + ic^I_{ij}$ is the complex stiffness coefficient. Following Carcione (2001) and Zhu and Tsvankin (2004), the elements of the quality-factor matrix can be defined as (no index summation is implied)

$$Q_{ij} \equiv \frac{c_{ij}}{c^I_{ij}} \,. \tag{4}$$

Assuming homogeneous wave propagation ($\mathbf{k} \parallel \mathbf{k}^I$), the wave vector can be expressed through the unit vector $\mathbf{n}$ in the slowness direction: $\tilde{\mathbf{k}} = \mathbf{n}\,\tilde{k}$. Then the Christoffel equation (3) becomes

$$\left[\tilde{G}_{ij} - \rho \tilde{V}^2 \delta_{ik}\right] \tilde{U}_k = 0 \,, \tag{5}$$

where $\tilde{V} = \frac{\omega}{\tilde{k}}$ is the complex phase velocity, and $\tilde{G}_{ij}$ are the elements of the complex Christoffel matrix:

$$\begin{aligned}
\tilde{G}_{11} &= \tilde{c}_{11} n_1^2 + \tilde{c}_{66} n_2^2 + \tilde{c}_{55} n_3^2 \,,\\
\tilde{G}_{22} &= \tilde{c}_{66} n_1^2 + \tilde{c}_{22} n_2^2 + \tilde{c}_{44} n_3^2 \,,\\
\tilde{G}_{33} &= \tilde{c}_{55} n_1^2 + \tilde{c}_{44} n_2^2 + \tilde{c}_{33} n_3^2 \,,\\
\tilde{G}_{12} &= (\tilde{c}_{12} + \tilde{c}_{66}) n_1 n_2 \,,\\
\tilde{G}_{13} &= (\tilde{c}_{13} + \tilde{c}_{55}) n_1 n_3 \,,\\
\tilde{G}_{23} &= (\tilde{c}_{23} + \tilde{c}_{44}) n_2 n_3 \,.
\end{aligned} \tag{6}$$

The components of the unit slowness (phase) vector $\mathbf{n}$ can be expressed through the polar phase angle θ and the azimuthal phase angle ϕ: $n_1 = \sin\theta\cos\phi$, $n_2 = \sin\theta\sin\phi$, $n_3 = \cos\theta$.

Note that although equation (5) has the same form as the Christoffel equation in nonattenuative (purely elastic) orthorhombic media, the velocity, polarization and stiffnesses are complex. As a result, plane-wave propagation in attenuative media is described by two coupled equations obtained by separating the real and imaginary parts of the Christoffel equation.

3 ATTENUATION COEFFICIENTS IN THE SYMMETRY PLANES

Suppose that the plane wave (2) propagates in the $[x_1, x_3]$-plane, so $n_1 = \sin\theta$, $n_2 = 0$, and $n_3 = \cos\theta$. Then the Christoffel equation (3) simplifies to

$$\begin{bmatrix}
\tilde{c}_{11}\tilde{k}_1^2 + \tilde{c}_{55}\tilde{k}_3^2 - \rho\omega^2 & 0 & (\tilde{c}_{13} + \tilde{c}_{55})\tilde{k}_1\tilde{k}_3 \\
0 & \tilde{c}_{66}\tilde{k}_1^2 + \tilde{c}_{44}\tilde{k}_3^2 - \rho\omega^2 & 0 \\
(\tilde{c}_{13} + \tilde{c}_{55})\tilde{k}_1\tilde{k}_3 & 0 & \tilde{c}_{55}\tilde{k}_1^2 + \tilde{c}_{33}\tilde{k}_3^2 - \rho\omega^2
\end{bmatrix}
\begin{Bmatrix} \tilde{U}_1 \\ \tilde{U}_2 \\ \tilde{U}_3 \end{Bmatrix} = 0 \,. \tag{7}$$

Equation (7) has the same form as the Christoffel equation for VTI media with VTI attenuation discussed in detail by Zhu and Tsvankin (2004, 2005a). The only difference between the two equations is that while for VTI media $\tilde{c}_{44} = \tilde{c}_{55}$, that is generally not the case for orthorhombic symmetry. However, the stiffness $\tilde{c}_{44}$ influences only the SH-wave polarized perpendicular to the propagation plane (see below),while $\tilde{c}_{55}$ contributes to the velocity and attenuation of the in-plane polarized waves (P and SV). Therefore, the well-known equivalence between the Christoffel equation in purely elastic VTI media and symmetry planes of orthorhombic media (e.g., Tsvankin, 1997, 2001) holds for attenuative models with the same symmetries of the real and imaginary parts of stiffness tensor.

Since the Christoffel matrix for wave propagation in the $[x_1, x_3]$-plane has four vanishing elements, equation (7) splits into two separate equations, one for the SH-wave polarized in the x_2-direction (the displacement component $\tilde{U}_2$), and the other for the in-plane polarized P- and SV-waves (the components $\tilde{U}_1$ and $\tilde{U}_3$). The solutions for the velocity and attenuation of all three modes can be obtained by simply adapting the results of Zhu and Tsvankin (2004, 2005a) for VTI media.

Assuming homogeneous wave propagation ($\tilde{\mathbf{k}} = \mathbf{n}\,\tilde{k}$), the Christoffel equation for the SH-wave takes the form

$$\left(\tilde{c}_{66}\sin^2\theta + \tilde{c}_{44}\cos^2\theta\right)\tilde{k}^2 - \rho\omega^2 = 0 \,. \tag{8}$$

Using the VTI result of Zhu and Tsvankin (2004, 2005a), the normalized attenuation coefficient of SH-waves in the $[x_1, x_3]$-plane can be obtained from equation (8) as

$$\mathcal{A}_{SH}^{(2)} = \sqrt{1 + (Q_{44}\,\alpha^{(2)})^2} - Q_{44}\,\alpha^{(2)} \,, \tag{9}$$

where the superscript (2) stands for the x_2-axis orthogonal to the propagation plane (the same convention as in

Tsvankin, 1997, 2001), and

$$\alpha^{(2)} \equiv \frac{(1+2\gamma^{(2)})\sin^2\theta+\cos^2\theta}{(1+2\gamma^{(2)})\dfrac{Q_{44}}{Q_{66}}\sin^2\theta+\cos^2\theta}\,.$$

For P- and SV-waves in the regime of homogeneous wave propagation, equation (7) reduces to

$$\begin{bmatrix} \left(\tilde{c}_{11}\sin^2\theta+\tilde{c}_{55}\cos^2\theta\right)\tilde{k}^2-\rho\omega^2 & (\tilde{c}_{13}+\tilde{c}_{55})\sin\theta\cos\theta\,\tilde{k}^2 \\ (\tilde{c}_{13}+\tilde{c}_{55})\sin\theta\cos\theta\,\tilde{k}^2 & \left(\tilde{c}_{55}\sin^2\theta+\tilde{c}_{33}\cos^2\theta\right)\tilde{k}^2-\rho\omega^2 \end{bmatrix} \begin{Bmatrix} \tilde{U}_1 \\ \tilde{U}_3 \end{Bmatrix} = 0\,. \tag{10}$$

The wavenumber obtained from equation (10) is described by an expression analogous to that in nonattenuative VTI media (e.g., Tsvankin, 2001):

$$\tilde{k} = \omega\sqrt{2\rho}\,\Big\{(\tilde{c}_{11}+\tilde{c}_{55})\sin^2\theta+(\tilde{c}_{33}+\tilde{c}_{55})\cos^2\theta \pm \sqrt{\left[(\tilde{c}_{11}-\tilde{c}_{55})\sin^2\theta-(\tilde{c}_{33}-\tilde{c}_{55})\cos^2\theta\right]^2+4(\tilde{c}_{13}+\tilde{c}_{55})^2\sin^2\theta\cos^2\theta}\Big\}^{-1/2}\,. \tag{11}$$

The normalized attenuation coefficients $\mathcal{A}^{(2)}_{P,SV}$ were derived from the complex part of equation (11) by Zhu and Tsvankin (2004, 2005a). For example, the P-wave coefficients $\mathcal{A}^{(2)}_{P}$ in the vertical and horizontal directions are given by

$$\mathcal{A}^{(2)}_{P}(\theta=0^\circ) = Q_{33}\left(\sqrt{1+1/Q_{33}^2}-1\right) \approx \frac{1}{2Q_{33}}, \tag{12}$$

$$\mathcal{A}^{(2)}_{P}(\theta=90^\circ) = Q_{11}\left(\sqrt{1+1/Q_{11}^2}-1\right) \approx \frac{1}{2Q_{11}}\,. \tag{13}$$

The SV-wave attenuation coefficient in both the vertical and horizontal directions is

$$\mathcal{A}^{(2)}_{SV}(\theta=0^\circ) = \mathcal{A}^{(2)}_{SV}(\theta=90^\circ) = Q_{55}\left(\sqrt{1+1/Q_{55}^2}-1\right) \approx \frac{1}{2Q_{55}}\,. \tag{14}$$

For plane-wave propagation in the $[x_2,x_3]$-plane ($n_1=0$, $n_2=\sin\theta$, and $n_3=\cos\theta$), the Christoffel equation (3) gives

$$\begin{bmatrix} \tilde{c}_{66}\tilde{k}_1^2+\tilde{c}_{55}\tilde{k}_3^2-\rho\omega^2 & 0 & 0 \\ 0 & \tilde{c}_{22}\tilde{k}_1^2+\tilde{c}_{44}\tilde{k}_3^2-\rho\omega^2 & (\tilde{c}_{23}+\tilde{c}_{44})\tilde{k}_1\tilde{k}_3 \\ 0 & (\tilde{c}_{23}+\tilde{c}_{44})\tilde{k}_1\tilde{k}_3 & \tilde{c}_{44}\tilde{k}_1^2+\tilde{c}_{33}\tilde{k}_3^2-\rho\omega^2 \end{bmatrix} \begin{Bmatrix} \tilde{U}_1 \\ \tilde{U}_2 \\ \tilde{U}_3 \end{Bmatrix} = 0\,. \tag{15}$$

The SH-wave, which is polarized in the x_1-direction, is described by the element $\tilde{c}_{66}\tilde{k}_1^2+\tilde{c}_{55}\tilde{k}_3^2-\rho\omega^2$ of the matrix in equation (15). It is clear from equations (7) and (15) that both the velocity and attenuation of the SH-wave can be obtained from the corresponding equations for the $[x_1,x_3]$-plane (or VTI media) by making the substitution $4 \rightarrow 5$ in the subscripts of the stiffnesses and elements Q_{ij}. For example, the normalized attenuation coefficient for homogeneous SH-wave propagation can be adapted from equation (9):

$$\mathcal{A}^{(1)}_{SH} = \sqrt{1+(Q_{55}\,\alpha^{(1)})^2}-Q_{55}\,\alpha^{(1)}\,, \tag{16}$$

where

$$\alpha^{(1)} \equiv \frac{(1+2\gamma^{(1)})\sin^2\theta+\cos^2\theta}{(1+2\gamma^{(1)})\dfrac{Q_{55}}{Q_{66}}\sin^2\theta+\cos^2\theta}\,.$$

The velocity and attenuation of P- and SV-waves in the $[x_2,x_3]$-plane are described by (for homogeneous wave propagation)

$$\begin{bmatrix} \left(\tilde{c}_{22}\sin^2\theta+\tilde{c}_{44}\cos^2\theta\right)\tilde{k}^2-\rho\omega^2 & (\tilde{c}_{23}+\tilde{c}_{44})\sin\theta\cos\theta\,\tilde{k}^2 \\ (\tilde{c}_{23}+\tilde{c}_{44})\sin\theta\cos\theta\,\tilde{k}^2 & \left(\tilde{c}_{44}\sin^2\theta+\tilde{c}_{33}\cos^2\theta\right)\tilde{k}^2-\rho\omega^2 \end{bmatrix} \begin{Bmatrix} \tilde{U}_2 \\ \tilde{U}_3 \end{Bmatrix} = 0\,. \tag{17}$$

The P- and SV-wave attenuation coefficients can be obtained from the equations for the $[x_1,x_3]$-plane using the following substitutions in the subscripts: $1 \rightarrow 2$ and $5 \rightarrow 4$.

The same substitutions were used by Tsvankin (1997, 2001) in his extension of the VTI velocity equations to the symmetry planes of orthorhombic media. The equivalence with vertical transverse isotropy is also valid for the complex Christoffel equation in the $[x_1,x_2]$ symmetry plane.

4 ATTENUATION-ANISOTROPY PARAMETERS

The Thomsen-style notation for velocity anisotropy suggested by Tsvankin (1997, 2001) helps to simplify the analytic description of a wide range of seismic signatures for orthorhombic media. Tsvankin's parameters provided a basis for developing efficient seismic inversion and processing methods operating with orthorhombic models (Grechka and Tsvankin, 1999; Grechka et al., 1999; Bakulin et al., 2000). Here, we extend his approach to attenuative orthorhombic media with the main goal of defining the parameter combinations that govern the directionally dependent attenuation coefficient.

Since our notation is designed primarily for reflection data, we choose the P- and S-wave attenuation coefficients in the vertical (x_3) direction ($\mathcal{A}_{P0}$ and $\mathcal{A}_{S0}$) as the reference isotropic quantities. The coefficient $\mathcal{A}_{S0}$ corresponds to the S-wave polarized in the x_1-direction, which may be either the fast or slow shear mode depending on the relationship between the stiffnesses c_{44} and c_{55}. According to equations (12) and (14), the approximate (accurate to the second order in $1/Q$) coefficients $\mathcal{A}_{P0}$ and $\mathcal{A}_{S0}$ are given by

$$\mathcal{A}_{P0} \equiv \frac{1}{2Q_{33}}, \tag{18}$$

$$\mathcal{A}_{S0} \equiv \frac{1}{2Q_{55}}. \tag{19}$$

To characterize the attenuation of waves propagating in the $[x_1, x_3]$-plane, we define three attenuation-anisotropy parameters analogous to the Thomsen-style parameters ϵ_Q, δ_Q, and γ_Q introduced for VTI media with VTI attenuation by Zhu and Tsvankin (2004, 2005a). The parameters $\epsilon_Q^{(2)}$ and $\gamma_Q^{(2)}$ (the superscript "(2)" stands for the x_2-axis perpendicular to the $[x_1, x_3]$-plane) determine the fractional difference between the normalized attenuation coefficients in the x_1- and x_3-directions for the P- and SH-waves, respectively. Another parameter, $\delta_Q^{(2)}$, is expressed through the second derivative of the P-wave attenuation coefficient in the vertical direction and, therefore, governs the P-wave attenuation for near-vertical propagation in the $[x_1, x_3]$-plane.

$$\epsilon_Q^{(2)} \equiv \frac{Q_{33} - Q_{11}}{Q_{11}}, \tag{20}$$

$$\delta_Q^{(2)} \equiv \frac{\frac{Q_{33} - Q_{55}}{Q_{55}} c_{55} \frac{(c_{13} + c_{33})^2}{(c_{33} - c_{55})} + 2\frac{Q_{33} - Q_{13}}{Q_{13}} c_{13}(c_{13} + c_{55})}{c_{33}(c_{33} - c_{55})} \tag{21}$$

$$\approx 4\,\frac{Q_{33} - Q_{55}}{Q_{55}}\, g^{(2)} + 2\,\frac{Q_{33} - Q_{13}}{Q_{13}} \left(1 + 2\delta^{(2)} - 2g^{(2)}\right), \tag{22}$$

$$\gamma_Q^{(2)} \equiv \frac{Q_{44} - Q_{66}}{Q_{66}}, \tag{23}$$

where equation (22) for $\delta_Q^{(2)}$ is simplified by assuming that the ratio $g^{(2)} \equiv \frac{c_{55}}{c_{33}}$ and the absolute value of Tsvankin's velocity-anisotropy parameter $\delta^{(2)}$ are small. Since the Christoffel equation in the $[x_1, x_3]$-plane has the same form as in VTI media, equations (20)–(23) are identical to the definitions of the corresponding VTI parameters. In contrast to VTI models, however, the parameters of orthorhombic media with the subscripts "55" and "44" are generally different, and one needs to use c_{55} and Q_{55} (not c_{44} or Q_{44}) in equation (21) and Q_{44} (not Q_{55}) in equation (23).

Similarly, we adapt the VTI definitions of Zhu and Tsvankin (2004, 2005a) to introduce three attenuation-anisotropy parameters in the $[x_2, x_3]$-plane:

$$\epsilon_Q^{(1)} \equiv \frac{Q_{33} - Q_{22}}{Q_{22}}, \tag{24}$$

$$\delta_Q^{(1)} \equiv \frac{\frac{Q_{33} - Q_{44}}{Q_{44}} c_{44} \frac{(c_{23} + c_{33})^2}{(c_{33} - c_{44})} + 2\frac{Q_{33} - Q_{23}}{Q_{23}} c_{23}(c_{23} + c_{44})}{c_{33}(c_{33} - c_{44})} \tag{25}$$

$$\approx 4\,\frac{Q_{33} - Q_{44}}{Q_{44}}\, g^{(1)} + 2\,\frac{Q_{33} - Q_{23}}{Q_{23}} \left(1 + 2\delta^{(1)} - 2g^{(1)}\right), \tag{26}$$

$$\gamma_Q^{(1)} \equiv \frac{Q_{55} - Q_{66}}{Q_{66}}. \tag{27}$$

In equation (26), $\delta^{(1)}$ is the velocity-anisotropy parameter defined in the $[x_2, x_3]$-plane (Tsvankin, 1997, 2001), and $g^{(1)} \equiv \frac{c_{44}}{c_{33}}$. Since the attenuation coefficient is supposed to be positive (otherwise, the amplitude will increase with distance), the diagonal components of the **Q** matrix have to be positive as well. This constraint implies the parameters $\epsilon_Q^{(1)}$, $\epsilon_Q^{(2)}$, $\gamma_Q^{(1)}$, and $\gamma_Q^{(2)}$ are always larger than -1.

The only component of the **Q**-matrix that is not involved in the definitions of the reference isotropic quantities and the attenuation-anisotropy parameters in the vertical symmetry planes is Q_{12}. Following the approach of Tsvankin (1997, 2001), we use Q_{12} to introduce one more anisotropy parameter, $\delta_Q^{(3)}$, which plays the role of the VTI parameter δ_Q in the $[x_1, x_2]$-plane (x_1 is treated as the symmetry axis of the equivalent VTI model):

$$\delta_Q^{(3)} \equiv \frac{\dfrac{Q_{11}-Q_{66}}{Q_{66}} c_{66} \dfrac{(c_{11}+c_{12})^2}{(c_{11}-c_{66})} + 2\dfrac{Q_{11}-Q_{12}}{Q_{12}} c_{12}(c_{12}+c_{66})}{c_{11}(c_{11}-c_{66})} \tag{28}$$

$$\approx 4\,\frac{Q_{11}-Q_{66}}{Q_{66}}\,g^{(3)} + 2\,\frac{Q_{11}-Q_{12}}{Q_{12}}\,(1+2\delta^{(3)}-2g^{(3)})\,, \tag{29}$$

where $\delta^{(3)}$ is another Tsvankin's velocity-anisotropy parameter defined in the $[x_1, x_2]$-plane, and $g^{(3)} \equiv \frac{c_{66}}{c_{11}}$. Although it is also possible to introduce the parameters $\epsilon_Q^{(3)}$ and $\gamma_Q^{(3)}$ in the $[x_1, x_2]$-plane, they would be redundant.

The nine attenuation-anisotropy parameters defined in equations (18)–(29), combined with Tsvankin's (1997, 2001) velocity-anisotropy parameters, are sufficient to fully characterize plane-wave attenuation in orthorhombic media. An additional practically important parameter responsible for the differential attenuation of the split S-waves in the vertical (x_3) direction is described in the next section.

5 APPROXIMATE ATTENUATION COEFFICIENTS IN THE SYMMETRY PLANES

The equivalence between plane-wave propagation in the symmetry planes of orthorhombic media and in VTI media means that the symmetry-plane attenuation coefficients of all three modes can be obtained by adapting the VTI equations of Zhu and Tsvankin (2004, 2005a). While the exact attenuation coefficients are rather complicated even for VTI models and do not provide insight into the influence of various attenuation-anisotropy parameters, much simpler solutions can be found under the following assumptions:

1. The magnitude of attenuation measured by the inverse Q_{ij} values or the parameters $\mathcal{A}_{P0}$ and $\mathcal{A}_{S0}$ is small.
2. Attenuation anisotropy is weak, which implies that the absolute values of all attenuation-anisotropy parameters introduced above are much smaller than unity.
3. Velocity anisotropy is also weak, so the absolute values of all Tsvankin's (1997, 2001) anisotropy parameters are much smaller than unity.

In limit of weak attenuation and small anisotropy parameters $\gamma^{(2)}$ and $\gamma_Q^{(2)}$ ($|\gamma^{(2)}| \ll 1$ and $|\gamma_Q^{(2)}| \ll 1$), the approximate SH-wave attenuation coefficient in the $[x_1, x_3]$-plane can be written as

$$\mathcal{A}_{SH}^{(2)} = \bar{\mathcal{A}}_{S0}\,(1+\gamma_Q^{(2)}\sin^2\theta)\,, \tag{30}$$

where

$$\bar{\mathcal{A}}_{S0} = \frac{1}{2Q_{44}} = \mathcal{A}_{S0}\,\frac{1+\gamma_Q^{(1)}}{1+\gamma_Q^{(2)}} \tag{31}$$

is the normalized attenuation coefficient for the vertically propagating shear wave polarized in the x_2-direction. Equation (30) is obtained by replacing the parameter γ_Q in the VTI result of Zhu and Tsvankin (2004, 2005a) by $\gamma_Q^{(2)}$ and using the appropriate isotropic reference value $\bar{\mathcal{A}}_{S0}$. Similarly, the corresponding linearized coefficient in the $[x_2, x_3]$-plane has the form

$$\mathcal{A}_{SH}^{(1)} = \mathcal{A}_{S0}\,(1+\gamma_Q^{(1)}\sin^2\theta)\,. \tag{32}$$

It should be emphasized that the term "SH-wave" refers to two different shear modes in the vertical symmetry planes (Tsvankin, 1997, 2001). For example, if $c_{44} > c_{55}$, then the fast shear wave S_1 represents an SH-wave in the $[x_1, x_3]$-plane where it is polarized in the x_2-direction. For wave propagation in the $[x_2, x_3]$-plane, however, the S_1-wave becomes an SV mode that has an in-plane polarization vector.

The difference between the attenuation coefficients of the vertically traveling split shear waves can be quantified by the *attenuation splitting parameter* $\gamma_Q^{(S)}$:

$$\gamma_Q^{(S)} \equiv \frac{\bar{\mathcal{A}}_{S0}-\mathcal{A}_{S0}}{\mathcal{A}_{S0}} = \frac{\gamma_Q^{(1)}-\gamma_Q^{(2)}}{1+\gamma_Q^{(2)}}\,. \tag{33}$$

The definition (33) is analogous to that of the widely used S-wave velocity splitting parameter $\gamma^{(S)}$ (Tsvankin, 1997, 2001). To keep the parameter $\gamma_Q^{(S)}$ positive, we assume that $\bar{\mathcal{A}}_{S0} > \mathcal{A}_{S0}$; otherwise, $\bar{\mathcal{A}}_{S0}$ and $\mathcal{A}_{S0}$ in equation (33) have to be switched. Although $\gamma_Q^{(S)}$ would be redundant as part of our notation for attenuative orthorhombic media, this parameter should play an important role in the attenuation analysis of reflection shear-wave data.

Substituting the attenuation-anisotropy parameters $\epsilon_Q^{(2)}$ and $\delta_Q^{(2)}$ into the VTI equations of Zhu and Tsvankin (2004, 2005a) yields the following approximate attenuation coefficients of the P- and SV-waves in the $[x_1, x_3]$-plane:

$$\mathcal{A}_P^{(2)} = \mathcal{A}_{P0}\left(1 + \delta_Q^{(2)} \sin^2\theta \cos^2\theta + \epsilon_Q^{(2)} \sin^4\theta\right), \tag{34}$$

$$\mathcal{A}_{SV}^{(2)} = \mathcal{A}_{S0}\left(1 + \sigma_Q^{(2)} \sin^2\theta \cos^2\theta\right), \tag{35}$$

where

$$\sigma_Q^{(2)} \equiv \frac{1}{g_Q^{(2)}}\left[2(1 - g_Q^{(2)})\,\sigma^{(2)} + \frac{\epsilon_Q^{(2)} - \delta_Q^{(2)}}{g^{(2)}}\right], \tag{36}$$

$g^{(2)} \equiv \dfrac{c_{55}}{c_{33}}$, $g_Q^{(2)} \equiv \dfrac{Q_{33}}{Q_{55}} = \dfrac{\mathcal{A}_{S0}}{\mathcal{A}_{P0}}$, and $\sigma^{(2)} \equiv \dfrac{\epsilon^{(2)} - \delta^{(2)}}{g^{(2)}}$. The approximate attenuation coefficients in equations (34) and (35) have exactly the same form as the corresponding linearized phase-velocity equations (Thomsen, 1986). However, as discussed by Zhu and Tsvankin (2004, 2005a), the dependence of the attenuation-anisotropy parameter $\delta_Q^{(2)}$ on the real parts of the stiffness coefficients reflects the coupling between the attenuation and velocity anisotropy. In contrast, the anisotropic phase-velocity function is practically independent of attenuation (see below).

The coefficients $\mathcal{A}_P^{(1)}$ and $\mathcal{A}_{SV}^{(1)}$ in the $[x_2, x_3]$-plane are obtained in the same way from the VTI results by using the attenuation-anisotropy parameters $\epsilon_Q^{(1)}$ and $\delta_Q^{(1)}$. For example,

$$\mathcal{A}_P^{(1)} = \mathcal{A}_{P0}\left(1 + \delta_Q^{(1)} \sin^2\theta \cos^2\theta + \epsilon_Q^{(1)} \sin^4\theta\right). \tag{37}$$

6 P-WAVE ATTENUATION OUTSIDE THE SYMMETRY PLANES

This section is devoted to the analysis of the P-wave attenuation coefficient for phase directions outside the symmetry planes. While the shear-wave attenuation coefficients can be studied numerically by solving the Christoffel equation, the area of validity of such plane-wave solutions in describing shear-wave amplitudes is significantly reduced because of the influence of point singularities (Crampin, 1991).

6.1 Influence of attenuation on phase velocity

As pointed out above, the attenuation coefficients depend not just on the quality-factor elements Q_{ij} but also on the velocity-anisotropy parameters. In contrast, the presence of attenuation has an almost negligible influence on the phase-velocity function. This result, discussed by Zhu and Tsvankin (2004, 2005a) for VTI media, remains valid for the symmetry planes of the orthorhombic model. Here, we demonstrate that attenuation-related distortions of phase velocity remain negligible outside the symmetry planes as well.

In the limit of weak attenuation ($\dfrac{1}{Q_{ij}} \ll 1$), the real part of the Christoffel equation (A-2) can be simplified by dropping terms quadratic in the inverse Q components. The resulting equation (A-3) is identical to the Christoffel equation for the reference nonattenuative medium, both within and outside the symmetry planes.

To evaluate the contribution of the higher-order attenuation terms, we compute the exact P-wave phase velocity for two orthorhombic models with strong attenuation. For the first model, the attenuation is isotropic with the uncommonly low quality factor $Q_{33} = Q_{55} = 10$ (Figure 1). Still, the maximum attenuation-related change in the phase velocity is limited to 0.5%, which is equal to $\dfrac{1}{2Q_{33}^2}$.

The second model has the same real part of the stiffness matrix, but this time accompanied by pronounced attenuation anisotropy (Figure 2). Although the deviation of the phase-velocity function from that in the reference nonattenuative medium increases away from the vertical, it remains insignificant (up to 1%) for the whole range of polar and azimuthal phase angles. Note, however, that this discussion does not take into account attenuation-related velocity dispersion.

Hence, seismic processing for orthorhombic media with orthorhombic attenuation can be divided into two steps. First, one can perform anisotropic velocity analysis and estimation of Tsvankin's parameters without taking attenuation into account (Grechka and Tsvankin, 1999; Grechka et al., 1999; Bakulin et al., 2000). Then the reconstructed

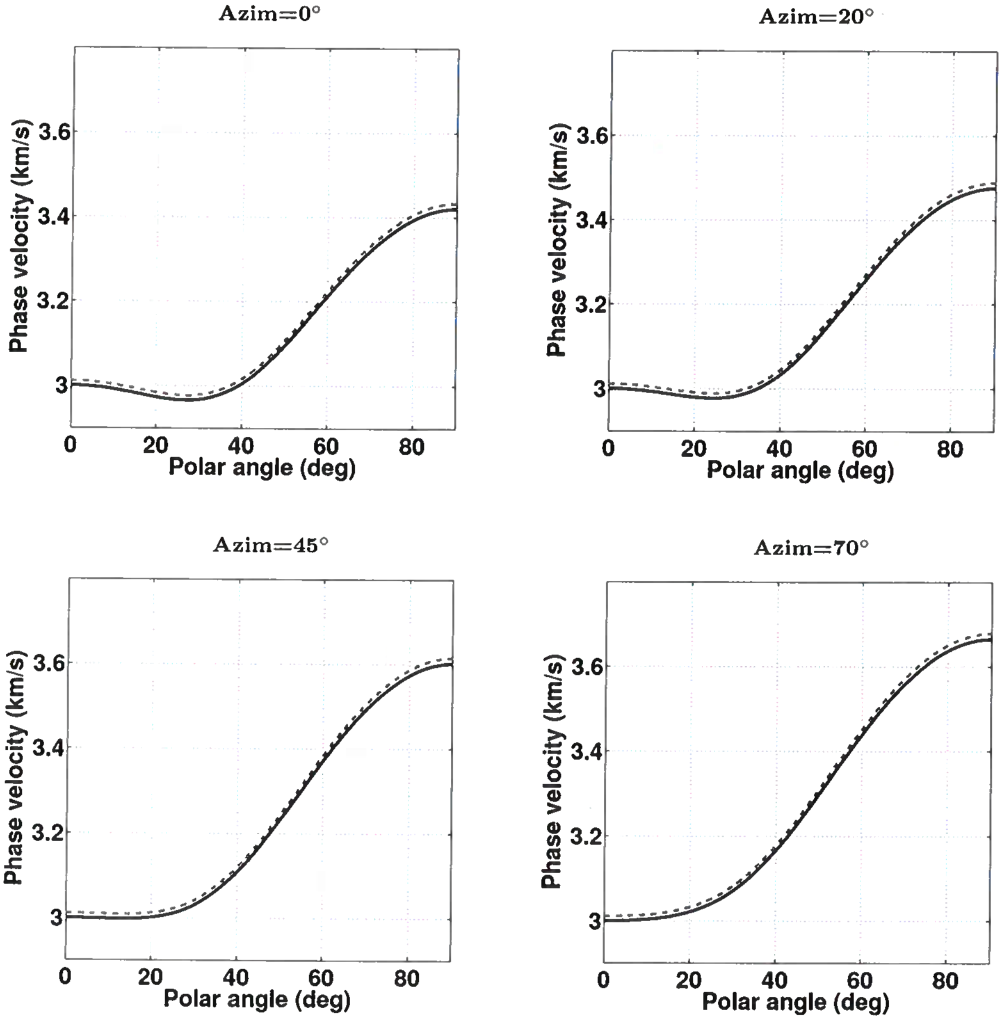

Figure 1. Influence of isotropic attenuation on the exact P-wave phase velocity computed from the Christoffel equation (5). Each plot corresponds to a fixed azimuthal phase angle. The solid curves mark the velocity for a nonattenuative orthorhombic model with the following Tsvankin's (1997, 2001) parameters: $V_{P0} = 3$ km/s, $V_{S0} = 1.5$ km/s, $\epsilon^{(1)} = 0.25$, $\epsilon^{(2)} = 0.15$, $\delta^{(1)} = 0.05$, $\delta^{(2)} = -0.1$, $\delta^{(3)} = 0.15$, $\gamma^{(1)} = 0.28$, and $\gamma^{(2)} = 0.15$. The dashed curves are computed for a model with the same velocity parameters and strong isotropic attenuation ($Q_{33} = Q_{55} = 10$; all attenuation-anisotropy parameters are set to zero).

anisotropic velocity model can be used in the processing of amplitude measurements and inversion for the attenuation-anisotropy parameters.

6.2 Approximate attenuation outside the symmetry planes

The linearized approximation for the P-wave attenuation coefficient can be extended for arbitrary propagation directions outside the symmetry plane under the assumption of weak attenuation and weak velocity and attenuation anisotropy. The approximate coefficient $\mathcal{A}_P$, expressed as a function of the polar phase angle θ and azimuthal phase angle ϕ, has the form (Appendix A)

$$\mathcal{A}_P(\theta,\phi) = \mathcal{A}_{P0}\left[1 + \delta_Q(\phi)\sin^2\theta\cos^2\theta + \epsilon_Q(\phi)\sin^4\theta\right] , \tag{38}$$

where

$$\epsilon_Q(\phi) = \epsilon_Q^{(1)}\sin^4\phi + \epsilon_Q^{(2)}\cos^4\phi + (2\epsilon_Q^{(2)} + \delta_Q^{(3)})\sin^2\phi\cos^2\phi , \tag{39}$$

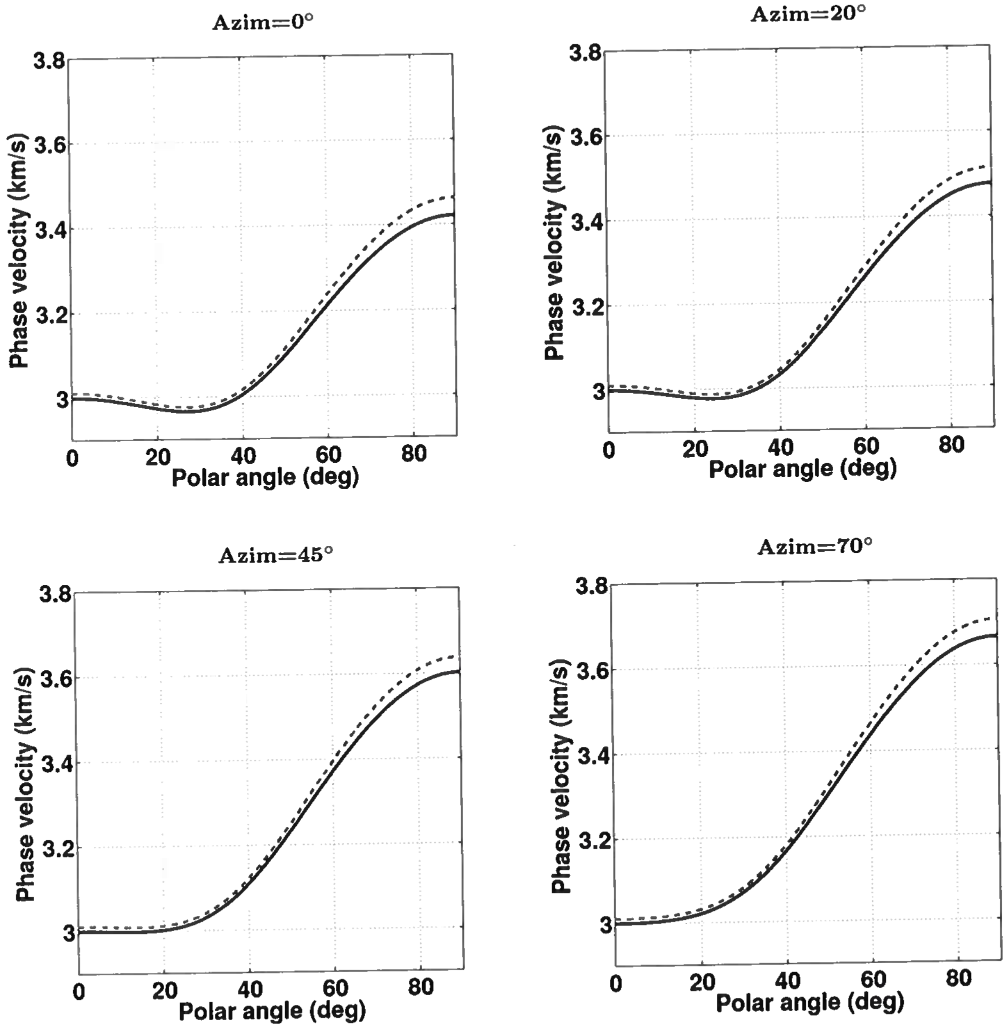
Azim=0°

Azim=20°

Azim=45°

Azim=70°

Figure 2. Influence of anisotropic attenuation on the exact P-wave phase velocity. The solid curves are the phase velocities for the nonattenuative orthorhombic model from Figure 1. The dashed curves are computed for a model with the same velocity parameters and strong orthorhombic attenuation: $Q_{33} = Q_{55} = 10$, $\epsilon_Q^{(1)} = \epsilon_Q^{(2)} = 0.8$, $\delta_Q^{(1)} = \delta_Q^{(2)} = \delta_Q^{(3)} = -0.5$, and $\gamma_Q^{(1)} = \gamma_Q^{(2)} = 0.8$.

$$\delta_Q(\phi) = \delta_Q^{(1)} \sin^2\phi + \delta_Q^{(2)} \cos^2\phi\,. \tag{40}$$

Evidently, the linearized P-wave attenuation coefficient in any vertical plane of orthorhombic media is described by the VTI equation (Zhu and Tsvankin, 2004, 2005a) with the azimuthally varying parameters $\epsilon_Q(\phi)$ and $\delta_Q(\phi)$. For wave propagation in the $[x_1, x_3]$-plane ($\phi = 0°$), $\epsilon_Q = \epsilon_Q^{(2)}$, $\delta_Q = \delta_Q^{(2)}$, and equation (38) reduces to equation (34). Similarly, for the $[x_2, x_3]$-plane ($\phi = 90°$), $\epsilon_Q = \epsilon_Q^{(1)}$, $\delta_Q = \delta_Q^{(1)}$, and equation (38) reduces to equation (37).

Remarkably, equations (38)–(40) have exactly the same form as the linearized P-wave phase-velocity equations (1.107)–(1.109) in Tsvankin (2001). This similarity is explained by the identical (orthorhombic) symmetry imposed on both the real and imaginary parts of the stiffness matrix and the assumption of homogeneous wave propagation. However, an important difference between the coefficient $\mathcal{A}_P$ and phase velocity is that the parameters $\delta_Q^{(1)}$, $\delta_Q^{(2)}$, and $\delta_Q^{(3)}$ include a contribution of the velocity anisotropy, while the velocity function is practically independent of attenuation. Also, as discussed below, the exact coefficient $\mathcal{A}_P$ is influenced by the velocity-anisotropy parameters even for fixed values of $\epsilon_Q^{(1,2)}$ and $\delta_Q^{(1,2,3)}$.

6.3 Attenuation for VTI and HTI media

Transversely isotropic models with both vertical (VTI) and horizontal (HTI) symmetry axis can be treated as special cases of orthorhombic media. For VTI media with VTI attenuation, all vertical planes are identical, and there is no velocity or attenuation variation in the horizontal (isotropy) plane:

$$\begin{aligned}
\epsilon^{(1)} &= \epsilon^{(2)} = \epsilon, \quad \epsilon_Q^{(1)} = \epsilon_Q^{(2)} = \epsilon_Q \\
\delta^{(1)} &= \delta^{(2)} = \delta, \quad \delta_Q^{(1)} = \delta_Q^{(2)} = \delta_Q, \\
\gamma^{(1)} &= \gamma^{(2)} = \gamma, \quad \gamma_Q^{(1)} = \gamma_Q^{(2)} = \gamma_Q, \\
\delta^{(3)} &= 0, \quad \delta_Q^{(3)} = 0 .
\end{aligned}$$

Then equations (38)–(40) yield the VTI result (Zhu and Tsvankin, 2004, 2005a): $\epsilon_Q(\phi) = \epsilon_Q$, $\delta_Q(\phi) = \delta_Q$, and

$$\mathcal{A}_P^{\mathrm{VTI}} = \mathcal{A}_{P0}\left(1 + \delta_Q \sin^2\theta \cos^2\theta + \epsilon_Q \sin^4\theta\right) . \tag{41}$$

Next, suppose that the symmetry axis of the TI medium (for both velocity and attenuation) points in the x_1-direction. In this case, the isotropy plane coincides with the $[x_2, x_3]$-plane, and

$$\begin{aligned}
\epsilon^{(1)} &= 0, \quad \epsilon_Q^{(1)} = 0, \\
\delta^{(1)} &= 0, \quad \delta_Q^{(1)} = 0, \\
\gamma^{(1)} &= 0, \quad \gamma_Q^{(1)} = 0 .
\end{aligned}$$

For this HTI model, the parameters $\delta^{(3)}$ and $\delta_Q^{(3)}$ are not independent because the $[x_1, x_2]$-plane is equivalent to the $[x_1, x_3]$-plane. If the velocity anisotropy is weak, $\delta^{(3)} = \delta^{(2)} - 2\epsilon^{(2)}$ (Tsvankin, 1997, 2001). For weak attenuation anisotropy, $\delta_Q^{(3)} = \delta_Q^{(2)} - 2\epsilon_Q^{(2)}$, and equation (39) becomes $\epsilon_Q(\phi) = \epsilon_Q^{(2)} \cos^4\phi + \delta_Q^{(2)} \sin^2\phi \cos^2\phi$. Then the P-wave attenuation coefficient (38) takes the form

$$\mathcal{A}_P^{\mathrm{HTI}} = \mathcal{A}_{P0}\left[1 + \delta_Q^{(2)} \cos^2\phi \sin^2\theta \cos^2\theta + \left(\epsilon_Q^{(2)} \cos^4\phi + \delta_Q^{(2)} \sin^2\phi \cos^2\phi\right) \sin^4\theta\right] . \tag{42}$$

6.4 Parameters for P-wave attenuation

The linearized P-wave attenuation coefficient (38) does not contain the parameters $\mathcal{A}_{S0}$, $\gamma_Q^{(1)}$, and $\gamma_Q^{(2)}$, which are primarily responsible for shear-wave attenuation. An important practical issue is whether or not this conclusion remains valid for models with strong attenuation and pronounced velocity and attenuation anisotropy. As illustrated by Figure 3, the dependence of $\mathcal{A}_P$ on the shear-wave vertical attenuation coefficient $\mathcal{A}_{S0}$ becomes noticeable only for extremely high attenuation (i.e., uncommonly small values of Q_{55}). The influence of the parameters $\gamma_Q^{(1)}$ and $\gamma_Q^{(2)}$ on the coefficient $\mathcal{A}_P$ (not shown here) for typical moderately attenuative models is also negligible.

Therefore, for a fixed orientation of the symmetry planes and fixed velocity parameters, P-wave attenuation is controlled by the reference value $\mathcal{A}_{P0}$ and five attenuation-anisotropy parameters – $\epsilon_Q^{(1)}$, $\epsilon_Q^{(2)}$, $\delta_Q^{(1)}$, $\delta_Q^{(2)}$, and $\delta_Q^{(3)}$. An equivalent result was obtained for velocity anisotropy by Tsvankin (1997, 2001), who showed that the P-wave phase-velocity function in orthorhombic media is governed just by the vertical velocity and five ϵ and δ parameters. However, while the velocity function is almost independent of attenuation, the P-wave attenuation coefficient does depend on the velocity anisotropy, even if all relevant attenuation-anisotropy parameters are held constant (see below).

6.5 Accuracy of the linearized solution

To evaluate the accuracy of the weak-anisotropy approximation (38) outside the symmetry planes, we compare it with the exact coefficient $\mathcal{A}_P$ [equation (5)] for a model with pronounced orthorhombic attenuation (Figure 4). The velocity parameters correspond to the moderately anisotropic model of Schoenberg and Helbig (1997). Since no measurements of the attenuation-anisotropy parameters are available, each of them was set to be twice as large as the corresponding velocity-anisotropy parameter (e.g., $\epsilon_Q^{(2)} = 2\epsilon^{(2)}$).

As expected, the weak-anisotropy approximation gives satisfactory results for near-vertical propagation directions with polar angles up to about 30°. The error becomes more significant for intermediate propagation angles in the range $30^\circ < \theta < 75^\circ$. When the vertical incidence plane is close to either vertical symmetry plane (i.e., the azimuth ϕ approaches 0° or 90°), the approximate solution also yields an accurate estimate of $\mathcal{A}_P$ near the horizontal direction. Overall, the error of the weak-anisotropy approximation for the full range of polar and azimuthal angles is less than 10%. Note that while the velocity anisotropy for this model is moderate (both $\epsilon^{(1)}$ and $\epsilon^{(2)}$ are about 0.3),

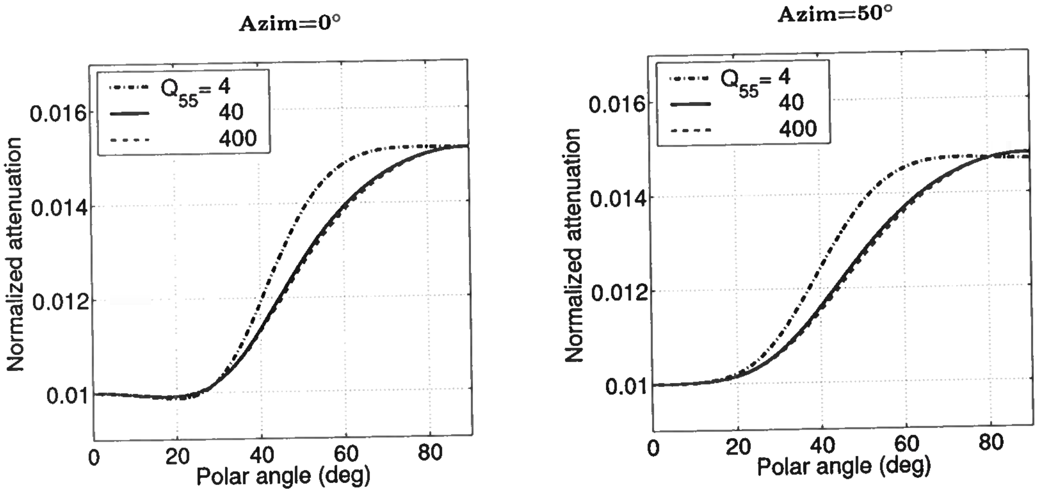

Figure 3. Influence of the parameter $\mathcal{A}_{S0} = 1/(2Q_{55})$ (marked on the plot) on the normalized P-wave attenuation coefficient. The velocity parameters correspond to an orthorhombic model formed by vertical cracks embedded in a VTI background (Schoenberg and Helbig, 1997): $V_{P0} = 2.437$ km/s, $V_{S0} = 1.265$ km/s, $\epsilon^{(1)} = 0.329$, $\epsilon^{(2)} = 0.258$, $\delta^{(1)} = 0.083$, $\delta^{(2)} = -0.078$, $\delta^{(3)} = -0.106$, $\gamma^{(1)} = 0.182$, and $\gamma^{(2)} = 0.0455$. The P-wave vertical attenuation coefficient is $\mathcal{A}_{P0} = 0.01$ ($Q_{33} = 50$); each attenuation-anisotropy parameter is twice the corresponding velocity-anisotropy parameter: $\epsilon_Q^{(1)} = 0.658$, $\epsilon_Q^{(2)} = 0.516$, $\delta_Q^{(1)} = 0.166$, $\delta_Q^{(2)} = -0.156$, $\delta_Q^{(3)} = -0.212$, $\gamma_Q^{(1)} = 0.364$, and $\gamma_Q^{(2)} = 0.091$.

the attenuation anisotropy is much more pronounced. This and other tests for a representative set of orthorhombic models confirm that equation (38) adequately describes P-wave attenuation under the assumption of homogeneous wave propagation.

To identify the source of errors in the weak-anisotropy approximation, we repeat the test in Figure 4 using a purely isotropic velocity model (Figure 5). The approximate solution (dashed lines) in Figure 5 coincides with that in Figure 4 because both models have identical attenuation-anisotropy parameters. The exact coefficient $\mathcal{A}_P$ (solid lines), however, is influenced by the velocity-anisotropy parameters in such a way that the error of the weak-anisotropy approximation becomes much smaller when the velocity field is isotropic (Figure 5).

Hence, the accuracy of the approximation (38) is controlled primarily by the strength of the velocity anisotropy, even if the magnitude of the attenuation anisotropy is much higher. This can be explained by the multiple linearizations in the velocity-anisotropy parameters involved in deriving equations (A4), (A7), and (A8).

It should be emphasized that the influence of different subsets of the velocity-anisotropy parameters on the attenuation coefficient varies with the azimuth ϕ. As illustrated in Figure 6, the contribution of the velocity-anisotropy parameters defined in the $[x_1, x_3]$-plane (the azimuth $\phi = 0°$) to the coefficient $\mathcal{A}_P$ decreases away from that plane and completely vanishes in the orthogonal direction. Note that according to the Christoffel equation (17), the P-wave attenuation coefficient in the $[x_2, x_3]$-plane ($\phi = 90°$) is indeed fully independent of the velocity- and attenuation-anisotropy parameters defined in the other two symmetry planes. Similarly, the maximum influence on $\mathcal{A}_P$ of the velocity-anisotropy parameters defined in the $[x_2, x_3]$-plane is observed for azimuths close to 90°.

7 DISCUSSION AND CONCLUSIONS

The attenuation coefficients of P-, S$_1$-, and S$_2$-waves in orthorhombic media with orthorhombic attenuation depend on the orientation of the symmetry planes, nine velocity parameters and nine components of the quality-factor matrix. The large number of independent parameters, compounded by the coupling between the attenuation and velocity anisotropy, makes the description of orthorhombic attenuation extremely difficult. Here, we demonstrated that the analysis of attenuation coefficients can be significantly simplified by introducing attenuation-anisotropy parameters similar to Tsvankin's parameters for the orthorhombic velocity function.

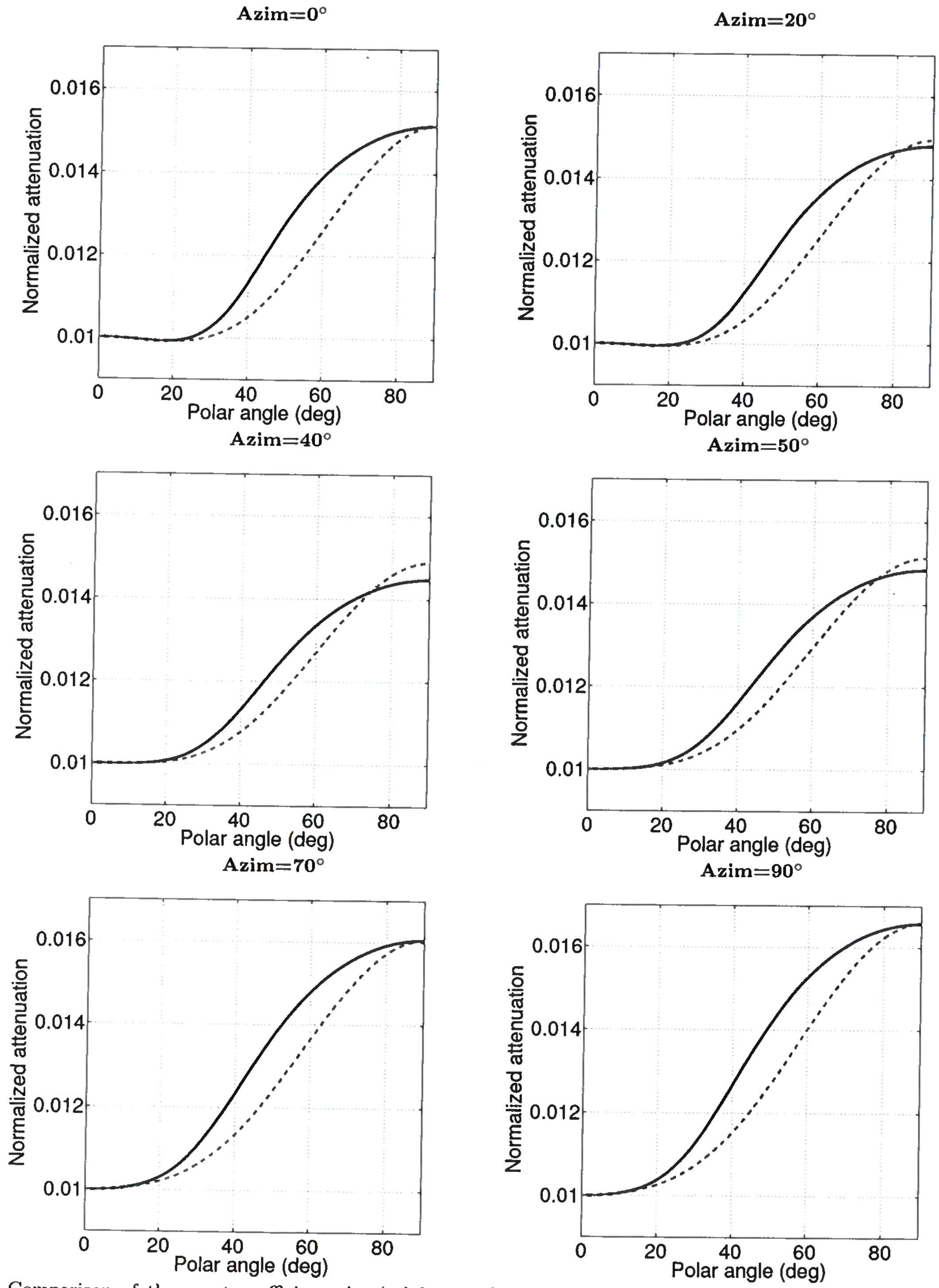

Figure 4. Comparison of the exact coefficient $\mathcal{A}_P$ (solid curves) with the linearized approximation (38) (dashed) for an orthorhombic medium with orthorhombic attenuation. The model parameters are the same as in Figure 3 ($Q_{55} = 40$).

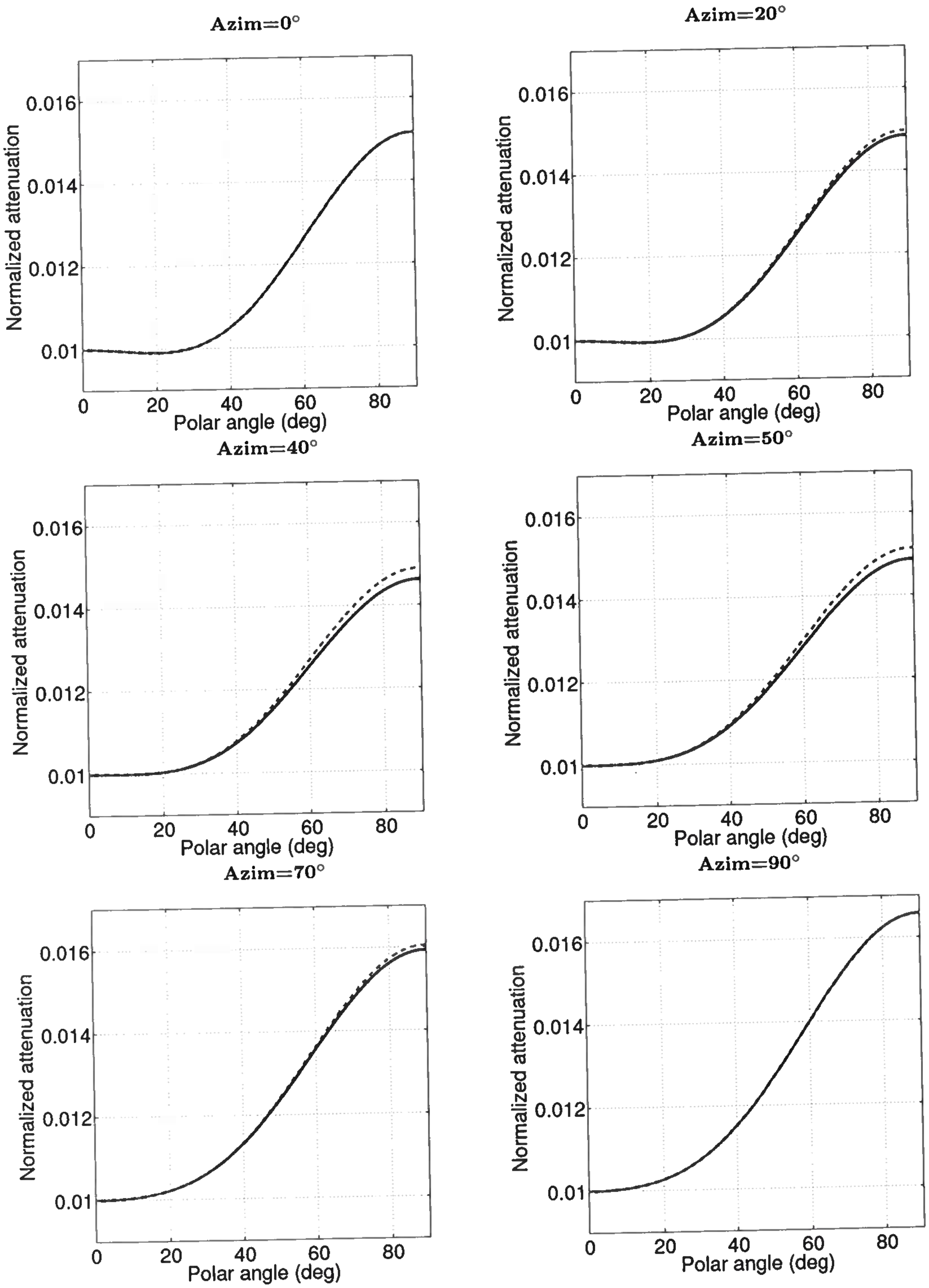

Figure 5. Comparison of the exact coefficient $\mathcal{A}_P$ (solid curves) with the linearized approximation (38) (dashed) for a medium with orthorhombic attenuation but a purely isotropic velocity function. The attenuation parameters are the same as in Figures 3 and 4, but the velocity $V_{P0} = 2.437$ km/s is constant in all directions.

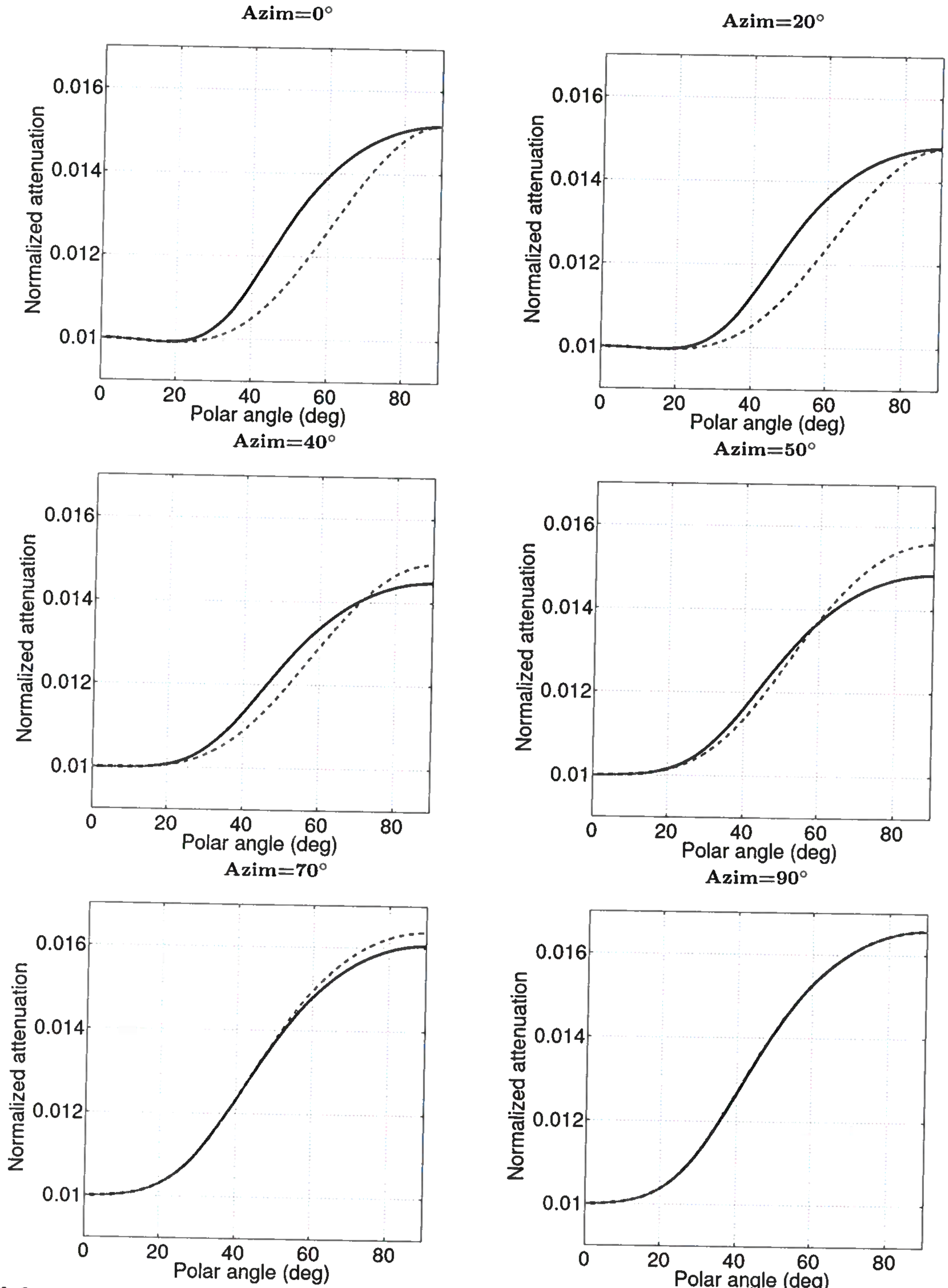

Figure 6. Influence of the velocity anisotropy on the exact attenuation coefficient $\mathcal{A}_P$. The solid curves are computed for the orthorhombic model with orthorhombic attenuation from Figures 3 and 4. The dashed curves are obtained by setting to zero the velocity-anisotropy parameters $\epsilon^{(2)}$, $\delta^{(2)}$, and $\gamma^{(2)}$ defined in the $[x_1, x_3]$-plane (azimuth = 0°); all other model parameters are unchanged.

The equivalence between the Christoffel equation in the symmetry planes of orthorhombic and VTI media, established previously for purely elastic media, holds in the presence of orthorhombic attenuation. Therefore, the symmetry-plane attenuation coefficients of all three modes can be obtained by simply adapting the known VTI equations. Also, the Thomsen-style VTI notation of Zhu and Tsvankin (2004, 2005a) can be extended to orthorhombic media following the approach suggested by Tsvankin (1997, 2001) for velocity anisotropy. The set of attenuation-anisotropy parameters introduced here includes two reference (isotropic) P- and S-wave attenuation coefficients in the x_3 direction, $\mathcal{A}_{P0}$ and $\mathcal{A}_{S0}$, and seven dimensionless anisotropy parameters, $\epsilon_Q^{(1,2)}$, $\delta_Q^{(1,2,3)}$, and $\gamma_Q^{(1,2)}$.

Adaptation of the linearized VTI equations leads to concise expressions for the symmetry-plane attenuation coefficients of P-, S_1-, and S_2-waves valid for weak attenuation and weak velocity and attenuation anisotropy. Furthermore, linearization of the Christoffel equation in the attenuation-anisotropy parameters yields the approximate P-wave attenuation coefficient $\mathcal{A}_P$ outside the symmetry planes as a simple function of $\mathcal{A}_{P0}$, $\epsilon_Q^{(1,2)}$, and $\delta_Q^{(1,2,3)}$. Interestingly, the linearized coefficient $\mathcal{A}_P$ expressed through the phase angles and attenuation-anisotropy parameters has the same form as the approximate P-wave phase-velocity function in terms of Tsvankin's velocity parameters. Also, as is the case for velocity anisotropy, the approximate P-wave attenuation coefficient in each vertical plane of orthorhombic media is given by the VTI equation with azimuthally varying parameters ϵ_Q and δ_Q.

This equivalence between the linearized equations for attenuation and velocity anisotropy stems from the identical (orthorhombic) symmetry of the real and imaginary parts of the stiffness tensor and the assumption of homogeneous wave propagation. Still, there are important differences between the treatment of velocity and attenuation anisotropy. Our analysis shows that in the absence of pronounced velocity dispersion the influence of attenuation (i.e., of the imaginary part of the stiffness tensor) on velocity is practically negligible. In contrast, the definitions of the attenuation-anisotropy parameters $\delta_Q^{(1,2,3)}$ include the velocity-anisotropy parameters $\delta^{(1,2,3)}$.

Also, although the velocity anisotropy does not explicitly contribute to the linearized expressions for attenuation, the exact attenuation coefficient $\mathcal{A}_P$ does vary with the velocity-anisotropy parameters even for fixed values of $\delta_Q^{(1,2,3)}$. Moreover, the accuracy of the linearized equation for $\mathcal{A}_P$ is controlled to a large degree by the strength of the velocity anisotropy. Numerical tests demonstrate that the approximate $\mathcal{A}_P$ remains close to the exact value even for strongly attenuative media provided the velocity anisotropy is relatively weak.

Thus, the P-wave attenuation coefficient is primarily governed by the orientation of the symmetry planes and six (instead of nine) attenuation-anisotropy parameters: $\mathcal{A}_{P0}$, $\epsilon_Q^{(1,2)}$, and $\delta_Q^{(1,2,3)}$. Still, due to the non-negligible influence of the velocity anisotropy on $\mathcal{A}_P$, inversion of attenuation measurements for orthorhombic media cannot be performed without anisotropic velocity analysis. Also, note that knowledge of the velocity field is required to correct for the difference between the phase attenuation coefficient studied here and the group attenuation coefficient responsible for the amplitude decay along seismic rays (Zhu and Tsvankin, 2004).

8 ACKNOWLEDGMENTS

We are grateful to members of the A(nisotropy)-Team of the Center for Wave Phenomena (CWP), Colorado School of Mines (CSM), for helpful discussions, and to Ken Larner (CSM) for his review of the manuscript. The support for this work was provided by the Consortium Project on Seismic Inverse Methods for Complex Structures at CWP and by the Chemical Sciences, Geosciences and Biosciences Division, Office of Basic Energy Sciences, U.S. Department of Energy.

REFERENCES

Akbar, N., Dvorkin, J., and Nur, A., 1993, Relating P-wave attenuation to permeability: Geophysics, **58**, 20–29.

Bakulin, A., Grechka, V., and Tsvankin, I., 2000, Estimation of fracture parameters from reflection seismic data. Part II: Fractured models with orthorhombic symmetry: Geophysics, **65**, 1803–1817.

Carcione, J. M., 2001, Wave fields in real media: wave propagation in anisotropic, anelastic, and porous media: Pergamon Press.

Crampin, S., 1991, Effects of singularities on shear-wave propagation in sedimentary basins: Geophysical Journal International, **107**, 531–543.

Grechka, V., Theophanis, S., and Tsvankin, I., 1999, Joint inversion of P– and PS–waves in orthorhombic media: Theory and a physical-modeling study: Geophysics, **64**, 146–161.

Grechka, V., and Tsvankin, I., 1999, 3-D moveout velocity analysis and parameter estimation for orthorhombic media: Geophysics, **64**, 820–837.

Lynn, H. B., Campagna, D., Simon, K. M., and Beckham, W. E., 1999, Relationship of P-wave seismic attributes, azimuthal anisotropy, and commercial gas pay in 3-D P-wave multiazimuth data, Rulison Field, Piceance Basin, Colorado: Geophysics, **64**, 1293–1311.

Mavko, G. M., and Nur, A., 1979, Wave attenuation in partially saturated rocks: Geophysics, **44**, 161–178.

Pointer T., Liu, E., and Crampin, S., 1996, Seismic wave propagation in media with interconnected cracks and pores: 66nd Annual International Meeting, Society of Exploration Geophysicists, Expanded Abstracts, 1846–1849.

Schoenberg, M., and Helbig, K., 1997, Orthorhombic media: Modeling elastic wave behavior in a vertically fractured earth: Geophysics, **62**, 1954–1974.

Thomsen, L., 1986, Weak elastic anisotropy: Geophysics, **51**, 1954–1966.

Tsvankin, I., 1997, Anisotropic parameters and P-wave velocity for orthorhombic media: Geophysics, **62**, 1292–1309.

Tsvankin, I., 2001, Seismic signatures and analysis of reflection data in anisotropic media: Elsevier.

Zhu, Y., and Tsvankin, I., 2004, Plane-wave propagation and radiation patterns in attenuative TI media: 74th Ann. Internat. Mtg., Soc. Expl. Geophys., Expanded Abstracts, 139–142.

Zhu, Y., and Tsvankin, I., 2005a, Plane-wave propagation in attenuative TI media: Geophysics, under review.

Zhu, Y., and Tsvankin, I., 2005b, Physical modeling and analysis of P-wave attenuation anisotropy in transversely isotropic media: CWP Project Review (this volume).

APPENDIX A: APPROXIMATE ATTENUATION OUTSIDE THE SYMMETRY PLANES OF ORTHORHOMBIC MEDIA

The complex Christoffel equation (5) for homogeneous wave propagation outside the symmetry planes can be rewritten as

$$\begin{aligned}
&[\,(c_{11}n_1^2 + c_{66}n_2^2 + c_{55}n_3^2)\mathcal{K}_{1,(1,6,5)} - \rho V^2 + i(c_{11}n_1^2 + c_{66}n_2^2 + c_{55}n_3^2)\mathcal{K}_{2,(1,6,5)}] \\
&\cdot\{\,[\,(c_{66}n_1^2 + c_{22}n_2^2 + c_{44}n_3^2)\mathcal{K}_{1,(6,2,4)} - \rho V^2 + i(c_{66}n_1^2 + c_{22}n_2^2 + c_{44}n_3^2)\mathcal{K}_{2,(6,2,4)}] \\
&\;\cdot\,[\,(c_{55}n_1^2 + c_{44}n_2^2 + c_{33}n_3^2)\mathcal{K}_{1,(5,4,3)} - \rho V^2 + i(c_{55}n_1^2 + c_{44}n_2^2 + c_{33}n_3^2)\mathcal{K}_{2,(5,4,3)}] - \\
&\quad[\,(c_{23} + c_{44})n_2n_3(\mathcal{K}_{1,(23,44)} + i\mathcal{K}_{2,(23,44)})]^2\} \\
&-[\,(c_{12} + c_{66})n_1n_2(\mathcal{K}_{1,(12,66)} + i\mathcal{K}_{2,(12,66)})] \\
&\cdot\{\,[\,(c_{12} + c_{66})n_1n_2(\mathcal{K}_{1,(12,66)} + i\mathcal{K}_{2,(12,66)})] \\
&\;\cdot\,[\,(c_{55}n_1^2 + c_{44}n_2^2 + c_{33}n_3^2)\mathcal{K}_{1,(5,4,3)} - \rho V^2 + i(c_{55}n_1^2 + c_{44}n_2^2 + c_{33}n_3^2)\mathcal{K}_{2,(5,4,3)}] - \\
&\quad[\,(c_{13} + c_{55})n_1n_3(\mathcal{K}_{1,(13,55)} + i\mathcal{K}_{2,(13,55)})] \cdot [(c_{23} + c_{44})n_2n_3(\mathcal{K}_{1,(23,44)} + i\mathcal{K}_{2,(23,44)})]\} \\
&+[\,(c_{13} + c_{55})n_1n_3(\mathcal{K}_{1,(13,55)} + i\mathcal{K}_{2,(13,55)})] \\
&\cdot\{\,[\,(c_{12} + c_{66})n_1n_2(\mathcal{K}_{1,(12,66)} + i\mathcal{K}_{2,(12,66)})] \cdot [(c_{23} + c_{44})n_2n_3(\mathcal{K}_{1,(23,44)} + i\mathcal{K}_{2,(23,44)})] - \\
&\quad[\,(c_{13} + c_{55})n_1n_3(\mathcal{K}_{1,(13,55)} + i\mathcal{K}_{2,(13,55)})] \\
&\quad[\,(c_{66}n_1^2 + c_{22}n_2^2 + c_{44}n_3^2)\mathcal{K}_{1,(6,2,4)} - \rho V^2 + i(c_{66}n_1^2 + c_{22}n_2^2 + c_{44}n_3^2)\mathcal{K}_{2,(6,2,4)}]\} = 0\,,
\end{aligned} \tag{A1}$$

where

$$\begin{aligned}
\mathcal{K}_1 &= 1 - \mathcal{A}^2 + \frac{2}{Q_{33}}\mathcal{A}\,, \qquad \mathcal{K}_2 = \frac{1 - \mathcal{A}^2}{Q_{33}} - 2\mathcal{A}\,, \\
\mathcal{K}_{1,(i,j,l)} &= \mathcal{K}_1 + 2\frac{\Delta_{(i,j,l)}}{Q_{33}}\mathcal{A}\,, \quad \mathcal{K}_{2,(i,j,l)} = \mathcal{K}_2 + \frac{\Delta_{(i,j,l)}}{Q_{33}}(1 - \mathcal{A}^2)\,, \\
\mathcal{K}_{1,(ij,kl)} &= \mathcal{K}_1 + 2\frac{\Delta_{(ij,kl)}}{Q_{33}}\mathcal{A}\,, \quad \mathcal{K}_{2,(ij,kl)} = \mathcal{K}_2 + \frac{\Delta_{(ij,kl)}}{Q_{33}}(1 - \mathcal{A}^2)\,, \\
\Delta_{(i,j,l)} &= \frac{c_{ii}n_1^2\dfrac{Q_{33} - Q_{ii}}{Q_{ii}} + c_{jj}n_2^2\dfrac{Q_{33} - Q_{jj}}{Q_{jj}} + c_{ll}n_3^2\dfrac{Q_{33} - Q_{ll}}{Q_{ll}}}{c_{ii}n_1^2 + c_{jj}n_2^2 + c_{ll}n_3^2}\,, \\
\Delta_{(ij,kl)} &= \frac{c_{ij}\dfrac{Q_{33} - Q_{ij}}{Q_{ij}} + c_{kl}\dfrac{Q_{33} - Q_{kl}}{Q_{kl}}}{c_{ij} + c_{kl}}\,.
\end{aligned}$$

Note that $\mathcal{A} \equiv k^I/k$ is on the order of the inverse Q-factor ($1/Q$). When the attenuation is weak ($\mathcal{A} \ll 1$), we obtain $\mathcal{K}_1 \approx 1$ and $\mathcal{K}_2 \approx \dfrac{1}{Q_{33}} - 2\mathcal{A}$ by dropping the quadratic and higher-order terms in $\mathcal{A}$. Assuming that Q_{33} and Q_{55} are of the same order (the common case), weak attenuation anisotropy implies the same order for all components Q_{ij}.

Hence, the magnitude of the terms $\Delta_{(i,j,l)}$ and $\Delta_{(ij,kl)}$ cannot be much larger than unity. Then the terms $\frac{\Delta_{(i,j,l)}}{Q_{33}}\mathcal{A}$, $\frac{\Delta_{(ij,kl)}}{Q_{33}}\mathcal{A}$, $\frac{\Delta_{(i,j,l)}}{Q_{33}}\mathcal{A}^2$, and $\frac{\Delta_{(ij,kl)}}{Q_{33}}\mathcal{A}^2$ are either quadratic or cubic in $\mathcal{A}$. Dropping these terms yields $\mathcal{K}_{1,(i,j,l)} \approx 1$, $\mathcal{K}_{2,(i,j,l)} \approx \frac{1+\Delta_{(i,j,l)}}{Q_{33}} - 2\mathcal{A}$, $\mathcal{K}_{1,(ij,kl)} \approx 1$, and $\mathcal{K}_{2,(ij,kl)} \approx \frac{1+\Delta_{(ij,kl)}}{Q_{33}} - 2\mathcal{A}$.

Next, we denote $\mathcal{C}_{(i,j,l)} = c_{ii}n_1^2 + c_{jj}n_2^2 + c_{ll}n_3^2$ and $\mathcal{C}_{(ij,kl)} = (c_{ij} + c_{kl})n_i n_j$ and simplify equation (A1) for weak attenuation and weak attenuation anisotropy as

$$
\begin{aligned}
&\left[\mathcal{C}_{(1,6,5)} - \rho V^2 + i\mathcal{C}_{(1,6,5)}\left(\frac{1+\Delta_{(1,6,5)}}{Q_{33}} - 2\mathcal{A}\right)\right] \\
&\left\{\left[\mathcal{C}_{(6,2,4)} - \rho V^2 + i\mathcal{C}_{(6,2,4)}(\frac{1+\Delta_{(6,2,4)}}{Q_{33}} - 2\mathcal{A})\right]\right. \\
&\left.\left[\mathcal{C}_{(5,4,3)} - \rho V^2 + i\mathcal{C}_{(5,4,3)}\left(\frac{1+\Delta_{(5,4,3)}}{Q_{33}} - 2\mathcal{A}\right)\right] - \mathcal{C}^2_{(23,44)}\left[1 + i\left(\frac{1+\Delta_{(23,44)}}{Q_{33}} - 2\mathcal{A}\right)\right]^2\right\} \\
&-\mathcal{C}_{(12,66)}\left[1 + \left(\frac{1+\Delta_{(12,66)}}{Q_{33}} - 2\mathcal{A}\right)\right] \\
&\left\{\mathcal{C}_{(12,66)}\left[1 + \left(\frac{1+\Delta_{(12,66)}}{Q_{33}} - 2\mathcal{A}\right)\right] \cdot \left[\mathcal{C}_{(5,4,3)} - \rho V^2 + i\mathcal{C}_{(5,4,3)}\left(\frac{1+\Delta_{(5,4,3)}}{Q_{33}} - 2\mathcal{A}\right)\right] -\right. \\
&\left.\mathcal{C}_{(13,55)}\left[1 + \left(\frac{1+\Delta_{(13,55)}}{Q_{33}} - 2\mathcal{A}\right)\right] \cdot \mathcal{C}_{(23,44)}\left[1 + i\left(\frac{1+\Delta_{(23,44)}}{Q_{33}} - 2\mathcal{A}\right)\right]\right\} \\
&+\mathcal{C}_{(13,55)}\left[1 + i\left(\frac{1+\Delta_{(13,55)}}{Q_{33}} - 2\mathcal{A}\right)\right] \\
&\left\{\mathcal{C}_{(12,66)}\left[1 + i\left(\frac{1+\Delta_{(12,66)}}{Q_{33}} - 2\mathcal{A}\right)\right] \cdot \mathcal{C}_{(23,44)}\left[1 + i\left(\frac{1+\Delta_{(23,44)}}{Q_{33}} - 2\mathcal{A}\right)\right] -\right. \\
&\left.\mathcal{C}_{(13,55)}\left[1 + i\left(\frac{1+\Delta_{(13,55)}}{Q_{33}} - 2\mathcal{A}\right)\right] \cdot \left[\mathcal{C}_{(6,2,4)} - \rho V^2 + i\mathcal{C}_{(6,2,4)}(\frac{1+\Delta_{(6,2,4)}}{Q_{33}} - 2\mathcal{A})\right]\right\} \\
&= 0\,.
\end{aligned}
\tag{A2}
$$

The real part of equation (A-2) is

$$
\begin{aligned}
&(c_{11}n_1^2 + c_{66}n_2^2 + c_{55}n_3^2 - \rho V^2) \\
\cdot\ &\left[(c_{66}n_1^2 + c_{22}n_2^2 + c_{44}n_3^2 - \rho V^2)(c_{55}n_1^2 + c_{44}n_2^2 + c_{33}n_3^2 - \rho V^2) - (c_{23} + c_{44})^2 n_2^2 n_3^2\right] \\
&-(c_{12} + c_{66})n_1 n_2 \\
\cdot\ &\left[(c_{12} + c_{66})n_1 n_2 (c_{55}n_1^2 + c_{44}n_2^2 + c_{33}n_3^2 - \rho V^2) - (c_{13} + c_{55})(c_{23} + c_{44})n_1 n_2 n_3^2\right] \\
&+(c_{13} + c_{55})n_1 n_3 \\
\cdot\ &\left[(c_{12} + c_{66})(c_{23} + c_{44})n_1 n_2 n_3^2 - (c_{13} + c_{55})n_1 n_3 (c_{66}n_1^2 + c_{22}n_2^2 + c_{44}n_3^2 - \rho V^2)\right] = 0\,,
\end{aligned}
\tag{A3}
$$

which is identical to the Christoffel equation for the reference nonattenuative medium.

The normalized attenuation coefficient $\mathcal{A}$ is obtained from the imaginary part of equation (A2):

$$
\mathcal{A} = \frac{1}{2Q_{33}}\left(1 + \frac{\mathcal{H}_u}{\mathcal{H}_d}\right),
\tag{A4}
$$

where

$$
\begin{aligned}
\mathcal{H}_u = {} & \Delta_{(1,6,5)}\mathcal{C}_{(1,6,5)}\left[(\mathcal{C}_{(6,2,4)} - \rho V^2)(\mathcal{C}_{(5,4,3)} - \rho V^2) - \mathcal{C}^2_{(23,44)}\right] \\
&+\Delta_{(6,2,4)}\mathcal{C}_{(6,2,4)}\left[(\mathcal{C}_{(1,6,5)} - \rho V^2)(\mathcal{C}_{(5,4,3)} - \rho V^2) - \mathcal{C}^2_{(13,55)}\right] \\
&+\Delta_{(5,4,3)}\mathcal{C}_{(5,4,3)}\left[(\mathcal{C}_{(1,6,5)} - \rho V^2)(\mathcal{C}_{(6,2,4)} - \rho V^2) - \mathcal{C}^2_{(12,66)}\right] \\
&-2\Delta_{(13,55)}\mathcal{C}^2_{(13,55)}(\mathcal{C}_{(6,2,4)} - \rho V^2) - 2\Delta_{(12,66)}\mathcal{C}^2_{(12,66)}(\mathcal{C}_{(5,4,3)} - \rho V^2) \\
&-2\Delta_{(23,44)}\mathcal{C}^2_{(23,44)}(\mathcal{C}_{(1,6,5)} - \rho V^2)
\end{aligned}
$$

$$+2\left(\Delta_{(13,55)}+\Delta_{(12,66)}+\Delta_{(23,44)}\right)\mathcal{C}_{(13,55)}\mathcal{C}_{(12,66)}\mathcal{C}_{(23,44)}\,, \tag{A5}$$

and

$$\begin{aligned}\mathcal{H}_d = \rho V^2\ &\left[(\mathcal{C}_{(1,6,5)}-\rho V^2)(\mathcal{C}_{(6,2,4)}-\rho V^2)+(\mathcal{C}_{(1,6,5)}-\rho V^2)(\mathcal{C}_{(5,4,3)}-\rho V^2)\right.\\ &\left.+(\mathcal{C}_{(6,2,4)}-\rho V^2)(\mathcal{C}_{(5,4,3)}-\rho V^2)-\mathcal{C}^2_{(12,66)}-\mathcal{C}^2_{(13,55)}-\mathcal{C}^2_{(23,44)}\right]\,.\end{aligned} \tag{A6}$$

The term $\dfrac{\mathcal{H}_u}{\mathcal{H}_d}$ in equation (A4) can be expressed through the velocity- and attenuation-anisotropy parameters. Assuming that the anisotropy is weak for both the velocity and attenuation, we keep only the linear terms in all anisotropy parameters to obtain

$$\mathcal{H}_u = c_{33}(c_{33}-c_{55})^2\left[\epsilon_Q^{(2)}n_1^4+\epsilon_Q^{(1)}n_2^4+(2\epsilon_Q^{(2)}+\delta_Q^{(3)})n_1^2n_2^2+\delta_Q^{(2)}n_1^2n_3^2+\delta_Q^{(1)}n_2^2n_3^2\right]\,, \tag{A7}$$

$$\begin{aligned}\mathcal{H}_d\ =\ & c_{33}(c_{33}-c_{55})\\ &\cdot\left\{(c_{33}-c_{55})\left(1+2\epsilon^{(2)}n_1^4+2\epsilon^{(1)}n_2^4+2\delta^{(2)}n_1^2n_3^2+2\delta^{(1)}n_2^2n_3^2+4\epsilon^{(2)}n_1^2n_2^2+2\delta^{(3)}n_1^2n_2^2\right)\right.\\ &+c_{33}\left[\epsilon^{(1)}(-2n_2^2+6n_2^4)+\epsilon^{(2)}(-2n_1^2+6n_1^4+12n_1^2n_2^2)\right.\\ &\qquad\left.+6\delta^{(1)}n_2^2n_3^2+6\delta^{(2)}n_1^2n_3^2+6\delta^{(3)}n_1^2n_2^2\right]\\ &\left.+c_{55}\left[\gamma^{(1)}(-2-2n_2^2)+\gamma^{(2)}(2-2n_1^2)\right]\right\}\,.\end{aligned} \tag{A8}$$

Note that since the term $\mathcal{H}_u$ is linear in the anisotropy parameters, it is sufficient to keep just the isotropic part of the term $\mathcal{H}_d$. Substitution of equations (A-7) and (A-8) into equation (A-4) yields the final form of the approximate P-wave attenuation coefficient given in the main text [equation (38)].

Physical modeling and analysis of P-wave attenuation anisotropy in transversely isotropic media

Yaping Zhu, Ilya Tsvankin, and Pawan Dewangan
Center for Wave Phenomena, Department of Geophysics,
Colorado School of Mines, Golden, CO 80401

ABSTRACT
The amplitudes and frequency content of seismic waves propagating through anisotropic formations may be strongly distorted by directionally dependent attenuation. Here, we present physical-modeling measurements of the P-wave attenuation coefficient in a transversely isotropic phenolic sample.

Using the spectral-ratio method, we estimated the group (effective) attenuation coefficient of P-waves transmitted through the sample for a wide range of propagation angles (from 0° to 90°) with the symmetry axis. Correction for the difference between the group and phase angles was used to obtain the normalized phase attenuation coefficient $\mathcal{A}$ that was inverted for the Thomsen-style attenuation-anisotropy parameters ϵ_Q and δ_Q. Whereas the symmetry axes of the angle-dependent coefficient $\mathcal{A}$ and of the velocity function have close orientations, the magnitude of attenuation anisotropy far exceeds that of velocity anisotropy. The quality factor Q increases more than tenfold from the symmetry (slow) direction to the isotropy plane (fast direction).

The robustness of our results depends critically on several factors, such as the availability of an accurate anisotropic velocity model and the adequacy of the "homogeneous" concept of wave propagation. The methodology discussed here can be extended to field measurements of anisotropic attenuation needed for AVO (amplitude variation with offset) analysis and seismic fracture detection.

Key words: attenuation, attenuation anisotropy, transverse isotropy, physical modeling

1 INTRODUCTION

Most existing publications on seismic anisotropy are devoted to the influence of angular velocity variation on the traveltimes and amplitudes of seismic waves. It is likely, however, that anisotropic formations are also characterized by directionally dependent attenuation related to the internal structure of the rock matrix or the presence of aligned fractures.

Various issues related to the analytic treatment of attenuation in anisotropic media were addressed by Borcherdt and Wennerberg (1985), Krebes and Le (1994), Carcione (2001), Červený and Pšenčík (2004) and others. For example, the quality factor Q, widely used as a measure of attenuation in isotropic media (e.g., Johnston and Toksöz, 1981), can be replaced by a *matrix* $\mathbf{Q}$ that describes anisotropic attenuation. Each element Q_{ij} of the quality-factor matrix is defined as the ratio of the real and imaginary parts of the corresponding stiffness coefficient (Carcione, 2001). Zhu and Tsvankin (2004, 2005) showed that the angle-dependent attenuation coefficients in transversely isotropic (TI) media can be obtained in a relatively simple form by using Thomsen-style attenuation parameters ϵ_Q, δ_Q, and γ_Q derived from the anisotropic $\mathbf{Q}$-matrix.

Although experimental measurements of attenuation, both in the field and on rock samples, are relatively rare, they indicate that the magnitude of attenuation anisotropy can exceed that of velocity anisotropy (e.g., Tao and King, 1990; Arts and Rasolofosaon, 1992; Prasad and Nur, 2003). For example, according to the measurements of Hosten et al. (1987) for an orthorhombic sample made of composite material, the quality factor for P-waves changes from $Q \approx 6$ in the vertical direction to $Q \approx 35$ in the horizontal direction. Hosten et al. (1987) also show that the symmetry of the attenuation coefficient closely follows that of velocity.

Here, we extend the spectral-ratio method to anisotropic media and apply it to P-wave transmission data acquired in a symmetry plane of a phenolic sample. Fitting the theoretical normalized attenuation coefficient $\mathcal{A}$ to the measurements for a wide range of propagation angles yields large absolute values of the Thomsen-style attenuation-anisotropy parameters ϵ_Q and δ_Q. Although the experiment was performed for a synthetic material, the results are indicative of the high potential of attenuation-anisotropy analysis for field seismic data.

2 THEORETICAL BACKGROUND

2.1 P-wave attenuation in TI media

Propagation of plane P- and SV-waves in TI media with TI attenuation is described by the Christoffel equation (Carcione, 2001; Zhu and Tsvankin, 2004, 2005):

$$(\tilde{c}_{11}\tilde{k}_1^2 + \tilde{c}_{55}\tilde{k}_3^2 - \rho\omega^2)(\tilde{c}_{55}\tilde{k}_1^2 + \tilde{c}_{33}\tilde{k}_3^2 - \rho\omega^2) - [(\tilde{c}_{13} + \tilde{c}_{55})\tilde{k}_1\tilde{k}_3]^2 = 0\,, \tag{1}$$

where ρ is the density, ω is the angular frequency, $\tilde{c}_{ij} = c_{ij} + ic^I_{ij}$ are the complex stiffness coefficients (the symbol " ˜ " denotes a complex quantity), and $\tilde{\mathbf{k}} = \mathbf{k} - i\mathbf{k}^I$ is the complex wave vector. Generally, the vectors $\mathbf{k}$ and $\mathbf{k}^I$ (the imaginary part $\mathbf{k}^I$ is sometimes called the *attenuation vector*) have different orientations, which means that the phase (slowness) direction does not coincide with the direction of maximum attenuation. In that case, wave propagation is usually called "inhomogeneous", and the angle between $\mathbf{k}$ and $\mathbf{k}^I$ is called the "inhomogeneity angle." Whereas the inhomogeneity angle represents a free parameter in plane-wave propagation, it is usually small for wavefields excited by point sources in weakly attenuative media.

As discussed in Carcione (2001) and Zhu and Tsvankin (2004, 2005), by solving the Christoffel equation (1) one obtains the (real) phase velocity $v = \dfrac{\omega}{k}$ and the normalized attenuation coefficient $\mathcal{A} = \dfrac{k^I}{k}$. The coefficient $\mathcal{A}$, which determines the rate of amplitude decay per wavelength, is expressed through the quality-factor matrix ($Q_{ij} \equiv \dfrac{c_{ij}}{c^I_{ij}}$) and the real parts c_{ij} of the stiffnesses $\tilde{c}_{ij}$. Even for relatively simple media in which both c_{ij} and c^I_{ij} have TI (hexagonal) symmetry, the attenuation coefficients of P- and SV-waves have a rather complicated form.

To facilitate the analytic description of TI attenuation, Zhu and Tsvankin (2004, 2005) developed a notation based on the same principle as the commonly used Thomsen (1986) parameters for velocity anisotropy. For P- and SV-waves, the set of Thomsen-style attenuation-anisotropy parameters includes two reference (isotropic) quantities $\mathcal{A}_{P0}$ and $\mathcal{A}_{S0}$ and the dimensionless coefficients ϵ_Q and δ_Q (Appendix A). The parameters $\mathcal{A}_{P0} \equiv 1/(2Q_{33})$ and $\mathcal{A}_{S0} \equiv 1/(2Q_{55})$ are the P- and S-wave attenuation coefficients (respectively) in the symmetry direction, while ϵ_Q and δ_Q control the angle variation of the attenuation coefficients between the symmetry axis and the isotropy plane. In the limit of small attenuation and weak anisotropy (for both velocity and attenuation), the P-wave attenuation coefficient can be significantly simplified by linearizing the solution of the Christoffel equation (1) in the anisotropy parameters (Zhu and Tsvankin, 2004, 2005):

$$\mathcal{A}_P = \mathcal{A}_{P0}\,(1 + \delta_Q \sin^2\theta\cos^2\theta + \epsilon_Q \sin^4\theta)\,, \tag{2}$$

where θ is the phase angle with the symmetry axis. Equation (2) is obtained under the assumption of "homogeneous" wave propagation ($\mathbf{k} \parallel \mathbf{k}^I$), which is sufficiently accurate for P-waves generated by a point source in a homogeneous, weakly attenuative, weakly anisotropic medium.

Equation (2) has exactly the same form as Thomsen's (1986) weak-anisotropy approximation for the P-wave phase velocity. The parameter δ_Q is responsible for the attenuation coefficient in near-vertical directions, while ϵ_Q controls $\mathcal{A}_P$ close to the horizontal plane. The definition of the parameter δ_Q, however, is more complicated than that of Thomsen's parameter δ and reflects the coupling between the attenuation and velocity anisotropy (Zhu and Tsvankin, 2004, 2005). If both ϵ_Q and δ_Q go to zero, the approximate coefficient $\mathcal{A}_P$ becomes isotropic (i.e., independent of angle).

2.2 Spectral-ratio method for anisotropic attenuation

The spectral-ratio method is often used to estimate the attenuation coefficient in both physical modeling and field surveys. For laboratory experiments, application of this method typically involves amplitude measurements made under identical conditions for the sample of interest and for a reference purely elastic (non-attenuative) sample.

The amplitude spectrum of an arrival recorded for the reference sample [denoted by the superscript "(0)"] can be written as

$$U^{(0)}(\omega) = S(\omega)\,G^{(0)}(\mathbf{x}^{(0)})\;e^{-\mathbf{k}^{(0)I}\cdot\mathbf{x}^{(0)}}\;e^{i(\omega t - \mathbf{k}^{(0)}\cdot\mathbf{x}^{(0)})}\,, \tag{3}$$

where $\mathbf{x}$ is the vector connecting the source and receiver, $S(\omega)$ is the spectrum of the source pulse, and the factor $G(\mathbf{x})$ incorporates the radiation pattern of the source and the geometrical spreading along the raypath. Similarly, the spectral amplitude for the attenuative sample (superscript "(1)") has the form

$$U^{(1)}(\omega) = S(\omega)\, G^{(1)}(\mathbf{x}^{(1)})\, e^{-\mathbf{k}^{(1)I}\cdot\mathbf{x}^{(1)}}\, e^{i(\omega t - \mathbf{k}^{(1)}\cdot\mathbf{x}^{(1)})}\,. \tag{4}$$

If the reference trace is acquired for a purely elastic medium with $\mathbf{k}^{(0)I} = 0$, the logarithm of the amplitude ratio becomes

$$\ln\left|\frac{U^{(1)}}{U^{(0)}}\right| = \ln\left(\frac{G^{(1)}}{G^{(0)}}\right) - \mathbf{k}^{(1)I}\cdot\mathbf{x}^{(1)}\,. \tag{5}$$

The frequency dependence of the ratio $G^{(1)}/G^{(0)}$ is usually considered to be negligible in certain frequency range. Then the slope of the function $\ln\left|\frac{U^{(1)}}{U^{(0)}}\right|$ in this frequency range yields the "local" value of the Q-factor in the direction $\mathbf{x}$. If this slope changes with frequency ω, then $k^{(1)I} = |\mathbf{k}^{(1)I}|$ is not a linear function of frequency ω, and the assumption of frequency-independent Q is not valid.

The normalized attenuation coefficient introduced above is given by

$$\mathcal{A} = \frac{k^I}{k} = \frac{k^{(1)I}}{\omega} v\,, \tag{6}$$

which is simply the slope of $k^{(1)I}$ in the frequency domain corrected by the source-receiver distance and scaled by the phase velocity in the direction $\mathbf{x}^{(1)}$.

In isotropic media with isotropic (angle-independent) attenuation, the group attenuation coefficient $k_G^I = |\mathbf{k}_G^I|$ measured along the raypath using the spectral-ratio method is the same as the phase (plane-wave) attenuation coefficient $k^I = |\mathbf{k}^I|$. For anisotropic media with anisotropic attenuation, however, these two coefficients are different. If wave propagation is homogeneous (i.e., the inhomogeneity angle is negligible), the group and phase attenuation coefficients are related by the equation $k_G^I = k^I \cos(\psi - \theta)$, where ψ and θ are the group and phase angles, respectively (Zhu and Tsvankin, 2004).

Here, we employ the following procedure of inverting P-wave attenuation measurements for the attenuation-anisotropy parameters. First, the logarithmic spectral ratio yields the amplitude decay factor in the group (ray) direction, $k_G^{(1)I} x^{(1)}$ [equation (5)]. Second, using the phase and group angles obtained from the known velocity parameters of the sample, we evaluate the phase attenuation coefficient k^I and normalize it by the corresponding real wavenumber k [equation (6)] to estimate the coefficient $\mathcal{A} = \frac{k^I}{k}$. Third, the measurements of $\mathcal{A}$ for a wide range of phase angles θ are inverted for the attenuation-anisotropy parameters ϵ_Q and δ_Q. Approximate values of the parameters ϵ_Q and δ_Q can be found in a straightforward way from the linearized equation (2). More accurate results, however, are obtained by nonlinear inversion based on the exact Christoffel equation (1).

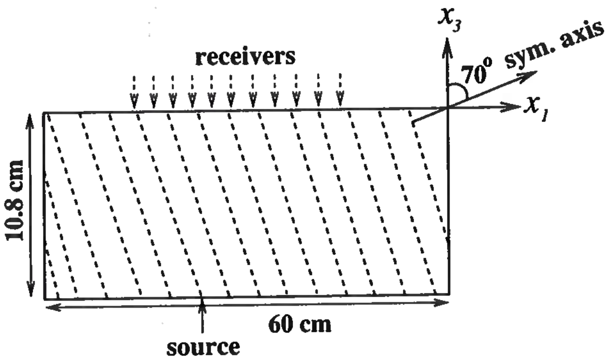

Figure 1. Physical model of a TI layer with the symmetry axis tilted at 70° (from Dewangan et al., 2005). The transmitted wavefield is excited by a transducer at the bottom of the model and recorded with a laser vibrometer.

Because of the coupling between attenuation and velocity anisotropy, estimation of the attenuation-anisotropy parameters requires knowledge of the anisotropic velocity field. Since the influence of attenuation on velocity is typically a second-order effect (Zhu and Tsvankin, 2005), anisotropic velocity analysis can be performed independently of attenuation measurements. Here, we use the results of Dewangan (2004) and Dewangan et al. (2005) who estimated the velocity-anisotropy parameters of our sample by inverting the reflection traveltimes of PP- and PS-waves.

3 EXPERIMENTAL SETUP

The goals of this experiment were to measure the directional dependence of the attenuation coefficient in a composite sample and to estimate the attenuation-anisotropy parameters. The material was XX-paper-based phenolic composed of thin layers of paper bonded with phenolic resin. This fine layering produces an effective anisotropic medium on the scale of the predominant wavelength. The sample was prepared by Dewangan (2004), who pasted phenolic blocks together at an angle, resulting in a transversely isotropic model with the symmetry axis tilted from the vertical by 70° (Figure 1).

Dewangan (2004) and Dewangan et al. (2005) show that the TTI model adequately explains the kinematics of multicomponent (P, S, and PS) data in the vertical measurement plane that contains the symmetry axis (the symmetry-axis plane). Although phenolic materials are generally known to be orthorhombic (e.g., Grechka et al., 1999), body-wave velocities and polarizations in the symmetry planes can be described by the corresponding TI equations (Tsvankin, 1997, 2001).

The original purpose of acquiring the transmission data used here (Figure 2a) was to verify the accuracy of the parameter-estimation results obtained by Dewangan (2004) and Dewangan et al. (2005). The P-wave source transducer was fixed at the bottom of the model, and the wavefield was recorded with a laser vibrometer at the top of the model with a sampling interval of 2 mm in the same azimuth as that of the symmetry axis. The spread of the receiver locations was wide enough to record the full range of propagation angles (from 0° to 90°) with respect to the (tilted) symmetry axis.

For attenuation analysis we separated the first (direct) arrival by applying a Gaussian window to the raw data. The amplitude spectrum of the windowed first arrival, obtained by filtering out the low ($f < 5$ kHz) and high ($f > 750$ kHz) frequencies, is shown in Figure 2b. An aluminum block with negligibly small attenuation served as the reference model. The spectrum of the reference trace acquired by a receiver located directly above the source (Figure 3) was used to estimate the attenuation coefficient by means of the spectral-ratio method described above.

The parameters of the TTI velocity model needed to process the attenuation measurements were obtained by Dewangan et al. (2005) from reflection PP and PS data (Figure 4). Tilted transverse isotropy is described by the the P- and S-wave velocities in the symmetry direction (V_{P0} and V_{S0}, respectively), Thomsen anisotropy parameters ϵ and δ defined with respect to the symmetry axis, the angle ν between the symmetry axis and the vertical, and the thickness z of the sample. The known values of $\nu = 70°$ and $z = 10.8$ cm were accurately estimated from the reflection data, confirming that the velocity-inversion algorithm is robust.

4 MEASUREMENTS OF ATTENUATION ANISOTROPY

4.1 Estimation of the attenuation-anisotropy parameters

For each receiver position at the surface of the phenolic sample, we divided the spectrum of the recorded trace by that of the reference trace (Figure 3), as suggested by equation (5). Records with a low signal-to-noise ratio were excluded from the analysis. We use the frequency band of 60–110 kHz to estimate the attenuation coefficient. According to the spectral-ratio method described above, the relevant elements Q_{ij} of the quality-factor matrix are assumed to be constant in that frequency band.

The normalized phase-attenuation coefficient $\mathcal{A}$, obtained after correcting for the difference between group and phase attenuation (it does not exceed 6%), exhibits a pronounced variation between the slow (0°) and fast (90°) directions (Figure 5). The largest attenuation coefficient is observed along the symmetry axis ($\theta = 0°$), where the P-wave phase velocity reaches its minimum value. Since the symmetry direction is orthogonal to the multiple thin layers bonded together

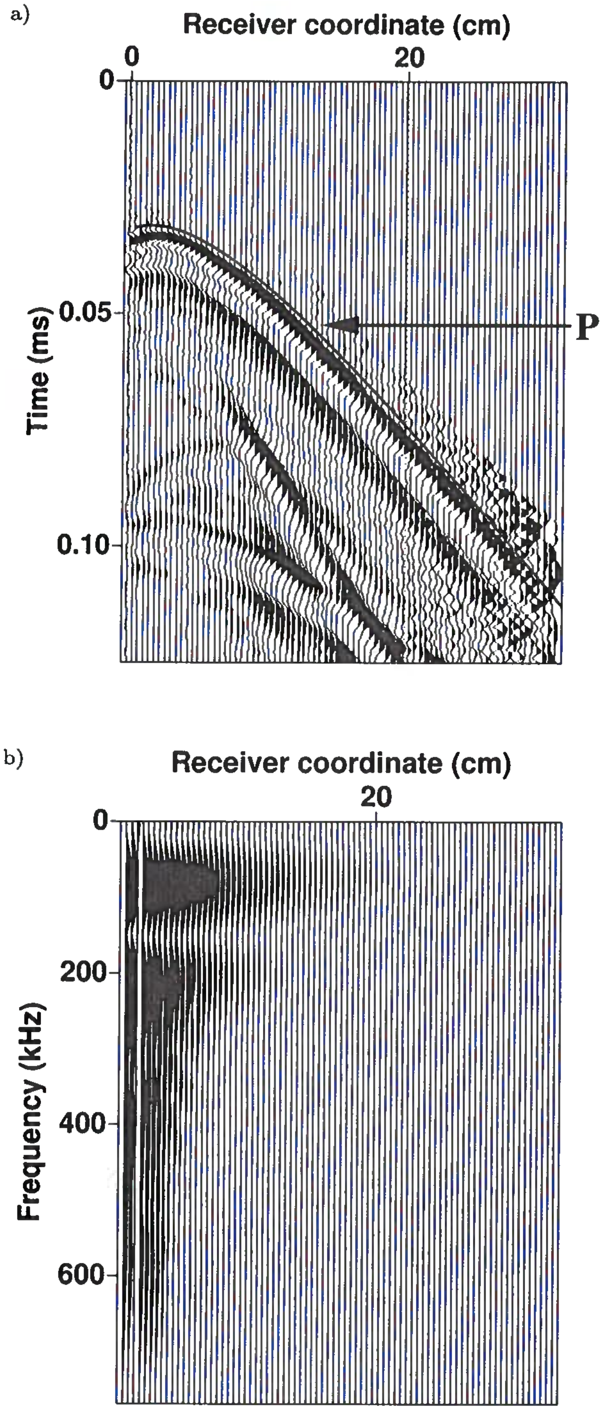

Figure 2. (a) Raw transmission data excited by a P-wave transducer, and (b) the amplitude spectrum of the windowed first arrival. The solid line is the P-wave traveltime modeled by Dewangan et al. (2005) using the inverted parameters from Figure 4. The time sampling interval is 2 μs, and the width of the Gaussian window is 40 samples.

a)

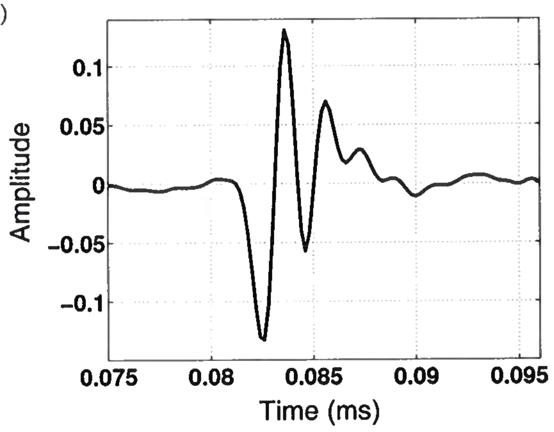

b)

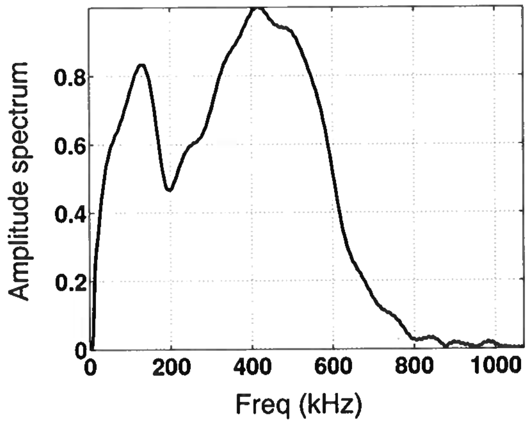

Figure 3. (a) Reference trace for vertical propagation through an aluminum block, and (b) its amplitude spectrum.

to form the model, the rapid increase in attenuation toward $\theta = 0°$ is expected.

The polar plot of the attenuation coefficient, shown in Figure 6, indicates that the symmetry axis of the function $\mathcal{A}(\theta)$ is close to that for the velocity measurements. Although we did not acquire data for angles over 90° to reconstruct a more complete angle variation of $\mathcal{A}(\theta)$, the direction orthogonal to the layering should represent the symmetry axis for all physical properties of the model. To quantify the attenuation anisotropy, we used the Christoffel equation (1) to estimate the best-fit parameters: $\mathcal{A}_{P0} = 0.16$ ($Q_{33} = 3.2$), $\epsilon_Q = -0.92$, and $\delta_Q = -1.84$. The weak-attenuation, weak-anisotropy approximation (2) yields similar values ($\mathcal{A}_{P0} = 0.16$, $\epsilon_Q = -0.86$, and $\delta_Q = -1.91$) despite the large angular variation of $\mathcal{A}(\theta)$ (Figure 6).

While the fact that the largest attenuation coefficient for this model is observed at the velocity minimum is predictable, the extremely low value of $Q_{33} = 3.2$ is somewhat surprising. It should be mentioned, however, that estimates of the attenuation coefficient near the symmetry axis may be distorted by the relatively low reliability of amplitude measurements at long offsets corresponding to small angles θ (Figure 1). Problems in applying our methodology for large source-receiver distances may be related to such factors as the frequency-dependent geometrical spreading and the increased influenced of heterogeneity. In general, the spectral-ratio method may not be adequate for describing the frequency spectrum of the long-offset data.

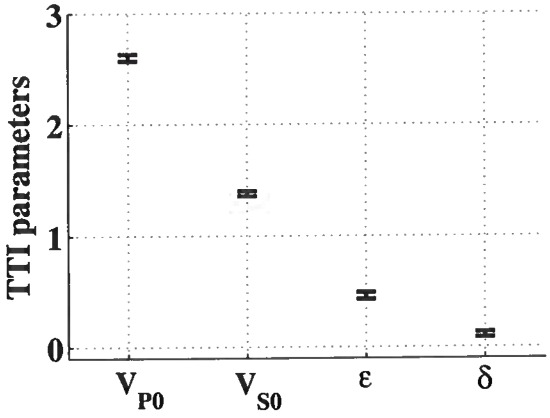

Figure 4. Parameters of the TTI model estimated from the reflection traveltimes of PP- and PS-waves in the symmetry-axis plane. The mean values are $V_{P0} = 2.6$ km/s, $V_{S0} = 1.38$ km/s, $\epsilon = 0.46$, and $\delta = 0.11$ (Dewangan et al., 2005). The error bars mark the standard deviations in each parameter obtained by applying the inversion algorithm to 200 realizations of input reflection traveltimes contaminated by Gaussian noise. The standard deviation of the noise times was equal to 1/8 of the dominant period of the reflection arrivals.

An essential assumption behind the estimates of the attenuation-anisotropy parameters is that wave propagation through the model is homogeneous, and the inhomogeneity angle is negligibly small. Although the modeled attenuation coefficient provides a good fit to the measured curve, it is not clear how significant the inhomogeneity angle for this model may be and how it can influence the parameter-estimation results.

4.2 Uncertainty analysis

It is important to evaluate the uncertainty of the attenuation measurements caused by errors in the velocity-anisotropy parameters. Using the standard deviations in the parameters V_{P0}, ϵ, δ, and ν provided by Dewangan et al. (2005), we repeated our inversion procedure for 50 realizations of the input TTI velocity model (Figure 7). Although the variation of the estimated attenuation coefficients in some directions is substantial, the mean values of the attenuation-anisotropy parameters obtained from the best-fit curve $\mathcal{A}(\theta)$ are close to those listed above. The standard deviations are 2% for $\mathcal{A}_{P0}$, 0.01 for ϵ_Q, and 0.06 for δ_Q, which indicates that the

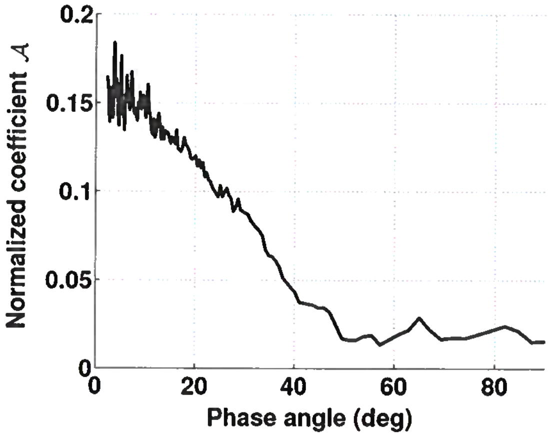

Figure 5. Measured normalized attenuation coefficient as a function of the phase angle.

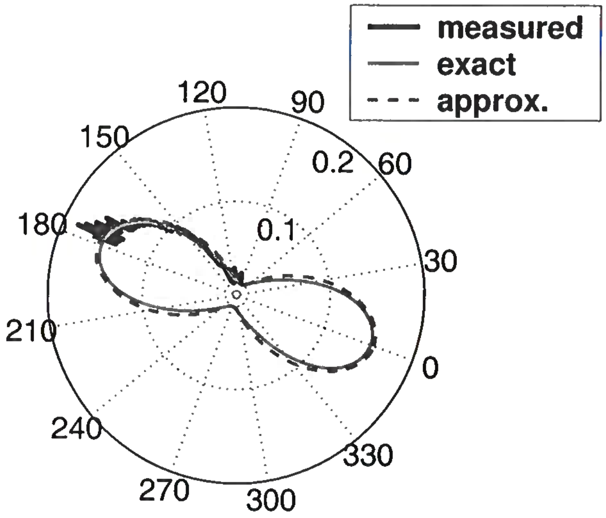

Figure 6. Attenuation measurements from Figure 5 (thick solid line) and the best-fit attenuation coefficients obtained using the Christoffel equation (1) (thin grey solid) and the approximation (2) (dashed).

influence of errors in the velocity field on our results is not significant.

Another potential source of uncertainty in the attenuation-anisotropy measurements is the choice of the frequency range used in the spectral-ratio method. Figure 8 shows the distribution of 50 realizations of the attenuation-anisotropy parameters obtained for variable upper and lower bounds of the frequency range. The means of the estimated parameters are $\mathcal{A}_{P0} = 0.16$ ($Q_{33} = 3.3$), $\epsilon_Q = -0.90$, and $\delta_Q = -1.94$, with the standard deviations equal to 3% for $\mathcal{A}_{P0}$, 0.06 for ϵ_Q, and 0.15 for δ_Q.

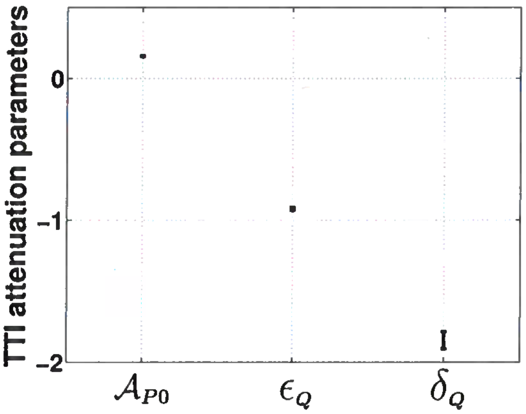

Figure 7. Influence of errors in the velocity model on the attenuation parameters. The error bars mark the standard deviations in each parameter obtained by applying our algorithm with 50 realizations of the input TTI velocity parameters. The standard deviations in the TTI parameters are taken from Dewangan et al. (2005).

The sensitivity of the attenuation-anisotropy parameters to moderate variations in the bounds of the frequency range is therefore not negligible. Note that since the parameter ϵ_Q for our model is close to -1, estimates of the normalized attenuation coefficient Q_{11} in the isotropy plane are unstable ($Q_{11} \rightarrow \infty$ when $\epsilon_Q \rightarrow -1$). Moderate variations of ϵ_Q within the errors bars in Figure 7 produce values of Q_{11} as low as 19.4 and as high as 93.5.

In accordance with the spectral-ratio method, we assume the quality-factor components Q_{ij} to be independent of frequency within the frequency range used for the analysis. The slope of the attenuation coefficient k^I in the frequency domain, however, is not constant, which implies that the attenuation-anisotropy parameters may vary with frequency.

A detailed analysis of the influence of noise in the data on attenuation estimates can be found in Vasconcelos and Jenner (2005).

5 DISCUSSION AND CONCLUSIONS

Since experimental measurements of attenuation are scarce, physical modeling of wave propagation through attenuative materials can provide useful insights into the magnitude and angular variation of the attenuation coefficient. Here, we applied the spectral-ratio method to P-waves transmitted through a transversely isotropic sample for a wide range of angles with the symmetry axis. After estimating the group (effective) attenuation along the raypath, we computed the corresponding phase (plane-wave) attenuation coefficient using a known TI velocity model. The difference between the phase and group attenuation, caused by the influence of velocity anisotropy, has to be accounted for in the

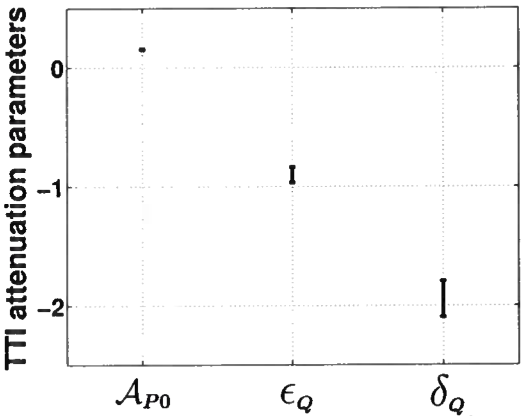

Figure 8. Influence of the frequency range used in the spectral-ratio method on the attenuation parameters. The error bars mark the standard deviations in each parameter obtained by applying our algorithm with 50 realizations of the upper and lower bounds of the frequency range. The upper bound was changed randomly between 88 kHz and 132 kHz, and the lower bound between 44 kHz and 66 kHz.

inversion of the attenuation coefficient for the medium parameters.

The reconstructed phase attenuation coefficient was normalized by the real wavenumber and used to estimate the Thomsen-style attenuation parameters $\mathcal{A}_{P0}$, ϵ_Q, and δ_Q introduced by Zhu and Tsvankin (2004, 2005). The large absolute values of both $\epsilon_Q = -0.92$ and $\delta_Q = -1.84$ reflect the high magnitude of the attenuation anisotropy, with the Q-factor increasing from 3.2 in the slow (symmetry-axis) direction to almost 40 in the fast (isotropy-plane) direction. This result corroborates the conclusions of some previous experimental studies (e.g., Hosten et al., 1987; Prasad and Nur, 2003) that attenuation is often more sensitive to anisotropy than is either phase velocity or reflection coefficient.

While the large difference between the attenuation coefficients in the two principal directions is unquestionable, the accuracy of our measurements strongly depends on several assumptions. First, the radiation pattern of the source and geometrical spreading are taken to be frequency-independent in the frequency range used in the spectral-ratio method. Since the sample is heterogeneous, it is desirable to test the validity of this assumption, particularly for relatively large source-receiver offsets. For example, the experiment can be redesigned by making measurements on two different-size samples of the same phenolic material. Then it would be possible to compute the spectral ratios for arrivals propagating in the same direction and recorded at different distances from the source. In this case, the potential frequency dependence of the radiation pattern would be removed from the attenuation measurement along with the spectrum of the source pulse, and no reference trace would be required.

Second, our analytic solutions for the attenuation coefficient are based on the common assumption of homogeneous wave propagation (i.e., the inhomogeneity angle is assumed to be negligible; see also Hosten et al., 1987). For strongly attenuative models with pronounced attenuation anisotropy, this assumption may cause errors in the interpretation of attenuation measurements. Also, if the model is layered, the inhomogeneity angle is governed by the boundary conditions and can be significant even for moderate values of the attenuation coefficients. Hence, future work should include investigations of the magnitude of the inhomogeneity angle and of its influence on the estimates of the attenuation-anisotropy parameters.

Third, our data-processing sequence did not include compensation for the possible contribution of attenuation to the coupling (i.e., reflection/transmission) coefficients at the source and receiver locations. In general, the attenuation-related frequency dependence of the reflection/transmission coefficients along the raypath can cause distortions in the results of the spectral-ratio method.

Finally, since this work was restricted to compressional data, we were unable to evaluate the strength of the shear-wave attenuation anisotropy and estimate the full set of Thomsen-style anisotropy parameters (Zhu and Tsvankin, 2004, 2005). A more complete characterization of attenuation anisotropy requires combining P-waves with either shear data or converted (e.g., reflected) PS-waves.

6 ACKNOWLEDGMENTS

We are grateful to Kasper van Wijk and Mike Batzle of the Institute of Experimental Geophysics (IEG) at CSM for their help in data acquisition and to Ivan Vasconcelos, Mike Batzle, and Manika Prasad (all of CSM) for useful discussions. The support for this work was provided by the Consortium Project on Seismic Inverse Methods for Complex Structures at CWP and by the Chemical Sciences, Geosciences and Biosciences Division, Office of Basic Energy Sciences, U.S. Department of Energy.

REFERENCES

Arts, R. J., and Rasolofosaon P. N. J., 1992, Approximation of velocity and attenuation in general anisotropic rocks: 62nd Annual International Meeting, Society of Exploration Geophysicists, Expanded Abstracts, 640–643.

Borcherdt, R. D., and Wennerberg, L., 1985, General P, type-I S, and type-II S waves in anelastic solids; Inhomogeneous wave fields in low-loss solids: Bulletin of the Seismological Society of America, **75**, 1729–1763.

Carcione, J. M., 2001, Wave fields in real media: Wave propagation in anisotropic, anelastic, and porous media: Pergamon Press.

Červený, V., and Pšenčík, I., 2004, Plane waves in viscoelastic anisotropic media. Part 1: Theory: Preprint.

Dewangan, P., 2004, Processing and inversion of mode-converted waves using the PP+PS=SS method: PhD thesis, Center for Wave Phenomena, Colorado School of Mines.

Dewangan, P., Tsvankin, I., Batzle, M., van Wijk, K., and Haney, M., 2005, PS-wave moveout inversion for tilted transversely isotropic media: A physical-modeling study: CWP Project Review (this volume).

Grechka, V., Theophanis, S. and Tsvankin, I., 1999, Joint inversion of P- and PS-waves in orthorhombic media: Theory and a physical modeling study: Geophysics, **64**, 146–161.

Hosten, B., Deschamps, M., and Tittmann B. R., 1987, Inhomogeneous wave generation and propagation in lossy anisotropic solids: application to the characterization of viscoelastic composite materials: Journal of the Acoustical Society of America, **82**, 1763–1770.

Krebes, E. S., and Le, L. H. T., 1994, Inhomogeneous plane waves and cylindrical waves in anisotropic anelastic media: Journal of Geophysical Research, **99**, 23899–23919.

Prasad, M., and Nur, A., 2003, Velocity and attenuation anisotropy in reservoir rocks: 73rd Annual International Meeting, Society of Exploration Geophysicists, Expanded Abstracts, 1652-1655.

Tao, G., and King, M. S., 1990, Shear-wave velocity and Q anisotropy in rocks: A laboratory study: International Journal of Rock Mechanics and Mining Sciences and Geomechanics Abstracts, **27**, 353–361.

Thomsen, L., 1986, Weak elastic anisotropy: Geophysics, **51**, 1954–1966.

Tsvankin, I., 1997, Anisotropic parameters and P–wave velocity for orthorhombic media: Geophysics, **62**, 1292–1309.

Tsvankin, I., 2001, Seismic signatures and analysis of reflection data in anisotropic media: Elsevier.

Vasconcelos, I., and Jenner, E., 2005, Estimation of azimuthally varying attenuation from surface seismic data: CWP Project Review.

Zhu, Y., and Tsvankin, I., 2004, Plane-wave propagation and radiation patterns in attenuative TI media: 74th Ann. Internat. Mtg., Soc. Expl. Geophys., Expanded Abstracts, 139–142.

Zhu, Y., and Tsvankin, I., 2005, Plane-wave propagation in attenuative TI media: Geophysics, under review.

APPENDIX A: THOMSEN-STYLE PARAMETERS FOR ATTENUATIVE TI MEDIA

The attenuation coefficients in transversely isotropic (TI) media with TI attenuation can be conveniently described using the Thomsen-style notation of Zhu and Tsvankin (2004, 2005). Instead of the five relevant components Q_{ij} of the quality-factor matrix, they defined two "isotropic" reference quantities ($\mathcal{A}_{P0}$ and $\mathcal{A}_{S0}$) and three dimensionless parameters (ϵ_Q, δ_Q, and γ_Q) describing attenuation anisotropy.

The reference parameters $\mathcal{A}_{P0}$ and $\mathcal{A}_{S0}$ represent the P- and S-wave attenuation coefficients (respectively) in the symmetry direction:

$$\mathcal{A}_{P0} = \frac{1}{2Q_{33}}\,, \tag{A1}$$

$$\mathcal{A}_{S0} = \frac{1}{2Q_{55}}\,. \tag{A2}$$

The parameter ϵ_Q denotes the fractional difference between the P-wave attenuation coefficients in the isotropy plane and along the symmetry axis:

$$\epsilon_Q \equiv \frac{1/Q_{11} - 1/Q_{33}}{1/Q_{33}} = \frac{Q_{33} - Q_{11}}{Q_{11}}\,. \tag{A3}$$

The parameter δ_Q is expressed through the curvature of the P-wave attenuation coefficient in the symmetry direction and, therefore, governs the angle variation of P-wave attenuation near the symmetry axis:

$$\delta_Q \equiv$$

$$\frac{\dfrac{Q_{33} - Q_{55}}{Q_{55}} c_{55} \dfrac{(c_{13} + c_{33})^2}{(c_{33} - c_{55})} + 2\dfrac{Q_{33} - Q_{13}}{Q_{13}} c_{13}(c_{13} + c_{55})}{c_{33}(c_{33} - c_{55})}\,. \tag{A4}$$

Note that the definition of δ_Q involves the real parts of the stiffnesses c_{ij} or the velocity-anisotropy parameters, which is indicative of the coupling between the attenuation coefficient and velocity anisotropy. The third anisotropic parameter, γ_Q, is responsible for the attenuation anisotropy of SH-waves.

The simplified P-wave attenuation coefficient in terms of the Thomsen-style parameters $\mathcal{A}_{P0}$, ϵ_Q, and δ_Q is given in the main text, equation (2).

PS-wave moveout inversion for tilted transversely isotropic media: A physical-modeling study

Pawan Dewangan*, Ilya Tsvankin*, Mike Batzle†, Kasper van Wijk†, and Matt Haney**

** Center for Wave Phenomena, Department of Geophysics, Colorado School of Mines, Golden, CO 80401-1887, USA*
† Institute for Experimental Geophysics, Department of Geophysics, Colorado School of Mines, Golden, CO 80401-1887, USA
*** Center for Wave Phenomena, Department of Geophysics, Colorado School of Mines, Golden, CO 80401-1887, USA*
(currently at Geophysical Technology Department, Sandia National Laboratories, Albuquerque, NM 87185-0750)

ABSTRACT

Mode-converted PS-waves can provide critically important information for velocity analysis in transversely isotropic (TI) media. Here we demonstrate, with physical-modeling data, that the combination of long-spread reflection traveltimes of PP- and PS-waves can be inverted for the parameters of a horizontal TI layer with a tilted symmetry axis. The 2D multicomponent reflection data are acquired over a phenolic sample manufactured to simulate the effective medium formed by a system of steeply dipping, penny-shaped cracks.

The reflection moveout of PS-waves in this model is asymmetric, and the moveout-asymmetry attributes play a crucial role in constraining the TI parameters. Applying the modified PP+PS=SS method to the PP and PS traveltimes recorded in the symmetry-axis plane, we compute the time and offset asymmetry attributes of the PS-waves along with the traveltimes of the pure SS reflections. Then the algorithm of Dewangan and Tsvankin is used to invert the combination of the moveout attributes of the PP-, SS-, and PS-waves for the medium parameters and thickness of the sample.

Our estimates of the tilt of the symmetry axis and layer thickness almost coincide with the actual values. The inverted model was also validated by reproducing the results of transmission experiments with both P- and SV-wave sources. In particular, the transmitted SV wavefield exhibits a prominent cusp (triplication) accurately predicted by the parameter-estimation results.

Key words: multicomponent data, mode conversions, physical modeling, velocity analysis, anisotropic media

1 INTRODUCTION

Transverse isotropy (TI) is a common anisotropic symmetry usually associated with shaly sediments, fine layering on a scale small compared to seismic wavelength, or aligned penny-shaped cracks (e.g., Thomsen, 1986; Helbig, 1994). In active tectonic areas, such as fold-and-thrust belts, the symmetry axis of TI formations is often tilted away from the vertical. Such tilted transversely isotropic (TTI) models are typical for the Canadian Foothills where they cause significant mispositioning of imaged reflectors (e.g., Isaac and Lawton, 1999; Vestrum *et al.*, 1999). An effective TTI medium also describes a system of parallel, dipping, penny-shaped cracks embedded in isotropic host rock (Angerer *et al.*, 2002), as well as progradational sequences.

While conventional migration algorithms can be readily extended to handle transverse isotropy, parameter estimation for TTI media remains a challenging problem. In particular, Grechka and Tsvankin (2000) show that P-wave reflection moveout alone does not constrain the parameters of a horizontal TTI layer, even if a wide range of source-receiver azimuths is available. Furthermore, supplementing P-wave data with wide-azimuth SV-wave traveltimes is still insufficient to make the inversion unique (Grechka and Tsvankin, 2000; Grechka *et al.*, 2002).

Important information for velocity analysis in TTI media is provided by mode-converted PS (PSV) data. Because of the deviation of the symmetry axis from both the vertical and horizontal directions, the moveout of PS-waves from horizontal reflectors becomes asymmetric (i.e., the PS-wave traveltime does not stay the same if the source and receiver are interchanged). As demonstrated by Dewangan and Tsvankin (2004a), moveout-asymmetry attributes of PS-waves can help to estimate all parameters of a horizontal TTI layer using solely reflection data. The algorithm of Dewangan and Tsvankin (2004a), based on a modification of the so-called "PP+PS=SS" method (Grechka and Tsvankin, 2002; Grechka and Dewangan, 2003), operates with long-offset PP and PS reflections acquired in the vertical plane that contains the symmetry axis (hereafter called the *symmetry-axis* plane).

Here, we show on physical-modeling data that the combination of PP and PS reflection traveltimes can indeed constrain all parameters of a horizontal TTI layer. Multicomponent, multioffset reflection seismic lines are acquired in the symmetry-axis plane of a phenolic sample to record long-spread moveouts of PP- and PS(PSV)-waves. Following the methodology of Dewangan and Tsvankin (2004a), the modified PP+PS=SS method is used to compute pure SS-wave reflection traveltimes and the asymmetry attributes of PS-waves. The moveout asymmetry information is then combined with the pure-mode (PP and SS) NMO velocities and zero-offset traveltimes to estimate the model parameters. The accuracy of the inverted TTI model is verified by matching the measured PP and PS traveltimes and reproducing the results of transmission experiments.

2 EXPERIMENTAL SETUP

To simulate a TTI layer, we used XX-paper-based phenolic composed of thin layers of paper bonded with phenolic resin. The effective medium due to this fine layering is anisotropic, and phenolic itself is known to have either TI or orthorhombic symmetry (Isaac and Lawton, 1999; Grechka *et al.*, 1999). The sample was prepared by cutting a large block of commercially available phenolic into smaller blocks and pasting them together at an angle to form a TTI medium. To simulate steeply dipping fractures similar to those identified by Angerer *et al.* (2002) on field data, the tilt ν of the symmetry axis from the vertical was chosen to be 70° (Figure 1).

The experiments were conducted in the Institute for Experimental Geophysics (IEG) at Colorado School of Mines (CSM). The measurements were made only in a vertical symmetry plane of the sample, where the velocities and polarizations are described by TI equations, even if the medium as a whole has orthorhombic symmetry. One reflection survey was acquired using source and receiver transducers (flat-faced cylindrical piezoelectric ultrasonic contact transducers). To generate P-waves, the source transducer was polarized vertically; shear (SV) waves were excited by a horizontal transducer.

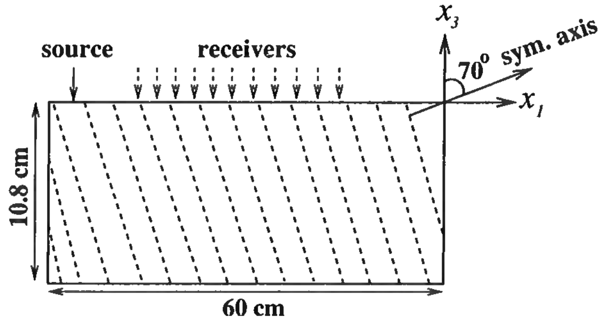

Figure 1. Physical model representing a horizontal TTI layer. The coordinate system is chosen in such a way that the symmetry axis is confined to the $[x_1, x_3]$-plane and is dipping in the negative x_1-direction. To simulate a reflection survey, the sources and receivers were placed on top of the sample in the symmetry-axis plane.

Another reflection data set was generated by the source transducer and recorded by a scanning laser vibrometer that measures the absolute particle velocity on the surface of the sample via the Doppler shift (Nishizawa *et al.*, 1997; Scales and van Wijk, 1999). The records of multiple shots were stacked to improve data quality. The scanning head is programmed to move the beam after each measurement, so that dense arrays of data can be recorded automatically. Therefore, data acquisition with the laser vibrometer is much more efficient compared with time-consuming transducer measurements, where relatively large receivers have to be moved manually.

3 SEISMIC REFLECTION EXPERIMENT

To study the moveout asymmetry of PS-waves and test the parameter-estimation methodology of Dewangan and Tsvankin (2004a), we acquired a multioffset 2D reflection survey in the symmetry-axis plane, as described above. The inversion algorithm operates on common-midpoint (CMP) gathers of PP- and PS-waves and requires the offset-to-depth ratio to reach at least two. Since recording a CMP gather involves moving both the source and receiver transducers, it is cumbersome and prone to error in positioning. Instead, we decided to collect shot gathers (Figure 1) and interpret them as CMP gathers, which is valid for laterally homogeneous media.

To verify that the lateral heterogeneity of the sample is negligible, we recorded a constant-offset P-wave section (Figure 2). The first arrival (the direct P-wave)

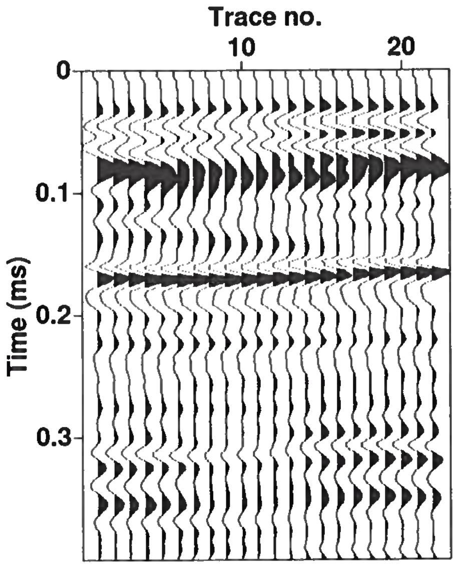

Figure 2. Constant-offset P-wave section acquired to validate the assumption of lateral homogeneity.

and the P-wave multiple at a time of about 0.17 ms exhibit relatively weak traveltime and waveform variations along the line. The waveform of the P-wave primary recorded around 0.08 ms is distorted because of its interference with the ground roll. The minor lateral variations in the waveforms may also be related to errors in receiver positioning and to scattering on air bubbles between imperfectly glued blocks.

Shot gathers of PP- and PS-waves were recorded by fixing the P-wave shot transducer at one end of the model and manually moving the receiver transducer with an increment of 1 cm until the offset reached 30 cm, which corresponds to an offset-to-depth ratio of 2.8 (Figure 1). The whole procedure was repeated by placing the source transducer at the other end of the model to record negative offsets. The traces for positive and negative offsets were then combined to form a split-spread CMP gather.

Another independent data set was obtained by replacing the receiver transducer with the laser vibrometer. The sampling interval for the vibrometer dataset was 2 mm; the maximum offset-to-depth ratio was limited to 2.5 (the maximum offset was 27 cm).

3.1 Vertical component (PP-waves)

For the vertical wavefield component recorded with the contact transducer (Figure 3a), the offset could not be smaller than 3 cm because of the finite transducer size. The minimum offset for the densely spaced data recorded with the laser vibrometer was 2 cm (Figure 3b). Since the vibrometer measures the vertical velocity at a point, it is possible to record closer to the source but the signal quality deteriorates at far offsets.

The two data sets in Figure 3 are quite similar, but identification of reflection events is hampered by their interference with the ground roll. To suppress the ground roll, we applied standard F-K dip filtering that significantly improved the quality of the section (Figure 4). The first arrival is the direct P-wave traveling with the horizontal velocity close to 2620 m/s. The strong ground roll clearly visible in Figure 3 travels with a velocity of 1285 m/s, which is slightly smaller than the shear-wave velocity along the symmetry axis. The P-wave primary reflection from the bottom of the block and the first multiple can be identified at zero-offset times of 0.064 ms and 0.128 ms, respectively. Since the laser dataset is more densely sampled and has better coherency, we used it for manually picking the traveltimes of the primary reflection.

The dominant frequency of the P-wave data decreases from 200 kHz at near offsets to around 40 kHz at far offsets, which indicates that the medium is strongly attenuative (Figure 5). Assuming a dominant frequency of 100 kHz, the units of time and distance used in our experiment should be scaled (multiplied) by 5000 to obtain the corresponding values for seismic field data with a frequency of 20 Hz; the equivalent thickness of the layer would be 540 m.

To estimate the P-wave normal moveout (NMO) velocity, we applied conventional hyperbolic velocity analysis (Figure 6). The influence of nonhyperbolic moveout was mitigated by muting out long offsets. The maximum offset-to-depth ratio used to compute the semblance in Figure 6a was close to one. The best-fit NMO velocity $V_{\mathrm{nmo},P}$, which flattens the near-offset primary and multiple reflections (Figure 6b), is 2350±50 m/s.

At large offsets, the NMO-corrected gather in Figure 6b is not flat, which indicates that the moveout curve is nonhyperbolic. This deviation from hyperbolic moveout in a single homogeneous layer indicates that the medium is anisotropic, and the anisotropy is not elliptical (e.g., Tsvankin, 2001).

The event arriving at $t_0 = 0.11$ ms with a lower moveout velocity than that of the P-waves may be interpreted as a converted PS mode. Since the PS-wave polarization vector at small and moderate offsets is close to the horizontal plane, this event is not prominent on the vertical component. To clearly identify mode-converted waves and pick their traveltimes, we recorded the horizontal component of the wavefield, as described in the next section.

3.2 Horizontal component (PS-waves)

The horizontal wavefield component from the vertical source was recorded with the same settings as the ver-

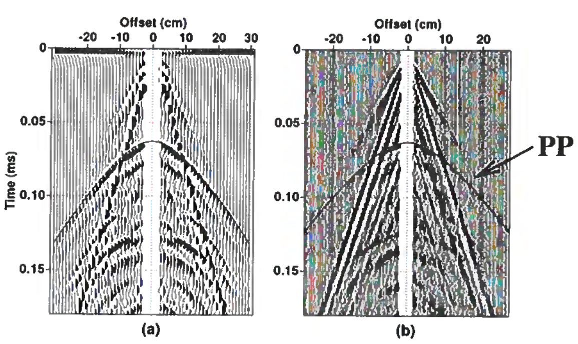

Figure 3. Vertical component of the wavefield. (a) Data recorded with the P-wave contact transducers; (b) densely sampled data recorded with the laser vibrometer. The first arrival is the direct P-wave; the PP-wave reflection from the bottom of the block (solid line) arrives at a zero-offset time of 0.064 ms.

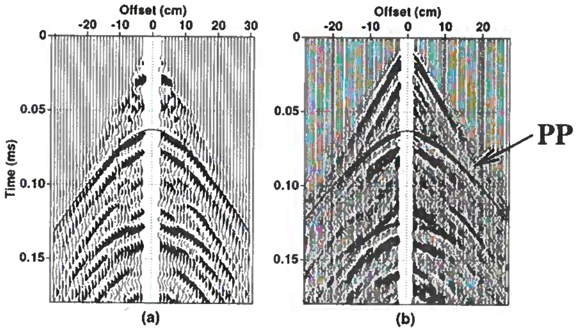

Figure 4. Data from Figure 3 after application of F-K filtering to suppress the ground roll.

tical component. The receiver transducer was oriented horizontally in the symmetry-axis plane to record mode-converted PS(PSV)-waves (Figure 7a). We verified that there was almost no energy on the crossline (transverse) component, which indicates that the data were indeed acquired in a symmetry plane of the medium. Also, shear-wave splitting along the symmetry axis was negligible, suggesting that the model is either TI or a special case of orthorhombic media with equal anisotropy coefficients $\gamma^{(1)}$ and $\gamma^{(2)}$ (Tsvankin, 1997, 2001). Because of the kinematic equivalence between the symmetry planes of orthorhombic and TI media, the parameter-estimation algorithm of Dewangan and Tsvankin (2004a) is valid for both plausible models.

So far, the laser vibrometer system available at CSM has not been used to record the horizontal component of the wavefield. This limitation, however, can be overcome by recording mode-converted SP-waves and treating their traveltimes (according to reciprocity) as those of the corresponding PS-waves. Instead of the P-wave transducer used before, a shear transducer served as the source and the laser vibrometer as the detector of the vertical wavefield component (Figure 7b). In the moveout analysis below, the traveltimes of the acquired SP-wave were substituted for those of the PS-wave, while the sign of the SP-wave source-receiver offset was reversed when constructing a split-spread PS-wave gather.

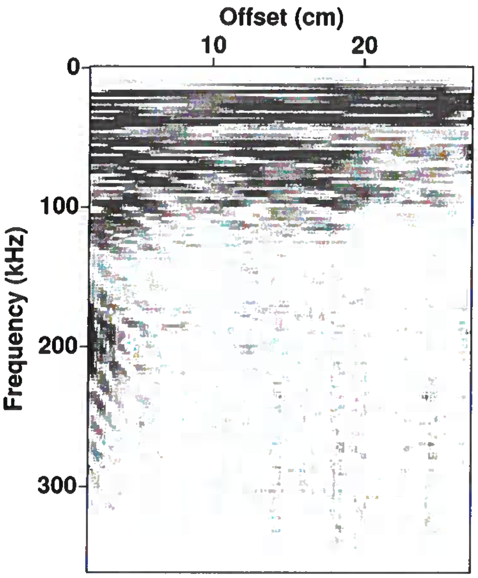

Figure 5. Amplitude spectra of the P-wave traces showing a decrease in frequency with offset.

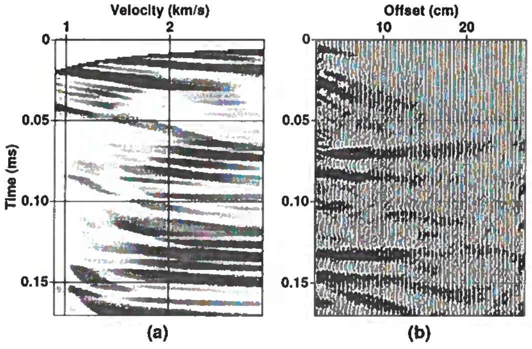

Figure 6. Conventional hyperbolic velocity analysis of the P-wave data. (a) Semblance panel computed for the maximum offset-to-depth ratio close to one; (b) the gather corrected for hyperbolic moveout using a moveout velocity of 2350 m/s.

Both acquired sections after application of F-K filtering are displayed in Figure 8. As was the case with the vertical component, there is close similarity between

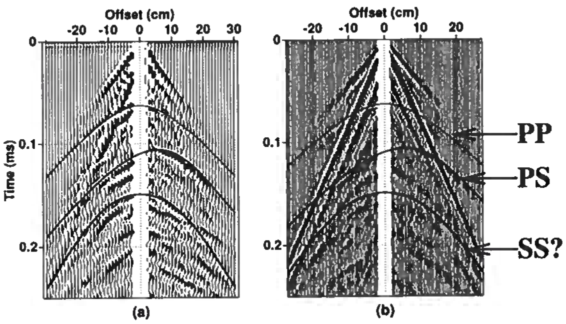

Figure 7. Horizontal component of the wavefield. Data recorded with: (a) the P-wave source transducer and S-wave receiver transducer; (b) the S-wave source transducer and the laser vibrometer as the receiver. The converted wave from the bottom of the model has an asymmetric moveout curve with the apex at 0.11 ms. The solid lines are the picked traveltimes of the PP, PS, and SS arrivals.

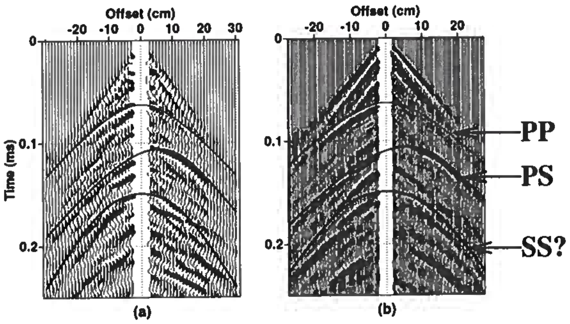

Figure 8. Data from Figure 7 after application of F-K filtering to suppress the ground roll. Negative offsets are displayed in reverse polarity to facilitate picking of PS traveltimes.

the two data sets recorded using different experimental setups. The moveout of the mode-converted PS- and SP-waves is strongly asymmetric, with a substantial difference between the traveltimes for positive and negative offsets. Since the model is laterally homogeneous, the PS-wave moveout asymmetry is caused entirely by the oblique orientation of the symmetry axis. Note that the moveout of converted waves is symmetric in any laterally homogeneous medium with a horizontal symmetry plane, including TI models with a vertical (VTI) and horizontal (HTI) symmetry axis (Grechka and Tsvankin, 2000; Dewangan and Tsvankin, 2004a).

The traveltime picks of the PS-wave, marked by the solid line in Figure 8, were made using the laser vibrometer dataset. Due to the moveout asymmetry, the minimum PS-wave traveltime is recorded at an offset of x=6 cm where the wavelet reverses its polarity. To facilitate visual correlation of PS traveltimes, we removed this polarity reversal from the sections in Figure 8.

The PP-wave primary reflection can be identified even on the horizontal component around the zero-offset time $t_{P0} = 0.064$ ms. It may also be possible to tentatively pick the SS-wave reflected arrival but, as expected, in Figure 8 it is much weaker than the converted modes.

3.3 Data processing

The key processing step was application of the PP+PS=SS method (Grechka and Tsvankin, 2002; Grechka and Dewangan, 2003) to compute the traveltimes of the pure SS (SVSV) reflections from the PP and PS data. The reflection traveltimes of both the PP-waves (on the vertical component) and the converted waves (on the horizontal component) were manually picked from the laser vibrometer dataset. To smooth the traveltimes and interpolate/extrapolate them at near offsets, we fitted a six-order polynomial to both PP and PS moveouts using the least-squares method.

The idea of the PP+PS=SS method is to identify two "reciprocal" PS-wave rays with the same reflection (conversion) point and combine their traveltimes with that of the PP-wave to compute the moveout of the SS-wave primary reflection. This can be accomplished by matching the reflection slopes on common-receiver gathers of PP- and PS-waves, as illustrated in Figure 9 (Grechka and Tsvankin, 2002). Since the PS rays recorded at points $x^{(3)}$ and $x^{(4)}$ have the same reflection point as the PP reflection $x^{(1)}Rx^{(2)}$, the traveltime τ_{SS} of the SS-wave (not physically excited in the survey) is determined from

$$\begin{aligned} \tau_{SS}(x^{(3)}, x^{(4)}) &= t_{PS}(x^{(1)}, x^{(3)}) + t_{PS}(x^{(2)}, x^{(4)}) \\ &- t_{PP}(x^{(1)}, x^{(2)}) \,, \end{aligned} \tag{1}$$

where t_{PS} and t_{PP} are the traveltimes of the PS and PP reflections, respectively. Note that application of this technique requires correlating PP and PS reflection events and picking their traveltimes, although explicit velocity information is not needed.

Alternatively, PP and PS arrivals with the same reflection point can be found by computing the time τ_{SS} in equation (1) for each desired SS-wave shot-receiver pair $(x^{(3)}, x^{(4)})$ and a wide range of the coordinates ($x^{(1)}$ and $x^{(2)}$) (Grechka and Dewangan, 2003; Dewangan and Tsvankin, 2004a):

$$\begin{aligned} \tau_{SS}(x^{(3)}, x^{(4)}) = \min_{x^{(1)},\, x^{(2)}} \Big(& t_{PS}(x^{(1)}, x^{(3)}) \\ & + t_{PS}(x^{(2)}, x^{(4)}) - t_{PP}(x^{(1)}, x^{(2)}) \Big) \,. \end{aligned} \tag{2}$$

The minimum of the function (2) in both the $x^{(1)}$ and $x^{(2)}$ directions allows us to identify the P-wave sources that generate the reciprocal PS arrivals with the same reflection point. The value of τ_{SS} corresponding to this minimum yields the SS traveltime from ($x^{(3)}$ to $x^{(4)}$).

We opted to apply the latter procedure to compute

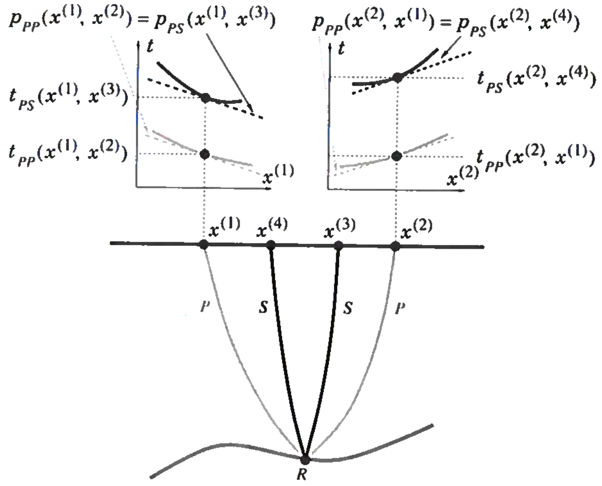

Figure 9. PP+PS=SS method is designed to find the source/receiver coordinates of the PP and PS rays with the same (albeit unknown) reflection point R. By matching the slopes on common-receiver gathers (i.e., the ray parameters) of the PP- and PS-waves, the method estimates the recording locations $x^{(3)}$ and $x^{(4)}$ of the PS arrivals that have the common P-wave legs with the PP reflection from $x^{(1)}$ to $x^{(2)}$ (after Grechka and Tsvankin, 2002).

the SS-wave traveltime as a function of the SS-wave offset $x_{SS} = |x^{(3)} - x^{(4)}|$ (Figure 10). Then, conventional hyperbolic velocity analysis was applied to the constructed SS arrivals to estimate their stacking velocity ($V_{\text{nmo},S} \approx 1780$ m/s) and zero-offset traveltime ($t_{S0} \approx 0.149$ ms).

Next, we followed the methodology of Dewangan and Tsvankin (2004a) in computing the time and offset asymmetry attributes of the PS-wave:

$$\Delta t_{PS}(x^{(3)}, x^{(4)}) = t_{PS}(x^{(1)}, x^{(3)}) - t_{PS}(x^{(2)}, x^{(4)})\,; \quad (3)$$

$$\begin{aligned}\Delta x_{PS}(x^{(3)}, x^{(4)}) &= |x_{PS}(x^{(1)}, x^{(3)})| \\ &- |x_{PS}(x^{(2)}, x^{(4)})|\,. \end{aligned} \quad (4)$$

The time asymmetry factor Δt_{PS} (Figure 11a) rapidly increases with offset and reaches about 20% of the zero-offset time. In contrast, the depth-normalized offset asymmetry Δx_{PS} reaches its maximum (by absolute value) at small SS-wave offsets (Figure 11b), as predicted by the analytic results of Dewangan and Tsvankin (2004a) for the symmetry axis deviating by more than 45° from the vertical. Note that the factor Δx_{PS} at zero offset ($x^{(3)} = x^{(4)}$) is twice the offset $x_{\min}$ corresponding to the minimum traveltime in the PS-wave CMP gather (Tsvankin and Grechka, 2000).

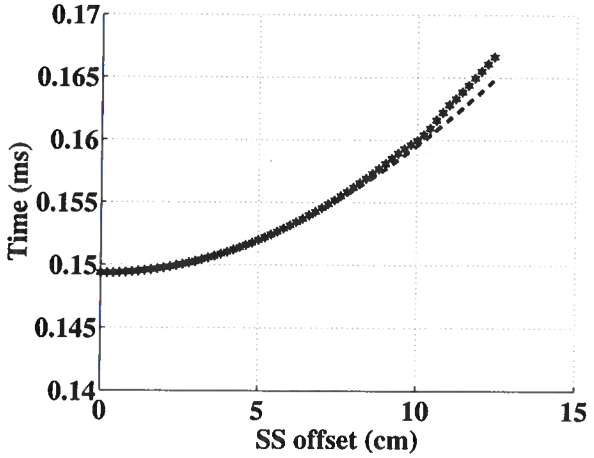

Figure 10. SS-wave traveltime computed using the PP+PS=SS method (stars) as a function of the SS-wave offset. The dashed line corresponds to the best-fit hyperbola with a moveout velocity of 1780 m/s.

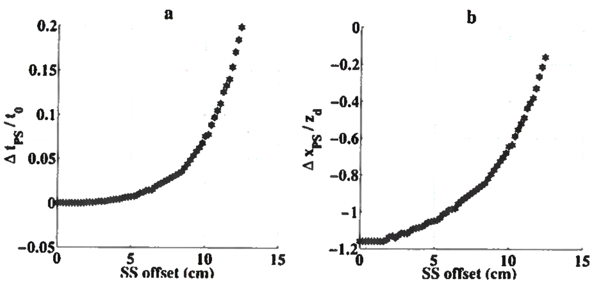

Figure 11. Moveout-asymmetry attributes of the PS-wave computed from equations (3) and (4). (a) The time asymmetry Δt_{PS} normalized by the zero-offset PS-wave time; (b) the corresponding offset asymmetry Δx_{PS} normalized by the layer thickness.

3.4 Parameter Estimation

The vector $\boldsymbol{d}$ of input data for the inversion procedure includes the NMO velocities and zero-offset times of the PP- and SS-waves and the asymmetry attributes of the PS-wave:

$$\begin{aligned}\boldsymbol{d} \;\equiv\; \Big\{ & V_{\text{nmo},P}\,,\, t_{P0}\,,\, V_{\text{nmo},S}\,,\, t_{S0}\,,\, \Delta t_{PS}(x_{SS})\,, \\ & \Delta x_{PS}(x_{SS}) \Big\}\,, \end{aligned} \quad (5)$$

The analytic expressions needed to model these quantities are given in Dewangan and Tsvankin (2004a), who used the offset $x_{\min}$ of the traveltime minimum instead of the asymmetry factor Δx_{PS}. Here, however, we prefer to operate with the function (array) $\Delta x_{PS}(x_{SS})$ that helps to obtain more accurate parameter estimates in the presence of noise (Dewangan and Tsvankin, 2004b).

The model vector $\boldsymbol{m}$ includes the five relevant TTI parameters and the layer thickness z:

$$\boldsymbol{m} \equiv \left\{ V_{P0}\,,\, V_{S0}\,,\, \epsilon\,,\, \delta\,,\, \nu,\, z \right\}, \tag{6}$$

where V_{P0} and V_{S0} are the velocities of P- and S-waves (respectively) in the symmetry direction, ϵ and δ are Thomsen anisotropy parameters, and ν (tilt) is the angle between the symmetry axis and the verical. To estimate the elements of $\boldsymbol{m}$, we applied the nonlinear inversion algorithm discussed in Dewangan and Tsvankin (2004a), with the misfit (objective) function given by

$$\begin{aligned} \mathcal{F} \equiv\ & \frac{(V^{\rm calc}_{{\rm nmo},P} - V^{\rm meas}_{{\rm nmo},P})^2}{(V^{\rm meas}_{{\rm nmo},P})^2} + \frac{(V^{\rm calc}_{{\rm nmo},S} - V^{\rm meas}_{{\rm nmo},S})^2}{(V^{\rm meas}_{{\rm nmo},S})^2} \\ & + \frac{(t^{\rm calc}_{P0} - t^{\rm meas}_{P0})^2}{(t^{\rm meas}_{P0})^2} + \frac{(t^{\rm calc}_{S0} - t^{\rm meas}_{S0})^2}{(t^{\rm meas}_{S0})^2} \\ & + \frac{\sum_0^{x^{\max}_{SS}} (\Delta t^{\rm calc}_{PS} - \Delta t^{\rm meas}_{PS})^2}{(\sum_0^{x^{\max}_{SS}} \Delta t^{\rm meas}_{PS})^2} \\ & + \frac{\sum_0^{x^{\max}_{SS}} (\Delta x^{\rm calc}_{PS} - \Delta x^{\rm meas}_{PS})^2}{(\sum_0^{x^{\max}_{SS}} \Delta x^{\rm meas}_{PS})^2}\,. \end{aligned} \tag{7}$$

Here, the superscripts "calc" and "meas" denote the calculated and measured quantities (respectively), and $x^{\max}_{SS}$ is the maximum offset of the constructed SS-wave that corresponds to the offset-to-depth ratio of the recorded PP data close to two.

The initial guesses for the vertical velocities and anisotropy coefficients were based on the isotropic relationships,

$$\begin{aligned} & V_{P0} = V_{{\rm nmo},P} = 2.35\,{\rm km/s}\,,\ V_{S0} = V_{{\rm nmo},S} = 1.78\,{\rm km/s}, \\ & \epsilon = 0,\ \delta = 0,\ z = V_{{\rm nmo},P}\, t_{P0}/2 = 7.52\,{\rm cm}\,. \end{aligned} \tag{8}$$

The initial tilt of the symmetry axis was randomly chosen between 50° and 85°. Although both the tilt ν and thickness z were known, they were estimated from the data to simulate a field experiment.

To assess the stability of the inversion, the algorithm was applied to multiple realizations of the input PP and PS traveltimes contaminated by random Gaussian noise with zero mean. The standard deviation of the noise was equal to 1/8 of the dominant period, which was assumed to be close to the accuracy of the traveltime picking. The inversion results for 200 realizations of the Gaussian noise are shown in Figure 12. The best-constrained parameter combination is the difference between ϵ and δ, which controls both the time and offset asymmetry (Dewangan and Tsvankin, 2004a). Note that the sample is strongly anisotropic, with the value of ϵ approaching 50%.

The PP- and PS-wave traveltimes computed for the estimated model are practically indistinguishable from the picked traveltimes at all offsets (Figures 4 and 8). Another indication of the high accuracy of the inversion procedure is that the errors in the known values of ν and z are almost negligible.

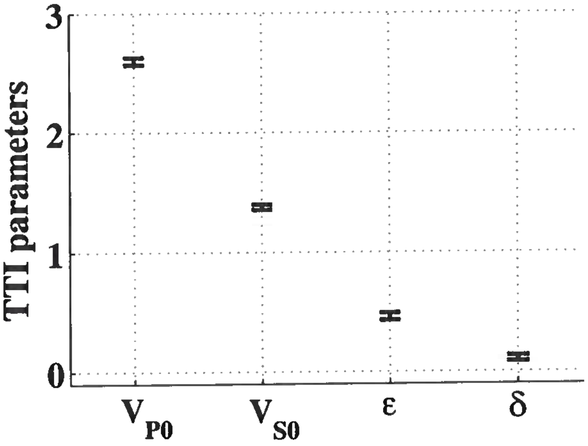

Figure 12. Thomsen parameters of the sample estimated from 2D PP and PS data in the symmetry-axis plane (the velocities are in km/s). The mean values are $V_{P0} = 2.6$ km/s, $V_{S0} = 1.38$ km/s, $\epsilon = 0.46$, and $\delta = 0.11$. The estimated tilt of the symmetry axis and layer thickness (not shown) are $\nu = 70°$ and $z = 10.9$ cm. The error bars correspond to the following standard deviations in each parameter: 2% for V_{P0}, V_{S0}, and z, 0.03 for ϵ and δ, and 1° for ν.

4 TRANSMISSION/CALIBRATION EXPERIMENT

To verify the estimated model using an independent data set, we conducted a transmission experiment on the same sample. The P-wave source transducer was fixed at the bottom of the model, while the laser vibrometer scanned the top with a regular interval of 2 mm. The experiment was set up in such a way that the first-arrival traveltime could be measured for the full range of propagation angles (0° – 90°) from the symmetry axis.

It is believed that laboratory experiments employing transducers of relatively large size may yield measurements of phase, not group velocity (Dellinger and Vernik, 1994). Our transducer, however, was small (15 mm) compared to the thickness of the model (108 mm), so the traveltimes should be determined by the corresponding group velocities. Therefore, to reproduce the results of the transmission experiment, we computed the group velocity V_G and the group angle ϕ for the inverted model using the standard TI equations (e.g., Tsvankin, 2001):

$$V_G = V \sqrt{1 + \left(\frac{1}{V}\,\frac{dV}{d\theta}\right)^2}\ ; \tag{9}$$

$$\tan\phi = \frac{\tan\theta + \frac{1}{V}\frac{dV}{d\theta}}{1 - \frac{\tan\theta}{V}\frac{dV}{d\theta}}\,, \tag{10}$$

where V and θ are the phase velocity and phase angle. It was assumed that ray bending was negligible, and the group angle ϕ corresponds to the source-receiver line.

Figure 13 shows the raw transmission data, with the zero- and far-offset receiver positions corresponding to the directions approximately perpendicular and parallel (respectively) to the symmetry axis. The first break is the direct P-wave followed by the relatively weak direct S-wave. The solid line marks the P-wave arrival time computed for the inverted TTI model using equations (9) and (10). Evidently, the estimated model parameters accurately predict the P-wave velocity in the transmission experiment that includes a wider range of propagation directions compared to the reflection data set.

It is interesting that the wavefront of the direct S-wave arrival in Figure 13 exhibits a cusp (triplication) at oblique angles with the symmetry axis. The existence and size of the cusp is mostly governed by the magnitude of the anisotropic parameter $\sigma \equiv (V_{P0}/V_{S0})^2\,(\epsilon - \delta)$ (Tsvankin, 2001; Thomsen, 2002) that reaches 1.24 for our model. While SV-wave cusps in TI media are well understood theoretically, their experimental observations are rare (e.g., Slater *et al.*, 1993).

To identify the cusp more clearly and measure the transmitted shear-wave traveltimes, we performed another transmission experiment, this time with the S-wave transducer as the source (Figure 14b). The transmitted wavefield was also computed (Figure 14a) for the inverted TTI model from Figure 12 using the spectral-element method (Komatitsch and Vilotte, 1998). Although the spectral-element code is 2D and cannot be expected to accurately reproduce the recorded amplitudes, the agreement between the measured and modeled wavefields in Figure 14 is excellent.

The spatial extent of the cusp in Figure 14 is significantly larger than that predicted by the group-velocity surface (i.e., by ray-theory modeling). This is consistent with the observation by Martynov and Mikhailenko (1984) that ray theory underestimates the actual size of the SV-wave cusp in TI media computed by solving the wave equation. The reflected PS data analyzed above do not exhibit cuspoidal behavior because the shear-wave group angles corresponding to the cusp are not reached during the P-to-S conversion at the bottom of the layer.

The ray-theoretical S-wave traveltimes computed for the inverted model (solid lines) match the observed arrivals only up to an offset of about 10 cm. To explain the discrepancy at larger offsets, we increased the frequency of the signal used in the spectral-element modeling (Figure 15). The higher-frequency wavefield shows two distinct arrivals with close traveltimes – the direct S-wave and the refracted P-wave. The interference of these waves on the lower-frequency section (Figure 14) produces a complicated wavelet that arrives ahead of the direct shear wave at large offsets. Another wave more clearly visible in Figure 15 is the P-wave multiple in the layer.

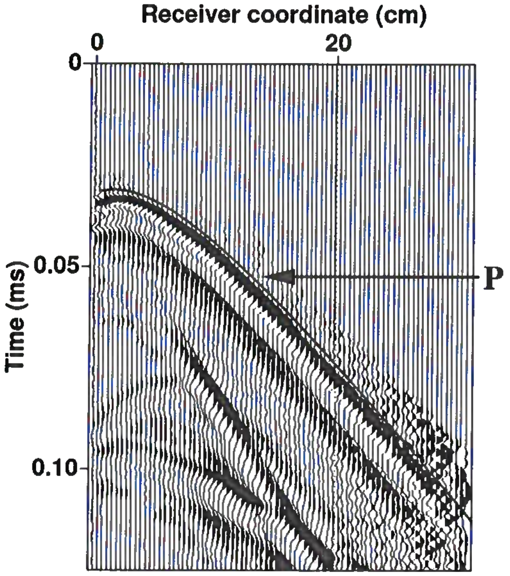

Figure 13. Transmitted wavefield excited by the P-wave transducer and recorded by the laser vibrometer at the top of the model. The solid line is the P-wave traveltime modeled using the inverted parameters from Figure 12.

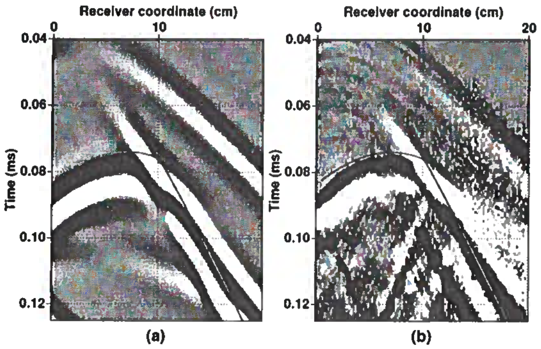

(a) (b)

Figure 14. Shear-wave cusp in the transmitted wavefield excited by the S-wave transducer. (a) The wavefield simulated with the spectral element method; (b) the wavefield recorded by the laser vibrometer. The solid line is the S-wave traveltime computed from the group-velocity surface for the inverted model in Figure 12.

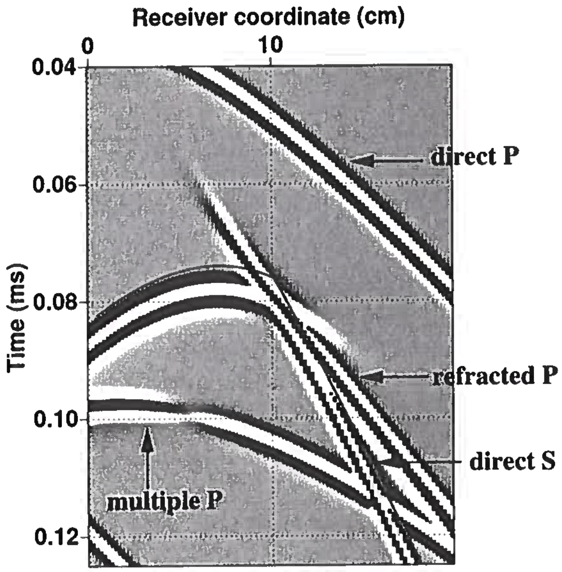

Figure 15. Same as Figure 14a, but the spectral-element modeling was performed with a higher-frequency wavelet.

5 DISCUSSION AND CONCLUSIONS

To estimate the anisotropic parameters of tilted TI media, P-wave reflection moveout can be combined with converted PS-waves. Here, we used 2D physical-modeling reflection data recorded over a horizontal layer of phenolic material to demonstrate that long-spread PP and PS (PSV) reflection traveltimes can be inverted in a stable way for the orientation of the symmetry axis and the pertinent Thomsen parameters. The large tilt of the symmetry axis from the vertical (70°) was designed to model the effective medium due to a system of steeply dipping, parallel cracks.

The data were acquired in the plane that contains the symmetry axis of the material (the "symmetry-axis plane") and processed using the modified version of the PP+PS=SS method developed by Dewangan and Tsvankin (2004a). In addition to the traveltimes of the pure SS reflections (which are not physically excited in the survey), this methodology produces the moveout-asymmetry attributes of the recorded PS arrivals. Our case study confirmed the conclusion of Dewangan and Tsvankin (2004a) that the combination of the PS-wave time and offset asymmetry factors with the NMO velocities and zero-offset times of the PP- and SS-waves makes it possible to estimate the medium parameters and layer thickness. Note that in field experiments the azimuth of the symmetry axis has to be estimated from the polarization of PS-waves or the azimuthal variation of such signatures as NMO velocities and AVO (amplitude variation with offset) gradients.

The sample proved to be strongly anisotropic, with the magnitude of P-wave velocity variations approaching 50% ($\epsilon = 0.46$, $\delta = 0.11$). The inversion algorithm provided accurate estimates of the known values of the tilt of the symmetry axis and the layer thickness. Still, to verify the parameter-estimation results, we conducted a transmission experiment using both P-wave and S-wave transducers. The P-wave group-velocity curve computed for the inverted model accurately matched the first breaks of the transmitted P-wave.

The wavefront of the transmitted SV-wave has a more complicated shape, with a cusp (triplication) between the symmetry axis and the isotropy plane. Although the observed cusp is noticeably wider than that predicted by the group-velocity surface calculated for the estimated model, this discrepancy is caused by the inadequacy of ray theory in describing triplications. More accurate modeling using the spectral-element method allowed us to reproduce the cusp and all other major features of the transmitted wavefield excited by the shear transducer. Since the shape and spatial extent of SV-wave cusps are highly sensitive to the medium parameters, the excellent agreement between the modeling results and recorded wavefield confirms the robustness of our inversion method.

6 ACKNOWLEDGMENTS

We are grateful to members of the A(nisotropy)-Team of the Center for Wave Phenomena (CWP), Colorado School of Mines (CSM), for helpful discussions and to Ken Larner (CSM) for his careful review of the manuscript. The support for this work was provided by the Consortium Project on Seismic Inverse Methods for Complex Structures at CWP and by the Chemical Sciences, Geosciences and Biosciences Division, Office of Basic Energy Sciences, U.S. Department of Energy. The experimental work was supported by the National Science Foundation (EAR-0111804, EAR-0337379) and the Army Research Office (DAAG55-98-1-0277, DAAD19-03-1-0292).

REFERENCES

Angerer, E., Horne, S. A., Gaiser, J. E., Walters, R., Bagala, S. and Vetri, L., 2002, Characterization of dipping fractures using PS mode-converted data: 72th Annual International Meeting, Society of Exploration Geophysicists, Expanded Abstracts, 1010–1013.

Bakulin, A., Grechka, V., and Tsvankin, I., 2000, Estimation of fracture parameters from reflection seismic data – Part I: HTI model due to a single fracture set: Geophysics, **65**, 1788–1802.

Dellinger, J. and Vernick, L., 1994, Do traveltimes in pulse-transmission experiments yield anisotropic group or phase velocities?: Geophysics, **59**, 1774–1779.

Dewangan, P., and Tsvankin, I. 2004a, Application of PS-wave moveout asymmetry in parameter estimation for tilted TI media – Part I: Horizontal TTI layer: Geophysics, under review.

Dewangan, P., and Tsvankin, I. 2004b, Application of PS-wave moveout asymmetry in parameter estimation for tilted TI media – Part II: Dipping TTI layer: Geophysics, under review.

Grechka, V., and Dewangan, P., 2003, Generation and processing of pseudo shear-wave data: Theory and case study: Geophysics, **68**, 1807–1816.

Grechka, V., Pech, A., and Tsvankin, I., 2002, Multicomponent stacking-velocity tomography for transversely isotropic media: Geophysics, **67**, 1564–1574.

Grechka, V., Theophanis, S. and Tsvankin, I., 1999, Joint inversion of P- and PS-waves in orthorhombic media: Theory and a physical modeling study: Geophysics, **64**, 146–161.

Grechka, V., and Tsvankin, I., 2000, Inversion of azimuthally dependent NMO velocity in transversely isotropic media with a tilted axis of symmetry: Geophysics, **65**, 232–246.

Grechka, V., and Tsvankin, I., 2002, PP+PS=SS: Geophysics, **67**, 1961–1971.

Helbig, K., 1994, Foundations of elastic anisotropy for exploration seismics: Pergamon Press.

Isaac, J. H., and Lawton, D. C., 1999, Image mispositioning due to dipping TI media: A physical seismic modeling study: Geophysics, **64**, 1230–1238.

Komatitsch, D., and Vilotte, J. P., 1998, The spectral-element method: An efficient tool to simulate the seismic response of 2D and 3D geological structures: Bulletin of the Seismological Society of America, **88**, 368–392.

Martynov, V. N., and Mikhailenko, B.G., 1984, Numerical modelling of elastic waves in anisotropic inhomogeneous media for the halfspace and the sphere: Geophysical Journal of the Royal Astronomical Society, **76**, 53–63.

Nishizawa O., Satoh, T., Lei, X., and Kuwahara, Y., 1997, Laboratory studies of seismic wave propagation in inhomogeneous media using a laser doppler vibrometer: Bulletin of the Seismological Society of America, **87**, 809–823.

Scales, J. A., and van Wijk, K., 1999, Multiple scattering attenuation and anisotropy of ultrasonic surface waves: Applied Physics Letters, **74**, 3899–3901.

Slater, C., Crampin, S., Brodov, L. Yu., and Kuznetsov, V. M., 1993, Observations of anisotropic cusps in transversely isotropic clay: Canadian Journal of Exploration Geophysics, **29**, 216–226.

Thomsen, L., 1986, Weak elastic anisotropy: Geophysics, **51**, 1954–1966.

Thomsen, L., 2002, Underst anding seismic anisotropy in exploration and exploitation: DISC (Distinuguished Instructor Short Course) Notes, Society of Exploration Geophysicists.

Tsvankin, I., 1997, Reflection moveout and parameter estimation for horizontal transverse isotropy: Geophysics, **62**, 614–629.

Tsvankin, I., 2001, Seismic signatures and analysis of reflection data in anisotropic media: Elsevier Science Publ. Co., Inc.

Tsvankin, I., and Grechka, V., 2000, Dip moveout of converted waves and parameter estimation in transversely isotropic media: Geophysical Prospecting, **48**, 257–292.

Vestrum, R. W., Lawton, D. C., and Schmid, R., 1999, Imaging structures below dipping TI media: Geophysics, **64**, 1239–1246.

Exact layer stripping of PP and PS reflections from dipping interfaces in anisotropic media

Pawan Dewangan and Ilya Tsvankin
Center for Wave Phenomena, Department of Geophysics,
Colorado School of Mines, Golden, CO 80401-1887

ABSTRACT

Building accurate interval velocity models is critically important for seismic imaging and AVO (amplitude variation with offset) analysis. Here, we adapt the so-called "PP+PS=SS" method to develop an exact technique for constructing the interval traveltime-offset function in a dipping anisotropic (target) layer beneath a horizontally layered overburden. Whereas the overburden is also supposed to have a horizontal symmetry plane, there are no restrictions on the type of anisotropy in the target layer.

It should be emphasized that the presented algorithm is entirely data-driven and does not require knowledge of the velocity field anywhere in the model. Other important advantages of our method compared to the generalized Dix equations include the ability to handle laterally heterogeneous target layers, long-offset data and mode-converted waves. Numerical tests confirm the high accuracy of the algorithm in computing the interval traveltimes of both PP- and PS-waves in a transversely isotropic layer with a tilted symmetry axis (TTI medium) beneath an anisotropic overburden.

In combination with existing inversion techniques for homogeneous TTI media, the layer stripping of PP and PS data can be used to estimate the interval parameters of TTI formations in such important exploration areas as the Canadian Foothills. Other potential applications of our methodology are in the dip-moveout inversion for the key time-processing parameter η and in the exact computation of the interval long-spread (nonhyperbolic) moveout that provides valuable information for anisotropic velocity analysis.

Key words: reflection moveout, velocity analysis, multicomponent data, mode conversions, anisotropic media

1 INTRODUCTION

Velocity analysis based on reflection moveout is routinely used for estimating subsurface velocity fields and imaging target reflectors. However, reflection traveltime in general and normal-moveout (NMO) velocity in particular represent effective quantities that are influenced by the medium properties along the entire raypath of the reflected wave. Interval parameter estimation for purposes of prestack and poststack migration requires application of layer-stripping (e.g., Dix, 1955; Liu, 1997; Grechka and Tsvankin, 2000; Sarkar and Tsvankin, 2004) or tomographic (e.g., Stork, 1991; Pech et al., 2002a,b) methods. Layer parameters are also needed for the inversion of the AVO (amplitude variation with offset) response, lithology discrimination and fracture detection using seismic data, etc.

In horizontally layered, isotropic media, the NMO velocity of reflected waves is equal to the root-mean-square (rms) of the interval velocities. This simple relationship, first discussed by Dix (1955), makes it possible to obtain the velocity in any layer using only the NMO velocities for the reflections from the top and bottom of this layer. A more general version of the Dix equation

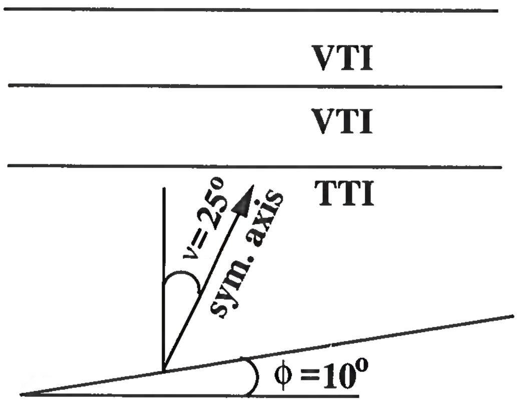

Figure 2. Transversely isotropic model used to test the layer-stripping algorithm for pure modes. The first layer has a vertical symmetry axis (VTI medium) and the following parameters: the symmetry-direction P-wave velocity $V_{P0} = 2$ km/s, the symmetry-direction S-wave velocity $V_{S0} = 1$ km/s, the thickness $z = 0.25$ km, and Thomsen anisotropy parameters $\epsilon = 0.2$ and $\delta = 0.1$. The second layer is also VTI with $V_{P0} = 4$ km/s, $V_{S0} = 2$ km/s, $z = 0.25$ km, $\epsilon = 0.15$, and $\delta = 0.05$; the third layer is dipping TTI with the symmetry axis tilted at $\nu = 25°$, the dip of the bottom $\phi = 10°$, $V_{P0} = 4$ km/s, $V_{S0} = 2$ km/s, $z = 0.5$ km, $\epsilon = 0.25$, and $\delta = -0.05$. The Thomsen parameters in the TTI layer are defined with respect to the symmetry axis (Dewangan and Tsvankin, 2004a,b).

restricted to isotropic media. Also, in contrast to the Dix-type equation (1), our algorithm can be applied to long-offset data and can handle a laterally heterogeneous target layer.

2.2 Numerical example

The layer-stripping algorithm was tested on PP-wave reflection data from the layered TI model in Figure 2. The traveltimes from the dipping reflector and the bottom of the overburden were computed by anisotropic ray tracing with a shot spacing of 25 m and a receiver spacing of 100 m (Figure 3). To conform with the 2D assumptions of the algorithm, the incidence plane coincides with the dip plane of the reflector and contains the symmetry axis of the TTI layer.

In our implementation of the layer stripping we follow the version of the PP+PS=SS method developed by Grechka and Dewangan (2003) and Dewangan and Tsvankin (2004a,b). For a given pair of points $[x^{(3)}, x^{(4)}]$, this algorithm searches for the coordinates $x^{(1)}$ and $x^{(2)}$ that minimize the interval traveltime in equation (4). This procedure was shown to produce the same results as the methodology based on reflection slopes discussed above (Dewangan and Tsvankin, 2004a,b). Substitution of the estimated coordinates $x^{(1)}$ and $x^{(2)}$ into equations (4) and (5) yields the interval traveltime in the target layer for the source and receiver located at points T and R. Although the depth of the top of the target layer is unknown, the goal of the layer stripping is achieved by obtaining the *horizontal* source/receiver coordinates needed to construct the interval traveltime function.

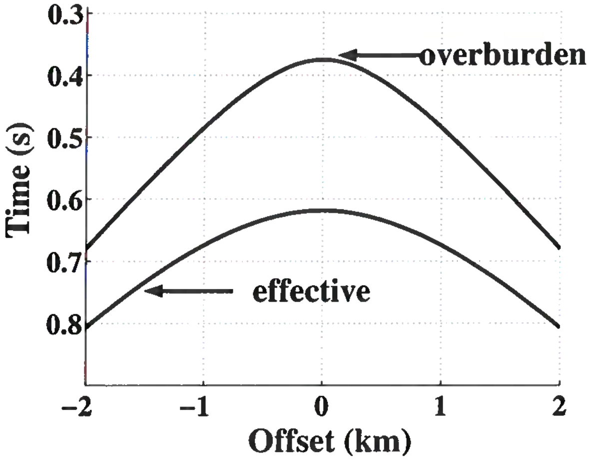

Figure 3. CMP gathers of the PP-wave reflections from the bottom of the second layer (marked "overburden") and the dipping reflector ("effective") for the model in Figure 2. The traveltimes were generated by an anisotropic ray-tracing code.

By repeating the above procedure to cover the whole recorded range of the source-receiver offsets for the dipping event, we compute the interval PP-wave traveltime for a number of the corresponding source/receiver pairs. These pairs do not necessarily form a common-midpoint (CMP), common-shot, or common-receiver gather and need to be sorted to analyze the interval traveltime in any desired configuration. This represents a complication compared with the PP+PS=SS method, in which the type of the output gather can be specified in advance.

To verify the accuracy of the layer stripping, we computed the interval PP-wave traveltime in the dipping layer and the corresponding source/receiver coordinates using ray tracing. The agreement between our method and the ray-tracing results is excellent (Figures 4 and 5). This and other synthetic tests we performed for a representative set of layered TI models confirm that the layer-stripping algorithm is exact and can be applied for large source-receiver offsets.

3 LAYER STRIPPING FOR MODE-CONVERTED WAVES

3.1 Layer-stripping algorithm

In contrast to the generalized Dix equations, our layer-stripping algorithm can be easily adapted for mode-converted (PS or SP) waves. Using the same model assumptions as those in the previous section, we consider

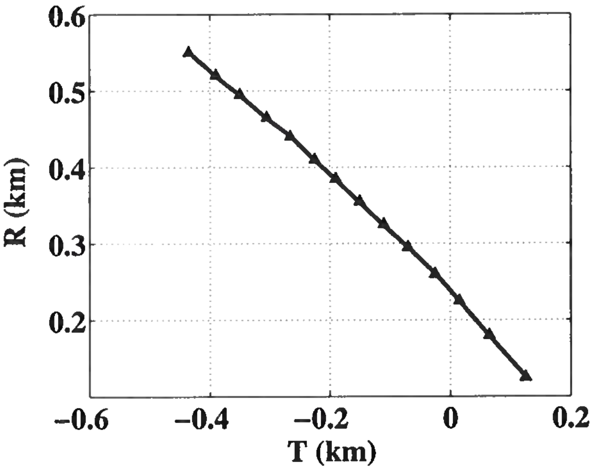

Figure 4. Source and receiver coordinates at the top of the target layer obtained for the model in Figure 2 for a range of surface points $[x^{(3)}, x^{(4)}]$. Here and in Figure 5 the triangles are the output of the layer-stripping algorithm; the solid line marks the results of ray tracing.

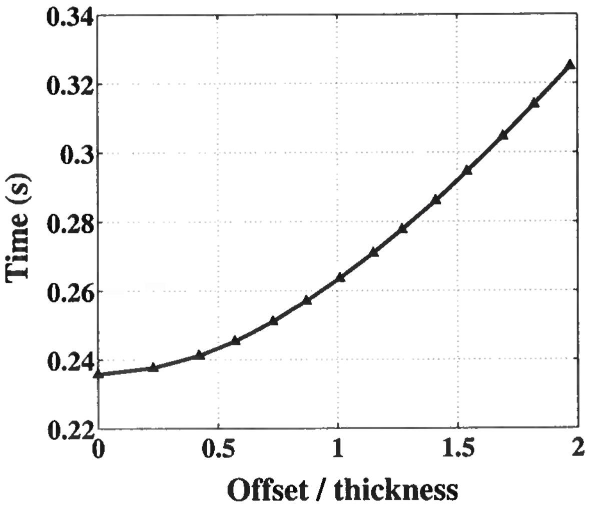

Figure 5. Interval PP-wave traveltime in the target layer as a function of offset for the source/receiver pairs from Figure 4.

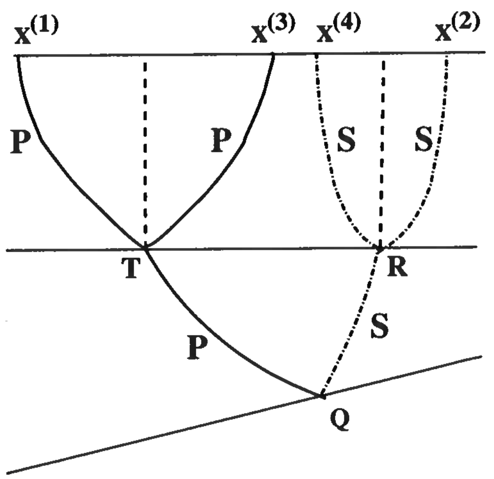

Figure 6. 2D ray diagram of the layer-stripping algorithm for PS-waves. The model is the same as that in Figure 1, with the overburden (the section above points T and R) composed of laterally homogeneous layers with a horizontal symmetry plane. The PS reflection from the dipping interface ($x^{(1)}TQRx^{(2)}$) and the PP reflection from the bottom of the overburden ($x^{(1)}Tx^{(3)}$) share the same downgoing leg ($x^{(1)}T$). The upgoing leg of the dipping PS event ($Rx^{(2)}$) coincides with a leg of the overburden SS reflection $x^{(2)}Rx^{(4)}$.

the PS-wave converted at a dipping reflector overlaid by a stack of horizontal layers with a horizontal symmetry plane (Figure 6). Since the upgoing leg of the PS mode represents a shear wave, the algorithm has to operate with both PP- and SS-waves reflected from the bottom of the overburden. In the absence of shear-wave excitation, the needed SS traveltimes ($t^{\rm ovr}_{SS}$) can be obtained by applying the PP+PS=SS method to the PP and PS data reflection data (Grechka and Tsvankin, 2002b; Grechka and Dewangan, 2003).

As in the previous section, we consider the reflection raypath $x^{(1)}TQRx^{(2)}$ from the dipping interface, but now the downgoing leg represents a P-wave, while the upgoing leg is an S-wave (Figure 6). By matching the time slopes at point $x^{(1)}$, we identify the overburden PP-wave reflection $x^{(1)}Tx^{(3)}$ that shares the segment $x^{(1)}T$ with the dipping PS event. The same procedure at point $x^{(2)}$ yields the reflected SS-wave $x^{(4)}Rx^{(2)}$ that has the same shear-wave segment $Rx^{(2)}$ as the PS-wave. Then the source/receiver coordinates T and R for the PS-wave propagating in the target layer can be found from equation (5), while the interval PS-wave traveltime can be expressed as

$$t^{\rm int}_{PS}(T,R) = t^{\rm eff}_{PS}(x^{(1)},x^{(2)}) - \frac{1}{2}\left[t^{\rm ovr}_{PP}(x^{(1)},x^{(3)}) + t^{\rm ovr}_{SS}(x^{(2)},x^{(4)})\right] . \tag{6}$$

Our implementation of this layer-stripping algorithm for PS-waves is similar to that described above for PP-waves.

Figure 7 shows ray-traced CMP gathers of the target PS event and the pure-mode reflections from the bottom of the overburden for the model in Figure 2. Note the the PS-wave moveout is asymmetric (i.e., the traveltime does not stay the same when the source and receiver positions are interchanged) because of combined influence of the reflector dip ($\phi = 10°$) and the tilt of the symmetry axis ($\nu = 25°$). This moveout asymmetry, however, is handled by our layer-stripping method that relies only on the symmetry of the reflection raypaths of the pure-mode reflections in the overburden.

The layer-stripped interval PS traveltimes and the corresponding source/receiver coordinates are close to

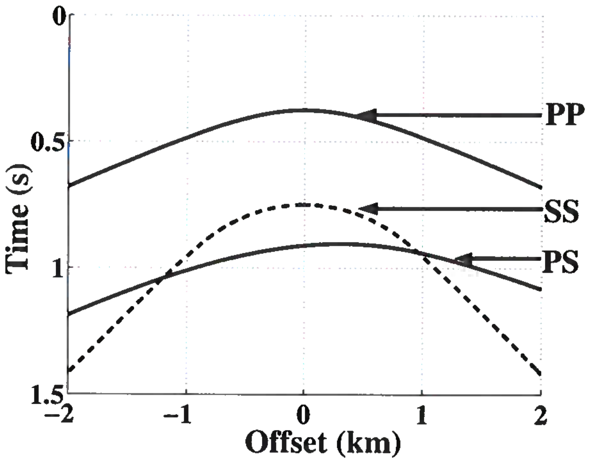

Figure 7. CMP gathers of reflected waves for the model in Figure 2 computed by anisotropic ray tracing. The PS-wave is converted at the dipping interface, while the PP- and SS-waves are reflected from the bottom of the overburden.

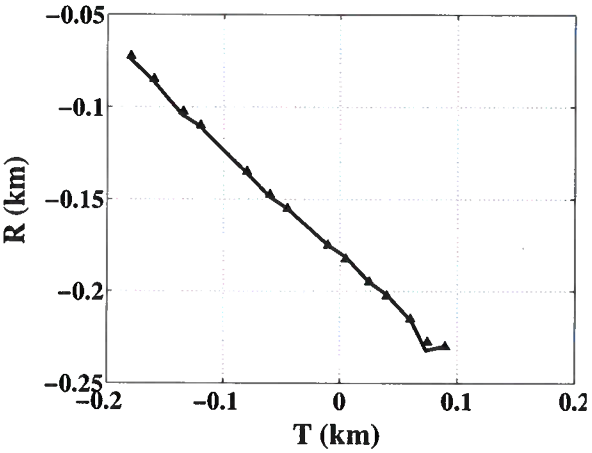

Figure 8. Source and receiver coordinates of the PS-wave at the top of the target layer obtained for the model in Figure 2. Here and in Figure 9 the triangles are the output of the layer-stripping algorithm applied to the data in Figure 7; the solid line marks the results of ray tracing.

the exact values computed by ray tracing (Figures 8 and 9). The minor deviations from the ray-tracing results are caused by interpolation errors related to the finite source and receiver sampling. The PS-wave traveltime function for the target layer, supplemented by the interval PP- and PS-wave moveouts, can serve as the input to the inversion algorithm of Dewangan and Tsvankin (2004b) designed to estimate the parameters of dipping TTI layers.

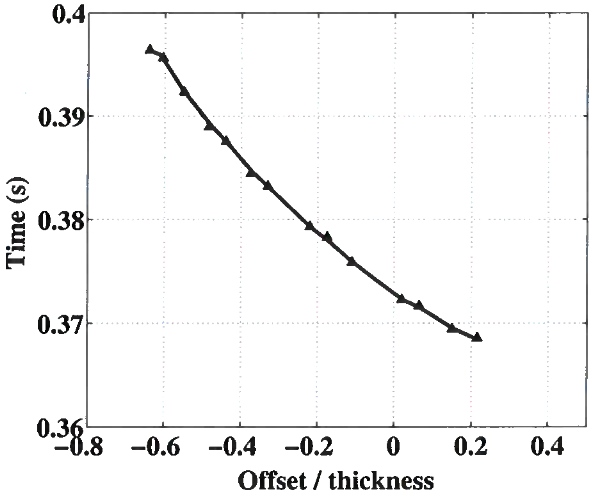

Figure 9. Interval PS-wave traveltime in the target layer as a function of offset for the source/receiver pairs from Figure 8.

4 DISCUSSION AND CONCLUSIONS

The principle of the PP+PS=SS method of Grechka and Tsvankin (2002b) and Grechka and Dewangan (2003) can be used to carry out exact layer stripping for dipping events in anisotropic media. The main assumptions of the algorithm introduced here are that the overburden is laterally homogeneous and has a horizontal symmetry plane (i.e., up-down symmetry) in each layer. The target layer above the dipping reflector, however, is allowed to be laterally heterogeneous without up-down symmetry, although the incidence plane has to coincide with a vertical symmetry plane for the whole model.

Under these assumptions, simple operations with reflection traveltimes can be used to identify the overburden events that have the same up- and downgoing legs as the reflection from the dipping interface. This allows us to perform kinematic downward continuation of the wavefield and obtain the interval traveltime-offset function without knowledge of the medium parameters. Numerical examples for layered transversely isotropic media with a vertical and tilted symmetry axis confirm that the algorithm gives exact results for both pure and converted modes. Although the testing was limited to PP- and PS-waves, the methodology can be also used for layer-stripping of SS and SP reflections excited by shear sources.

In contrast to the existing layer-stripping techniques that employ the generalized Dix equation, our algorithm is not restricted to the hyperbolic portion of the moveout curve. Therefore, it can yield exact *long-offset* interval traveltimes of both horizontal and dipping events in symmetry planes of anisotropic media. Note that existing layer-stripping methods for long-spread data are derived for the quartic moveout coefficient in layer-cake models and cannot handle reflector dip (Tsvankin, 2001).

The 2D algorithm discussed here can be extended to wide-azimuth data using the 3D version of the PP+PS=SS method outlined by Grechka and Tsvankin (2002b) and Grechka and Dewangan (2003). It should be mentioned, however, that our methodology operates with individual traveltimes, which makes it more complicated and computer-intensive than the Dix-type layer stripping. Hence, if the velocity model of the overburden is known and only conventional-spread P-wave data are available, it is more efficient to apply the generalized Dix equations of Alkhalifah and Tsvankin (1995) and Grechka et al. (1999).

An important application of the above results is in velocity analysis for tilted TI layers using multicomponent (PP and PS) data. Dewangan and Tsvankin (2004a,b) showed that the asymmetry attributes of PS-waves, combined with pure-mode moveout signatures, can provide sufficient information for parameter estimation in a homogeneous TTI medium. The layer-stripping algorithm introduced here can help to implement their inversion technique for realistic vertically heterogeneous models with a stratified overburden above the dipping target TTI layer.

Our method can also help to overcome the limitations of the generalized Dix equation in the dip-moveout inversion for the time-processing parameter η in VTI media. Because of the need to compute the interval NMO velocities in the overburden for non-existent reflectors, Dix-type algorithms designed to estimate η using dipping events have to rely on the presence of both horizontal and dipping interfaces in each layer (Alkhalifah and Tsvankin, 1995; Tsvankin, 2001). This requirement, which is often difficult to satisfy in practice, can be removed by replacing the generalized Dix equation with our velocity-independent layer-stripping technique.

5 ACKNOWLEDGMENTS

We are grateful to members of the A(nisotropy)-Team of the Center for Wave Phenomena (CWP), Colorado School of Mines (CSM), for helpful discussions. The support for this work was provided by the Consortium Project on Seismic Inverse Methods for Complex Structures at CWP and by the Chemical Sciences, Geosciences and Biosciences Division, Office of Basic Energy Sciences, U.S. Department of Energy.

REFERENCES

Alkhalifah, T., 1997, Velocity analysis using nonhyperbolic moveout in transversely isotropic media: Geophysics, **62**, 1839–1854.

Alkhalifah, T., and Tsvankin, I., 1995, Velocity analysis in transversely isotropic media: Geophysics, **60**, 1550–1566.

Dewangan, P., and Tsvankin, I., 2004a, Application of PS-wave moveout asymmetry in parameter estimation for tilted TI media – Part I: Horizontal TTI layer: Geophysics, under review.

Dewangan, P., and Tsvankin, I., 2004b, Application of PS-wave moveout asymmetry in parameter estimation for tilted TI media – Part II: Dipping TTI layer: Geophysics, under review.

Dix, C.H., 1955, Seismic velocities from surface measurements: Geophysics, **20**, 68–86.

Grechka, V., and Dewangan, P., 2003, Generation and processing of pseudo shear-wave data: Theory and case study: Geophysics, **68**, 1807–1816.

Grechka, V., Pech, A., and Tsvankin, I., 2002a, P–wave stacking-velocity tomography for VTI media: Geophysical Prospecting, **50**, 151–168.

Grechka, V., Pech, A., and Tsvankin, I., 2002b, Multicomponent stacking-velocity tomography for transversely isotropic media: Geophysics, **67**, 1564–1574.

Grechka, V., and Tsvankin, I., 2000, Inversion of azimuthally dependent NMO velocity in transversely isotropic media with a tilted axis of symmetry: Geophysics, **65**, 232–246.

Grechka, V., and Tsvankin, I., 2002a, NMO-velocity surfaces and Dix-type formulas in anisotropic heterogeneous media: Geophysics, **67**, 939–951.

Grechka, V., and Tsvankin, I., 2002b, PP+PS=SS: Geophysics, **67**, 1961–1971.

Grechka, V., Tsvankin, I., and Cohen, J.K., 1999, Generalized Dix equation and analytic treatment of normal-moveout velocity for anisotropic media: Geophysical Prospecting, **47**, 117–148.

Hake, H., Helbig, K., and Mesdag, C. S., 1984, Three-term Taylor series for $t^2 - x^2$ curves over layered transversely isotropic ground: Geophysical Prospecting, **32**, 828-850.

Liu, Z., 1997, An analytical approach to migration velocity analysis: Geophysics, **62**, 1238–1249.

Sarkar, D., and Tsvankin, I., 2004, Migration velocity analysis in factorized VTI media: *Geophysics*, 69, 708–718.

Shah, P.M., 1973, Use of wavefront curvature to relate seismic data with subsurface parameters: Geophysics, **38**, 812–825.

Stork, C., 1991, Reflection tomography in the post migrated domain: Geophysics, **57**, 680-692.

Tsvankin, I., 2001, Seismic signatures and analysis of reflection data in anisotropic media: Elsevier Science Publ. Co., Inc.

Tsvankin, I., and Thomsen, L., 1994, Nonhyperbolic reflection moveout in anisotropic media: Geophysics, **59**, 1290–1304.

Small-angle AVO response of PS-waves in tilted TI media

Jyoti Behura and Ilya Tsvankin
Center for Wave Phenomena, Colorado School of Mines, Golden, CO 80401

ABSTRACT

Field records for small source-receiver offsets often contain intensive converted PS-waves that cannot be generated in laterally homogeneous isotropic models. Among the most likely physical reasons for this converted energy is the presence of anisotropy on either side of the reflector. Here, we study the small-angle reflection coefficients of the split converted PS$_1$- and PS$_2$-waves (R_{PS_1} and R_{PS_2}) for a horizontal interface separating two transversely isotropic media with arbitrary orientations of the symmetry axis.

The normal-incidence reflection coefficients $R_{PS_1}(0)$ and $R_{PS_2}(0)$ vanish when both halfspaces have a horizontal symmetry plane, which happens if the symmetry axis is vertical or horizontal (i.e., if the medium is VTI or HTI). For a tilted symmetry axis in either medium, however, the magnitude of the reflection coefficients can reach substantial values close to 0.1, even if the strength of anisotropy is moderate. To study the influence of the orientation of the symmetry axis and the anisotropy parameters, we develop concise weak-contrast, weak-anisotropy approximations for the reflection coefficients and compare them with exact numerical results.

In particular, the analytic solutions show that the contributions of the Thomsen parameters ϵ and δ to the coefficients $R_{PS_1}(0)$ and $R_{PS_2}(0)$ are governed by simple functions of the symmetry-axis tilt ν, which have the same form for both halfspaces. If the symmetry-axis orientation and anisotropy parameters do not change across the interface, the normal-incidence reflection coefficients are insignificant, regardless of the strength of the velocity and density contrast. The AVO (amplitude variation with offset) gradients of the PS-waves are mostly influenced by the anisotropy of the incidence medium that causes shear-wave splitting and determines the partitioning of energy between the PS$_1$ and PS$_2$ modes.

Because of their substantial amplitude, small-angle PS reflections in TI media contain valuable information for anisotropic AVO inversion of multicomponent data. Our analytic solutions provide a foundation for linear AVO-inversion algorithms and can be used to guide nonlinear inversion based on the exact reflection coefficients.

Key words: converted wave, transverse isotropy, TTI media, reflection coefficient, AVO intercept, AVO gradient, azimuthal AVO

Introduction

In a number of case studies, significant converted wave energy was observed at zero and near-zero offsets (e.g., Thomsen, 2002). This phenomenon can be explained by several factors, including heterogeneity and the presence of nongeometrical waves (Tsvankin, 1995). However, neither heterogeneity nor nongeometrical waves can account for normal-incidence PS-wave reflections for layer-cake subsurface models and large distances between the source and the interface.

Here, we study the influence of anisotropy on the amplitude of PS-waves at small source-receiver offsets. We restrict ourselves to the TTI (transverse isotropy with a tilted symmetry axis) model and analyze the influence of the orientation of the symmetry axis and the anisotropy parameters on the PS-wave reflection coefficients. The main focus of the paper is on the normal-incidence PS-wave reflection coefficient that vanishes only when the reflector coincides with a symmetry plane in both halfspaces. If the reflector is horizontal, generation of converted energy at vertical incidence requires the symmetry axis in at least one of the halfspaces to deviate from both the vertical and horizontal directions.

We employ exact computation of the reflection coefficients as well as linearized solutions that help to understand the influence of various model parameters on the PS-wave reflectivity. Approximate reflection and transmission coefficients for isotropic media can be found in Aki and Richards (2002) and Shuey (1985). Banik (1987), Thomsen (1993) and Rüger (1996, 1997, 1998) derived approximate P-wave reflection coefficients for VTI (TI with a vertical symmetry axis) and HTI (TI with a horizontal symmetry axis) media. Rüger's results can be also applied in the symmetry planes of orthorhombic media. Pšenčík and Vavryčuk (1998) and Vavryčuk and Pšenčík (1998) obtained weak-contrast, weak-anisotropy P-wave reflection and transmission coefficients for arbitrarily anisotropic media.

Closed-form solutions for the reflection coefficients of PS-waves in isotropic media can be found in Donati (1998), Larsen *et al.* (1999), Alvarez *et al.* (1999) and Nefedkina and Buzlukov (1999). Rüger (1996) developed approximate expressions for the PS-wave reflection coefficients in VTI media and the symmetry planes of HTI media. However, as mentioned above, the normal-incidence reflection coefficients of mode conversions go to zero in both VTI and HTI media.Weak-contrast, weak-anisotropy approximations for PS-wave reflection and transmission coefficients in arbitrarily anisotropic media were presented by Vavryčuk (1999), Jílek (2000) and Artola *et al.* (2003). Jílek (2001) also developed algorithms for the joint inversion of PP- and PS-wave reflection coefficients in azimuthally anisotropic media.

Jílek (2000) and Vavryčuk (1999) pointed out that the normal-incidence PS-wave reflection coefficients do not vanish for nonzero stiffnesses c_{34} and/or c_{35} on either side of the reflector. Artola *et al.* (2003) demonstrated the presence of normal-incidence PS-wave energy in synthetic seismograms computed for azimuthally anisotropic models. Here, we show that the tilt of the symmetry axis in TI media can create relatively strong zero-offset PS reflections from horizontal interfaces. Application of the weak-contrast, weak-anisotropy approximations helps to identify the parameter combinations responsible for both zero-offset reflection coefficients and AVO gradients of PS-waves.

1 ANALYTIC BACKGROUND

We start by setting up the system of linear equations that can be used to compute the exact reflection/transmission coefficients from the boundary conditions. The approximate (linearized) reflection/transmission coefficients are then obtained by applying the first-order perturbation theory.

1.1 Exact solution of the reflection/transmission problem

The reflection/transmission problem for a given incident wave is solved by satisfying the boundary conditions at the reflector. For a welded contact of the two halfspaces, these boundary conditions are the continuity of traction and displacement, which can be written in the following compact form:

$$\mathbf{C}\cdot\mathbf{U}=\mathbf{B}, \tag{1}$$

where $\mathbf{C}$ corresponds to the displacement-stress matrix for the reflected and transmitted waves, $\mathbf{B}$ is the displacement-stress vector of the incident wave, and $\mathbf{U}$ is the vector of the reflection and transmission coefficients of the waves P, S$_1$ and S$_2$:

$$\mathbf{C}=\begin{bmatrix} g_1^{(1)} & g_1^{(2)} & g_1^{(3)} & -g_1^{(4)} & -g_1^{(5)} & -g_1^{(6)} \\ g_2^{(1)} & g_2^{(2)} & g_2^{(3)} & -g_2^{(4)} & -g_2^{(5)} & -g_2^{(6)} \\ g_3^{(1)} & g_3^{(2)} & g_3^{(3)} & -g_3^{(4)} & -g_3^{(5)} & -g_3^{(6)} \\ X_1^{(1)} & X_1^{(2)} & X_1^{(3)} & -X_1^{(4)} & -X_1^{(5)} & -X_1^{(6)} \\ X_2^{(1)} & X_2^{(2)} & X_2^{(3)} & -X_2^{(4)} & -X_2^{(5)} & -X_2^{(6)} \\ X_3^{(1)} & X_3^{(2)} & X_3^{(3)} & -X_3^{(4)} & -X_3^{(5)} & -X_3^{(6)} \end{bmatrix}, \tag{2}$$

$$\mathbf{B}=-\begin{bmatrix} g_1^{(0)}, & g_2^{(0)}, & g_3^{(0)}, & X_1^{(0)}, & X_2^{(0)}, & X_3^{(0)} \end{bmatrix}^T, \tag{3}$$

$$\mathbf{U}=\begin{bmatrix} R_{S1}, & R_{S2}, & R_P, & T_{S1}, & T_{S2}, & T_P \end{bmatrix}^T. \tag{4}$$

Here the superscript denotes the reflected/transmitted modes according to the following convention:
0–incident wave; 1–reflected S$_1$-wave; 2–reflected S$_2$-wave; 3–reflected P-wave; 4–transmitted S$_1$-wave; 5–transmitted S$_2$-wave; 6–transmitted P-wave. In equation (2), g(N) and X(N) are the polarization and amplitude-normalized traction vectors, respectively, obtained by solving the Christoffel equation. Equation (1) can be solved numerically for $\mathbf{U}$ to compute the reflection/transmission coefficients.

1.2 Weak-contrast, weak-anisotropy approximation

The main goal of using linearized approximations here is to gain physical insight into the dependence of the reflection coefficients on the medium parameters and incidence angle. Following the approach of Vavryčuk and Pšenčík (1998) and Jílek (2000), we linearize the boundary conditions by assuming a weak contrast in the elastic parameters across the interface and weak anisotropy in both halfspaces (see Appendix A). A homogeneous isotropic full space divided by a fictitious planar interface is taken as the background medium. The elastic parameters $a_{ijkl} = c_{ijkl}/\rho$ (density-normalized stiffness coefficients) are expressed as small perturbations δa_{ijkl} from the background values. The exact boundary conditions [equation (1)] are then linearized in terms of the small perturbations to find approximate PS-wave reflection coefficients.

Consider an incident P-wave traveling in the negative z-direction in the $[x, z]$-plane; the reflector coincides with the plane $z = 0$. The slowness vectors of the incident, reflected, and transmitted waves in the background medium can be written as follows (Figure 1):

$$\begin{aligned} \mathbf{p}^{0(0)} &= \mathbf{p}^{0(6)} = [\ p_1^0,\ \ 0,\ \ -p_3^{0P}\ ]\,, \\ \mathbf{p}^{0(1)} &= \mathbf{p}^{0(2)} = [\ p_1^0,\ \ 0,\ \ p_3^{0S}\ ]\,, \\ \mathbf{p}^{0(3)} &= [\ p_1^0,\ \ 0,\ \ p_3^{0P}\ ]\,, \\ \mathbf{p}^{0(4)} &= \mathbf{p}^{0(5)} = [\ p_1^0,\ \ 0,\ \ -p_3^{0S}\ ]\,. \end{aligned} \tag{5}$$

The P-wave unit polarization vectors in the isotropic background are given by

$$\begin{aligned} \mathbf{g}^{0(0)} &= \mathbf{g}^{0(6)} = \alpha\,\mathbf{p}^{0(0)}, \\ \mathbf{g}^{0(3)} &= \alpha\,\mathbf{p}^{0(3)}, \end{aligned} \tag{6}$$

where α is the P-wave velocity in the background.

1.3 Polarization angle

The SV- and SH-components are obtained by projecting the S-wave polarization vector in the background onto the incidence $[x, z]$ plane and the direction orthogonal to it, respectively. In anisotropic media, however, for the perturbation approach to work, the chosen polarization vectors in the background isotropic medium ($\mathbf{g}^{0(1)}$ and $\mathbf{g}^{0(2)}$) should be close to the actual polarizations ($\mathbf{g}^{(1)}$ and $\mathbf{g}^{(2)}$) (Jech and Pšenčík, 1989). So the SV and SH-wave polarizations ($\mathbf{g}^{SV}$ and $\mathbf{g}^{SH}$) in the background isotropic medium have to be rotated by an angle Φ called the "polarization angle," which is defined uniquely (except for singular directions), as shown by Jech and Pšenčík (1989). Since the polarization angle is neither a linear function of the perturbations δa_{ijkl} nor is it necessarily small, the presence of Φ complicates the computation of the analytic expressions for the PS-wave reflection coefficients.

If the polarization angle is known, the polarization vectors of the S_1^0 and S_2^0-waves ($\mathbf{g}^{0(1)}$ and $\mathbf{g}^{0(2)}$) can be determined by rotating the SV- and SH-wave polarization vectors counter-clockwise by the angle Φ in the plane perpendicular to the background slowness vector $\mathbf{p}^{0(1)}$ (Figure 1). Thus, $\mathbf{g}^{0(1)}$ and $\mathbf{g}^{0(2)}$ are given by

$$\begin{aligned} \mathbf{g}^{0(1)} &= [\ \beta p_3^{0S}\cos\Phi,\quad \sin\Phi,\quad -\beta p_1^0\cos\Phi\ ]\,, \\ \mathbf{g}^{0(2)} &= [\ -\beta p_3^{0S}\sin\Phi,\quad \cos\Phi,\quad \beta p_1^0\sin\Phi\ ]\,, \end{aligned} \tag{7}$$

where β is the S-wave velocity in the background. Equa-

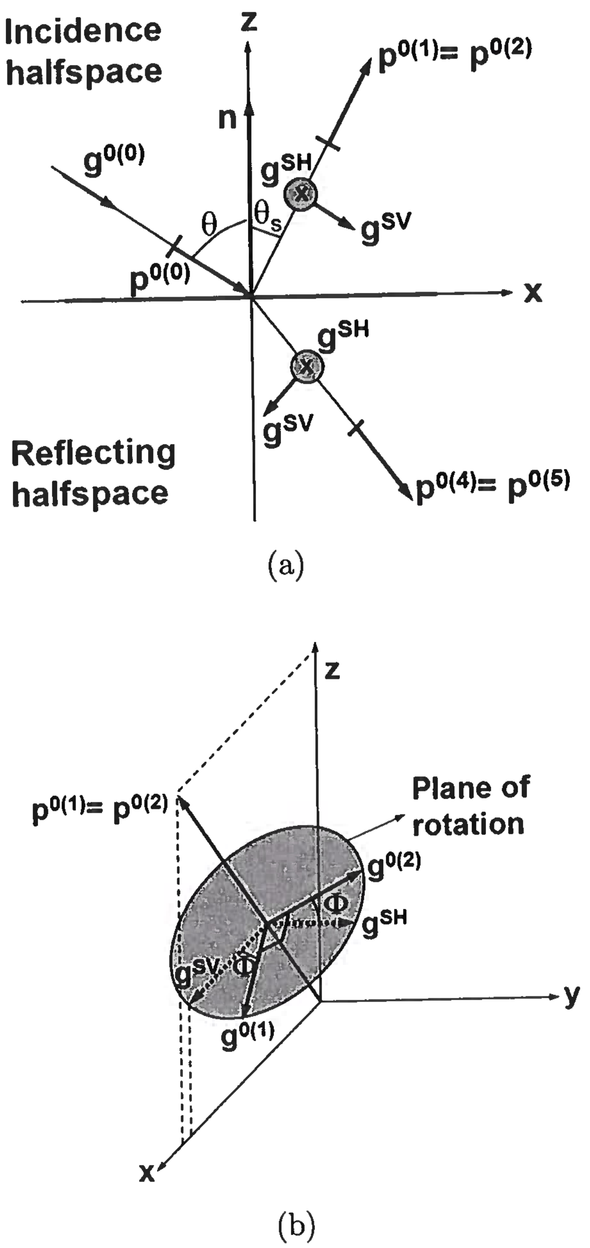

Figure 1. (a) Conventions used in solving the reflection/transmission problem. The incidence $[x, z]$-plane contains the interface normal $\mathbf{n}$ and the background P-wave slowness vector $\mathbf{p}^{0(0)}$. The background S-wave slowness vectors are denoted by $\mathbf{p}^{0(1)} = \mathbf{p}^{0(2)}$ (reflected) and $\mathbf{p}^{0(4)} = \mathbf{p}^{0(5)}$ (transmitted); θ and θ_s are the phase angles of the incident P-wave and reflected S-wave. The polarization vector of the incident P-wave in the background medium is $\mathbf{g}^{0(0)}$, while the SV- and SH-wave polarizations vectors are $\mathbf{g}^{SV}$ and $\mathbf{g}^{SH}$, respectively. (b) $\mathbf{g}^{0(1)}$ and $\mathbf{g}^{0(2)}$ are the chosen polarization vectors of the reflected S_1- and S_2-waves, respectively, in the background medium. These vectors are obtained by rotating $\mathbf{g}^{SV}$ and $\mathbf{g}^{SH}$ by the angle Φ (polarization angle) in the plane orthogonal to the slowness vector $\mathbf{p}^{0(1)}$. If the incidence halfspace is isotropic or VTI, $\Phi = 0$ [after Jílek (2000)].

tion (7) shows that when the medium is isotropic and $\Phi = 0$ (Jech and Pšenčík, 1989), S_1^0 reduces to SV and S_2^0 reduces to SH. Similarly, the polarization vectors of the transmitted S-waves can be written as

$$\mathbf{g}^{0(4)} = \left[\ -\beta p_3^{0S} \cos\Psi, \quad \sin\Psi, \quad -\beta p_1^0 \cos\Psi\ \right],$$
$$\mathbf{g}^{0(5)} = \left[\ \beta p_3^{0S} \sin\Psi, \quad \cos\Psi, \quad \beta p_1^0 \sin\Psi\ \right], \qquad (8)$$

where Ψ is the corresponding polarization angle. Since we are concerned with the reflected S-waves only, computation of Ψ is unnecessary because $\mathbf{g}^{0(4)}$ and $\mathbf{g}^{0(5)}$ are not involved in the linearized reflection coefficients [equation (A11)].

When the incidence halfspace is anisotropic, Φ is generally nonzero. If the medium is TTI, the polarization vector of the PS_1-wave lies in the plane formed by the symmetry axis and the PS_1 slowness vector (i.e., it is the PSV-wave in the coordinate system in which the symmetry axis is taken as vertical) while the PS_2-wave would be polarized orthogonal to that plane. (Note that PS_1 is not necessarily the fast PS mode.) Thus, in this case Φ is the angle between the background SV-wave polarization vector and the plane formed by $\mathbf{p}^{0(1)}$ and the symmetry axis of the incident TTI halfspace. Using simple vector algebra and dropping the cubic and higher-order terms in $\sin\theta$, we find

$$\cos\Phi \approx \frac{1}{2g^2 A}\left(2g^2\cos\phi_1 \sin\nu_1 + 2g\cos\nu_1 \sin\theta + \cos\phi_1 \sin\nu_1 \sin^2\theta\right), \qquad (9)$$

where

$$A \equiv \left(\sin^2\nu_1 + \frac{\cos\phi_1 \sin 2\nu_1 \sin\theta}{g} + \frac{(\cos^2\nu_1 - \sin^2\nu_1 \cos^2\phi_1)\sin^2\theta}{g^2}\right)^{1/2}.$$

Here ν_1 and ϕ_1 are the tilt (i.e., the angle with the vertical) and azimuth, respectively, of the symmetry axis of the incidence TI halfspace, and $g \equiv \alpha/\beta$. Although Φ can be computed from equation (9), its presence complicates the approximate PS-wave reflection coefficients. Although Φ is independent of the anisotropic parameters (except for the tilt of the symmetry axis), it depends on the incidence angle in a rather complicated way. For an incident TTI halfspace, $\Phi \neq 0$ whenever the incidence plane is different from the vertical symmetry-axis plane (i.e., from the vertical plane that contains the symmetry axis) of the incidence halfspace.

In general, Φ cannot be linearized in θ without assuming that $\sin^2\nu_1$ is sufficiently large, except for the special case of normal incidence ($\theta = 0$) when Φ reduces to ϕ_1 [equation(9)]. This complication prevents us from deriving fully linearized oblique-incidence reflection coefficients for TI media with arbitrary orientation of symmetry axis. For an incident VTI halfspace ($\nu_1 = 0°$) $\Phi = 0$, and for an incident HTI halfspace ($\nu_1 = 90°$), Φ can be linearized in terms of the medium parameters [equation (9)]. The orientation of the symmetry axis of the reflecting TI halfspace does not pose any problems in the linearization of the reflection coefficients because it does not contribute to Φ. Because of the above constraints, linearized PS-wave reflection coefficients for oblique incidence angles are given here only if the incidence halfspace is isotropic, VTI, HTI, or TTI with the symmetry axis confined to the incidence plane. For oblique incidence of P-waves in all other models, we analyze only the exact reflection coefficients.

2 NORMAL-INCIDENCE REFLECTION COEFFICIENT

The normal-incidence reflection coefficient is also called the "intercept" in amplitude-variation-with-offset (AVO) analysis. The general linearized equation for small-angle PS-wave reflection coefficients can be written as (Thomsen, 2002),

$$R_{PS} \quad = \quad R_{PS}(0) + G\sin\theta\,, \qquad (10)$$

where $R_{PS}(0)$ is the normal-incidence reflection coefficient and G is the AVO gradient. In this section, we discuss the normal-incidence reflection coefficient; the AVO gradient is analyzed next.

2.1 Isotropic/TTI interface

Consider the model that includes an incidence isotropic halfspace overlying a reflecting TTI halfspace. The normal-incidence PS-wave in this case is polarized in the symmetry-axis plane of the reflecting halfspace (Figure 2). In general, the reflected PS-wave can be represented as the vector sum of the PSV- and PSH-waves. For normal incidence, however, the incidence plane is undefined, and it is convenient to study the PS-wave as a whole.

The linearized PS-wave normal-incidence reflection coefficient is given by

$$R_{PS}(0) \quad = \quad \frac{g^2 \sin 2\nu_2\left[\cos 2\nu_2\,(\delta_2 - \epsilon_2) + \epsilon_2\right]}{4(1+g)} \qquad (11)$$

$$\quad = \quad \frac{g^2}{4(1+g)}\,\frac{1}{V_{P0,2}}\,\left.\frac{dV_{P,2}(\theta)}{d\theta}\right|_{\theta=0} \qquad (12)$$

where $V_{P,2}$ is the P-wave phase velocity in the reflecting halfspace. It is interesting that the normal-incidence PS-wave reflection coefficient is proportional to the first derivative of the P-wave phase velocity computed at $\theta = 0$. Although this derivative is supposed to be linearized to make equation (12) equivalent to equation (11), the accuracy of the weak-contrast, weak-anisotropy approximation can be increased by using the exact value of this derivative in equation (12) (Figure 3).

The very existence of the normal-incidence PS reflection is caused by the tilt of the symmetry axis away

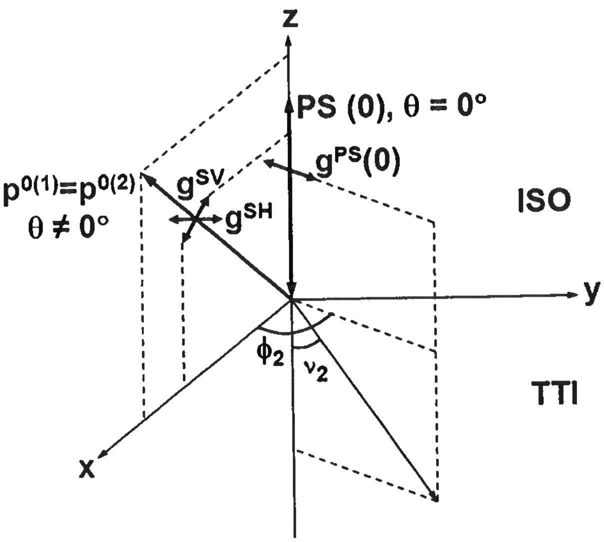

Figure 2. For an isotropic incidence halfspace overlying a TTI reflecting halfspace, the PS-wave at normal incidence is polarized (vector g^{PS}) in the symmetry-axis plane. For oblique incidence, we analyze the two components of the PS-wave (PSV and PSH) separately.

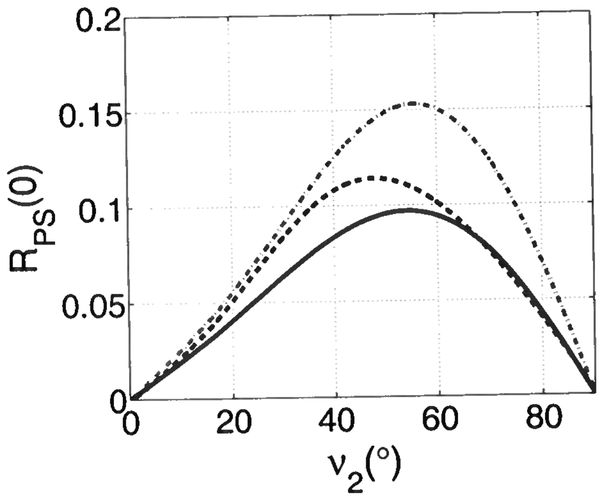

Figure 3. Accuracy of the weak-contrast, weak-anisotropy approximation for the normal-incidence PS-wave reflection coefficient. The solid black line is the exact coefficient for an isotropic/TTI interface, the dashed black line is computed using equation (12) with the exact first derivative of the P-wave phase velocity, and the dash-dotted gray line marks the fully linearized approximation (11). The parameters of the incidence isotropic halfspace are $V_{P,1} = 2.9$ km/s, $V_{S,1} = 1.5$ km/s, and $\rho_1 = 2$ gm/cm^3. The parameters of the reflecting TTI halfspace are $V_{P0,2} = 3.3$ km/s, $V_{S0,2} = 1.8$ km/s, $\rho_2 = 2.2$ gm/cm^3, $\epsilon_2 = 0.4$, $\delta_2 = 0.2$, $\gamma_2 = 0.11$, and $\phi_2 = 30°$.

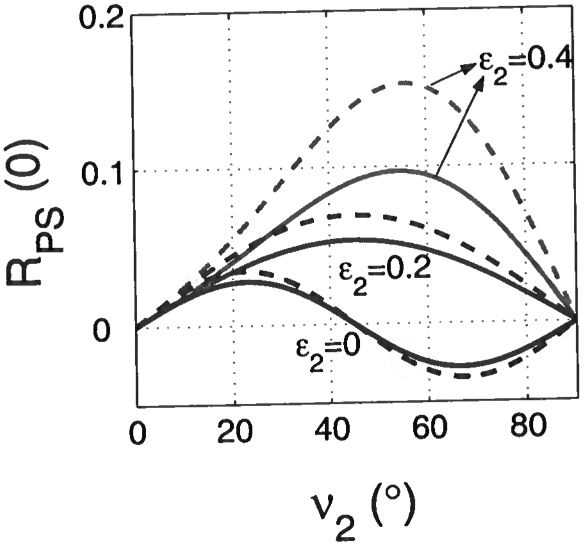

Figure 4. The normal-incidence PS-wave reflection coefficient for an isotropic/TTI interface as a function of tilt ν_2 of the symmetry axis and the parameter ϵ_2. The solid lines mark the exact $R_{PS}(0)$, the dashed lines represent the linearized approximation (11). The parameters of the incidence isotropic halfspace are $V_{P,1} = 2.9$ km/s, $V_{S,1} = 1.5$ km/s, and $\rho_1 = 2$ gm/cm^3. The parameters of the reflecting TTI halfspace are $V_{P0,2} = 3.3$ km/s, $V_{S0,2} = 1.8$ km/s, $\rho_2 = 2.2$ gm/cm^3, $\delta_2 = 0.2$, $\gamma_2 = 0.11$, and $\phi_2 = 30°$.

from the vertical and horizontal directions. Therefore, $R_{PS}(0)$ goes to zero for both VTI ($\nu_2 = 0°$) and HTI ($\nu_2 = 90°$) media; the dependence on ν_2 may have minima and maxima at intermediate tilts. For the model in Figure 4, $R_{PS}(0)$ attains values as high as 0.1 for $\epsilon_2 = 0.4$; in general, the magnitude of $R_{PS}(0)$ increases with ϵ_2. Apart from the anisotropy parameters, the normal-incidence reflection coefficient also increases with $g \equiv \alpha/\beta$.

The linearized $R_{PS}(0)$ is close to the exact value for models approaching VTI and HTI, but the approximation deteriorates for higher absolute values of $R_{PS}(0)$ (Figures 3 and 4). The accuracy of the linearized expressions also decreases with g, and the approximation may break down for soft rocks with high V_P/V_S ratios.

The dependence of $R_{PS}(0)$ on the parameters ϵ_2, δ_2 and ν_2 in Figures 4 and 5 can be explained using approximation (11). The influence of ϵ_2 and δ_2 on $R_{PS}(0)$ strongly depends on the tilt ν_2 of the symmetry axis (Figure 6). If the function of ν_2 multiplied with ϵ_2 and δ_2 becomes zero, the corresponding anisotropy parameter makes no contribution to $R_{PS}(0)$. For example, according to approximation (11), δ_2 should have no influence on the $R_{PS}(0)$ at $\nu_2 = 45°$, which is confirmed by the exact $R_{PS}(0)$ in Figure 5. For small tilts ν_2, δ_2 has a greater influence on $R_{PS}(0)$ than does ϵ_2, while for larger ν_2, ϵ_2 largely determines the value of $R_{PS}(0)$.

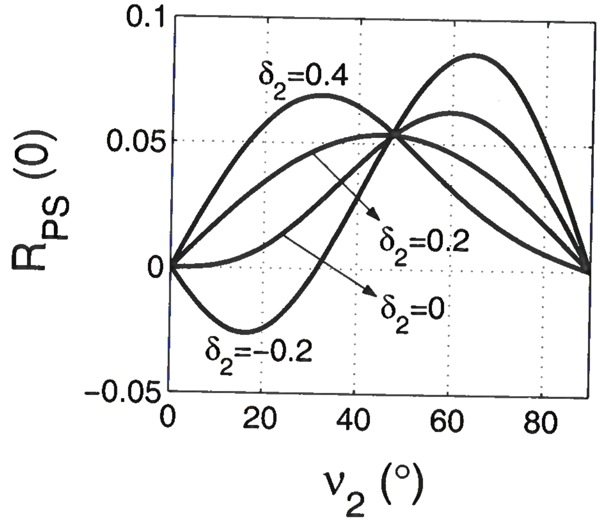

Figure 5. Exact coefficient $R_{PS}(0)$ for an isotropic/TTI interface as a function of the tilt ν_2 and the parameter δ_2. Except for δ_2 and $\epsilon_2 = 0.2$, the model parameters are the same as in Figure 4.

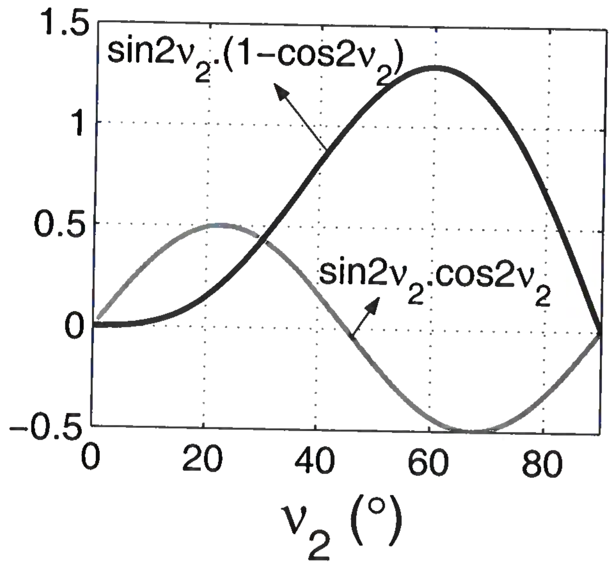

Figure 6. Functions of ν_2 multiplied with ϵ_2 (black line) and δ_2 (gray line) in equation (11). These curves help to explain the influence of ϵ_2 and δ_2 on $R_{PS}(0)$ for different tilts ν_2 in Figures 4 and 5.

This dependence of $R_{PS}(0)$ on ϵ and δ is explained by the behavior of the P-wave phase-velocity function in TI media. At small angles with the symmetry axis, P-wave velocity is controlled by δ, while the contribution of ϵ increases toward the isotropy plane (e.g., Tsvankin, 2001).

2.2 TTI/TTI interface

Next, we consider the normal-incidence PS reflection for a model in which the incidence halfspace is also TTI. In isotropic media, an incident P-wave excites a single converted (PSV) mode because the symmetry prohibits the generation of PSH conversions. When the incidence halfspace is anisotropic, the PS reflection splits into the PS_1 and PS_2 modes that have different normal-incidence reflection coefficients ($R_{PS_1}(0)$ and $R_{PS_2}(0)$) and AVO gradients. To understand the influence of the parameters of both halfspaces, we study the linearized approximations for $R_{PS_1}(0)$ and $R_{PS_2}(0)$.

2.2.1 Special case of aligned symmetry planes

If the azimuth of the symmetry axis is the same above and below the reflector ($\phi_1 = \phi_2$), the vertical plane that contains both symmetry axes represents a plane of symmetry for the whole model. In this case, the P-wave at normal incidence excites only one (PS_1) wave polarized in the symmetry-axis plane:

$$\begin{aligned} R_{PS_1}(0) &= \frac{g^2}{4(1+g)}\{-\sin 2\nu_1\left[\cos 2\nu_1\left(\delta_1-\epsilon_1\right)+\epsilon_1\right] \\ &\quad +\sin 2\nu_2\left[\cos 2\nu_2\left(\delta_2-\epsilon_2\right)+\epsilon_2\right]\} \qquad (13) \\ &= \frac{g^2}{4(1+g)}\left(-\frac{1}{V_{P0,1}}\frac{dV_{P,1}(\theta)}{d\theta}\bigg|_{\theta=0}\right. \\ &\quad \left.+\frac{1}{V_{P0,2}}\frac{dV_{P,2}(\theta)}{d\theta}\bigg|_{\theta=0}\right), \qquad (14) \end{aligned}$$

$$R_{PS_2}(0) = 0. \qquad (15)$$

The coefficient $R_{PS_1}(0)$ is a function of both tilts (ν_1 and ν_2) and all anisotropy parameters except for γ_1 and γ_2 – the parameters responsible for SH-wave propagation in TI media.

$R_{PS_1}(0)$ vanishes when each of the halfspaces is either VTI or HTI, and the reflector represents a symmetry plane for the whole model. The term involving ν_1, ϵ_1, and δ_1 in equation (13) coincides by absolute value with that involving ν_2, ϵ_2, and δ_2. So the conclusions drawn above for ν_2, ϵ_2, and δ_2 (Figure 6) apply to ν_1, ϵ_1, and δ_1 as well. If both TI halfspaces have the same orientation of the symmetry axes and the same parameters ϵ and δ, $R_{PS_1}(0)$ vanishes, even though there may be a jump in the other parameters across the interface. This result, however, is valid only in the weak-contrast, weak-anisotropy limit.

2.2.2 General TTI/TTI model

Suppose the symmetry axis has an arbitrary orientation in both halfspaces. Then a P-wave at normal-incidence excited both PS modes, and the approximate solutions

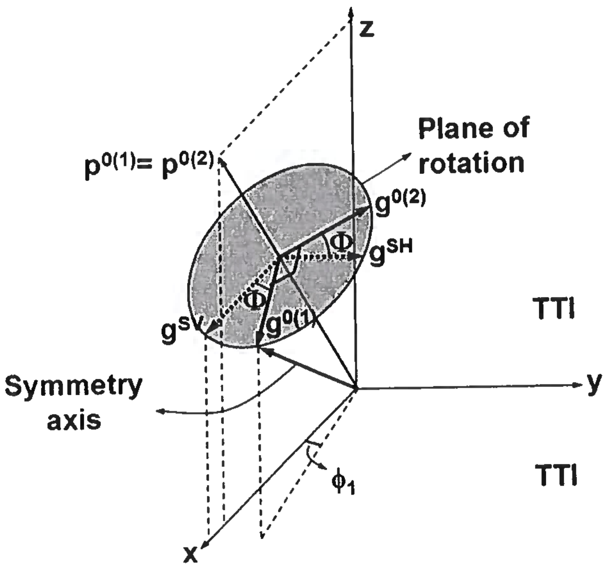

Figure 7. For an incidence TI halfspace, $\mathbf{g}^{0(1)}$ lies in the plane formed by the slowness vector and the symmetry axis (i.e., it would correspond to the SV-wave, if the symmetry axis were vertical), while $\mathbf{g}^{0(2)}$ is perpendicular to this plane (SH-wave).

for $R_{PS_1}(0)$ and $R_{PS_2}(0)$ are as follows:

$$R_{PS_1}(0) = \frac{g^2}{4(1+g)}\{-\sin 2\nu_1 \left[\cos 2\nu_1 (\delta_1 - \epsilon_1) + \epsilon_1\right] + \cos(\phi_2 - \phi_1) \sin 2\nu_2 \left[\cos 2\nu_2 (\delta_2 - \epsilon_2) + \epsilon_2\right]\} \quad (16)$$

$$= \frac{g^2}{4(1+g)} \left(- \frac{1}{V_{P0,1}} \frac{dV_{P,1}(\theta)}{d\theta}\bigg|_{\theta=0} + \cos(\phi_2 - \phi_1) \frac{1}{V_{P0,2}} \frac{dV_{P,2}(\theta)}{d\theta}\bigg|_{\theta=0} \right), \quad (17)$$

$$R_{PS_2}(0) = \frac{g^2}{4(1+g)}\{\sin(\phi_2 - \phi_1) \sin 2\nu_2 \left[\cos 2\nu_2 (\delta_2 - \epsilon_2) + \epsilon_2\right]\} \quad (18)$$

$$= \frac{g^2}{4(1+g)} \sin(\phi_2 - \phi_1) \frac{1}{V_{P0,2}} \frac{dV_{P,2}(\theta)}{d\theta}\bigg|_{\theta=0}. \quad (19)$$

It is clear from the symmetry of the above model (TTI/TTI), that the normal-incidence reflection coefficients should depend just on the difference $\phi_2 - \phi_1$ which is confirmed by equations (16)–(19). Indeed, a simultaneous azimuthal rotation of both symmetry axes can only change the azimuthal direction of the polarization vectors of the PS-waves. When the vertical symmetry planes of the two TI halfspaces coincide ($\phi_1 = \phi_2$), equations (17) and (19) reduce to equations (14) and (15), respectively. Note that the terms involving the tilt of the symmetry axis and the anisotropy parameters in equations (16) and (18) have the same form as the corresponding terms for the simpler isotropic/TTI model examined above.

3 AVO GRADIENTS

The AVO gradients of the split PS-waves can be computed numerically by estimating the best-fit initial slope of the exact reflection coefficient expressed as a function of $\sin\theta$. In the linearized weak-anisotropy, weak-contrast approximation, the gradient G is obtained explicitly as the multiplier of $\sin\theta$ [equation (10)]. The linearized approximations for the PS-wave AVO gradients are given in Appendix B.

3.1 Isotropic/TTI interface

For the isotropic/TTI interface, only the gradient G_{PS_1} contains both isotropic and anisotropic terms, while G_{PS_2} is purely anisotropic [equations (B1) and (B2)]. The expression for G_{PS_1} reduces to the familiar gradient for isotropic media (e.g., Nefedkina and Buzlukov, 1999), if $\epsilon_2 = \delta_2 = \gamma_2 = 0$.

In the linearized approximation, the reflection coefficients for isotropic media coincide with the isotropic terms in the coefficients for the isotropic/TTI interface. Numerical testing shows that the AVO gradient is not significantly distorted by the anisotropy for common values of the vertical-velocity ratio g (Figure 8). The influence of the anisotropy in the reflecting halfspace changes primarily the normal-incidence coefficient $R_{PS}(0)$ that goes to zero in the isotropic model. Although the AVO gradients of both PS-waves vary with azimuth, their average values are close to those for isotropic media, and the magnitude of the azimuthal variations is relatively small.

Since the dependence of the AVO gradients on the parameters of the reflecting medium is rather complicated, in particular for the PS$_1$-wave [equation (B1)], we studied the behavior of the exact gradients using numerical modeling. As was the case for $R_{PS}(0)$, the influence of ϵ_2 on both G_{PS_1} and G_{PS_2} increases with the tilt ν_2, while that of δ_2 becomes smaller. The contribution of γ_2 to both AVO gradients also increases with ν_2.

The PS$_2$-wave vanishes for a reflecting VTI halfspace when the reflected PS-wave is polarized in the symmetry-axis plane of the incidence medium. Therefore, the gradient G_{PS_2} increases as the symmetry axis deviates from the vertical. G_{PS_2} also goes to zero when the symmetry axis is confined to the incidence plane or is perpendicular to it.

3.2 TTI/TTI interface

The AVO gradients of the PS$_1$- and PS$_2$-waves for a TTI/TTI interface [equations (B3) and (B4)] are de-

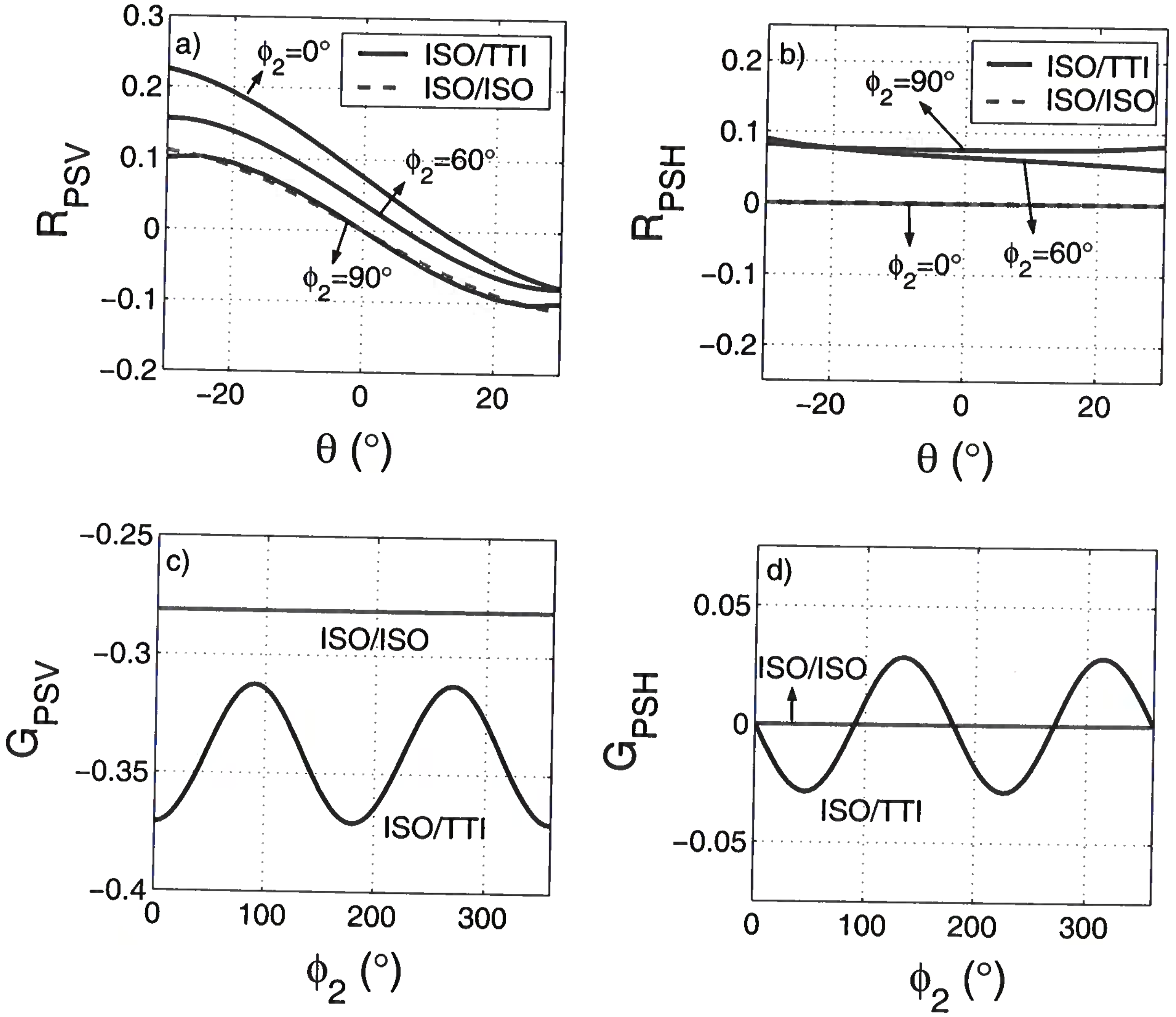

Figure 8. Exact PS-wave reflection coefficients (top row) and AVO gradients (bottom row) for isotropic/isotropic and isotropic/TTI interfaces. The velocity and density contrasts for both models are the same: $\Delta\rho = 0.2$ gm/cm^3, $\bar{\rho} = 2.1$ gm/cm^3, $\Delta\beta = 0.3$ km/s, $\beta = 1.65$ km/s, $\Delta\alpha = 0.4$ km/s, $\alpha = 3.1$ km/s, and $g = 1.88$. The anisotropy parameters of the reflecting TTI halfspace are $\epsilon_2 = 0.3, \delta_2 = 0.15, \gamma_2 = 0.11$, and $\nu_2 = 60°$.

rived in Appendix B for the special case of the incidence plane containing the symmetry axis of the upper halfspace. We also present numerical results for an arbitrary orientation of the symmetry axis of the incidence medium.

In agreement with the linearized approximations (B3) and (B4), the anisotropy parameters ϵ_1 and δ_1 influence only G_{PS_1} while γ_1 influences only G_{PS_2} (Figures 9 and 10). To explain this result valid for an arbitrary orientation of the symmetry axis of the incidence halfspace, note that the PS$_1$-wave would be the PSV mode if the symmetry axis were vertical, and the PS$_2$-wave would be the PSH (transversely polarized) mode. The P- and SV-wave propagation in TI media is governed only by ϵ and δ, while the SH-wave velocity is controlled by γ (Tsvankin, 2001).

As shown earlier, when the incidence medium is isotropic, the gradient G_{PS_1} contains both isotropic and anisotropic terms, while G_{PS_2} is purely anisotropic. If the incidence halfspace is TTI with the symmetry axis not confined to the incidence plane, then there are no purely isotropic terms in either gradient, as demonstrated for the special case of the HTI reflecting medium by equations (B5) and (B6). The influence of the anisotropy in the upper halfspace leads to a substantial deviation of the gradients computed for a TTI/TTI interface from those for the corresponding isotropic model (compare Figures 11 and 8).

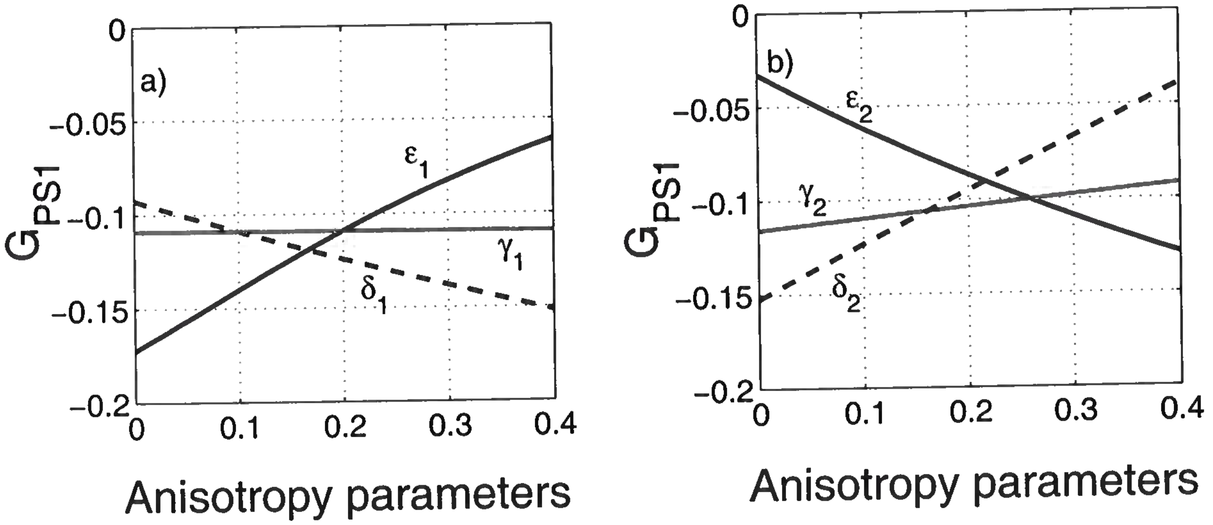

Figure 9. Exact AVO gradient of the PS_1-wave for a TTI/TTI interface as a function of the anisotropy parameters in the (a) incidence and (b) reflecting halfspaces. The incidence plane makes the angle $\phi_1 = 60°$ with the symmetry-axis plane of the incidence halfspace. The medium parameters of the incidence TTI halfspace are $V_{P0,1} = 2.9$ km/s, $V_{S0,1} = 1.5$ km/s, $\rho_1 = 2$ gm/cm^3, $\epsilon_1 = 0.2, \delta_1 = 0.1, \gamma_1 = 0.1$, and $\nu_1 = 60°$. The parameters of the reflecting halfspace are $V_{P0,2} = 3.3$ km/s, $V_{S0,2} = 1.8$ km/s, $\rho_2 = 2.2$ gm/cm^3, $\epsilon_2 = 0.3, \delta_2 = 0.15, \gamma_2 = 0.11, \nu_2 = 30°$, and $\phi_2 = 30°$.

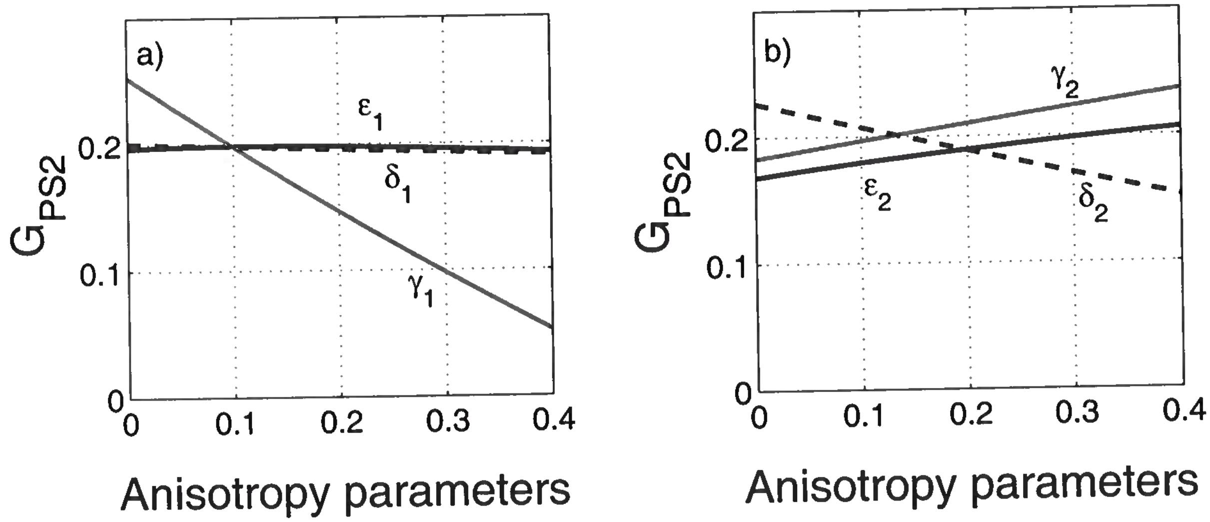

Figure 10. Exact AVO gradient of the PS_2-wave for a TTI/TTI interface as a function of the anisotropy parameters in the (a) incidence and (b) reflecting halfspaces. The model is the same as in Figure 9.

4 DISCUSSION AND CONCLUSIONS

In the absence of lateral heterogeneity, anisotropy is the most likely reason for significant PS-wave energy at zero and small offsets observed in many multicomponent data sets. Here, we analyze the small-angle PS-wave AVO response for the most common type of anisotropy: transverse isotropy with a tilted symmetry axis (TTI medium). If the reflector does not coincide with a symmetry plane in either halfspace, a P-wave at normal incidence always generates reflected PS-waves. To examine the influence of the anisotropy parameters on the normal-incidence PS-wave reflection coefficient and AVO gradient, we employ linearized analytic solutions (obtained using weak-contrast, weak-anisotropy approximations) supported by numerical modeling of the exact reflection coefficient.

If the incidence halfspace is isotropic, the reflected PS-wave is polarized in the symmetry-axis plane of the

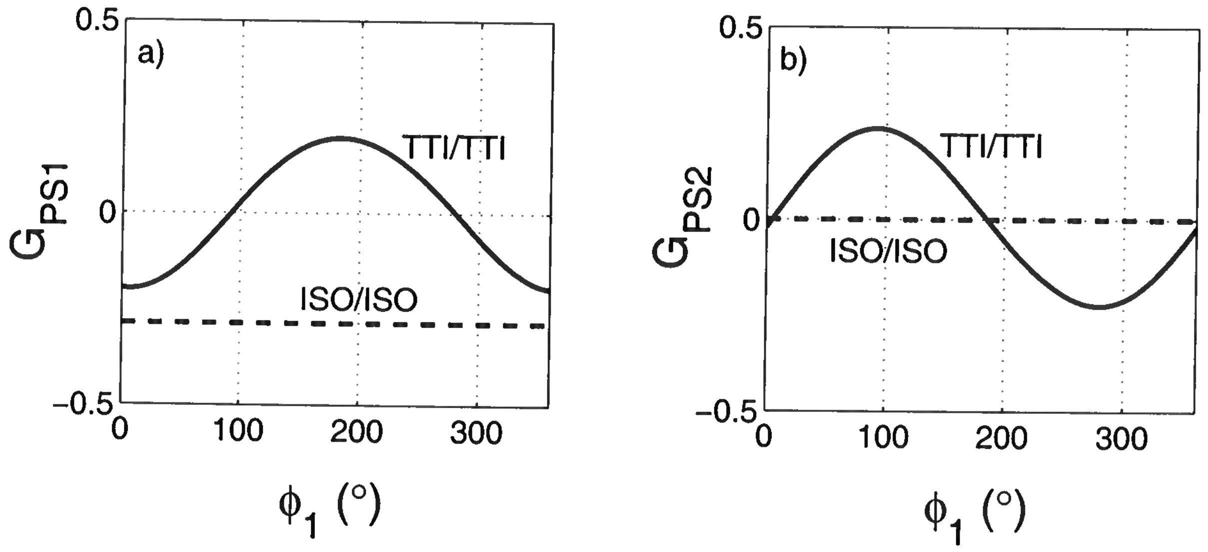

Figure 11. Exact AVO gradients of the (a) PS$_1$- and (b) PS$_2$-waves as functions of the azimuth ϕ_1 for a TTI/TTI interface (black solid line) and isotropic/isotropic interface (black dashed line). The parameters of the isotropic model are $V_{P,1} = 2.9$ km/s, $V_{S,1} = 1.5$ km/s, $\rho_1 = 2$ gm/cm^3, $V_{P,2} = 3.3$ km/s, $V_{S,2} = 1.8$ km/s, and $\rho_2 = 2.2$ gm/cm^3. For the TTI/TTI interface, the parameters are $V_{P0,1} = 2.9$ km/s, $V_{S0,1} = 1.5$ km/s, $\rho_1 = 2$ gm/cm^3, $\epsilon_1 = 0.2, \delta_1 = 0.1, \gamma_1 = 0.1, \nu_1 = 60°$, $V_{P0,2} = 3.3$ km/s, $V_{S0,2} = 1.8$ km/s, $\rho_2 = 2.2$ gm/cm^3, $\epsilon_2 = 0.3, \delta_2 = 0.15, \gamma_2 = 0.11, \nu_2 = 30°$, and $\phi_2 = 30°$.

reflecting TTI medium. The normal-incidence reflection coefficient $R_{PS}(0)$ vanishes when the reflecting TI halfspace is VTI or HTI, because in that case the model as a whole has a horizontal symmetry plane. The coefficient $R_{PS}(0)$ rapidly increases as the symmetry axis deviates from both the vertical and horizontal directions. Closed-form approximations and numerical modeling show that $R_{PS}(0)$ can reach values close to 0.1 for moderate values of the anisotropy parameters typical for shale formations. When the tilt ν_2 of the symmetry axis is relatively small, the coefficient $R_{PS}(0)$ is mostly controlled by δ_2, with the contribution of ϵ_2 becoming dominant for larger values of ν_2.

When both halfspaces are anisotropic (TTI), a P-wave at normal incidence excited two split PS-waves (PS$_1$ and PS$_2$) with the polarizations governed by the orientation of the symmetry axis in the incidence medium. The reflection coefficients of both PS-waves are functions of the difference between the azimuths of the symmetry axes ($\phi_2 - \phi_1$) and do not depend on either azimuth individually. The linearized normal-incidence reflection coefficient goes to zero when the two halfspaces have the same orientation of the symmetry axis and the same parameters ϵ and δ, even though there may be a jump in the velocities and densities across the interface.

We also discussed the azimuthally varying AVO gradients of PS-waves responsible for the small-angle reflection response. If the symmetry axis of the incidence halfspace is confined to the vertical incidence plane (or if the incidence halfspace is isotropic), the AVO gradient of the PS$_1$(PSV)-wave includes both purely isotropic and anisotropic terms, while the PS$_2$(PSH)-wave AVO gradient is entirely anisotropic. For an arbitrary symmetry-axis orientation, however, neither AVO gradient contains purely isotropic terms since the contributions of the velocity and density contrasts are multiplied with functions of the symmetry-axis azimuth ϕ_1. The AVO gradients are mostly influenced by the anisotropy in the incidence medium that causes shear-wave splitting and pronounced azimuthal variation of the reflection coefficients of both PS-waves.

The linearized approximations developed here not only provide physical insight into the behavior of the PS-wave reflection coefficients, but can be also used to quickly evaluate the PS-wave amplitudes for a wide range of TTI models. Potentially, these analytic expressions can help in the AVO inversion of PP and PS data for TTI media that can be implemented using the approach suggested by Jílek (2001) for anisotropic models with a horizontal symmetry plane.

5 ACKNOWLEDGMENTS

We are grateful to members of the A(nisotropy)-Team of the Center for Wave Phenomena (CWP), Colorado School of Mines and P. Jílek (BP Americas) for helpful discussions. The support for this work was provided by the Consortium Project on Seismic Inverse Methods for Complex Structures at CWP and by the Chemical Sciences, Geosciences and Biosciences Division, Office of Basic Energy Sciences, U.S. Department of Energy.

REFERENCES

Aki, K., and Richards, P. G. 1980, Quantitative Seismology: Theory and methods: Vol.1. W. N. Freeman & Co., San Francisco.

Alvarez, K., Donati, M., and Aldana, M. 1999, AVO analysis for converted waves: 69th Annual Internat. Mtg., Soc. Expl. Geophys., Expanded Abstracts, 876-879.

Artola, F. V. A., Leiderman, R., Fontoura, S. A. B., and Silva, M. B. C. 2003, Zero-offset C-wave reflectivity in horizontally layered media: 73rd Annual Internat. Mtg., Soc. Expl. Geophys., Expanded Abstracts, 761-764.

Banik, N. C. 1987, An effective anisotropy parameter in transversely isotropic media: Geophysics, **52**, 1654-1664.

Donati, S. M. 1998, Making AVO analysis for converted waves a practical issue: 68th Annual Internat. Mtg., Soc. Expl. Geophys., Expanded Abstracts, 2060-2063.

Jech, J., and Pšenčík, I. 1989, First-order perturbation method for anisotropic media: Geophys. J. Int., **99**, 369-376.

Jílek, P. 2000, Converted PS-wave reflection coefficients in anisotropic media: CWP Annual Project Review, CWP-340, 275-299.

——, 2001, Modeling and inversion of converted-wave reflection coefficients in anisotropic media: A tool for quantitative AVO analysis: Ph.D. Thesis, Center for Wave Phenomena, Colorado School of Mines, Golden, Colorado.

Larsen, A. J., Margrave, F. G., and Lu, H-X. 1999, AVO analysis by simultaneous P-P and P-S weighted stacking applied to 3C-3D seismic data: 69th Annual Internat. Mtg., Soc. Expl. Geophys., Expanded Abstracts, 721-724.

Nefedkina, T., and Buzlukov, V. 1999, Seismic dynamic inversion using multiwave AVO data: 69th Annual Internat. Mtg., Soc. Expl. Geophys., Expanded Abstracts, 888-891.

Pšenčík, I., and Vavryčuk, V. 1998, Weak contrast PP wave displacement R/T coefficients in weakly anisotropic elastic media: Pure Appl. Geophys., **151**, 699-718.

Rüger, A. 1996, Reflection coefficients and azimuthal AVO analysis in anisotropic media: Ph.D. Thesis, Center for Wave Phenomena, Colorado School of Mines, Golden, Colorado.

——, 1997, P-wave reflection coefficients for transversely isotropic models with vertical and horizontal axis of symmetry: Geophysics, **62**, 713-722.

——, 1998, Variation of P-wave reflectivity with offset and azimuth in anisotropic media: Geophysics, **63**, 935-947.

Shuey, R. T. 1985, A simplification of Zoeppritz-equations: Geophysics, **50**, 609-614.

Thomsen, L. 1993, Weak anisotropic reflections: In: Offset dependent reflectivity (Castagna and Backus, Eds.), SEG, Tulsa.

——, 2002, Understanding seismic anisotropy in exploration and exploitation: Distinguished Instructor Short Course (DISC), No. 5, SEG and EAGE.

Tsvankin, I. 1995, Seismic wavefields in layered isotropic media: Samizdat Press, Colorado School of Mines.

——, 2001, Seismic signatures and analysis of reflection data in anisotropic media: Elsevier Science.

Vavryčuk, V. 1999, Weak-contrast reflection/transmission coefficients in weakly anisotropic elastic media: P-wave incidence: Geophys. J. Int., **138**, 553-562.

Vavryčuk, V., and Pšenčík, I. 1998, PP-wave reflection coefficients in weakly anisotropic elastic media: Geophysics, **63**, 2129-2141.

APPENDIX A: PERTURBATION APPROACH APPLIED TO THE REFLECTION/TRANSMISSION PROBLEM

The approximate linearized reflection and transmission coefficients are derived by using an isotropic full space as the reference medium. A horizontal planar interface (reflector) divides the full space into two halfspaces, which are perturbed to obtain two weakly anisotropic media:

$$a_{ijkl}^{(I)} = a_{ijkl}^{0} + \delta a_{ijkl}^{(I)} , \tag{A1}$$

$$\rho^{(I)} = \rho^{0} + \delta\rho^{(I)} , \tag{A2}$$

$$|\delta a_{ijkl}^{(I)}| << \|a_{ijkl}^{0}\| , \tag{A3}$$

$$|\delta\rho^{(I)}| << \rho^{0} . \tag{A4}$$

In equation (A4), the index I ($I = 1, 2$) stands for the incidence and reflecting halfspaces, respectively, and $a_{ijkl}^{(I)}$ and ρ^{0} are the density-normalized stiffness coefficients and density of the background isotropic medium. Since the perturbations from the isotropic background in both halfspaces are small, the approximation involves both weak anisotropy and weak elastic contrast between the halfspaces. Using these approximations, the polarization ($\mathbf{p}^{(N)}$) and slowness vectors ($\mathbf{g}^{(N)}$) can be linearized as follows:

$$\begin{aligned} &\mathbf{g}^{(N)} \approx \mathbf{g}^{0(N)} + \delta\mathbf{g}^{(N)}, \\ &\mathbf{p}^{(N)} \approx \mathbf{p}^{0(N)} + \delta\mathbf{p}^{(N)}, \end{aligned} \tag{A5}$$

where $\mathbf{g}^{0(N)}$ and $\mathbf{p}^{0(N)}$ are the polarization and slowness vectors of waves propagating in the background isotropic medium, and $\delta\mathbf{g}^{(N)}$ and $\delta\mathbf{p}^{(N)}$ are their linear perturbations. Analytic expressions for the perturbations $\delta\mathbf{g}^{(N)}$ and $\delta\mathbf{p}^{(N)}$ in terms of $\delta a_{ijkl}^{(I)}$ are given in Vavryčuk and Pšenčík (1998) and Jílek (2000). Substituting these linearized expressions into equation (1) of the main text yields

$$(\mathbf{C}^{0} + \delta\mathbf{C})(\mathbf{U}^{0} + \delta\mathbf{U}) = \mathbf{B}^{0} + \delta\mathbf{B} . \tag{A6}$$

Here, $\mathbf{C}^{0}$ is the stiffness matrix of the background medium and $\delta\mathbf{U}$ is the perturbation of the reflection and transmission coefficients in the background isotropic medium ($\mathbf{U}^{0}$). As the background is homogeneous, $\mathbf{U}^{0}$ is given by

$$\mathbf{U}^{0} = \left[\begin{array}{cccccc} 0, & 0, & 0, & 0, & 0, & 1 \end{array}\right]^{T} . \tag{A7}$$

Expanding equation (A6) and retaining only the leading terms in small quantities results in the following equation:

$$\delta\mathbf{U} = (\mathbf{C}^{0})^{-1}(\delta\mathbf{B} - \delta\mathbf{C} \cdot \mathbf{U}^{0}) , \tag{A8}$$

where

$$\delta\mathbf{C} = \begin{bmatrix} \delta g_1^{(1)} & \delta g_1^{(2)} & \delta g_1^{(3)} & -\delta g_1^{(4)} & -\delta g_1^{(5)} & -\delta g_1^{(6)} \\ \delta g_2^{(1)} & \delta g_2^{(2)} & \delta g_2^{(3)} & -\delta g_2^{(4)} & -\delta g_2^{(5)} & -\delta g_2^{(6)} \\ \delta g_3^{(1)} & \delta g_3^{(2)} & \delta g_3^{(3)} & -\delta g_3^{(4)} & -\delta g_3^{(5)} & -\delta g_3^{(6)} \\ \delta X_1^{(1)} & \delta X_1^{(2)} & \delta X_1^{(3)} & -\delta X_1^{(4)} & -\delta X_1^{(5)} & -\delta X_1^{(6)} \\ \delta X_2^{(1)} & \delta X_2^{(2)} & \delta X_2^{(3)} & -\delta X_2^{(4)} & -\delta X_2^{(5)} & -\delta X_2^{(6)} \\ \delta X_3^{(1)} & \delta X_3^{(2)} & \delta X_3^{(3)} & -\delta X_3^{(4)} & -\delta X_3^{(5)} & -\delta X_3^{(6)} \end{bmatrix} , \tag{A9}$$

$$\delta\mathbf{B} = -\left[\begin{array}{cccccc} \delta g_1^{(0)}, & \delta g_2^{(0)}, & \delta g_3^{(0)}, & \delta X_1^{(0)}, & \delta X_2^{(0)}, & \delta X_3^{(0)} \end{array}\right]^{T} . \tag{A10}$$

Therefore, the perturbed vector of the reflection/transmission coefficients is obtained as

$$\begin{aligned} \delta\mathbf{U} = (\mathbf{C}^{0})^{-1} \Big[\; & \delta g_1^{(6)} - \delta g_1^{(0)}, \quad \delta g_2^{(6)} - \delta g_2^{(0)}, \quad \delta g_3^{(6)} - \delta g_3^{(0)}, \\ & \delta X_1^{(6)} - \delta X_1^{(0)}, \quad \delta X_2^{(6)} - \delta X_2^{(0)}, \quad \delta X_3^{(6)} - \delta X_3^{(0)} \; \Big] . \end{aligned} \tag{A11}$$

APPENDIX B: APPROXIMATE PS-WAVE AVO GRADIENTS IN TI MEDIA

Here, we present linearized expressions for the PS$_1$- and PS$_2$-wave AVO gradients (G_{PS_1} and G_{PS_2}) obtained in the weak-contrast, weak-anisotropy limit. If the incidence halfspace is isotropic, PS$_1$ becomes the PSV-wave with an in-plane polarization, and PS_2 becomes the transversely polarized PSH-wave.

$$\begin{aligned} G_{PSV} &= G_{PS_1} = -\frac{2\,\Delta\beta}{g\beta} - \frac{(2+g)\,\Delta\rho}{2g\overline{\rho}} - \frac{2\,\sin^2\nu_2\,\sin^2\phi_2\,\gamma_2}{g} \\ &\quad + \frac{g}{16(1+g)}\,\{(3+2g)\delta_2 + (3-2g)\cos 4\nu_2\,(\delta_2-\epsilon_2) - (1+2g)\epsilon_2 \\ &\qquad + 2\cos 2\nu_2\,[\delta_2 + 2(-1+2g)\cos 2\phi_2\,\sin^2\nu_2\,(\delta_2-\epsilon_2) + 2\epsilon_2] \\ &\qquad + 4\cos 2\phi_2\,\sin^2\nu_2\,(2g\delta_2 - \epsilon_2 - 2g\epsilon_2)\}\,, \end{aligned} \tag{B1}$$

$$\begin{aligned} G_{PSH} &= G_{PS_2} = \frac{\sin^2\nu_2\,\sin 2\phi_2\,\gamma_2}{g} \\ &\quad + \frac{g\sin^2\nu_2\,\sin 2\phi_2}{4(1+g)}\,\{[2g + (-1+2g)\,\cos 2\nu_2](\delta_2-\epsilon_2) - \epsilon_2\}\,. \end{aligned} \tag{B2}$$

The AVO gradients for a TTI/TTI interface are given here only for the incidence plane containing the symmetry axis of the incidence TTI halfspace ($\phi_1 = 0°$):

$$\begin{aligned} G_{PS_1} &= -\frac{2\Delta\beta}{g\beta} - \frac{(2+g)\Delta\rho}{2g\overline{\rho}} - \frac{2\sin^2\nu_2\,\sin^2\phi_2\,\gamma_2}{g} \\ &\quad + \frac{g}{16(1+g)}\{-4(1+g)(\delta_1-\epsilon_1) + 4(-1+g)\,\cos 4\nu_1\,(\delta_1-\epsilon_1) \\ &\qquad -8\cos 2\nu_1\,\epsilon_1 + 3\delta_2 - \epsilon_2 + 2g(\delta_2-\epsilon_2) + 2\cos 2\nu_2\,(\delta_2+2\epsilon_2) \\ &\qquad +4\cos 2\phi_2\,\sin^2\nu_2\,\{-\epsilon_2 + [2g + (-1+2g)\cos 2\nu_2](\delta_2-\epsilon_2)\} \\ &\qquad +(3-2g)\cos 4\nu_2\,(\delta_2-\epsilon_2)\}\,, \end{aligned} \tag{B3}$$

$$\begin{aligned} G_{PS_2} &= \frac{\sin^2\nu_2\,\sin 2\phi_2\,\gamma_2}{g} \\ &\quad + \frac{g\sin^2\nu_2\sin 2\phi_2}{4(1+g)}\{[2g + (-1+2g)\cos 2\nu_2](\delta_2-\epsilon_2) - \epsilon_2\}\,. \end{aligned} \tag{B4}$$

If the symmetry axis of the upper halfspace deviates from the incidence plane, fully linearized AVO gradients can still be derived for the special case of the incidence HTI medium:

$$\begin{aligned} G_{PS_1} &= -\frac{2\Delta\beta\,\cos\phi_1}{g\beta} - \frac{(2+g)\Delta\rho\,\cos\phi_1}{2g\overline{\rho}} - \frac{2\sin^2\nu_2\,\sin(\phi_2-\phi_1)\,\sin\phi_2\,\gamma_2}{g} \\ &\quad + \frac{g}{16(1+g)}\{4\sin^2\nu_2\,\cos(2\phi_2-\phi_1)\,\{[2g + (-1+2g)\cos 2\nu_2](\delta_2-\epsilon_2) - \epsilon_2\} \\ &\qquad + \cos\phi_1\,[-8\delta_1 + 16\epsilon_1 + 3\delta_2 - \epsilon_2 + 2g(\delta_2-\epsilon_2) \\ &\qquad +2\cos 2\nu_2\,(\delta_2+2\epsilon_2) - (-3+2g)\cos 4\nu_2\,(\delta_2-\epsilon_2)]\}\,, \end{aligned} \tag{B5}$$

$$\begin{aligned} G_{PS_2} &= \frac{2\Delta\beta\,\sin\phi_1}{g\beta} + \frac{(2+g)\Delta\rho\,\sin\phi_1}{2g\overline{\rho}} - \frac{2\sin\phi_1\,\gamma_1}{g} \\ &\quad + \frac{2\sin^2\nu_2\,\cos(\phi_2-\phi_1)\,\sin\phi_2\,\gamma_2}{g} \\ &\quad + \frac{g}{16(1+g)}\,\{4\sin^2\nu_2\,\sin(2\phi_2-\phi_1)\,\{[2g + (-1+2g)\cos 2\nu_2](\delta_2-\epsilon_2) - \epsilon_2\} \\ &\qquad - \sin\phi_1[3\delta_2 - \epsilon_2 + 2g(\delta_2-\epsilon_2) + 2\cos 2\nu_2\,(\delta_2+2\epsilon_2) \\ &\qquad - (-3+2g)\cos 4\nu_2\,(\delta_2-\epsilon_2)]\}\,. \end{aligned} \tag{B6}$$

CWP-510

On common-offset pre-stack time migration with curvelets

Huub Douma and Maarten V. de Hoop
Center for Wave Phenomena, Colorado School of Mines, Golden, CO 80401-1887, USA

ABSTRACT
Recently, curvelets have been introduced in the field of applied harmonic analysis and shown to optimally sparsify smooth (C_2, i.e., twice continuously differentiable) functions away from singularities along smooth curves. In addition, it was shown that the curvelet representation of wave propagators is sparse. Since the wavefronts in seismic data lie mainly along smooth surfaces (or curves in two dimensions), and since the imaging operator belongs to the class of operators that is sparsified by curvelets, curvelets are plausible candidates for simultaneous sparse representation of both the seismic data and the imaging operator. In this paper, we study the use of curvelets in pre-stack time migration, and show that simply translating, rotating and dilating curvelets according to the pre-stack map time-migration equations we developed earlier, combined with amplitude scaling, provides a reasonably accurate approximation to time-migration. We demonstrate the principle in two dimensions but emphasize that extension to three dimensions is possible using 3D equivalents of curvelets. We treat time-migration in an attempt to learn the basic characteristics of seismic imaging with curvelets, as a preparation for future imaging in heterogeneous media with curvelets.

Key words: Pre-stack time-migration, common-offset, curvelets, map migration, translation, rotation, dilation

Introduction

In the high-frequency approximation, seismic waves propagate along rays in the subsurface. The local slopes of reflections in seismic data, measured at the surface, determine (together with the velocity of the medium at the surface), the directions in which we need to 'look into the earth' from the surface, to find the location and orientation of the reflector in the subsurface where the reflection occured. The determination of a reflector position *and* orientation from the location of a reflection in the data *and* the local slope, is generally referred to as map migration (Kleyn, 1977). For an overview of literature on this topic, and for an explanation of the applicability condition of map migration, we refer to Douma & de Hoop (2005).

Given the slopes at the source and at the receiver locations, map migration provides a one-to-one mapping from the surface seismic measurements, i.e., locations, times and slopes, to the reflector position and orientation in the image (provided the medium does not allow different reflectors to have identical surface seismic measurements (location, times and slopes) that persist in being identical under small perturbations of the reflectors; see Douma & de Hoop (2005) for an explanation of this condition). This is in sharp contrast to migration techniques that do not make explicit use of the slopes in the data, such as Kirchhoff methods, where the data is summed over diffraction surfaces [see, e.g., Bleistein *et al.* (2000)]; such mappings are many-to-one because all points along the diffraction surface are mapped to one output location. The benefit of the explicit use of the local slopes in the data, is exploited in several seismic applications such as parsimonious migration (Hua & McMechan, 2001; Hua & McMechan, 2003), controlled directional reception (CDR) (Zavalishin, 1981; Harlan & Burridge, 1983; Sword, 1987; Riabinkin, 1991), and stereo tomography (Billette & Lambaré, 1998; Billette *et al.*, 2003). This list is certainly not complete and many more applications exist. In all these methods, the slopes are estimated from the data using additional processing techniques such as local slant-stacking, multidimensional prediction-error filters (Claerbout, 1992, p.186-201) or plane-wave destruction filters (Fomel, 2002; Claerbout, 1992, p.93-97).

Recently, in the field of harmonic analysis, Candès and Guo (2002) and Candès and Donoho (2000; 2004b) introduced a tight frame of curvelets (see appendix B for an explanation of tight frames), which provide an essentially optimal representation of objects that are twice continuously differentiable (C^2) away from discontinuities along C^2 edges. Due to the wave character of seismic data, the reflections recorded in seismic data lie mainly along smooth surfaces (or curves in 2D), just as geologic interfaces in the subsurface lie primarily along smooth surfaces. Therefore, it is plausible to assume that seismic data and their images can be sparsely represented using curvelets. This was earlier also noted by Herrmann (2003a; 2003b). Of course, at points where the recorded wavefronts have caustic points or at point-like discontinuities in the subsurface (e.g. along faults), the level of sparsity achieved with a curvelet representation naturally will be somewhat less than the sparsity achieved for the smooth parts of the wavefronts or geologic interfaces. Since curvelets are anisotropic 2D extensions of wavelets and thus have a direction associated with them, using curvelets as building blocks of seismic data, the slopes in the data are built into the representation of the data; a simple projection of the data onto the curvelet frame (combined with an intelligent thresholding scheme to separate signal from noise) then gives the directions associated with the recorded wavefronts.

Smith (1998) and later Candès and Demanet (2002) have shown that curvelets sparsify a certain class of Fourier integral operators. Since the seismic imaging operator can be constructed from Fourier integral operators that belong to this class, and since reflections in seismic data lie mainly along smooth curves, it seems that curvelets are plausible candidates for simultaneous compression of seismic data and the imaging operator. Curvelets have a multiresolution character just like wavelets do. This means that curvelets of different scales have different dominant wavelengths. It is known that waves with a certain dominant wavelength are sensitive to variations in the medium with certain lengths scales only; i.e., a wave with a dominant wavelength of say 100 meters is hardly sensitive to variations in the medium on the scale of one centimeter. Therefore curvelets of different scales are sensitive to media with variations on different scales. This allows the possibility to filter the background velocity with filters related to the dominant wavelength of the curvelets (i.e., the scale of the curvelets), and propagate curvelets of different scales through different media. Smith (1998) has shown that the propagation of a curvelet through such a filtered medium is governed by the Hamiltonian flow associated with the center of the curvelet. Here the center of the curvelet is its center in phase-space, meaning the center location of the curvelet combined with the center direction. This means that a curvelet is treated as if it was a particle with an associated momentum (or direction). For each filtered medium, this observation reduces to the statement of Candès and Demanet (2004) that the propagation of a curvelet (through an infinitely smooth medium) is "well-approximated by simply translating the center of the curvelet along the corresponding Hamiltonian flow." In fact, the procedure just outlined yields a leading order contribution to the solution of the wave equation (Smith, 1998). Hence this procedure admits wave-equation-based seismic imaging with curvelets.

For homogeneous media the above mentioned filtering is unnecessary. For such media, wave-equation based seismic imaging is really the same as Kirchhoff-style imaging. In this paper, we study the use of curvelets in homogeneous media (i.e., in time migration) and verify the statement that curvelets can be treated as particles with associated directions (or momenta) in an imaging context. We focus on the simple case of homogeneous media in an attempt to learn the basic characteristics of seismic imaging with curvelets, as a preparation for imaging in heterogeneous media with curvelets. This work is a follow-up on earlier work (Douma & de Hoop, 2004) that showed that (at least for time-migration) the kinematics of seismic imaging with curvelets are governed by map migration. This paper is a report on research in progress on pre-stack time imaging with curvelets.

In this paper we first present an intuitive description of curvelets, with examples of digital curvelets from the digital curvelet transform (Candès *et al.*, 2005). A detailed treatment of the construction of real-valued curvelets is included in appendix A. Subsequently, we show an example of the use of curvelets as building blocks of seismic data, and explain the relation between curvelets and map migration. We proceed to explain our current understanding of common-offset (CO) pre-stack time migration with curvelets, and introduce a transformation that consists of translations, rotations and dilations of curvelets to perform such migration. This transformation is largely based on map migration. Finally, we present numerical examples that show the use of this transformation for time-imaging with curvelets, and finish with a discussion and conclusion of the results.

Curvelets

In this section we explain intuitively what curvelets are, how they are constructed, and their main properties. Appendix A provides a detailed treatment of their construction in the frequency domain, which closely follows

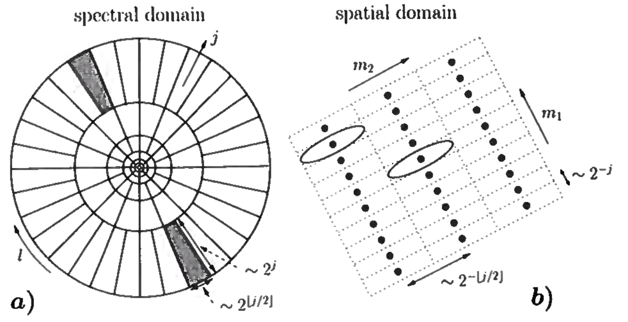

Figure 1. Tilings of the curvelet frame in the spectral domain (a) and the spatial domain (b). In the frequency domain a curvelet is supported 'near' a wedge on a polar grid (i.e. the actual support extends slightly further than the indicated wedge), where the width of the wedge is proportional to $2^{\lfloor j/2 \rfloor}$ and its length is proportional to 2^j. On the support of such a wedge, a local Fourier basis provides a Cartesian 'tiling' of the spatial domain (shown schematically in b). The essential support of a curvelet in the spatial domain is indicated by an ellipse (while again the actual support extends beyond this ellipse).

the original treatment of the construction of real-valued curvelets by Candès and Donoho (2004b) but provides additional explanations and derivations to guide the non-specialist (i.e., not harmonic analysts). We include this extensive appendix because most of the literature on the construction of curvelets is rather dense and thus aim to make the construction of curvelets more accessible to a broader audience. For a short summary of (the more general) complex-valued curvelets, we refer the reader to Candès and Demanet (2004).

In wavelet theory [e.g., Mallat (1998)], a 1D signal is decomposed into wavelets, where a wavelet is 'localized' in both the independent variable *and* its Fourier dual, say time and frequency; such localization is of course understood within the limits imposed by the Heisenberg uncertainty principle. These wavelets can be translated along the time axis through a translation index, and dilated in their frequency content through a scale index. They are uniquely determined by both indices: the translation index m determines their location along, say, the time axis, while the scale index j determines their location along, say, the frequency axis.

Curvelets are basically 2D *anisotropic* (see below) extensions to wavelets, that have a direction associated with them. Just like wavelets are 'localized' in one variable *and* its Fourier dual, curvelets are 'localized' in two variables *and* their two Fourier duals. Analogously to wavelets, curvelets can be translated and dilated. The dilation is given also by a scale index j, and, since we are in 2D, the translation is indexed by two indices m_1 and m_2; we defer from the standard notation k_1 and k_2 to avoid confusion with the wave-vector components. A main difference between curvelets and wavelets is that curvelets can be rotated. This rotation is indexed by an angular index l. The relation between these indices and the location of the curvelet in the spatial and spectral domains is shown in Figure 1a and b. A curvelet is uniquely determined by all four indices (j, l, m_1, m_2).

As explained in appendix A, curvelets satisfy the anisotropic scaling relation width $\approx$ length^2 in the spatial domain (where we ignore the dimensional difference between width and length^2). This is generally refered to as the *parabolic scaling.* This anisotropic character of curvelets is the key to the proof from Candès and Donoho (2004b) that curvelets provide the sparsest representations of C^2 (i.e., twice continuously differentiable) functions away from edges along piecewise C^2 curves. The search for sparse representations of such functions in the field of image analysis was the original motivation for their construction, as wavelets fail to sparsely represent such functions (Candès & Donoho, 2004b) due to their isotropic character. The anisotropic scaling relation is the key difference between wavelets and curvelets.

Curvelets are constructed through the following sequence of operations. First, the spectral domain is bandpass filtered (i.e. in the radial direction) into dyadic annuli (or subbands); this means that the radial widths of two neighboring annuli differs by a factor of two, the outer annulus having twice the radial width as the inner annulus. Each subband is subsequently subdivided into angular wedges (see Figure 1a), where the number of wedges in each subband is determined by the frequency content (or the scale index j) of the subband. The number of wedges in a subband with scale j is $2^{\lfloor j/2 \rfloor}$, where the notation $\lfloor p \rfloor$ denotes the integer part of p. This means that the number of wedges in a subband increases only every other scale. This is a consequence of the dyadic nature of the subband filtering done in the first step combined with the desired parabolic scaling. Subsequently, each wedge is multiplied by a 2D orthonormal Fourier basis for the rectangle that just covers the support of the wedge. According to the discrete Fourier transform, this basis has the fewest members if the area of this rectangle is minimum, since then the product of both sampling intervals in space is largest. Therefore, the orientation of this rectangle rotates with the angular wedge and the spatial tiling associated with the local Fourier basis is oriented along the direction associated with the angular wedge (see Figure 1b); that is, the spatial tiling associated with each angular wedge depends on the particular orientation of the wedge. The subband filtering gives curvelets their multiresolution character (just like with wavelets), whereas the subdivision of these subbands into angular wedges provides them with orientation. The local Fourier basis over the support of the angular wedge, allows the curvelets to be translated in space. Curvelets are in essence a tiling of phase-space; i.e., a tiling of two variables *and* its two Fourier duals. The tiling is non-trivial in that the sampling of phase space is polar in the spectral domain, but Cartesian in the spatial domain. As explained in appendix A, curvelets are essentially 'Heisenberg cells' in phase-space.

An angular wedge in the frequency domain has length proportional to 2^j (i.e., in the radial direction) and width proportional to $2^{\lfloor j/2 \rfloor}$ (see appendix A for the derivation). This means that in the spatial domain the curvelet is oscillatory in the direction of the main $\boldsymbol{k}$-vector (i.e., the $\boldsymbol{k}$-vector pointing to the middle of the angular wedge in the frequency domain), while it is smooth in the orthogonal direction. In some of the papers on curvelets, they are therefore referred to as (Candès & Demanet, 2004) "little needle(s) whose envelope is a specified 'ridge' ... which displays an oscillatory behavior across the main ridge". Intuitively, we can roughly think of curvelets as small pieces of bandlimited plane waves. The difference between this rough description and the actual interpretation lies, of course, in the fact that a bandlimited plane wave has associated with it one $\boldsymbol{k}$ direction only, whereas a curvelet is associated with a small range of $\boldsymbol{k}$ vectors. A better description is the term 'coherent wave packet' which was around even before the first ever construction of curvelets [e.g. Smith (1997; 1998)], and dates back to the work of Córdoba and Fefferman (Córdoba & Fefferman, 1978). The frequency domain tiling of the curvelet frame is the same as the dyadic parabolic decomposition or second dyadic decomposition (Gunther Uhlmann, personal communication) used in the study of Fourier Integral Operators [see e.g. Stein (1993)], that was around long before the construction of the curvelet frame (Fefferman, 1973).

Curvelets form a tight frame for functions in $L^2(\mathbb{R}^2)$ (see appendix B for a quick introduction to tight frames, and appendix A for the derivation of this tight frame). This means that, much like in the case of an orthonormal basis, we have a reconstruction formula

$$f = \sum_{\mu \in M} (f, c_\mu)\, c_\mu \;, \quad (f, c_\mu) = \int_{\mathbb{R}^2} f(\boldsymbol{x}) c_\mu^*(\boldsymbol{x}) d\boldsymbol{x} \;, \qquad (1)$$

where c_μ denotes a curvelet with multi-index $\mu = (j, l, m_1, m_2)$, the superscript $*$ denotes taking the complex conjugate, M is an index-set, and $f(x_1, x_2) \in L^2(\mathbb{R}^2)$. Thus, we can express an arbitrary function in $L^2(\mathbb{R}^2)$ as a superposition of curvelets. The term (f, c_μ) is the coefficient of curvelet c_μ given by the projection of the function f on curvelet c_μ with multi-index $\mu = (j, l, m_1, m_2)$. Of course, $(\cdot,\cdot)$ given in equation (1) is the familiar inner product on $L^2(\mathbb{R}^2)$.

Digital curvelets versus continuous curvelets

In the construction of continuous curvelets, the sampling of the spectral domain is done in polar coordinates, while the sampling of the spatial domain is Cartesian (see Figure 1a and b). From a computational point of view, this combination is not straightforward to implement. Combining Cartesian coordinates in both domains is straightforward and is standard in data processing. Therefore, for the purpose of digital curvelet transforms, the polar coordinates in the spectral domain are replaced with Cartesian coordinates. Also, in the field of image analysis [where the digital curvelet transform was developed (Candès & Donoho, 2004a; Candès *et al.*, 2005)], images usually have Cartesian spatial coordinates to begin with, hence it is natural to have Cartesian coordinates in the spectral domain also, since this allows straightforward application of Fast Fourier Transform algorithms. Of course, this holds for seismic data too.

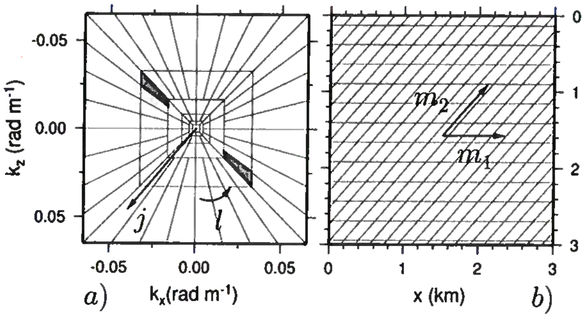

Figure 2. Tilings for digital curvelets in the spectral domain (a) and the spatial domain (b). For digital curvelets, the concentric dyadic circles in the spectral domain are replaced with concentric dyadic squares, and the Cartesian spatial grid is sheared.

To go from polar coordinates to Cartesian coordinates in the spectral domain, the concentric circles in Figure 1a are replaced with concentric squares (see Figure 2a); hence the rotational symmetry is replaced with a sheared symmetry. As a consequence, the Cartesian sampling in the spatial domain is no longer a rotated Cartesian grid, but is a sheared Cartesian grid (cf. Figure 1b and Figure 2b)*. This construction allows a rapidly computable digital curvelet transform. Whether this digital analog of the continuous curvelets introduces artefacts due to the loss of the rotational symmetry in the spectral domain (this is most severe near the corners of the concentric squares) is currently unclear to us. For more details on the implementation of digital curvelet transforms, we refer to Candès and Donoho (2004a) and Candès *et al.* (2005).

Examples of digital curvelets

Figure 3 shows examples of digital curvelets. The left column shows curvelets in the spatial domain, while the right column shows their associated spectra. Superimposed on the spectra, the spectral tiling of the digital curvelet transform is shown. The middle column shows

---

*Here the centers of the cells are the actual possible locations of the centers of the curvelets in space.

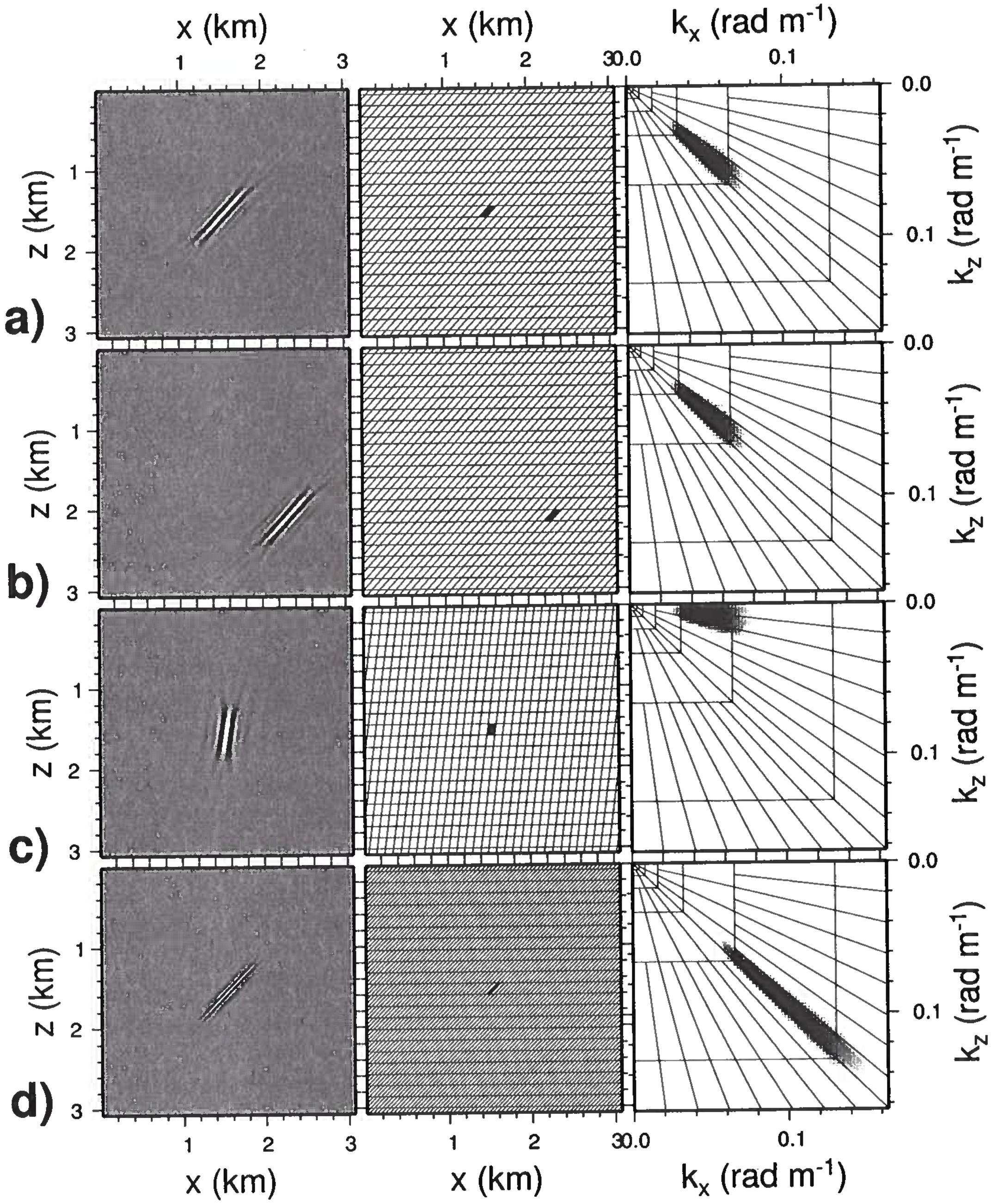

Figure 3. First column: curvelets in the spatial domain. Second column: associated spatial lattices, and spatial cells colored according to the value of the coefficient. Third column: amplitude spectra and frequency-domain tilings. First row: a curvelet. Second row: curvelet from Figure (a) with different translation indices. Third row: curvelet from Figure (a) with a different angular index. Fourth row: curvelet from Figure (a) with a different (higher) scale index (here the translation indices and the angular index are in fact also different, since they depend on the scale index).

the associated spatial lattice for each of the curvelets, where the centers of the cells are the actual possible locations of the centers of the curvelets in space. Here the spatial cells on the spatial lattice are colored according to the coefficient of the curvelet (here always one); black equals one and white equals zero. Figure 3b shows a translated version of the curvelet in Figure 3a; the spectral tile is the same, but the spatial tile has changed, i.e., indices j and l are held constant, but the translation indices m_1 and m_2 are different. Figure 3c shows a rotated version of the curvelet in Figure 3a; now the spatial location is the same, but the spectral

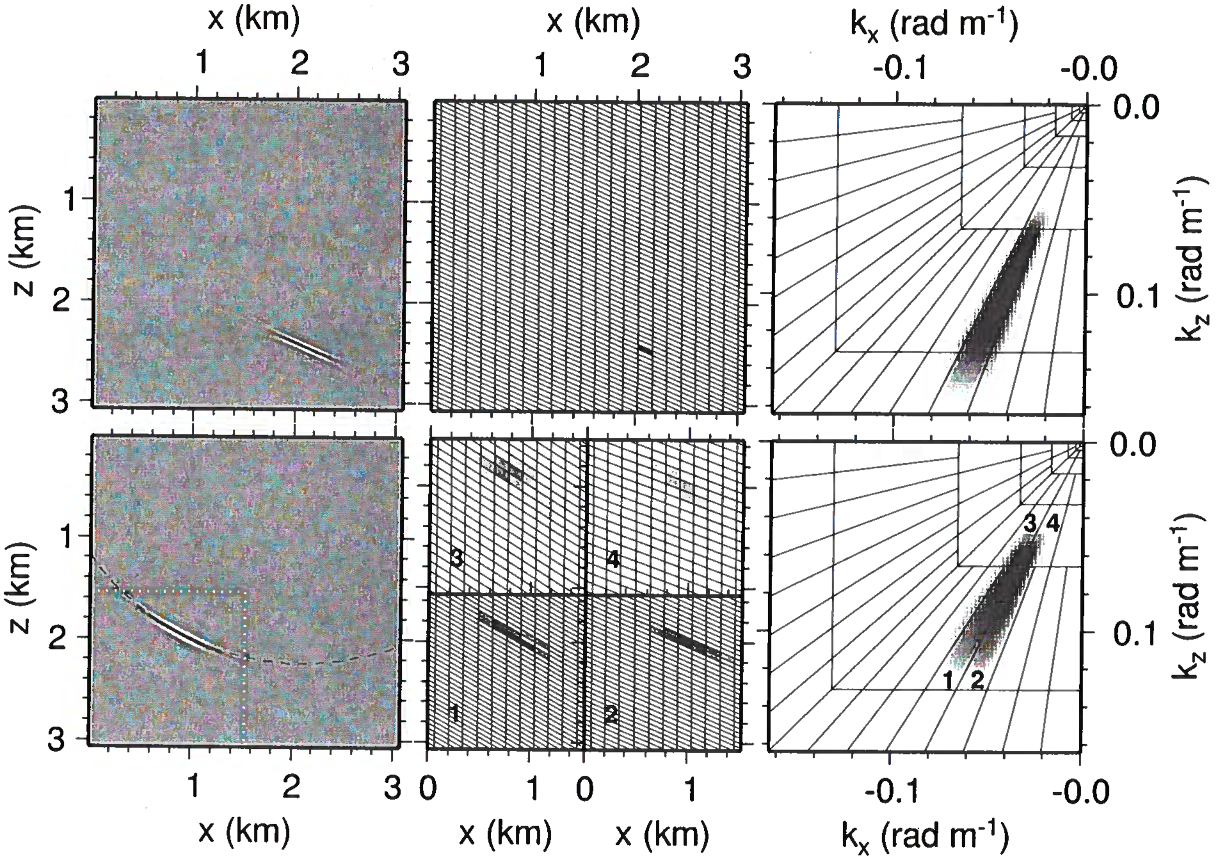

Figure 4. Top row: a curvelet with a dominant frequency of about 30 Hz (left, shown in depth $z = vt_u/2$, for consistency), the normalized absolute value of the coefficient on the spatial lattice (middle), and its amplitude spectrum (right). Bottom row: CO Kirchhoff migration of the curvelet in the top row. The middle panel in this row shows the coefficients on the spatial lattice in the lower left quadrant of the leftmost panel (indicated with the dotted lines in the leftmost panel) for each of the numbered wedges (labeled '1' to '4') in the spectrum (right). The Kirchhoff migration of a curvelet determines only *part of the isochron*, and shows that a curvelet is not mapped onto one other curvelet, but rather several other curvelets. The resulting curvelets are clustered together both in space and spectrum, at least for the constant media case shown here, indicating that a curvelet remains curvelet-like after CO Kirchhoff time migration.

tile has moved within the same concentric squares, i.e., indices j, m_1, and m_2 are the same, but index l has changed. Notice how the spatial lattice changes as we change the angular index l. Finally, Figure 3d shows a dilated version of the curvelet shown in Figure 3a; the spatial location is the same, but the spectral tile has moved outward into a neighboring annulus (or subband), i.e. the scale index j is increased by one. Since the neighboring annulus is subdivided into more wedges, the angular index l has also changed, although the direction of the curvelet is essentially the same. Similarly, since the larger scale has a finer spatial sampling associated with it, the translation indices m_1 and m_2 have also changed, while the curvelet location is essentially the same.

Curvelets remain curvelet-like when subjected to our class of operators

The action of operators belonging to the class of Fourier integral operators that can be sparsely represented using curvelets, which includes the CO time migration operator, can be described in terms of propagation of singularities along a Hamiltonian flow. The remark in the introduction thus applies: The action on a curvelet of a particular scale can be approximated by flowing out the center of the curvelet in phase space in accordance with the Hamiltonian associated with the medium filtered for this scale. This means that, in the appropriately filtered media, curvelets remain fairly localized in both the spatial domain and the spectral domain. Hence, the propagated curvelet can be constructed by using neighboring curvelets only, where neighboring is understood in the context of phase-space; i.e., a neighboring curvelet is a

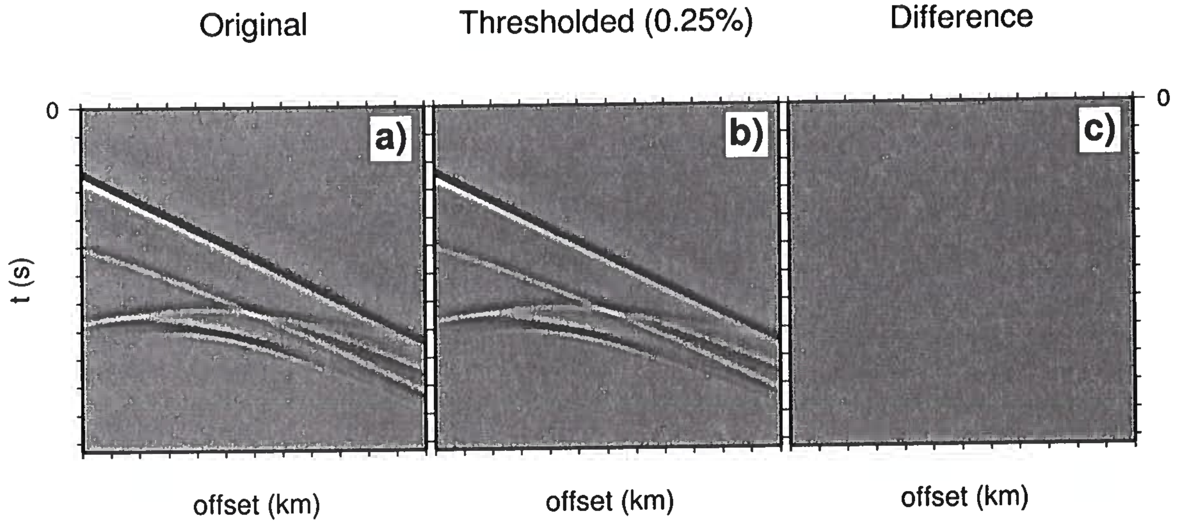

Figure 5. Synthetic common-shot gather with cusped wavefront: original (a), reconstructed using only the 0.25 % largest curvelet coefficients (b), and the difference (c). The reconstruction with 0.25 % of the curvelets is almost identical to the original common-shot gather. In this example, using only 0.25 % of the curvelets results in about 30 times fewer curvelets than input samples in the gather.

curvelet that is close in the spatial domain and has orientation close to the orientation of the curvelet that is propagated along the central ray.

For homogeneous media, filtering is unnecessary, and the above observation applies to the same medium for curvelets of all scales. To illustrate this, Figure 4 shows the result of CO Kirchhoff migration of a curvelet [taken from Douma and de Hoop (2004)]. The top row shows the input curvelet in space (the vertical axis was converted to depth using $z = vt_u/2$ for convenience), and its associated amplitude spectrum. Again the coefficient of the curvelet is shown in the middle panel, just as in Figure 3. The left-most panel of the bottom row shows the CO Kirchhoff migrated curvelet. Notice how the migrated curvelet is clearly localized in space and determines *only part of the isochron*, in sharp contrast to the whole isochron if a single sample (or a 'spike') would be used as input to the migration. This confirms that curvelets are indeed a more appropriate choice for building blocks of seismic data than are 'spikes' (that are currently used to represent seismic data). The spectrum of the migrated curvelet (bottom right) is clearly localized after the migration, and overlies four wedges in the curvelet tiling of the spectrum, indicating some leakage into neighboring curvelets in the spectral domain. The middle panel shows the coefficients for the spatial area in the lower left quadrant of the leftmost figure (outlined by the dotted lines), for the wedges labeled '1' through '4'. Indeed there is also some leakage to neighboring curvelets in space, but again this can be considered small. This confirms that curvelets remain localized in both the spatial and spectral domain (i.e., they remain 'curvelet-like') after pre-stack time migration.

Curvelets as building blocks of seismic data

Seismic reflections in seismic data lie primarily along smooth surfaces (or curves in two dimensions). Even diffractions from discontinuities in the earth's subsurface, such as edges of geologic interfaces caused by faulting, lie along smooth surfaces. This is a direct consequence of the wave-character of seismic data. As mentioned in the introduction, it is intuitive that curvelets can be used to sparsely represent seismic data, since curvelets provide the sparsest representations of smooth (C^2) functions away from edges along piecewise C^2 curves (Candès & Donoho, 2004b). Throughout this work, we simply adopt this intuition and illustrate this with a simple synthetic example below.

Figure 5a shows part of a synthetic common-shot gather, where the wavefront has a cusp. This data relates to a model with a syncline shaped reflector. Figure 5b shows the reconstructed gather where only the 0.25 % largest curvelet coefficients were used. For the particular example shown, this relates to a compression ratio of about 30; i.e., we used 30 times less curvelets than there are sample values in the original gather, to reconstruct the data. From Figure 5c it is clear that the difference between the original and reconstructed data is close to zero. This exemplifies that, using curvelets as building blocks of seismic data, the data can be sparsely represented with curvelets, with much fewer curvelets than the data has samples, and with essentially no residual, even in areas where the wavefront has cusps.

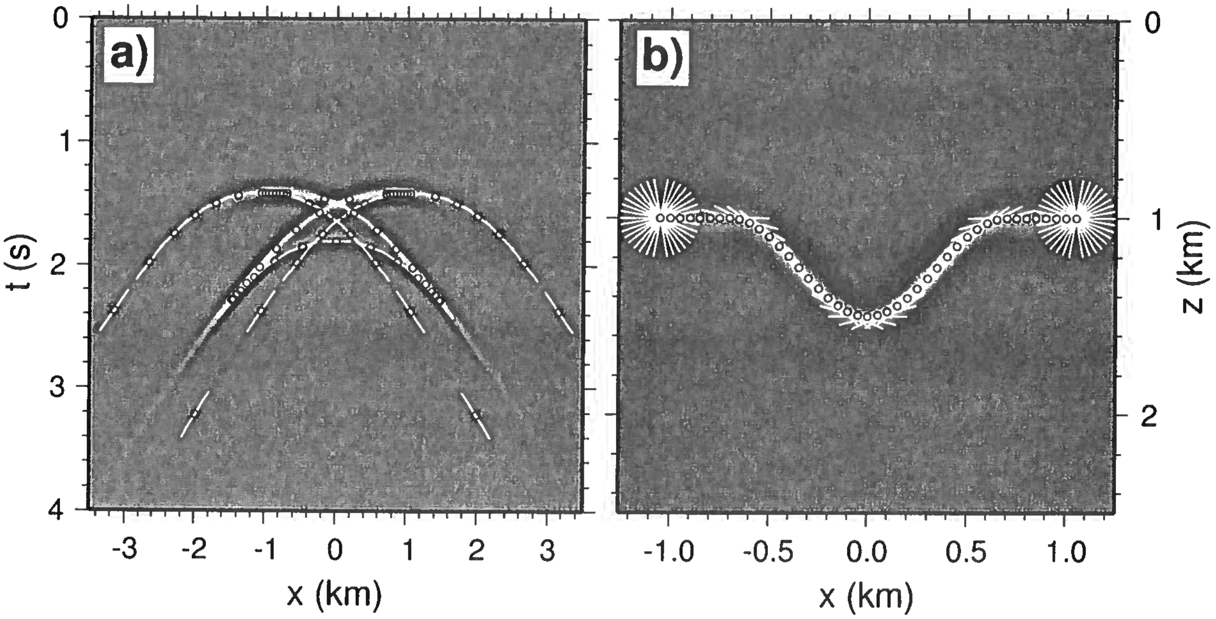

Figure 6. Common offset ($h = 1000$ m) data (a) and migrated data (b) from a syncline shaped reflector embedded in a constant velocity ($v = 2000$ m/s) medium, and demigrated and migrated line elements superposed on the data and migrated data, respectively. The excellent agreement between the demigrated line elements and the seismic data (a), and the migrated line elements and the migrated data (b), indicate the validity of the common-offset map time-demigration and migration equations, respectively.

In our example, we have applied a hard thresholding to the data; we simply did not use 99.75 % of the curvelets. At first sight one might think that therefore the compression ratio should be 400. However, the curvelet transform is redundant, meaning that if all curvelets are used to reconstruct the data, there are more curvelets than sample points in the data. Different digital implementations of the curvelet transform have different redundancies (Candès *et al.*, 2005). (In this particular example, the apparent compression ratio (400) and the associated implied redundancy of $400/30 \approx 13$ is so large only because a lot of zero-padding was necessary to make the number of samples in the gather both horizontally and vertically equal to an equal power of 2; the actual redundancy of the used transform is about 3.) The hard thresholding that we used in our example, will in practice certainly not be ideal to determine the threshold level, especially in a practical situation where we have noise. Here, we refrain from any denoising issues, and focus on the imaging with curvelets. Hence, we assume that an intelligent thresholding of the data has already determined the significant curvelet coefficients in the data.

We emphasize that by using curvelets as building blocks of seismic data, the local slopes (or 'directions') in the data are built into the data representation. Other than a straightforward projection of the data onto the curvelet frame (combined with an intelligent thresholding procedure), no additional processing steps are required to extract the local slopes from the data, such as local slant stacking in CDR (Zavalishin, 1981; Harlan & Burridge, 1983; Sword, 1987; Riabinkin, 1991), stereotomography (Billette & Lambaré, 1998; Billette *et al.*, 2003), and parsimonious migration (Hua & McMechan, 2001; Hua & McMechan, 2003), or multidimensional prediction-error filters (Claerbout, 1992, p.186-201) and plane-wave destruction filters (Fomel, 2002; Claerbout, 1992, p.93-97). Therefore, curvelets provide an appropriate reparameterization of seismic data, that have the wave-character of the data built into them.

2D Common-offset map time migration

Douma & de Hoop (2005) present explicit expressions for common-offset map time migration (i.e., migration in a medium with constant velocity), that use only the slope in a common-offset gather (and the velocity), rather than the slope in a common-offset gather *and* the slope in a common-midpoint gather (and the velocity), such as the equations presented by Sword (1987, p.22). The expressions in three dimensions from Douma & de

Hoop (2005) simplify in two dimensions to

$$\begin{aligned} x_m &= x_u - \left(\frac{vt_u}{2}\right)^2 \frac{\Lambda_u}{h}, & (2)\\ t_m &= \sqrt{\left[1-\left(\frac{vt_u\Lambda_u}{2h}\right)^2\right]\left\{t_u^2-\left(\frac{2h}{v}\right)^2\right\}}, & (3)\\ p_m &= \frac{2p_ut_u\left(\dfrac{|\Lambda_u-1|\,|\Lambda_u+1|}{|\Lambda_u-1|+|\Lambda_u+1|}\right)}{\sqrt{\left[1-\left(\frac{vt_u\Lambda_u}{2h}\right)^2\right]\left\{t_u^2-\left(\frac{2h}{v}\right)^2\right\}}} & (4)\end{aligned}$$

in which

$$\begin{aligned} \Lambda_u &= \Lambda_u\left(p_u,\Theta_u,h\right)\\ &= \frac{1}{2\sqrt{2}p_uh}\sqrt{\Theta_u\left(1-\sqrt{1-\frac{64\left(p_uh\right)^4}{\Theta_u^2}}\right)}, & (5)\end{aligned}$$

with

$$\begin{aligned} \Theta_u &= \Theta_u\left(t_u,p_u,h\right)\\ &= t_u^2+\left(\frac{2h}{v}\right)^4\frac{1}{t_u^2}-2\left(\frac{2h}{v}\right)^2\left(1-\left(vp_u\right)^2\right). & (6)\end{aligned}$$

In these expressions x_u, t_u, and $p_u = \frac{1}{2}\partial t_u/\partial x_u$ are the midpoint location, two-way (unmigrated) traveltime, and the (unmigrated) slope in a CO section, respectively, while x_m, t_m and $p_m = \frac{1}{2}\partial t_m/\partial x_m$ are their migrated counterparts. Also, h denotes the half-offset and v is the medium velocity. Equations (2)-(4) are explicit expressions that determine the migrated reflector coordinates (x_m, t_m, p_m) from the specular reflection coordinates (x_u, t_u, p_u), given h and v. Equations (2)-(4) do not use the offset horizontal slowness $p_h = \frac{1}{2}\partial t_u/\partial h$, such that in practice, only p_u needs to be estimated, and the slope in a common-midpoint gather can be ignored. It is possible to derive map migration equations that use the offset horizontal slowness p_h instead of the velocity (Sergey Fomel, personal communication). In this way, map time-migration can be done *without knowledge of the medium velocity.* This idea dates back to the work of Ottolini (1983). In the context of pre-stack time-migration with curvelets, this would require 3D equivalents of curvelets for 2D imaging since both p_u and p_h would need to be known.

Figure 6a shows a common-offset gather ($h = 1000$ m) from synthetic data generated from a syncline model with constant velocity above the reflector. On top of the reflections, line elements are drawn tangent to the reflections. Each of these line elements determines a local slope, p_u, while the center of the line determines the two-way traveltime t_u and the common-midpoint location x_u. Using equations (2)-(4) and the velocity $v = 2000$ m/s, the migrated location (x_m, z_m), with $z_m = vt_m/2$, and the local dip angle $\tan\phi = vp_m$ can be determined (ϕ is the angle with the horizontal measured clockwise positive). Figure 6b shows the migrated common-offset equivalent of the data shown in Figure 6a, with the migrated line elements, determined using x_m, t_m, and p_m, drawn on top of the image. The migrated line elements accurately follow the directions in the image, indicating that equations (2)-(4) accurately capture the kinematics of CO time migration in a high-frequency approximate sense. Note that the line elements from diffractions of the edges of the syncline in Figure 6a, are all mapped to the same location but with different orientations. This is identical to building a (band-limited) delta-function with plane waves from all directions; i.e., the Fourier transform of a delta function has all directions.

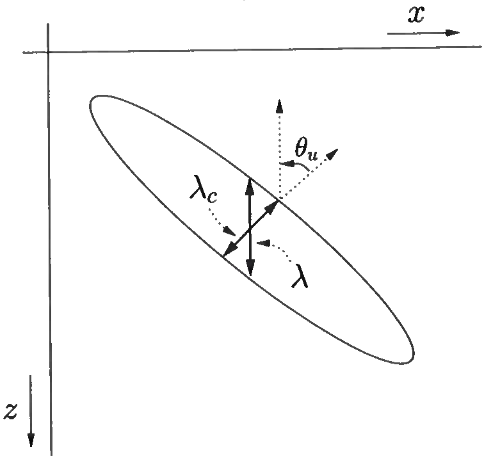

Figure 7. The width of the curvelet in the direction perpendicular to its 'main ridge' determines wavelength λ_c, while the vertical width of the curvelet determines the wavelength λ relevant to seismic migration. It follows that $\lambda_c = \lambda\cos\theta_u$ and hence $\omega = \omega_c\cos\theta_u$.

Knowing that each curvelet has a (few) direction(s) associated with it, we aim to replace the line elements in Figure 6 with curvelets, and see to what extent moving curvelets around according to the map migration equations (2)-(4), gives us a good time migrated image. We are thus aiming to lift the applicability of map migration beyond velocity model building, and show its use for pre-stack (here CO) time imaging with curvelets. This was also mentioned by Douma and de Hoop (2004).

2.5-D Common-offset time migration with curvelets

As mentioned in the previous section, the CO map time-migration equations (2)-(4) use the slope in the CO domain only. This implies that the flow from a curvelet in the data domain to the image domain is determined by one slope only. Therefore, the following scheme for time-imaging with curvelets emerges. Using curvelets as building blocks of seismic data, the directions (or local slopes) in the data follow from a straightforward projec-

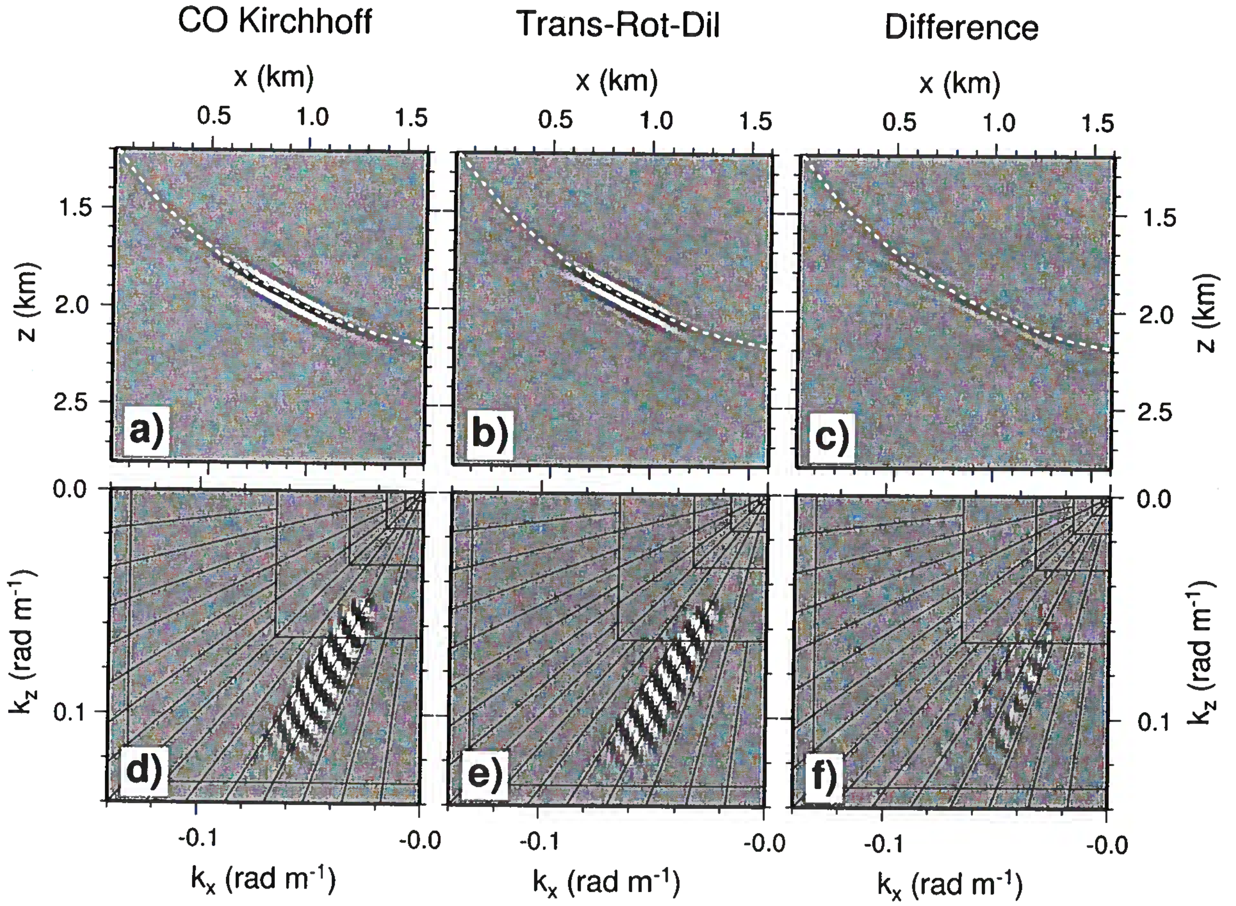

Figure 8. CO Kirchhoff migration of the curvelet shown in Figure 4 (a), TRD transformation of this curvelet (b), and the difference (c). The bottom row shows the real part of the spectrum for the CO Kirchhoff migrated curvelet (d), the TRD transform (e), and the difference (f). The TRD transform gives a good approximation to the Kirchhoff migrated curvelet.

tion of the data onto the curvelet frame. Thresholding of the curvelet coefficients then gives the curvelets associated with the main wavefronts in the data, and thus the directions associated with these wavefronts also. Subsequently, these directions can be used in our map migration equations (2)-(4) (together with an estimate of the velocity), to determine the migrated location and orientation of the curvelet. Hence, these equations determine a translation and a rotation of the curvelet.

It is known (e.g., Bleistein *et al.* (2000), p.223 and p.235) that after pre-stack migration, the length of the $\boldsymbol{k}$-vector changes according to

$$|\boldsymbol{k}| = \omega \nabla_y \phi(\boldsymbol{y}, \boldsymbol{x}_s, \boldsymbol{x}_r) = \frac{\omega}{v(\boldsymbol{y})} \cos\theta(\boldsymbol{y}, \boldsymbol{x}_s, \boldsymbol{x}_r)\ , \qquad (7)$$

where ω is the angular frequency, $\boldsymbol{x}_{s,r}$ are the source and receiver locations, $\boldsymbol{y}$ is the output location in the image, $\phi(\boldsymbol{y}, \boldsymbol{x}_s, \boldsymbol{x}_r)$ is the two-way traveltime from the source location $\boldsymbol{x}_s$ to the reflector at $\boldsymbol{y}$ to the receiver position $\boldsymbol{x}_r$, $v(\boldsymbol{y})$ is the velocity at output location $\boldsymbol{y}$, and $\theta(\boldsymbol{y}, \boldsymbol{x}_s, \boldsymbol{x}_r)$ is the half opening-angle between the ray from the source to the scattering point, and the ray from the receiver to the scattering point. The term $\cos\theta(\boldsymbol{y}, \boldsymbol{x}_s, \boldsymbol{x}_r)$ is usually referred to as the ***obliquity*** factor. In 2D, for a constant background velocity and a CO acquisition geometry, equation (7) simplifies to $|\boldsymbol{k}| = \frac{\omega}{v}\cos\theta(x_m, t_m, x_u, h)$, where h is the half offset, x_u the common midpoint location along the 2D acquisition profile, and the angle $\theta(x_m, t_m, x_u, h)$ is given by

$$\theta(x_m, t_m, x_u, h) = \frac{1}{2}\left\{\tan^{-1}\left(\frac{2\,(x_u + h - x_m)}{vt_m}\right) - \tan^{-1}\left(\frac{2\,(x_u - h - x_m)}{vt_m}\right)\right\}\ . \qquad (8)$$

A curvelet has dominant wavelength λ_c in the direction orthogonal to the curvelet (see Figure 7). However, the dominant wavelength λ in the vertical direction determines the frequency relevant to migration. It follows that $\lambda_c = \lambda\cos\theta_u$, which gives

$$\omega = \omega_c \cos\theta_u\ , \qquad (9)$$

where θ_u is the phase-angle (measured clockwise positive with the vertical) of the curvelet in the data domain.

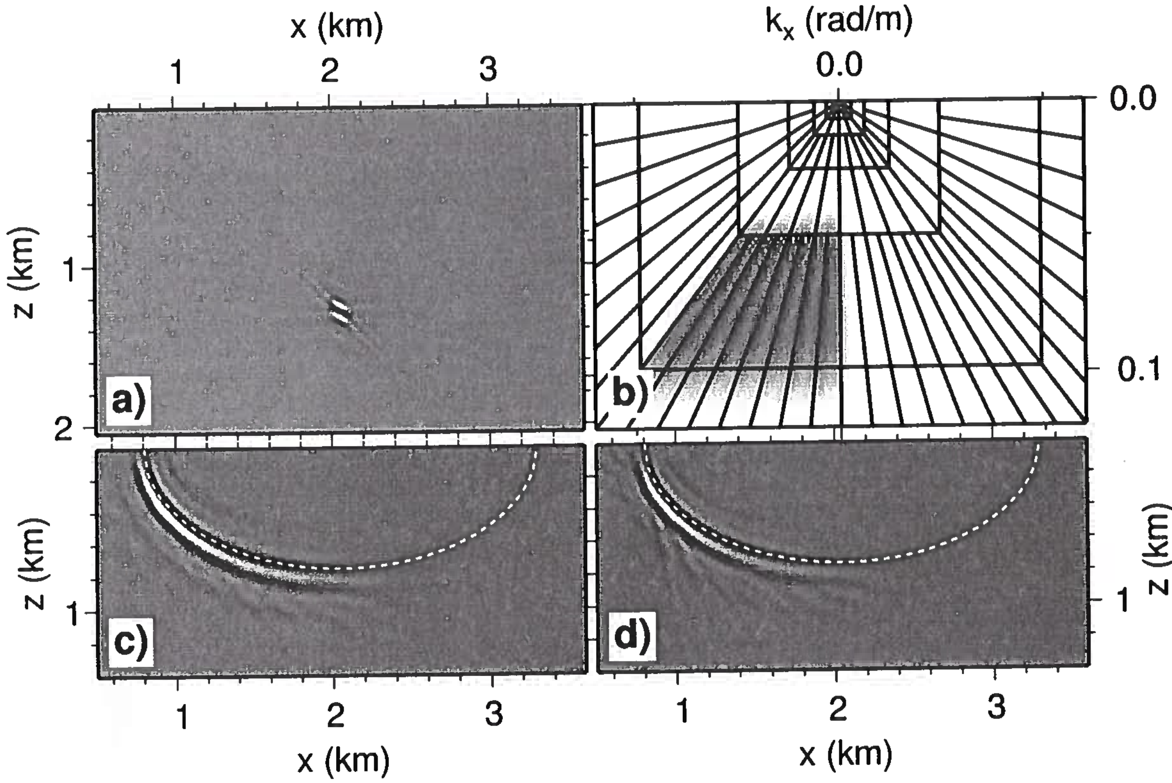

Figure 9. Superposition of 8 curvelets (a), the associated amplitude spectrum (b), the CO Kirchhoff migrated result (c), and the result from the amplitude corrected TRD transform (d). The amplitude corrected TRD transform gives a decent approximation to the Kirchhoff migrated result, and the interference between different curvelets results in a reasonably smooth isochron. Since we used only curvelets with $\boldsymbol{k}$-vectors pointig to the left, only the left part of the isochron is constructed.

Combining equations (7) and (9) it follows that, after migration, the length of the $\boldsymbol{k}$-vector can be written as

$$|\boldsymbol{k}| = \frac{\omega_c}{v(\boldsymbol{y})} \cos\theta(x_m, t_m, x_u, h)\sqrt{1-(v(\boldsymbol{y})p_u)^2}\,, \qquad (10)$$

where we used $\cos\theta_u = \sqrt{1-(v(\boldsymbol{y})p_u)^2}$. This means that the curvelet needs to be dilated (or stretched) in the image domain with dilation factor D, given by

$$D = \frac{1}{\cos\theta(x_m, t_m, x_u, h)\sqrt{1-(vp_u)^2}}\,. \qquad (11)$$

where we specialized to the constant background velocity case. Therefore, CO pre-stack time migration with curvelets can be done by translating and rotating the curvelets in the data domain according to the map migration equations (2)-(4), and dilating the curvelets with a stretch factor given by equation (11). In these equations, the parameters x_u, t_u, and p_u are the position (x and t) and direction of the center of the curvelet respectively. Throughout this paper, we refer to the translation, rotation and dilation of a curvelet as the *TRD transformation* of a curvelet.

The TRD transformation of a curvelet provides the kinematics of imaging with curvelets, but ignores the dynamics, often referred to as the 'true amplitude' part of seismic imaging. For constant background velocities and a CO acquisition geometry, Bleistein *et al.* (2000) show that the equation for 2.5-D Kirchhoff inversion for reflectivity is given by [their equation (6.3.25); note the missing division with the velocity v in the phase function]

$$\begin{aligned}\beta(\boldsymbol{y}) &= \frac{1}{\sqrt{2\pi}}\int\int A(\boldsymbol{y}, x_u, \omega; h)e^{-i\omega[r_s+r_g]/v} \times \ldots \\ &\quad u_S\left(x_g, x_s, \omega\right) dx_u d\omega,\end{aligned} \qquad (12)$$

with

$$\begin{aligned}A(\boldsymbol{y}, x_u, \omega; h) &= \frac{4y_3\sqrt{r_s+r_g}\left(r_s^2+r_g^2\right)}{\left(v\, r_s r_g\right)^{3/2}} \times \ldots \\ &\quad \cos\theta(\boldsymbol{y}, x_u, h)\sqrt{|\omega|}e^{i\frac{\pi}{4}\mathrm{sgn}\omega}\,,\end{aligned} \qquad (13)$$

where $\boldsymbol{y} = (y_1, y_3)$ is the output location in the image domain, x_u is the midpoint location along the 2D acquisition profile, $r_{s,g}$ are the distance from the output location $\boldsymbol{y}$ to the source and receiver at $x_s = (x_u - h, 0)$ and $x_r = (x_u + h, 0)$, respectively, and u_S is the (singly) scattered data. To find the amplitude correction for the migration of a curvelet, we would therefore need to use a curvelet as scattered data u_S, and evaluate the

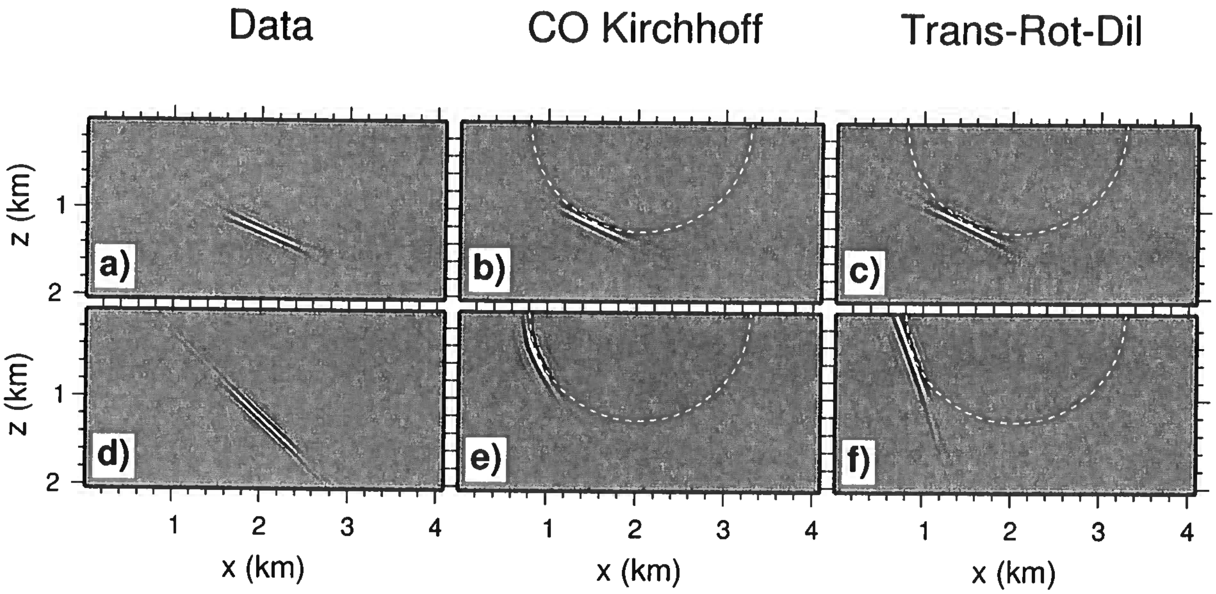

Figure 10. A shallow dipping curvelet (a) and a steep dipping curvelet (d), their CO Kirchhoff migrated counterparts [(b) and (e), respectively], and the TRD transformed counterparts [(c) and (f), respectively]. The steeper dipping curvelet is more strongly bended towards the isochron than is the shallower dipping curvelet.

integrals in equation (12). A natural way to evaluate the oscillatory integral in equation (12), is to use the method of stationary phase [e.g. Bleistein (1984, p.77-81) and Bleistein *et al.* (2000, p.127-135)]. Such an analysis should reveal the amplitude correction for the migrated curvelet. At the moment of writing this report, we have not done such an analysis. Therefore, for the purpose of generating the results in this report, we simply scale the curvelet with $A(y, x_u, \omega; h)$ knowing that ultimately we want to do the stationary phase analysis.

Numerical examples

Figure 8a shows the 2.5-D CO Kirchhoff migrated curvelet from Figure 4 in more detail, while Figure 8d shows the real part of the associated spectrum. We plot the real part of the spectrum instead of the amplitude spectrum, to see the phase information and amplitude information combined in one plot. Figure 8b shows the result of the TRD transformation of the same curvelet, where the translation and rotation is determined by the map migration equations (2)-(4), and the dilation is determined by the stretch factor given in equation (11). Figure 8c shows the difference between the Kirchhoff migrated curvelet and the TRD transformed curvelet. Before subtraction, both images were normalized to have maximum amplitude one, such that the difference only shows relative amplitude differences between both images. Figures 8e and f show the real part of the amplitude spectra of the images shown in Figures 8b and c.

It is clear that for this particular curvelet, the TRD transformation of the curvelet gives a reasonable approximation to the Kirchhoff result. The maximum amplitude of the difference between both methods is about 20% of the maximum amplitude in the Kirchhoff image. From the lines of equal phase in the spectra, we see that the curvelet is slightly bent due to the migration, whereas the TRD transformation does not take this bending into account (cf. Figures 8d and e). The main difference in the spectrum occurs on the edges of the support of the curvelet in the frequency domain, where this bending is strongest. Overall, for this particular curvelet, the TRD transformation gives a satisfactory approximate image when compared to the Kirchhoff result.

Even though Figure 8 shows good results for one (particular) curvelet, this does not show the interference between different curvelets. Figure 9a shows a superposition of 8 curvelets, with the same central location in space, and the same scale index, but different directions (or angular indices). The vertical axis is here again converted from two-way traveltime to depth. Figure 9b shows the amplitude spectrum of all 8 curvelets combined, and it is clear that we used curvelets that have leftward pointing $\boldsymbol{k}$-vectors only. Figure 9c shows the 2.5-D CO Kirchhoff migrated result, while Figure 9d shows the result of our TRD transformation combined with an amplitude scaling given by equation (13). As expected, the Kirchhoff result gives the left part of the isochron only. Comparing Figures 9c and d, the TRD transformation combined with the amplitude correction of equation (13) gives a reasonable approximation to the

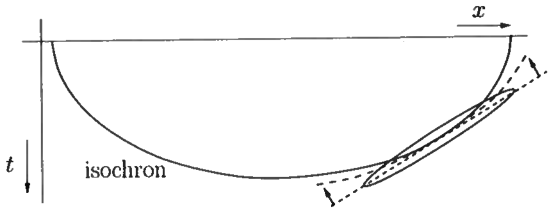

Figure 11. The observed bending of curvelets, mostly for the steeper dips in the data, could possibly be corrected for by bending the curvelet towards the isochron as depicted.

Kirchhoff migrated result. The interference of the different curvelets (of the same scale) is good, and compares favorably to the Kirchhoff result, although the comparison seems better for the shallower dipping part of the isochron. At the steeper parts of the isochron, the destructive interference between different curvelets away from the isochron, is somewhat less effective and leaves the tails of the curvelets somewhat visible.

In order to see the differences between the results for the steeper dipping curvelets and the shallower ones, Figure 10 shows the comparison between the Kirchhoff result and our TRD transformation for both a shallow and a steep dipping curvelet. Here we did zero-offset migration, to avoid the curvature of the isochron being different at different locations on the isochron; i.e., a semi-circle has constant curvature everywhere. Figure 10 shows that the steeper dipping curvelet is significantly 'bent' towards the isochron, while the shallower dipping curvelet is hardly bent at all. As a result, the TRD transform does better for the shallower dipping curvelets than for the steeper dipping ones, as it does not include any such bending.

It remains to be seen how severe the error is if we ignore this bending, and use our TRD transform on a synthetic data-set with many curvelets. In this case, there would be interaction between curvelets from several different scales, i.e., with different frequency content. We have not performed such a test yet, since this requires the proper frequency weighting for curvelets of different scales. As we mentioned earlier, this frequency weighting should follow from a stationary phase evaluation of equation (12) with a curvelet as scattered data u_S. At the moment of writing this report we have not done such a calculation. In case future tests using a combination of the amplitude correction, obtained in this manner, and the TRD transform would show that an omitted bending correction in the TRD transform causes large differences with the Kirchhoff result, we could introduce an extra bending correction to bend the curvelets towards the isochron as depicted in Figure 11.

Discussion

In this paper, the TRD transform is calculated using a brute-force approach in the spatial domain. For the significant curvelet coefficients, we apply an inverse curvelet transform, and transform the resulting curvelet in the spatial domain according to our TRD transform. This approach allows us to show the proof of concept of imaging with curvelets using our TRD transform, but does not provide an efficient way of such imaging with curvelets. Ultimately one would want to calculate the TRD transform in the curvelet frame, although an approach that makes use of the finite support of the curvelets in the spectral domain seems also worth investigating.

Even though the curvelets used in this paper are 2D, they can be extended to higher dimensions. Figure 12 shows an example of a 3D curvelet in both the spatial domain (a) and the spectral domain (b). In the spatial domain, 3D equivalents of curvelets look like circular disks that are smooth along the disk and oscillatory orthogonal to the disk. Roughly speaking they are smoothed circular pieces of a bandlimited plane wave in 3D[†]. Therefore, replacing the 2D map migration equations with their 3D equivalents, the TRD transform can be extended to 3D, hence allowing 3D CO pre-stack time-imaging with curvelets. Decomposing a 3D CO volume of data into 3D curvelets, the same procedure as outlined in this paper can be used to image 3D seismic data with 3D equivalents of curvelets. Of course, the proper 3D amplitude correction should be used in this case.

Even though in this paper we show results from migration only, modeling or demigration with curvelets works in the same way. In this case the TRD transform is defined according to the map demigration equations (Douma & de Hoop, 2005).

Conclusion

We have presented first examples of the use of curvelets in CO pre-stack time migration. A simple numerical example confirmed that curvelets can be used as building blocks for seismic data that allow for a sparse representation of such data. Since curvelets are roughly like pieces of bandlimited plane waves, the wave-character of the seismic data, i.e., that it is bandlimited and that the recorded wavefronts have directions associated with them, can be built into the representation of the data. Therefore, in essence, curvelets are an appropriate reparameterization of seismic data, that allow the wave-character of the data to be built into the representation of the data. Knowing that the local directions (or slopes) in the data (for a fixed scattering angle and azimuth, or offset and azimuth in homogeneous media) can be mapped one-to-one from the data to the image

---

[†] This rough description of course ignores that each curvelet has a small range of $\boldsymbol{k}$-vectors associated with it, rather than only a single $\boldsymbol{k}$ direction, as has a plane wave.

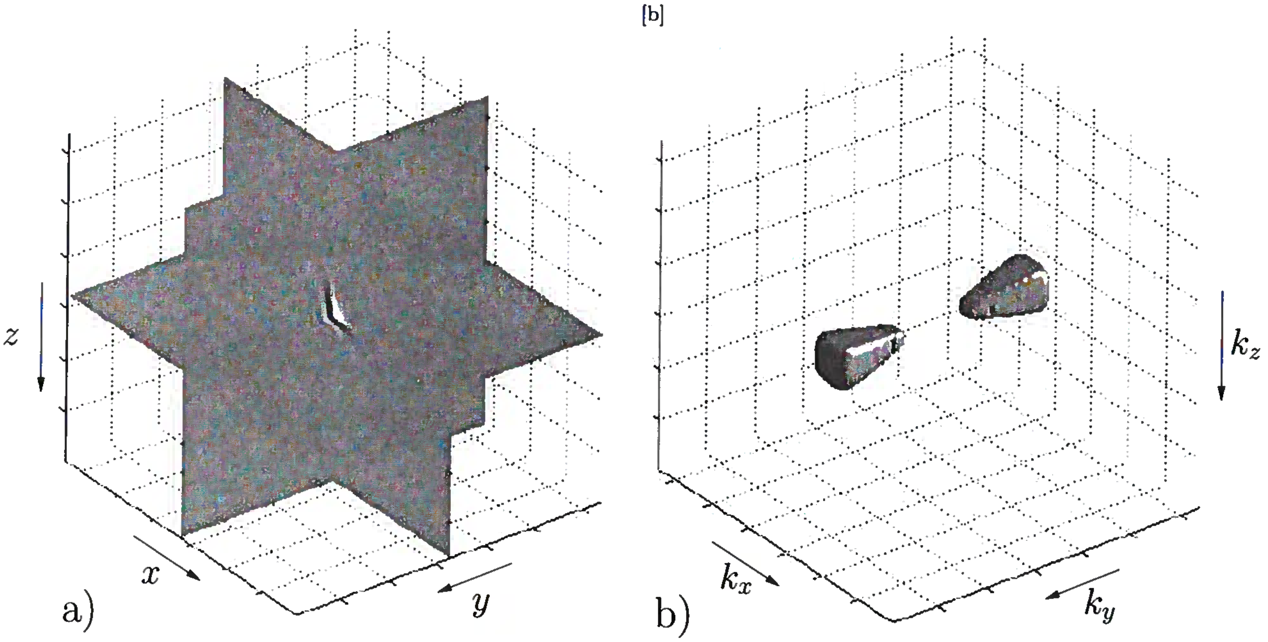

Figure 12. A 3D curvelet in space (a) and its associated amplitude spectrum (b). In the spatial domain, 3D equivalents of curvelets look like circular disks that are smooth along the disk and oscillatory orthogonal to the disk.

domain using map migration, we have studied the use of map migration to perform CO pre-stack time migration with curvelets.

The numerical tests of 2D CO pre-stack time imaging with curvelets we presented, showed that a simple translation, rotation, and dilation approach (which we refer to as the TRD transformation) of curvelets, largely determined by the 2D CO pre-stack map migration equations, provides a reasonably accurate approximation to the Kirchhoff migrated result, at least on a per scale basis, i.e., for curvelets with similar frequency content. Our results for CO pre-stack time migration with curvelets in 2D, through our TRD transformation, can be extended to 3D using 3D equivalents of curvelets.

Acknowledgments

The authors thank Roel Snieder for his critical review of the paper, and Emmanuel Candès for providing us with his Matlab implementation of the digital curvelet transform via unequally spaced fast Fourier transforms. This work was partly supported by Total E & P and the sponsors of the Consortium Project on Seismic Inverse Methods for Complex Structures at the Center for Wave Phenomena.

REFERENCES

Billette, F., & Lambaré, G. 1998. Velocity macro-model estimation from seismic reflection data by stereotomography. *Geophysical Journal International*, **135**, 671–690.

Billette, F., Le Bégat, S., Podvin, P., & Lambaré, G. 2003. Practical aspects and applications of 2D stereotomography. *Geophysics*, **68**, 1008–1021.

Bleistein, N. 1984. *Mathematical methods for wave phenomena.* Academic Press, Inc.

Bleistein, N., Cohen, J.K., & Stockwell, J.W.Jr. 2000. *Mathematics of Multidimensional Seismic Imaging, Migration, and Inversion.* Springer.

Candès, E. J., & Demanet, L. 2004. The curvelet representation of wave propagators is optimally sparse. *submitted, and can be downloaded from Candès website.*

Candès, E. J., & Donoho, D. L. 2004a. DCTvUSFFT: Digital Curvelet Transform via Unequispaced Fast Fourier Transforms. *Technical Report, California Institute of Technology.*

Candès, E. J., & Donoho, D. L. 2004b. New tight frames of curvelets and optimal representations of objects with piecewise C^2 singularities. *Comm. on Pure and Appl. Math.*, **57**, 219–266.

Candès, E. J., & Guo, F. 2002. New multiscale transforms, minimum total variation synthesis: Applications to edge-preserving image reconstruction. *Signal Processing*, **82**, 1519–1543.

Candès, E. J., Demanet, L., Donoho, D., & Ying, L. 2005. Fast discrete curvelet transforms. *preprint.*

Candès, E.J., & Donoho., D.L. 2000. *Curvelets - a surprisingly effective nonadaptive representation for objects* *with edges.* Vanderbilt University Press. Pages 105–120.

Claerbout, J. F. 1992. *Earth soundings analysis: Processing versus inversion.* Blackwell Scientific Publications, Inc.

Córdoba, A., & Fefferman, C. 1978. Wave packets and Fourier Integral Operators. *Comm. PDE's*, **3**, 979–1005.

Douma, H., & de Hoop, M. V. 2005. Explicit expressions for pre-stack map time-migration in isotropic and VTI media and the applicability of map depth-migration in heterogeneous anisotropic media. Accepted for publication in *Geophysics.*

Douma, H., & de Hoop, M.V. 2004. Wave-character preserving pre-stack map migration using curvelets. *In: Expanded Abstracts 74th annual international meeting of the SEG.* Soc. Expl. Geophys.

Fefferman, C. 1973. A note on spherical summation multipliers. *Israel J. Math.*, **15**, 44–52.

Fomel, S. 2002. Applications of plane-wave destruction filters. *Geophysics*, **67**(6), 1946–1960.

Harlan, W., & Burridge, R. 1983. A tomographic velocity inversion for unstacked data. *Stanford Exploration Project report SEP-37, 1-7.*

Hernández, E., & Weiss, G. 1996. *A first course on wavelets.* CRC Press, Inc.

Herrmann, F. 2003a. Optimal imaging with curvelets. *In: Expanded Abstracts.* Soc. Expl. Geophys.

Herrmann, Felix J. 2003b. *Multifractional splines: application to seismic imaging.* SPIE. Pages 240–258.

Hua, B., & McMechan, G. A. 2001. Parsimonious 2D poststack Kirchhoff depth migration. *Geophysics*, **66**, 1497–1503.

Hua, B., & McMechan, G. A. 2003. Parsimonious 2D prestack Kirchhoff depth migration. *Geophysics*, **68**, 1043–1051.

Kleyn, A.H. 1977. On the migration of reflection time contour maps. *Geophysical Prospecting*, **25**, 125–140.

Mallat, S. G. 1998. *A wavelet tour of signal processing.* First edn. Academic Press, USA.

Ottolini, R. 1983. Velocity independent seismic imaging. *Stanford Exploration Project report SEP-37, 1-7.*

Riabinkin, L.A. 1991. *Fundamentals of resolving power of controlled directional reception (CDR) of seismic waves.* Society of Exploration Geophysicists (Tulsa), Geophysics Reprint Series. Pages 36–60.

Smith, H. 1997. A Hardy space for Fourier integral operators. *J. Geom. Anal.*, **7**.

Smith, H. 1998. A parametrix construction for wave equations with $C^{1,1}$ coefficients. *Ann. Inst. Fourier*, **48**, 797–835.

Stein, E. M. 1993. *Harmonic Analysis: Real-variable methods, orthogonality, and oscillatory integrals.* Second edn. Princeton University Press.

Strang, G., & Nguyen, T. 1997. *Wavelets and filter banks.* Revised edn. Wellesley-Cambridge Press.

Sword, C. H. 1987. *Tomographic determination of interval velocities from reflection seismic data: the method of controlled directional reception.* Ph.D. thesis, Stanford Exploration Project, Stanford University.

Zavalishin, B.R. 1981. Perfection of methods for constructing seismic images using controlled directional reception. *Soviet Geology and Geophysics*, **22**, 98–104.

APPENDIX A: CURVELETS

In this appendix, we explain curvelets and their construction. This treatment closely follows the construction of real-valued curvelets from Candès and Donoho (2004b), except from some added derivations and explanations to clarify the construction of curvelets for the non-specialist. We deviate in some places from the original treatment to clarify certain details. For example, we immediately use the 'splitting at every other scale' (that will become clear later).

Before treating the construction of curvelets, we mention that we want to be able to reconstruct a signal in a function space $\mathcal{X}$ with zero error; i.e., we want the curvelets to satisfy the reconstruction formula

$$f = \sum_{\mu \in M} (f, c_\mu)\, c_\mu \quad , \tag{A1}$$

where c_μ denotes a curvelet with multi-index μ (and M some index-set), and $f \in \mathcal{X}$. It is known [e.g., Hernández and Weiss (1996, pp.334-336) and appendix B in this paper] that if $\mathcal{X}$ is a Hilbert space, this is equivalent to requiring

$$\|f\|^2_{\mathcal{X}} = \sum_{\mu \in M} |(f, c_\mu)|^2 \ , \quad \forall f \in \mathcal{X} \, . \tag{A2}$$

to hold. The latter expression implies that the energy of the signal f is conserved through the decomposition (A1); in other words, the curvelets c_μ should be a 'partition of unit energy'. Condition (A2) is the definition of a (normalized) tight frame (see appendix B for a thorough explanation of tight frames). Hence, for the curvelets to satisfy the reconstruction formula (A1), we want them to constitute a partition of unit energy.

Curvelets can be thought of as 2D (anisotropic) extensions to wavelets. Just like wavelets are 'localized' in one variable *and* its Fourier dual, curvelets are 'localized' in two variables *and* their two Fourier duals. Such localization is of course understood within the limits imposed by the Heisenberg uncertainty principle. Choosing the variables to be x and z, such localization is obtained through tiling of the spatial domain (x, z) and the spectral domain (k_x, k_z). We treat the spectral localization first, followed by the spatial one.

Let $\chi_{j,l}(\boldsymbol{k})$ be a window (or tile) in the spectral domain, with j an index related to the radial (i.e., scale) direction, and l an index related to the angular direction; i.e. the localization in the spectrum is dealt with in polar coordinates r and θ. In order for the curvelets to constitute a tight frame (see appendix B), the windows $\chi_{j,l}(\boldsymbol{k})$ must satisfy

$$\sum_{j} \sum_{l} |\chi_{j,l}(\boldsymbol{k})|^2 = 1, \ j \in J, l \in L, \tag{A3}$$

such that $\chi_{j,l}(\boldsymbol{k})$ indeed is a partition of unit energy. The window $\chi_{j,l}(\boldsymbol{k})$ is constructed through multiplication of an angular window $\nu(\theta)$ and a radial window ing

$$u_{j,m}\left(k_x,k_z\right) = \frac{2^{-3j/4}}{2\pi\sqrt{\delta_1\delta_2}} e^{i\pi(m_1+1/2)2^{-j}k_x/\delta_1} e^{im_2k_z2^{-\lfloor j/2\rfloor}/\delta_2},$$

Using this definition, and denoting by $R_{\theta_{j,l}}$ the rotation by angle $\theta_{j,l}$, the curvelet is then in the frequency domain defined as

$$\hat{c}_\mu(\boldsymbol{k}) = 2\pi\chi_{j,l}(\boldsymbol{k})u_{j,m}\left(R^*_{\theta_{j,l}}\boldsymbol{k}\right), \quad \mu=(j,l,m), \qquad \text{(A9)}$$

where $\hat{c}_\mu$ denotes the Fourier transform of the curvelet $c_\mu \in L^2(\mathbb{R}^2)$. These are the 'fine' scale curvelets. The coarse scale curvelets are then defined as $\hat{c}_{\mu_0}(\boldsymbol{k}) = 2\pi\chi_0(\boldsymbol{k})u_m(\boldsymbol{k})$, with $u_m(\boldsymbol{k}) = (2\pi\delta_0)^{-1}e^{i(m_1k_x/\delta_0+m_2k_z/\delta_0)}$. Here, δ_0 is again some appropriate constant determining the sampling rate (or translations steps) in the spatial domain. Note that here δ_0 determines the sampling rate in both the x and z direction, since the coarse scale curvelets (or better wavelets) are isotropic.

Using the definition of curvelets given in equation (A9), it can be shown that curvelets form a (normalized) tight frame. From equation (A9) it is clear that in L^2 we have

$$\sum_{m_1,m_2}\left|\left(\hat{f},\hat{c}_\mu\right)\right|^2 = (2\pi)^2\cdot\int\left|\hat{f}(\boldsymbol{k})\right|^2|\chi_{j,l}(\boldsymbol{k})|^2\,d\boldsymbol{k},$$

where we used that $\left(u_{j,m}\left(R^*_{\theta_{j,l}}\boldsymbol{k}\right)\right)_{m\in\mathbb{Z}^2}$ is, by construction, an orthonormal basis for L^2 over the support of $\chi_{j,l}(\boldsymbol{k})$, i.e., $\left|u_{j,m}\left(R^*_{\theta_{j,l}}\boldsymbol{k}\right)\right|^2 = 1$. Using that the $\chi_{j,l}(\boldsymbol{k})$ constitute a partition of unity by equation (A8), it then follows that

$$\begin{aligned}
&\textstyle\sum_{j\geq0}\sum_{l=0}^{2^{\lfloor j/2\rfloor-1}}\sum_{m_1,m_2}\left|\left(\hat{f},\hat{c}_{(j,l,m_1,m_2)}\right)\right|^2 = \\
&(2\pi)^2\textstyle\sum_{j\geq0}\sum_{l=0}^{2^{\lfloor j/2\rfloor-1}}\int\left|\hat{f}(\boldsymbol{k})\right|^2|\chi_{j,l}(\boldsymbol{k})|^2\,d\boldsymbol{k} \\
&= (2\pi)^2\int\left|\hat{f}(\boldsymbol{k})\right|^2\left[\textstyle\sum_{j\geq0}\sum_{l=0}^{2^{\lfloor j/2\rfloor-1}}|\chi_{j,l}(\boldsymbol{k})|^2\right]d\boldsymbol{k} \\
&= (2\pi)^2\int\left|\hat{f}(\boldsymbol{k})\right|^2d\boldsymbol{k} = (2\pi)^2\left\|\hat{f}\right\|_2^2.
\end{aligned}$$

This tells us that $(\hat{c}_\mu)_{\mu\in M}$ (with $\mu=(j,l,m_1,m_2)$ a multi-index) is a tight frame for $L^2(\mathbb{R}^2)$. Here, M is a multi-index set that has the appropriate ranges for j, l, m_1 and m_2. Finally, using the Parseval formula and the Plancherel formula for $L^2(\mathbb{R}^2)$, i.e., $\left(\hat{f},\hat{c}_\mu\right) = (2\pi)^2(f,c_\mu)$ and $\left\|\hat{f}\right\|_2^2 = (2\pi)^2\|f\|_2^2$, respectively, it follows that for $f\in L^2(\mathbb{R}^2)$

$$\sum_{\mu\in M}|(f,c_\mu)|^2 = \|f\|_2^2\,. \qquad \text{(A10)}$$

This shows that $(c_\mu)_{\mu\in M}$ is a normalized tight frame for $L^2(\mathbb{R}^2)$, giving us the reconstruction formula (A1).

APPENDIX B: TIGHT FRAMES IN HILBERT SPACES

Let $\mathcal{H}$ be a Hilbert space, and let $(\cdot,\cdot)$ denote the inner product on $\mathcal{H}$. A collection of elements $\{e_j\}_{j\in J}$ in $\mathcal{H}$, with J an index set, is called a **frame**, if there exist constants A and B, $0 < A \leq B < \infty$, such that

$$A\|f\|^2_{\mathcal{H}} \leq \sum_{j\in J}|(f,e_j)|^2 \leq B\|f\|^2_{\mathcal{H}} \quad \forall f\in\mathcal{H}, \qquad \text{(B1)}$$

where A and B are called **frame bounds**, and where $\|\cdot\|_{\mathcal{H}}$ denotes the norm on $\mathcal{H}$ induced by the inner product. If the frame bounds are equal ($A=B$), the frame is called **tight**. E.g., the four vectors $\phi_1=(0,1)$, $\phi_2=(1,0)$, $\phi_3=\left(\frac{\sqrt{2}}{2},\frac{\sqrt{2}}{2}\right)$, and $\phi_4=\left(-\frac{\sqrt{2}}{2},\frac{\sqrt{2}}{2}\right)$, form a tight frame for $\mathbb{R}^2$ with frame bounds $A=B=2$, since it follows that $\sum_{i=1}^4|(f,\phi_i)|^2 = 2\|f\|^2$. Here the frame bounds measure the 'redundancy' of the frame in $\mathbb{R}^2$, i.e., four vectors in two dimensions have a redundancy of two.

It is known that the linear span of frame elements is dense in $\mathcal{H}$ [e.g., Hernández and Weiss (1996, p.399)]. This means, that any element $f\in\mathcal{H}$ can essentially be written as a linear combination of the frame elements, and that the difference between this linear combination and f has a measure zero. If the frame elements were also linearly independent, they would form a basis for $\mathcal{H}$. It is clear that the frame elements e_j are not a basis, since adding the zero vector to $\{e_j\}_{j\in J}$ does not alter the inequalities in (B1). Of course, adding any vector to a basis, would destroy the linear independence of the basis, meaning it no longer would be a basis. When both frame bounds equal one ($A=B=1$), the frame is called a **normalized** tight frame. Each orthonormal basis is obviously a normalized tight frame, but the converse is not generally true, since the frame elements need not be linearly independent.

Even though the frame elements do not need to be normal, it follows that they must satisfy $\|e_j\| \leq \sqrt{B}$, $\forall j\in J$. To see this, let $f=e_k$ for some $k\in J$, and use frame condition (B1) to see that $\|e_k\|^4 = |(e_k,e_k)|^2 \leq \sum_{j\in J}|(e_k,e_j)|^2 \leq B\|e_k\|^2$. Therefore we have $\|e_k\| \leq \sqrt{B}$, $\forall k\in J$. If the frame is a normalized tight frame (i.e., $A=B=1$), we must have $\|e_k\|\leq 1$. Hence, for a normalized tight frame, the linear independence of a basis is traded for the condition $\|e_k\|\leq 1$, $\forall k\in J$.

If a normalized tight frame has $\|e_k\|=1$, $\forall k\in J$, it follows that $\{e_j\}_{j\in J}$ is an orthonormal basis for $\mathcal{H}$. To see this, observe that for fixed $k\in J$, $1 = \|e_k\|^4 = |(e_k,e_k)|^2 \leq \sum_{j\in J}|(e_k,e_j)|^2 \leq 1$. Therefore, we have $\sum_{j\in J}|(e_k,e_j)|^2 = |(e_k,e_k)|^2 + \sum_{j\neq k,j\in J}|(e_k,e_j)|^2 = \|e_k\|^2 + \sum_{j\neq k,j\in J}|(e_k,e_j)|^2 = 1$, and thus $\sum_{j\neq k,j\in J}|(e_k,e_j)|^2 = 0$. This implies $(e_k,e_j)=0$, $\forall k\in J$ and $k\neq j$. Since k is arbitrary, and since $\|e_k\|=1$, it follows that $\{e_j\}_{j\in J}$ is an orthonormal basis for $\mathcal{H}$.

It is known [e.g., Hernández and Weiss (1996, pp.334-336)] that for a Hilbert space $\mathcal{H}$ and a family of elements $\{e_j\}_{j\in J}$ in $\mathcal{H}$, the condition

$$\|f\|^2_{\mathcal{H}} = \sum_{j\in J} |(f, e_j)|^2 \quad \forall f \in \mathcal{H}, \tag{B2}$$

is necessary and sufficient for

$$f = \sum_{j\in J} (f, e_j)\, e_j \quad , \tag{B3}$$

to hold[‡]; in other words, statements (B2) and (B3) are equivalent. This tells us that for a tight frame with frame bound A, we have reconstruction formula (B3), for if we have $\sum_{j\in J} |(f, e_j)|^2 = A\,\|f\|^2_{\mathcal{H}}$, simply defining $e'_j = e_j/\sqrt{A}$, gives $\sum_{j\in J} \left|(f, e'_j)\right|^2 = \|f\|^2_{\mathcal{H}}$. From the equivalence of statements (B2) and (B3), we then have $f = \sum_{j\in J} \left(f, e'_j\right) e'_j = \dfrac{1}{A}\sum_{j\in J} (f, e_j)\, e_j$; i.e., for a tight frame we have reconstruction formula (B3). For a normalized tight frame ($A = 1$), we simply have $f = \sum_{j\in J} (f, e_j)\, e_j$, and thus also the reconstruction formula (B3). Note that this reconstruction formula is identical to the reconstruction formula for an orthonormal basis, but that here the frame elements are not orthogonal; i.e., you can have reconstruction formula (B3) with linearly dependent elements of $\mathcal{H}$, provided (B2) holds.

Even though we showed that the reconstruction formula (B3) holds for (normalized) tight frames, it should be mentioned that a similar reconstruction formula can be found if the frame is not tight. We refer the reader to (Mallat, 1998, chapter 5), (Hernández & Weiss, 1996, Chapter 8), or (Strang & Nguyen, 1997, Section 2.5) for treatments of non-tight frames.

[‡] Here the equality means that the sum on the right-hand side of equation (B3) converges to an element $f \in \mathcal{H}$.

Time reversed imaging for perturbed media

Kurang Mehta, Roel Snieder and Ken Larner
Center for Wave Phenomena, Department of Geophysics, Colorado School of Mines, Golden, CO 80401-1887

ABSTRACT

Time reversed imaging is a technique in which we propagate a pulse through a medium, record the signal and then back-propagate the time-reversed signal through the same medium to refocus the energy at the original source location. The refocusing is independent of the medium, provided that the medium remains the same during back-propagation. When the velocity for back-propagation is different from that for the forward propagation, the waves refocus at a different location. Based on the shift in the location of the refocused pulse, we can estimate the velocity perturbation. For a single source and single receiver, the shift is proportional to the distance between the source and the receiver and the velocity perturbation. When we consider a larger aperture, however, the shift in the refocused energy depends on a geometric factor related to the receiver array as well. For a given source-receiver distance and velocity perturbation, the shift in the location of the refocused pulse increases with increasing aperture angle. If we look at the problem using ray theory, the increase in the aperture angle should result in decrease in the shift of the refocused pulse; this is where ray theory tends to misguide us. The explanation for the increase in the shift of the refocused pulse location with increased aperture angle is simple when we look at the problem from a wave-front point of view. For an unperturbed medium, presence of a random heterogeneity in the model enhances the quality of focusing.

Key words: Effective aperture, Wave propagation in random medium, Focusing, Migration.

1 TIME REVERSED IMAGING

Time reversed imaging is a technique in which we propagate a pulse through a medium, record the signal, and then back-propagate the time-reversed signal through the same medium to refocus the energy at the original source location. The refocusing takes place in time and space and occurs in homogeneous as well as heterogeneous media. The refocused pulse in a medium is independent of the characteristics of the medium, provided that we use the same medium for the forward and for the back-propagation (Haider et al., 2004). A striking observation is that for a heterogeneous medium, inhomogeneities in the medium enhance the degree of refocusing (Fink et al., 2001). Parvulescu (1995) applied the technique called *matched-signal processing*, based on the same principle, to ocean acoustics.

Time reversed imaging has found applications in several fields of science and engineering, for instance, in medical imaging. It can be used for non-invasive destruction of kidney stones, the detection of defects in metals, and mine detection in the ocean (Fink, 1997). Conventional methods for detection and destruction of the kidney stones use x-rays and ultrasound, respectively. The time reversed imaging technique can be used as a non-invasive destruction method to refocus energy on the kidney stone by using a group of time-reversal mirrors. The kidney stone receives a signal sent by a source and scatters it in all directions. The mirror array picks up the scattered signal, amplifies it, and sends the signal back to refocus the energy at the source of the scattered waves, i.e., the kidney stone. Other medical application of time reversed imaging include acoustically induced hyperthermia for tumor treatment (Porter et al., 1999). Apart from medical applications, time reversed imaging is also used for secure communication (Parvulescu, 1995 ; Edelmann et al., 2001 ; Song et al., 2002 ; Kim et al., 2001).

The back-propagation of a signal is mathematically the same as the process of migration in geophysics (Borcea et al., 2003). In time reversed imaging, the signal recorded at the receiver array is back-propagated through the same medium to refocus energy at the original source location. In migration, in contrast, the reflected waves are back-propagated numerically using an estimate of the velocity of the subsurface. Migrating with a wrong velocity model images the waves at wrong locations. This is exactly what would happen if we would not use the same velocity model during back-propagation in time reversed imaging. In migration, for such cases, a process called *migration velocity analysis* (MVA) (Zhu et al., 1998) is carried out to aid in estimating velocity, aimed at improved imaging.

In time reversed imaging, when we use the same medium for both forward and backward propagation, we get the refocusing of energy at the location of the original source. However, just as in migration, when we back-propagate using a velocity different from the forward propagation velocity, the waves refocus at other locations. The difference in the forward and backward velocities can be estimated from the shift of the refocused pulse compared to the original source location and, hence, can be used for applications including velocity analysis and time-lapse monitoring of velocity changes.

Coda wave interferometry is another technique used for monitoring time-lapse changes (Snieder, 2004). In coda wave interferometry, we use a single source and a receiver to study the velocity changes. The changes are monitored by the correlation of the coda waves recorded in the unperturbed and perturbed medium, respectively. This technique is based on the high sensitivity of multiply scattered waves to small changes in a medium and can be used for monitoring changes in volcanic interiors (Snieder et al., 2004). For a single receiver, time reversed imaging at the source location is the same as convolution with the time-reversed signal, which is the same as correlation with the originally recorded signal. The shift in the location of the refocused pulse for a perturbed medium is related to the deviation of the correlation peak from the origin, which gives the measure of the velocity perturbation. Hence for a single source and receiver, time reversed imaging is identical to coda wave interferometry. If, instead, we have an array of receivers forming an aperture, the shift in the location of the refocused pulse depends on the aperture angle along with the distance between source and receiver and the velocity perturbation. The next section derives the shift in the location of the refocused pulse, followed by a simulation test to validate the expression obtained. A physical interpretation explains why rays misguide us in understanding how this shift varies with aperture angle.

2 EXPRESSION FOR THE LOCATION OF THE REFOCUSED PULSE

We start with a simple model to study the effect of a velocity perturbation on the location of the refocused pulse. The model is acoustic, two-dimensional, and homogeneous. We allow a source pulse to propagate through the homogeneous medium using the 2-D wave equation and record the field at a distance R with an array of receivers. This wave-field recorded at the receivers is then time-reversed and back-propagated through the same medium to refocus the energy at the source location.

Let the source be a symmetric pulse such as a Ricker wavelet $S(t)$, given by

$$S(t) = \frac{\partial^2}{\partial t^2}\left[\exp\left(-\alpha^2 t^2/2\right)\right]. \tag{1}$$

We propagate this pulse over a distance R and record the wave-field on a circular array of receivers. The receivers are placed along a circle with a source at the center and radius R that extends up to a fixed aperture angle $\pm\Phi$ as shown in Fig. 1. The wave-field in the far field can be represented using the 2-D asymptotic behavior of the Hankel function (Snieder, 2nd. ed. ; Arfken et al., 4th. ed.):

$$u(R) \quad = \quad \frac{\exp[i(kR - \pi/4)]}{\sqrt{8\pi k R}} S(\omega), \tag{2}$$

where k is the wavenumber. When this wave-field is reversed in time, it acts as our new source signal.

Reversing in time in the time domain is equivalent to complex conjugation in the frequency domain. If $S(t)$ is the wave-field in time domain, then it can be represented in the frequency domain using the Fourier transform,

$$\begin{aligned} S(\omega) &= \int_{-\infty}^{\infty} S(t)e^{i\omega t}dt \\ \Leftrightarrow S(t) &= \left(\frac{1}{2\pi}\right)\int_{-\infty}^{\infty} S(\omega)e^{-i\omega t}dw. \end{aligned}$$

Time reversing the wave-field is equivalent to changing t to $-t$. Hence, the time-reversed wave-field is

$$\begin{aligned} S^{TR}(t) \equiv S(-t) &= \left(\frac{1}{2\pi}\right)\int_{-\infty}^{\infty} S(\omega)e^{+i\omega t}dw \\ &= \left(\frac{1}{2\pi}\right)\int_{-\infty}^{\infty} S(-\omega)e^{-i\omega t}dw. \end{aligned}$$

For a real signal, $S(-\omega)$ equals the complex conjugate $S^*(\omega)$,

$$S^{TR}(t) \quad = \quad \left(\frac{1}{2\pi}\right)\int_{-\infty}^{\infty} S^*(\omega)e^{-i\omega t}dw.$$

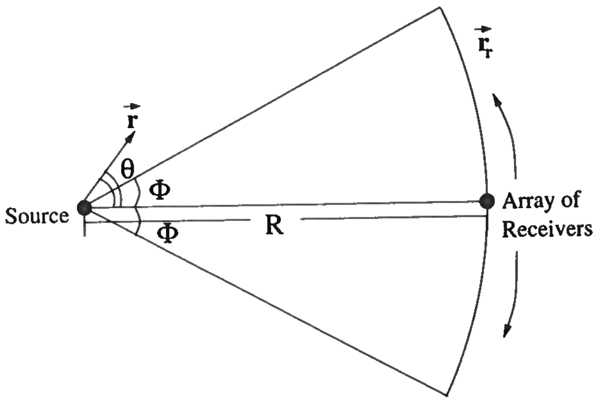

Figure 1. Model showing the source and an array of receivers placed at a distance R for a limited aperture angle Φ.

This shows that the time-reversed signal in the time domain is equivalent to complex conjugation in the frequency domain. Hence, the wave-field recorded by the array of receivers shown in Fig. 1, when reversed in time, is equivalent to complex conjugation of Eq. (2):

$$u^*(R) \quad = \quad \frac{\exp[-i(kR-\pi/4)]}{\sqrt{8\pi kR}}S^*(\omega). \tag{3}$$

If we back-propagate this wave-field with the same velocity as the forward propagating velocity, we refocus the waves at the original source location. When we back-propagate with a different velocity, the energy will refocus at a location other than the original source location. Let us see what information this shift in the location of the refocused pulse gives us about the velocity perturbation. The back-propagated wave-field radiated by each of the receivers is obtained by convolving this time-reversed signal and the Green's function. To compute the total back-propagated wave-field, we need to sum over all receivers that have recorded the forward propagating wave. For the receivers that are densely sampled over the receiver array, we approximate the summation over all the receivers by integration over the aperture angle Φ in order to simplify further calculations. Hence, in the frequency domain, the back-propagated wave-field at location $\mathbf{r}$ corresponds to

$$\begin{aligned} P(\mathbf{r},\omega) &= \int_{-\Phi}^{\Phi} G(\mathbf{r},\mathbf{r_r}(\phi))u^*(R)d\phi \\ &= \frac{S^*(\omega)}{8\pi}\int_{-\Phi}^{\Phi}\left[\frac{\exp\left[i(k'|\mathbf{r}-\mathbf{r_r}|-kR)\right]}{\sqrt{k'|\mathbf{r}-\mathbf{r_r}|}\sqrt{kR}}\right]d\phi, \end{aligned} \tag{4}$$

where ϕ goes from -Φ to Φ, $\mathbf{r_r}$ is the receiver location and k and k' are the wavenumbers associated while forward and back-propagation, respectively.

We are interested in the refocusing point close to the original source location. This requires that $R \gg r$ and hence the term $|\mathbf{r}-\mathbf{r_r}|$ in the expression can be approximated up to second-order accuracy in (r/R) as

$$|\mathbf{r}-\mathbf{r_r}| = R\left[1-\left(\frac{r}{R}\right)\cos(\theta-\phi)+ \frac{1}{2}\left(\frac{r^2}{R^2}\right)\sin^2(\theta-\phi)\right], \tag{5}$$

where θ is the angle defined in Fig. 1. This term is present in both the denominator and the numerator of Eq. (4). In the denominator, we ignore the dependence of $|\mathbf{r}-\mathbf{r_r}|$ on (r/R) and approximate it to be equal to R. This approximation results in an error of the order (r/R), which can be ignored as $R \gg r$. In the numerator, the term $|\mathbf{r}-\mathbf{r_r}|$ is multiplied with the wavenumber k in the argument of an exponent. Ignoring the (r/R) and $(r/R)^2$ terms in the numerator of Eq. (4) would result in errors of the order of (r/λ) and $(r^2/\lambda R)$ respectively, which may be significant. (λ is the wavelength of the pulse.) We, therefore, express the term $|\mathbf{r}-\mathbf{r_r}|$ in the exponent using Eq. (5). With this simplification, the denominator becomes a constant scaling factor except for $|\omega|$. Leaving out this scaling factor, the back-propagated wave-field becomes the following integral over all the receivers.

$$P(\mathbf{r},\omega) = \frac{S^*(\omega)}{|\omega|}\int_{-\Phi}^{\Phi}\exp\left[-i\left\{k'r\cos(\theta-\phi)- \frac{1}{2}\left(\frac{k'r^2}{R}\right)\sin^2(\theta-\phi)-R(k'-k)\right\}\right]d\phi. \tag{6}$$

By replacing the wavenumbers $k=\omega/c$ and $k'=\omega/c'$, we can also rewrite the back-propagated wave-field as

$$P(\mathbf{r},\omega) = \frac{S^*(\omega)}{|\omega|}\int_{-\Phi}^{\Phi}\exp\left[-i\omega\left\{\left(\frac{r}{c'}\right)\cos(\theta-\phi)- \frac{1}{2}\left(\frac{r^2}{Rc'}\right)\sin^2(\theta-\phi)-R\left(\frac{1}{c'}-\frac{1}{c}\right)\right\}\right]d\phi,$$

where c is the velocity for the forward propagation and c' is the velocity for back-propagation. To represent the refocused energy in the time domain we integrate over all frequencies (Snieder, 2004). The wave-field can be represented in the time domain in terms of a function f as

$$P(\mathbf{r},t) = \int_{-\Phi}^{\Phi} f\left[t+\left(\frac{r}{c'}\right)\cos(\theta-\phi)-R\left(\frac{1}{c'}-\frac{1}{c}\right)- \frac{1}{2}\left(\frac{r^2}{Rc'}\right)\sin^2(\theta-\phi)\right]d\phi, \tag{7}$$

where f is defined as

$$f(t) \quad = \quad \int_{-\infty}^{\infty}\frac{S^*(\omega)}{|\omega|}e^{-i\omega t}d\omega.$$

The function f is a function of time and space that can be expressed in terms of x and z as follows:

$$f\left[t+\left(\frac{r}{c'}\right)\cos(\theta-\phi)-\frac{1}{2}\left(\frac{r^2}{Rc'}\right)\sin^2(\theta-\phi)-R\left(\frac{1}{c'}-\frac{1}{c}\right)\right]$$

$$=f\left[t+\left(\frac{z}{c'}\right)\cos\phi+\left(\frac{x}{c'}\right)\sin\phi-\left(\frac{1}{2c'R}\right)(x\cos\phi-z\sin\phi)^2-R\left(\frac{-\delta c}{cc'}\right)\right],$$

where

$$\begin{aligned} z &= r\cos\theta, \\ x &= r\sin\theta, \\ \delta c &\equiv c'-c. \end{aligned}$$

This function f can be approximated using a Taylor's series expansion up to second order in ξ, where

$$\xi=\left(\frac{z}{c'}\right)\cos\phi+\left(\frac{x}{c'}\right)\sin\phi-\left(\frac{1}{2c'R}\right)(x\cos\phi-z\sin\phi)^2-R\left(\frac{-\delta c}{cc'}\right). \qquad (8)$$

When we insert this representation into Eq. (7) and integrate over ϕ, we obtain an expression for the back-propagated wave-field at an arbitrary location (x, z) close to the source location. We are interested in the location of the refocused pulse which we define as given by the maximum value of this wave-field at time $t = 0$. Since the medium is homogeneous and the acquisition geometry is symmetric with respect to $x = 0$, the peak is located on the X-axis; hence we set $x = 0$ in the wave-field representation. This reduces the resultant wave-field representation to an expression involving terms in z and t only. We are interested in examining the shift in the location of the refocused pulse in the z-direction. This shift can be computed in two steps. The first step involves evaluating the wave-field at time $t = 0$. This wave-field is then solved for its maximum as a function of z. As a result, we get the shift in the location of the refocused pulse,

$$\delta z \cong \frac{-2\left(\frac{\sin\Phi}{\Phi}\right)R\left(\frac{\delta c}{c}\right)}{\left(1+\frac{\sin 2\Phi}{2\Phi}\right)}. \qquad (9)$$

A stepwise derivation of this result is shown in Appendix A.

This expression for the shift in the location of the refocused pulse holds for any source pulse that is symmetric at $t = 0$. When the forward and backward propagating velocities are the same ($\delta c = 0$), the location of the refocused pulse is the same as that of the source pulse ($\delta z = 0$), as supported in Eq. (9). For a small aperture angle, $(\sin\Phi)/\Phi$ and $(\sin 2\Phi)/2\Phi \rightarrow 1$; hence in the limit of $\Phi \rightarrow 0$, the shift of the refocused pulse is a function of just the distance R and the velocity perturbation δc.

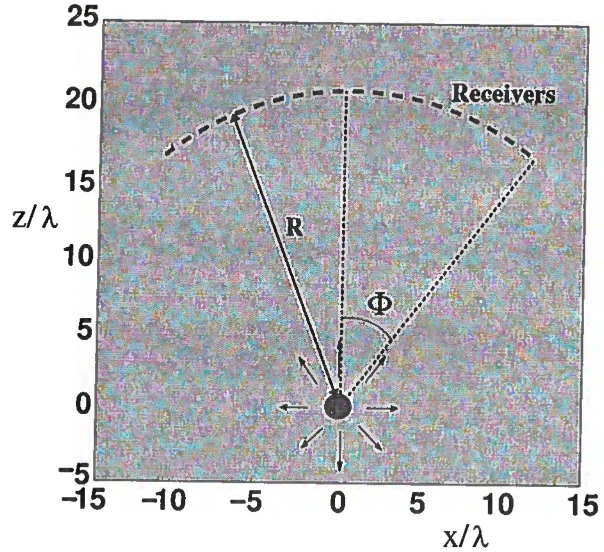

Figure 2. Initial conditions of the simulation test model showing a source pulse at the origin with an array of receivers forming an aperture Φ at a distance R.

$$\lim_{\Phi\rightarrow 0}\delta z = -R\left(\frac{\delta c}{c}\right). \qquad (10)$$

Let us consider this case of small Φ, or equivalently just a single receiver (Fig. 8). Suppose we excite the source pulse and record the signal at a distance R using a single receiver. If this recorded signal is back-propagated with same velocity, then the back-propagated wave-field refocuses at the original source location. If, instead, the back-propagation velocity is different from the forward-propagation velocity ($c' \neq c$, $\delta c \neq 0$), the back-propagated waves travel over a distance,

$$\begin{aligned} R_{back} &= c't \\ &= (c+\delta c)t \\ &= ct+t\delta c \\ &= R-\left(-R\left(\frac{\delta c}{c}\right)\right). \end{aligned} \qquad (11)$$

Hence, the relative shift in the location of the refocused pulse is $-R(\delta c/c)$, which agrees with Eq. (10).

3 ILLUSTRATION USING NUMERICAL SIMULATION

Eq. (9) gives the expression for the location of the refocused pulse. Let us compare the results obtained from this expression with a numerical simulation. The simulation uses a simple finite-difference scheme for the 2-D wave equation with absorbing boundary conditions (Clayton et al., 1997). The geometry of the simulation

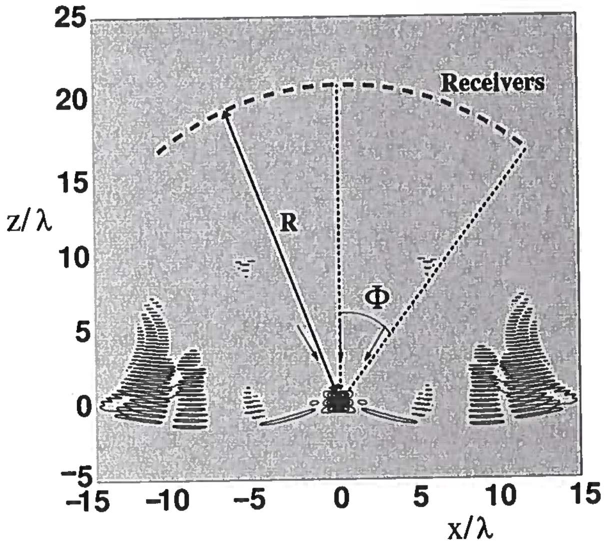

Figure 3. Energy refocusing at the source location (along with some low amplitude noise caused by imperfect absorbing boundary conditions) obtained after the wave-field recorded by the receivers is back-propagated using the correct back-propagating velocity.

is shown in Fig. 2. As the medium is homogeneous, we specify a constant velocity for forward propagation. The source radiation pattern is isotropic, as illustrated by the arrows. The receiver array, located at a distance $R = 20\lambda$ where λ is the wavelength of the pulse, records the wave-field. The aperture angle Φ for this test is 35°. When this wave-field is time-reversed and back-propagated using the same velocity as for forward propagation, the waves refocus at the original source location as shown in Fig. 3. We also see some low amplitude numerical noise near the sides, which is caused by reflection from the imperfectly absorbing boundaries. Even though its location is preserved, the shape of the refocused pulse differs from that of the original pulse in Fig. 2. There are two reasons for this distortion. First, the receiver array has a finite aperture $\Phi = 35°$. During forward propagation, the source propagates in all the possible directions, while in back-propagation the energy propagates only from a certain slice of directions. Second, according to Eq. (6), for a given source spectrum $S(\omega)$, the refocused pulse is proportional to $S^*(\omega)/|\omega|$. This distortion is even clearer in Fig. 4 which is a detailed view of Fig. 3.

Let us see what happens when we back-propagate with a different velocity. Suppose the back-propagating velocity c' is low compared to the velocity c for the forward propagation. When the back-propagating velocity is lower than the forward propagating velocity, the refocusing occurs at a location closer to the receiver array compared to the original source location, which is indicated by a circle as shown in Fig. 5. If we imagine the model space as a human face, the shape of the refocused pulse is similar to a frown; hence, in seismic migration, this shape is commonly referred to as a frown (Zhu et al., 1998). Fig. 6 shows the refocused pulse when the back-propagating velocity is higher than velocity for the forward propagation. The refocusing in this case occurs at a location farther from the receiver array, and the shape of the refocused pulse resembles a smile (Zhu et al., 1998).

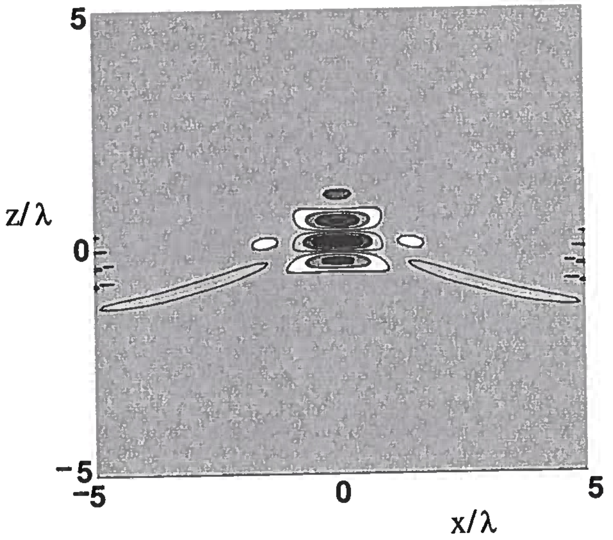

Figure 4. Detailed view of the refocused pulse obtained by back-propagating the wave-field using the correct velocity. This shows the distortion in the shape of the refocused pulse.

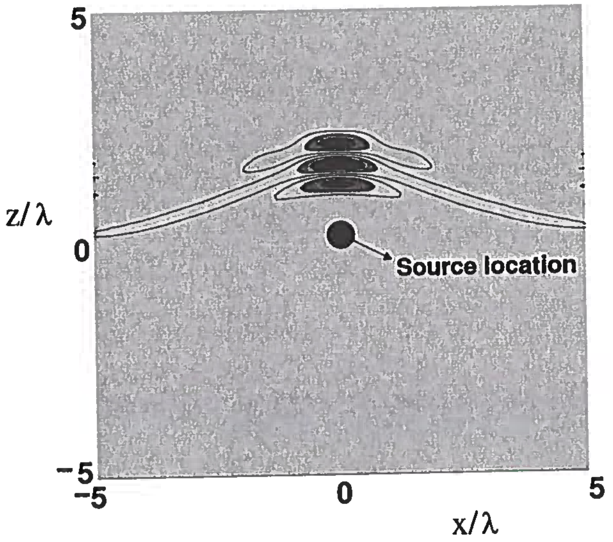

Figure 5. Refocused pulse obtained when the recorded wave-field is back-propagated using a lower velocity than that for forward-propagation.

Table 1 shows the agreement of the shift in the location of the refocused pulse obtained from Eq. (9) and

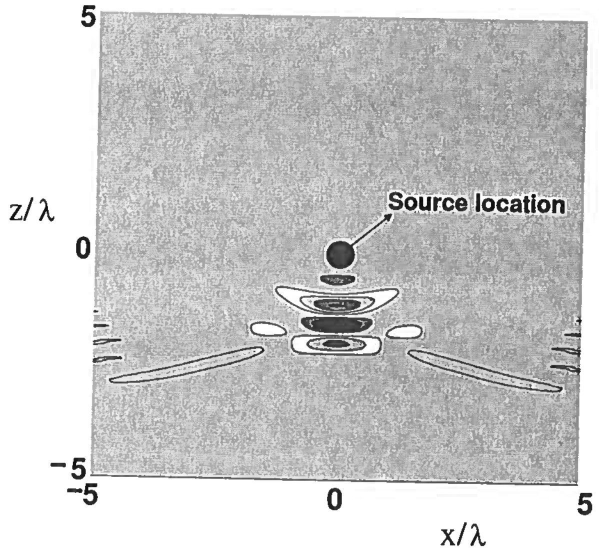

Figure 6. Refocused Pulse obtained when the recorded wave-field is back-propagated using a higher velocity than that for forward-propagation.

$\delta c/c$	$-\delta z/R(theoretical)$	$-\delta z/R(numerical)$
-0.04	-0.042	-0.044
-0.02	-0.021	-0.021
0.00	0	0
0.02	0.021	0.021
0.04	0.042	0.044

Table 1. Comparison of theoretical and numerical results showing relative shift in the location of the refocused pulse for different relative velocity perturbations. The aperture angle is 35°.

the simulation test results for different velocity perturbations at a specific aperture angle (35°). This result holds true for any aperture angle ranging from as small as 5°, which mimics the case of a single receiver, up to 90°. Apart from the distortion in the shape of the refocused pulse, the shift in its location obtained from the simulation test agrees with Eq. (9).

The change in the location of the refocused pulse with a change in the velocity for two extreme cases (5° and 90°) is demonstrated graphically in Fig. 7. The solid line shows the shift in the location of the refocused pulse as given in Eq. (9) whereas the points show the shift obtained from the numerical simulations. The shift obtained from the simulation test for 5° aperture angle is shown in circles, whereas for 90° it is shown as diamonds. The simulation test results agree with Eq. (9) for small velocity perturbations up to an accuracy of

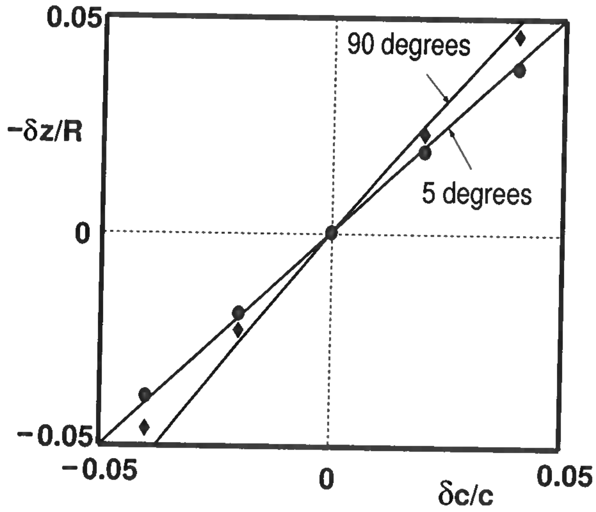

Figure 7. Relative shift in the location of the refocused pulse as a function of relative perturbation in the back-propagating velocity. The relative shift obtained from numerical simulation are denoted by diamonds for 90° aperture angle and by circles for 5°

$$\frac{|0.044 - 0.042|}{|0.042|} = 5\%. \tag{12}$$

For larger aperture angles, as we increase the velocity perturbation, the theoretical expression loses accuracy and hence starts deviating from the simulation test results. This is because as we increase the velocity perturbation, the second order approximation in ξ (Eq. (8)) used in the Taylor's expansion of the function f and the expansion of $|\mathbf{r} - \mathbf{r_r}|$ in Eq. (5) is inaccurate.

4 WHY DO RAYS MISGUIDE US?

The numerical simulation shows that Eq. (9) gives the shift in the location of the refocused pulse with an accuracy of up to 5%. In high-quality *migration velocity analysis*, this is a typical accuracy which gets worse as we deal with more complex media. This result is, however, accurate under certain conditions which include a bound on the relative velocity perturbation of about ±5%. It also depends on the normalized distance (R/λ) between the source and the receivers and, more important, the aperture angle Φ. The angle Φ is a crucial parameter in estimating the shift in the location of the refocused pulse.

Let us start by analyzing the influence of the aperture angle on the refocused pulse in terms of ray theory. Consider first a very small aperture or, equivalently a single receiver. Eq. (10) shows that for a very small aperture angle Φ, the velocity perturbation while back-propagation results in a relative shift of $R(\delta c/c)$ in the location of the refocused pulse. Fig. 8 gives a pictorial representation of this case. The forward propagation is

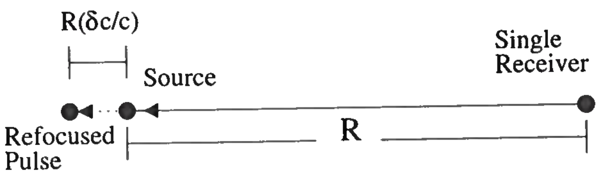

Figure 8. Shift in the location of the refocused pulse when the wave-field is recorded by a single receiver and back-propagated using higher velocity (based on rays)

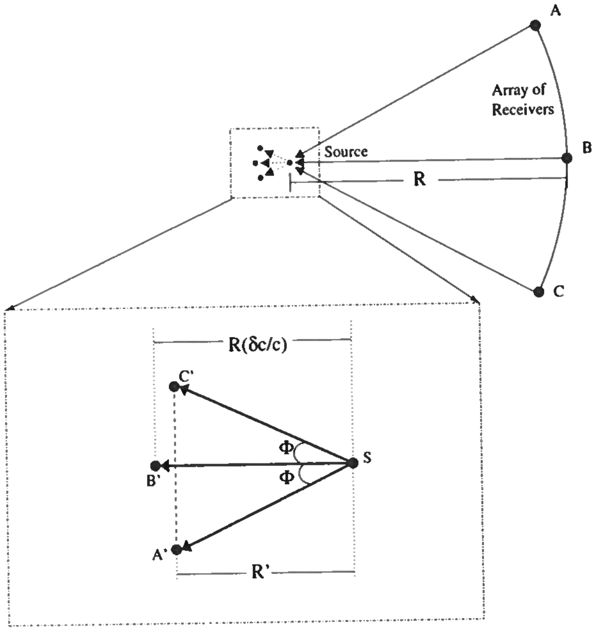

Figure 9. Shift in the location of the refocused pulse when the wave-field is recorded by an array of receivers and back-propagated using higher velocity (based on rays)

carried out with a velocity c. When we back-propagate with velocity $c' > c$, the shift in the location of the refocused pulse depends on the product of distance R and the velocity difference δc as shown in the derivation for Eq. (11).

A more complicated case involves an array of receivers forming a finite aperture angle instead of using a single receiver, as shown in Fig. 9. We have already seen that if we have only receiver B, then the shift in the location of the refocused pulse is $R(\delta c/c)$ indicated by B'. Let us start by examining the contribution of the receivers A and C placed at the two ends of the receiver array. The rays coming from A and C also travel a distance of $R(\delta c/c)$, indicated by A' and C', respectively. The detailed view shows the source S and the shift in the location of the refocused pulse for data from just receivers A, B, and C. This is shown by three rays in thick arrows each having the same length $R(\delta c/c)$. Even though all the three rays have the same length, the component of the rays S-A' and S-C' in the direction of S-B' extends only up to a distance $R' = R(\delta c/c)\cos(\Phi) < R(\delta c/c)$. This suggests that in the presence of only two receivers placed at the two ends of the receiver array, the shift in the location of the refocused pulse is smaller than in that of a single receiver.

With finite aperture angle, however, a number of receivers are placed between A and C along the circular boundary. Rays coming from all the receivers travel a distance of $R(\delta c/c)$, but the contribution to the shift in the direction of S-B' from each of these receivers is $R(\delta c/c)\cos(\phi)$, where ϕ is the angle depending on the receiver location. This distance is always less than $R(\delta c/c)$. Hence, ray theory suggests that as we increase the aperture angle formed by the array of receivers, the shift in the location of the refocused pulse decreases.

Let us see if our results agree with this explanation. The slope of the two straight lines in Fig. 7 represents the ratio $(-\delta z)/(R(\delta c/c))$. If we follow the explanation based on the ray theory, then as we increase the aperture angle, the shift in the location of the refocused pulse reduces; hence, the slope of the line should reduce. Instead, what we see in Fig. 7 is that the slope increases with increasing aperture angles (90°).

Let us take one step back and consider the expression for the position of the refocused pulse, Eq. (9), which can also be rewritten as

$$G(\Phi) \quad \equiv \quad \frac{-\delta z}{R\left(\frac{\delta c}{c}\right)} = \frac{2\left(\frac{\sin\Phi}{\Phi}\right)}{\left(1+\frac{\sin 2\Phi}{2\Phi}\right)}. \tag{13}$$

Fig.10 shows that $G(\Phi)$ is unity for $\Phi = 0$, which is the same as a slope of unity for smaller angles in Fig. 7, and then increases, indicating that as the aperture angle increases, the distance of the refocused pulse from the original pulse increases. This observation is supported in Fig. 7 which also shows an increase in the slope with increase in the aperture angle. This is, however, contradicted by the reasoning based on the ray theory.

Let us now view the picture in terms of wave-front propagation. For the single receiver, as shown in Fig. 11, the explanation remains the same as in ray theory and hence the shift in the location of the refocused pulse is $R(\delta c/c)$. The scenario is different when we consider more receivers forming a larger aperture as shown in Fig. 12. Similar to what we did for the explanation using ray theory, consider just two receivers A and C placed at the two ends. The detailed view in Fig. 12 shows the *wavefronts* coming from receivers A, B and C. The source is indicated by S and the dotted *wavefronts* indicate no velocity perturbation. The solid wavefronts A'-A", B'-B" and C'-C" are the three wavefronts from A, B and C, respectively. All three wavefronts are displaced by a distance of $R(\delta c/c)$ in their respective directions of propagation. It is the interference of the three wave-fronts that contributes to the refocused pulse. The wavefront propagating from the receiver A (A'-A") has displacement in the direction of B'-B" given by $R'' = [R(\delta c/c)/cos(\Phi)] > R(\delta c/c)$. A similar expla-

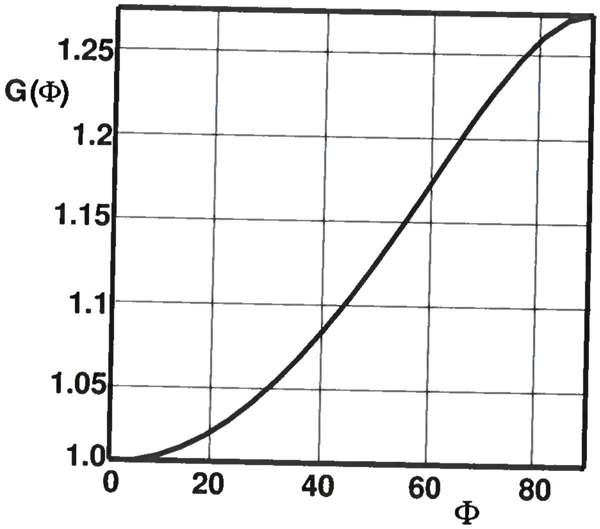

Figure 10. Relative shift in the location of the refocused pulse normalized by relative velocity perturbation as a function of angle Φ

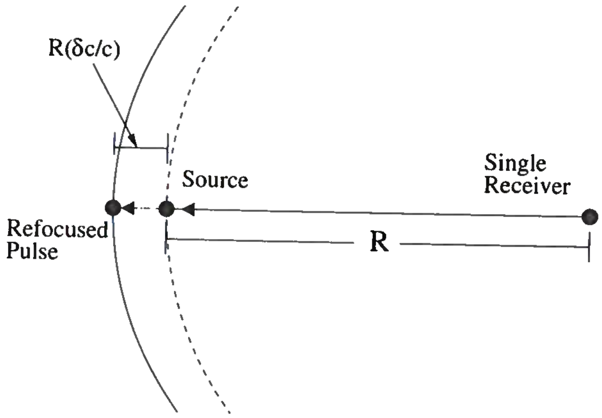

Figure 11. Shift in the location of the refocused pulse when the wave-field is recorded by a single receiver and back-propagated using higher velocity (based on wave fronts)

nation can be given for the wave-front C'-C"; hence we have a constructive interference at a distance R'' from the source, yielding the refocusing. This distance R'' can be referred to as apparent displacement. Hence, for a larger aperture, the refocused pulse is shifted by a distance greater than $R(\delta c/c)$. This explanation is consistent with Eqs. (9) and (10) and supports the results shown in Figs. 7 and 10. This, however, is just an extreme case where we consider only two receivers placed at the two ends. When we consider the whole receiver array, the wave-fronts coming from all the receivers will be displaced by a distance of $R(\delta c/c)$ in their direction of propagation resulting in constructive interference at an effective distance $[R(\delta c/c)/\cos(\Phi)]$ with the angle Φ varying with the aperture of the receiver array. This distance may be less than or equal to R'', but will definitely be greater than $R(\delta c/c)$. Thus, if we consider all the wave-fronts coming from the whole receiver array, the shift in the location of the refocused pulse will increase with increase in the aperture angle. So, the results obtained from the theory and numerical simulation agree with the explanation based on wave-front propagation.

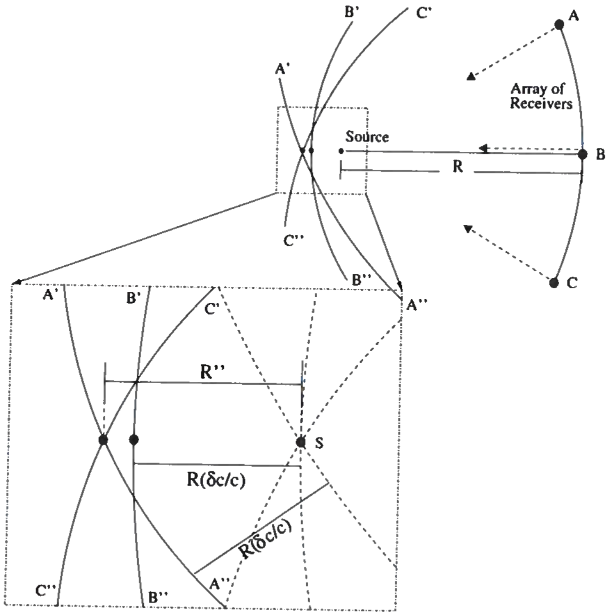

Figure 12. Shift in the location of the refocused pulse when the wave-field is recorded by an array of receivers and back-propagated using higher velocity (based on wave fronts)

5 RELATION TO MIGRATION

Time-reversed imaging is mathematically the same as *migration* in the field of geophysics (Borcea et al., 2003). The numerical simulation shows that if the recorded wave-field is back-propagated (migrated) using the correct velocity, then the waves are imaged at the correct position. This is demonstrated in Fig. 3 which shows the refocused pulse for a homogeneous medium with a considerably large aperture.

The refocusing for a homogeneous medium is governed by the aperture of the receiver array. Changing the shape of the aperture from circular (as in the simulations) to linear (as in migration) does not fundamentally alter the refocusing. Reducing the aperture size, however, leads to smearing of the refocused pulse, even though it focuses at the correct position. This becomes clear by comparing Fig. 13, showing refocusing with a smaller aperture, with Fig. 3. When a strong heterogeneity, characterized by velocity variations, is present in the model, then even with the small aperture size, the quality of refocusing improves as compared to that for a homogeneous medium. Fig. 14 illustrates the improved

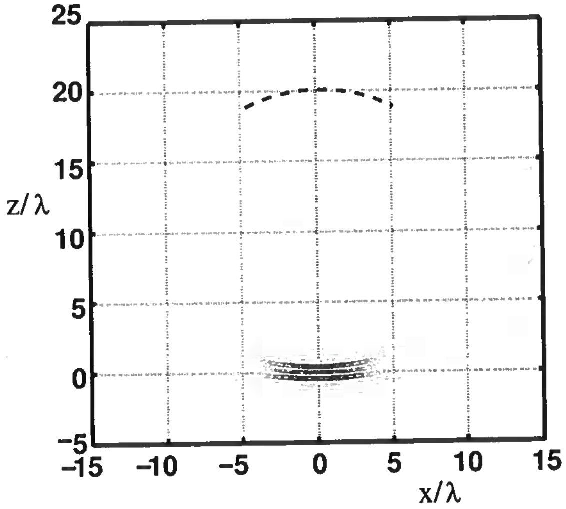

Figure 13. Refocused pulse gets smeared because of reduction in the aperture size formed by the array of receivers.

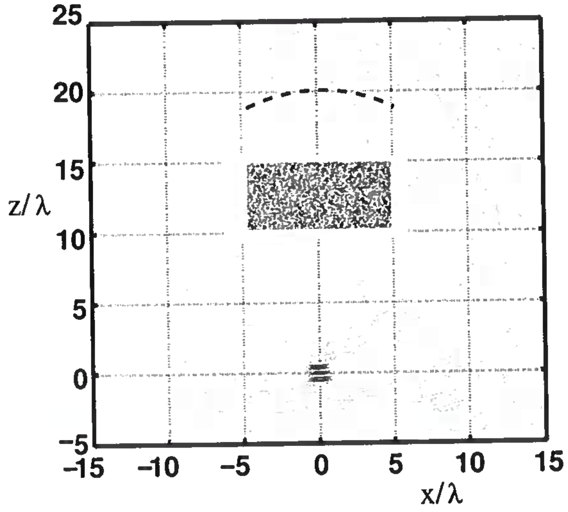

Figure 14. Improved refocusing is obtained due to the presence of a random heterogeneity both while forward- and back-propagation. This improvement is because of the scattering in the random medium.

focusing for a heterogeneous medium. The heterogeneous block, here, is random and characterized by Gaussian correlated velocity variations. The improved focusing is due to the scattering inside the random medium giving rise to the coda waves. For both forward- and back-propagation, scattering allows energy, in the form of coda waves, to arrive at and depart from a larger range of directions which would be absent for propagation in in homogeneous media. Hence, randomness in the medium, in effect enlarges the aperture angle.

After forward propagation, the wave-field recorded by the receivers can be written in the frequency domain as $u = SG$ where S is the source spectrum and G is the Green's function of the medium. The time window for recording the wave-field is long enough to capture both the direct arrival and the coda waves. Decomposing the Green's function into the direct wave and the coda, this can also be written as

$$u = S(G_o + G_{coda}).$$

With ±20% velocity variations in our random medium and a correlation length of the order of a tenth of the wavelength of the source pulse, the amplitude of the direct arrival is around twice that of the coda waves. When the recorded wave-field is time-reversed and back-propagated through the same medium, the resulting wave-field can be written as,

$$\begin{aligned} u^*G &= S^*(G_o^* + G_{coda}^*)(G_o + G_{coda}) \\ &= S^*(G_o^*G_o + G_{coda}^*G_{coda} + G_{coda}^*G_o \\ &\quad + G_o^*G_{coda}), \end{aligned} \tag{14}$$

where u^* is the time-reversed wave-field (asterisk denotes the complex conjugate) and G is the Green's function of the same medium. The third term is the cross-correlation of coda waves during forward-propagation and the direct arrival during back-propagation. Similarly, the fourth term is the cross-correlation of direct arrival during forward-propagation and the coda waves during back-propagation. Since the phase information encoded in G_o and G_{coda} is unrelated, these terms do not contribute to the refocusing and we will refer to it as focusing-noise. Hence, if the entire recorded wave-field is back-propagated, the refocused wave-field is described by the four terms in Eq. (14) out of which only the first two terms represents refocusing.

Fig. 15 shows the refocused pulse when only the coda waves are back-propagated. Even in the absence of the direct arrival, the waves refocus in the presence of the random medium. A comparison of Figs. 14 and 15 show that refocusing is actually better when we back-propagate only the coda waves as opposed to back-propagating the entire wave-field. When only the coda waves are back-propagated, Eq. (14) reduces to $u^*G = S^*(G_{coda}^*G_{coda} + G_{coda}^*G_o)$. Hence, the refocused coda waves do not contain noise represented by the fourth term in Eq. (14) when only the coda waves are back-propagated. This explains the improvement in focusing by muting the direct wave. If only the direct arrival is back-propagated, Eq. (14) becomes $u^*G = S^*(G_o^*G_o + G_o^*G_{coda})$. The first term in the equation indicates that waves refocus at the correct location with some noise described by the second term. However, focusing deteriorates because it is the back-propagation of the coda waves (represented by the second term in Eq. (14)) that improves the focusing when we back-propagate through the same medium.

In migration, the velocity model is characterized by the best velocity estimates without knowledge of the

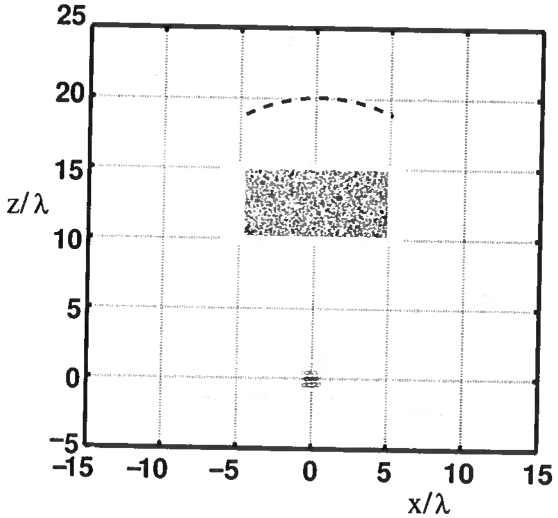

Figure 15. In the presence of heterogeneity both while forward- and back-propagation, back-propagation of only the coda waves also gives better refocusing.

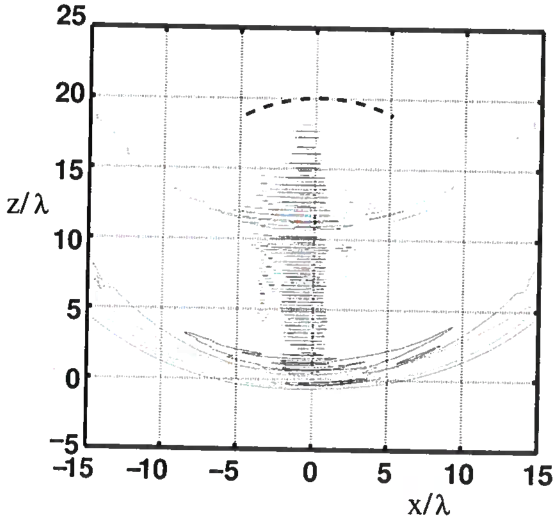

Figure 16. When the direct wave is back-propagated through a homogeneous medium, the waves refocus at the correct location, although they are smeared.

precise velocity variations associated with heterogeneity in the subsurface. Data acquisition from a subsurface is equivalent to forward propagation where the reflectors, which we are trying to image, act as secondary sources. When these data are migrated, the velocities used are only an estimate and thus do not account for the precise velocity variations. Since migration depends on the smooth background velocity only (Tarantola, 1986), back-propagation of the direct arrival in the absence of the random medium most closely resembles migration. For this situation, Eq. (14)) becomes $u^*G = S^*(G_o^*G_o)$ which indicates that the waves refocus at the correct depth although they are smeared due to limited aperture. This is shown in Fig. 16.

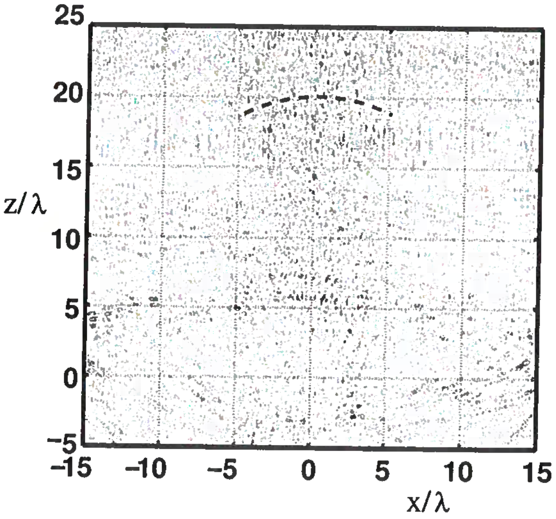

Figure 17. Energy is scattered all around when only the coda waves are back-propagated through a homogeneous medium.

We next check if the use of coda waves in migration improves focusing. When the coda waves are back-propagated through a homogeneous medium, Eq. (14) reduces to $u^*G = S^*(G_{coda}^*G_o)$ which is one of the terms representing focusing-noise. This is shown in Fig. 17 where the energy is scattered all around, with no trace of the original source location. Thus, improved refocusing is possible only when the medium is the same both while forward and back-propagation. In migration, it is unlikely to know the precise details about variations of velocity in the heterogeneity. Hence, use of coda waves in migration does not help improve, and can harm, refocusing. The direct arrival images features acceptably with only a coarse estimate of the velocity model.

The principle of time-reversed imaging is used in *virtual source imaging* (Bakulin et al., 2004) that is to image the deeper earth independent of the near-surface complex overburden. Bakulin and Calvert suggested that the near-surface complex overburden, which is difficult to quantify in terms of velocity, does help improve the quality of the virtual source. The numerical simulations in this paper have shown that the presence of a random heterogeneity improves the refocusing even with a small aperture provided that the model remains the same during forward- and back-propagation. The near-surface complexity plays the same role in virtual source experiment as the random medium in the simulations, and the number of sources on the surface for the virtual source experiment is equivalent to the aperture size in the simulations. This supports the fact that increased overburden complexity does enhance the quality of the virtual source with less sources on the surface.

6 CONCLUSION

The principle idea of time reversed imaging is the refocusing of the energy at the same location as the source when the forward and back-propagating media are the same. Based on the same idea, we have formulated an expression for the shift in the location of the refocused pulse caused by velocity perturbation during back-propagation. The shift mainly depends on the distance between source and receivers, the aperture angle formed by the receiver array and the velocity perturbation. For a single source-receiver pair, the shift is directly proportional to the velocity perturbation and the source-receiver separation only. For more receivers, however, the aperture angle plays an important role in estimating the shift in the location of the refocused pulse. For the same source-receiver distance and velocity perturbation, as we increase the aperture angle, the shift in the location of the refocused pulse increases. An explanation based on the ray theory yields an underestimate of the shift. In contrast, the variation in the shift of the refocused pulse with change in aperture angle is explained well in terms of the constructive interference of wavefronts. For an unperturbed medium, heterogeneity in the model enhances the quality of focusing provided the same velocity model is used during forward- and back-propagation. However, this improvement cannot be used in migration because in that application the details of the heterogeneity is not known. In virtual source imaging, however, the near-surface heterogeneity helps to better focus the waves onto the virtual source position.

7 ACKNOWLEDGMENTS

We thank the support provided by the sponsors of the Consortium Project on Seismic Inverse Methods for Complex Structures at the Center for Wave Phenomena. We also appreciate the comments and discussions with Matt Haney.

REFERENCES

Arfken, G. B., and Weber, H. J., *Mathematical Methods for Physicists* (Academic Press, San Diego, CA, 1995), 4th. ed.

Bakulin, A., and Calvert, R., "Virtual source: new method for imaging and 4D below complex overburden", Expanded abstracts of the 2004 SEG-meeting, 2477–2480 (2004).

Borcea, L., Papanicolaou, G., and Tsogka C., "Theory and Applications of Time Reversal and Interferometric Imaging", Inverse Problems **19**, S139–S164 (2003).

Clayton, R., and Engquist, B., "Absorbing Boundary Conditions for Acoustic and Elastic wave equations", Bulletin of the Seismological Society of America **67**, 1529-1540 (1997).

Edelmann, G. F., Hodgkiss, W. S., Kim S., Kuperman, W. A., Song, C., and Akal, T., "Underwater Acoustic Communication Using Time Reversal", Oceans 2001, Hawaii (2001).

Fink, M., "Time Reversed Acoustics", Physics Today **50**, 34–40 (1997).

Fink, M., and Prada, C., "Acoustic time-reversal mirrors", Inverse Problems **17**, R1–R38 (2001).

Haider, M. A., Mehta, K. J., and Fouque, J. P., "Time-Reversal Simulations for Detection in Randomly Layered Media", Waves in Random Media **14**, 185–198 (2004).

Kim, S., Kuperman, W. A., Hodgkiss, W. S., Song, H. C., Edelmann, G.F., Akal, T., Millane, R. P., and Di Iorio, D., "A Method for Robust Time-Reversal Focusing in a Fluctuating Ocean", Oceans 2001, Hawaii (2001).

Parvulescu, A., "Matched-signal("MESS") processing by the ocean", J. Acoust. Soc. Am. **98**, 943–960 (1995).

Porter, M., Roux, P., Song, H., and Kuperman, W., "Tumor Treatment by Time Reversal Acoustics", IEEE Proc. ICASSP-99 VI-2107, Phoenix, Arizona (1999).

Snieder, R., "Coda Wave Interferometry", McGraw-Hill Yearbook of Science and Technology 2004, 54–56 (2004).

Snieder R., "Extracting the Green's function from the correlation of coda waves: A derivation based on stationary phase", Physical Review **69**, 046610 (2004).

Snieder, R., and Hagerty, M., "Monitoring change in volcanic interiors using coda wave interferometry: Application to Arenal Volcano, Costa Rica", Geophysical Research Letters **31**, L09608 (2004).

Snieder, R. K., *A Guided Tour of Mathematical Methods for the Physical Sciences* (Cambridge University Press, Cambridge, United Kingdom, 2004), 2nd. ed.

Song, H. C., Kuperman, W. A., Hodgkiss, W. S., Akal, T., Kim, S., and Edelmann G. F., "Recent Results from Ocean Acoustic Time Reversal Experiments", 6th European Conference on Underwater Acoustics, Gdanski, Poland (2002).

Tarantola, A.,"A Strategy for Nonlinear Inversion of Seismic Reflection Data", Geophysics **51**, 1893-1903 (1986).

Zhu, J., Lines, L. R., and Gray, S. H., "Smiles and Frowns in migration/velocity analysis", Geophysics **63**, 1200–1209 (1998).

APPENDIX A:

The wave-field in the time domain is given by Eq. (7). When the function f is represented with a second-order Taylor series in (r/R) and integrated over all the receivers, we get the following expression for the back-propagated wave-field.

$$P(\mathbf{r},t) \quad = \quad 2\Phi f(t) + \dot{f}(t)I_1 + \frac{1}{2}\ddot{f}(t)I_2, \tag{A1}$$

where I_1 and I_2 are functions of space. As a result, the wave-field is the sum of three terms. We need to calculate this wave-field at time $t = 0$. Also, we know that because of the symmetry of the receiver positions with respect to $x = 0$, the peak location will occur at $x = 0$. Hence, we can set $x = 0$ in the expression for the wave-field. In the second and third terms of the wave-field, the integrals I_1 and I_2 are given by

$$I_1 = \int_{-\Phi}^{\Phi} \left[\left(\frac{z}{c'}\right) \cos\phi - \left(\frac{z^2}{2c'R}\right) \sin^2\phi + R\left(\frac{\delta c}{cc'}\right) \right] d\phi$$
$$= \left(\frac{2z}{c'}\right) \sin\Phi + 2R\Phi\left(\frac{\delta c}{cc'}\right) - \left(\frac{z^2}{2Rc'}\right)\left[\Phi + \left(\frac{\sin 2\Phi}{2}\right)\right],$$

$$I_2 = \int_{-\Phi}^{\Phi} \left[\left(\frac{z}{c'}\right) \cos\phi - \left(\frac{z^2}{2c'R}\right) \sin^2\phi + R\left(\frac{\delta c}{cc'}\right) \right]^2 d\phi$$
$$= \left(\frac{z^2}{c'^2}\right) \left\{ \Phi + \left(\frac{\sin 2\Phi}{2}\right) - \left(\frac{\delta c}{c}\right)\left[\Phi - \left(\frac{\sin 2\Phi}{2}\right)\right] \right\}$$
$$+4R\left(\frac{\delta c}{cc'}\right)\left(\frac{z}{c'}\right)\sin\Phi - 2\Phi R^2 \left(\frac{\delta c}{cc'}\right)^2.$$

In the integral I_2, we are considering only the terms up to second order in z. When we insert these values of I_1 and I_2 in Eq. (A1) and set $t = 0$, we get the wave-field as a quadratic function of z as follows:

$$P(z,t) = A + Bz + Dz^2, \tag{A2}$$

where

$$A = \Phi\left[2f(0) + 2R\dot{f}(0)\left(\frac{\delta c}{cc'}\right) - R^2\ddot{f}(0)\left(\frac{\delta c}{cc'}\right)^2\right],$$
$$B = \left(\frac{2\sin\Phi}{c'}\right)\left[\dot{f}(0) + \ddot{f}(0)R\left(\frac{\delta c}{cc'}\right)\right],$$
$$D = \dot{f}(0)\left\{\frac{-\Phi}{2Rc'}\left[1 - \left(\frac{\sin 2\Phi}{2\Phi}\right)\right]\right\} + \ddot{f}(0)\left[\left(\frac{\Phi}{2c'^2}\right)K_1\right],$$

and

$$K_1 = 1 + \left[\frac{\sin 2\Phi}{2\Phi}\right] - \left(\frac{\delta c}{c}\right)\left[1 - \frac{\sin 2\Phi}{2\Phi}\right].$$

As the source pulse is symmetric with respect to the origin, its first derivative vanishes at time $t = 0$; hence $\dot{f}(0) = 0$. The maximum value of the wave-field $P(z,t)$ at time $t = 0$ can be found by equating its first z-derivative to zero. When solved for z, this gives the shift in the location of the refocused pulse. Hence, this shift is $\delta z = -B/2D$ where the values of B and D at time $t = 0$ are given by,

$$B = \ddot{f}(0)\left[\frac{2\sin\Phi}{c'}\right] R\left(\frac{\delta c}{cc'}\right),$$
$$D = \ddot{f}(0)\left[\left(\frac{\Phi}{2c'^2}\right)K_1\right].$$

Given the values of B and D, we can compute δz as follows:

$$\delta z = \frac{-2\left(\frac{\sin\Phi}{\Phi}\right)R\left(\frac{\delta c}{c}\right)}{\left(1 + \frac{\sin 2\Phi}{2\Phi}\right) - \left(\frac{\delta c}{c}\right)\left(1 - \frac{\sin 2\Phi}{2\Phi}\right)}.$$

The term $\ddot{f}(0)$ drops in the expression for δz, which indicates that the shift in the location of the refocused pulse is independent of frequency. For small values of velocity perturbation $(\delta c/c)$, we can ignore the second term in the denominator; and hence,

$$\delta z \cong \frac{-2\left(\frac{\sin\Phi}{\Phi}\right)R\left(\frac{\delta c}{c}\right)}{\left(1 + \frac{\sin 2\Phi}{2\Phi}\right)}. \tag{A3}$$

CWP-512

Velocity smoothing before depth migration: Does it help or hurt?

Ken Larner and Carlos Pacheco
Center for Wave Phenomena, Colorado School of Mines, Golden, CO 80401

ABSTRACT

Previous studies of the sensitivity of depth migration to smoothing of the migration-velocity model have treated smoothing of an initially correct model. Aside from the relatively small amount of smoothing that is needed for imaging with Kirchhoff migration and that does no harm to imaging with finite-difference migration, smoothing of the model changes the model from the true one, so those studies have shown the less smoothing the better. Because we never know the subsurface velocity function with perfect accuracy, imaging is always compromised to some extent by error in the migration-velocity model. Given that reality, perhaps some amount of smoothing of the inevitably erroneous velocity model could improve quality of the migrated image.

We have performed a number of tests of imaging with erroneous velocity models for a simple synthetic 2D model of reflectors beneath salt. The salt layer has a chirp-shape boundary so that we could assess imaging quality as a function of lateral wavelength of velocity variation in the overburden. Errors that we introduce into the velocity model include lateral and vertical shifting of the chirp-shape (usually top-of-salt) boundary, and erroneous amplitude of the chirp, including random errors in the chirp shape. Primarily with poststack migration of modeled exploding-reflector, we assess sub-salt image quality for migrations with many different smoothings of erroneous velocity models. We find that, depending on the type and size of error in the shape of the top-of-salt boundary, as well as the lateral wavelength of the chirp, smoothing of the erroneous velocity model before migration can benefit image quality, sometimes substantially. The form of error that can most benefit from smoothing is error in the shape, as opposed to position, of the salt boundary. This observation, based on numerous tests with exploding-reflector data, is supported by a small number of tests with smoothing of the erroneous velocity model in prestack migration.

Key words: velocity smoothing, depth migration

1 INTRODUCTION

No factor is of larger importance to imaging quality in depth migration than accuracy of the velocity model used for the migration. Velocity information, however, is inevitably erroneous to some extent. Finding sufficiently accurate velocity for migration is an especially difficult task in complex regions such as beneath salt in the Gulf of Mexico, an impediment to efficient exploration and development there (Paffenholz, 2001).

Because information about the spatial variation of subsurface velocity can never be known in detail, in practice estimated velocities are routinely smoothed over space prior to using them for migration. Moreover, because Kirchhoff-type migration algorithms obtain their traveltime information from some form of ray tracing, the velocities used must be spatially smoothed to insure stability in the ray computations.

Any smoothing changes the subsurface velocity model and hence the migration result, so too much smoothing will certainly lead to distortion in migrated images. Of importance, then, is to know how much smoothing of the migration velocity field becomes too much.

Various studies, notably those of Versteeg (1993), Gray (2000), and Paffenholz et al. (2001), have aimed at providing guidance on the appropriate amount of spatial smoothing of velocity for depth migration. A common conclusion of those studies, all of which involved smoothing of known velocities in complex two-dimensional (2D) synthetic datasets such as the Marmousi, Sigsbee2, and SEG-EAGE salt models, is that the appropriate amount of smoothing is both model- and depth-dependent. The study of Gray (2000), which focused on Kirchhoff migration, found that, although some smoothing is necessary for that approach, "too little smoothing produced a better image than too much smoothing" because too much smoothing will change the velocity model substantially, perhaps to the extent of removing geologic plausibility.

Because Versteeg (1993) did his migrations with a wavefield-migration approach, which had no dependence on ray tracing, smoothing of the velocity was not essential to overcome a deficiency of the migration method. Paralleling a conclusion of Jannane et el. (1989), Versteeg argued that the velocity model need not include spatial wavelengths smaller than an amount governed by the wavelengths for frequencies in the data, with further dependence on the complexity of the velocity model. His tests showed that smoothing of the known velocity model up to a certain amount (about 200 m for realistic frequencies in the Marmousi data set) was quite acceptable.

In their migration tests with the Sigsbee2 model, Paffenholz et al. (2001) demonstrated the clear superiority of wavefield migration (e.g., finite-difference migration) over Kirchhoff migration when the migration velocity model is known perfectly, but "the advantage of wavefield migration disappears if the (salt) velocity contains errors." They also showed degradation in sub-salt imaging when the migration-velocity model used is erroneous, either because of error in the shape of the salt or because smoothing of the correct model is too large to some extent.

In all of the studies mentioned above, the tests with smoothing for migration involved smoothing of the known, true velocity model. Recall, however, that one of the reasons for smoothing is that we cannot know the true velocity structure in detail – and sometimes we have rather poor information about the velocity structure. It therefore is appropriate to conduct studies in which the smoothing is applied not to the known, correct velocity model but to models that are erroneous. Then, depending on complexity of the velocity model, amount of error in that model, depth of target beneath the erroneous overburden, and frequency content in the data, some degree of smoothing is likely optimal in the sense of yielding a better image of the target than is use of either less or more smoothing.

In the study here, we perform migrations with smoothed versions of erroneous velocity models and make a start at answering the question "does smoothing of the erroneous velocity field help or hurt the quality of the migrated result?"

As in the references mentioned above, our tests make use of synthetic data. Most of our models, however, are much more simple than those in the published studies, with little attempt to mimic realistic subsurface structure. We introduce errors in the shape of the modeled salt and migrate the data when different degrees of spatial smoothing are applied to the erroneous velocity models.

In order to perform enough tests to draw general conclusions here, most of tests entail 2D modeling and migration. Moreover, for reasons discussed below, most involve poststack migrations of data generated under the exploding-reflector assumption.

2 GENERIC MODEL

The simple (we might say simplistic) model, on which we focus most of the tests is exemplified by any of the six models shown in Figure 1. This model, which we call the *generic model*, looks like no salt structure and sub-salt configuration in the real subsurface. It consists of a sub-horizontal, high-velocity 'salt layer', with a chirp-shape for either the top or bottom of salt, beneath a homogeneous layer and above a half-space. That half-space is also homogeneous, except for four sets of embedded reflecting segments, the targets we wish to image. Each set consists of five plane-dipping reflecting segments, with dips ranging from 0 to 40 degrees, in 10-degree increments. One of the upper two sets has reflector dip increasing from left to right, and the other has dip increasing from right to left. This pattern of target reflector dip allows us to assess the relationship between wavelength of lateral velocity variation in the overburden and sub-salt image quality, as well as illumination issues, as they relate to reflector dip. The lower two sets of reflectors have the same form as the upper ones; they are included so that we can observe changes in the quality of imaging with target depth beneath the salt. Use of a chirp shape for the top or bottom of the salt allows systematic analysis of sub-salt image quality as a function of lateral wavelength of salt shape.

Use of such a simple model has its advantages and disadvantages. The model avoids many of the complexities of data from a Marmousi or even Sigsbee2 model, not to mention those in true salt areas. Moreover, use of the chirp shape allows somewhat systematic assessment of modeled sub-salt imaging. The primary disadvantage of the generic model is that it cannot come close to modeling realistic salt shape, let alone the many issues that confound sub-salt imaging.

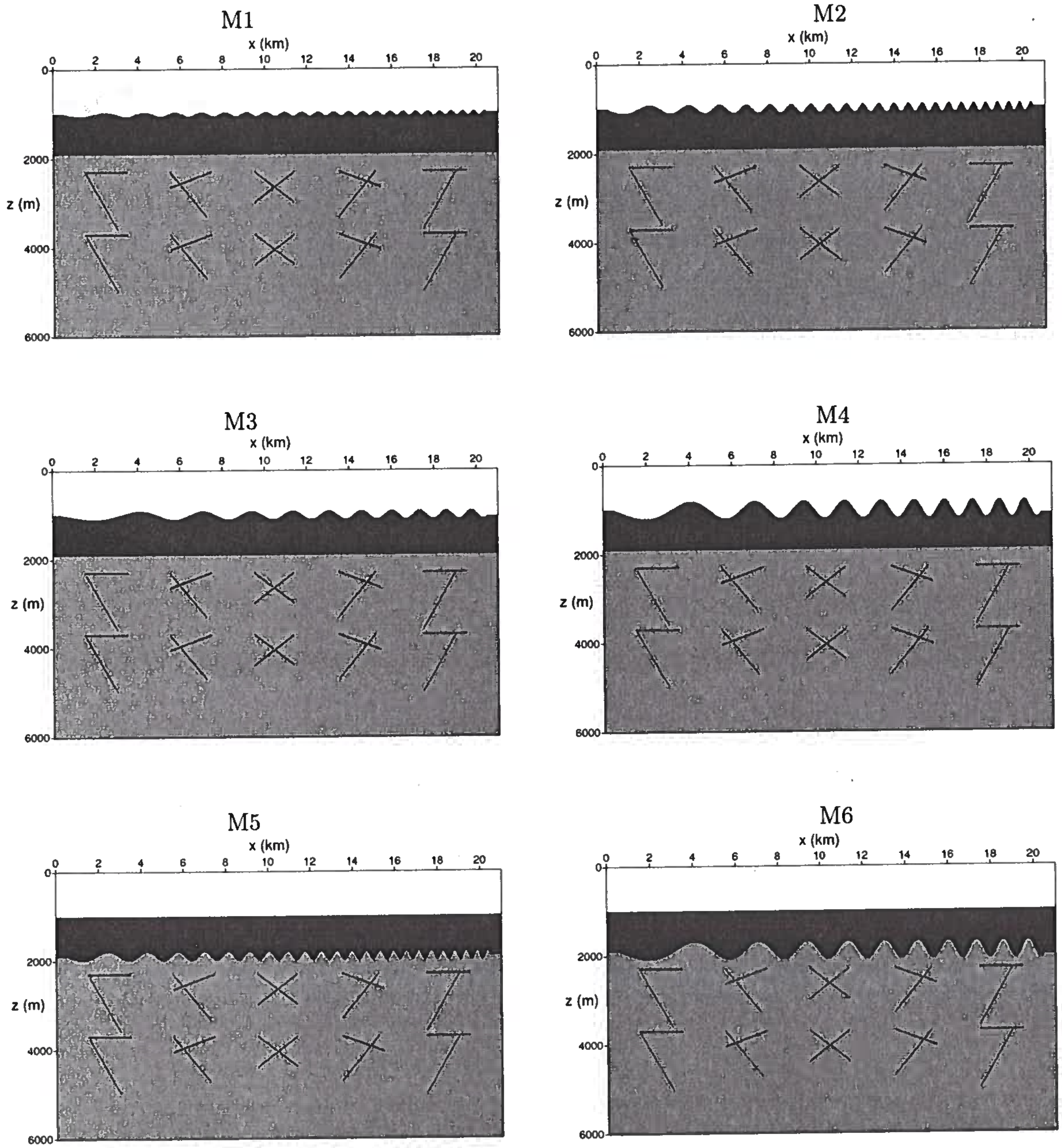

Figure 1. Velocity models M1-M6 used to generate the synthetic data. Lateral position is denoted by x, and depth by z.

Simple as it is, the generic model nevertheless is characterized by enough parameters that comprehensive study of imaging would require a large number of tests of models with many different combinations of values for those parameters. Parameters of the generic model include

- average depth of the top and bottom of the salt
- velocities of the salt and of the layers above and below
- parameters of the chirp-shape top or bottom of salt, specifically
  - amplitude of the chirp
  - range of spatial wavelengths of the chirp
- target depths

Our study can only spottily cover the large combi-

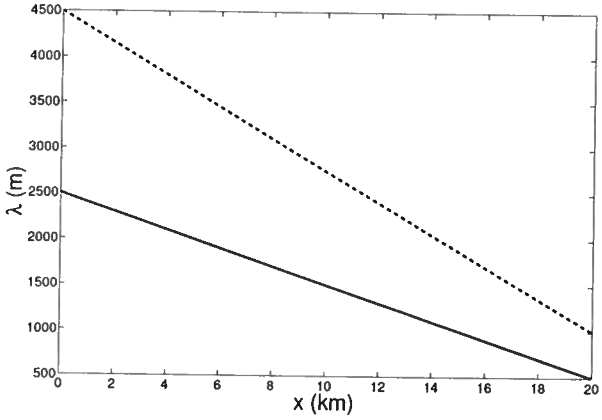

Figure 2. Range of spatial wavelengths for the two chirps used in our study. The solid line shows wavelength λ as a function of lateral position for models M1, M2, and M5; the dashed line shows wavelength for models M3, M4, and M6.

nation of pertinent values for these many parameters. Moreover, none of the six models in Figure 1 exhibits the large structural size of the salt in, for example, the Sigsbee2 model. So, the study is a mere start.

When we consider the different forms of error in the velocity models and differing amounts of smoothing of those erroneous models, the number of tests to perform could further multiply greatly. Errors could arise in all of the parameters (except for the sub-salt reflector description) listed above. For example, the chirp-shape top of salt used for the migration-velocity model could be shifted laterally or vertically from the true position, or have erroneous amplitude.

Our tests with the generic model all involve the six models in Figure 1. All six have velocities of 2000 m/s, 4500 m/s, and 3500 m/s for the top layer, salt layer, and half-space, respectively. For all six models, the average depth of the top and bottom of the salt is 1000 m and 1900 m, respectively. Models M1, M2, and M5 have the same range of spatial wavelength for the chirp, and Models M3, M4, and M6 have a higher range of spatial wavelength. The variation of spatial wavelength with horizontal location is shown in Figure 2. Other differences among the six models are in the amplitude of the chirp shape. Table 1 summarizes the parameter values for the chirp in each model.

Another important parameter for the tests would be the range of frequencies contained in the seismic wavelet used in the wavefield modeling. All of our tests involve just one choice of input wavelet – a Ricker wavelet, with dominant frequency of 15 Hz.

model	λ_{max} (m)	λ_{min} (m)	h (m)	top	bottom
M1	2500	500	50	X	
M2	2500	500	100	X	
M3	4500	1000	100	X	
M4	4500	1000	200	X	
M5	2500	500	50		X
M6	2500	500	100		X

Table 1. Chirp parameters for the generic velocity model used in the study. The parameter h is the ampliitude of the chirp, i.e., the peak departure of salt-boundary depth from its average value.

3 ZERO-OFFSET VERSUS EXPLODING-REFLECTOR DATA

Ultimately one might prefer that a study of the sensitivity of sub-salt imaging to errors in the velocity model be done with 3D prestack depth migration applied to modeled 3D data. The cost of such a study is clearly prohibitive, certainly in this decade. Among the many other complexities of such a study would be the issue of how to define a useful 3D extension of the chirp model.

Our study therefore is strictly limited to 2D. Even 2D prestack depth migration imposes too large a computational cost for other than a small number of token comparison tests with the generic model. In order to do enough comparisons, we limited the study primarily to imaging with poststack migration. The simplification doesn't stop here, however. We can envision three different forms of input to poststack migration: (1) modeled data from many source-to-receiver offsets that have been stacked, (2) zero-offset (ZO) data extracted from normal-moveout-corrected and unstacked modeled data, and (3) exploding-reflector (ER) modeled data. We did tests with all three forms, but the largest number with exploding-reflector data.

The choice of exploding-reflector data may seem puzzling. One reason for this choice is that generation of ER data is least computationally costly. We use a finite-difference code, second-order in time, fourth-order in space, for the modeling; the cost of modeling zero-offset data would be essentially the same as that of modeling a full prestack data set. But there is another reason for choosing exploding-reflector data over extracted zero-offset data.

Seismic data that result from ER modeling are largely equivalent to, but differ in important respects from, either ZO or common-midpoint (CMP) stacked data, particularly in the presence of strong lateral velocity variation (Kjartasson & Rocca, 1979) and (Spetzler & Snieder, 2001). Moreover, the pattern of multiples and the relative amplitudes of the primaries and multiples differ among the three forms of data.

So, why do we consider a study using ER data to be useful? Because poststack migration is based on the exploding-reflector assumption, such migration of zero-offset data would be erroneous even if the migration velocity were correct. In contrast, because poststack (i.e., zero-offset) migration and exploding-reflector modeling of primaries are essentially exact inverses of one another, we can count on accurate migration of ER primaries when we use the correct migration velocities. Therefore, sensitivity of imaging to errors in velocity, including smoothing of erroneous velocity, is best isolated when we apply poststack migration to ER data.

That ER and ZO data differ from one another, as do the results of poststack migration applied to these two forms of data, is exhibited in Figures 3 and 4. The differences between the ER and ZO sections for models M1, M2, and M4, in Figure 3, are striking. Particularly for models with larger chirp amplitude and in regions of the model with smaller chirp wavelength, sub-salt reflections show more numerous triplications characteristic of caustics and multi-pathing in the overburden. The exploding-reflector sections exhibit less loss of amplitude with time and more complete expression of the diffractions than do the zero-offset sections. Since migration aims to collapse diffractions, the distorted and incomplete diffractions in the ZO data will be poorly collapsed in poststack-migrated results. The stronger amplitudes at late time in the ER data result from the weaker geometric spreading from sources that are, in effect, placed on the exploding reflectors than the spreading from the surface line sources for the ZO data. Finally, as expected, the timing and amplitudes of multiples in the exploding-reflector sections differ from those in the counterpart zero-offset sections. The multiples in these data are internal ones. Surface multiples are largely absent because absorbing boundary conditions (Clayton & Engquist, 1977) were used for all boundaries.

The results of poststack (i.e., zero-offset) depth migration of the exploding-reflector and zero-offset sections using the true velocity for the migration are shown in Figure 4, again for models M1, M2, and M4. We used an f-x domain, finite-difference depth-migration algorithm (Claerbout, 1985) for both migrations. For all models, depth migration of the exploding-reflector data yields high-quality imaging of the primaries, with artifacts related to migration of the multiples. In contrast, depth migration of the zero-offset sections results in degraded imaging of the sub-salt reflectors, especially in regions of the model where the chirp has smaller wavelength. Since these migrations were performed using the correct velocity model, the compromised migrated ZO data offer a poor starting point for study of sub-salt imaging when smoothed, erroneous velocity models are used for the migration.

Using equation (12) of Spetzler and Snieder (2004), we calculated approximate focal depths (depths at which caustics and triplications start to appear) for the six velocity models used in the study. Although only roughly approximate because that equation assumes 1D lateral slowness variations and point sources, these computed focal depths give a measure of the relative complexity of the various models and of wavefields in them. For our generic models, this complexity, which depends on the depth and lateral variation of the velocity anomaly, is controlled mainly by the geometry of the chirp. Figure 5 shows the focal depths below the surface as a function of lateral position x for the six chirp models. Model M2, for example, has caustics that appear at the shallowest depth, whereas caustics arise deeper for the models with milder chirp shape, and for chirp shape at the base rather than the top of the salt. The relatively poor image, in Figure 4, of the migrated zero-offset data for Model 2, as compared with the migrated images for models M1 and M4, suggests dependence of image quality on model complexity. (Again, the imaging problem arises because zero-offset migration is based on the exploding-reflector idea.) Also, as seen in Figure 5, the levels of complexity of models M1 and M4 are equivalent. Consistent with this observation, the image quality of the depth-migrated zero-offset sections for these models is comparable.

When errors are present in the velocity model, t he degradation of migrated ER data will differ from that in (1) poststack-migrated ZO data, (2) prestack-migrated ZO data, and (3) prestack-migrated full-offset data. Even with the correct velocity model the quality of imaging can be compromised in each of these treatments of data. We've already seen in Figure 4 that, because poststack migration is founded on the ER assumption, poststack-migrated ZO data is erroneous even when the correct velocity model is used for migration. Prestack-migrated ZO data do not suffer from that shortcoming, but can exhibit image distortion and artifacts arising from insufficient pre-migration muting of wide-angle reflections and refractions prior to the migration, limited aperture for the (shot-record) migration, and variations in wavefield illumination beneath the salt. Prestack-migrated, full-offset data can also be distorted because of variable illumination, insufficient muting, and limited migration aperture. These data, however, have the advantage that the worst of these problems are mitigated to some extent by destructive interference of offset-dependent distortions and artifacts after stacking the migrated data for all offsets.

4 LENGTH SCALES FOR VELOCITY SMOOTHING

For finite-difference migration, if we knew the velocity model perfectly we would have no need to smooth the velocities. Smoothing could only alter the model from

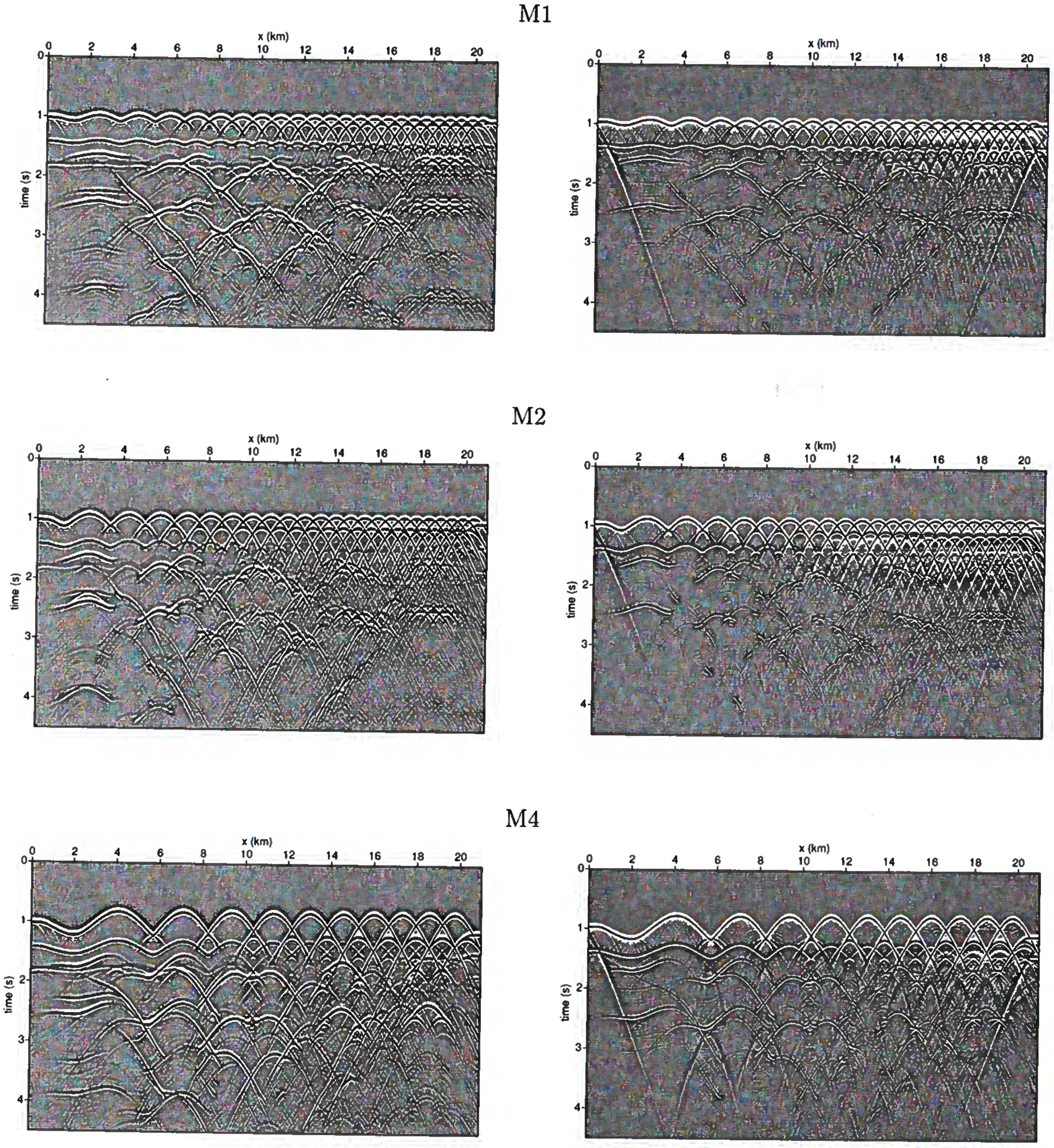

Figure 3. Exploding-reflector sections (left) and zero-offset sections (right) for models M1, M2, and M4.

the true one, resulting in erroneous migration — the more smoothing the poorer the image. Versteeg (1993), however, showed that there is little harm done with an amount of spatial smoothing that is small in relation to the wavelengths in the signal and fineness of detail in the velocity model. Even for Kirchhoff migration, Gray (2000) pointed out that smoothing too little is better than smoothing too much.

Before addressing smoothing of erroneous velocity models, let us see how much smoothing of our correct generic models is acceptable for the depth migration. Given the range of complexities suggested for the models in Figure 5, we expect that the appropriate amount of smoothing will differ from one model to another.

We smooth the velocity functions using a two-dimensional Gaussian-shaped operator similar to the

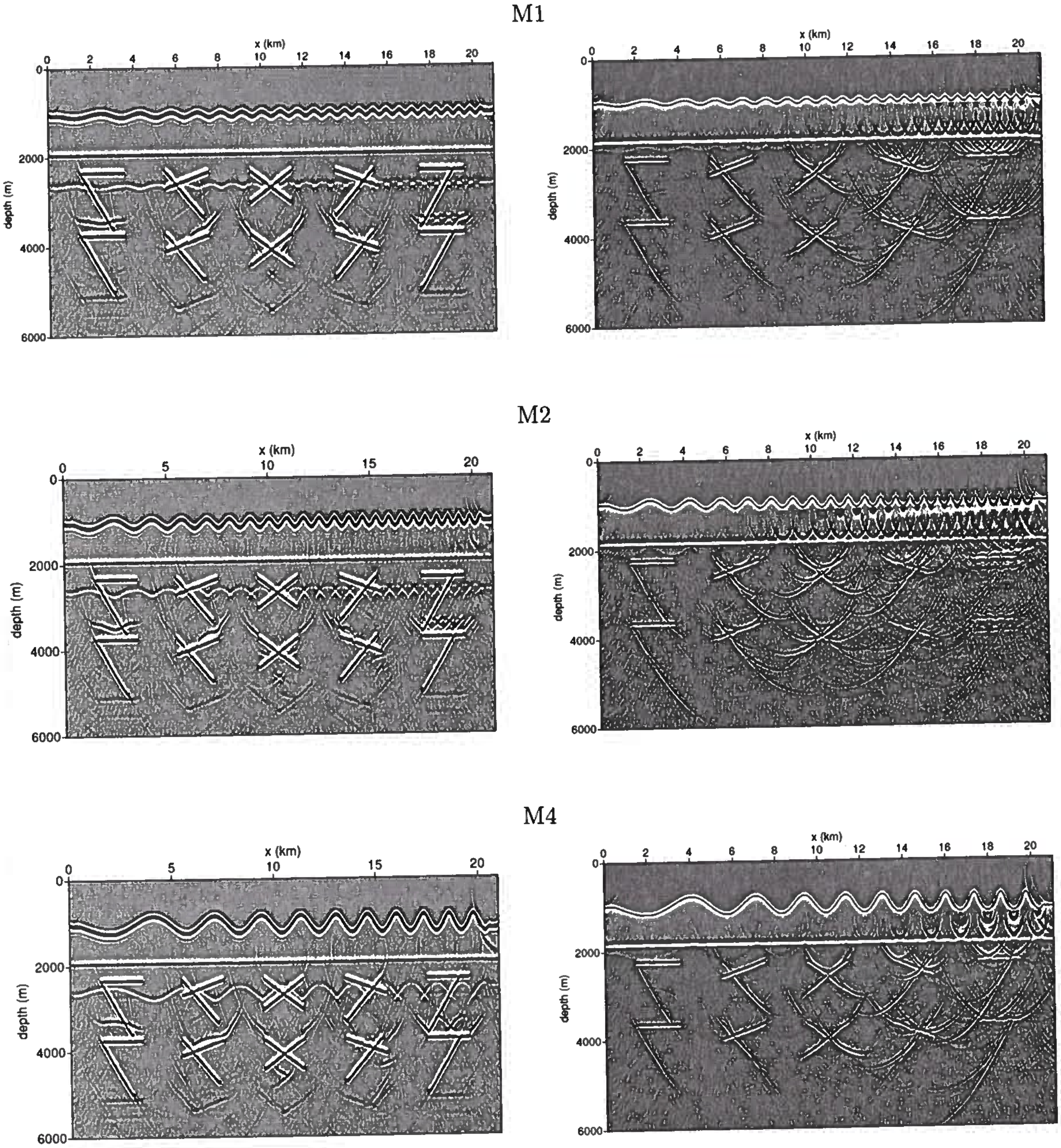

Figure 4. Finite-difference, zero-offset depth migrations of exploding-reflector data (left) and zero-offset data for models M1, M2, and M4 using the correct velocity model.

one described in Vertsteeg (1993). We first convert the velocities to slownesses and then convolve the slownesses with a two-dimensional Gaussian filter of the form $\exp[-(x^2 + z^2)/(a/2)^2]$. With this definition, a is the diameter at which the amplitude of the Gaussian operator has decreased to e^{-1} of its peak value.

Although we did tests with all six models shown in Figure 1, here we focus attention primarily on models M2 and M4, the ones with the largest amplitude chirp shape for the top of salt. The conclusions drawn from tests for these two models have general counterparts from those for the other models. Figures 6 and 7 show depth-migrated exploding-reflector sections for models M2 and M4 after applying different amounts of smooth-

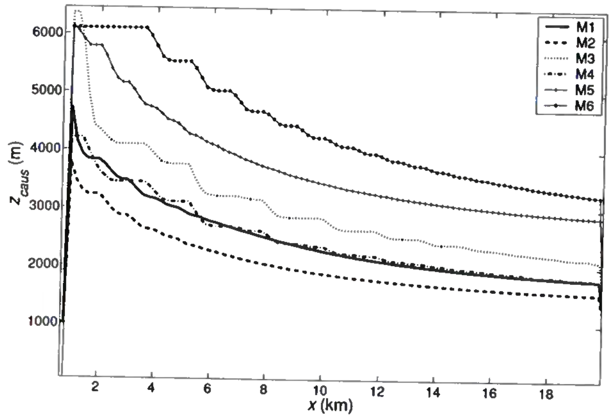

Figure 5. Focal depths z_{caus} for the velocity models in Figure 1. We associate shallower focal depth with larger model complexity.

ing to the correct velocity model. Not surprising, as the degree of smoothing increases, the quality of the imaged sub-salt reflectors worsens; for any given amount of smoothing, the degradation is model-dependent. The more complex the overburden model (i.e., the shallower the computed focal depth shown in Figure 5), the faster the image degrades with increased smoothing. Thus, for a given amount of smoothing, the degradation for model M2 is more severe than that for model M4. For both, the degradation is worse beneath the shorter-wavelength portion of the chirp. For these two models, the maximum smoothing diameter that yields acceptable imaging is about 160 m. For the remaining models, a smoothing diameter of 200 m, and even larger, yields acceptable imaging of the target reflections.

The models in which the bottom rather than the top of the salt has the chirp shape can be smoothed as much as 400 m without introducing significant distortion of the imaged sub-salt reflections. One reason for this is the closer proximity of the chirp boundary to the targets. Another is that the impedance contrast, and consequently the lateral velocity variation, is smaller for the models with chirp-shape bottom rather than top of the salt.

We note that our observations and impressions of image quality are subjective, based on assessment of four characteristics of imaged reflectors: their locations, sharpness of imaged events, distortion in imaged reflector shape, and contaminating artifacts.

As seen especially in Figure 7, the deeper targets suffer somewhat larger distortion than do the shallower ones. The farther waves have propagated through the velocity model the more complicated they become. Keep in mind that it is not the complexity of the velocity model directly above a reflector that influences the quality of imaging, but rather the complexity along the dominant ray directions. Thus the steep reflectors on the right side of the figures are better imaged than are the horizontal ones. Conversely, the horizontal reflectors at the left are better imaged than are the dipping ones there.

Another aspect of smoothing, seen in Figure 8, are gaps in the imaged bottom of the salt for model M2 migrated using velocities smoothed with a=160 m. The smoothed velocity model does not have the detail necessary to honor all the ray bending and multi-pathing that occurs at the chirp interface. As a result, migrating with the smoothed velocity model creates illumination gaps in the bottom-of-salt reflection.

To summarize, for migration with finite-differences, smoothing of the true velocity model can only degrade the imaging quality; it cannot improve it. For the generic velocity models with chirp-shape top of salt, the maximum amount of smoothing that produces an acceptably depth-migrated image is that with $a \approx 200$ m. This maximum acceptable smoothing, however, depends on the complexity of the model. In agreement with the results of Versteeg (1993) and Gray (2000), the less complex the model, the more smoothing that is acceptable. Again, however, in practice we cannot know the velocity model in detail. Next we investigate what happens when we smooth erroneous velocity models.

5 SMOOTHING OF ERRONEOUS VELOCITY MODELS: EXPLODING-REFLECTOR DATA

Here, we again consider poststack depth migration of exploding-reflector data generated for the generic velocity models. We first migrate using the erroneous velocity model and then repeat the migration after applying different amounts of smoothing to the erroneous velocity model. We introduced errors of the following kind to the generic velocity models:

- lateral and vertical shifts of the chirp-shape top or bottom salt boundary,
- erroneous amplitude of the chirp-shape boundary,
- random perturbations added to the chirp,
- erroneous velocity of the salt layer.

As simple as is our generic velocity model, the list of model parameters shown in Section 3, plus all the scale lengths (Fresnel zone, chirp wavelength, smoothing diameter, scale length of the velocity error, depth of the targets) involved in the problem make systematic analysis of depth migration for different smoothings of erroneous migration velocities a large task. We show only a few selected examples that illustrate main observations of the study.

The benefit or harm done by velocity smoothing depends on the type of error. For migration of field data in practice, velocity models will have a combination of all the forms of error that we introduce individually in this study.

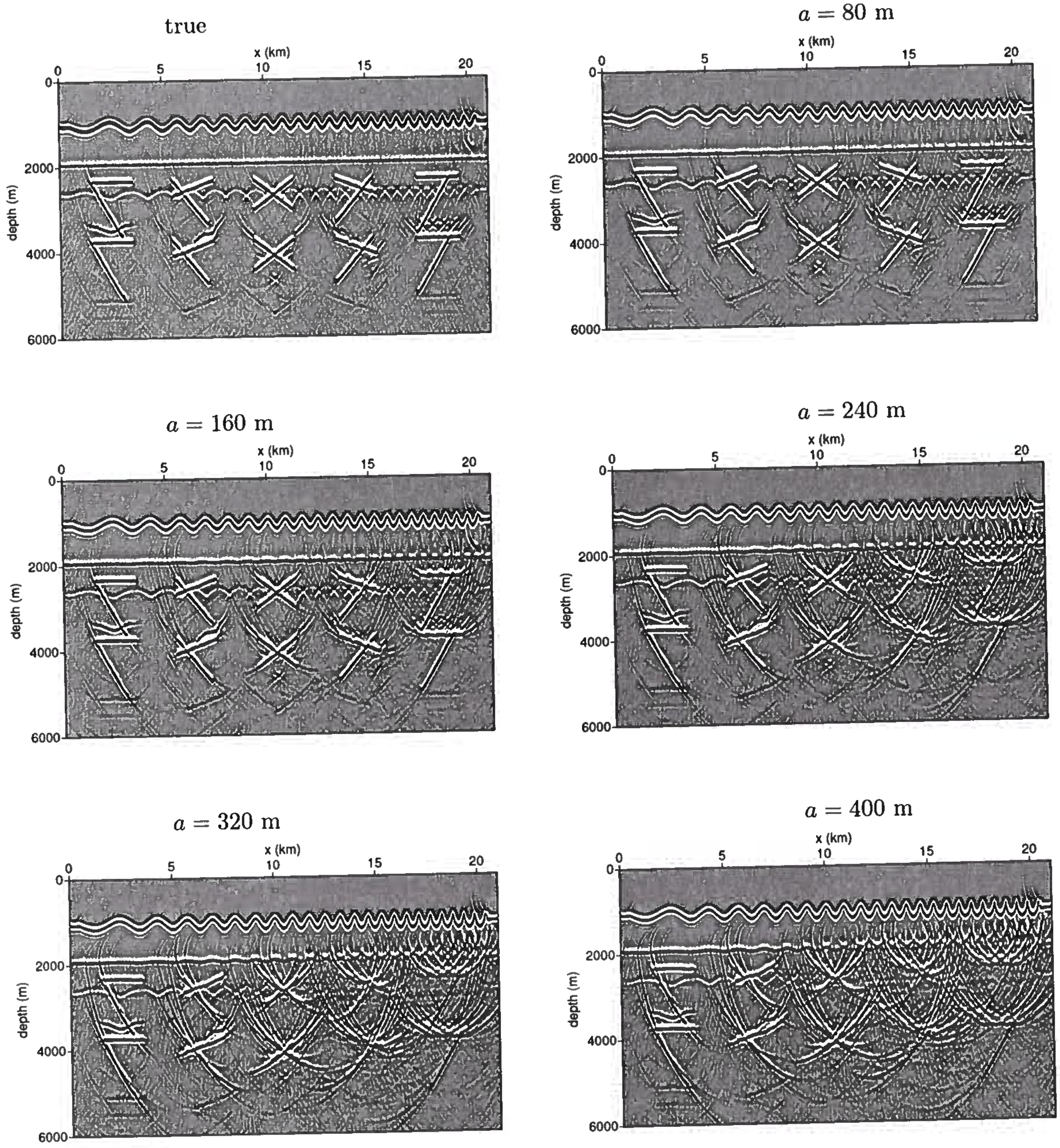

Figure 6. Depth-migrated exploding-reflector sections for model M2 using the correct velocity model and after different amounts of smoothing have been applied to that correct model. The diameter of the two-dimensional Gaussian smoothing operator is denoted by a.

Some types error in the velocity model have relatively small influence on the migrated image. For example, vertical shifts of the salt boundary and constant error in the velocity of the sediments surrounding the salt body have relatively little influence on sub-salt image quality. These two types of error primarily cause error in reflector depth without severely distorting or defocusing the image. Pon and Lines (2004) and Paffenholz et al. (2001) obtained similar results with their modeled data sets. Smoothing of these erroneous velocity models has much the same influence on the quality of imaging as does smoothing of the correct velocity models. Increasing the degree of smoothing in this case only further degrades image quality.

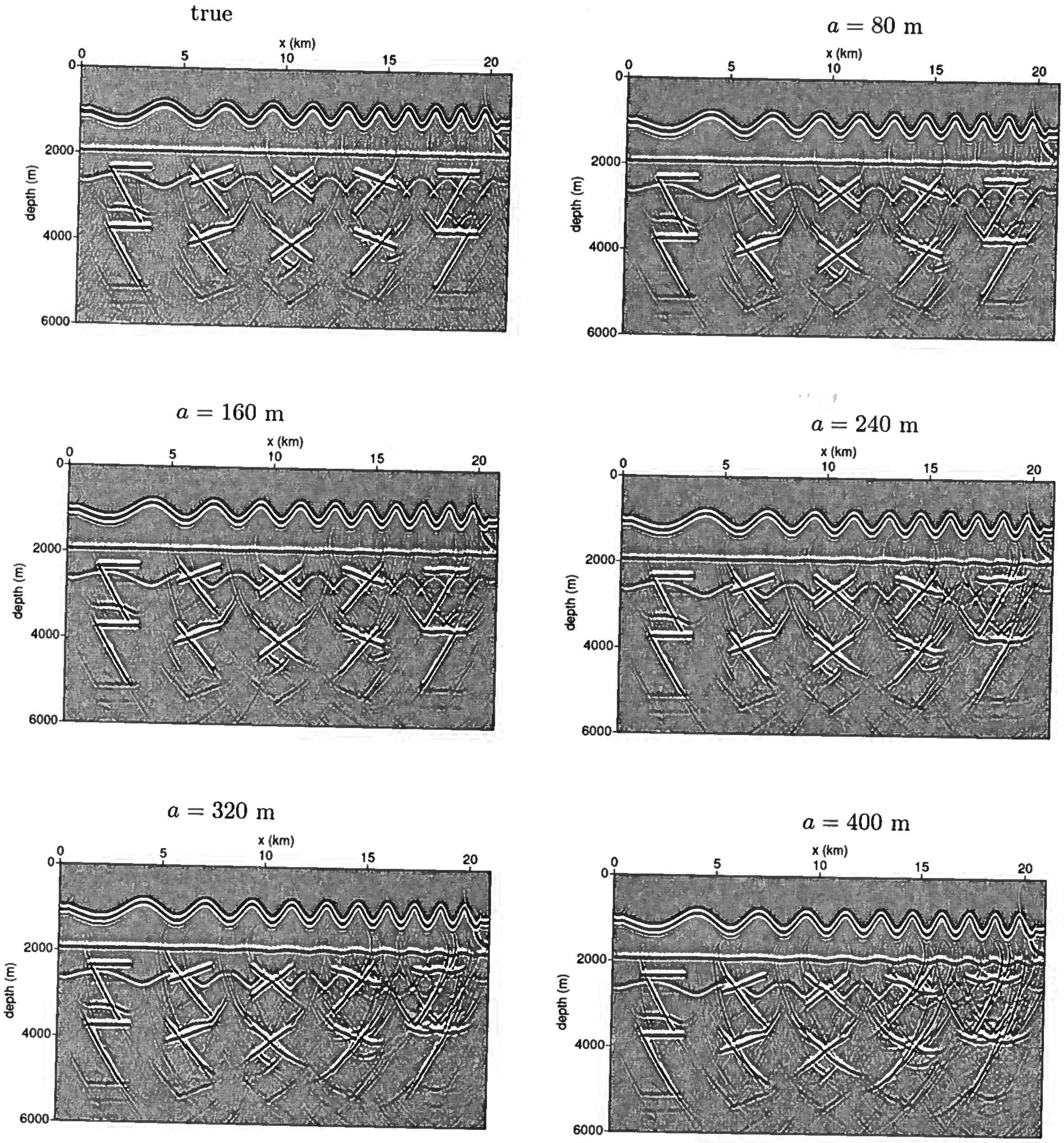

true

$a = 80$ m

$a = 160$ m

$a = 240$ m

$a = 320$ m

$a = 400$ m

Figure 7. Same as Figure 6, but for model M4.

In contrast, consistent with the results of Paffenholz et al., we find that lateral shift of the chirp model can cause significant degradation of sub-salt imaging, as do errors in the geometry of the chirp boundary. In general, a given amount of lateral shift of the boundary causes larger degradation of the sub-salt image than does a comparable vertical shift.

As we shall see, where error in the velocity model causes substantial degradation of the migrated image. smoothing the erroneous velocity model can improve the quality of the migrated image. Where it causes too severe degradation, once again no smoothing can help.

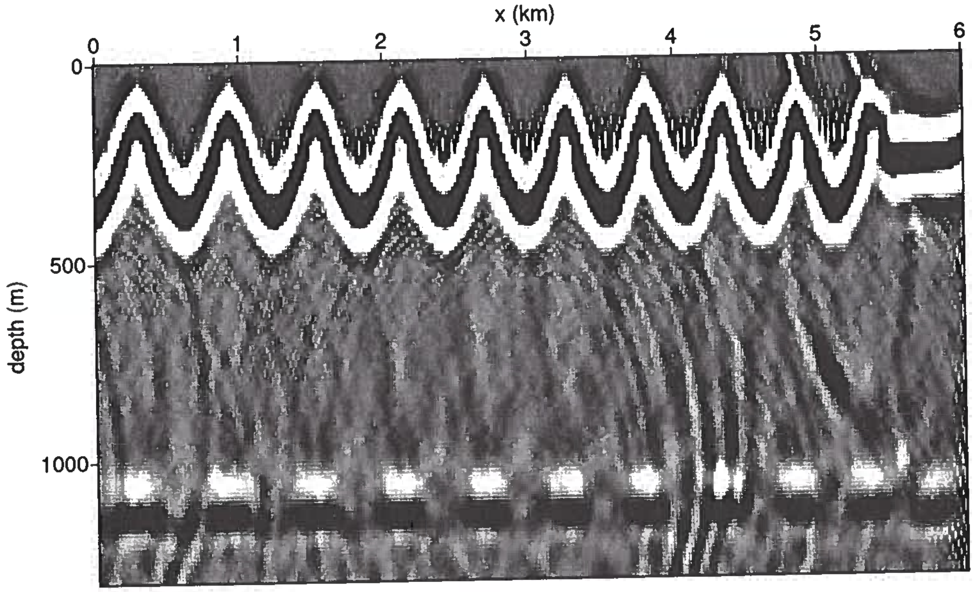

Figure 8. Close view of the top and bottom of salt in the migrated image of model M2 for velocity smoothing with a=160 m. Note the gaps in the image of the base of salt, in part the result of mistreatment of variable illumination at the salt base.

5.1 Lateral shift of the chirp

A constant lateral shift of the entire salt boundary is an unrealistic error in practice. Applied to our chirp-shape top-of-salt boundary, however, a constant shift allows us to study the influence of such an error systematically as a function of lateral velocity variation in the overburden.

Figure 9 shows the depth-migrated sections for model M4 using the correct velocity model and that model laterally shifted by different amounts, from 20 to 100 m. Note that even a shift of only 40 m (trace spacing in the exploding-reflector section is 20 m) introduces distortions in the depth-migrated image. As expected, image degradation is larger beneath the small-wavelength region of the chirp and deeper in the section. Increasing the amount of lateral shift leads to worsened image quality beneath the longer-wavelength portions of the chirp. We next smooth the shifted velocity models and assess the quality of sub-salt imaging in the resulting migrations. Figure 10 shows migrations with smoothed versions of the model that was erroneously shifted laterally by 40 m. Smoothing with a of 160 to 240 m improves the image quality for many of the sub-salt targets, but smoothing by larger amounts results in reduced quality of the migrated section. Smoothing of velocity models with larger lateral shifts (not shown here) produced similar results although the improvement introduced by smoothing becomes harder to recognize for larger shifts. The data quality is so much compromised for large lateral shift that smoothing can have little influence. The image quality is already so poor that it would take a large amount of smoothing to make it much worse.

5.2 Exaggerated chirp amplitude

The type of velocity error we consider next is that caused by incorrect amplitude of the chirp-shape top of salt. Figures 11 and 12 show depth-migrated images of exploding-reflector data for models M2 and M4, each with the amplitude of the chirp-shape top of salt too large by 50 m, and with various amounts of smoothing. The images for the erroneous models are significantly degraded from those generated with the correct migration velocity, more so for model M2 (with short spatial wavelength of chirp) than for model M4. Smoothing of the erroneous velocities for model M2 results in improved image quality for smoothing diameter up to about 320 m, but degrades the quality for larger smoothing. The degree of improvement varies across the model. For model M4, improvement in imaging for some targets is best with a as large as 640 m. Note also that the region of largest improvement generally progresses toward the left (i.e., toward longer spatial wavelength of chirp) as the amount of smoothing increases.

For this 50-m error in chirp amplitude, we performed migrations of models M1 through M4 (the four models with chirp-shape top of salt) and smoothing ranging from a = 80 m to 1240 m in increments of 40 m. From subjective visual impressions of migrated sec-

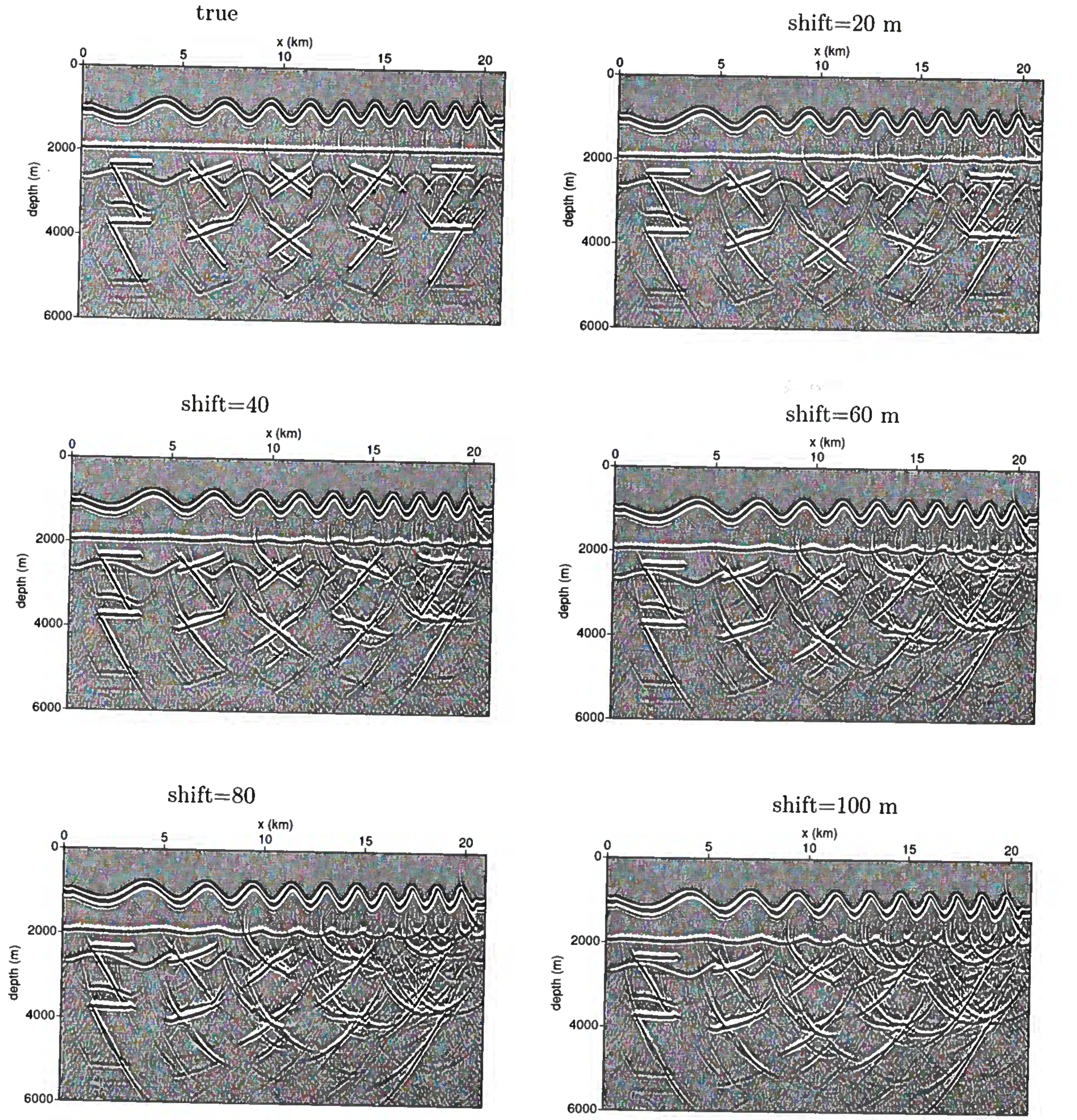

true

shift=20 m

shift=40

shift=60 m

shift=80

shift=100 m

Figure 9. Depth-migrated exploding-reflector sections for model M4 using the correct velocity and different amounts of lateral shift of that model.

tions for the different amounts of smoothing, we made rough estimates of smoothing diameter that yields the best imaging of the different target reflectors across the model. Figure 13 shows the estimated optimum smoothing diameters for the four models, as a function of lateral position x. Comparison of the curves (linearly interpolated between the subjectively inferred values) in this figure with the curves in Figure 5 shows some degree of correlation between the focal depths in Figure 5 (a measure of model complexity) and the optimum smoothing diameters in Figure 13 for this particular form of velocity error: generally the shallower the focal depth (i.e., the greater the model complexity), the smaller the smoothing diameter that is best.

Versteeg (1993) showed that the lower the complexity of the velocity field, the larger the amount of smooth-

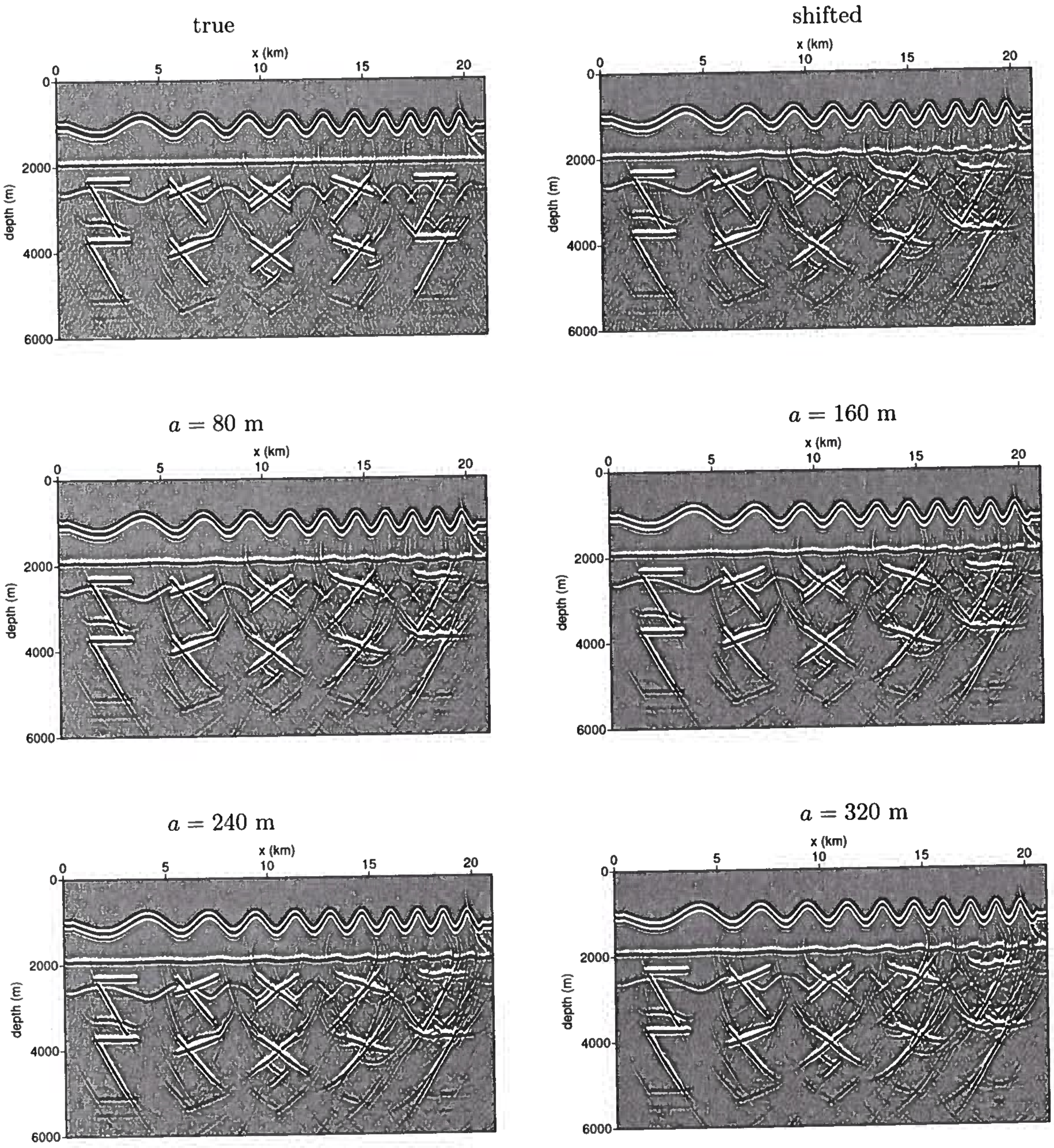
true

shifted

$a = 80$ m

$a = 160$ m

$a = 240$ m

$a = 320$ m

Figure 10. Depth-migrated exploding-reflector sections for model M4 using the correct velocity model, for that model laterally shifted by 40 m, and for various degrees of smoothing applied to the laterally shifted model.

ing of the velocity model that is acceptable for imaging. Here, we find a counterpart result: the lower the complexity of the velocity field, the larger the amount of smoothing that yields the best imaging when the initial model is in error. In tests with larger error in chirp amplitude (100-m too large), we found a similar correlation between model complexity and optimum amount of smoothing.

5.3 Random perturbation of the chirp

The final type of error in the migration-velocity model that we show is a random perturbation of the chirp-

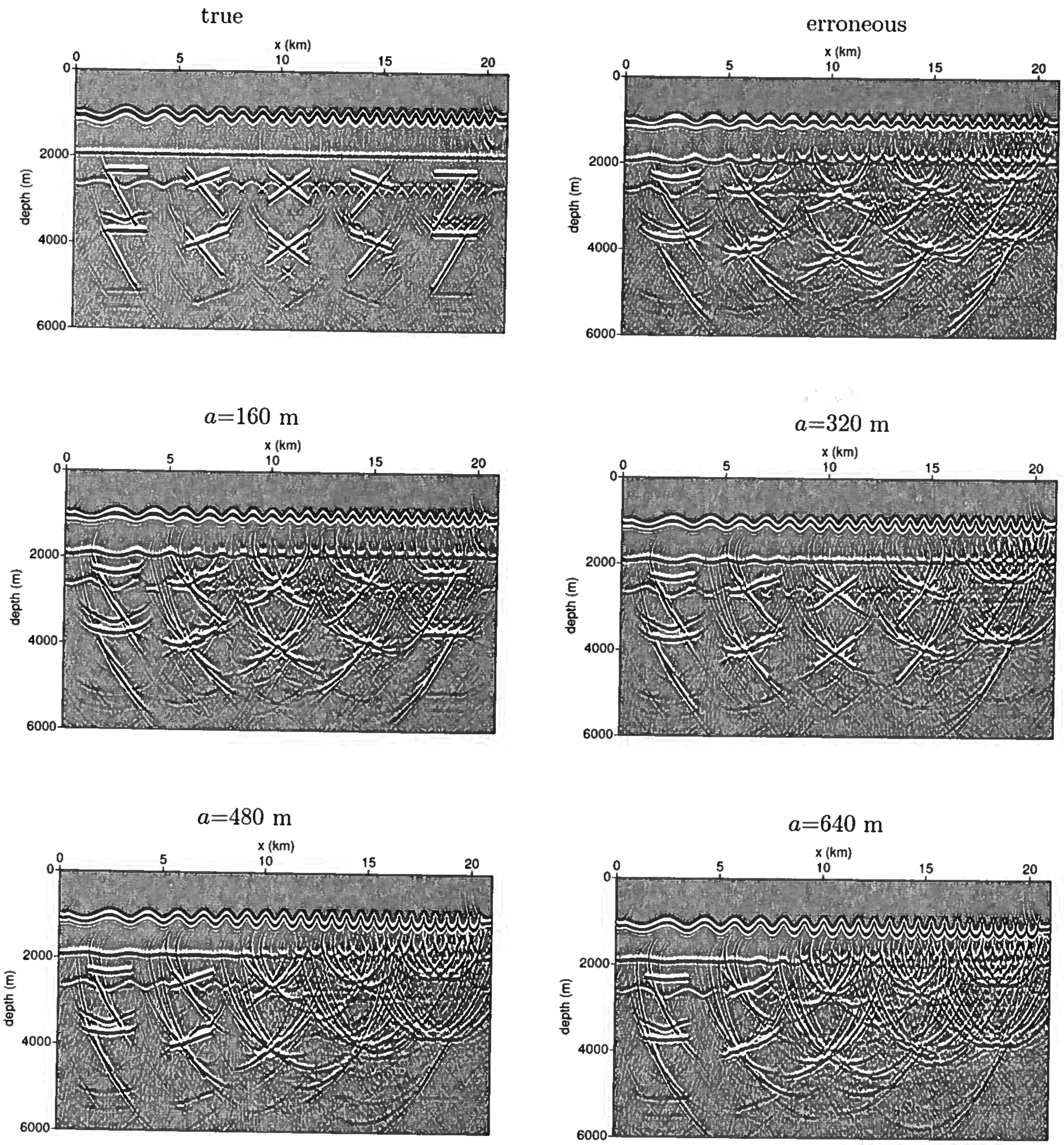

true

erroneous

a=160 m

a=320 m

a=480 m

a=640 m

Figure 11. Depth-migrated exploding-reflector sections for model M2 with true velocity, for an erroneous velocity model caused by chirp amplitude exaggerated by 50 m (a 50 percent exaggeration), and for smoothed versions of the erroneous velocity model.

shape top of the salt. We distorted the shape by adding a laterally bandlimited, Gaussian-distributed depth error to the chirp. For the test results shown in Figures 14, 15, and 16, the correlation length $l = 100$ m, where l is the lag at which the autocorrelation of the random depth variation decreases by a factor e^{-1} of its peak value. The correlation length is a measure of lateral scale length of velocity error. For these tests, the standard deviation of the random depths prior to bandlimiting is $\sigma = 50$ m.

Figures 14 and 15 show migrated sections using the true velocity model, a model with random error added to the depth of the chirp, and variously smoothed versions of the erroneous velocity function for models M2 and M4. For both models, migration with the erro-

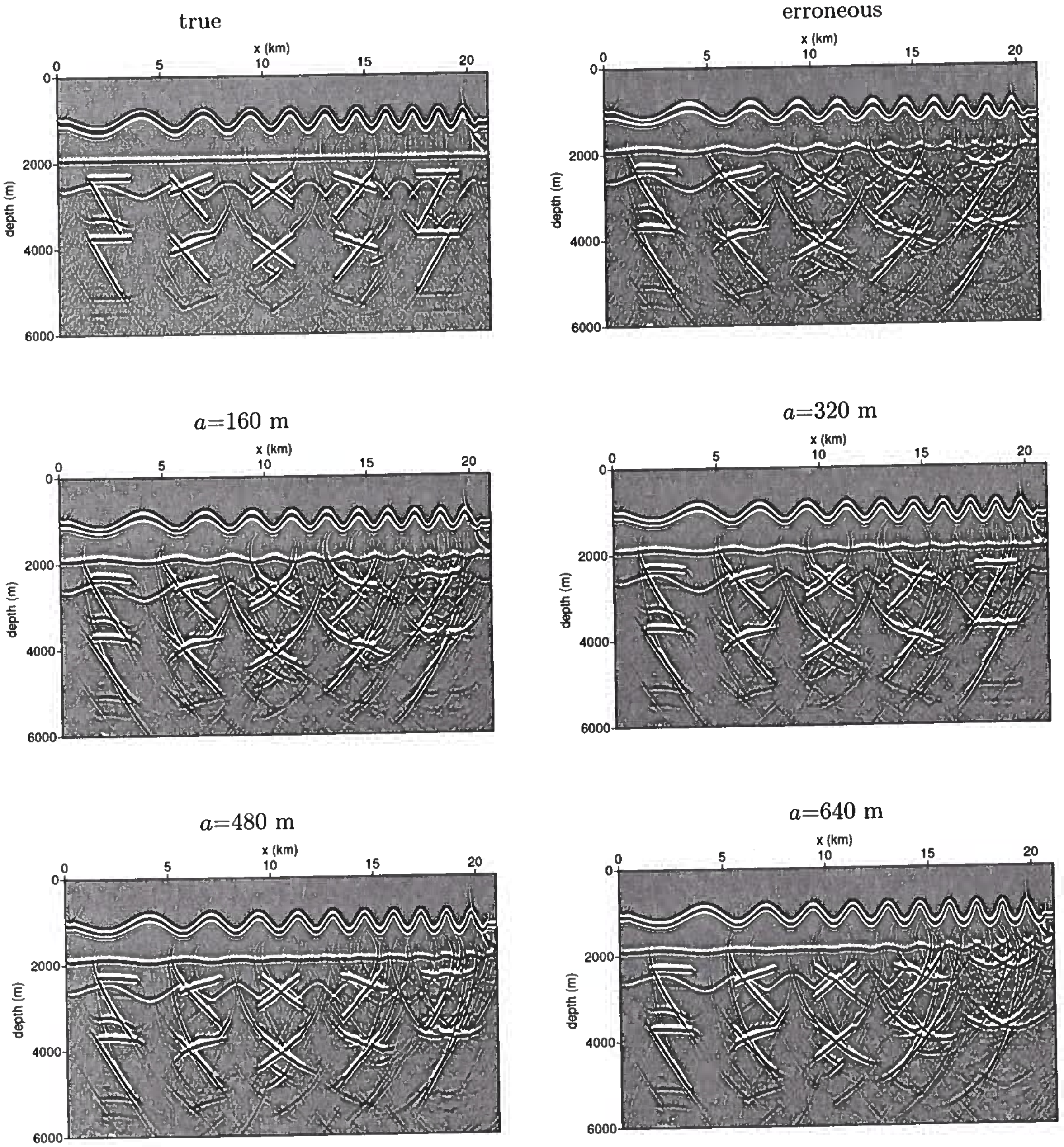

true

erroneous

a=160 m

a=320 m

a=480 m

a=640 m

Figure 12. Same as Figure 11 but for model M4. The 50-m increase in chirp amplitude represents a 25 percent exaggeration of the amplitude for this model.

neous velocity function yields severely distorted imaging of the sub-salt reflections. For model M2 (Figure 14), which has the shorter-wavelength chirp-shape top of salt, smoothing of the erroneous velocity model yields, at best, marginal improvement, with optimal smoothing varying from a = 160 m to at least 640 m for reflectors from right to left. The improvement brought about by smoothing the erroneous model is more evident in the results for model M4, shown in Figure 15. As smoothing increases from a = 160 m to 640 m, targets that are best imaged again are those beneath progressively longer-wavelength portions of the chirp.

Model M3 has chirp shape spanning the same range of wavelengths as those in model M4, but with smaller-amplitude chirp. Compared to results for similarly considered models M2 and M4, migration for data from

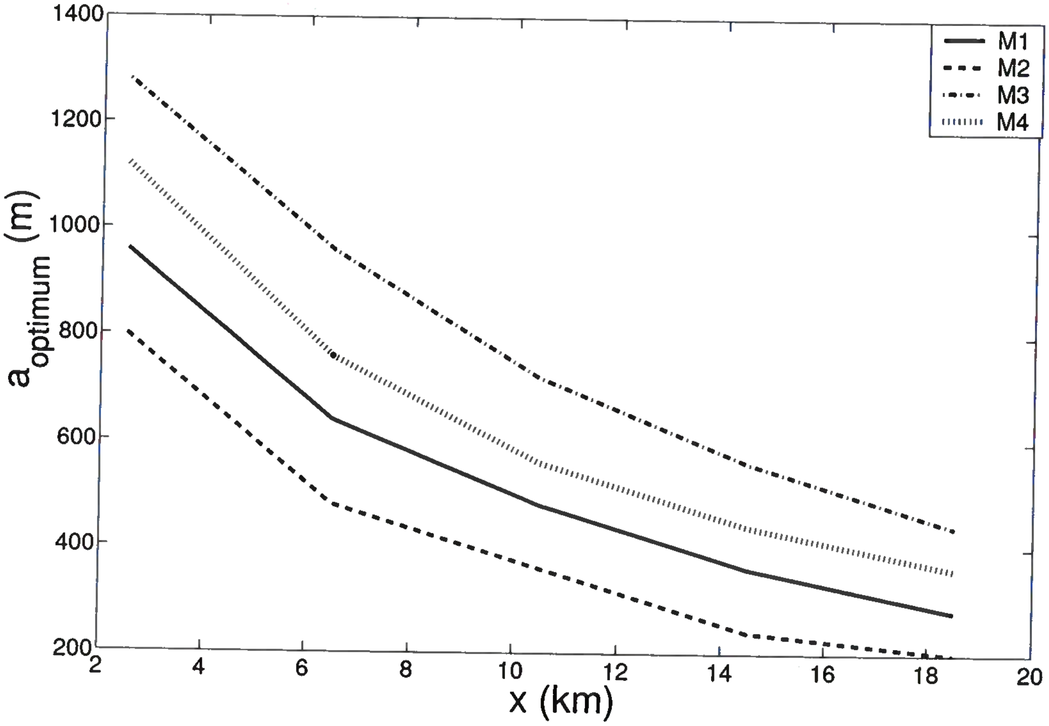

Figure 13. Optimum smoothing diameters for migration-velocity error caused by chirp amplitude that is 50-m too large, for models M1-M4.

model M3 (Figure 16) exhibits more distortion of sub-salt events when the randomly erroneous velocity model is used. Migration with variously smoothed versions of the erroneous model, however, yields substantial improvement in sub-salt images. The pattern of improved quality of imaging for various smoothings of the erroneous velocity model is similar to that seen in Figures 14 and 15, but the improvement here is dramatic. In particular, much of the sub-salt region is best imaged with smoothing using $a = 320$ and 640 m, with $a = 640$ m yielding the best result for lateral positions $x < 10$ km. Even broader smoothing might have resulted in a better image yet. We found similar behavior for other choices of correlation distance and amplitude of the random perturbations. Smoothing of the migration-velocity model *can* help in imaging.

6 SMOOTHING OF AN ERRONEOUS VELOCITY MODEL: PRESTACK MIGRATION

In all of the above tests, we have used poststack-migrated exploding-reflector data to assess the influence of smoothing of erroneous velocity models on sub-salt image quality. Such data and migration require so relatively little computation that we could perform a large number of tests. Despite being useful for our study, exploding-reflector data cannot be acquired in the field nor can they be obtained from field data. They are a fiction. Next we show results for one example of a similar study of the influence of smoothing, but with prestack migration performed on synthetic multi-offset data.

Using finite-difference code, we modeled shot records for a simulated 2D survey across the top of model M4, each shot having 500 channels, with 10-m group interval, and 80-m shot spacing. Migration was performed with a shot-record f-x domain algorithm (Claerbout, 1985). We then sorted the migrated data into common-image gathers and stacked the gathers. Figure 17 shows the prestack-migrated image for model M4 using the correct velocity model. The quality of imaging for the target reflectors is excellent, superior to that obtained in poststack migration of exploding-reflector data for model M4 (Figure 4), primarily because imaged multiples are much weaker in the prestack result.

For this test, we generated the erroneous velocity model by exaggerating the amplitude of the top-of-salt chirp in model M4 by 100 m, a 50 percent increase from the true chirp amplitude. Prestack migration with this erroneous velocity model is shown in the upper left of Figure 18. With this level of velocity error, the shape of the horizontal bottom of the salt is greatly distorted toward the left of the section, and toward the right the bottom of the salt is virtually not imaged. Similar obser-

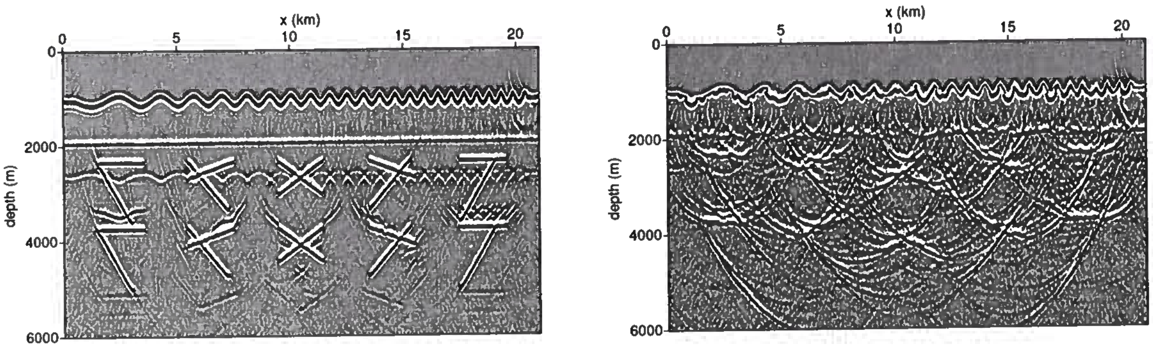
true

erroneous

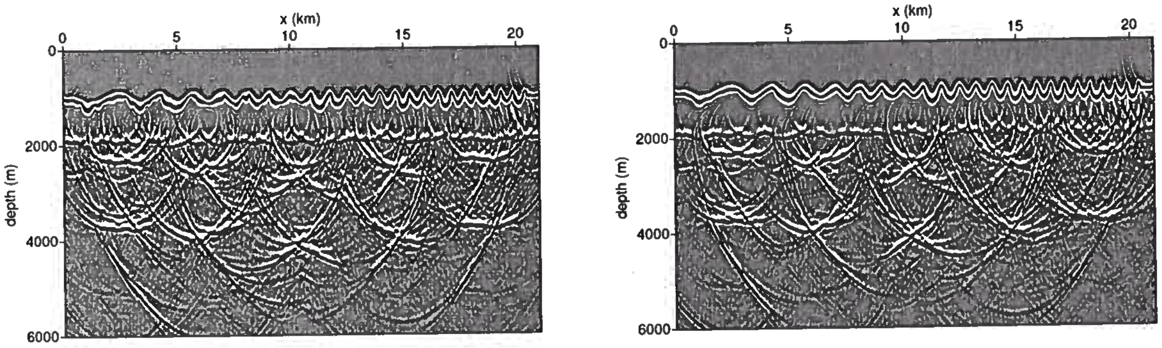
a=160 m

a=320 m

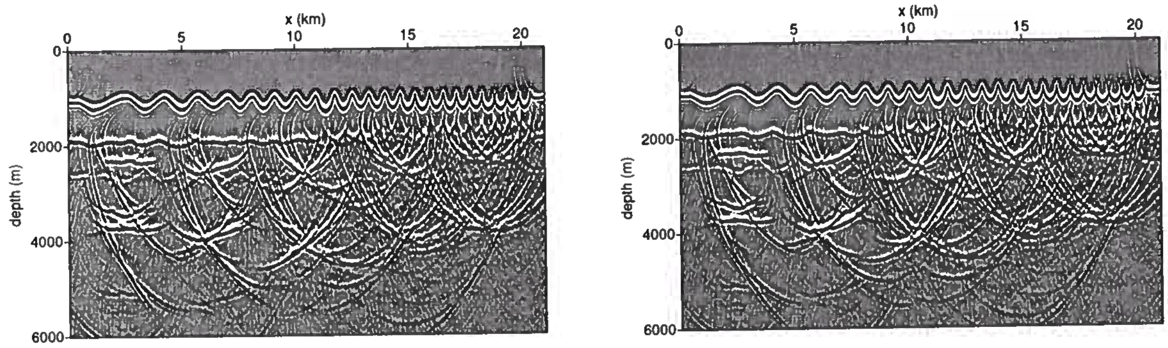
a=480 m

a=640 m

Figure 14. Depth-migrated exploding-reflector sections for model M2 with the true velocity, for an erroneous velocity model with random error ($l = 100$ m, $\sigma = 50$ m), and for variously smoothed versions of the erroneous velocity model.

vations hold for the sub-salt reflectors. The remainder of the figure shows the results of prestack migration using the erroneous velocity model smoothed with what we might consider to be large amounts of smoothing: $a = 240$, 480, and 720 m. Velocity smoothing clearly improves the quality of the migrated images, with $a = 480$ m yielding the best imaging of the right portion of the subs-salt section (beneath the shorter-wavelength portion of the chirp), and $a = 720$ m yielding the best imaging beneath the longer-wavelength portion. The best images show distortion of the shapes of the target reflectors, but these reflectors nevertheless are far better imaged than when no smoothing is applied to the erroneous velocity model.

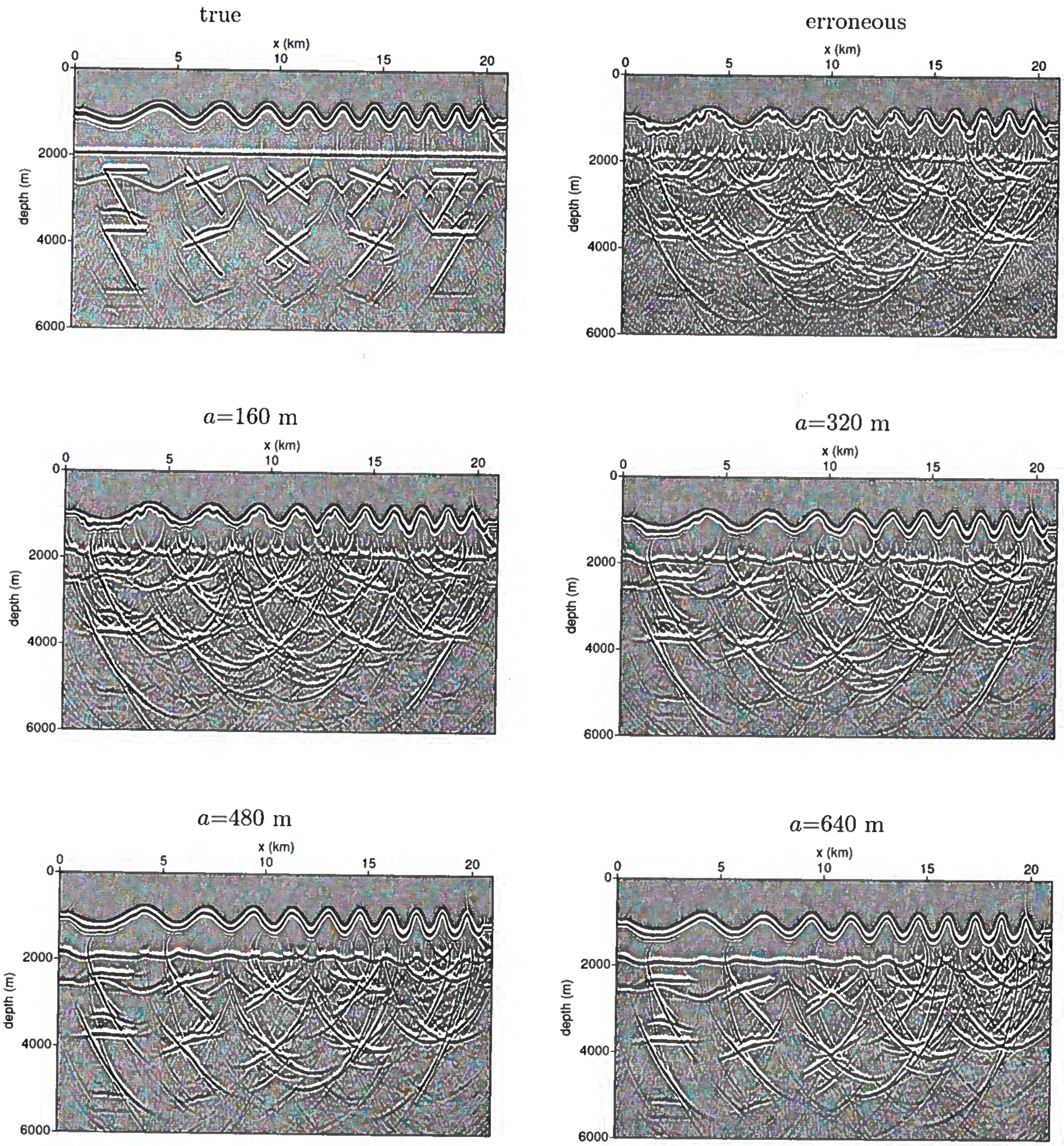

Figure 15. Same as Figure 14 but for model M4.

Prestack migration with the erroneous velocity model resulted in more severe degradation of image quality than did poststack migration of the exploding-reflector data. This could be due in part to mistacking that arises when the incorrect velocity model is used. In any case, the data are far better imaged with use of smoothed migration velocities in the migration.

7 DISCUSSION AND CONCLUSIONS

Despite the limited nature of this study — 2D, primarily poststack migration of exploding-reflector data, just one choice of wavelet, simple chirp-shape top or bottom of salt with limited range and choice of spatial wavelength, small number of and forms for perturbations from the true velocity model, and simple model of subsurface structure — results for tests with the generic

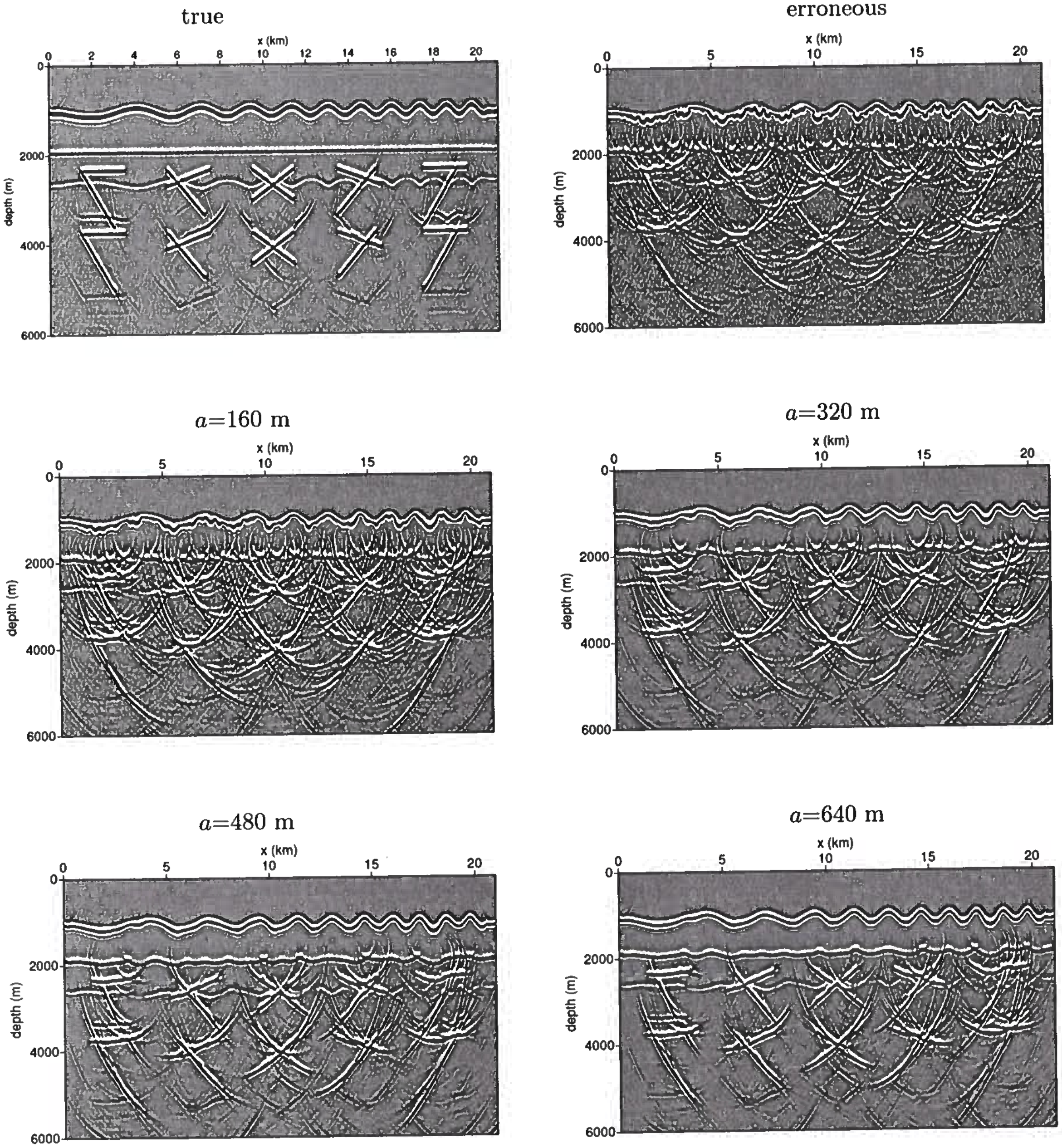

Figure 16. Same as Figure 14 but for model M3.

model give clear indication that, for some types of velocity error, smoothing of velocities for migration velocity model *can* improve image quality, sometimes significantly. The amount of smoothing that is optimum in the sense that it gives imaging superior to that when either less or more smoothing is used depends on the size and type of error in the migration-velocity model as well as on the lateral wavelength of the true velocity structure in the overburden.

The optimal choice for smoothing to address imaging degradation caused by use of an erroneous velocity model can be considerably larger than either (1) that needed to overcome shortcomings of ray tracing for Kirchhoff migration or (2) the amount of smoothing that would be acceptable for any migration algorithm

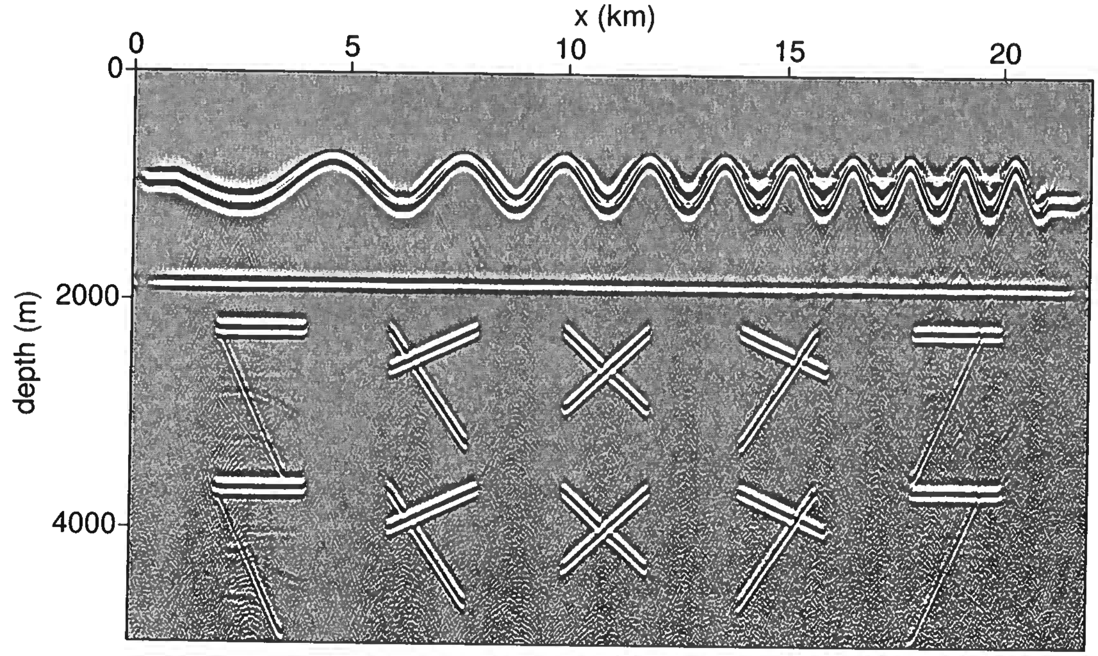

Figure 17. Prestack migrated image for model M4 using the correct velocity model. Compare with Figure 4.

when the initial migration-velocity model was perfectly accurate. Because the velocity function for migration is never fully accurate in practice, *some* degree of smoothing is always appropriate. Moreover, although it will be difficult in practice to pin down an optimal spatial extent of smoothing, that amount can well be larger than is often used in practice — even considerably larger than the spatial size of the errors in the migration-velocity model.

Use of the generic chirp-shape salt boundary allowed us to do simple tests, e.g., velocity error modeled as lateral shift of the boundary, in a systematic effort to gain an idea of the relationship between optimum amount of smoothing and scale of the velocity variations. For even this simple model, we have seen dramatic differences between zero-offset data modeled based on the exploding-reflector assumption and those modeled with wavefields generated by individuals shots. A significant manifestation of the difference arises from variations in the spatial distribution of subsurface illumination. These differences in the two forms of modeled data in turn give rise to marked difference in image quality when the data are depth-migrated with a poststack algorithm (which is based on the exploding-reflector) using a migration-velocity function that is known perfectly.

Although we did only a few tests of smoothing erroneous velocity models for use in prestack migration, use of smoothed velocities generally helped to improve the quality of images — greatly so for the one test with prestack migration shown here. This is consistent with what we found (although to a lesser extent) for poststack migration of exploding-reflector data. The consistency is comforting given that most of our tests were with exploding-reflector data, which cannot be obtained from field data. Supporting the results from the poststack migrations of exploding-reflector data, the amount of smoothing that is best can be considerably larger than might have been suspected from the spatial size of errors and detail in the velocity model.

A general ranking of the influence of the different types of velocity error on image quality is as follows. Constant vertical shift of the top of salt or constant error in velocity of the overburden causes relatively little degradation. Smoothing of the velocity model will not improve imaging for these types of error any more than it would if the velocity model were perfectly accurate. Lateral shift of the top of salt causes image distortion that can be not only large, but such that imaging is not amenable to improvement by velocity smoothing. Error in amplitude of the chirp-shape top of salt, including random perturbation of the salt shape, can also cause large distortions in the sub-salt image, but the imaging can be substantially improved through use of smoothed

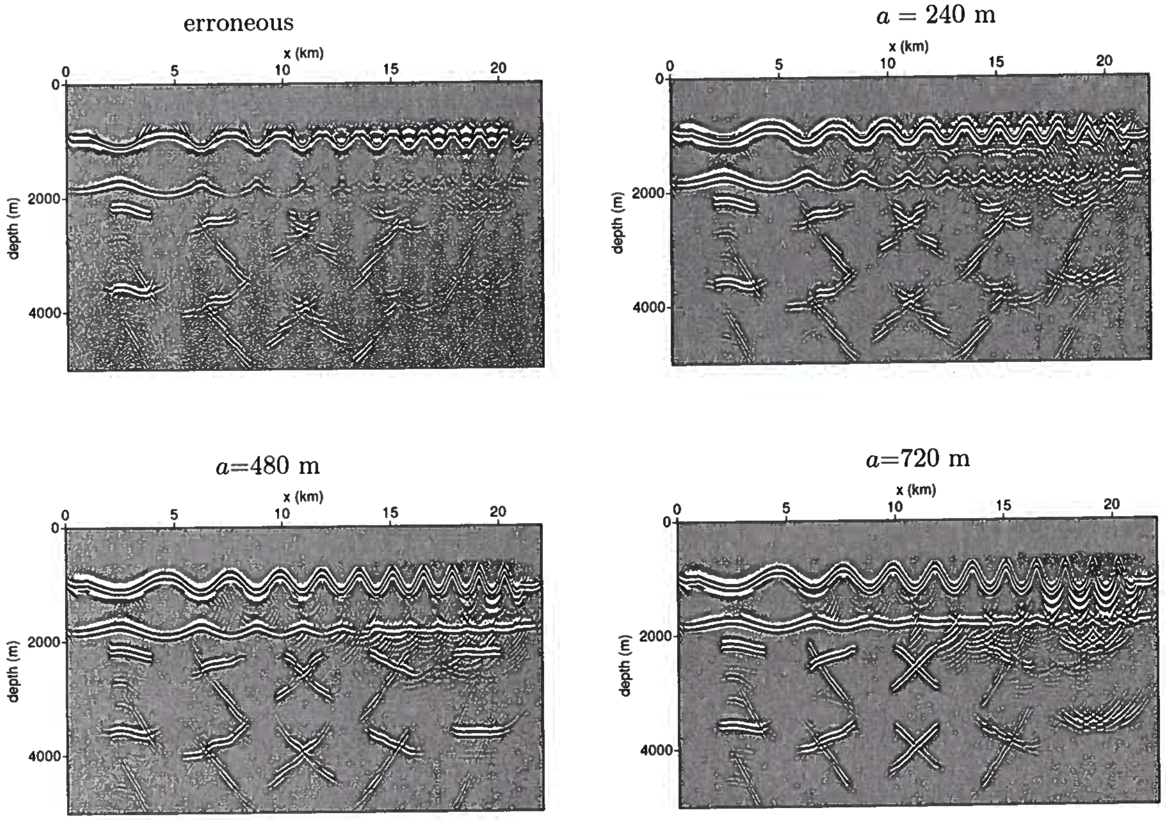
erroneous

$a = 240$ m

a=480 m

a=720 m

Figure 18. Prestack-migrated image for model M4 using the erroneous velocity model with chirp amplitude exaggerated by 100 m, and for the erroneous velocity model smoothed with operator diameter a=240, 480, and 720 m.

velocities, even broadly smoothed. Of course these general comments about the influences of the different types of error and the benefits of smoothing for these types of error are all dependent on the magnitude of the velocity error of any given type.

Any smoothing of a derived migration-velocity model yields velocities that are erroneous. That's clearly true if the derived velocities somehow happened to be perfectly accurate. A conclusion from the tests here is that, since the migration-velocity model is necessarily inaccurate, it is better that detail in the initial velocity model be smoothed prior to migration — thus yielding a smoothly erroneous model — than to trust in use of the detailed model. Moreover, the amount of smoothing needed to help the imaging is likely greater than that inferred from previous studies involving smoothing of perfectly accurate velocities. The observation of Gray (2000) nevertheless still holds that too much smoothing will alter the velocity model from the 'true' one to the extent that image quality will be harmed. The optimal amount of smoothing to use remains as difficult model- and data-dependent choice.

REFERENCES

Claerbout, J. 1985. *Imaging the Earth's Interior.* Blackwell.

Clayton, R., & Engquist, B. 1977. Absorbing boundary conditions for acoustic and elastic wave equations. *Bull. Seis. Soc. Am.*, **67**, 1529–1540.

Gray, S. 2000. Velocity smoothing for depth migration: how much is too much? Calgary, Alberta, Canada: CSEG Publication.

Jannane, M. et. al. 1989. Short note: Wavelengths of earth structures that can be resolved from seismic reflection data. *Geophysics*, **54**(7), 906–910.

Kjartasson, E., & Rocca, F. 1979. The exploding reflector model and laterally variable media. *In: Stanford Exploration Project No. 16.* Stanford University.

Paffenholz, J. 2001. Sigsbee2 synthetic subsalt dataset: image quality as function of migration algorithm and velocity model error. San Antonio, Texas, USA: 71st SEG Annual International Meeting.

Pon, S., & Lines, L.R. 2004. Sensitivity analysis of seismic depth migrations: Canadian Structural Model. Calgary, Alberta, Canada: CSEG Publication.

Spetzler, J., & Snieder, R. 2001. The formation of caustics in two- and three-dimensional media. *Geophys. J. Int*, **144**, 175–182.

Spetzler, J., & Snieder, R. 2004. Tutorial: The Fresnel volume and transmitted waves. *Geophysics*, **69**(3), 653–663.
Versteeg, R. J. 1993. Sensitivity of prestack depth migration to the velocity model. *Geophysics*, **58**(6), 873–882.

CWP-513

A fault caught in the act of burping

Matthew M. Haney[1], Roel Snieder[1], Jon Sheiman[2], and Steven Losh[3]
[1] *Center for Wave Phenomena and Department of Geophysics, Colorado School of Mines, Golden, CO 80401, USA*
[2] *Shell International Exploration and Production, Houston, TX 77025, USA*
[3] *Department of Earth and Atmospheric Sciences, Cornell University, Ithaca, NY 14853, USA*

ABSTRACT

We report on the first direct observation of a migrating fluid pulse inside a fault zone that, based on previous evidence, is suspected to be a conduit for fluids ascending from depth. We find that areas of high fault-plane reflectivity from a fault at the South Eugene Island Block 330 field, offshore Louisiana, systematically moved up the fault 1 km between 1985 and 1992. The updip movement can be explained by the presence of a high pressure fluid pulse ascending a vertically permeable fault zone. These fault burps play a central role in hydrocarbon migration.

Key words: hydrocarbon migration, fault zones, seismic reflectivity

INTRODUCTION

Faults display a split-personality as both impediments to fluid flow and, at times, preferential pathways for flow. Both behaviors are invoked in the petroleum industry to explain how hydrocarbons move (Hooper, 1991) from the location at which they are generated (e.g., by flowing along faults) into fault-bounded reservoirs (Holland *et al.*, 1990) where they are trapped (e.g., by a lack of flow across faults). In the Gulf of Mexico, growth faults cutting through low permeability sediments provide a means for hydrocarbons generated in deep, pressurized source rocks to migrate into shallow reservoirs.

Despite the fact that fault-hosted fluid flow is still poorly understood, several studies, both theoretical and observational, have put our understanding of the interaction of fluids and faults on firmer footing. One popular model, introduced by Rice (1992) and discussed by Revil and Cathles (2002), maintains that fluids may intermittently propagate as shock waves along faults at geologically fast rates (from m/yr to km/yr). The shock waves are excited in the subsurface when the rock permeability is a strongly nonlinear function of fluid pressure - a characteristic of highly fractured zones, such as fault zones. Nur and Walder (1992) refer to intermittent times of intense fault-hosted fluid flow as "fault burps", a descriptive term that we adopt for this paper. As with Nur and Walder (1992), Finkbeiner *et al.* (2001) choose to view these episodic flow events in terms of pore pressure buildup followed by release when the Coulomb failure criterion is exceeded. Such behavior is reminiscent of the fault-valve model of Sibson (1990), in which fluid flow along faults is episodic and initiated by an increase in fault zone permeability in response to fault slip. Recently, Miller *et al.* (2004) have shown how a combination of Rice's shock wave model and Sibson's fault-valve model explains the upward movement of aftershock epicenters along a fault in the deep crust beneath Italy.

Several lines of evidence taken at the South Eugene Island Block 330 field, offshore Louisiana, indicate that faults there have hosted significant vertical fluid flow over the last 250,000 years, continuing to the present day. The evidence includes (a) oil seeps from the fault scarps along the ocean floor (Anderson *et al.*, 1995), (b) thermal anomalies associated with the spatial patterns of the fault scarps (Anderson *et al.*, 1991), (c) reports from drilling of anomalously high pore pressure confined to one of the fault planes (Losh *et al.*, 1999), (d) a year-to-year variation in the fluid chemistry of hydrocarbons produced from the same reservoir (Whelan *et al.*, 2001), and (e) geochemical anomalies seen in core samples taken from fault zones (Losh *et al.*, 1999). We present an additional set of data - seismic reflection images - that indicate fast (> 100 m/yr) fluid movement along growth faults. Previously, we have demonstrated that reflections from the fault-planes that appear in seismic data from South Eugene Island Block

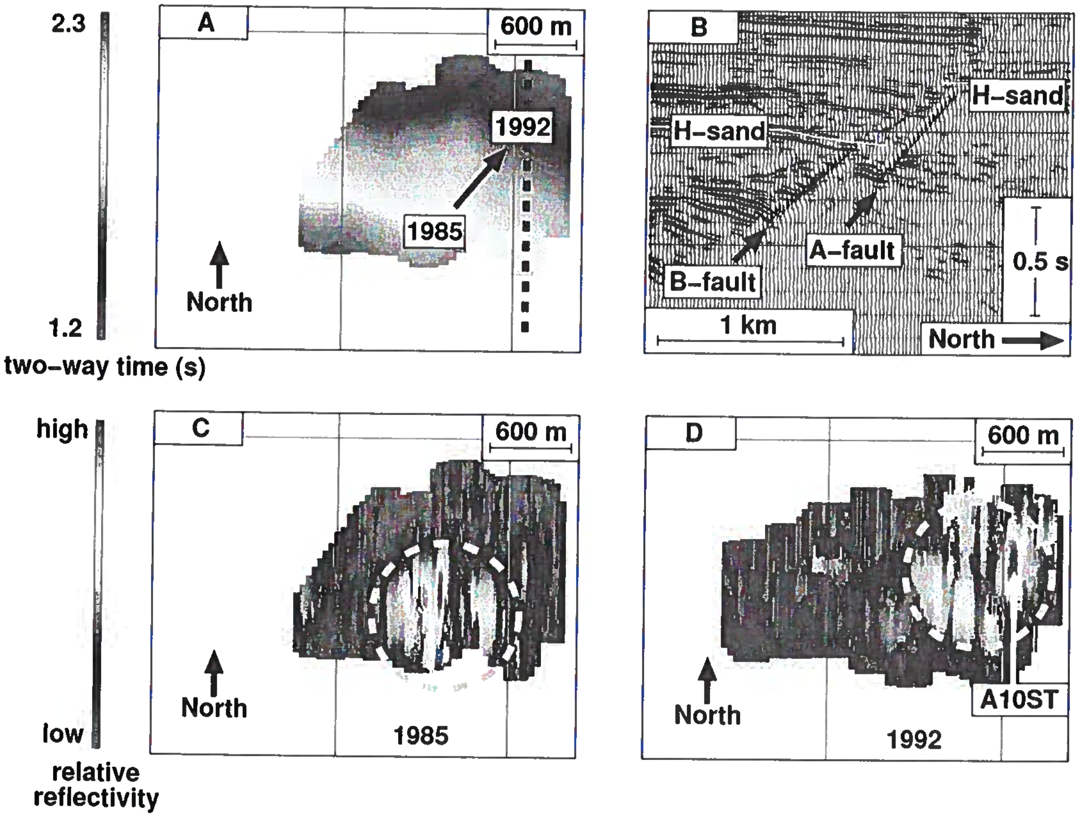

Figure 1. (A) Map of the two-way reflection time (TWT) to the B-fault plane. Using the approximation 100 m depth ~ 0.1 s TWT (Losh *et al.*, 1999), this map shows the structure of the B-fault, most notably the down-to-the-SW dip. (B) Overlay of the dip-filtered seismic reflection image (black & white wiggle plot) on top of the original image (red & blue variable density plot) along the dashed line in (A). The dip-filtering highlights the fault-plane reflections from the B-fault and a nearby fault known as the A-fault. The H-sand is shown to indicate throw. (C) Map of the B-fault, as in (A), but with reflectivity from the fault-plane in 1985 plotted instead of TWT. The area of highest reflectivity is circled in gold. (D) Map of the B-fault reflectivity, as in (C), but from 1992. The data extend over a slightly larger area than in (C); however, the spatial perspective is identical. The area of highest reflectivity, circled in gold, is shifted roughly 1 km NE in the updip direction relative to its location in 1985, as is expected for a fluid pulse ascending the B-fault. This movement is depicted by the arrow in (A). Also shown is the location of the A10ST well intersection, where exceptionally high fluid pressures were encountered while drilling into the B-fault zone in 1993 (Losh *et al.*, 1999).

330 contain information about the distribution of fluid pressures across faults (Haney *et al.*, 2004).

FLUID MIGRATION AS SEEN IN TIME LAPSE SEISMIC DATA

The South Eugene Island field is an ideal location for this study. Multiple vintages of seismic reflection surveys can be interpreted in the context of abundant fluid pressure, geochemical, and other data. Much of the available data is due to a multifaceted drilling project conducted by the Global Basins Research Network (GBRN) in the 1990s (Anderson *et al.*, 1995). During late 1993, GBRN intentionally drilled into and successfully cored some of the growth faults at South Eugene Island. Normal faults that transect the field separate upthrown sediments saturated by highly-pressurized fluids from normally-pressurized dowthrown sediments; the faults are typically at the same pressure as the upthrown sediments (Losh *et al.*, 1999). However, exceptionally pressurized fluid was encountered in one penetration of a growth fault, the B-fault, in the A10ST well (Anderson *et al.*, 1995; Losh *et al.*, 1999). Losh *et al.* (1999) stated that "the isolated pocket of anomalously high fluid pressure in the A10ST well may represent a spatially limited pulse of anomalously pressured fluid."

To test the hypothesis of a moving fluid pulse, or fault burp, we isolate the fault-plane reflections from the B-fault in images derived from seismic surveys taken in 1985 and 1992 and look for indications of movement. First, we pick the fault plane in the 3D seismic reflection images (Figure 1A). We then proceed by dip-filtering the seismic reflection images in the direction of the B-fault (Figure 1B). This dip-filtering step serves to accentuate the fault-plane reflections while simultaneously attenuating the reflections from the sedimentary layers. The final step is to extract the amplitude of the fault-plane reflection along the B-fault in a small time-window around the picked fault-plane. In Figures 1C and 1D, we show reflectivity as a function of position on the fault-plane for both datasets. Patches of high reflectivity, or "bright spots", are known to be associated with the presence of fluids (Dobrin, 1976).

The most striking pattern in the fault reflectivity maps of Figures 1C and 1D is the northeast movement of the highest reflectivity areas between 1985 and 1992. This movement, in the up-dip direction, is to be expected for a fluid pulse ascending the B-fault. From the reflectivity maps at the B-fault, we estimate the movement of the fluid pulse to be on the order of 1 km between 1985 and 1992, for an average velocity of ~ 140 m/yr. In the next section, we describe how we estimated this velocity for the pulse. Such fast fluid flow up a growth fault at South Eugene Island is in line with the study by Finkbeiner *et al.* (2001). In their study, Finkbeiner *et al.* (2001) analyzed in situ stress data and pressure measurements and showed that overpressure in some of the deep reservoirs abutting the B-fault could induce frictional failure on the fault plane. The fast movement of fluids up a permeable fault also agrees with a nonlinear permeability model first discussed by Rice (Rice, 1992). In this model, the fluid pulse is a shock wave that moves with velocity v given by

$$v = \frac{k_o(1-\phi_o)g(\rho_g-\rho_f)\sin\alpha}{\eta_f\beta\phi_o} \times \left[\frac{\exp(-\sigma_f/\sigma^*)-\exp(-\sigma_i/\sigma^*)}{\sigma_i-\sigma_f}\right], \quad (1)$$

where k_o is the permeability at zero effective stress, ϕ_o is the porosity at zero effective stress, g is gravitational acceleration, ρ_g is the density of the rock grain, ρ_f is the density of the fluid, α is the dip of the fault, η_f is the dynamic viscosity of the fluid, β is a parameter describing the linear dependence of porosity on effective stress (Elliott, 1999), σ_i is the initial effective stress state ahead of the pulse, σ_f is the final effective stress state behind the pulse, and σ^* is a parameter describing the exponential dependence of permeability on effective stress (Rice, 1992; Revil & Cathles, 2002). We note that models by Finkbeiner *et al.* (2001) and Rice (1992) are not the only ones of relevance to the behavior we observe along the B-fault at South Eugene Island. Currently, a "vug-wave" model is being developed (Losh *et al.*, 2005) that describes a fluid pulse which is mechanically coupled with the shear strain in the fault. This model has the potential to bridge the link between what we have observed at South Eugene Island and the phenomenon of "slow" or "silent" earthquakes that show sudden aseismic slip (Cervelli *et al.*, 2002).

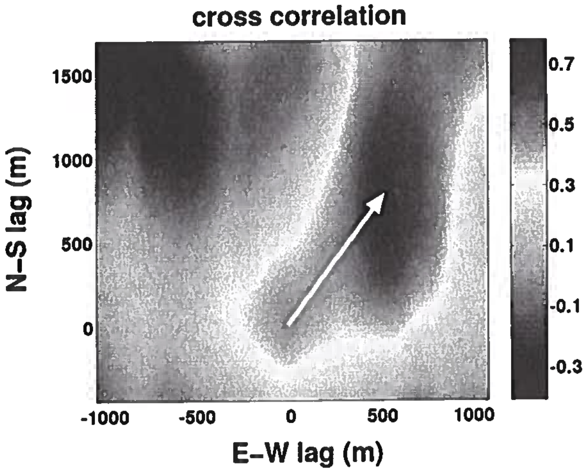

Figure 2. Spatial cross correlation of the 1985 and 1992 B-fault amplitude maps shown in Figures 1C and 1D. There is a maximum in the cross correlation when the spatial lag is 1 km to the NE (the up-dip direction of the A-fault). At the maximum, the correlation coefficient is 0.78, which is close to the value 0.80 for a horizontal reflector known as the O-sand at zero spatial lag (see Figure 3). The correlation shown here can be seen visually in Figures 1C and 1D.

QUANTIFYING THE PULSE MOVEMENT

In Figure 2, we plot the spatial cross correlation of the amplitude maps from the B-fault. There is a local maximum at 1 km spatial lag in the NE direction. This corresponds to what is seen visually in Figures 1C and 1D. The value of the correlation at the maximum is 0.78, which is close to the correlation value of 0.80 computed for a horizontal reflector known as the O-sand at zero-lag (see Figure 3). The zero-lag correlation for the B-fault amplitude maps, as shown in Figure 2, is 0.45. The fact that the correlation is as high as 0.80 for the O-sand in its zero-lag position supports the similarity of the two surveys and their processing schemes. In another study (Haney *et al.*, 2005), we tested how the presence of noise, a lack of DMO processing, and application of AGC degraded migrated amplitudes. The application of AGC most severely altered the relative amplitudes. Though an AGC appears to have been applied to the

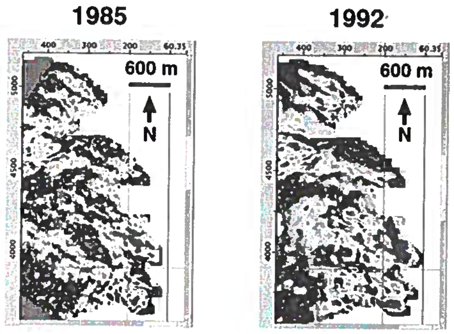

Figure 3. A comparison of the O-sand amplitude in the 1985 and 1992 surveys. The O-sand is a gently dipping sedimentary layer boundary at ~ 2.3 s TWT. Hence, the O-sand abuts the B-fault in the lower part of the B-fault plane displayed in Figure 1A. The consistency of the amplitudes in these two images, compared to the changing amplitudes along the B-fault shown in Figures 1C and 1D, supports the interpretation of relative amplitude changes in the two surveys. Though we only show the O-sand here, this consistency holds for the other sedimentary layer boundaries as well.

1985 data, it obviously did not damage the amplitudes from the O-sand enough to bring its correlation below 0.80. We have also checked the K-sand and found good amplitude agreement in its zero-lag position. Both the O- and K-sands are in the same depth interval as the B-fault plane.

The similarity of the amplitudes in the 1985 and 1992 surveys at the O-sand support the hypothesis that the 1 km of movement seen at the B-fault is an actual change in reflectivity; however, we need to show that the 1 km of movement in the seismic image is not the result of over- or under-migration, given typical errors in migration velocities. Note that the 1 km of movement up the B-fault, which dips at 45°, is equivalent to 700 m of lateral movement. To explore the issue of over- or under-migration, we first make the approximation that the shooting lines in the 1985 and 1992 seismic surveys were in the dip direction. This means the action of 3D migration on the reflection from the B-fault is purely a vertical and lateral movement in a single vertical plane. We then use the expression for the lateral movement applied to a time sample in a stacked section by a constant-velocity 2D migration, denoted Δx_m (Yilmaz, 1987)

$$\Delta x_m = \frac{p t_{in} v_m^2}{4}. \tag{2}$$

In equation (2), t_{in} is the two-way time of the input point, v_m is the migration velocity, and p is the time dip of the fault-plane reflection. The time dip is given by

$$p = \frac{2\sin\theta}{v}, \tag{3}$$

where θ is the dip of the fault-plane and v is the true subsurface velocity, not necessarily equal to the migration velocity v_m. Given the true subsurface velocity, the amount of lateral movement applied by migration should be

$$\Delta x = \frac{p t_{in} v^2}{4}. \tag{4}$$

The difference in the amount of lateral movement applied by migration, Δx_m, and the amount of lateral movement that should be applied, Δx, is the error in the lateral placement of the input point Δx_e due to an incorrect migration velocity

$$\Delta x_e = \Delta x_m - \Delta x = \frac{p t_{in}(v_m^2 - v^2)}{4}. \tag{5}$$

Denoting the depth of the time sample in the stacked section as z, t_{in} is given by

$$t_{in} = \frac{2z}{v\cos\theta}. \tag{6}$$

Therefore, using equation (3) and (6), equation (5) may be written as

$$\Delta x_e = z\tan\theta\left[\left(\frac{v_m}{v}\right)^2 - 1\right]. \tag{7}$$

To estimate the amount of error in lateral positioning due to over- or under-migration at the B-fault, we use the approximate depth z and dip θ of the fault given by 2 km and 45°, respectively. From equation (7), a ±5% error in migration velocity results in a lateral positioning error of ~200 m, less than the 700 m of lateral movement we observe at the B-fault in the 1985 and 1992 seismic surveys. Given that the geology above the B-fault is essentially a vertically-varying, compacting stack of sediments and that a considerable number of wells with wireline data passed through this section, we feel that a ±5% error in migration velocity is a conservative estimate of the error. In fact, a 700 m error in lateral positioning requires a ±17.5% error in migration velocity, much too large for a target in a 1D geologic setting above salt. Furthermore, the movement of the pulse observed in the 1985 and 1992 data, if an artifact of incorrect migration velocities, would require that the errors in the two data sets be negatively correlated. For example, if the 1985 data had a −5% error in migration velocity (under-migration) and the 1992 data had a +5% error in migration velocity (over-migration), the residual mis-positioning between the two surveys would still only be 400 m. If both surveys had a +5% error in migration velocity, there would be no apparent lateral movement. We therefore conclude that 1 km of movement up the B-fault is significant enough to stand out in the presence of typical positioning errors due to incorrect migration velocities.

CONCLUSION

At a location on the B-fault plane at the South Eugene Island Block 330 field, where anomalously high pore pressures have been reported in the fault zone (Anderson *et al.*, 1995; Losh *et al.*, 1999), areas of high reflectivity appear to move up the fault-plane, as would be expected for an ascending, pressure-driven fluid pulse. The seismic waves are able to sense these different pressure domains due to the effective stress controlling the elastic properties of the soft Plio-Pleistocene sediments (Haney *et al.*, 2005). This observation gives additional credence to the dynamic fluid injection hypothesis (Whelan *et al.*, 2001) and points to natural flow processes in sedimentary basins that occur on production time scales.

The movement seen in the 1985 and 1992 seismic data warrants more extensive study of the faults at South Eugene Island. One possibility in the future is to go to the fault scarps on the ocean floor with a small submersible and take samples of the fluids coming directly out of the fault scarps, since Anderson *et al.* (1994) report oil seeps that correlate with their location. The shallow water depth at South Eugene Island (< 100 m) makes such an investigation using a submersible possible. Submersibles have proven to be useful in sub-sea geological studies, as shown by Chaytor *et al.* (2004) in the Pacific ocean and Roberts (2001) in the Gulf of Mexico. Other data sets to incorporate into future fault studies are prestack data, especially for doing AVO analysis on a fault-plane reflection, and microseismicity data. Without question, future studies on faults should incorporate time-lapse measurements to capture the essence of faults as dynamic and quickly-changing zones.

ACKNOWLEDGMENTS

Supported by a research grant from Shell International Exploration and Production, whom also provided the 1992 seismic data. The 1985 data, originally acquired by Pennzoil, is currently in the public domain. We thank R. Anderson, W. He, S. Naruk, J. Busch, and S. Wilkins for help and discussions.

REFERENCES

Anderson, R. N., He, W., Hobart, M. A., Wilkinson, C. R., & Roice, H. R. 1991. Active fluid flow in the Eugene Island area, offshore Louisiana. *The Leading Edge*, **10**, 12–17.

Anderson, R. N., Flemings, P., Losh, S., Austin, J., & Woodhams, R. 1994. Gulf of Mexico growth fault drilled, seen as oil, gas migration pathway. *Oil & Gas Journal*, **92**, 97–103.

Anderson, R. N., Billeaud, L. B., Flemings, P. B., Losh, S., & Whelan, J. K. 1995. *Results of the Pathfinder Drilling Program into a Major Growth Fault, Part of the GBRN/DOE Dynamic Enhanced Recovery Project in Eugene Island 330 Field, Gulf of Mexico.* Lamont-Doherty Earth Observatory: Global Basins Research Network.

Cervelli, P., Segall, P., Johnson, K., Lisowski, M., & Miklius, A. 2002. Sudden aseismic fault slip on the south flank of Kilauea volcano. *Nature*, **415**, 1014–1018.

Chaytor, J. D., Goldfinger, C., Huftile, G. J., Romsos, C. G., & Meiner, M. 2004. Submerged Shorelines of Pilgrim Banks and the Northern Channel Islands, Southern California Continental Borderland, as Vertical Tectonic Strain Markers. *In: EOS Trans. AGU, 85(47), Fall Meet. Suppl., Abstract T13C-1398.* AGU.

Dobrin, M. B. 1976. *Introduction to geophysical prospecting.* New York: McGraw-Hill.

Elliott, D. A. 1999. *Hydrofracture Permeability Response and Maximum Previous Consolidation Stress Estimations for Faulted and Micro-Faulted Silty-Shales Taken from the Eugene Island Block 330 Field Pathfinder Well in the Gulf of Mexico.* MSc Thesis, University of California, San Diego.

Finkbeiner, T., Zoback, M. D., Stump, B., & Flemings, P. 2001. Stress, pore pressure and dynamically-constrained hydrocarbon column heights in the South Eugene Island 330 Field, Gulf of Mexico. *AAPG Bulletin*, **85**, 1007–1031.

Haney, M., Sheiman, J., Snieder, R., Naruk, S., Busch, J., & Wilkins, S. 2004. Fault-plane reflections as a diagnostic of pressure differences in reservoirs: a case study from South Eugene Island Block 330. *Pages O-07 of:* Engelder, T., Konstanty, J., & Grauls, D. (eds), *Proceedings of the EAGE special session on Fault and Top Seals.* EAGE.

Haney, M., Snieder, R., & Ampuero, J. 2005. Spectral element modeling of fault-plane reflections arising from fluid pressure distributions. *in: CWP Project Review.*

Holland, D. S., Leedy, J. B., & Lammlein, D. R. 1990. Eugene Island Block 330 field-USA, offshore Louisiana. *Pages 103–143 of:* Beaumont, E. A., & Foster, N. H. (eds), *Structural traps III, tectonic fold and fault traps: AAPG Treatise of Petroleum Geology Atlas of Oil and Gas.* AAPG.

Hooper, E. C. D. 1991. Fluid migration along growth faults in compacting sediments. *J. of Pet. Geology*, **14**, 161–180.

Losh, S., Eglinton, L., Schoell, M., & Wood, J. 1999. Vertical and Lateral Fluid Flow Related to a Large Growth Fault. *AAPG Bulletin*, **83**, 244–276.

Losh, S., Phipps-Morgan, J., & Haney, M. 2005. High-Pressure Fluid Pulses in an Active Fault, Offshore Louisiana Gulf of Mexico. *In: AGU Chapman Conference on radiated energy and the physics of earthquake faulting.*

Miller, S. A., Collettini, C., Chiaraluce, L., Cocco, M., Barchi, M., & Kaus, B. J. P. 2004. Aftershocks driven by a high-pressure CO_2 source at depth. *Nature*, **427**, 724–727.

Nur, A., & Walder, J. 1992. Hydraulic Pulses in the Earth's Crust. *Pages 461–474 of:* Evans, B., & Wong, T.-F. (eds), *Fault Mechanics and Transport Properties of Rocks.* San Diego: Academic Press.

Revil, A., & Cathles, L. M. 2002. Fluid transport by solitary waves along growing faults: A field example from the South Eugene Island Basin, Gulf of Mexico. *Earth* *and Planetary Science Letters*, **202**, 321–335.

Rice, J. R. 1992. Fault Stress States, Pore Pressure Distributions, and the Weakness of the San Andreas Fault. *Pages 475–503 of:* Evans, B., & Wong, T.-F. (eds), *Fault Mechanics and Transport Properties of Rocks*. San Diego: Academic Press.

Roberts, H. H. 2001. Fluid and gas expulsion o the northern Gulf of Mexico continental slope: Mud-prone to mineral-prone responses. *Pages 131–143 of:* Paull, C. K., & Dillon, W. P. (eds), *Natural Gas Hydrates: Occurence, distribution, and dynamics*. Geophysical Monograph 124. San Francisco: AGU.

Sibson, R. H. 1990. Conditions for fault-valve behavior. *Pages 15–28 of:* Knipe, R. J., & Rutter, E. H. (eds), *Deformation Mechanisms, Rheology and Tectonics*. Geological Society Special Publication, no. 54. Oxford: Alden Press.

Whelan, J. K., Eglinton, L., Kennicutt, II, M. C., & Qian, Y. 2001. Short-time-scale (year) variations of petroleum fluids from the U. S. Gulf Coast. *Geochim. Cosmochim. Acta*, **65**, 3529–3555.

Yilmaz, Ö. 1987. *Seismic Data Processing*. Tulsa: Society of Exploration Geophysicists.

Spectral element modeling of fault-plane reflections arising from fluid pressure distributions

Matthew Haney[1], Roel Snieder[1], and Jean-Paul Ampuero[2]
[1] *Center for Wave Phenomena, Colorado School of Mines, Golden, CO 80401*
[2] *Geosciences Department, Princeton University, Princeton, NJ 08544*

ABSTRACT

In order to better understand the origin of fault-plane reflections in compacting sedimentary basins, we have numerically modeled the elastic wavefield via the spectral element method (SEM) for several different fault models. Using well log data from the South Eugene Island field, offshore Louisiana, we derive empirical relationships between the elastic parameters (e.g., P-wave velocity, density) and effective stress along both normal compaction and unloading paths. These empirical relationships guide the numerical modeling and allow us to investigate the effect of fluid pressure. We chose to simulate the elastic wave equation via SEM since irregular model geometries can be accommodated and slip boundary conditions at an interface, such as a fault or fracture, are implemented naturally. The method of including a slip interface retains the desirable qualities of SEM in that it is explicit in time and does not require the inversion of a large matrix.

We perform a complete numerical study by forward modeling shot gathers over a realistically-sized Earth model using SEM and then processing the simulated data to reconstruct post-stack time-migrated images of the kind that are routinely interpreted in the petroleum industry. We dip filter the seismic images to highlight the fault-plane reflections prior to making amplitude maps on the fault plane. With these amplitude maps, we compare the reflectivity from the different fault models to diagnose which contributes most to the observed fault reflectivity. To lend physical meaning to the value of compliance for a slipping fault, we propose an equivalent-layer model under the assumption of weak scattering. This allows us to use the empirical relationships between density, velocity, and effective stress from the South Eugene Island field to relate a slipping interface to an amount of pore pressure in a fault zone.

Key words: fault zones, fluid pressures, spectral element method

INTRODUCTION

Seismic data acquisition and processing have evolved to the point that fault-plane reflections are often imaged under favorable conditions, such as above salt in the Gulf of Mexico (Liner, 1999). Reflections originating from fault zones hold important information about fluid movement along faults or the capacity of a fault to act as a seal (Haney *et al.*, 2004). For prospect evaluation, faults are associated with uncertainty in petroleum systems by virtue of their split personality as both hydrocarbon traps and pathways for hydrocarbons to move from deep kitchens into shallower, economically producible reservoirs. Any light that seismic data can shed on the situation would be useful.

To gain a stronger grasp on the factors at play in causing fault-plane reflectivity, we have pursued a complete numerical study of seismic wave interaction with fault models. By complete, we do not simply model the entire elastic wavefield with high fidelity, but additionally process the data back into its time-migrated image, which is the point at which many geoscientists in the petroleum industry gain access to and begin examining seismic data. We model the wavefield with an implementation of the spectral element method (SEM) written by Dimitri Komatitsch and Jean-Pierre Vilotte at the Institut de Physique du Globe in Paris, France. Further improvements have been made to the original code by the third author in the course of his graduate work (Ampuero, 2002). Processing of the elastic wavefield output by the SEM code has been accomplished with Seismic Un*x (Stockwell, 1997).

We sketch the theory behind SEM and, after discussing the dip-filtering step we employ to highlight the fault-plane reflections, present results for different fault models. These models represent examples and combinations of three types of heterogeneity expected at faults. These three types are:

(i) juxtaposition (sand/shale or shale/sand) contacts
(ii) pressure contrast ΔP across the fault
(iii) a slipping fault

We expect from the outset that these various types of heterogeneity show up differently in dip-filtered seismic images. For instance, since the juxtaposition contacts exist over the length scale of a typical bed thickness and have positive (sand/shale) or negative (shale/sand) reflection coefficients, the smoothing of the dip-filter (Oppenheim & Schafer, 1975) should act to suppress their contribution to the fault-plane reflectivity. In fact, the specular contribution to the average reflected intensity from a fault-plane between two vertically shifted layered media with a random reflection coefficient series is zero. In practice, away from this idealized model, reflectivity from juxtaposition contacts should be relatively suppressed compared to the other two models. This is desirable since the juxtaposition contacts do not carry information on the intrinsic properties of the fault zone. The other two types of heterogeneity, pressure contrasts and slip at the fault plane, which are related to pore pressure distributions at the fault, are not attacked by the dip filter in the same way as are the juxtaposition contacts.

In the first section of this paper, we discuss empirical relationships between pore pressure and three basic rock properties - porosity, density, and sonic velocity. The data for this analysis come from wells drilled at the South Eugene Island field, offshore Louisiana. These relationships form the basis for the models used in the subsequent SEM simulations. The fact that pore pressure largely controls rock matrix properties in compacting sedimentary basins allows methods for imaging seismic reflections to indirectly measure spatially varying pore pressure distributions. The variation of the three rock properties with effective stress reveals a hysteretic behavior that occurs during the compaction of sediments. Evidence for both plastic (irreversible) and elastic (reversible) deformation exists in the available well data and pressure tests. These two regimes point to different underlying causes of overpressure (Hart *et al.*, 1995). For these dual deformation mechanisms, we construct two empirical relationships between each rock property and pore pressure - one valid for each regime.

Vertical effective stress

Pore pressures that exceed the hydrostatic pressure, or overpressures, lead to a lowering of density and seismic velocity and may contribute to the reflectivity associated with fault zones. Pennebaker (1968) was among the first geoscientists to demonstrate the ability of seismic stacking velocities to detect fluid pressures in the subsurface. Terzaghi (1943), however, had previously discussed the basic principle, that of an effective stress acting on the rock frame. According to Terzaghi's principle, the effective stress determines rock properties (e.g., *P*-wave velocity). Terzaghi defined the effective stress to be the difference between the confining stress, σ_v, and the pore pressure p:

$$\sigma_d = \sigma_v - p. \tag{1}$$

The subscript v stands for *vertical* since, in extensional regimes, the maximum stress is in the vertical direction (the weight of the overburden). The quantity σ_d is also called the differential stress. Equation (1) states that rocks of similar composition but at different confining stress and pore pressure have the same velocity so long as the difference between the confining stress and pore pressure is the same. Hence, high pore pressure, which lowers effective stress, leads to lower seismic velocities.

Following the work of Terzaghi, rock physicists began to question whether the effective stress governing rock properties is not simply the difference between the confining stress and the pore pressure (Wang, 2000). Today, the most general effective-stress law is instead

$$\sigma_e = \sigma_v - np, \tag{2}$$

where the parameter n is called the *effective stress coefficient.* Carcione *et al.* (2001) state that the value of n can differ for each physical quantity (e.g., permeability, compressibility, or shear modulus), and that it depends linearly on the differential stress of equation (1). Currently, the effective-stress coefficient is a controversial topic that is still being sorted out by the rock physics community. For the remainder of this paper, we do not distinguish between differential stress, σ_d, and effective stress, σ_e; that is, we take $n = 1$ in equation (2).

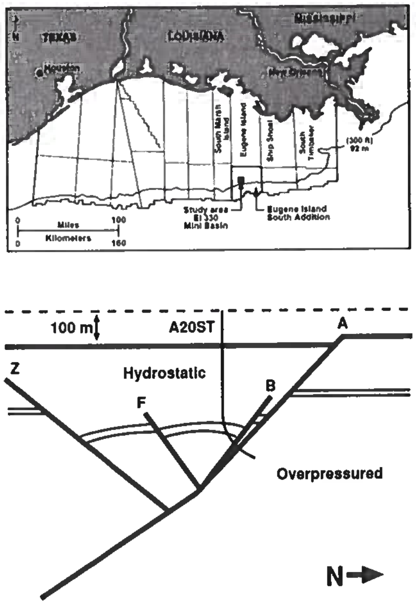

Figure 1. Regional map (top), from Anderson *et al.* (1995), and cartoon depth section (bottom) of the subsurface at South Eugene Island. The four main faults discussed in this thesis are shown in the bottom panel as the A, B, F, and Z faults. Throw across the faults is depicted by the layer running from left to right. Most of the wells at South Eugene Island were drilled into the shallow, hydrostatic section; the A20ST well was unusual in that it was continued through the A-fault system and into the deep overpressured compartment.

1 POROSITY VERSUS DEPTH

As suggested by its name, compaction acts to reduce the porosity of sediments as they are buried; however, this process can continue only as long as fluids in the diminishing pore space are allowed to be expelled. Such would be the case in normally pressured, hydrostatic sediments in which the fluids are in communication up to the seafloor. Once the movement of the fluids out of the pore space is opposed, as in a compartment sealed-off by low permeability or high capillary-entry-pressure shales or fault gouge, the porosity remains constant with burial depth if the fluid is more or less incompressible. This situation is called *undercompaction* (Huffman, 2002). Undercompaction means the sediments are "frozen" in time and are simply buried in their unchanging earlier compaction state (Bowers, 1995). To compound the situation, if fluid from outside the undercompacted sediments is pumped into the pore space, or if hydrocarbons are generated from within the undercompacted sediments, a process called *unloading* occurs (Huffman, 2002). Whereas undercompaction can only cease the reduction of porosity (Bowers, 1995), unloading can actually reverse the trend and increase porosity. Although unloading can reverse the trend, it cannot reclaim all of the previously lost porosity. This is because the compaction process has a large *irreversible* component. In contrast, unloading and loading of sediments by pumping fluid into and then depressurizing the pore space is a reversible process, insofar as the fluid does not cause hydrofracturing.

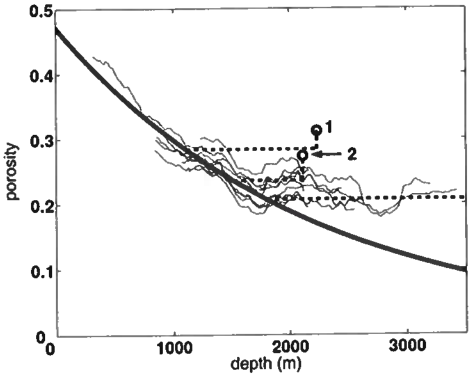

Figure 2. Porosity versus depth at South Eugene Island. The thick, solid line is the best-fit normal compaction trend using Athy's Law (Athy, 1930). The faint solid lines are density-derived porosity values from 11 wells at South Eugene Island. To obtain the porosity, we assume that the solid grains have a density of 2650 kg/m^3 and the fluid has a density of 1000 kg/m^3, as in Revil and Cathles (2002). There is a clear break from the shallow, exponentially decreasing porosity trend at a depth of 1800 m, at which point the porosity remains constant with increasing depth, as shown by the flat dashed line. The two circles are density-derived porosities from the upthrown block to the north of the minibasin at South Eugene Island. The dashed lines connecting the circles to the main compaction trend are the interpreted porosity histories of the samples. They show a period of undercompaction, depicted as a horizontal line deviating from the normal compaction trend, followed by a vertical unloading path due to a late-stage pore-pressure increase.

We have examined wireline data taken in wells at the South Eugene Island field, offshore Louisiana, for indicators of overpressure, such as constant porosity as a function of depth. Previous work by Hart *et al.* (1995) shows the crossover from hydrostatic to overpressured conditions in porosities derived from sonic velocities. We take a slightly different, perhaps more straightforward approach based on the density log. The South Eugene Island field is a Plio-Pleistocene minibasin formed by salt withdrawal and has yielded more than 300 million barrels of oil in its lifetime. A cartoon depiction of the subsurface at South Eugene Island is displayed in Figure 1, in addition to a regional map. The main part of the field is a vertical stack of interbedded sand and mostly shale layers bounded by two large growth faults to the north and south.

Figure 2 shows porosity derived from density logs taken in the following wells at South Eugene Island: A13, A20ST, A14OH, A15, A23, A6, B10, B1, B2, B7, and B8. Because the geology in the minibasin is essentially horizontally layered, we ignore the fact that some wells may be miles away from each other and simply look at the depth variation of their porosity. In all the well logs shown in this paper, we have done some smoothing with depth (over $\sim$ 100 m) to remove any short-range lithologic influences (e.g., sand versus shale) on the density and velocity. To obtain the porosity from the density log, we take the solid grains to have a density of 2650 kg/m^3 and the fluid to have a density of 1000 kg/m^3, as in Revil and Cathles (2002). There is a clear break from the shallow, decreasing porosity trend at a depth of 1800 m. Based on the work of Stump *et al.* (1998), we assume that this is the onset of overpressures in the sedimentary section, beneath a shale bed located above a layer called the JD-sand. We fit an exponential trend to the porosity values above 1800 m, known as Athy's Law (Athy, 1930), to get the normal compaction trend in the hydrostatically pressured sediments

$$\phi^c(z) = 0.47\ e^{-0.00046\ z}, \tag{3}$$

where, in this equation, the depth z is in meters. The superscript c in equation (3) refers to the fact that this functional relationship characterizes normal compaction. In the porosity-versus-depth plot of Figure 2, this relationship holds for any movement towards the right on the normal compaction curve and any purely right-going horizontal deviations from the normal compaction curve. For purely right-going horizontal deviations, the depth z used in equation (3) is equal to the depth at which the horizontal deviation started. The two circles in Figure 2, represent samples taken in the A20ST well and are connected to the normal compaction curve by both horizontal and vertical lines. The vertical lines show the departure of the samples from the normal compaction trend. We return to these in the next section.

The sediments deeper than 1800 m in Figure 2 maintain a nearly constant porosity of around 0.2 during subsequent burial (a horizontal deviation from the compaction trend). Though the depth of the sediments increases with burial, the effective stress experienced by the sediments does not seem to change. Hence, the additional weight of the overburden with increasing depth is borne by the fluids trapped in the pore space. As a result, the pore pressure increases with the vertical gradient of the overburden stress and is said to have a *lithostatic gradient.* This point is illustrated graphically in Figure 3. In this plot, we make the crude approximation that the lithostatic gradient (or total weight density), ρg, is twice as large as the hydrostatic gradient (or fluid weight density), $\rho_f g$, with g the acceleration of gravity. Since $\rho g = 2\rho_f g$, the effective stress is equal to the hydrostatic stress down to 1800 m. At that point, the effective stress stays constant with depth due to undercompaction; therefore, the pore pressure must increase at the rate of the lithostatic stress in order to satisfy Terzaghi's law, equation (1). In doing so, overpressure, or pore pressure in excess of hydrostatic, is created below 1800 m.

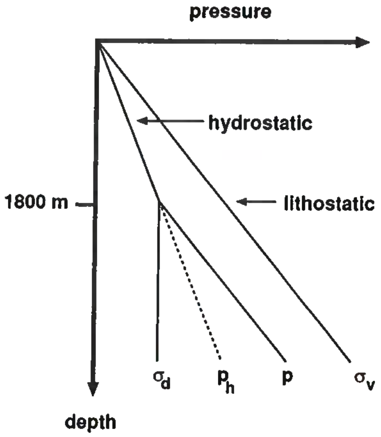

Figure 3. A depth section of the pressure regime for pure undercompaction. The symbols are as follows: σ_d is the effective stress, P_h is the hydrostatic pressure, P is the pore pressure, and σ_v is the overburden, or lithostatic, stress. Note that, before 1800 m, the effective stress stays constant, as seen from the porosity versus-depth-plot in Figure 2, and the pore pressure increases at a rate equal to that of the overburden stress.

2 DENSITY VERSUS VERTICAL EFFECTIVE STRESS

Since density is a parameter widely used in the field of seismic wave propagation, we study the variability of the bulk density in this section. By looking at bulk density, we also avoid the assumption concerning the solid and fluid densities needed to obtain the porosity. In contrast to the preceding section, we want to see how density changes with effective stress, instead of depth. To accomplish this, we take only the measurements that are shallower than 1800 m, where the pore pressure is, by all indications, hydrostatic. Therefore we know the pore pressure and can calculate the effective stress. In overpressured compartments, since the pore pressure is unknown, direct measurements by Repeat Formation Tests (RFTs) are necessary to calculate the effective stress.

We rewrite equation (3) in terms of density and effective stress using the relationships

$$\rho = \rho_s(1-\phi) + \phi\rho_f, \tag{4}$$

and

$$\sigma_d = \rho_f g z, \tag{5}$$

where ρ is the bulk density and ρ_s and ρ_f are the densities of the solid and fluid components. Note that the relationship for σ_d holds only under hydrostatic con-

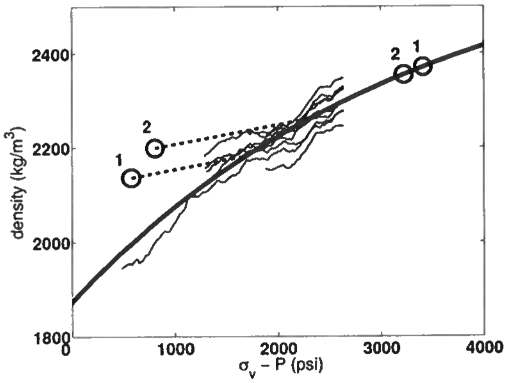

Figure 4. Density versus effective stress at South Eugene Island. The thick solid line is the same normal compaction trend shown in Figure 2, except transformed into density and effective stress. The faint solid lines are also the same as in Figure 2, except that they are now limited to the hydrostatic depths down to 1800 m. The circles represent two pressure measurements, labeled 1 and 2, which were made in the overpressured upthrown block where a density log also existed. For each pressure measurement, we plot the data point twice - one where it should lie on the normal compaction curve were it to have been normally pressured, and the other where it actually does plot because of severe overpressure. Note that sample 1 is from a greater depth than sample 2.

ditions. From these relationships and equation (3), we obtain the normal compaction curve for density

$$\rho^c(\sigma_d) = \rho_s - 0.47\ (\rho_s - \rho_f)\ e^{-0.0003\sigma_d}, \qquad (6)$$

where ρ_s and ρ_f are the densities of the solid and fluid components, taken as 2650 kg/m^3 and 1000 kg/m^3 respectively, and σ_d is in psi. We plot this normal compaction curve in Figure 4 together with the density measurements. Also, in Figure 4, we show as circles two data points obtained from RFT pressure measurements and density log measurements in the overpressured upthrown block. We show the circles in two locations - one on the normal compaction trend where they would plot if the measurements were at hydrostatically pressured locations, and the other where they actually plot because of severe overpressures being present in the upthrown block.

At this point, we don't know exactly how the samples taken in the upthrown block came to be off the normal compaction trend. Using a laboratory measurement of the unloading coefficient by Elliot (1999) on a core sample taken near the locations of samples 1 and 2, the path that these samples took to their present locations can be estimated. Elliot (1999) characterized the unloading, or elastic swelling, for the porosity of the core samples to be

$$\phi^u(\sigma_d) = \phi_0\,(1 - \beta\sigma_d)\,, \qquad (7)$$

where ϕ_0 and β characterize the deviation of the unloading path from the normal compaction trend. Note the superscript u, in contrast to equation (3), indicating the unloading path instead of the normal compaction trend. Elliot (1999) found that $\phi_0 = 0.37$ and $\beta = 0.98 \times 10^{-8}$ Pa^{-1} for the unloading path. Though these parameters describe the porosity, we use them to find the slope of the unloading path for density using the relationships between porosity and density described earlier. After finding this slope, we can construct the unloading path for the density from equation (6) and the slope

$$\begin{aligned}\rho^u(\sigma_d) \quad = \quad & 0.04\ (\sigma_d - \sigma_{max}) + \rho_s \\ & -0.47\ (\rho_s - \rho_f)\ e^{-0.0003\sigma_{max}}. \qquad (8)\end{aligned}$$

This expression contains an extra parameter σ_{max} that refers to the value of the effective stress when the sample began to be unloaded. We do not know σ_{max} for samples 1 and 2, but we do know that σ_{max} must lie on the main compaction trend. Hence, we can construct linear unloading paths for the density, as shown by the dashed lines in Figure 4. With these unloading paths, we can then find the value for the maximum past effective stress σ_{max}. It is worth mentioning that the maximum past effective stress for sample 1 comes out to be ~ 1500 psi by our approach of using Elliott's experimental results. In an independent measurement, Stump *et al.* (2002) performed uniaxial strain tests on a core sample taken from the same location as sample 1 to find the maximum past effective stress. Stump *et al.* (2002) report a value of 1248 psi for this sample, close to our estimate of ~ 1500 psi; visually, the discrepancy lies within the error bars of the normal compaction curve's fit to the density log data.

With the estimate of the maximum past effective stress, we can also return to Figure 2 and find the depth at which samples 1 and 2 left the normal compaction trend, since in the hydrostatic zone the depth is a linearly scaled version of the effective stress. These depths correspond to a slightly lower porosity than that of samples 1 and 2. We interpret this as being the result of a late stage porosity increase and represent it as a vertical unloading path for samples 1 and 2 in Figure 2.

3 SONIC VELOCITY VERSUS VERTICAL EFFECTIVE STRESS

For the purposes of modeling faults and to make inferences about the distribution of pore pressure from seismic interval velocity inversions, accurate pore-pressure-versus-velocity relationships are critical (Dutta, 1997). In general, sonic velocity has a normal compaction curve and unloading paths as a function of effective stress that are similar to those we just described for the density well log data. To obtain these relationships, we proceed as for the density logs: 1) We take 12 shallow wells to make up a data set of sonic velocity versus effective stress. 2) We select the depth range with hydrostatic pressures and plot the sonic velocity versus effective stress. 3) We fit this with a power law relation for the normal com-

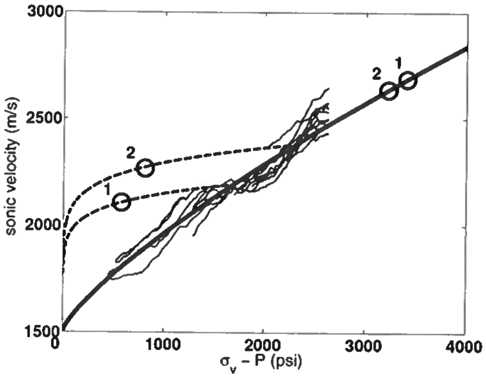

Figure 5. Sonic velocity versus effective stress at South Eugene Island. The thick solid line represents the normal compaction curve fitted to the shallow well data, shown in the faint solid lines. We also plot samples 1 and 2 both where they should fall on the normal compaction trend, were they to be normally pressured, and where they actually plot due to the severe overpressure where they were obtained. Using the estimate for past maximum effective stress from the density plot and the Bowers-type relation (Bowers, 1995) shown in equation (10), we are able to construct the velocity unloading curves, shown as dashed lines.

paction trend. 4) We then look at where the two samples from the overpressured upthrown block lie and construct unloading curves using the estimate for the maximum past effective stress that we obtained in the previous section on density. The wells we use for characterizing the sonic velocity come from A20ST, A14OH, A23, A6, B10, B1, B2, B7, B8, A1, B14, and B20.

In Figure 5, we plot the normal compaction trend for sonic velocity as a thick solid line described by the power law equation (Bowers, 1995)

$$v_p^c(\sigma_d) = 1500 + 2.3\, \sigma_d^{0.77}, \tag{9}$$

where v_p is in m/s and σ_d is in psi. Note again the superscript c for the normal compaction relation. We also construct the unloading curve for v_p following the relationship first suggested by Bowers (1995)

$$v_p^u(\sigma_d) = 1500 + 2.3 \left[\sigma_{max}\left(\frac{\sigma_d}{\sigma_{max}}\right)^{1/6.2}\right]^{0.77}, \tag{10}$$

where σ_d and σ_{max} are in psi and v_p is again in m/s.

To model elastic waves, one other parameter is needed in addition to ρ and V_P; for instance, a seismologist would naturally want the shear velocity. In the absence of information on the shear wave velocity v_s and pressure in the shallow, hydrostatic sediments, we assume that

$$v_s(\sigma_d) = v_p(\sigma_d) - 1500, \tag{11}$$

where this relationship holds on both the normal compaction curve and the unloading path. The data presented by Zimmer *et al.* (2002) for unconsolidated sands supports this assumption, in that the dependence they found for v_s on effective stress is essentially a down-shifted version of the v_p curve. An additional piece of supporting evidence comes from the only v_s data available at South Eugene Island, a shear log from the A20ST well, where samples 1 and 2 were taken. There, the ratio of v_p/v_s from the sonic and shear logs falls between 3 to 3.5 in the overpressured upthrown block. Inserting the values for v_p at samples 1 and 2 into equation (11) to get v_s and finding the corresponding ratio of v_p/v_s, we get $v_p/v_s = 3.48$ at sample 1 and $v_p/v_s = 2.96$ at sample 2, within the range of the ratios observed in the sonic and shear logs.

To summarize, we have established two empirical relationships between each of three basic rock properties and pore pressure at the South Eugene Island field. Most important for subsequent numerical modeling of wave propagation, we have found relationships for the density ρ and the sonic velocity v_p on both the normal compaction and unloading paths. Without shallow information on the shear velocity v_s, we must make the assumption that it is a down-shifted version of the $v_p(\sigma_d)$ relationship. From looking at the density-derived porosity-versus-depth-relationship, we are able to conclude that the deep, overpressured sediments below the JD-sand are predominately overpressured because of compaction disequilibrium, since their porosity did not change appreciably with depth. In contrast, both compaction disequilibrium and unloading have contributed to the current overpressured state of the sediments on the upthrown side. The latter conclusion is in agreement with a previous study by Hart *et al.* (1995) on porosity and pressure at South Eugene Island. We use the empirical relationships between the elastic parameters and fluid pressure to simulate fault-plane reflections from different pressure distributions in the subsurface.

4 THE SPECTRAL ELEMENT METHOD

Numerical modeling of wave propagation in the Earth can be based on either the weak (Zienkiewicz & Taylor, 2000) or strong (Boore, 1970) forms of the elastodynamic equations of motion. By weak and strong, we mean the integrated or differential forms of the equations of motion. The spectral element method (SEM), though based on the weak form, combines favorable aspects of both strong and weak formulations. For instance, SEM naturally handles general geometries and exotic boundary conditions. In the finite-difference method (based on the strong form), it is notoriously difficult to implement a linear-slip boundary condition (Coates & Schoenberg, 1995) or any general boundary condition for that matter (Boore, 1970; Kelly *et al.*, 1976). On the other hand, SEM does not require the inversion of a large matrix, a property usually identified with finite-difference methods. Formally, this last property of SEM means that its mass matrix is diagonal and its computational cost is relatively small. Note that

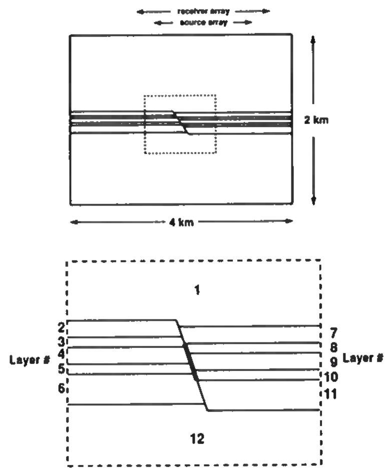

Figure 6. The entire numerical model with a zoom-in of the normal fault. The zoom area is shown on the entire numerical model with a dashed rectangle. The lengths of the source and receiver arrays are shown by extended arrows. Eleven sources evenly spaced over 2000 m (200-m shot interval) and 241 receivers over 3000 m (12.5-m receiver interval). In the zoom, the layers are labeled with numbers 1-12 corresponding to the material properties for models listed in subsequent tables. For models with a slipping fault, the portion of the fault plane that slips is shown by a thicker line in the zoom.

SEM does this in a way similar to mass-lumping (Karniadakis & Sherwin, 1999), which has been used to diagonalize finite-element schemes. SEM has the additional property of spectral convergence, meaning that, as the polynomial order of the basis functions is increased, the numerical error goes down exponentially (Karniadakis & Sherwin, 1999).

The term "spectral element" indicates that SEM is a mixture of finite-element and spectral methods (Komatitsch & Vilotte, 1998). As a result, there are two parameters relevant to the mesh in SEM: the size of the elements and polynomial degree ($n-1$, where n is the number of zero crossings of the basis functions used within each element). Komatitsch and Tromp (2003) refer to these parameters when they speak of the global mesh and the local mesh. Concerning the local mesh, there is a known trade-off between accuracy and numerical cost (Seriani & Priolo, 1994), which suggests that polynomial degrees no higher than 10 should be used within the elements. For the numerical examples in this paper, we use a polynomial degree of eight.

5 MODELING OF A FAULT

As an example of the ability of SEM to model seismic scale structures, we discuss a complete modeling and processing sequence for a simple fault model. The SEM forward modeling has been run in serial (one node for each shot) on a 32-processor pentium IV Xeon (3.0-GHz) cluster. All of the processing has been performed on a workstation using the Seismic Un*x package (Stockwell, 1997). Figure 6 depicts the geometry of the model. The normal fault we model has a vertical throw of 20 m, a value characteristic of a small fault. The model shown in Figure 6 has been previously studied by Townsend *et al.* (1998) in order to assess changes in seismic attributes caused by faults disrupting the lateral continuity of events.

We mesh the interior of the computational grid shown in Figure 6 using a freely available mesh program developed by INRIA, called EMC2. The program can be downloaded at:

http://www-rocq.inria.fr/gamma/cdrom/www/emc2/eng.htm.

For the examples in this paper, we use a semi-structured mesh since the fault geometries modeled are not overly complex. A semi-structured mesh is desirable when possible since the accuracy of SEM depends on the Jacobian of the transformation between a generally shaped element and a standard rectangular element over which the integration is performed. Though the mesh has structure, it honors the slanted boundaries of the fault. After initial construction of the mesh, the quadrangle elements are regularized so that their shapes mimic rectangles as closely as possible. At the fault, the possibility exists for the fault to experience linear-slip (Schoenberg, 1980). With SEM, we can incorporate this aspect by using a split-node (Andrews, 1999). In Appendix A, we show how to incorporate a linear-slip interface into a finite-element algorithm with a split-node. We also show that the presence of a linear-slip interface modifies the numerical stability criterion, a fact that is also true for SEM.

Since the SEM code is elastic, both primary and converted waves show up on the vertical component of the displacement seismograms. We mute the converted waves in order to proceed with conventional P-wave time-processing. We subtract off the direct waves by running a homogeneous subsurface simulation with the elastic properties of layer 1 of Figure 6. After this step, we perform a geometrical-spreading correction, NMO, DMO, and stack to simulate zero-offset data. With the simulated zero-offset section, we proceed with a constant-velocity migration using the velocity of the overburden (layer 1). Hence, a source of error in this simulation originates from the slight undermigration of the deepest reflectors and the fault-plane reflection. We chose to migrate with constant velocity since we have interpreted time-migrated seismic sections in the Gulf of Mexico (Haney *et al.*, 2004) and wanted the SEM modeling to mimmick the data as closely as possible. With this full suite of forward modeling and processing capabilities, we apply SEM to study various normal fault models. Before going into the details of the mod-

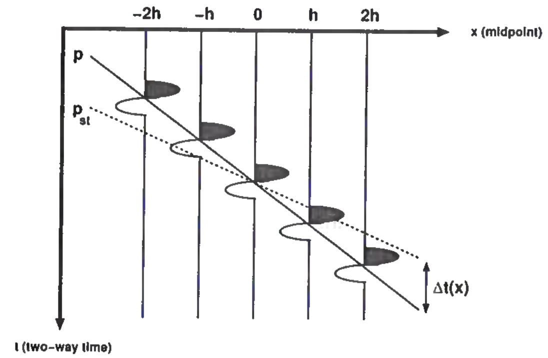

Figure 7. Dipping event with true dip direction given by the slanted solid line. The event is summed along a direction given by the dashed line, and the result is placed at the intersection of the two lines at the center trace. When there is a difference in the two dips, the true dip p and the stacking dip p_{st}, a time shift Δt is induced that varies linearly with midpoint x. In this example, the seismic data exist at equally-spaced, discrete midpoint locations.

eling, though, we present the type of dip-filter we use to isolate the migrated fault-plane reflections.

6 DIP FILTERING

Using an array-based approach, we show in this section the form of the dip filter that we apply to migrated images to accentuate the fault-plane reflections. Figure 7 shows a dipping event in a post-stack seismic image. The function of the dip filter is to stack along the dashed line and place the stack result at the intersection of the solid and dashed lines; where the coordinate system is chosen such that the midpoint is equal to 0. Note that, in Figure 7, the dip filter emphasizes a direction different from the dip of the event. This difference induces a time shift at the m-th input trace (shown as a vertical arrow). Suppose that the true dip, the dip of the event, is p (dimension s m^{-1}) and the dip of the stacking curve is p_{st}. The time shift at the m-th input trace is thus

$$\Delta t_m = (p - p_{st})\, mh, \tag{12}$$

where h is the midpoint spacing and m is the discrete variable running over midpoint location. Assuming that the dipping event has a constant waveform $f(t)$, the result of the summation, $g(t)$, over the stacking curve can be written as

$$\begin{aligned} g(t) \quad = \quad & \frac{1}{2n+1}\,[f(t-\Delta t_{-n}) + \cdots + f(t-\Delta t_{-1}) + \\ & f(t) + f(t-\Delta t_1) + \cdots + f(t-\Delta t_n)]\,, \end{aligned} \tag{13}$$

where $2n+1$ is the length of the dip filter in terms of the number of traces. In the example shown in Figure 7, $n = 2$. When we again take the Fourier transform over time and move to the ω-x domain, equation (13) becomes

$$G(\omega) = F(\omega)K(\omega), \tag{14}$$

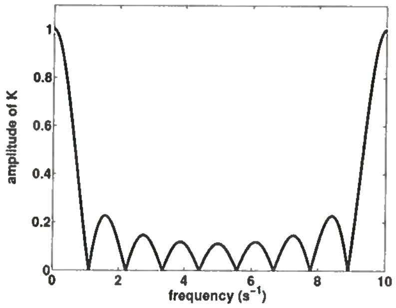

Figure 8. Representative amplitude spectrum for the dip filter. The parameters used for this plot were $n = 4$ and $\Delta t = 0.1$. Note that the first aliased frequency for this choice of Δt is at $f = 10$ Hz.

with the Fourier transforms of $f(t)$ and $g(t)$ shown as $F(\omega)$ and $G(\omega)$ and the transfer function, K, given by

$$K(\omega) = \frac{1}{2n+1} \sum_{m=-n}^{n} e^{i\omega(p-p_{st})mh}. \tag{15}$$

Since the time shifts in equation (15) are linear in m, the series can be evaluated exactly.

Using the geometric series, equation (15) can be written as

$$\begin{aligned} K(\omega) \quad = \quad & \frac{1}{2n+1}\left[\frac{1-e^{i\omega(n+1)(p-p_{st})h}}{1-e^{i\omega(p-p_{st})h}} + \right. \\ & \left. \frac{1-e^{-i\omega(n+1)(p-p_{st})h}}{1-e^{-i\omega(p-p_{st})h}} - 1\right]. \end{aligned} \tag{16}$$

Putting the first two terms in the brackets of equation (16) under a common denominator and simplifying further yields a filter similar to that obtained for convolution with a boxcar, or rectangular window (Oppenheim & Schafer, 1975)

$$\begin{aligned} K(\omega) \quad = \quad & \frac{1}{2n+1}\left[2\frac{\sin[\omega(n+1)(p-p_{st})h/2]}{\sin[\omega(p-p_{st})h/2]} \times \right. \\ & \left. \cos[\omega n(p-p_{st})h/2] - 1\right]. \end{aligned} \tag{17}$$

This filter is real because of the symmetric summation about its output point and can be better understood by making the substitution $\Delta t = (p - p_{st})h$ in equation (17)

$$\begin{aligned} K(\omega) \quad = \quad & \frac{1}{2n+1}\left[2\frac{\sin[\omega(n+1)\Delta t/2]}{\sin[\omega\Delta t/2]} \times \right. \\ & \left. \cos[\omega n\Delta t/2] - 1\right]. \end{aligned} \tag{18}$$

The amplitude spectrum of the dip filter is shown in Figure 8 for certain values of n and Δt.

A dip filter in terms of ω and k is needed to enhance fault-plane reflections on a migrated time section. The filter in equation (17) is only in terms of ω. To get the k dependence, we exploit the fact that $p = -k/\omega$ (Hatton *et al.*, 1986). This means that linear features with a dip p in the t-x domain get mapped into linear features with the negative dip in the ω-k domain. Substituting

$p = -k/\omega$ into equation (17) gives

$$K(\omega, k) = \frac{1}{2n+1}\left[2\frac{\sin[(n+1)(\omega p_{st}+k)h/2]}{\sin[(\omega p_{st}+k)h/2]} \cos[n(\omega p_{st}+k)h/2] - 1\right]. \qquad (19)$$

This is the form of a dip filter that corresponds to stacking $2n+1$ traces centered about the output point along a dip p_{st}.

7 SEM MODELING OF REFLECTED WAVES

The dip filter operation discussed in the previous section has been applied to simulated seismic images in the ω-k domain. An alternative procedure would be a combination of interpolation and slant stacking in the t-x domain; however, the ω-k dip filter is sufficiently accurate, as we show here. Figure 9 shows a plot of the simulated reflection images for the two of the models presented in this chapter next to their dip-filtered versions that highlight the fault-plane reflection. The dip filter applied to these plots has a length of 21 traces and the adata and filter have a trace-to-trace spacing of 6.25 m (the midpoint spacing); this sampling avoids any aliasing problems and attacks all events not having the dip (slope) of the fault-plane reflection. In particular, it attacks the horizontal reflections.

The upper panels of Figure 9 are for a model of a pressure difference across the fault, which acts like a traditional seismic interface. The lower panels of Figure 9 are for a model of a linear-slip interface, which, in contrast to the pressure difference model, reflects the derivative of the incident wave (see Appendix B for details). A slice cut out of the dip-filtered images in the direction perpendicular to the fault-plane (shown as a white arrow in the right-hand panels of Figure 9) helps in assessing the accuracy of the numerically simulated fault-plane reflections. In Figure 10, we plot the reflected waveforms together with either the incident wave or the derivative of the incident wave, depending on whether the model contains the pressure difference or slip at the fault. The agreement seen between the waveforms in Figure 10 demonstrates that the SEM modeling, processing, and dip-filtering together produce an accurate reflected waveform from the fault plane.

In the following three sections, we examine reflectivity from the fault plane for a juxtaposition-contrast model, three pore-pressure contrast models, and four slipping-fault models embedded in one of the pore-pressure-contrast models. The purpose of this modeling exercise is to get a feeling for which type of reflectivity should dominate at a general fault. We also perform the processing of the SEM modeled data contaminated with certain errors to see how maps of the amplitude along the fault are affected.

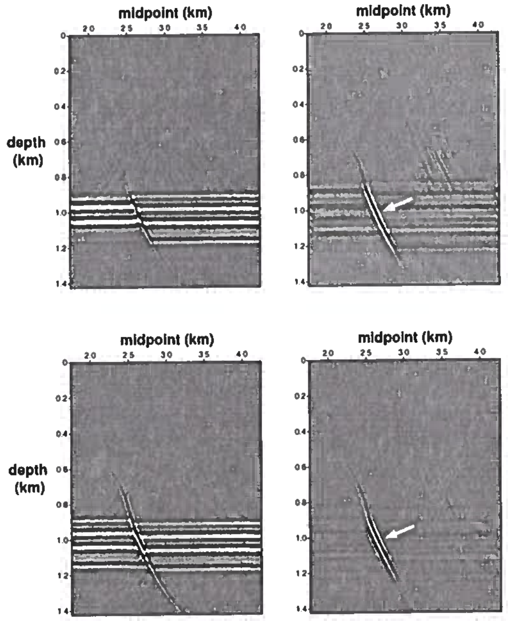

Figure 9. Migrated seismic images from Model 2 (top panels) and Slip-Model A embedded in Model 1 (bottom panels). Their dip-filtered versions, used to highlight the fault-plane reflections, are shown in the right-hand panels. Slip-Model A is for a slipping fault (see Table 5), which is embedded in Model 1 (see Table 1). Model 2 is for a pore-pressure contrast across the fault (see Table 2). The traces in Figure 10 are sliced from these images in a direction normal to the fault-plane, as shown by an arrow in the dip-filtered images. The horizontal events in the upper panels appear to be not as well suppressed as the lower panels simply because the fault-plane reflection is stronger in the bottom panel and, as a result, the amplitude clip for the display is higher.

8 AMPLITUDE OF WAVES REFLECTED FROM A JUXTAPOSITION CONTACT

Table 1 shows the parameters of a juxtaposition model for the subsurface geometry shown in Figure 6. There are two rock types in this example, an acoustically hard shale (ρ = 2280 kg/m^3, v_p = 2750 m/s, and v_s = 1250 m/s) and an acoustically soft sand (ρ = 2240 kg/m^3, v_p = 2600 m/s, and v_s = 1100 m/s). The values for the sand are taken from a well log that intersected a sand layer at the South Eugene Island field known as the JD-sand. The shale values come from the lower bounding shale beneath the JD-sand. In Figure 11, we plot these well logs at the depth of this lithologic contact. These two layers are at hydrostatic conditions, which at this depth is nominally 2800 psi.

In Figure 12, we plot the reflected amplitude from the juxtaposition model within a small window (100 ms) of the fault-plane for four different processing scenarios. The first scenario, shown in the upper-left panel of Figure 12, compares the extracted amplitude on the fault

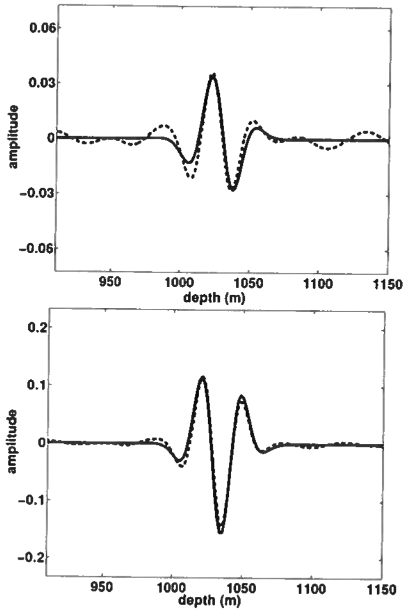

Figure 10. The reflected waves from Model 2 (top), a pore pressure contrast, and Slip-Model A embedded in Model 1 (bottom), a slipping fault, are shown in dashed lines. The reflected waveforms for these two models are different in shape. The reflected waveform for Model 2 should be the wavelet, which is plotted in the top panel as a solid line for comparison with the numerical result. The waveform for Slip-Model A embedded in Model 1 should be the the derivative of the wavelet, which is plotted in the bottom panel as a solid line for comparison. The agreement between the numerical results for the fault-plane reflections and the expected waveforms validates the sequence of modeling, processing, and dip-filtering used here.

Layer	Thickness (m)	ρ (kg/m^3)	v_p (m/s)	v_s (m/s)
1	900	2240	2600	1100
2	50	2280	2750	1250
3	30	2240	2600	1100
4	50	2280	2750	1250
5	30	2240	2600	1100
6	90	2280	2750	1250
7	50	2280	2750	1250
8	30	2240	2600	1100
9	50	2280	2750	1250
10	30	2240	2600	1100
11	90	2280	2750	1250
12	850	2240	2600	1100

Table 1. Model 1 for the SEM modeling. The throw between the upthrown (layers 2 through 6) and downthrown (layers 7 through 11) sediments is 20 m. The sediments on both sides of the fault are at hydrostatic pore pressure. The geometry of the model is given in Figure 6. The values are taken from the JD-sand and its lower bounding shale at a depth of 2 km. The pore pressure is $\sim$ 2800 psi at that location.

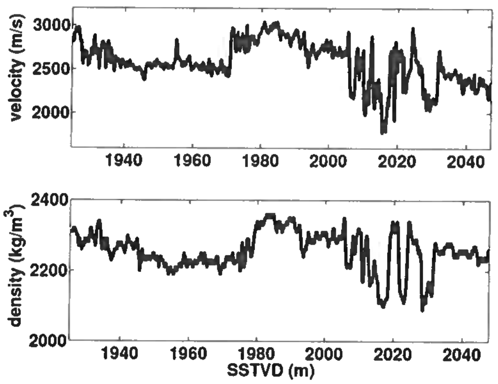

Figure 11. Velocity and density logs in the A20ST well at the South Eugene Island field showing the interface between the JD-sand and its lower bounding shale at 1975 m sub-sea true vertical depth (SSTVD). The log information at this contact is used to construct the sand/shale model in Table 1. These logs also cut through a growth fault zone known as the B-fault at around 2020 m SSTVD.

plane of the noise-free dip-filtered image with the amplitude extracted after 20% Gaussian noise was added to the original image before dip filtering. As can be seen, the dip-filtering step is robust in the presence of random noise, giving roughly the $1/\sqrt{n}$ attenuation of noise exploited in stacking. The processing is such that the amplitude of the reflected waves is an indication of the reflection coefficient at the boundary giving rise to the reflected wave, at least within any changes induced by amplitude variations with offset (AVO) in the stack. The pattern of the amplitude map reflects the spatially varying presence of juxtaposition contacts for this model, as the amplitude wildly oscillates up and down. The second scenario, shown in the lower-left panel of Figure 12, compares the extracted amplitude on the fault-plane of the noise-free dip-filtered image with automatic gain control (AGC) applied to the amplitude extracted after 20% Gaussian noise was added to the original image before dip filtering and AGC. The AGC operates in a time window of 200 ms. In this panel, the true-amplitude degrading nature of the AGC is clear (the absolute value of the amplitude is completely different from the result without AGC); however, along the fault some of the same qualitative patterns are present. The same can be said for the third scenario in the upper-right panel of Figure 12. In this panel, everything is the same as in the upper-left panel, except that DMO has been omitted in the processing sequence. The omission of DMO serves to dampen the fault-plane reflections as a result of mis-stacking. The lower-right panel of Figure 12 is the same as in the lower-left panel, except that DMO has again been omitted in the processing sequence. This is the most extreme and problematic of the processing sequences, with AGC and without DMO; the patterns on the fault-plane seen in the upper-left panel are barely recognizable.

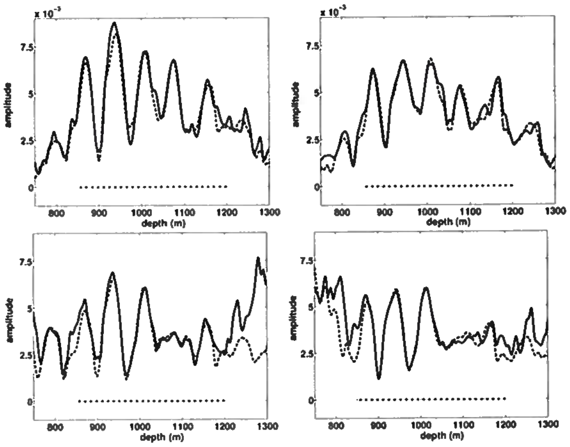

Figure 12. Amplitude along fault-plane for Model 1 shown in Table 1, the juxtaposition contact model, with four different processing scenarios. The amplitude is plotted as a function of depth on the fault-plane, and the extent of the fault-plane is shown by a horizontal line in the bottom portion of each plot. The processing scenarios are: 1) upper-left panel: amplitude extracted from the noise-free image (dashed) and from the image with 20% additive Gaussian noise (solid), 2) lower-left panel: amplitude extracted from the noise-free image with AGC applied (dashed) and from the image with 20% Gaussian noise added in before applying AGC (solid), 3) upper-right panel: amplitude extracted from the noise-free image without DMO included in the processing sequence (dashed) and from the image with 20% additive Gaussian noise, but no DMO (solid), and 4) lower-right panel: amplitude extracted from the noise-free image with AGC applied but no DMO (dashed) and from the image with 20% Gaussian noise added before applying AGC but no DMO (solid). There is no slip at the fault.

9 AMPLITUDE OF WAVES REFLECTED FROM A PORE-PRESSURE CONTRAST ACROSS A FAULT

In Tables 2, 3, and 4 are three different models that incorporate pore pressure contrasts of 600 psi, 300 psi, and 150 psi, respectively, across the fault. The aim of using these models is to see how small a pore pressure contrast can be and still be detectable in the fault-plane reflectivity. These figures are relevant to studying the fault-plane reflectivity at South Eugene Island since pressure measurements taken near the large, minibasin-bounding growth fault, known as the A-fault, show a 780 psi increase in pore pressure over 18 m in going from the hydrostatically pressured downthrown sediments to the overpressured upthrown sediments (Losh *et al.*, 1999). With the pore-pressure contrasts in the three models being 600 psi, 300 psi, and 150 psi, the effective stress values can be computed using a hydrostatic pressure of 2800 psi (the same as for the juxtaposition model covered in the previous section). The juxtaposition model can be thought of as having a 0 psi pore-pressure difference across the fault. The values of the densities and velocities used in the three models are consistent with the effective stress relationships derived in the introduction assuming that the mechanism of overpressure is pure undercompaction.

Layer	Thickness (m)	ρ (kg/m^3)	V_P (m/s)	V_S (m/s)
1	900	2240	2600	1100
2	50	2240	2570	1070
3	30	2210	2380	880
4	50	2240	2570	1070
5	30	2210	2380	880
6	90	2240	2570	1070
7	50	2280	2750	1250
8	30	2240	2600	1100
9	50	2280	2750	1250
10	30	2240	2600	1100
11	90	2280	2750	1250
12	850	2240	2600	1100

Table 2. Model 2 for the SEM modeling. The geometry of the model is given in Figure 6. There is 20 m of throw between the upthrown (layers 2 through 6) and downthrown (layers 7 through 11) sediments, in addition to 600 psi of pore pressure difference. The difference in pore pressures is the result of the upthrown sediments being overpressured. The densities and velocities of layers 2 through 6 are relatively lower than the normally compacted, hydrostatically pressured layers 7-11 on the downthrown side. To relate the velocities and densities to pressure, the mechanism of overpressure is taken to be purely compaction disequilibrium.

Layer	Thickness (m)	ρ (kg/m^3)	V_P (m/s)	V_S (m/s)
1	900	2240	2600	1100
2	50	2260	2660	1160
3	30	2225	2490	990
4	50	2260	2660	1160
5	30	2225	2490	990
6	90	2260	2660	1160
7	50	2280	2750	1250
8	30	2240	2600	1100
9	50	2280	2750	1250
10	30	2240	2600	1100
11	90	2280	2750	1250
12	850	2240	2600	1100

Table 3. Model 3 for the SEM modeling. The geometry of the model is given in Figure 6. Same as Table 2 except that the pore pressure difference is 300 psi.

In Figure 13 are plotted the maximum reflected amplitude from Model 2 (ΔP = 600 psi) within a small window (100 ms) of the fault-plane for four different processing scenarios. These different processing scenarios are the same as in the previous section on juxtaposition contrasts. The scenarios include the presence and absence of 20% additive Gaussian noise with the full processing sequence (upper-left panel of Figure 13), the application of AGC (lower-left panel of Figure 13), the omission of DMO in the processing sequence (upper-

Layer	Thickness (m)	ρ (kg/m^3)	V_P (m/s)	V_S (m/s)
1	900	2240	2600	1100
2	50	2270	2705	1205
3	30	2232	2545	1045
4	50	2270	2705	1205
5	30	2232	2545	1045
6	90	2270	2705	1205
7	50	2280	2750	1250
8	30	2240	2600	1100
9	50	2280	2750	1250
10	30	2240	2600	1100
11	90	2280	2750	1250
12	850	2240	2600	1100

Table 4. Model 4 for the SEM modeling. The geometry of the model is given in Figure 6. Same as Table 2 except that the pore-pressure difference is 150 psi.

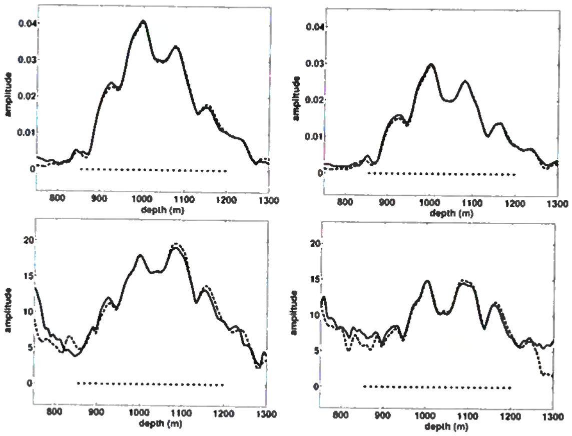

Figure 13. Amplitude along fault-plane for Model 2 shown in Table 2, a model with a pore pressure contrast of 600 psi across the fault, with four different processing scenarios (the same ones as in Figure 12). See the caption for Figure 12 for details about the amplitudes plotted and about the four scenarios.

right panel of Figure 13), and the combined application of AGC and the omission of DMO in the processing sequence (lower-right panel of Figure 13).

In these plots, the effect of the juxtaposition contacts shows up in this model as a high frequency wobble on top of the low frequency trend due to the presence of a ΔP across the fault. This means that a pore-pressure difference of 600 psi is sufficient enough to dominate the reflectivity attributable to juxtapositions. This occurs for two reasons: the ΔP is large enough across the fault and the dip filter preferentially attacks the juxtapositions since they change in polarity along the fault plane. From the plots in Figure 13, the most severe processing artifact, in the sense of destroying the relative amplitude pattern, is the AGC.

In Figure 14 are plotted four different models of ΔP across the fault: 600 psi in the upper-left panel (Model 2), 300 psi in the upper-right panel (Model 3), 150 psi in the lower-left panel (Model 4), and 0 psi (the juxtaposition model, Model 1) in the lower-right panel. All of these amplitude maps are plotted both with (solid line) and without (dashed line) 20% Gaussian additive noise. Comparison of the plots shows essentially linear reduction of reflection amplitudes with reduction in pore-pressure contrast. For a pore-pressure contrast as small as 150 psi, it is difficult to tell if a contrast exists. Specifically, note the similarity of the lower-left (150 psi) and lower-right (0 psi) panels, especially in the degree with which the wobbles due to the juxtapositions contribute to the fault reflectivity.

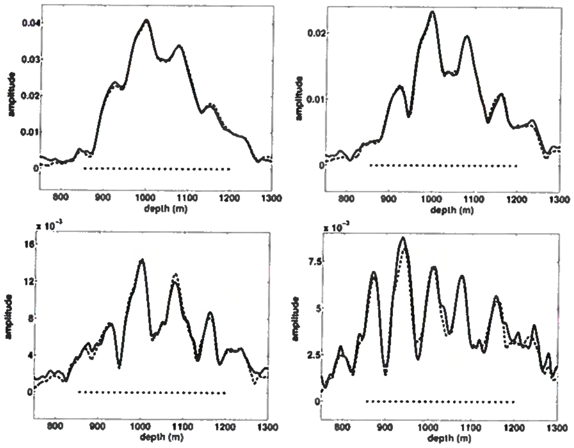

Figure 14. Amplitude along fault-plane for Models (clockwise from the upper left) 2 (upper-left), 3 (upper-right), 4 (lower-left), and 1 (lower-right). The amplitude is plotted as a function of depth on the fault-plane and the extent of the fault-plane is shown with a horizontal line in the bottom portion of each plot. These models represent the situations of: 600-psi pore-pressure difference across the fault (Model 2, upper-left), 300-psi pore-pressure difference across the fault (Model 3, upper-right), 150-psi pore-pressure difference across the fault (Model 4, lower-left), and 0 psi pore pressure difference across the fault; in other words, the juxtaposition contact model (Model 1, lower-right), There is no slip at the fault.

10 AMPLITUDE OF WAVES REFLECTED FROM A LINEAR-SLIP FAULT

We use the abilities of the SEM code to accommodate slip at an interface to model four different slipping interfaces, as described in Table 5, in terms of their normal and tangential (shear) compliances. We label these models in order from the most to the least slipping as Slip-Model A, B, C, and D. The examples here have the linear-slip interface embedded in layered Model 2, described previously (ΔP = 600psi). The entire fault-plane does not slip, only a portion of it as shown in

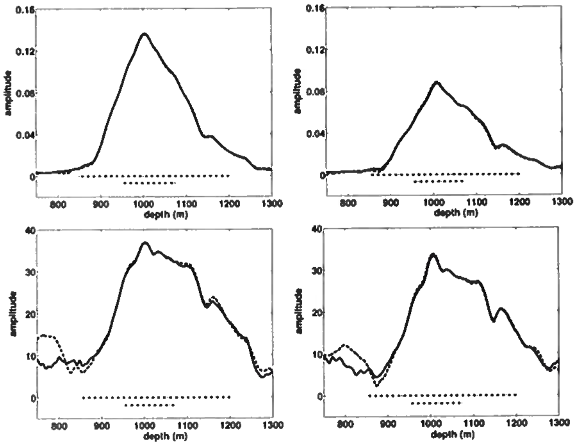

Figure 15. Amplitude along fault-plane for Slip-Model A (see Table 5) at a fault embedded in Model 2 (see Table 2) for four different processing scenarios. The amplitude is plotted as a function of depth on the fault-plane and the extent of the fault-plane is shown with a long horizontal line in the bottom portion of each plot. The sub-portion of the fault that slips is shown beneath this line with a shorter horizontal line. The processing scenarios are the same as those described in the caption for Figure 12. The Slip-Model uses slip at the fault to represent weakness caused by elevated pore pressure.

Figure 6. In the next section, we present a weak scattering model to relate the value of the compliances to pore pressures in a thin fault zone. For now, these values are simply parameters describing the degree of bonding between the surfaces on either side of the linear-slip interface.

The amplitude of the fault-plane reflection from Slip-Model A embedded in Model 2 is displayed in Figure 15 for the four processing scenarios outlined earlier in the sections on juxtaposition contacts and pore pressure difference across the fault: 20% noise (upper-left panel), AGC (lower-left panel), no DMO (upper-right panel), and AGC and no DMO (lower-right panel). The fault-plane extends over the long horizontal line at the bottom of the plots in Figure 15. The shorter horizontal line signifies the part of the fault plane that slips. Note that the location of the maximum reflectivity occurs in the part of the fault that is slipping. Also, since the reflection from Slip-Model A, embedded in Model 2, is relatively large compared to the fault-plane reflection for Model 2 alone (as shown in the upper-left plot of Figure 13 - an amplitude of 0.14 versus 0.04), the sources of noise and error in the processing do not degrade the amplitude map severely in any of the scenarios. This highlights the efficiency of Slip-Model A in reflecting energy compared to the purely ΔP contrast of Model 2.

The amplitude maps for Slip-Models A, B, C, and D are shown in Figure 16. As the normal and shear compliances are decreased in going from Slip-Model A to Slip-Model D, the amplitude of the fault-plane reflection attributable to a slipping interface redcues in the about the same proportion. This occurs because the reflection coefficient is proportional to the compliance for a relatively weakly slipping interface (see Appendix B, equation (B6)). For the the smallest compliance, Slip-Model D, the magnitude of the reflection is on the same order as that of the reflection caused by the ΔP present in Model 2 (shown in the upper-left plot of Figure 13). Hence, this would seem to be a lower limit for compliance for slipping behavior to dominate any ΔP across the fault.

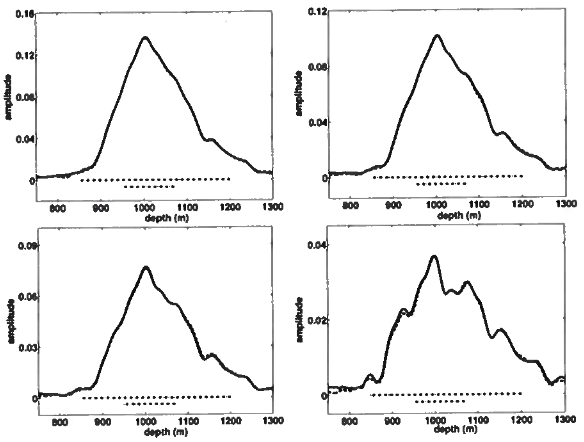

Figure 16. Amplitude along fault-plane for Slip-Models A (upper-left), B (upper-right), C (lower-left), and D (lower-right) shown in Table 15 at a fault embedded in Model 2 having a pore pressure contrast of 600 psi across the fault. The amplitude is plotted as a function of depth on the fault-plane and the extent of the fault-plane is shown with a long horizontal line in the bottom portion of each plot. The sub-portion of the fault that slips is shown beneath this line with a shorter horizontal line. The maximum amplitude occurs near the center of the slipping portion of the fault in each slip-model. The amplitude map also resembles a triangle since it is in essence the convolution of two boxcar functions: the slipping portion of the fault-plane and the dip filter. In moving from Slip-Model A to D, the compliance of the fault slip becomes smaller and, as a result, the reflection magnitude scales in the same proportion, as predicted by equation (B6) in Appendix B for a weakly slipping interface. The Slip-Models use slip at the fault to represent weakness due to elevated pore pressure.

11 RELATING LINEAR-SLIP TO A PRESSURIZED FAULT

The values for the compliances used in the numerical modeling and shown in Table 5 do not, up to this point, have any physical meaning in terms of the pressure locally at the fault. In this section, we relate a slipping interface to an effective-layer model that demonstrates much of the same wave-scattering behavior. With an effective layer described in terms of its thickness, density, and velocity, the empirical relationships between

Slip-Model	normal compliance, η_N (m Pa^{-1})	tangential compliance, η_T (m Pa^{-1})
A	5.0×10^{-10}	1.0×10^{-9}
B	3.5×10^{-10}	7.0×10^{-10}
C	2.5×10^{-10}	5.0×10^{-10}
D	1.0×10^{-10}	2.0×10^{-10}

Table 5. Four different slip interfaces described in terms of their normal and tangential compliances. These have been used in the SEM modeling.

effective stress and density, and effective stress and velocity, derived in the introduction can give the compliance values a physical meaning. The derivation here is for normally incident P-waves, but can be extended to P-waves incident at an angle. We focus on normally incident P-waves since the seismic imaging discussed in previous sections utilized PP-scattered waves at small incidence angles.

The effective-layer model begins from a weak scattering assumption. For a thin layer, if the interface reflection coefficients at the upper and lower boundary are small, then the entire series of reverberations (Aki & Richards, 1980) within the layer can be neglected. The total reflection coefficient from the thin layer can thus be approximated simply as the sum of the reflections off the upper and lower interface. For the case when the thin layer is sandwiched between two identical media,

$$R_{tot} \approx R_{PP} \;-\; R_{PP}\,\exp\left(\frac{2i\omega h}{\alpha_L}\right), \tag{20}$$

where R_{PP} is the P-wave to P-wave (PP) reflection coefficient at the upper interface (the reflection at the lower interface is $-R_{PP}$), ω is the frequency, h is the thickness of the thin layer, and α_L is the P-wave velocity in the thin layer. In equation (20), we have assumed that the impedance difference between the thin layer and the host medium is small enough that the transmission coefficients in moving from the host medium into the thin layer and vice versa are close to 1. This is consistent with the weak-scattering assumption made above.

The next approximation relies on the layer being sufficiently thin. If, for the argument of the exponential term in equation (20),

$$\frac{2\omega h}{\alpha_L} \ll 1, \tag{21}$$

then the exponential can be expanded to first order in a Taylor series

$$\exp\left(\frac{2i\omega h}{\alpha_L}\right) \approx 1 + \frac{2i\omega h}{\alpha_L}. \tag{22}$$

Note that the condition in equation (21) states that $1 \gg 4\pi h/\lambda_L$, where λ_L is the wavelength of the wave in the thin layer. Hence, the condition means that only a fraction of a wavelength fits in the layer. Inserting the Taylor series approximation into equation (20) gives

$$R_{tot} \approx -R_{PP}\,\frac{2i\omega h}{\alpha_L}. \tag{23}$$

This expression shows that the total reflection from a thin weak layer is proportional to the derivative of the incident wave. Widess has discussed this fact in a famous paper on vertical seismic resolution (Widess, 1973).

From equation (B6) in Appendix B, the PP reflection coefficient for a weakly-slipping interface between two identical media (the host medium) is

$$R^s_{PP} \approx \frac{i\omega\eta_N\rho\alpha}{2}, \tag{24}$$

where ω is the frequency, η_N is the normal compliance, ρ is the density of the host medium, α is the P-wave velocity of the host medium, and the superscript s indicates that this is the reflection coefficient for a slipping interface. This equation comes with its own assumption, namely that the dimensionless normal compliance is much smaller than 1, $\omega\eta_N\rho\alpha \ll 1$. Equating this expression to equation (23) gives

$$\frac{i\omega\eta_N\rho\alpha}{2} = -R_{PP}\,\frac{2i\omega h}{\alpha_L}. \tag{25}$$

By canceling common factors and solving this for η_N, the normal compliance, we get

$$\eta_N = -\frac{4h}{\rho\alpha\alpha_L}\,R_{PP}. \tag{26}$$

In the weak scattering approximation, we can substitute a weak-scattering approximation for the interface reflection coefficient R_{PP}. This can be obtained from equation (B6) in Appendix B

$$R_{PP} = \frac{1}{2}\left(\frac{\Delta\rho}{\bar{\rho}} + \frac{\Delta\alpha}{\bar{\alpha}}\right), \tag{27}$$

where $\Delta\rho = \rho_L - \rho$, $\bar{\rho} = (\rho_L + \rho)/2$, $\Delta\alpha = \alpha_L - \alpha$, and $\bar{\alpha} = (\alpha_L + \alpha)/2$. Rewriting equation (27) in terms of the properties of the layer and host medium,

$$R_{PP} = \frac{\rho_L - \rho}{\rho_L + \rho} + \frac{\alpha_L - \alpha}{\alpha_L + \alpha}. \tag{28}$$

Substituting into equation (26) for R_{PP} yields

$$\eta_N = \frac{4h}{\rho\alpha\alpha_L}\left(\frac{\rho - \rho_L}{\rho + \rho_L} + \frac{\alpha - \alpha_L}{\alpha + \alpha_L}\right). \tag{29}$$

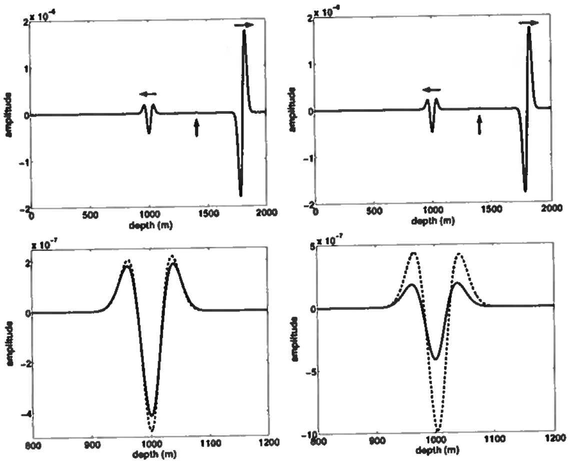

Figure 17. A test of the effective layer for a linear-slip fracture for a normally-incident P-wave. These traces are computed with a finite-element implementation of normally-incident P-waves. The upper-left panel shows a transmitted plane wave (traveling to the right) and a reflected plane wave (traveling to the left) from a horizontal thin bed of 10-m thickness with density and velocity values from Table 9. The background medium has *alpha* = 2675 m/s and ρ = 2260 kg/m^3 (the average values of the hydrostatic sand/shale layers shown in Table 1). The upper-right plot shows the same picture for the equivalent linear-slip interface with compliance calculated from equation (29). In the lower-left panel, a zoom in of the reflected waves for the thin bed (solid) and the equivalent linear-slip interface (dashed) are shown. The reflection from the equivalent linear-slip interface, equation (29), is in error by 15%. The lower-right panel shows the comparison between the reflection from the thin bed (solid) and the equivalent linear-slip interface (dashed) from Schoenberg (1980). The reflection from Schoenberg's equivalent linear-slip interface, equation (30), is in error by 135% likely because it is a strong scattering approximation.

Since η_N is always greater than zero, the effective thin layer can have relatively lower density $\rho > \rho_L$ and lower velocity $\alpha > \alpha_L$ than the host medium. This holds for a locally pressurized fault, since velocity and density decrease with increase in pore pressure.

It is interesting to compare equation (29) with the expression by (1980) for the compliance of a thin weak layer. Schoenberg (1980) relates the compliance to the properties of the layer by stating that, in the limit of $h \to 0$ and $\rho_L \alpha_L^2 \to 0$, the effective compliance of the thin layer is

$$\eta_N = \frac{h}{\rho_L \alpha_L^2}. \tag{30}$$

Equation (30) is somewhat different than equation (29), most notably in that equation (30) contains material properties of the layer only and not those of the host medium. The source of the difference between these two expressions is that the result of Schoenberg (1980) holds as $h \to 0$ and $\rho_L \alpha_L^2 \to 0$; that is, it is a strong-scattering approximation. The approximation that we have made in equation (29) is a weak-scattering one. A weak-scattering approximation should be more appropriate for an overpressurized fault since, according to the pore pressure relationships described in the introduction, $\rho_L \alpha_L^2 \to 0$ cannot happen for any value of the pore pressure. Schoenberg's analogous conditions for shear waves may be more realistic, since the shear velocity goes to nearly zero at zero effective stress (Zimmer *et al.*, 2002).

Using a finite-element implementation of normally-incident P-waves, we can test the above approximation by comparing the reflection from a weakly slipping fracture with the reflection from its effective weak thin layer. We use a 10-m thick layer with α_L = 2077 m/s and ρ_L = 2124 kg/m^3 in a background medium of α = 2675 m/s and ρ = 2260 kg/m^3. The layer thickness, α_L, and ρ_L are taken from the results in Table 9 described below. The background medium parameters are the average values of the sand/shale sequence in Table 1. The normal compliance η_N predicted by our weak-scattering model, equation (29), for these parameters is 5×10^{-10} m Pa^{-1}. For the Schoenberg model, equation (30), the normal compliance comes out to be 1.1×10^{-9} m Pa^{-1}. The source frequency in the simulation is peaked at 20 Hz, just as it was in the SEM modeling shown earlier in this chapter. The result of the finite-element simulation is shown by the traces in Figure 17. We find that our weak-scattering effective-layer model is in much better agreement than Schoenberg's model (Schoenberg, 1980). Our model is in error by 15% while the Schoenberg model is in error by 136%. This supports the weak-scattering model for equivalent thin layers and weakly slipping interfaces.

Using the effective-stress relationships we estimated at South Eugene Island for ρ_L and α_L in the case of unloading, $\rho_L^u(\sigma_d)$ and $\alpha_L^u(\sigma_d)$, and fixing the depth (or, equivalently the lithostatic stress σ_v) so that the effective stress varies only with pore pressure ($\sigma_d = \sigma_v - p$), the compliance of a fracture can be put in terms of the thickness of the layer and the pore pressure

$$\eta_N(h, P) = \frac{4h}{\rho \alpha \alpha_L^u(P)} \left(\frac{\rho - \rho_L^u(P)}{\rho + \rho_L^u(P)} + \frac{\alpha - \alpha_L^u(P)}{\alpha + \alpha_L^u(P)} \right). \tag{31}$$

Note that we use the unloading relationships for ρ_L and α_L. This is because a locally pressurized fault likely results from fluid migrating up the fault. Hence, the correct curve to use is the unloading curve (Revil & Cathles, 2002). This curve requires another parameter, the maximum past effective stress σ_{max} that the fault rock experienced before being unloaded to its current state. With this information, the slip models used in the previous modeling section can be related to an effective layer described by four parameters: fault zone of thickness h, fixed depth z, excess fluid pressure $P - P_h$, and maximum past effective stress σ_{max}. Figure 18 shows how, given a maximum past effective stress σ_{max} and fault zone thickness h, one can construct equivalent compliances for the velocity and density values traced out along the unloading curve as a function of effective stress. To convert from effective stress to pore pressure, knowledge of the depth z or lithostatic level σ_V in necessary.

From this weak equivalent layer, we find that the pore-pressure value corresponding to a linear-slip interface is not unique - it depends on three other parameters besides the pressure. In Tables 6 through 9, we fix two of these parameters - the depth of the fault zone (1850 m) and the thickness of the fault zone (10 m). The tables show the values of the effective thin layer for each Slip-Model, A through D, while varying σ_{max} between the different tables: σ_{max} = 2800 psi in Table 6, σ_{max} = 2400 psi in Table 7, σ_{max} = 2000 psi in Table 8, and σ_{max} = 1600 psi in Table 9. They also show the effective stress corresponding to those values of velocity and density along the unloading path, and use the depth to convert to pore pressure. We do not show results for the variation with thickness h since it is mundane, as seen in equation (29). The variation with depth z is also fairly unimportant since it changes only the value of the pore pressure for a given effective stress. As seen in Tables 6 through 9, certain values of the compliance cannot even exist for some values of σ_{max} since the compliance does not fall in the range of possible compliances based on the values of density and velocity. This is shown in Figure 18, where in the bottom panel the possible compliance values corresponding to the unloading path in the upper figures does not extend all the way to zero. Hence, some small compliance values cannot be modeled for those choices of h, z, and σ_{max}. In order to get smaller compliance values, the thickness of the fault would need to be made smaller because the compliance, from equation (29), scales with h. From the Tables 6 through 9, we find that the earlier that the rock in the fault zone began to be unloaded, i.e., the smaller the σ_{max}, the larger the compliance can be for smaller amounts of pore pressure. Hence, the more efficient the pressurized fault zone can be in scattering seismic waves for a small amount of pore pressure increase.

In the A10ST well at South Eugene Island, the effective stress in the B-fault zone was measured at as low as 166 psi (Losh *et al.*, 1999). In fact, Losh *et al.* (1999) state that "... the fault itself ... is at significantly lower vertical effective stress than the downthrown sediments." In other words, the fault itself is overpressured. Hence, some of the low values for effective stress shown in Tables 6 through 9, while unusual, are entirely possible for the growth faults at South Eugene Island. Anomalously low effective stresses of 575 psi and 807 psi were also measured in the nearby A20ST well as it crossed the A-fault system (Losh *et al.*, 1999).

Slip-Model	ρ (kg/m^3)	v_p (m/s)	σ_e (psi)	p (psi)
A	2204	2019	11	5490
B	2207	2175	88	5412
C	2216	2293	322	5178
D	2269	2472	1655	3845

Table 6. Four different slip-interfaces described in terms of their effective layer parameters assuming a thickness of 10 m. The estimates are made under the assumption that the fault rock began its unloading path after reaching a maximum vertical effective stress of 2800 psi. velocity and pore pressure derived in the introduction are used to relate these compliances to vertical effective stress σ_e and pore pressure p at South Eugene Island. Also, for the four tables, the pore-pressure estimate assumes a depth of 1850 m, where the overburden stress is 5500 psi and the hydrostatic pressure is 2800 psi.

Slip-Model	ρ (kg/m^3)	v_p (m/s)	σ_e (psi)	p (psi)
A	2178	2037	31	5469
B	2186	2192	238	5262
C	2208	2301	775	4725

Table 7. Four different slip-interfaces described in terms of their effective layer parameters assuming a thickness of 10 m. The estimates are made under the assumption that the fault rock began its unloading path after reaching a maximum vertical effective stress of 2400 psi. There is no effective-layer model for Slip-Model D along this unloading path.

12 CONCLUSION

We have presented a complete numerical modeling experiment by utilizing an SEM implementation of the 2D elastic wave equation and processing the resulting waveforms into their time-migrated images. We derived a simple dip filter and used it to isolate fault-plane reflections. We then exploited the relationships between the elastic parameters, density and velocity, to create physically meaningful models of sealing faults that maintain a ΔP of up to 600 psi. For these ΔP models, we as-

Slip-Model	ρ (kg/m^3)	v_p (m/s)	σ_e (psi)	p (psi)
A	2149	2058	109	5391
B	2172	2203	700	4800
C	2218	2292	1829	3671

Table 8. Four different slip-interfaces described in terms of their effective layer parameters assuming a thickness of 10 m. The estimates are made under the assumption that the fault rock began its unloading path after reaching a maximum vertical effective stress of 2000 psi. There is no effective-layer model for Slip-Model D along this unloading path.

Slip-Model	ρ (kg/m^3)	v_p (m/s)	σ_e (psi)	p (psi)
A	2124	2077	453	5047

Table 9. Four different slip-interfaces described in terms of their effective layer parameters assuming a thickness of 10 m. The estimates are made under the assumption that the fault rock began its unloading path after reaching a maximum vertical effective stress of 1600 psi. There are no effective layer models for Slip-Models B, C, and D along this unloading path.

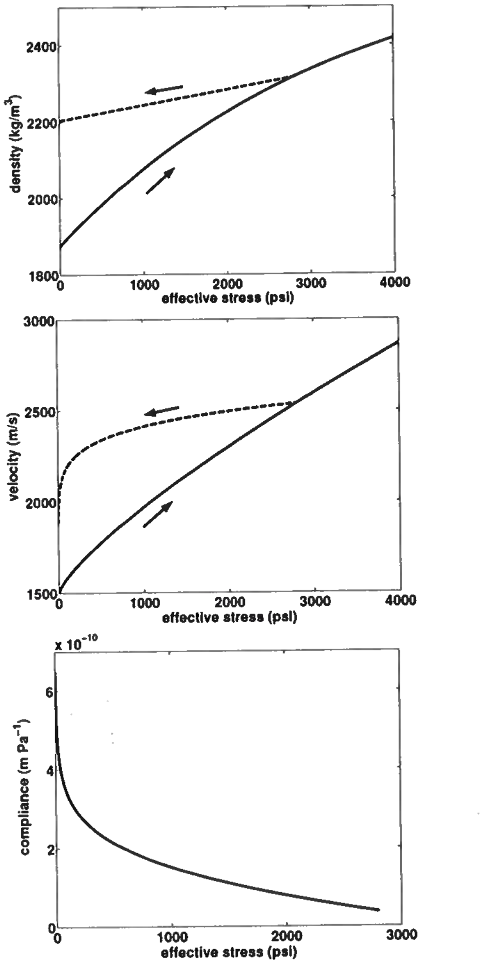

Figure 18. The unloading paths for density and velocity used for the values in Table 6. Also shown is the compliance for the effective layer model along the unloading path for a 10-m thick fault using equation (29). Note that the compliance values end at 2800 psi - the maximum past effective stress σ_{max} for this model.

sumed that the overpressure mechanism is purely due to undercompaction. In the course of this modeling, we found that the minimum ΔP necessary to give rise to substantial fault-plane reflections is on the order of 150 psi. Taking advantage of the SEM modeling code's ability to accommodate linear-slip interfaces, we selected four different values of the normal and shear compliances for the fault interface. We find that the slipping interfaces are more efficient at scattering seismic energy than are the pore pressure differences across the fault for compliance values above $\sim 10^{-10}$ m Pa^{-1}. Unsatisfied with the lack of physical insight into the meaning of a compliance, we derived, from a weak-scattering model, an equivalent thin, weak layer that gives virtually the same reflection as a linear-slip interface under certain conditions. We used this equivalent layer model to relate the values of the compliance to realistic values of pore pressure at South Eugene Island. To do so required extensive use of the effective-stress relationships for the unloading paths. In closing, we conclude that the smaller the past maximum effective stress is for the fault zone, the more efficient the fault can be at scattering seismic waves. This makes sense physically in that the overpressured fault rock is being poroelastically perturbed (by, for instance, fluid migrating up the fault) from a more extreme initial state.

ACKNOWLEDGMENTS

Jon Sheiman provided valuable input and thanks go out to him. Andrey Bakulin first brought the idea of a weak scattering model of a fracture to the authors' attention. Shell International Exploration and Production has provided funding for this research.

REFERENCES

Aki, K., & Richards, P. 1980. *Quantitative Seismology*. San Francisco: W. H. Freeman and Company.

Alterman, Z. S., & Loewenthal, D. 1970. Seismic Waves in a Quarter and Three-Quarter Plane. *Geophys. J. R. astr. Soc.*, **20**, 101.

Ampuero, J. P. 2002. *Etude physique et numérique de la nucléation des séismes*. PhD Thesis, Université Paris 7, Paris, France.

Andrews, D. J. 1999. Test of two methods for faulting in finite-difference calculations. *Bull. Seism. Soc. Am.*, **89**, 931–937.

Boore, D. M. 1970. *Finite-difference solutions to the equations of elastic wave propagation, with applications to Love waves over dipping interfaces*. PhD Thesis, MIT.

Bowers, G. L. 1995. Pore Pressure Estimation from Velocity Data: Accounting for Overpressure Mechanisms Besides Undercompaction. *SPE Drilling & Completion*, **June**, 89–95.

Carcione, J. M., & Tinivella, U. 2001. The seismic response to overpressure: a modeling study based on laboratory, well, and seismic data. *Geophysical Prospecting*, **49**, 523.

Chaisri, S., & Krebes, E. S. 2000. Exact and approximate formulas for *P-SV* reflection and transmission coefficients for a nonwelded contact interface. *JGR*, **105**, 28045.

Coates, R. T., & Schoenberg, M. 1995. Finite-difference modeling of faults and fractures. *Geophysics*, **60**, 1514.

Demirbag, E., Çoruh, C., & Costain, J. K. 1993. Inversion of *P*-Wave AVO. *Pages 500–540 of:* Castagna, J. P., & Backus, M. M. (eds), *Offset-dependent reflectivity - theory and practice of AVO analysis.* Tulsa: SEG.

Dutta, N. C. 1997. Pressure prediction from seismic data: implications for seal distribution and hydrocarbon exploration and exploitation in the deepwater Gulf of Mexico. *Pages 187–199 of:* Moeller-Pederson, P., & Koestler, A. G. (eds), *Hydrocarbon Seals: Importance for Exploration and Production.* Singapore: Elsevier.

Elliott, D. A. 1999. *Hydrofracture Permeability Response and Maximum Previous Consolidation Stress Estimations for Faulted and Micro-Faulted Silty-Shales Taken from the Eugene Island Block 330 Field Pathfinder Well in the Gulf of Mexico.* MSc Thesis, University of California, San Diego.

Groenenboom, J. 1998. *Acoustic Monitoring of Hydraulic Fracture Growth.* PhD Thesis, Delft University.

Haney, M., Sheiman, J., Snieder, R., Naruk, S., Busch, J., & Wilkins, S. 2004. Fault-plane reflections as a diagnostic of pressure differences in reservoirs: a case study from South Eugene Island Block 330. *Pages O-07 of:* Engelder, T., Konstanty, J., & Grauls, D. (eds), *Proceedings of the EAGE special session on Fault and Top Seals.* EAGE.

Hart, B. S., Flemings, P. B., & Deshpande, A. 1995. Porosity and pressure: Role of compaction disequilibrium in the development of geopressures in a Gulf Coast Pleistocene basin. *Geology*, **23**, 45–48.

Hatton, L., Worthington, M. H., & J., Makin. 1986. *Seismic Data Processing: Theory and Practice.* Oxford: Blackwell Science.

Huffman, A. R. 2002. The Future of Pressure Prediction Using Geophysical Methods. *Pages 217–233 of:* Huffman, Alan, & Bowers, Glenn (eds), *Pressure regimes in sedimentary basins and their prediction.* AAPG Memoir, no. 76. Tulsa: AAPG.

Karniadakis, G. E., & Sherwin, S. J. 1999. *Spectral/HP Element Methods for CFD.* Oxford: Oxford University Press.

Kelly, K. R., Ward, R. W., Treitel, S., & Alford, R. M. 1976. Synthetic seismograms: A finite-difference approach. *Geophysics*, **41**, 2.

Komatitsch, D., & Tromp, J. 2003. Introduction to the spectral-element method for three-dimensional seismic wave propagation. *Geophys. J. Int.*, **139**, 806.

Komatitsch, D., & Vilotte, J. P. 1998. The spectral element method: An efficient tool to simulate the seismic response of 2D and 3D geological structures. *BSSA*, **88**, 368–392.

Liner, C. L. 1999. *Elements of 3-D Seismology.* Tulsa: PennWell.

Losh, S., Eglinton, L., Schoell, M., & Wood, J. 1999. Vertical and Lateral Fluid Flow Related to a Large Growth Fault. *AAPG Bulletin*, **83**, 244–276.

Oppenheim, A. V., & Schafer, R. W. 1975. *Digital Signal Processing.* Englewood Cliffs, New Jersey: Prentice-Hall.

Pennebaker, E. S. 1968. Seismic data indicate depth, magnitude of abnormal presures. *World Oil*, **166**, 73.

Press, W. H., Flannery, B. P., Teukolsky, S. A., & Vetterling, W. T. 1992. *Numerical Recipes in C: the Art of Scientific Computing.* Cambridge: Cambridge University Press.

Revil, A., & Cathles, L. M. 2002. Fluid transport by solitary waves along growing faults: A field example from the South Eugene Island Basin, Gulf of Mexico. *Earth and Planetary Science Letters*, **202**, 321–335.

Schoenberg, M. 1980. Elastic wave behavior across linear slip interfaces. *J. Acoust. Soc. Am.*, **68**, 1516–1521.

Seriani, G., & Priolo, E. 1994. Spectral element method for acoustic wave simulation in hetrogeneous media. *Finite Elements in Analysis and Design*, **16**, 337–348.

Shuey, R. T. 1985. A simplification of the Zoeppritz equations. *Geophysics*, **50**, 609.

Stockwell, Jr., J. W. 1997. Free software in education; a case study of CWP7SU: Seismic Unix. *The Leading Edge*, **16**, 1045–1049.

Stump, B., Flemings, P., Finkbeiner, T., & Zoback, M. 1998. Pressure differences between overpressured and bounding shales of the Eugene Island 330 field (offshore Louisiana, USA) with implications for fluid flow induced by sediment loading. *in: Overpressures in petroleum exploration: workshop proceedings, eds. A. Mitchell and D. Grauls, Elf Exploration Production Memoir 22.*

Stump, B. B., & Flemings, P. B. 2002. Consolidation State, Permeability, and Stress Ratio as Determined from Uniaxial Strain Experiments on Mudstone Samples from the Eugene Island 330 Area, Offshore Louisiana. *Pages 131–144 of:* Huffman, Alan, & Bowers, Glenn (eds), *Pressure regimes in sedimentary basins and their prediction.* AAPG Memoir, no. 76. Tulsa: AAPG.

Terzaghi, K. 1943. *Theoretical Soil Mechanics.* New York: Wiley.

Thomsen, L. 1993. Weak anisotropic reflections. *Pages 200–240 of:* Castagna, J. P., & Backus, M. M. (eds), *Offset-dependent reflectivity - theory and practice of AVO analysis.* Tulsa: SEG.

Townsend, C., Firth, I. R., Westerman, R., Kirkevollen, L., Harde, M., & Anderson, T. 1998. Small seismic-scale fault identification and mapping. *in: Faulting, Fault Sealing and Fluid Flow in Hydrocarbon Resrvoirs, eds. G. Jones, Q. J. Fisher, and R. J. Knipe, Geological Society Special Publication No. 147.*

Wang, H. F. 2000. *Theory of Linear Poroelasticity.* Princeton: Princeton University Press.

Wang, Y. 1999. Approximations to the Zoeppritz equations and their use in AVO analysis. *Geophysics*, **64**, 1920–1932.

Widess, M. B. 1973. How Thin is a Thin Bed? *Geophysics*, **38**, 1176.

Worthington, M. H., & Hudson, J. A. 2000. Fault properties from seismic *Q*. *Geophys. J. Int.*, **143**, 937.

Zienkiewicz, O. C., & Taylor, R. L. 2000. *The Finite Element Method.* Vol. 1. Oxford: Butterworth-Heinemann.

Zimmer, M., Prasad, M., & Mavko, G. 2002. Pressure and porosity influences on $V_P - V_S$ ratio in unconsolidated sands. *The Leading Edge*, **21**, 178.

APPENDIX A: STABILITY OF A SPLIT NODE

To obtain a typical stability condition for a split node, we consider the simple case of a finite-element implementation of the 1D scalar wave equation. This case can be thought of as that of a normally incident SH-wave on a fracture. The linear basis functions ϕ used here are given as

$$\phi_K(z) = \begin{cases} (z - z_{K-1})/h & \text{if } z_{K-1} \leq z \leq z_K, \\ (z_{K+1} - z)/h & \text{if } z_K \leq z \leq z_{K+1}, \\ 0 & \text{otherwise,} \end{cases} \tag{A1}$$

where h is the grid spacing. After applying the weak formulation to the 1D wave equation and integrating in space, the resulting matrix equation to be solved in time is

$$M\ddot{\vec{u}} = -c^2 K \vec{u}, \tag{A2}$$

where M and K are the mass and stiffness matrices, $c^2 = \mu/\rho$ is the squared wavespeed (assumed to be constant here), and u is the (out of plane) displacement field ($u = u_y$). For the linear basis functions used here, the entries of these matrices can be calculated exactly. For the (consistent) mass matrix, $M_{J,K}$, the non-zero entries are

$$\int_0^L \phi_K \phi_J dz = 2h/3 \qquad \text{for } J = K \tag{A3}$$

$$\int_0^L \phi_K \phi_J dz = h/6 \qquad \text{for } J = K+1, J = K-1. \tag{A4}$$

where h is the spatial grid spacing (assumed to be constant). This means that M is symmetric and tridiagonal. Similarly, the stiffness matrix, $S_{J,K}$, is also symmetric tridiagonal and the non-zero entries are

$$\int_0^L \frac{\partial \phi_K}{\partial z} \frac{\partial \phi_J}{\partial z} dz = 2/h \qquad \text{for } J = K \tag{A5}$$

$$\int_0^L \frac{\partial \phi_K}{\partial z} \frac{\partial \phi_J}{\partial z} dz = -1/h \qquad \text{for } J = K+1, J = K-1. \tag{A6}$$

For a single split node, the matrices M and K have some structure. In fact, the left hand side of equation (A2) is

$$\begin{bmatrix} \ddots & \ddots & & & & & & \\ \ddots & 2h/3 & h/6 & & & & & \\ & h/6 & 2h/3 & h/6 & & & & \\ & & h/6 & h/3 & 0 & & & \\ & & & 0 & h/3 & h/6 & & \\ & & & & h/6 & 2h/3 & h/6 & \\ & & & & & h/6 & 2h/3 & \ddots \\ & & & & & & \ddots & \ddots \end{bmatrix} \begin{bmatrix} \vdots \\ \ddot{u}_{m-2} \\ \ddot{u}_{m-1} \\ \ddot{u}_m \\ \ddot{u}_{m+1} \\ \ddot{u}_{m+2} \\ \ddot{u}_{m+3} \\ \vdots \end{bmatrix} \tag{A7}$$

where the spatial location on the grid is indicated by the subscripts $m-1$, m, etc. In equation (A7), the split node is located between the gridpoints m and $m+1$. Similarly, the right hand side of equation (A2) is

$$-c^2 \begin{bmatrix} \ddots & \ddots & & & & & & \\ \ddots & 2/h & -1/h & & & & & \\ & -1/h & 2/h & -1/h & & & & \\ & & -1/h & 1/h & 0 & & & \\ & & & 0 & 1/h & -1/h & & \\ & & & & -1/h & 2/h & -1/h & \\ & & & & & -1/h & 2/h & \ddots \\ & & & & & & \ddots & \ddots \end{bmatrix} \begin{bmatrix} \vdots \\ u_{m-2} \\ u_{m-1} \\ u_m \\ u_{m+1} \\ u_{m+2} \\ u_{m+3} \\ \vdots \end{bmatrix} \tag{A8}$$

We use the expressions in equations (A7) and (A8) to find the stability criterion for a split node. To further simplify the calculation, we lump the mass matrix shown in equation (A7) so that the left hand side of equation (A2) is instead

$$\begin{bmatrix} \ddots & \ddots & & & & & & \\ \ddots & h & 0 & & & & & \\ & 0 & h & 0 & & & & \\ & & 0 & h/2 & 0 & & & \\ & & & 0 & h/2 & 0 & & \\ & & & & 0 & h & 0 & \\ & & & & & 0 & h & \ddots \\ & & & & & & \ddots & \ddots \end{bmatrix} \begin{bmatrix} \vdots \\ \ddot{u}_{m-2} \\ \ddot{u}_{m-1} \\ \ddot{u}_m \\ \ddot{u}_{m+1} \\ \ddot{u}_{m+2} \\ \ddot{u}_{m+3} \\ \vdots \end{bmatrix} \tag{A9}$$

The lumping is accomplished by summing the rows and placing the result on the main diagonal. This essentially reduces the finite-element scheme into a finite-difference scheme. The difference is that care has been taken with the inclusion of a split-node and, as seen in the next paragraph, the boundary condition at the split-node can be accounted for in an entirely straightforward manner. This is in contrast to the "fictitious lines" in Alterman and Lowenthal (1970) and Kelly *et al.* (1976).

Setting the m-th rows of the matrix/vector multiplications depicted in equations (A8) and (A9) equal to each other, in accordance with the equation of motion, equation (A2), gives the spatially discretized equation of motion at the split node

$$\frac{h}{2}\ddot{u}_m = \frac{c^2}{h}u_{m-1} - \frac{c^2}{h}u_m. \tag{A10}$$

Note that there is currently no communication across the split node, between the gridpoint at m and at $m+1$. Interaction between these gridpoints is accomplished by including the traction σ_{yz} between the nodes with the slip law

$$u_{m+1} - u_m = \eta\sigma_{yz}, \tag{A11}$$

where the coupling is described by the free parameter η (the compliance). Note that $\eta = 0$ is a welded contact and $\eta = \infty$ is a stress-free boundary. Using the slip law and Hooke's Law $\mu\ \partial u/\partial z = \sigma_{yz}$, the traction at the split node can be included into equation (A10)

$$\frac{h}{2}\ddot{u}_m = \frac{c^2}{h}u_{m-1} - \frac{c^2}{h}u_m + \frac{c^2}{\mu\eta}(u_{m+1} - u_m). \tag{A12}$$

A time integration scheme must be chosen for equation (A12). An explicit scheme is obtained by evaluating all the u-terms on the right hand side at the previous timestep, denoted n. For notational purposes, we show u_{m-1} evaluated at timestep n by $u_{m-1,n}$. For the left hand side, we choose the second difference approximation to $\ddot{u}_m$ centered at timestep n

$$\ddot{u}_m = \frac{u_{m,n+1} - 2u_{m,n} + u_{m,n-1}}{\Delta t^2}, \tag{A13}$$

where Δt is the time spacing. The algorithm outlined here is to be solved for $u_{m,n+1}$ in equation (A13) by knowing the displacements at timesteps n and $n-1$. Such a multistep algorithm can be seen as equivalent to a single-step algorithm with prediction.

Inserting equation (A13) into equation (A12) results in the complete finite-element stencil

$$\frac{h}{2\Delta t^2}u_{m,n+1} - \frac{h}{\Delta t^2}u_{m,n} + \frac{h}{2\Delta t^2}u_{m,n-1} = \frac{c^2}{h}u_{m-1,n} - \frac{c^2}{h}u_{m,n} + \frac{c^2}{\mu\eta}(u_{m+1,n} - u_{m,n}). \tag{A14}$$

To investigate the stability of this scheme, we study the exponential growth or decay of the odd eigenmodes of u. These eigenmodes are antisymmetric with respect to the slipping interface. We chose the odd eigenmodes since the symmetric modes have no slip. If there wasn't a slipping interface and the medium was homogeneous, harmonic functions would be inserted for both the spatial and temporal variation of u; for the case of slipping interface, care has to be taken in treating the spatial variation since the medium is not homogeneous. This extra care amounts to determining an additional free parameter at the interface, as demonstrated shortly.

An odd eigenmode for a single linear-slip interface located at the depth z_s is

$$\begin{aligned} u(z,t) &= \tilde{U}(z)e^{i\omega t} \\ \tilde{U}(z) &= \operatorname{sgn}(z-z_s)\sin(k|z-z_s|+\phi), \end{aligned} \tag{A15}$$

where $\tilde{U}(z)$ is the spatial variation of the odd eigenmode, ϕ is a free parameter determined from the linear-slip boundary condition of equation (A11), k is the wavenumber, and ω is the frequency. As stated above, the slip interface is between the m and $m+1$ gridpoints, which are both located at the depth z_s. To be precise, the m gridpoint is obtained in the limit $z \to z_s$ for values $z < z_s$. Similarly, the $m+1$ gridpoint is obtained in the limit $z \to z_s$ for values $z > z_s$. Mathematically, this is the difference between a left-hand and right-hand limit. It matters in the context of equation (A15) since the signum function is discontinuous at $z = z_s$.

Taking the proper limits, the spatial components of an odd eigenmode at the m and $m+1$ gridpoints are

$$\begin{aligned} \tilde{U}_m &= -\sin\phi, \\ \tilde{U}_{m+1} &= \sin\phi. \end{aligned} \tag{A16}$$

From these equations, it can be seen that ϕ drives the magnitude of the slip discontinuity. We now use the relationships in equation (A16) to determine ϕ from the linear-slip boundary condition of equation (A11). For this, we need the shear stress component σ_{yz}, which by Hooke's Law is equal to $\mu\ \partial u/\partial z$. In other words, we need the value of the derivative of u at z_s. From equation (A15)

$$\frac{\partial\tilde{U}}{\partial z} = k\cos(k|z-z_s|+\phi). \tag{A17}$$

Therefore, at z_s, $\sigma_{yz} = \mu k\cos\phi$. Inserting this expression for σ_{yz} and the relationships in equation (A16) into the boundary condition of equation (A11) yields

$$\tan\phi = \frac{\eta\mu k}{2}. \tag{A18}$$

From this equation, $\sin\phi$ and $\cos\phi$ can be found

$$\begin{aligned} \sin\phi &= \frac{\pm\eta\mu k}{\sqrt{\eta^2\mu^2k^2+4}} \\ \cos\phi &= \frac{\pm 2}{\sqrt{\eta^2\mu^2k^2+4}}. \end{aligned} \tag{A19}$$

Since it does not matter, we take the postive sign in equation (A19).

We are now in a position to write down the discrete forms of the antisymmetric eigenmodes at the gridpoints $m-1$, m, and $m+1$ using equation (A15)

$$\begin{aligned} u_{m+1,n} &= \sin\phi\ e^{i\omega n\Delta t} \\ u_{m,n} &= -\sin\phi\ e^{i\omega n\Delta t} \\ u_{m-1,n} &= -\sin(kh+\phi) = -(\sin kh\cos\phi + \cos kh\sin\phi)\ e^{i\omega n\Delta t}, \end{aligned} \tag{A20}$$

where the time t is discretized by timestep n and time spacing Δt. Using equation (A19) and the substitution

$$\zeta^n = e^{i\omega n\Delta t}, \tag{A21}$$

equation (A20) can be written finally as

$$\begin{aligned} u_{m+1,n} &= \frac{\eta\mu k}{\sqrt{\eta^2\mu^2k^2+4}}\,\zeta^n \\ u_{m,n} &= \frac{-\eta\mu k}{\sqrt{\eta^2\mu^2k^2+4}}\,\zeta^n \\ u_{m-1,n} &= -\frac{2\sin kh + \eta\mu k\cos kh}{\sqrt{\eta^2\mu^2k^2+4}}\,\zeta^n. \end{aligned} \tag{A22}$$

In equation (A22), the variation with timestep n is trivial, requiring only a change in the exponent of ζ. Taking the information in equation (A20), using it in equation (A14), and organizing terms yields

$$\begin{aligned} 0 \;=\; & \Big[\frac{h\eta\mu k}{2\Delta t^2}\zeta^2 + \frac{c^2}{h}(\eta\mu k - 2\sin kh - \eta\mu k\cos kh)\zeta \\ & -\frac{h\eta\mu k}{\Delta t^2}\zeta + 2c^2k\zeta + \frac{h\eta\mu k}{2\Delta t^2}\Big]\,\zeta^{n-1}. \end{aligned} \tag{A23}$$

In order to have non-trivial solutions, the terms inside the brackets in equation (A23) must equal zero.

Dividing equation (A23) by the coefficient of the ζ^2 term and setting the terms inside the brackets to zero gives

$$0 = \zeta^2 - 2[1 - \frac{\Delta t^2c^2}{h^2\eta\mu k}(\eta\mu k - \eta\mu k\cos kh - 2\sin kh) - \frac{2\Delta t^2c^2}{\mu\eta h}]\zeta + 1. \tag{A24}$$

For the numerical scheme to be stable, the two roots of equation (A24) should have magnitudes less than or equal to 1. This means that solutions are not exponentially growing in time. Let's find the conditions such that this is the case.

Note that equation (A24) has the general form

$$0 = \zeta^2 - v\zeta + 1, \tag{A25}$$

where the coefficient v is a complex number. Denote the two (possibly complex) roots of equation (A25) ζ_1 and ζ_2. From the quadratic formula, it is known that for any v

$$\begin{aligned} \zeta_1 + \zeta_2 &= v \\ \zeta_1\zeta_2 &= 1. \end{aligned} \tag{A26}$$

These equalities are a particular example of what are known as Viète's formula's and are analogous to the trace of a matrix being equal to the sum of its eigenvalues and the determinant being equal to the product of its eigenvalues. With help of the triangle inequality, the two equalities in equation (A26) can be recast in terms of the magnitudes of ζ_1 and ζ_2, shown as $|\zeta_1|$ and $|\zeta_2|$. For the first equality of equation (A26)

$$|\zeta_1| + |\zeta_2| \geq |\zeta_1 + \zeta_2| = |v|. \tag{A27}$$

And, for the second equality

$$|\zeta_1|\;|\zeta_2| = |\zeta_1\zeta_2| = |1| = 1. \tag{A28}$$

This is necessary since it is the magnitude of the roots of equation (A24) that determine the stability of the algorithm. Since we need both $|\zeta_1| \leq 1$ and $|\zeta_2| \leq 1$ for stability, equation (A28) tells us that

$$|\zeta_1| = 1 \quad\text{and}\quad |\zeta_2| = 1. \tag{A29}$$

This makes sense because we are solving a wave equation whose solutions should not decay with time. Using this information together with equation (A27) gives

$$2 = |\zeta_1| + |\zeta_2| \geq |v| \tag{A30}$$

or in other words,

$$|\frac{v}{2}| \leq 1. \tag{A31}$$

Applying this stability criterion, valid for the general quadratic form of equation (A25), to the expression describing the roots in equation (A24) gives

$$|1 - \frac{\Delta t^2c^2}{h^2\eta\mu k}(\eta\mu k - \eta\mu k\cos kh - 2\sin kh) - \frac{2\Delta t^2c^2}{\mu\eta h}| \leq 1. \tag{A32}$$

From this expression, note that in the limit of low frequencies $kh \to 0$ (which corresponds to waves that are well sampled by the grid), this stability criterion is always satisfied. Typically we look for instabilities to occur for waves that are near the spatial Nyquist frequency ($kh = \pi$). For this frequency, equation (A32) becomes

$$|1 - \frac{2\Delta t^2 c^2}{h^2} - \frac{2\Delta t^2 c^2}{\mu\eta h}| \leq 1. \tag{A33}$$

The term inside the absolute value on the left hand side of equation (A33) is real-valued; therefore, the inequality may be rewritten as two simultaneous inequalities

$$-1 \leq 1 - \frac{2\Delta t^2 c^2}{h^2} - \frac{2\Delta t^2 c^2}{\mu\eta h} \leq 1. \tag{A34}$$

Since the terms being subtracted from 1 in the middle of equation (A34) are both positive, the right hand inequality is always satisfied and may be ignored. The other inequality is meaningful

$$\begin{aligned} -1 &\leq 1 - \frac{2\Delta t^2 c^2}{h^2} - \frac{2\Delta t^2 c^2}{\mu\eta h} \\ \frac{2\Delta t^2 c^2}{h^2} + \frac{2\Delta t^2 c^2}{\mu\eta h} &\leq 2 \\ \frac{\Delta t^2 c^2}{h^2}\left(1 + \frac{h}{\mu\eta}\right) &\leq 1 \\ \frac{c\Delta t}{h}\sqrt{1 + \frac{h}{\mu\eta}} &\leq 1 \\ c\Delta t &\leq \frac{h}{\sqrt{1 + (h/\mu\eta)}} \end{aligned} \tag{A35}$$

This stability criterion has the same general form as that for a regular node that is not split ($c\Delta t \leq h$). However, the compliance of the split node η does enter into the stability criterion uniquely in the inverse square root appearing on the right hand side. For a free surface, $\eta = \infty$ and the factor with the compliance vanishes and the stability criterion can be met. As the compliance approaches zero, though, the denominator becomes large and the stability criterion becomes harder to satisfy. For given values of c, h, μ, and Δt, there is a lower value for compliance η_{min} past which the algorithm becomes unstable at the split node. This precludes the possibility of a welded interface ($\eta = 0$), though for certain values of c, h, μ, and Δt, η_{min} may be so small that an effectively welded interface can be realized.

APPENDIX B: LINEARIZED REFLECTION COEFFICIENTS FROM A LINEAR-SLIP INTERFACE

As demonstrated in Groenenboom (1998), fractures act as an interface over which slip occurs during the passage of a seismic wave. Therefore, a good place to begin modeling fractures is with linear-slip theory. Schoenberg (1980) formally introduced the concept of a linear-slip interface to the exploration seismology community. The linear-slip interface is characterized by the following boundary condition for the SH case:

$$u_y^+ - u_y^- = k_T \sigma_{yz}, \tag{B1}$$

$$\sigma_{yz}^+ = \sigma_{yz}^-, \tag{B2}$$

where k_T is called the shear (or transverse) compliance of the linear-slip interface. In equations (B1) and (B2), the superscript (-) refers to the side of the interface on which the wave is incident, (+) the other side of the interface, u_y is the displacement out of the plane of wave propagation, and σ_{yz} is the shear stress. The shear compliance, k_T, quantifies the degree of slip along the interface. For $k_T = 0$, the interface is welded ($u_y^+ = u_y^-$), and for $k_T = \infty$, it is a free surface. Hence, a linear-slip interface is a general interface condition that includes the usual welded case. In a recent case study from the North Sea, Worthington and Hudson (2000) have modeled a fault zone as a series of closely spaced linear-slip interfaces.

A common tool to diagnose the elastic properties of a reflecting interface in exploration seismology is called amplitude-versus-offset, or AVO. Linearized expressions of reflection coefficients for small changes in the elastic properties across an interface have proven useful in linear AVO-inversion (Demirbag *et al.*, 1993). The linearized expressions provide a set of basis functions in terms of incidence/reflection angle that can be used in a standard least-squares inversion (as described in Chapter 15 of Press *et al.* (1992)). Here, we discuss the linearized approximation of the reflection coefficients for an interface which allows slip. The formulas can be seen as generalizations of existing expressions for welded (no-slip) interfaces.

The linearized reflection coefficient for an SH-wave at a planar interface between two isotropic halfspaces, obtained by enforcing equations (B1) and (B2) for a harmonic elastic disturbance and keeping first order terms in the elastic contrasts and the slip-discontinuity, is:

$$R_{SH} \approx -\frac{1}{2}\left(\frac{\Delta\rho}{\rho}+\frac{\Delta\beta}{\beta}\right)+\frac{1}{2}\frac{\Delta\beta}{\beta}\tan^2\theta - i\frac{\omega k_T\rho\beta}{2}\cos\theta, \tag{B3}$$

where $\Delta\beta$ and $\Delta\rho$ are the changes in S-velocity and density at the interface, β and ρ are the average S-velocity and density of the two halfspaces, ω is the angular frequency of the incident wave, k_T is the shear compliance of the interface, and θ is the reflection/incidence angle. The approximation in equation (B3) holds for small relative changes in the medium parameters ($\Delta\beta/\beta$, $\Delta\rho/\rho \ll 1$), small dimensionless compliance ($\omega k_T\rho\beta \ll 1$), and small angles of incidence (surely not greater than the critical angle). For a welded interface ($k_T = 0$), equation (B3) agrees with Thomsen's expression (Thomsen, 1993) for the case of isotropic halfspaces. We do not show the lengthy derivation of equation (B3); the technique for obtaining linearized reflection coefficients is outlined in (Wang, 1999).

Seismologists usually assume that interfaces are welded and, as a result, reflection coefficients are *real* and *frequency-independent*. As seen from equation (B3), neither of these characteristics are true when slip occurs at the interface. The third term in equation (B3) is the contribution to the reflection coefficient from slip. There is a factor of $i\omega$ in the third term since the linear-slip interface can be obtained in the limit of a thin, low shear strength bed (Schoenberg, 1980) whose reflection, as pointed out a long time ago by Widess (1973), is the derivative of the incident wave.

To overcome the complication of having a complex-valued reflection coefficient, it may be instructive to study the squared magnitude of equation (B3)

$$\begin{aligned} |R_{SH}|^2 \approx\ & \frac{1}{4}\left(\frac{\Delta\rho}{\rho}+\frac{\Delta\beta}{\beta}\right)^2 - \frac{1}{4}\frac{\Delta\beta}{\beta}\left(\frac{\Delta\rho}{\rho}+\frac{\Delta\beta}{\beta}\right)\tan^2\theta + \frac{1}{4}\left(\frac{\Delta\beta}{\beta}\right)^2\tan^4\theta \\ & + \frac{\omega^2 k_T^2\rho^2\beta^2}{4}\cos^2\theta. \end{aligned} \tag{B4}$$

The angle dependencies in equation (B4) can be modified to reveal which terms are sensitive at zero-offset, near-offsets, and far-offsets. This is the approach taken by Shuey (1985). To highlight the angle dependencies, we use the following identities:

$$\begin{aligned} \cos^2\theta &= 1-\sin^2\theta, \\ \tan^2\theta &= \sin^2\theta + \tan^2\theta\,\sin^2\theta, \\ \tan^4\theta &= \tan^2\theta\,\sin^2\theta + \tan^4\theta\,\sin^2\theta. \end{aligned}$$

Equation (B4) can then be rewritten as:

$$\begin{aligned} |R_{SH}|^2 \approx\ & \frac{1}{4}\left[\left(\frac{\Delta\rho}{\rho}+\frac{\Delta\beta}{\beta}\right)^2 + \omega^2 k_T^2\rho^2\beta^2\right] \\ & -\frac{1}{4}\left[\frac{\Delta\beta}{\beta}\left(\frac{\Delta\rho}{\rho}+\frac{\Delta\beta}{\beta}\right) + \omega^2 k_T^2\rho^2\beta^2\right]\sin^2\theta \\ & -\frac{1}{4}\frac{\Delta\beta}{\beta}\frac{\Delta\rho}{\rho}\tan^2\theta\,\sin^2\theta \\ & +\frac{1}{4}\left(\frac{\Delta\beta}{\beta}\right)^2\tan^4\theta\,\sin^2\theta. \end{aligned} \tag{B5}$$

The first term in equation (B5) dominates at zero offset ($\theta \approx 0$). At near-offsets ($0 < \theta < 35°$), the second term, proportional to $\sin^2\theta$, becomes important. The third and fourth terms in equation (B5) are sensitive at far-offsets ($35° < \theta$). Since only the first two terms contain k_T, it can be said that far-offsets are not affected by slip at an interface for the SH case.

For the P-SV-case, the linear-slip interface is described by the boundary conditions:

$$\begin{aligned} u_z^+ - u_z^- &= k_N\sigma_{zz}, \\ \sigma_{zz}^+ &= \sigma_{zz}^-, \\ u_x^+ - u_x^- &= k_T\sigma_{xz}, \\ \sigma_{xz}^+ &= \sigma_{xz}^-, \end{aligned}$$

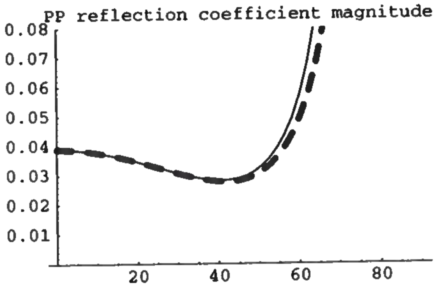

Figure A1. The linearized reflection coefficient as a function of angle (thick, dashed line) and the exact reflection coefficient for a welded interface (k_T, $k_N = 0$).

elastic property	value
density of incident medium	2300 kg/m^3
P-velocity of incident medium	2800 m/s
S-velocity of incident medium	1400 m/s
density of reflecting medium	2400 kg/m^3
P-velocity of reflecting medium	2900 m/s
S-velocity of reflecting medium	1450 m/s

Table A1. The earth model used to compute the reflection coefficients.

where now two compliances, the normal (k_N) and shear (k_T) compliance, describe the linear-slip interface. The linearized PP-reflection coefficient at a planar interface between two isotropic halfspaces that results is:

$$\begin{aligned} R_{PP} \approx\; & \left[\frac{1}{2} - 2\left(\frac{\beta}{\alpha}\right)^2 \sin^2\theta\right] \frac{\Delta\rho}{\rho} + \frac{1}{2}\sec^2\theta\,\frac{\Delta\alpha}{\alpha} - 4\left(\frac{\beta}{\alpha}\right)^2 \sin^2\theta\,\frac{\Delta\beta}{\beta} \\ & + i\left[\frac{1}{2} - 2\left(\frac{\beta}{\alpha}\right)^2 \sin^2\theta\right] \sec\theta\;\omega k_N \rho\alpha \\ & - 2i\left(\frac{\beta}{\alpha}\right)^3 \cos\theta\,\sin^2\theta\;\omega k_T \rho\beta, \end{aligned} \tag{B6}$$

where $\Delta\alpha$, $\Delta\beta$, and $\Delta\rho$ are the changes in P-velocity, S-velocity, and density of the two halfspaces, α, β, and ρ are the average P-velocity, S-velocity, and density of the two halfspaces, ω is the angular frequency of the incident wave, k_T and k_N are the shear and normal compliances of the interface, and θ is the reflection/incidence angle. The approximation in equation (B6) holds for small relative changes in the medium parameters ($\Delta\alpha/\alpha$, $\Delta\beta/\beta$, $\Delta\rho/\rho \ll 1$), small dimensionless shear compliance ($\omega k_T \rho\beta \ll 1$), small dimensionless normal compliance ($\omega k_N \rho\alpha \sec\theta \ll 1$), and small angles of incidence. Note that the condition for a small dimensionless normal compliance has an angular dependence. For a welded interface (k_T, $k_N = 0$), the imaginary terms in equation (B6) vanish and the linearized PP-reflection coefficient agrees with equation 5.44 of Aki and Richerds (1980). Again, we omit the lengthy derivation of equation (B6), but it follows from Wang (1999).

In Figures 1 through 3, we compare the linearized PP-reflection coefficient to the exact PP-reflection coefficient for the parameters shown in Table II while varying the amount of slip (the value of the compliance) at the interface. Since the reflection coefficient for an interface with slip is frequency dependent, we set the frequency of the incident wave to 10 Hz for all the examples. The elastic contrasts resulting from the parameters listed in Table II are sufficiently small to expect agreement between the linearized approximation and the exact reflection coefficient at small incidence/reflection angles. The formulas for the exact PP-reflection coefficient, including possible slip, can be found in Chaisri and Krebes (2000).

Shown in Figure (A1) is the magnitude of the exact PP-reflection coefficient as a function of angle for a welded interface (with elastic contrasts from Table II) and its linearized approximation. Figure (A1) is the typical case

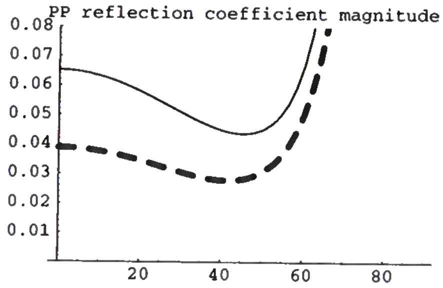

Figure A2. The linearized reflection coefficient as a function of angle (thick, dashed line) for a welded interface (k_T, $k_N = 0$) and the exact reflection coefficient for an interface with the same elastic contrasts, but with some slip ($k_T = 5.0 \times 10^{-10}$ m/Pa and $k_N = 2.5 \times 10^{-10}$ m/Pa). By not including slip in linearized reflection coefficient, it underestimates the magnitude of the exact reflection coefficient.

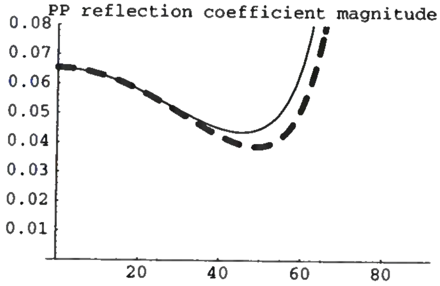

Figure A3. The linearized reflection coefficient as a function of angle (thick, dashed line) for an interface with the elastic contrasts from Table I and having linear-slip behavior ($k_T = 5.0 \times 10^{-10}$ m/Pa and $k_N = 2.5 \times 10^{-10}$ m/Pa). The expression for the linearized reflection coefficient including slip is taken from equation (B6). The exact reflection coefficient for the same interface is also shown. By including slip in the linearized reflection coefficient, the approximation agrees well with the exact solution up to about 45°.

assumed in AVO studies, that of a welded interface, and the approximation is seen to be in good agreement for angles out to about 50°. In Figure (A2), we plot the same linearized reflection coefficient as in Figure (A1), assuming a welded interface; however, for the exact reflection coefficient, we include a small amount of slip by using non-zero values for the compliances: $k_T = 5.0 \times 10^{-10}$ m/Pa and $k_N = 2.5 \times 10^{-10}$ m/Pa. By small, we mean that the dimensionless compliances, $\omega k_T \rho\beta$ and $\omega k_N \rho\alpha \sec\theta$, are much less than one. Without the contribution of slip at the interface, the linearized reflection coefficient underestimates the exact reflection coefficient.

Using equation (B6), the magnitude of the linearized reflection coefficient for an interface with slip can be compared to the exact reflection coefficient. The comparison is shown in Figure (A3). The inclusion of slip in the expression for the linearized reflection coefficient has resulted in better agreement with the exact reflection coefficient (good agreement up to 45°). Qualitatively, from looking at Figure (A2), the presence of non-weldedness at an interface causes the AVO intercept to increase (magnitude at zero-offset is greater) and the AVO gradient to increase (the curve steepens with increasing angle) from their values for the case of no slip. These linearized reflection coefficients for an interface with slip give some insight into the influence of the various elastic contrasts and compliances that is unavailable from the complicated exact expressions. Also, the linearized formulas should be useful in a least-squares, linear inversion of AVO for rock and fracture properties.

Seismic signatures of two orthogonal sets of vertical microcorrugated fractures

Rodrigo Felício Fuck and Ilya Tsvankin
Center for Wave Phenomena, Department of Geophysics, Colorado School of Mines, Golden, CO 80401

ABSTRACT

Conventional fracture-characterization techniques operate with the idealized model of penny-shaped (rotationally invariant) cracks and ignore the roughness (microcorrugation) of fracture surfaces. Here, we develop analytic solutions based on the linear-slip theory to examine wave propagation through an effective triclinic medium that contains two microcorrugated, vertical, orthogonal fracture sets in isotropic background rock.

The compliance matrix off-diagonal elements associated with the corrugation cause the deviation of the polarization vectors of the vertically traveling S-waves from the horizontal plane. Also, the shear-wave splitting coefficient at vertical incidence becomes sensitive to fluid saturation, especially for tight, low-porosity host rock. In contrast to the model with two orthogonal sets of penny-shaped cracks, the NMO (normal-moveout) ellipses of all three reflection modes (P, S_1, S_2) are rotated with respect to the fracture strike directions. Another unusual property of the fast shear wave S_1, which can help to distinguish between models with one and two microcorrugated fracture sets, is the misalignment of the semi-major axis of its NMO ellipse and the polarization vector at vertical incidence. The model analyzed here may adequately describe the orthogonal fracture sets at Weyburn Field in Canada, where the axes of the P-wave NMO ellipse deviate from the S_1-wave polarization direction. Our results can be used to identify the underlying physical model and, potentially, estimate the combinations of fracture parameters constrained by wide-azimuth, multicomponent seismic data.

Key words: fracture characterization, microcorrugated fractures, wide-azimuth data, multicomponent seismic, NMO ellipse, AVO gradient

1 INTRODUCTION

A key element in reservoir characterization is identification of fluid pathways that control the production of hydrocarbons. Since such pathways are often formed by fracture networks and joints, detection and analysis of fractures using seismic data is an important area of reservoir geophysics (e.g. Lynn et al., 1995; Pérez et al., 1999; Mallick et al., 1998; DeVault et al., 2002). In a series of three papers, Bakulin et al. (2000a,b,c) outlined several practical approaches to estimating fracture parameters from surface seismic and VSP (vertical seismic profiling) data. Using the linear-slip theory of Schoenberg (1980), they represented the equations describing the NMO (normal-moveout) ellipses and AVO (amplitude-variation-with-offset) gradients of reflected waves in terms of fracture compliances and orientations. These analytic expressions helped Bakulin et al. (2000a,b,c) to devise fracture-characterization methods based on the inversion of multicomponent, mutliazimuth reflection data.

The work of Bakulin et al. (2000a,b,c) was largely focused on the idealized model of rotationally invariant fractures (i.e., oblate spheroids), which have perfectly smooth surfaces and are often called "penny-shaped cracks." Grechka et al. (2003) extended the results of Bakulin et al. (2000a) by considering a single set of the most general vertical fractures allowed by the linear-slip formalism. Physically, such "general" fractures have rough (microcorrugated) surfaces and are described by a compliance matrix that has nonzero off-diagonal elements. The results of Grechka et al. (2003) show that fracture rheology has a strong impact on velocities and reflection moveout of pure modes, as well as on the shear-wave splitting coefficient. For instance, if the fractures are rotationally invariant, the axes of the NMO ellipses from horizontal reflection events are always parallel and perpendicular to the fracture strike. By contrast, for a set of general fractures only the NMO ellipse of the fast shear wave S_1 maintains its alignment with the fractures, while the ellipses of the P- and S_2-waves may have different orientations.

While the methodology of Grechka et al. (2003) helps to treat realistic fracture rheology, their results are limited to effective media that include only one general fracture set. Many naturally fractured reservoirs, however, contain two (or even more) systems of fractures, which are often orthogonal to each other (Schoenberg and Sayers, 1995; Grechka and Tsvankin, 2003). Here, we study the effective triclinic medium formed by two vertical, orthogonal, microcorrugated fracture sets embedded in isotropic background rock.

Our motivation for investigating this model comes from analysis of multicomponent, multiazimuth reflection data acquired at Weyburn Field in Canada. Borehole imaging and geological information reveal the presence of two dominant fracture sets, which are interpreted as approximately orthogonal over most of the field (Cardona, 2002). The assumption that both fracture sets are rotationally invariant cannot explain the misalignment of P-wave NMO ellipses and the fast S-wave polarization direction observed by Cardona (2002) in some parts of the reservoir. Making the fractures microcorrugated can help to develop an effective model that accounts for this anomaly without introducing a third fracture system.

The objective of this paper is to analyze the influence of two orthogonal sets of microcorrugated fractures on the NMO ellipses and AVO gradients of reflected waves, as well as on the shear-wave splitting coefficient. By applying the weak-anisotropy approximation, we derive closed-form analytic expressions for these common seismic signatures in terms of the fracture compliances. Although the feasibility study by Grechka and Tsvankin (2003) indicates that the individual compliances of two general fracture sets cannot be resolved even from the complete effective stiffness tensor, our results can assist in retrieving certain combinations of the compliances and identifying the presence of a second fracture set.

2 EFFECTIVE MODEL

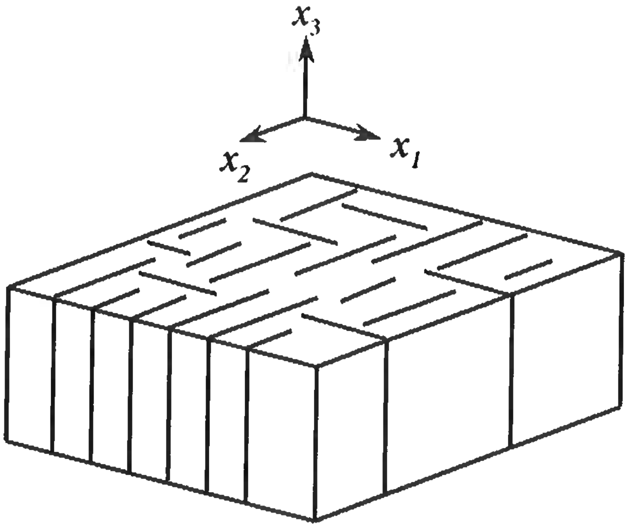

Figure 1. Illustration of a model of two sets of vertical fractures orthogonal to each other in an isotropic background. Since the linear-slip theory does not account for the interaction of fracture sets, fractures are not supposed to intersect each other.

The model considered here includes two orthogonal sets of vertical fractures of the most general rheology embedded in a purely isotropic background (Figure 1). To compute the elastic stiffnesses for the fractured model, we employ the linear-slip theory introduced by Schoenberg (1980), Schoenberg and Sayers (1995), and others (see Appendix A). According to the linear-slip formalism, fractures can be described as non-welded interfaces that cause discontinuities in the displacement field (i.e., slips). The slips are proportional to the product of the (continuous) tractions that act across the fractures and to the excess fracture compliances.

The most general mathematical description of a fracture set in the linear-slip theory is a 3×3 symmetric matrix of the excess compliances (Grechka et al., 2003):

$$\mathbf{K} = \begin{pmatrix} K_N & K_{NV} & K_{NH} \\ K_{NV} & K_V & K_{VH} \\ K_{NH} & K_{VH} & K_H \end{pmatrix}, \qquad (1)$$

where K_N is the normal compliance responsible for relating the normal traction (stress) across the fracture surface to the normal slip, and K_V and K_H are the tangential compliances that relate the shear stresses to the tangential slips. The off-diagonal compliances incorporate the mechanical effects of irregularities and asperities on the fracture surfaces (Figure 2) by coupling normal slips to shear stresses and vice-versa (Schoenberg and Douma, 1988; Nakagawa et al., 2000).

Fractures are usually classified in accordance with the structure of their compliance matrix $\mathbf{K}$ [equation (1)]. If at least one of the off-diagonal elements does not vanish, the fractures are sometimes called "monoclinic" (Schoenberg and Douma, 1988). Fractures described by a diagonal matrix $\mathbf{K}$ are called "orthotropic"

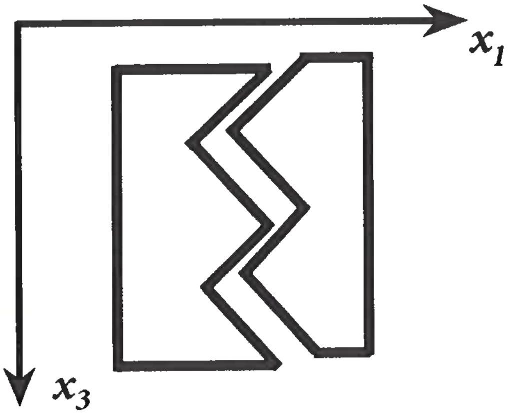

Figure 2. Idealized fracture with corrugations that are offset from one face to the other (adapted from Schoenberg and Douma, 1988). In such a model, normal slips (discontinuities in displacement) are coupled to shear stresses and vice-versa. For example, the slip in the x_3-direction will cause the coupling of the fracture faces and, therefore, shear stress in the x_1-direction.

or simply "diagonal"; rotationally invariant fractures are a special subset of diagonal fractures corresponding to equal tangential compliances $K_V = K_H$.

The stiffness matrix of the effective model is obtained by adding the compliance matrices of the two corrugated fracture sets to that of the isotropic background (Appendix B):

$$\mathbf{c} = \begin{pmatrix} c_{11} & c_{12} & c_{13} & \chi c_{24} & c_{15} & c_{16} \\ c_{12} & c_{22} & c_{23} & c_{24} & \chi c_{15} & c_{26} \\ c_{13} & c_{23} & c_{33} & \chi c_{24} & \chi c_{15} & c_{36} \\ \chi c_{24} & c_{24} & \chi c_{24} & c_{44} & 0 & c_{46} \\ c_{15} & \chi c_{15} & \chi c_{15} & 0 & c_{55} & c_{56} \\ c_{16} & c_{26} & c_{36} & c_{46} & c_{56} & c_{66} \end{pmatrix} \qquad (2)$$

where

$$\chi \equiv \frac{\lambda}{(\lambda + 2\mu)} .$$

Equation (2) demonstrates that the effective model has the most general, triclinic symmetry (i.e., it does not have axes of rotational symmetry or symmetry planes), with only one vanishing elastic constant, $c_{45} = c_{54}$. This is not surprising since even a single set of microcorrugated fractures creates an effective triclinic medium. Nonetheless, only 14 out of the 20 elastic constants are independent because the effective model is constructed using two Lamé parameters of the isotropic background (λ and μ) and 12 fracture compliances (six for each fracture set). Note that if the fracture azimuth is unknown, it is also necessary to introduce an orientation angle that defines the azimuth of one of the sets in our coordinate frame.

By dividing the matrix $\mathbf{c}$ into 3×3 submatrices $\mathbf{C}_{MN}$, it can be represented in block form:

$$\mathbf{c} = \left(\begin{array}{c|c} \mathbf{C}_{NN} & \mathbf{C}_{NT} \\ \hline \mathbf{C}_{NT}^T & \mathbf{C}_{TT} \end{array} \right), \qquad (3)$$

The influence of the complex fracture rheology in our model on the structure of the stiffness matrix can be understood by comparing the matrix (3) with that for the effective orthorhombic medium due to two orthogonal sets of *rotationally invariant* fractures (Bakulin et al., 2000b):

$$\mathbf{c}^{\text{orth}} = \left(\begin{array}{c|c} \mathbf{C}_{NN}^{\text{orth}} & \mathbf{0} \\ \hline \mathbf{0} & \mathbf{C}_{TT}^{\text{orth}} \end{array} \right). \qquad (4)$$

Here, the matrix $\mathbf{C}_{TT}^{\text{orth}}$ is diagonal, and c_{66} contained in $\mathbf{C}_{TT}^{\text{orth}}$ is a linear combination of c_{44} and c_{55}.

The expressions for the effective stiffness elements c_{ij} in equation (2) can be simplified by linearizing the exact results in the normalized compliances which are called *fracture weaknesses* (Bakulin et al., 2000a). The weaknesses vary from zero for unfractured medium to unity for intensely fractured rock in which the body-wave velocities go to zero in a certain direction. Since the weaknesses for typical fractured formations are much smaller than unity, they can be conveniently used in developing linearized approximations for seismic signatures. Definitions of the fracture weaknesses are given in Appendix B, as well as the resulting linearized c_{ij} elements.

3 VERTICAL WAVE PROPAGATION

The phase velocities and polarization vectors of vertically propagating plane waves can be obtained by solving the Christoffel equation for the effective medium described by the stiffness matrix (2). Applying the first-order perturbation theory (e.g., Jech and Pšenčik, 1989; Pšenčik and Vavryčuk, 2002) yields the following simplified expressions for the vertical velocities of the P-, S$_1$-, and S$_2$-waves:

$$V_P \approx V_{Pb} \left[1 - \frac{1}{2} \left(\Delta_{N_1} + \Delta_{N_2} \right) \chi^2 \right], \qquad (5)$$

$$V_{S1} \approx V_{Sb} \left(1 - \frac{\Delta_{V_2}}{2} \right), \qquad (6)$$

$$V_{S2} \approx V_{Sb} \left(1 - \frac{\Delta_{V_1}}{2} \right), \qquad (7)$$

where V_{Pb} and V_{Sb} are the P- and S-wave velocities in the isotropic background, whereas Δ_{N_i} and Δ_{V_i} correspond to the normal and vertical weaknesses of fracture sets 1 and 2, as indicated by the index i. Although the vertical velocities are influenced by the presence of fractures, equations (5)–(7) do not contain off-diagonal weaknesses and coincide with the linearized velocities for rotationally invariant fractures (Bakulin et al. (2000b)).

In contrast, the body waves polarization vectors ($\mathbf{U}_m$), contain first-order contributions of the off-diagonal compliances Δ_{NV_i}:

$$\mathbf{U}_P \approx (a\,\Delta_{NV_1},\, a\,\Delta_{NV_2}, 1)^T\,, \tag{8}$$

$$\mathbf{U}_{S1} \approx (0, 1,\, -a\,\Delta_{NV_2})^T\,, \tag{9}$$

$$\mathbf{U}_{S2} \approx (1, 0,\, -a\,\Delta_{NV_1})^T\,, \tag{10}$$

where

$$a \equiv \frac{(1-2g_b)}{(1-g_b)}\sqrt{g_b}\,, \qquad g_b \equiv \left(\frac{V_{Sb}}{V_{Pb}}\right)^2.$$

Because of the corrugation of fracture surfaces, the P-wave polarization vector deviates from the vertical, and the vertically propagating shear waves are no longer polarized in the horizontal plane. Equations (9) and (10), however, show that the shear-wave polarization vectors are still confined to the planes of the two fracture sets.*

Therefore, Alford-style rotation of the horizontal displacement components of near-offset S-wave reflections can be used to estimate the fracture azimuths. To measure the vertical components of the shear-wave polarization vectors, which are indicative of the presence of microcorrugated fractures, it is necessary to apply 3D polarization analysis.

3.1 Shear-wave splitting

The shear-wave splitting coefficient (γ^S) at vertical incidence is defined as (Thomsen, 1988; Tsvankin, 2001)

$$\gamma^S \equiv \frac{V_{S1}^2 - V_{S2}^2}{2V_{S2}^2}\,, \tag{11}$$

where V_{S1} is the velocity of the fast shear wave. Applying the second-order perturbation theory (Farra, 2001) in terms of the fracture weaknesses yields

$$\gamma^S \approx \frac{1}{2}\Bigg\{(\Delta_{V_1} - \Delta_{V_2})(1 + \Delta_{V_1} - \Delta_{V_2}) - g_b\left[(\Delta_{VH_1}^2 - \Delta_{VH_2}^2) + (\Delta_{NV_1}^2 - \Delta_{NV_2}^2)\,\frac{(3-4g_b)}{1+g_b}\right]\Bigg\} \tag{12}$$

As expected, γ^S at vertical incidence vanishes when the two fracture sets are identical. If the terms quadratic in the weaknesses are dropped from equation (12), the splitting coefficient reduces to the difference between the diagonal tangential weaknesses Δ_{V_1} and Δ_{V_2} [see equations (9) and (10)]. Therefore, to the first order γ^S coincides with the splitting coefficient for rotationally invariant fractures, which is controlled by the difference between the fracture densities of the two sets (Thomsen (1988); Bakulin et al. (2000a,b)).

However, if the second-order terms are substantial, γ^S is also influenced by the off-diagonal weaknesses Δ_{VH_i} and Δ_{NV_i}. Note that the weakness Δ_{NV_i} depends on saturation and takes different values for fractures filled with compressible gas, brine, or oil (Bakulin et al. (2000c)).† Therefore, the vertical-incidence splitting coefficient for microcorrugated fractures with relatively large off-diagonal weaknesses may serve as an indicator of fluid saturation.

As illustrated by Figure 3, the exact coefficient γ^S can vary by as much as 50% over the entire range of plausible values of Δ_{NV_1} (Δ_{NV_2} was fixed). For a tight (non-porous) host rock, $\Delta_{NV_1} = 0$ corresponds to fractures filled with incompressible fluid such as brine, whereas nonzero values of Δ_{NV_1} describe fractures at least partially saturated with gas (Bakulin et al., 2000c). Although the weak-anisotropy approximation (12) correctly reproduces the overall character of the curve $\gamma^S(\Delta_{NV_1})$, it understimates the sensitivity of the shear splitting to the weakness Δ_{NV_1}.

If the saturation of both fracture sets changes simultaneously and Δ_{NV_2} varies similarly to Δ_{NV_1}, the splitting coefficient becomes less sensitive to fluid content. Also, when the host rock has pore space hydraulically connected to the fractures, the weaknesses Δ_{NV_i} do not necessarily vanish even for incompressible saturating fluids (Cardona, 2002; Gurevich, 2003). As a consequence, for porous rocks the variation of γ^S with saturation may be less pronounced than that suggested by Figure 3. Finally, γ^S becomes less sensitive to the off-diagonal compliances and saturation for softer rocks (e.g., marine sediments) with smaller values of the ratio g_b.

4 NMO ELLIPSES FOR HORIZONTAL REFLECTORS

Important information for fracture detection is provided by azimuthally varying traveltimes (moveout) of reflected waves, in particular by their normal-moveout (NMO) ellipses. For a horizontal, homogeneous layer of arbitrary anisotropic symmetry, the NMO velocity of pure (non-converted) reflection modes as a function of the azimuth α is given by (Grechka et al., 1999):

$$V_{\text{nmo}}^{-2} = W_{11}\cos^2\alpha + 2W_{12}\sin\alpha\cos\alpha + W_{22}\sin^2\alpha\,, \tag{13}$$

---

*Due to the limitations of the first-order perturbation theory, the shear-wave polarization vectors are no longer orthogonal, despite being perpendicular to the P-wave polarization vector. Also, the perturbed polarization vectors were not normalized; still, to the first order in the fracture weaknesses, the magnitude of the vectors $\mathbf{U}_P$, $\mathbf{U}_{S1}$ and $\mathbf{U}_{S2}$ is equal to unity.

†Equation (12) is more accurate than equation (30) of Bakulin et al. (2000c) because it includes terms quadratic in the weaknesses.

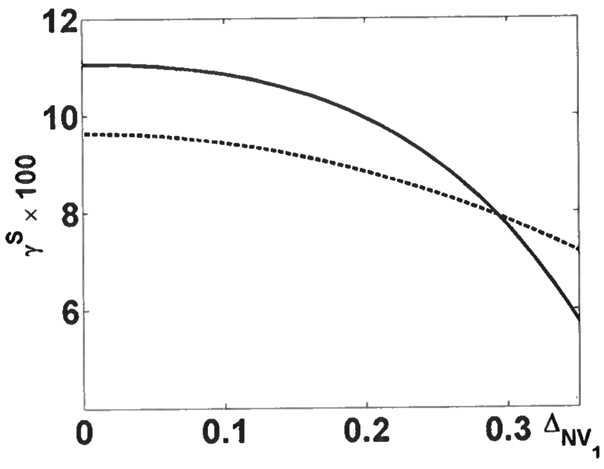

Figure 3. Variation of the shear-wave splitting coefficient (γ^S) for vertical propagation as a function of the weakness Δ_{NV_1}. The solid line is the exact γ^S from equation (11), where the velocities are computed from the Christoffel equation; the dashed curve is the approximation (12). The model parameters are $V_{Pb} = 3$ km/s , $V_{Sb} = 1.5$ km/s, $\Delta_{N_1} = 0.5$, $\Delta_{V_1} = \Delta_{H_1} = 0.25$ and $\Delta_{NH_1} = \Delta_{VH_1} = 0.1$. Each weakness of the second fracture set except for Δ_{NV_2} is equal one-third of the corresponding weakness of the first set; $\Delta_{NV_2} = 1/3\Delta_{NH_1}$.

where $\mathbf{W}$ is a symmetric 2×2 matrix:

$$\mathbf{W} = \frac{q}{q_{,12}^2 - q_{,11}q_{,22}} \begin{pmatrix} q_{,22} & -q_{,12} \\ -q_{,12} & q_{,11} \end{pmatrix}. \qquad (14)$$

Here, q is the vertical component of the slowness vector $\mathbf{p} = [p_1, p_2, q]$ of the zero-offset ray and $q_{,ij}$ denote the following partial derivatives evaluated at zero offset:

$$q_{,ij} \equiv \frac{\partial^2 q(p_1, p_2)}{\partial p_i \partial p_j}. \qquad (15)$$

The vertical slowness and its derivatives can be obtained from the Christoffel equation, as discussed by Grechka et al. (1999). If the eigenvalues of the matrix $\mathbf{W}$ are positive (the most typical case), equation (13) describes an ellipse in the horizontal plane.

To analyze the dependence of the NMO ellipses on the medium parameters, it is convenient to linearize equation (14) in the fracture weaknesses [equations (B1)–(B6)]. For P-waves, the linearized matrix $\mathbf{W}$ takes the form

$$\mathbf{W}^P \approx \frac{1}{V_{Pb}^2} \begin{pmatrix} W_{11}^P & W_{12}^P \\ W_{12}^P & W_{22}^P \end{pmatrix}, \qquad (16)$$

where

$$W_{11}^P = 1 + \Delta_{N_1}\left(1 - 4g_b^2\right) + \Delta_{N_2}\left(1 - 2g_b\right)^2 + 4g_b\,\Delta_{V_1}, \qquad (17)$$

$$W_{12}^P = 2\left(\Delta_{NH1} + \Delta_{NH_2}\right)\left(1 - 2g_b\right)\sqrt{g_b}, \qquad (18)$$

$$W_{22}^P = 1 + \Delta_{N_2}\left(1 - 4g_b^2\right) + \Delta_{N_1}\left(1 - 2g_b\right)^2 + 4g_b\,\Delta_{V_2}. \qquad (19)$$

The structure of equations (17)–(19) can be understood from the "addition rule" formulated by Bakulin et al. (2000b). To find the linearized weak-anisotropy approximation for most seismic signatures (one exception is discussed below), the anisotropic terms due to each fracture set can be simply added together taking into account the fracture orientation. This recipe can be used to obtain equations (17)–(19) from the P-wave NMO ellipse for a single set of microcorrugated fractures given in equation (56) of Grechka et al. (2003).

For the fast shear wave S_1 the matrix $\mathbf{W}$ becomes

$$\mathbf{W}^{S1} \approx \frac{1}{V_{Sb}^2} \begin{pmatrix} W_{11}^{S1} & W_{12}^{S1} \\ W_{12}^{S1} & W_{22}^{S1} \end{pmatrix}, \qquad (20)$$

with

$$W_{11}^{S1} = 1 + \Delta_{H_1} + \Delta_{H_2} - \mathcal{A}, \qquad (21)$$

$$W_{12}^{S1} = \sqrt{g_b}\left(2\Delta_{NH_2} - \mathcal{C}\right), \qquad (22)$$

$$W_{22}^{S1} = 1 - 3\Delta_{V_2} + 4g_b\,\Delta_{N_2} - \mathcal{B}. \qquad (23)$$

Here,

$$\mathcal{A} \equiv \mathcal{D}\,\Delta_{VH_1}^2, \qquad (24)$$

$$\mathcal{B} \equiv \mathcal{D}\,\Delta_{VH_2}^2, \qquad (25)$$

$$\mathcal{C} \equiv \mathcal{D}\,\Delta_{VH_1}\Delta_{VH_2}, \qquad (26)$$

$$\mathcal{D} \equiv \frac{g_b}{\left(\Delta_{V_1} - \Delta_{V_2}\right)}. \qquad (27)$$

Although the factors $\mathcal{A}$, $\mathcal{B}$, and $\mathcal{C}$ are proportional to products of the weaknesses Δ_{VH_i}, their denominator contains the difference in the tangential weaknesses Δ_{V_i} [see equation (27)]. For that reason, $\mathcal{A}$, $\mathcal{B}$, and $\mathcal{C}$ have to be retained in the linearized approximation for the NMO ellipse $\mathbf{W}^{S1}$. In such a case, the addition rule discussed above is not valid, and the approximate NMO ellipse of the S_1-wave cannot be obtained as the sum of the contributions of each fracture set.

The linearized matrix $\mathbf{W}$ for the S_2-wave is given by

$$\mathbf{W}^{S2} \approx \frac{1}{V_{Sb}^2} \begin{pmatrix} W_{11}^{S2} & W_{12}^{S2} \\ W_{12}^{S2} & W_{22}^{S2} \end{pmatrix}, \qquad (28)$$

where

$$W_{11}^{S2} = 1 - 3\Delta_{V_1} + 4g_b\,\Delta_{N_1} + \mathcal{A}, \qquad (29)$$

$$W_{12}^{S2} = \sqrt{g_b}\left(2\Delta_{NH_1} + \mathcal{C}\right), \qquad (30)$$

$$W_{22}^{S2} = 1 + \Delta_{H_1} + \Delta_{H_2} + \mathcal{B}. \qquad (31)$$

Equations (16)–(31) show that only the presence of the off-diagonal weaknesses can explain the misalignment of the NMO ellipses with the fracture planes. If both fracture sets were rotationally invariant, the matrices $\mathbf{W}$ for all three modes [equations (16), (20), and (28)] would be diagonal, and the axes of the NMO

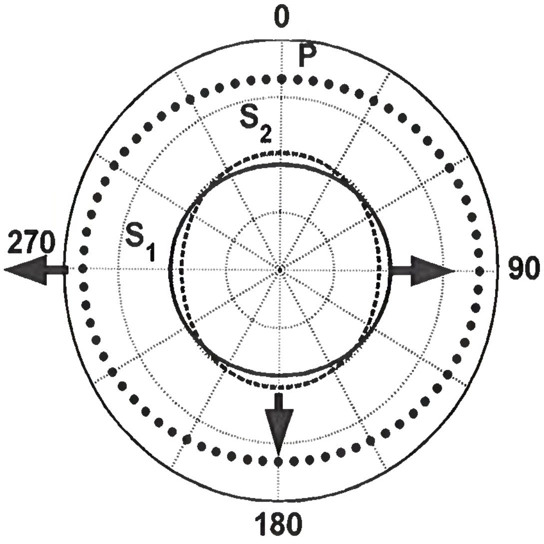

Figure 4. Exact NMO ellipses for an effective orthorhombic model formed by two vertical, orthogonal sets of rotationally invariant fractures. The semi-major axes (black arrows) of the P- and S_1-wave NMO ellipses are parallel to the strike of the dominant fractured set (azimuth 90°). The parameters are $V_{Pb} = 2$ km/s, $V_{Sb} = 1$ km/s, $\Delta_{N_1} = 0.25$, and $\Delta_{V_1} = \Delta_{H_1} = 0.12$. Each weakness of the second fracture set is equal to one-third of the corresponding weakness of the first set. The radius of the external circle corresponds to 2 km/s.

ellipses would be parallel to the fracture strike directions. In an effective orthorhombic medium due to two orthogonal sets of rotationally invariant fractures, the semi-major axes of the NMO ellipses of the P- and S_1-waves (see Figure 4) are aligned with the strike of the dominant fracture set (Bakulin et al., 2000b).

By contrast, when both fracture sets are microcorrugated, all three NMO ellipses generally have different orientations, and none of them is aligned with the fracture azimuths (Figure 5). The deviation of the semi-major axis of the NMO ellipse from the azimuth of the dominant fracture sets reaches 40° for the S_2-wave, 30° for the P-wave and 20° for the S_1-wave. The weak-anisotropy approximations for the NMO ellipses are close to the exact solutions for the full range of azimuths (Figure 6). The error of the approximate solution, caused primarily by the misalignment of the axes of the exact and approximate NMO ellipses, is noticeable only for the slow wave S_2. The higher accuracy of the approximation for the S_1-wave compared to that for the S_2-wave is not surprising since equations (22) and (23) for the matrix elements W_{12}^{S1} and W_{22}^{S1} become exact for one set of fractures (Grechka et al., 2003).

The orientation of the NMO ellipse of the fast wave S_1 can help to distinguish between the models with one or two microcorrugated fracture sets. If the second set does not exist, then $\Delta_{NH_2} = \Delta_{VH_2} = 0$, and the

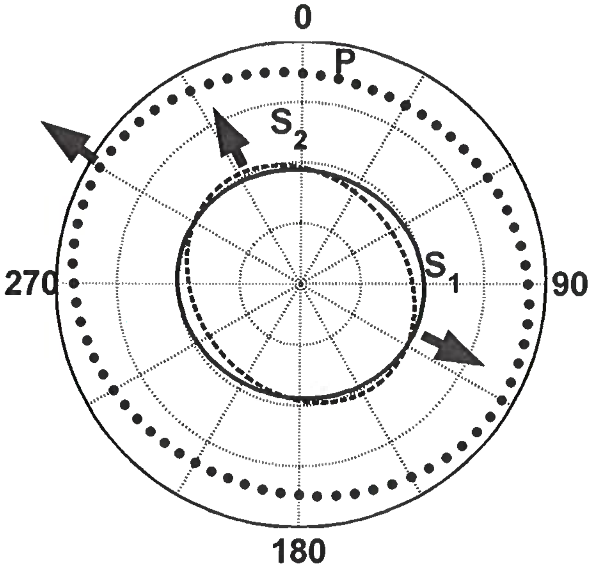

Figure 5. Exact NMO ellipses for two vertical, orthogonal sets of microcorrugated fractures. The strike azimuth of the dominant fracture set is 90°. The parameters are V_{Pb}=2 km/s, V_{Sb}=1 km/s, $\Delta_{N_1} = 0.25$, $\Delta_{V_1} = \Delta_{H_1} = 0.12$, $\Delta_{NV_1} = \Delta_{NH_1} = 0.17$, and $\Delta_{VH_1} = 0.12$. Each weakness of the second fracture set is equal to one-third of the corresponding weakness of the first set.

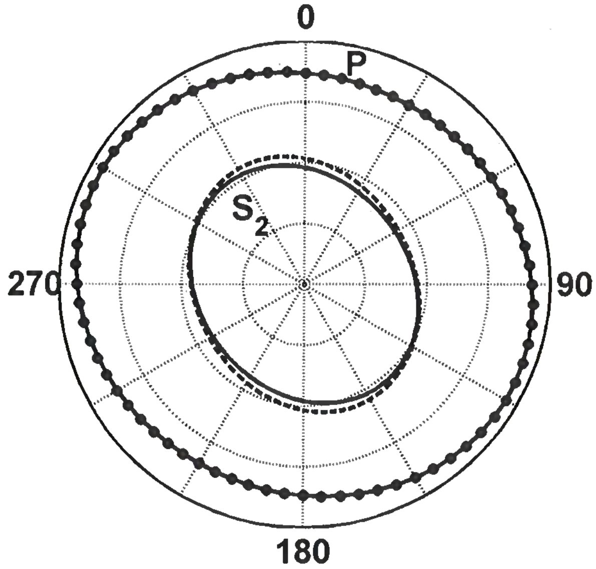

Figure 6. Comparison between the exact NMO ellipses of the P- and S_2-waves from Figure 5 (solid lines) and the weak-anisotropy approximations (dots for the P-wave and the dashed line for the S_2-wave). The approximations are computed from equations (17)–(19) and (29)–(31). The exact and approximate NMO ellipses of the S_1-wave (not shown) practically coincide with each other.

element W_{12} for the S$_1$-wave vanishes [equations (22) and (26)]. In this case, the matrix $\mathbf{W}^{S1}$ [equation (20)] becomes diagonal, and the semi-major axis of the NMO ellipse of the S$_1$-wave is parallel to both the fast shear-wave polarization direction [equation (9)] and the fracture strike. Moreover, for the model with one set of microcorrugated fractures, the S$_1$-wave vertical velocity coincides with the NMO velocity in the fracture strike direction. This result, discussed by Grechka et al. (2003), follows from equations (6) and (20).

Grechka et al. (2000) defined the Thomsen-style parameters $\zeta^{(i)}$ $(i = 1, 2, 3)$ responsible for the orientations of the NMO ellipses of pure modes in a horizontal monoclinic layer with a horizontal symmetry plane. Equations (16)–(31) can be used to generalize their result for our triclinic model because the elements W_{12} include the parameters $\zeta^{(i)}$ and additional correction terms for the shear waves. Using equations (B21) and (B24), the element W_{12}^P [equation (18)] responsible for the rotation of the P-wave NMO ellipse with respect to the x_1-axis can be represented as

$$W_{12}^P = -2\frac{c_{36}}{c_{33}} = -2\zeta^{(3)}\,, \tag{32}$$

which coincides with the expression for W_{12}^P in Grechka et al. (2000). For our model, the parameter $\zeta^{(3)}$ is proportional to the sum of the weaknesses Δ_{NH_1} and Δ_{NH_2}.

Similarly, the off-diagonal elements W_{12}^{S1} and W_{12}^{S2} for shear waves [equations (22) and (30)] can be expressed through the parameters $\zeta^{(1)}$ and $\zeta^{(2)}$:

$$W_{12}^{S1} = -2\,\frac{c_{16} - c_{36}}{2V_{Pb}^2\, g_b,} + \mathcal{C} = -2\frac{\zeta^{(1)}}{g_b} + \mathcal{C}\,, \tag{33}$$

$$W_{12}^{S2} = -2\,\frac{c_{26} - c_{36}}{2V_{Pb}^2 g_b} - \mathcal{C} = -2\frac{\zeta^{(2)}}{g_b} - \mathcal{C}\,, \tag{34}$$

where $\mathcal{C}\,(\Delta_{V_i}, \Delta_{VH_i})$ [equation (26)] is an additional correction factor that accounts for the nonzero stiffnesses c_{46} and c_{56} in the triclinic model [equation (3)]. The parameters $\zeta^{(1)}$ and $\zeta^{(2)}$ depend on the weaknesses Δ_{NH_2} and Δ_{NH_1}, respectively.

Our approximations for the NMO ellipse of both S-waves break down when tangential weaknesses Δ_{V_1} and Δ_{V_2} are identical and the weaknesses $\Delta_{VH_i} \neq 0$. In this case, the parameter $\mathcal{D}$ [equation (27)] goes to infinity, which reflects the fact that a point shear-wave sigularity develops in a close vicinity of the zero-offset ray. An analysis of the influence of singularities on normal moveout for models with orthogonal sets of penny-shaped cracks can be found in Bakulin et al. (2000b).

5 P-WAVE REFLECTION COEFFICIENT

Another seismic signature that can be effectively used in fracture detection is the azimuthally varying reflection coefficient, in particular the AVO (amplitude variation with offset) gradient responsible for small- and moderate-offset reflection amplitudes. Here, we present a linearized expression for the P-wave AVO response in our model and discuss its dependence on the fracture weaknesses.

We consider an isotropic incidence halfspace above the triclinic medium described by equation (2) and assume a weak contrast in the elastic properties across the interface and weak anisotropy (i.e., small fracture weaknesses) in the reflecting halfspace. The weak-contrast, weak-anisotropy approximation for the P-wave reflection coefficient in arbitrary anisotropic media is derived in Vavryčuk and Pšenčik (1998). By combining their general result with the linearized stiffness coefficients for our model [equations (B10)–(B30)], we find the P-wave reflection coefficient R_{PP} as a function of the phase incidence angle θ:

$$\begin{aligned} R_{PP} &= A + B\sin^2\theta + C\sin^2\theta\,\tan^2\theta \\ &= A_{\text{iso}} + (B_{\text{iso}} + B_{\text{ani}})\sin^2\theta \\ &\quad + (C_{\text{iso}} + C_{\text{ani}})\sin^2\theta\tan^2\theta\,. \end{aligned} \tag{35}$$

Here, $A = A_{\text{iso}}$ is the normal-incidence reflection coefficient that is not influenced by anisotropy, B is the AVO gradient, and C is the so-called "curvature" (large-angle) term. Both B and C can be separated into the isotropic (subscript "iso") and anisotropic (subscript "ani") parts, with the anisotropic part of the AVO gradient given by

$$\begin{aligned} B_{\text{ani}}(\phi) = g_b \{ &- [(1 - 2g_b)\,\Delta_{N_1} + \Delta_{V_1}]\cos^2\phi \\ &- \frac{1}{2\sqrt{g_b}}\,(\Delta_{NH_1} + \Delta_{NH_2})\,(1 - 2g_b)\sin 2\phi \\ &+ [\Delta_{V_2} - 2\Delta_{V_1} - (1 - 2g_b)\,\Delta_{N_2}]\sin^2\phi\}\ , \end{aligned} \tag{36}$$

where ϕ is the azimuthal phase angle measured from the x_1-axis. The anisotropic curvature term is expressed as

$$\begin{aligned} C_{\text{ani}}(\phi) = -g_b \Bigg\{ &\left(\Delta_{N_1}\cos^4\phi + \Delta_{N_2}\sin^4\phi\right)(1 - g_b) \\ &+ \frac{1}{2\sqrt{g_b}}\Bigg[\Big(\Delta_{NH_1} + \Delta_{NH_2}\,(1 - 2g_b)\Big)\cos^2\phi \\ &+ \frac{1}{2}\Big(\Delta_{H_1} + \Delta_{H_2} + (\Delta_{N_1} + \Delta_{N_2})\,(1 - 2g_b)\Big)\sin 2\phi \\ &+ \Big(\Delta_{NH_1}\,(1 - 2g_b) + \Delta_{NH_2}\Big)\sin^2\phi\Bigg]\sin 2\phi\Bigg\}. \end{aligned} \tag{37}$$

There are similarities between equations (36) and (37) and equations (16)–(19) for the P-wave NMO ellipse. First, $B_{\text{ani}}(\phi)$ traces out a curve close to an ellipse in the horizontal plane, with $B_{\text{ani}}^{-2}(\phi)$ being exactly elliptical. Second, the only off-diagonal weaknesses appearing in the linearized equations for both the reflection coefficient and NMO ellipse are Δ_{NH_1} and Δ_{NH_2}. Third, the "principal direction" of the curve $B_{\text{ani}}(\phi)$

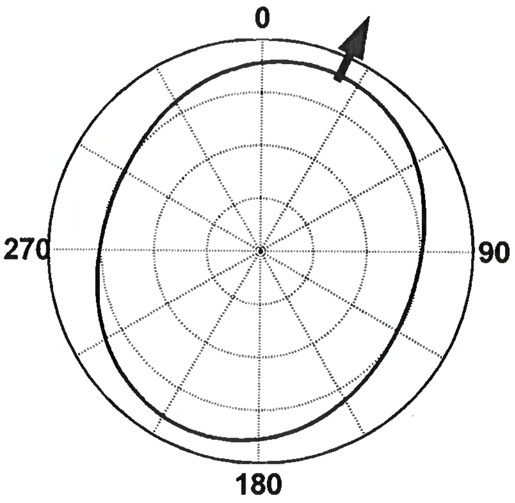

Figure 7. Azimuthal variation of the P-wave AVO gradient for our triclinic model computed from equation (36). The strike azimuth of the dominant fracture set is 90°; the direction of the largest gradient (black arrow) is close to 65°. The parameters are $V_{Pb}/V_{Sb} = 3$, $\Delta_{N_1} = 0.25$, $\Delta_{V_1} = \Delta_{H_1} = 0.12$, and $\Delta_{NH_1} = 0.05$. Each weakness of the second fracture set is equal to one-third of the corresponding weakness of the first set.

is rotated with respect to the horizontal coordinate axes (i.e., with respect to the fracture azimuths) only when $\Delta_{NH_1} \neq 0$ or $\Delta_{NH_2} \neq 0$. Furthermore, the rotation angle of both the NMO ellipse [equation (18)] and AVO gradient [equation (36)] is controlled by the sum $\Delta_{NH_1} + \Delta_{NH_2}$. As shown above, the rotation angle can be also expressed through the anisotropy coefficient $\zeta^{(3)}$ [equation (32)].

The example in Figure 7 illustrates the orientation and shape of the AVO gradient from equation (36). The curve $B_{\text{ani}}(\phi)$ is close to an ellipse with the semi-major axis deviating by about 65° from the strike of the dominant fracture set. If the weaknesses Δ_{NH_1} and Δ_{NH_2} are set to zero, the direction of the largest (by absolute value) AVO gradient is perpendicular to the dominant fracture set. Despite the small value of $\Delta_{NH_1} = 0.05$, the contribution of the off-diagonal weaknesses is sufficient for rotating this direction by about 25°.

6 DISCUSSION AND CONCLUSIONS

We studied seismic signatures of an effective medium formed by two sets of vertical, orthogonal fractures with microcorrugated surfaces embedded in isotropic host rock. Each fracture set is described by the most general compliance matrix allowed within the framework of the linear-slip theory, with the off-diagonal compliance elements responsible for the character and degree of corrugation. The effective model is triclinic and has no symmetry planes, although only 14 stiffness elements are independent.

By applying expansions in the fracture weaknesses (normalized compliances), we derived closed-form analytic expressions for shear-wave splitting, the NMO ellipses of horizontal reflection events, and the P-wave reflection coefficient. These weak-anisotropy approximations provide valuable insight into the influence of the fracture rheology on seismic signatures commonly used in reservoir characterization. For instance, the presence of the off-diagonal compliances makes the shear-wave splitting coefficient γ^S at vertical incidence sensitive (to the second order) to fluid saturation. The variation of γ^S with saturation may be substantial in tight, high-velocity formations where fluids cannot easily move from the fractures into pore space.

The fracture compliances also control the orientation and eccentricity of the NMO ellipses of the reflected P-, S_1-, and S_2-waves. In particular, the contributions of the off-diagonal compliances Δ_{NH_i} and Δ_{VH_i} $(i = 1, 2)$ lead to the rotation of the NMO ellipses with respect to the fracture strike directions. In contrast to the effective orthorhombic medium formed by two orthogonal sets of penny-shaped cracks, all three NMO ellipses in our model have different orientations. Extending the results of Grechka et al. (2000) for monoclinic models, we expressed the rotation angles of the NMO ellipses in triclinic media through the anisotropy parameters $\zeta^{(1)}$, $\zeta^{(2)}$, and $\zeta^{(3)}$.

Analysis of the NMO ellipse of the fast shear wave S_1 suggests a simple way to distinguish between models with one and two microcorrugated fracture sets. For a single set of fractures, the semi-major axis of the S_1-wave NMO ellipse and the polarization vector of the S_1-wave at vertical incidence are parallel to each other and to the fracture strike. This is no longer the case for the model with two fracture sets where the angle between the polarization vector and the semi-major axis of the NMO ellipse for the S_1-wave can reach 20-30°.

For P-waves, the principal azimuthal directions of both the NMO ellipse and AVO gradient depend on the sum of the off-diagonal weaknesses Δ_{NH_1} and Δ_{NH_2}. If both Δ_{NH_1} and Δ_{NH_2} vanish, then the NMO ellipse and AVO gradient are aligned with the fracture strike directions, as is always the case for penny-shaped cracks. Whereas the azimuthally varying P-wave AVO gradient typically traces out a quasi-elliptical curve, the large-angle AVO term has a much more complicated azimuthal dependence.

The results of this work can be instrumental in developing inversion algorithms for estimating the fracture parameters from multicomponent seismic data. As demonstrated by Grechka and Tsvankin (2003), the inversion for all 14 independent parameters of this model is ill-posed. Even if all 21 elastic constants of the triclinic medium are recovered with high accuracy, it is impossible to resolve the fracture weaknesses individually. The equations presented here, however, can help to estimate certain parameter combinations and verify whether the underlying physical model is appropriate.

As discussed above, comparison of the NMO ellipse and polarization directions of the S_1-wave makes it possible to discriminate between the effective models with one and two sets of microcorrugated fractures. Generalizing the results of Bakulin et al. (2000b) and Grechka et al. (2003), it may be possible to invert seismic data for the velocity ratio g_b and the differences between the diagonal weaknesses Δ_{N_i}, Δ_{V_i} and Δ_{H_i} of the two sets, if the vertical velocities are available. Also, the P-wave ellipses and AVO gradient can potentially constrain the sum of weaknesses Δ_{NH_i}.

The weaknesses Δ_{NV_i} do not appear in the linearized equations for any of the NMO ellipses or the P-wave AVO gradient and contribute only to the second-order term in the shear-wave splitting coefficient. The only quantities that contain first-order contributions of Δ_{NV_i} are the vertical components of the S-wave polarization vectors, which may be difficult to measure on field data. Likewise, the weaknesses Δ_{VH_i} are contained only in relatively small terms in the equations for the shear-wave NMO ellipses and for the splitting coefficient γ^S. Therefore, estimation of the weaknesses Δ_{VH_i} and Δ_{NV_i} is likely to be unstable. As pointed out by Grechka et al. (2003), both Δ_{VH} and Δ_{NV} for a single fracture set can be obtained from VSP data using the slowness surface of P-waves. It is not clear, however, if such an algorithm can be extended to the more complicated model treated here.

7 ACKNOWLEDGEMENTS

We are grateful to members of the A(nisotropy)-team of the Center for Wave Phenomena (CWP) at Colorado School of Mines (CSM) for helpful discussions and to Tom Davis, Ken Larner, John Stockwell and Ivan Vasconcelos (all from CSM) for their reviews of the manuscript. Rodrigo Fuck's graduate studies at CSM were funded by CAPES under the scholarship BEX1340-0/00. This work was also supported by the Consortium Project on Seismic Inverse Methods for Complex Structures at CWP and by the Chemical Sciences, Geosciences and Biosciences Division, Office of Basic Energy Sciences, U.S. Department of Energy.

REFERENCES

Bakulin, A., Grechka, V., and Tsvankin, I., 2000a, Estimation of fracture parameters from reflection seismic data - Part I: HTI model due to a single fracture set: Geophysics, **65**, 1788–1802.

—, 2000b, Estimation of fracture paramenters from reflection seismic data - Part II: Fractured models with orthorhombic symmetry: Geophysics, **65**, 1803–1817.

—, 2000c, Estimation of fracture paramenters from reflection seismic data - Part III: Fractured models with monoclinic symmetry: Geophysics, **65**, 1818–1830.

Cardona, R., 2002, Fluid substitution theories and multicomponent seismic characterization of fractured reservoirs: Ph.D. thesis, Colorado School of Mines.

DeVault, B., Davis, T. L., Tsvankin, I., Verm, R., and Hilterman, F., 2002, Multicomponent AVO analysis, Vacuum field, New Mexico: Geophysics, **67**, 701–710.

Farra, V., 2001, High-order perturbations of the phase velocity and polarization of qP and qS waves in anisotropic media: Geophysical Journal International, **147**, 93–104.

Grechka, V., Bakulin, A., and Tsvankin, I., 2003, Seismic characterization of vertical fractures described as general linear-slip interfaces: Geophysical Prospecting, **51**, 117–129.

Grechka, V., Contreras, P., and Tsvankin, I., 2000, Inversion of normal moveout for monoclinic media: Geophysical Prospecting, **48**, 577–602.

Grechka, V., and Tsvankin, I., 2003, Feasibility of seismic characterization of multiple sets: Geophysics, **68**, 1399–1407.

Grechka, V., Tsvankin, I., and Cohen, J. K., 1999, Generalized Dix equation and anlaytic treatment of normal-moveout velocity for anisotropic media: Geophysical Prospecting, **47**, 117–148.

Gurevich, B., 2003, Elastic properties of saturated porous rocks with aligned fractures: Journal of Applied Geophysics, **54**, 203–218.

Hood, J. A., 1991, A simple method for decomposing fracture-induced anisotropy: Geophysics, **56**, 1275–1279.

Jech, J., and Pšenčik, I., 1989, First-order perturbation method for anisotropic media: Geophysical Journal International, **99**, 369–376.

Lynn, H., , Simon, K. M., Layman, M., Schneider, R., Bates, C. R., and Jones, M., 1995, Use of anisotropy in P-wave and S-wave data for fracture characterization in a naturally fractured gas reservoir: The Leading Edge, **14**, 887–893.

Mallick, S., Craft, K. L., Meister, L. J., and Chambers, R. E., 1998, Determination of the principal directions of azimuthal anisotropy from P-wave seismic data: Geophysics, **63**, 692–706.

Nakagawa, S., Nihei, K. T., and Myer, L. R., 2000, Shear-induced conversion of seismic waves across single fractures: International Journal of Rock Mechanics and Mining Sciences, **37**, 203–218.

Pérez, M. A., Grechka, V., and Michelena, R. J., 1999, Fracture detection in a carbonate reservoir using a variety of seismic methods: Geophysics, **64**, 1266–1276.

Pšenčik, I., and Vavryčuk, V., 2002, Approximate relation between the ray vector and the wave normal in weakly anisotropic media: Studia Geophysica et Geodaetica, **46**, 793–807.

Schoenberg, M., 1980, Elastic wave behavior across linear slip interfaces: Journal of Acoustical Society of America, **68**, 1516–1521.

Schoenberg, M., and Douma, J., 1988, Elastic wave propagation in media with parallel fractures and aligned cracks: Geophysical Prospecting, **36**, 571–590.

Schoenberg, M., and Muir, F., 1989, A calculus for finely layered anisotropic media: Geophysics, **54**, 581–589.

Schoenberg, M., and Sayers, C. M., 1995, Seismic anisotropy of fractured rock: Geophysics, **60**, 204–211.

Thomsen, L., 1988, Reflection seismology over azimuthally anisotropic media: Geophysics, **53**, 304–313.

Tsvankin, I., 2001, Seismic signatures and analysis of reflection data in anisotropic media: Elsevier Science, Inc.

Vavryčuk, V., and Pšenčik, I., 1998, PP-wave reflection coefficients in weakly anisotropic elastic media: Geophysics, **63**, 2129–2141.

APPENDIX A: OVERVIEW OF THE LINEAR-SLIP THEORY

The linear-slip theory (Schoenberg, 1980; Schoenberg and Sayers, 1995) is designed to find an equivalent (long-wavelength) representation of a medium that contains one or several fracture sets. Fractures are treated as planar and parallel surfaces of weakness, and it is assumed that interaction between fractures can be ignored. The fracture length is taken to be infinite, while fracture apertures have to be small compared to the dominant seismic wavelength. According to the linear-slip theory, the jumps in the displacement vector $[u_i]$ (i.e., "slips") across a fracture are to the first order proportional to the (continuous) stresses σ_{jk}:

$$[u_i] = h K_{ij} \sigma_{jk}\, n_k, \tag{A1}$$

where $\mathbf{n}$ is the normal to the fracture plane, h is the average spacing between fractures, and K_{ij} are called the "compliances" of the fracture set. The effective compliance tensor $\mathbf{s}$ of a fractured medium is then found as the sum of the background compliance $\mathbf{s}_b$ and the excess compliances $\mathbf{s}_{f_i}$ of all fracture sets (e.g., Schoenberg and Muir, 1989; Hood, 1991):

$$\mathbf{s} = \mathbf{s}_b + \sum_{i=1}^{N} \mathbf{s}_{f_i}. \tag{A2}$$

The compliances K_{ij} of each fracture set are mapped onto the corresponding compliance tensor s_{ijkl} using Hooke's law (Schoenberg and Sayers, 1995):

$$s_{ijkl} = \frac{1}{4}\left(K_{ik} n_l n_j + K_{jk} n_i n_l + K_{il} n_j n_k + K_{jl} n_i n_k\right). \tag{A3}$$

Equation (A1) indicates that $\mathbf{K}$ is a 3×3 matrix that has to be symmetric and nonnegative definite because of the symmetries of the compliance tensor. Hence, a fracture system can be described by up to six independent compliance elements. The diagonal terms of the matrix relate the jumps in the normal displacement ("normal slips") to the normal tractions acting across the surface of the fractures, as well as the tangential slips to the shear stresses. The off-diagonal elements are responsible for the coupling of the normal slips and shear stresses and vice-versa. Hereafter, we follow the notation of Grechka et al. (2003):

$$K_{11} \rightarrow K_N\,; \quad K_{22} \rightarrow K_V\,; \quad K_{33} \rightarrow K_H\,;$$
$$K_{12} \rightarrow K_{NV}\,; \quad K_{13} \rightarrow K_{NH}\,; \quad K_{23} \rightarrow K_{VH}\,.$$

Here, we consider two vertical, orthogonal fracture sets oriented in such a way that that the x_1-axis is perpendicular to the first set. The summation in equation (A2) is more conveniently carried out using the condensed Voigt notation, which allows the compliance tensor to be replaced by a 6×6 compliance matrix. Then the compliances matrices for the two sets take the form

$$s_{f1} = \begin{pmatrix} K_{N_1} & 0 & 0 & 0 & K_{NV_1} & K_{NH_1} \\ 0 & 0 & 0 & 0 & 0 & 0 \\ 0 & 0 & 0 & 0 & 0 & 0 \\ 0 & 0 & 0 & 0 & 0 & 0 \\ K_{NV_1} & 0 & 0 & 0 & K_{V_1} & K_{VH_1} \\ K_{NH_1} & 0 & 0 & 0 & K_{VH_1} & K_{H_1} \end{pmatrix}, \tag{A4}$$

$$s_{f2} = \begin{pmatrix} 0 & 0 & 0 & 0 & 0 & 0 \\ 0 & K_{N_2} & 0 & K_{NV_2} & 0 & K_{NH_2} \\ 0 & 0 & 0 & 0 & 0 & 0 \\ 0 & K_{NV_2} & 0 & K_{V_2} & 0 & K_{VH_2} \\ 0 & 0 & 0 & 0 & 0 & 0 \\ 0 & K_{NH_2} & 0 & K_{VH_2} & 0 & K_{H_2} \end{pmatrix}. \tag{A5}$$

The compliance matrix of the isotropic background can be written as

$$s_b = \begin{pmatrix} E^{-1} & -\nu/E & -\nu/E & 0 & 0 & 0 \\ -\nu/E & E^{-1} & -\nu/E & 0 & 0 & 0 \\ -\nu/E & -\nu/E & E^{-1} & 0 & 0 & 0 \\ 0 & 0 & 0 & \mu^{-1} & 0 & 0 \\ 0 & 0 & 0 & 0 & \mu^{-1} & 0 \\ 0 & 0 & 0 & 0 & 0 & \mu^{-1} \end{pmatrix}, \tag{A6}$$

where E is Young's modulus and ν is Poisson's ratio, which can be expressed through the Lamé parameters λ and μ:

$$E = \frac{\mu\,(3\lambda + 2\mu)}{\lambda + \mu}\,; \tag{A7}$$

$$\nu = \frac{\lambda}{2\,(\lambda + \mu)}\,. \tag{A8}$$

APPENDIX B: LINEARIZED STIFFNESS MATRIX FOR TWO ORTHOGONAL FRACTURE SETS

Wave phenomena are more conveniently described using the effective stiffness matrix that can be obtained by inverting the compliance matrix (A2). To simplify the resulting stiffness matrix, all stiffness elements can be linearized in the normalized quanitites called fracture *weaknesses.* Following Grechka et al. (2003), the weaknesses for our model can be defined as

$$\Delta_{N_i} \equiv \frac{(\lambda + 2\mu)\, K_{N_i}}{1 + (\lambda + 2\mu)\, K_{N_i}} \,, \tag{B1}$$

$$\Delta_{V_i} \equiv \frac{\mu K_{V_i}}{1 + \mu K_{V_i}} \,, \tag{B2}$$

$$\Delta_{H_i} \equiv \frac{\mu K_{H_i}}{1 + \mu K_{H_i}} \,, \tag{B3}$$

$$\Delta_{NV_i} \equiv \frac{\sqrt{\mu\,(\lambda + 2\mu)} K_{NV_i}}{1 + \sqrt{\mu\,(\lambda + 2\mu)} K_{NV_i}} \,, \tag{B4}$$

$$\Delta_{NH_i} \equiv \frac{\sqrt{\mu\,(\lambda + 2\mu)} K_{NH_i}}{1 + \sqrt{\mu\,(\lambda + 2\mu)} K_{NH_i}} \,, \tag{B5}$$

$$\Delta_{VH_i} \equiv \frac{\sqrt{\mu\,(\lambda + 2\mu)} K_{VH_i}}{1 + \sqrt{\mu\,(\lambda + 2\mu)} K_{VH_i}} \,, \tag{B6}$$

where the subscript $i = 1, 2$ refers to the number of the fracture set. Since the matrix $\mathbf{K}$ has to be nonnegative definite, the weaknesses satisfy the inequalities

$$\Delta_{IJ}^2 \le \Delta_I \Delta_J \,, \tag{B7}$$

where I and J denote the subscripts N, V, and H.

Using equations (A2) and (A4)–(A6) and linearizing the stiffness matrix $\mathbf{c} \equiv \mathbf{s}^{-1}$ in the fracture weaknesses [equations (B1)–(B6)], we obtain

$$\mathbf{c} \approx \begin{pmatrix} c_{11} & c_{12} & c_{13} & \chi c_{24} & c_{15} & c_{16} \\ c_{12} & c_{22} & c_{23} & c_{24} & \chi c_{15} & c_{26} \\ c_{13} & c_{23} & c_{33} & \chi c_{24} & \chi c_{15} & c_{36} \\ \chi c_{24} & c_{24} & \chi c_{24} & c_{44} & 0 & c_{46} \\ c_{15} & \chi c_{15} & \chi c_{15} & 0 & c_{55} & c_{56} \\ c_{16} & c_{26} & c_{36} & c_{46} & c_{56} & c_{66} \end{pmatrix}, \tag{B8}$$

where

$$\chi \equiv \frac{\lambda}{\lambda + 2\mu} \,. \tag{B9}$$

The linearized stiffness elements are given by

$$c_{11} \approx (\lambda + 2\mu)\left(1 - \Delta_{N_1} - \chi^2 \Delta_{N_2}\right) , \tag{B10}$$

$$c_{12} \approx \lambda\,(1 - \Delta_{N_1} - \Delta_{N_2}) \,, \tag{B11}$$

$$c_{13} \approx \lambda\,(1 - \Delta_{N_1} - \chi\,\Delta_{N_2}) \,, \tag{B12}$$

$$c_{14} \approx -\Delta_{NV_2} \sqrt{\lambda \mu \chi} \,, \tag{B13}$$

$$c_{15} \approx -\Delta_{NV_1} \sqrt{\mu\,(\lambda + 2\mu)} \,, \tag{B14}$$

$$c_{16} \approx -\sqrt{\mu\,(\lambda + 2\mu)}\,(\Delta_{NH_1} + \chi\,\Delta_{NH_2}) \,, \tag{B15}$$

$$c_{22} \approx (\lambda + 2\mu)\left(1 - \Delta_{N_2} - \chi^2 \Delta_{N_1}\right) , \tag{B16}$$

$$c_{23} \approx \lambda\,(1 - \chi\,\Delta_{N_1} - \Delta_{N_2}) \,, \tag{B17}$$

$$c_{24} \approx -\Delta_{NV_2} \sqrt{\mu\,(\lambda + 2\mu)} \,, \tag{B18}$$

$$c_{25} \approx -\Delta_{NV_1} \sqrt{\lambda \mu \chi} \,, \tag{B19}$$

$$c_{26} \approx -\sqrt{\mu\,(\lambda + 2\mu)}\,(\chi\,\Delta_{NH_1} + \Delta_{NH_2}) \,, \tag{B20}$$

$$c_{33} \approx (\lambda + 2\mu)\left[1 - \chi^2 (\Delta_{N_2} + \Delta_{N_1})\right] , \tag{B21}$$

$$c_{34} \approx -\Delta_{NV_2} \sqrt{\lambda \mu \chi} \,, \tag{B22}$$

$$c_{35} \approx -\Delta_{NV_1} \sqrt{\lambda \mu \chi} \,, \tag{B23}$$

$$c_{36} \approx -\sqrt{\lambda \mu \chi}\,(\Delta_{NH_1} + \Delta_{NH_2}) \,, \tag{B24}$$

$$c_{44} \approx \mu\,(1 - \Delta_{V_2}) \,, \tag{B25}$$

$$c_{45} \approx 0 \,, \tag{B26}$$

$$c_{46} \approx -\mu\,\Delta_{VH_2} \sqrt{\frac{\mu}{(\lambda + 2\mu)}} \,, \tag{B27}$$

$$c_{55} \approx \mu\,(1 - \Delta_{V_1}) \,, \tag{B28}$$

$$c_{56} \approx -\mu\,\Delta_{VH_1} \sqrt{\frac{\mu}{(\lambda + 2\mu)}} \,, \tag{B29}$$

$$c_{66} \approx \mu\,(1 - \Delta_{H_1} - \Delta_{H_2}) \,. \tag{B30}$$

If the weaknesses of the second fracture set are equal to zero, the linearized effective stiffnesses given above reduce to those obtained by Grechka et al. (2003) for a single microcorrugated fracture set orthogonal to the x_1-axis. Another special case is that of rotationally invariant fractures, for which the off-diagonal weaknesses vanish and the tangential weaknesses Δ_{V_i} and Δ_{H_i} are equal to each other. If both fracture sets are made rotationally invariant, our stiffness matrix becomes identical to that in Bakulin et al. (2000b).